

Mixing and Attenuation of Upwelling Groundwater Contaminants in the Hyporheic Zone

Katherine Yoana Santizo

Dissertation submitted to the faculty of the Virginia Polytechnic Institute and State University in
partial fulfillment of the requirements for the degree of

Doctor of Philosophy

In

Civil Engineering

Erich T. Hester, Chair

Mark A. Widdowson

Amy J. Pruden-Bagchi

Madeline E. Schreiber

Kyle B. Strom

February 15, 2021

Blacksburg, VA

Keywords: Mixing zones, mixing-dependent reactions, mixing-controlled reactions, hyporheic zone, groundwater, attenuation

Mixing and Attenuation of Upwelling Groundwater Contaminants in the Hyporheic Zone

Katherine Yoana Santizo

Academic Abstract

The hyporheic zone is the reactive interface between surface water and groundwater found beneath streams and rivers, where chemical gradients and an abundant biological presence allow beneficial attenuation of contaminants. Such attenuation often requires reactants from surface water and groundwater to mix, but few studies have explored the controls on mixing of upwelling groundwater water in the hyporheic zone and its potential to foster mixing-dependent reactions. The goals of this dissertation are therefore to evaluate the effects of (1) hydraulic controls and (2) reaction kinetic controls on hyporheic mixing and mixing-dependent reactions, and (3) use two-dimensional visualization techniques to quantify patterns of hyporheic mixing and mixing-dependent reactions. These objectives were addressed by hyporheic zone simulations using a laboratory sediment mesocosm and numerical models. In the laboratory, a hyporheic flow cell was created to observe both conservative dye mixing and abiotic mixing-dependent reaction. The numerical models MODFLOW and SEAM3D were then used to simulate the experimental data to better understand hydraulic and transport processes underlying laboratory observations and provide sensitivity analysis on hydraulic and reaction kinetic parameters. Visualization techniques showed a distinct mixing zone developing over time for both conservative and reactive conditions. Mixing zone thickness in both conditions depended on surface water head drop and the ratio of boundary inflows of surface water and groundwater (inflow ratios). The abiotic reaction caused the mixing zone to shift even under steady-state hydraulics indicating that hyporheic zone mixing-dependent reactions affect the location of mixing as chemical transformations take place. The numerical model further showed the production zone to be thicker than the mixing zone and located where reactants had already been depleted. Finally, mapping of two-dimensional microbial respiration (i.e., electron acceptor utilization) patterns in streambed sediments using dissolved oxygen and carbon dioxide planar optodes showed that coupling multiple such 2D chemical profiles can enhance understanding of microbial processes in the hyporheic zone. Temporal dynamics for these chemical species revealed development of spatial heterogeneity in microbial respiration and hence microbial activity. Our results show key hydrologic and biogeochemical

controls on hyporheic mixing and mixing-dependent reactions. These reactions represent a last opportunity for attenuation of groundwater borne contaminants prior to entering surface water.

Mixing and Attenuation of Upwelling Groundwater Contaminants in the Hyporheic Zone

Katherine Yoana Santizo

General Audience Abstract

The boundary between surface water and groundwater beneath streams and rivers is known to have an abundant biological presence that allows for beneficial reduction of contaminants when chemicals combine. This combination of chemicals due to mixing of the waters is an important characteristic of the boundary area (defined as the hyporheic zone). However, controls on mixing and the impact on contaminant reduction are not fully understood. Therefore, the goals of this dissertation are to evaluate (1) the effects of varying water level and flow and (2) the effects of the rates of the reaction on mixing of chemicals and chemical transformation, and (3) use two-dimensional visualization processes to quantify the reactions and mixing occurring at the boundary area of surface water and groundwater. We used both laboratory and numerical model simulations to study mixing at the boundary area. The two-dimensional visualization in both laboratory and numerical models show distinct regions where mixing occurred between the surface water and groundwater. The extent of the mixing (mixing thickness) was most dependent on the flow ratio between the upward groundwater and downward surface water. The observations were made with non-varying surface and groundwater flow rates but changes on the mixing thickness and location were seen throughout the duration of the experiments revealing that chemical reaction dynamics have an influence on the mixing process. Ultimately, these types of reactions represent a last opportunity for attenuation of groundwater borne contaminants prior to entering surface water.

Dedication

This dissertation is dedicated to my parents, Miguel and Silvia Santizo, who have encouraged and believed in me. Also, to my partner, Mynor Medrano, and cats, Comet and Nova, who have provided unwavering support throughout my journey.

Esta tesis está dedicado a mis padres, Miguel y Silvia Santizo, que me han brindado su ánimo y han creído en mí. También a mi pareja, Mynor Medrano, y gatos, Comet y Nova, quien han sido un gran apoyo.

Acknowledgements

I am in great appreciation to all those who have encouraged and helped me throughout my academic journey.

I am thankful for the support and encouragement from my parents and sisters. They have been a steady source of motivation and love. Equally, my partner has been patient and provided solace when needed the most. My cats who have provided unconditional love and emotional support.

I would like to acknowledge some of my early academic support who I could not have started this journey without. Jeffrey Heilweil whose advice and encouragement led me to my undergraduate career. Enrique Guzman, Dr. Phyllis Brady, and Dr. Micaela Morgan who ensured I continued my pursuit for knowledge and inspired me to obtain a doctorate degree.

I am greatly indebted to the faculty, staff, and administration at Virginia Tech. I want to especially thank Dr. Erich Hester and Dr. Mark Widdowson who encouraged and advised me as I grew as a researcher. Dr. Amy Pruden, Dr. Madeline Schreiber, and Dr. Kyle Strom who served as committee members and provided insightful guidance. Also, Dr. Paolo Scardina who provided invaluable mentorship.

In addition, I want to also acknowledge all the administrators and staff in the CEE Department who helped ensure that my journey was as smooth as possible. Also, the Multicultural Academic Opportunities Program and New Horizons Scholars Program who provided funding and vital moral support especially Renee Cloyd and Dr. Catherine Amelink.

Last, but not least, I would like to thank all my friends and colleagues who provided inspiration, laughter, and comfort throughout. There are countless of you who have left their grain in ensuring my success and I could not be more thankful for the support you all provided. To name a few, Pamela Sue Swank, Dr. Carlos Mantilla Peña, Dr. Javier Gonzalez-Rocha, Dr. Lindy Cranwell, Dr. Daniel Herrera, Anthony Millican, Brianna Hibbler, Hani Awni, Lexi Russell, Kim and Vlad Barrera, Kevin Madson, Genesis Vasquez, Denean Kelson, Oscar Gomez, Dr. Max Stephenson, Maria Amaya, and Dr. Larry Pranger. To the writing groups that made sure I made it, I could not have done it without you.

Table of Contents

Academic Abstract	i
General Audience Abstract	iii
Dedication	v
Acknowledgements	vi
Chapter 1. Introduction	1
1.1 Mixing, Dispersion, Dilution, and Spreading	2
1.2 Attenuation of Upwelling Groundwater Contaminants in the Hyporheic Zone	3
1.3 Key Controls of Mixing and Mixing-dependent Reactions in Hyporheic Zones	8
1.4 Measuring Mixing and Mixing-dependent Reactions	9
1.5 Research Motivation and Summary of Attributions	11
References	13
Chapter 2. Hyporheic transverse mixing zones and dispersivity: laboratory and numerical experiments of hydraulic controls	21
Key Points	21
Abstract	22
2.1 Introduction	23
2.2 Methods	25
2.2.1 Laboratory Experiments	25
2.2.2 Numerical Modeling	30
2.3 Results	33
2.3.1 Steady State Conditions	33
2.3.2 Transient Conditions	37
2.4 Discussion and Analysis	40
2.4.1 Dispersion Coefficient, Peclet Number, and Dilution Index, and Relation to Mixing Zone Thickness	40
2.4.2 Magnitude of Hyporheic Transverse Dispersion	42
2.4.3 Effect of Hydraulic Controls	43
2.4.4 Effect of Transient Head Variation	45
2.4.5 Limitations and Applications	47
2.5 Conclusions	49
Acknowledgements	50
References	51

Chapter 3. Abiotic mixing-dependent reaction in a laboratory simulated hyporheic zone	59
Abstract.....	59
Key Points	60
3.1 Introduction	61
3.1.1 Hyporheic Mixing-Dependent Reactions and Their Quantification	62
3.1.2 Imaging in Subsurface Experiments	63
3.1.3 Purpose of Study	64
3.2 Materials and Methods	64
3.2.1 Laboratory Apparatus	64
3.2.2 Experiments	67
3.2.3 Measurements	68
3.2.4 Data Analysis	70
3.3 Results	71
3.3.1 Sediment DO Distributions (Planar Optode)	71
3.3.2 Concentration Profiles and Oxidic Fronts	73
3.3.3 Mixing Zone Thickness	76
3.4 Discussion and Analysis	78
3.4.1 Relative Dominance of Advection, Dispersion, and Reaction Processes	78
3.4.2 Dynamic Hyporheic Reactive Mixing Zones	81
3.4.3 Novelty and Limitations of Approach	83
3.4.4 Application	86
3.5 Conclusions	87
Acknowledgements	89
References.....	90
Chapter 4. Numerical modeling of an abiotic hyporheic mixing-dependent reaction: chemical evolution of mixing and reactant production zones	99
Abstract.....	100
4.1 Introduction	101
4.2 Methods	103
4.2.1 Model Domain and Governing Equations	103
4.2.2 Model Inputs, Calibration, and Outputs	106
4.2.3 Sensitivity Analysis and Coefficients	107
4.3 Results	109

4.3.1 Basecase Head and Concentration Distributions and Match to Laboratory Observations	109
4.3.2 Temporal Trends.....	113
4.3.3 Mixing and Production Zone Front Location Sensitivity	114
4.3.4 Mixing and Production Zone Thickness Sensitivity	116
4.4 Discussion and Analysis.....	118
4.4.1 Temporal Evolution of Reactive Mixing Zones.....	118
4.4.2 Mass Consumption and Production	121
4.5 Novelty and Limitations	123
4.6 Conclusions.....	124
References.....	126
Chapter 5. Imaging of biotic reactions in the subsurface: Two-dimensional O₂ and CO₂ dynamics of aerobic respiration	129
5.1. Introduction.....	129
5.1.1 Relations among Hyporheic Hydrology, Biogeochemistry, and Microbiology	129
5.1.2 Advances in Observational Methodology	130
5.1.3 Objectives of Chapter	131
5.2 Methods.....	131
5.2.1 Planar Optodes, Chemical Sensors, and Aquarium Tank	131
5.2.2 Stern-Volmer Method.....	133
5.2.3 Camera, Lighting, and Software System	133
5.2.4 Sediment and Water Collection	135
5.2.5 Assembly of Water, Sediment, Nutrients, and Carbon Source.....	136
5.2.6 Calibration Curves.....	137
5.2.7 Batch Experiments.....	139
5.3 Results and Discussion.....	141
5.3.1 Trial 1: 72-hr DO/pCO ₂ Distribution in Silica Sand with 0.01 M C ₆ H ₁₂ O ₆ and 0.13 M KH ₂ PO ₄	141
5.3.2 Trial 2: 18-hr DO/pCO ₂ Distribution in Streambed Sediment and Silica Sand with 0.1 M C ₆ H ₁₂ O ₆ and 0.08 M KH ₂ PO ₄	144
5.3.3 Comparison of Trials.....	147
5.4 Conclusion and Future Outlook	148
References.....	150
Chapter 6. Conclusion	153

6.1 Summary of Research Work.....	153
6.2 Engineering Significance and Implications	156
6.3 Future Work.....	159
References.....	161
Appendix A. Steady-State MATLAB Codes for Chapter 2: Hyporheic transverse mixing zones and dispersivity.....	164
Contents for High Head Drop: Steady State	164
1. Importing Data.....	164
2. First Normalization.....	165
3. Block Processing.....	166
4. Second Normalization.....	167
5. Interpolation and Mixing Zone Width Calculation	170
Contents for Mid Head Drop: Steady State.....	170
1. Importing Data.....	171
2. First Normalization.....	171
3. Block Processing.....	172
4. Second Normalization.....	173
5. Interpolation and Mixing Zone Width Calculation	176
Contents for Low Head Drop: Steady State	176
1. Importing Data.....	177
2. First Normalization.....	177
3. Block Processing.....	178
4. Second Normalization.....	179
5. Interpolation and Mixing Zone Width Calculation	182
Appendix B. Supporting Information on Chapter 3 publication	183
B.1 Calibration Information	184
B.1a. Sulfate Spectrophotometer Calibration	184
B.1b. Dissolved Oxygen (DO) Planar Optode Calibration	184
B.2 Supplemental Results.....	186
B.3 Parameter Estimations and Dimensionless Numbers	188
B.3a. Values calculated from experiment	188
B.3b. Dimensionless number calculations	190
References.....	192

Appendix C. MATLAB codes for analysis of laboratory simulated mixing-dependent abiotic reaction	193
Controls: Fall 2018, head drop: 6.0cm	193
Abiotic Reaction: Fall 2018, head drop: 6.0cm	203
Controls: Fall 2018, head drop: 4.5cm	213
Abiotic Reaction: Fall 2018, head drop: 4.5cm	223
Appendix D. Microbial Growth/Respiration in Abiotic Experiments	233
Appendix E. Additional set-up images for laboratory simulated mixing-dependent abiotic reaction	237
Appendix F. Trials of Microbial Respiration for Biotic Experiments	240
Appendix G. Set of Images from Biotic Experiments in Chapter 5	248
Trial 1: CO₂ time 23-45 hours from 72-hr experiment in 20 min increments	248
Trial 2: CO₂ time 0-18 hours from 18-hr experiment in 20 min increments	257
Trial 1: O₂ time 0-18 hours from 72-hr experiment in 20 min increments	264
Trial 2: O₂ time 0-18 hours from 18-hr experiment in 20 min increments	272
Appendix H. Preliminary Research for Experiments using Resazurin	280
REU Student Report: Summer 2016	280
Supporting Data for Student Report	291

Chapter 1. Introduction

Understanding subsurface environmental processes has been of significant interest given their influence on transport, physiochemical transformation, and biological transformation of solutes. The interconnections among these processes are crucial in the shallow subsurface as their interplay dominates biogeochemical cycles (e.g., carbon, oxygen, nitrogen, and phosphorus). Furthermore, shallow subsurface biogeochemical processes near stream and river systems interact with groundwater, benefit ecosystem health, and vary spatially and temporally with hydrological and microbial conditions. Surface (stream/river) water and groundwater interact underneath the channel in an area called the hyporheic zone (Figure 1.1). The hyporheic zone exhibits a unique mix of characteristics of both surface water and groundwater and is affected by processes taking place in both areas. Due to redox gradients and a diverse and abundant biological presence, the hyporheic zone is often highly reactive relative to surface water and deeper groundwater for attenuation of contaminants (Caruso et al., 2017; Conant et al., 2004; Ellis & Rivett, 2007; Freitas et al., 2015; Landmeyer et al., 2010; Stegen et al., 2016, 2018; Zarnetske et al., 2011).

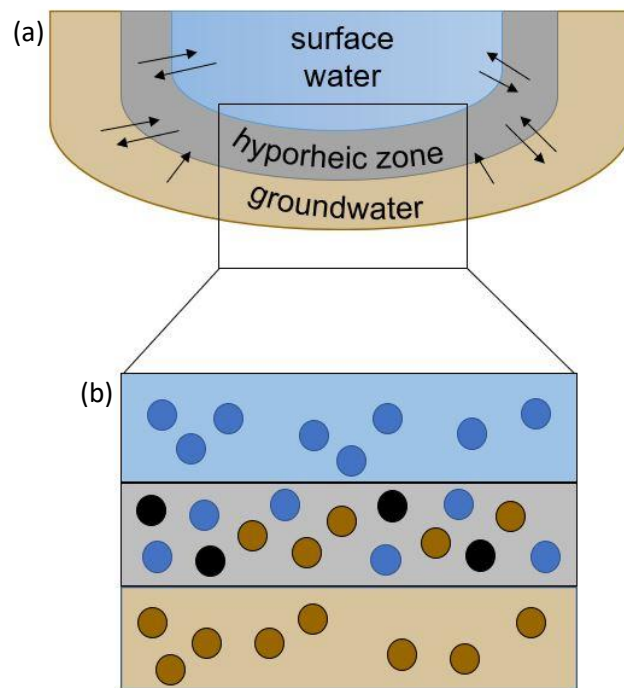


Figure 1.1 (a) Schematic of the hyporheic zone showing the interface and exchange between surface water and groundwater, and (b) interface close-up showing compounds interacting within the hyporheic zone to depict mixing and transformation. The blue and brown dots represent surface

water and groundwater compounds, respectively. The black dots represent transformation that occurs from a reaction between the blue and brown compounds due to the mixing.

1.1 Mixing, Dispersion, Dilution, and Spreading

One of the main drivers of biogeochemical processes in the hyporheic zone and deeper groundwater is mixing. Mixing is defined as the meeting of different source waters and resulting comingling of solutes (Abarca & Clement, 2009; Hester et al., 2017; Rolle et al., 2013b). Mixing in porous media has been studied extensively (Anna et al., 2014; Bandopadhyay et al., 2018; Cirpka et al., 2008, 2015; Hochstetler et al., 2013; B. A. Robinson & Viswanathan, 2003; G. Robinson et al., 2016; Su et al., 2020; Ye et al., 2016). Robinson et al. (2016) and Abarca and Clement (2009) both looked at the influence of mixing on salt wedges in the seawater-freshwater interface. Cirpka et al (2008), Anna et al. (2014), and Hochstetler et al. (2013) focused on mixing in shallow groundwater, observing how hydrological parameters control mixing. Mixing has also been studied in the hyporheic zone, in particular how curvilinear flowpaths, sediment heterogeneity, and varying flow conditions impact mixing (Bandopadhyay et al., 2018; Hester et al., 2017; Su et al., 2020).

Since mixing is an important process in the subsurface it must be distinguished from other processes that also effect contaminant attenuation such as dispersion, dilution, and spreading (Chiogna et al., 2012; Cirpka & Kitanidis, 2000; Hester et al., 2017). Yet, many studies lump mixing together with these other processes, thus not distinguished their separate contributions. For example, when transverse hyporheic dispersion has been modeled the coefficients used are large and therefore may confuse mixing with spreading (Hester et al., 2013, 2017; Laura K. Lautz & Siegel, 2006). Spreading is the deformation of a solute plume without increasing its overall volume (e.g., fingering), while mixing increases the plume volume by increasing the dilution of the plume's solutes through the process of molecular diffusion along the plume margins (e.g., along fingers) (Cirpka & Kitanidis, 2000; Dentz et al., 2011; Kitanidis, 1994).

Mixing has been extensively studied in groundwater (Chiogna & Rolle, 2017; Cirpka et al., 2008; Hochstetler et al., 2013; Lu et al., 2009; Rolle et al., 2013a; Ye et al., 2016) but less in the hyporheic zone. Yet the hyporheic zone has unique characteristics due to its proximity to surface water that may enhance mixing (e.g., solute mixing) such as rapid head fluctuations, shear and curvilinear flow, sediment movement and its enhancement of heterogeneity, steep head

gradients, and turbulence. Thus, studies that focus on mixing specific processes in the hyporheic zone are needed.

Moreover, mixing is important for chemical transformation and contaminant attenuation, especially in the hyporheic zone as it is the last chance for reduction of upwelling groundwater contaminants before they enter surface water. Thus there is interest in controls that enhance mixing-dependent (mixing-controlled) reactions (Chiogna & Rolle, 2017; Hester et al., 2014; Marzadri et al., 2016). Mixing-dependent reactions occur where mixing of source waters is required to supply all necessary reactants/solutes. In the hyporheic zone, mixing-dependent reactions occur between reactants in upwelling groundwater and downwelling surface water (Hester et al., 2013, 2014, 2019; Santizo et al., 2020; Sheibley et al., 2003).

Similar to mixing, mixing-dependent reactions were first studied in deeper aquifers where groundwater contaminant plumes attenuate due to mixing of solutes along the plume fringe (Bauer et al., 2009; Castro-Alcalá et al., 2012; Cirpka et al., 1999, 2008). Sediment heterogeneity has been extensively studied as an enhancer to mixing, mixing-dependent reactions, and groundwater attenuation. Ye et al. (2015) showed that mixing was enhanced by the presence of high permeability zones and that spatial arrangement of the high permeability zone affects plume fringe reactions (i.e., mixing-dependent reactions). Werth et al. (2006) specifically showed that heterogeneity through high permeability zone increased mixing and groundwater reactions. In addition, they concluded that transverse mixing was variable and therefore an important control for mixing-dependent reactions. Ye et al. (2016) studied mixing and mixing-dependent reactions under helical flows. The distortion of flow due to helical flow paths showed significant enhancement to mixing-dependent reactions and reduction of contaminants. Finally, Bauer et al. (2008) performed laboratory experiments to observe mixing-dependent biodegradation as a result of chemical gradients and spatial distribution of microorganisms via solute port sampling in a microcosm. These studies illustrate that there are multiple controls on mixing and mixing-dependent reactions.

1.2 Attenuation of Upwelling Groundwater Contaminants in the Hyporheic Zone

Groundwater contaminants have been studied extensively to understand their extent, chemical and physical characteristics, and flow patterns among other things (Conant et al., 2004;

Freitas et al., 2015; Hynds et al., 2014; Lapworth et al., 2012). In the last decades, how groundwater contaminants affect the health and ecology of streams as they upwell into the stream has also been of interest (Xiao et al., 2015; Zemo et al., 2017). Additionally, how groundwater contaminants interact within the hyporheic zone and their potential attenuation has been a growing interest. Some of the groundwater contaminants of focus in these studies have been organic compounds, chlorinated compounds, and agricultural compounds as these are some of the most prevalent industrial contaminants to impair groundwater (Aisopou et al., 2015; Conant et al., 2004; Ellis & Rivett, 2007; Freitas et al., 2015; Landmeyer et al., 2010; Rasmussen et al., 2016; Zemo et al., 2017).

Attenuation of groundwater contaminants entering surface water is important for water quality as they can impair the stream leading to ecological and human impact (Hynds et al., 2014; Landmeyer et al., 2010; Lapworth et al., 2012; Zhang et al., 2017). Groundwater is contaminated in a similar manner as surface water through point and non-point sources. Common point sources include landfill waste, industrial waste, and mining residual. Non-point sources, similar to surface water, include agricultural and storm runoff (Kennedy et al., 2009; Zarnetske et al., 2015).

Groundwater contaminants can be attenuated and transformed through a range of processes as they upwell into a river, depending on the type of contaminant. For instance, organic compounds may either dissolve into the water mixture based on their solubility in water or sorb to sediment media. Heavy metals and fertilizers also have the potential to be retained via sorption (Creswell et al., 2008; Gandy et al., 2007; Mahar et al., 2016; Mulligan et al., 2001). However, studies have shown that sorbed compounds can subsequently desorb in response to hydrological changes (Herzog et al., 2018; Perujo et al., 2017; Schaper et al., 2019). Additionally, flora in streambeds or stream margins can reduce contaminant concentrations via phytoremediation. Many of these processes are physicochemical and could be reversed. Therefore, irreversible chemical transformation is sought out for contaminants where reactions occur through natural attenuation.

Natural attenuation tends to occur due to the microorganisms present in the subsurface which therefore play an important role in the hyporheic zone and overall subsurface biogeochemical processes. Redox reactions and gradients are often important, where electron donors and acceptors drive many of the reactions as electron donors give an electron and energy becoming oxidized while the electron acceptors receive the electron given becoming reduced.

When solutes from both surface water and groundwater interact with microorganisms contained within the sediment, redox gradients develop, where electron donors and acceptors are exchanged as mixing takes place. Thus, redox gradients enhance the potential for attenuation. Many studies focus on conditions where mixing-dependent reactions may be responsible for observed natural attenuation of multiple groundwater pollutants that approach rivers via the hyporheic zone (Conant et al., 2004; Danczak et al., 2016; Hester et al., 2014; Li et al., 2017; Sawyer & Cardenas, 2009). The natural attenuation, however, is not always beneficial as hyporheic zone studies have also shown methylation of mercury, nitrification, and Arsenic mobilization due to the redox gradients formed (Brown et al., 2007; Creswell et al., 2008; Hartland et al., 2015; Hinkle et al., 2014; Zarnetske et al., 2012). In all cases, beneficial and non-beneficial mixing-dependent reactions require mixing of solutes to develop the conditions for redox gradient formation. While it has been noted that both types of attenuation may occur, this dissertation thus focuses on beneficial mixing-dependent reactions in the hyporheic zone where pollutants are reduced due to the reactions and redox gradients formed.

1.2.1 Organic and Chlorinated Groundwater Contaminants

Organic and chlorinated groundwater contaminants are ubiquitous, especially near urban rivers, due to their use in industry (e.g., dry cleaners, oil & gas, wastewater treatment plant effluent). As such, natural attenuation and bioremediation of such compounds is important as these compounds tend to be ecotoxic. Studies that have observed such contaminants have shown that attenuation and bioremediation is possible and that transformation into daughter products is achieved when the groundwater contaminant plume transverses the hyporheic zone.

Landmeyer et al. (2010) showed that fuel-related contaminants (methyl tert-butyl ether (MTBE), tert-butyl alcohol (TBA), and tert-amyl methyl ether (TAME)) discharging into a river attenuated as it passed through the hyporheic zone. They concluded that hyporheic zone attenuation should be considered for assessment of remediation efforts as these fuel-oxygenating contaminants experienced substantial attenuation in the hyporheic zone under oxic and anoxic conditions. In addition, Schaper et al. (2019) observed trace organic compounds (e.g., metformin, epoxy-carbamazepine) in the hyporheic zone and hypothesized that the oxic shallow hyporheic zone would provide the largest potential for attenuation. They were able to demonstrate that most of the tracer organic compounds under investigation were significantly reduced within the first 40 cm of the hyporheic zone.

Earlier studies by Conant et al. (2004) and Ellis and Rivett (2007) mapped the occurrence of chlorinated volatile organic compounds (VOCs) along reaches of the streambed and bank. Conant et al. (2004) measured vertical profiles of tetrachloroethylene (PCE) and its derivatives and showed that in upgradient (deeper) locations the plume did not undergo appreciable reaction. Instead, as the plume approached the surface water and traversed the hyporheic zone, chemical concentrations decreased and daughter products (e.g., dichloroethane (DCE)) were produced. Freitas et al. (2015) showed a similar phenomenon at the River Tame with TCE, cis-DCE, vinyl chloride (VC), ethene, and ethane levels decreasing over time as contaminated groundwater approached the riverbed from beneath. They demonstrated the ability to attenuate incoming chlorinated substances, with attenuation capacity varying in space. Overall, organic and chlorinated contaminants have been shown to have attenuation potential in the hyporheic zone which may be further explored and managed as synthetic organics such as pharmaceutical and personal care products seem to be an increasing contaminant concern.

1.2.2 Agricultural Groundwater Contaminants

The agricultural nutrients nitrogen and phosphorus are a major focus in upwelling groundwater due to their impact on habitats and inducing of eutrophication. Management and reduction of agricultural nutrients in watersheds is of high concern in places around the world where eutrophication frequently impacts species habitat and recreation opportunities (Alexander et al., 2000; Cardenas et al., 2008; Dahm et al., 1998; Dodds, 2006; Gomez-Velez et al., 2015; Harvey et al., 2013; Kennedy et al., 2009; Kessler et al., 2012). Hyporheic zone management and restoration is a focus to ensure reduction of agricultural nutrients in impacted watersheds.

Naranjo et al. (2015), observed nitrogen concentrations (NO_3 , NH_4) and dissolved oxygen (DO) in the Truckee River to determine the influence of hyporheic mixing and mean residence time on nitrogen transformations. They concluded that low flow inhibited the extent of mixing and high flow (modeled through a storm event) allowed for an increase of mixing due to the increase of surface water that flows through the hyporheic flow cell. Hester et al. (2014) simulated mixing-dependent and non-mixing-dependent hyporheic denitrification, the reduction of nitrate to nitrogen gas with nitrite and nitrous oxide as intermediates, and related biogeochemical processes via MODFLOW/SEAM3D. This study showed that mixing-dependent denitrification of upwelling

NO₃ was dependent on dissolved organic carbon availability and sufficient hydraulic conductivity. In addition, Puckett et al. (2008) did an extensive study of multiple sites to determine the influence of water flow rates and residence times on NO₃ removal. NO₃ in groundwater was reduced but not entirely removed, therefore a portion flowed into surface water. Residence times and electron donor availability were key controls on NO₃ removal. The electron donor and residence times are both characteristics of reactions kinetics as they deal with concentrations available for electron transfers to occur for the reactions and inform the solute contact time with reaction time.

Unlike nitrogen, phosphorus reduction takes place through retention mechanisms that reduce phosphorus in surface water, the most significant being sorption, where phosphorus is neither an electron donor nor acceptor but rather binds/adheres to the soil matrix. Perujo et al. (2017) observed the link between physiochemical and microbial processes, specifically the influence of sediment heterogeneity on phosphorus transport. They determined that finer sediment with low hydraulic conductivity allowed for greater amounts of phosphorus retention while reducing microbial processes. The opposite was true for coarser sediments with higher hydraulic conductivity. Jarvie et al. (2012) modeled phosphorus retention using the Illinois River under varying flow rates. They showed that phosphorus retention was higher at low flow rates, but retained phosphorus was then remobilized under high flows. Therefore, there is a balance between optimal retained phosphorus and remobilized phosphorus that needs to be considered (Herzog et al., 2018; Jarvie et al., 2012; Parker et al., 2018; Perujo et al., 2017).

1.2.3 Metals as Groundwater Contaminants

A variety of transformations of metals and related cations are known to occur in the hyporheic zone (Creswell et al., 2008; Gandy et al., 2007; Hinkle et al., 2014; L. K. Lautz & Fanelli, 2008). Mining contaminants such as heavy metals are major source of pollution in areas with a history of mining in the 19th and 20th centuries. Mining contaminants are highly detrimental to aquatic health of streams (Gandy et al., 2007), thus microbial and biogeochemical processes in the hyporheic zone that can aid remediation efforts are of interest. Gandy et al. (2007) further showed that redox conditions are a main contribution to precipitation and adsorption processes of metals in the hyporheic zone.

Lautz and Fanelli (2008) showed that redox conditions unique to the hyporheic zone (i.e., oxic/anoxic interfaces) allow for manganese and iron oxidation via microbially-mediated reactions. Fuller and Harvey (2000) showed that iron oxide concentrations decreased in their study while sorption was insignificant. Mercury dynamics within the hyporheic zone have been researched to determine their influence on mercury methylation (Creswell et al., (2008); Hinkle et al., (2014)). Hinkle et al. (2014) studied the dynamics of mercury cycling in the hyporheic zone and concluded that it is dependent on mobilization and attenuation of dissolved organic carbon (DOC). Creswell et al. (2008) showed that mercury methylation peaked during late summer when microbial reduction of iron and sulfate ions were high.

1.2.4 Emerging Groundwater Contaminants

Emerging contaminants have received heightened attention due to their concern in water bodies (Antweiler et al., 2014; Burke et al., 2014; Lapworth et al., 2012; Writer, et al., 2011a; Writer, et al., 2011b). Lapworth et al. (2011) discussed the potential of the hyporheic zone to address emerging organic contaminants. For example, Burke et al. (2014) demonstrated that the hyporheic zone was able to reduce concentrations of organic compounds such as acesulfame, diclofenac, and metoprolol. Writer et al. (2011a) demonstrated biodegradation of steroidal hormones and alkylphenols in biofilms and sediments of streams. The study concluded that the sediment was more effective than the water column at attenuating the compounds 17 β -estradiol, estrone, 17 α -ethynylestradiol, 4-nonylphenol, 4-nonylphenolmonowxthoyle and 4-nonylphenoldiethoxyle. In a follow up study, Writer et al. (2011b) concluded that stream biofilms and sediments have similar attenuation ability as the interaction with the microbial biomass and mixing of reactants allowed for attenuation. Therefore, understanding how to enhance attenuation in the hyporheic zone via mixing will provide insight to benefit water quality.

1.3 Key Controls of Mixing and Mixing-dependent Reactions in Hyporheic Zones

Understanding controls on mixing and thus mixing-dependent reactions is important for maximizing contaminant attenuation. Many controls are hydrological in nature, including hydraulic conductivity, residence times, and water exchange rates (Azinheira et al., 2014; Cardenas et al., 2004; Chen et al., 2018; Hester et al., 2019; Hester & Doyle, 2008; Hou et al.,

2017; Kalbus et al., 2009; Santizo et al., 2020; Saup et al., 2019; Stegen et al., 2018, 2016). Other controls are biogeochemical such as kinetic rates, chemical concentrations, and microorganism diversity and abundance (Hou et al., 2017; Mermillod-Blondin et al., 2015; Saup et al., 2019; Stegen et al., 2016).

The extent of gaining, heterogeneity, and residence times all influence the extent of mixing (Crispell & Endreny, 2009; Fox et al., 2016; Galloway et al., 2019; Hester et al., 2019; Su et al., 2020). Su et al. (2020) measured effects of heterogeneity, surface water velocity, and upwelling groundwater on hyporheic mixing. It was determined that upwelling groundwater and surface water velocity influenced and enhanced mixing more than sediment heterogeneity. In Hester et al. (2019), the influence of surface water fluctuations and sediment heterogeneity on mixing-dependent denitrification were modeled. The models showed that surface water fluctuations led to more enhancement of denitrification than did sediment heterogeneity because fluctuations controlled mixing lengths. More recently, turbulence and bedform celerity have been shown to impact mixing by controlling flow velocities and therefore rate of water entering the hyporheic zone (Roche et al., 2019; Shen et al., 2020; Wolke et al., 2020).

Such hydrological controls have been linked to microbial processes in the hyporheic zone as well. Stegen et al. (2016) showed that the mixing of waters changed organic carbon availability which altered microbial communities and enhanced microbial respiration (consumption of organic carbon by microorganisms to produce energy). Saup et al. (2019) showed that mixing created hotspots for microbial communities during spring snowmelt. The spring snowmelt increased flow rates and downwelling surface water which enhanced oxygenation of subsurface media allowing for higher microbial respiration. The connection between hydrological and biogeochemical processes shows the importance of integrating both disciplines within hyporheic zone studies.

1.4 Measuring Mixing and Mixing-dependent Reactions

Accurate measurements of mixing in laboratory or field settings are an important methodological foundation needed for research on mixing-dependent reactions. Over the years, a variety of complementary methods have been devised. These include mixing zone thickness/length, mixing areas, dimensionless numbers, dispersivity, dilution index, flux-related

dilution index, and critical dilution index (Chiogna et al., 2011, 2012; Hester et al., 2014; Marzadri et al., 2016; Rolle et al., 2009; Santizo et al., 2020; Ye et al., 2016).

Chiogna et al. (2011) used critical dilution index to relate conservative tracer mixing to an instantaneous mixing-dependent reaction in a heterogeneous aquifer. They concluded that critical dilution index successfully developed a relationship between conservative mixing and mixing-dependent reaction with the critical dilution index also informing the amount of mixing needed for a complete attenuation. In a follow-up study, Chiogna et al. (2012) observed how mixing could be quantified using a flux-related dilution index in the context of a reactive plume. They concluded that the flux-related dilution index varied based on the evolution of the concentration profile of the plume but independent of plume location. However, the flux-related dilution index may be hard to obtain from field and laboratory experiments as it relies on detailed knowledge of location and magnitude of mass fluxes. In comparison, mixing, mixing widths, and location are more practical measurements that can be taken in field, laboratory, and modeling experiments. Using these measurements to relate mixing to attenuation can be helpful in understanding what processes are occurring and therefore what may enhance the attenuation.

Multiple visualization techniques have been used to estimate dispersion coefficients, dispersivities, concentration profiles, and mixing processes (Abarca & Clement, 2009; Bauer et al., 2009; Castro-Alcalá et al., 2012; Robinson et al., 2016). A recent visualization technique is planar optodes, which are thin reactive films that provide two-dimensional mapping of chemical concentrations from which mixing zones, areas, and thicknesses can be measured (Galloway et al., 2019; Kaufman et al., 2017; Lehto et al., 2017; Santizo et al., 2020; Wolke et al., 2020). Wolke et al. (2020) and Galloway et al. (2019) both calculated mixing areas between 25-75% DO concentration whereas Santizo et al. (2020) calculated mixing-zone thickness from 16-84% DO concentration. While visualization techniques are practical for laboratory or field studies, there is a lack of consensus regarding which concentrations and locations should be used for mixing calculations. Therefore, additional theory linking mixing studies and metrics will allow a more rigorous analysis of mixing zones, mixing-dependent reactions, and applications such as enhancing contaminant attenuation.

1.5 Research Motivation and Summary of Attributions

1.5.1 Research Motivation

The motivation for this dissertation was to observe mixing and mixing-dependent reactions in the hyporheic zone and address knowledge gaps in the current literature to provide insight into their controls. As stated earlier, mixing is an important subsurface environmental process that aids contaminant attenuation and as such understanding what controls mixing and mixing-dependent reactions will further implementation of hyporheic mixing for attenuation of contaminants entering surface water. Chapter 2 focus on conservative mixing in the hyporheic zone and Chapter 3-4 focus on an abiotic mixing-dependent reaction in the hyporheic zone. Chapter 5 explores using coupled planar optodes to observe biotic reactions in the subsurface.

1.5.2 Organization of Dissertation and Attributions

This dissertation entails three studies that enhance our understanding of mixing and mixing-dependent reactions in the shallow submerged sediments of the hyporheic zone. An additional study builds a framework to use a new technology to improve visualization and measurements of microbial processes in the hyporheic zone. The chapters are as follow:

- Chapter 2: Hyporheic transverse mixing zones and dispersivity: laboratory and numerical experiments of hydraulic controls
Simulates hyporheic mixing zones using visualization of conservative tracers in laboratory experiments and numerical simulations to understanding underlying processes. This manuscript has been submitted to *Journal of Contaminant Hydrology*.
 - Abenezzer Nida performed the laboratory experiments; Katherine Santizo developed analysis methods and performed analysis of laboratory results, helped with numerical model set up and calibration, and edited the manuscript; Erich T. Hester took the lead in writing the manuscript and calculating dilution-index and Peclet number; and Mark A. Widdowson was the lead in creating numerical model and model outputs.
- Chapter 3: Abiotic mixing-dependent reaction in a laboratory simulated hyporheic zone

Simulates hyporheic mixing zones using visualization of abiotic mixing-dependent oxygen consumption reactions in laboratory experiments. This manuscript was published in *Water Resources Research* in August 2020.

- Katherine Santizo took the lead on writing the manuscript, developed laboratory methods, conducted the laboratory experiments and data analysis; Erich T. Hester and Mark A. Widdowson helped develop the manuscript and guided laboratory experiments.
- Chapter 4: Numerical modeling of an abiotic hyporheic mixing-dependent reaction: chemical evolution of mixing and reactant production zones
Simulates laboratory abiotic mixing-dependent hyporheic oxygen consumption reactions from Chapter 3 using a numerical model and conducts a sensitivity analysis on reaction kinetics and hydraulics. This manuscript is in preparation for submission.
 - Katherine Santizo took the lead on writing the manuscript, performed the numerical simulations and data analysis, Mark A. Widdowson helped develop and calibrate the model and provided feedback on analysis and manuscript, Erich T. Hester helped develop the manuscript and guided analysis on the numerical model.
- Chapter 5: Imaging of biotic reactions in the subsurface: Two dimensional O₂ and CO₂ dynamics of aerobic respiration
Builds a framework to use planar optodes to obtain two-dimensional dissolved oxygen and carbon dioxide concentrations from microbial respiration in the hyporheic zone. This study is not currently being prepared for publication.
 - Katherine Santizo performed the experiments, collected the stream samples, and performed data analysis. Erich T. Hester and Mark A. Widdowson guided laboratory experiments and provided feedback on written chapter.

References

- Abarca, E., & Clement, T. P. (2009). A novel approach for characterizing the mixing zone of a saltwater wedge. *Geophysical Research Letters*, *36*(6).
<https://doi.org/10.1029/2008GL036995>
- Aisopou, A., Bjerg, P. L., Sonne, A. T., Balbarini, N., Rosenberg, L., & Binning, P. J. (2015). Dilution and volatilization of groundwater contaminant discharges in streams. *Journal of Contaminant Hydrology*, *172*, 71–83. <https://doi.org/10.1016/j.jconhyd.2014.11.004>
- Alexander, R. B., Smith, R. A., & Schwarz, G. E. (2000). Effect of stream channel size on delivery of nitrogen to the Gulf of Mexico. *Nature*, *403*, 758–761.
- Anna, P. De, Jimenez-martinez, J., Tabuteau, H., Turuban, R., Borgne, T. Le, Derrien, M., & Me, Y. (2014). Mixing and Reaction Kinetics in Porous Media : An Experimental Pore Scale Quantification. <https://doi.org/10.1021/es403105b>
- Antweiler, R. C., Writer, J. H., & Murphy, S. F. (2014). Evaluation of wastewater contaminant transport in surface waters using verified Lagrangian sampling. *Science of the Total Environment*, *470–471*, 551–558. <https://doi.org/10.1016/j.scitotenv.2013.09.079>
- Azinheira, D. L., Scott, D. T., Hession, W., & Hester, E. T. (2014). Comparison of effects of inset floodplains and hyporheic exchange induced by in-stream structures on solute retention. *Water Resources Research*, *50*(7), 6168–6190.
<https://doi.org/10.1002/2013WR014400>
- Bandopadhyay, A., Davy, P., & Le Borgne, T. (2018). Shear Flows Accelerate Mixing Dynamics in Hyporheic Zones and Hillslopes. *Geophysical Research Letters*, *45*(21), 11659–11668.
<https://doi.org/10.1029/2018GL079914>
- Bauer, R. D., Rolle, M., Kürzinger, P., Grathwohl, P., Meckenstock, R. U., & Griebler, C. (2009). Two-dimensional flow-through microcosms - Versatile test systems to study biodegradation processes in porous aquifers. *Journal of Hydrology*, *369*(3–4), 284–295.
<https://doi.org/10.1016/j.jhydrol.2009.02.037>
- Brown, B. V., Valett, H. M., & Schreiber, M. E. (2007). Arsenic transport in groundwater, surface water, and the hyporheic zone of a mine-influenced stream-aquifer system. *Water Resources Research*, *43*(11), 1–14. <https://doi.org/10.1029/2006WR005687>
- Burke, V., Greskowiak, J., Asmuß, T., Bremermann, R., Taute, T., & Massmann, G. (2014). Temperature dependent redox zonation and attenuation of wastewater-derived organic micropollutants in the hyporheic zone. *Science of the Total Environment*, *482–483*(1), 53–61. <https://doi.org/10.1016/j.scitotenv.2014.02.098>
- Cardenas, M. B., Wilson, J. L., & Zlotnik, V. A. (2004). Impact of heterogeneity, bed forms, and stream curvature on subchannel hyporheic exchange. *Water Resources Research*, *40*(8), 1–14. <https://doi.org/10.1029/2004WR003008>
- Cardenas, M. B., Cook, P. L. M., Jiang, H., & Traykovski, P. (2008). Constraining denitrification in permeable wave-influenced marine sediment using linked hydrodynamic and biogeochemical modeling. *Earth and Planetary Science Letters*, *275*(1–2), 127–137.
<https://doi.org/10.1016/j.epsl.2008.08.016>

- Caruso, A., Boano, F., Ridolfi, L., Chopp, D. L., & Packman, A. (2017). Biofilm-induced bioclogging produces sharp interfaces in hyporheic flow, redox conditions, and microbial community structure. *Geophysical Research Letters*, *44*(10), 4917–4925. <https://doi.org/10.1002/2017GL073651>
- Castro-Alcalá, E., Fernández-García, D., Carrera, J., & Bolster, D. (2012). Visualization of mixing processes in a heterogeneous sand box aquifer. *Environmental Science and Technology*, *46*(6), 3228–3235. <https://doi.org/10.1021/es201779p>
- Chen, X., Cardenas, M. B., & Chen, L. (2018). Hyporheic exchange driven by three-dimensional sandy bedforms: sensitivity to and prediction from bedform geometry. *Water Resources Research*, *54*(6), 4131–4149.
- Chiogna, G., & Rolle, M. (2017). Entropy-based critical reaction time for mixing-controlled reactive transport. *Water Resources Research*, *53*(8), 7488–7498. <https://doi.org/10.1002/2017WR020522>
- Chiogna, G., Cirpka, O. A., Grathwohl, P., & Rolle, M. (2011). Relevance of local compound-specific transverse dispersion for conservative and reactive mixing in heterogeneous porous media. *Water Resources Research*, *47*(7). <https://doi.org/10.1029/2010WR010270>
- Chiogna, G., Hochstetler, D. L., Bellin, A., Kitanidis, P. K., & Rolle, M. (2012). Mixing, entropy and reactive solute transport. *Geophysical Research Letters*, *39*(20), 1–6. <https://doi.org/10.1029/2012GL053295>
- Cirpka, O. A., & Kitanidis, P. K. (2000). Characterization of mixing and dilution in heterogeneous aquifers by means of local temporal moments. *Water Resources Research*, *36*(5), 1221–1236. <https://doi.org/10.1029/1999WR900354>
- Cirpka, O. A., Frind, E. O., & Helmig, R. (1999). Numerical simulation of biodegradation controlled by transverse mixing. *Journal of Contaminant Hydrology*, *40*(2), 159–182. [https://doi.org/10.1016/S0169-7722\(99\)00044-3](https://doi.org/10.1016/S0169-7722(99)00044-3)
- Cirpka, O. A., Schwede, R. L., Luo, J., & Dentz, M. (2008). Concentration statistics for mixing-controlled reactive transport in random heterogeneous media. *Journal of Contaminant Hydrology*, *98*(1–2), 61–74. <https://doi.org/10.1016/j.jconhyd.2008.03.005>
- Cirpka, O. A., Chiogna, G., Rolle, M., & Bellin, A. (2015). Transverse mixing in three-dimensional nonstationary anisotropic heterogeneous porous media. *Water Resources Research*, *51*(1), 241–260. <https://doi.org/10.1002/2014WR015331>
- Conant, B., Cherry, J. A., & Gillham, R. W. (2004). A PCE groundwater plume discharging to a river: Influence of the streambed and near-river zone on contaminant distributions. *Journal of Contaminant Hydrology*, *73*(1–4), 249–279. <https://doi.org/10.1016/j.jconhyd.2004.04.001>
- Creswell, J. E., Kerr, S. C., Meyer, M. H., Babiarz, C. L., Shafer, M. M., Armstrong, D. E., & Roden, E. E. (2008). Factors controlling temporal and spatial distribution of total mercury and methylmercury in hyporheic sediments of the Allequash Creek wetland, northern Wisconsin. *Journal of Geophysical Research: Biogeosciences*, *113*(G2), n/a-n/a. <https://doi.org/10.1029/2008jg000742>

- Crispell, J. K., & Endreny, T. A. (2009). Hyporheic exchange flow around constructed in-channel structures and implications for restoration design. *Hydrological Processes*, *23*, 1158–1168. <https://doi.org/10.1002/hyp.7230>
- Dahm, C. N., Grimm, N. B., Marmonier, P., Valett, H. M., & Vervier, P. (1998). Nutrient dynamics at the interface between surface waters and groundwaters. *Freshwater Biology*, *40*(3), 427–451. <https://doi.org/10.1046/j.1365-2427.1998.00367.x>
- Danczak, R. E., Sawyer, A. H., Williams, K. H., Stegen, J. C., Hobson, C., & Wilkins, M. J. (2016). Seasonal hyporheic dynamics control coupled microbiology and geochemistry in Colorado River sediments. *Journal of Geophysical Research: Biogeosciences*, *121*(12), 2976–2987. <https://doi.org/10.1002/2016JG003527>
- Dentz, M., Le Borgne, T., Englert, A., & Bijeljic, B. (2011). Mixing, spreading and reaction in heterogeneous media: A brief review. *Journal of Contaminant Hydrology*, *120–121*, 1–17.
- Dodds, W. K. (2006). Eutrophication and trophic state in rivers and streams. *Limnology and Oceanography*, *51*, 671–680.
- Ellis, P. A., & Rivett, M. O. (2007). Assessing the impact of VOC-contaminated groundwater on surface water at the city scale. *Journal of Contaminant Hydrology*, *91*(1–2), 107–127. <https://doi.org/10.1016/j.jconhyd.2006.08.015>
- Fox, A., Laube, G., Schmidt, C., Fleckenstein, J. H., & Arnon, S. (2016). The effect of losing and gaining flow conditions on hyporheic exchange in heterogeneous streambeds. *Water Resources Research*, *52*, 7460–7477. <https://doi.org/10.1002/2014WR015716>
- Freitas, J. G., Rivett, M. O., Roche, R. S., Durrant, M., Walker, C., & Tellam, J. H. (2015). Heterogeneous hyporheic zone dechlorination of a TCE groundwater plume discharging to an urban river reach. *Science of the Total Environment*, *505*, 236–252. <https://doi.org/10.1016/j.scitotenv.2014.09.083>
- Galloway, J., Fox, A., Lewandowski, J., & Arnon, S. (2019). The effect of unsteady streamflow and stream-groundwater interactions on oxygen consumption in a sandy streambed. *Scientific Reports*, *9*(1). <https://doi.org/10.1038/s41598-019-56289-y>
- Gandy, C. J., Smith, J. W. N., & Jarvis, A. P. (2007). Attenuation of mining-derived pollutants in the hyporheic zone: A review. *Science of the Total Environment*, *373*(2–3), 435–446. <https://doi.org/10.1016/j.scitotenv.2006.11.004>
- Gomez-Velez, J. D., Harvey, J. W., Cardenas, M. B., & Kiel, B. (2015). Denitrification in the Mississippi River network controlled by flow through river bedforms. *Nature Geoscience*, *8*(12), 941–945. <https://doi.org/10.1038/ngeo2567>
- Hartland, A., Larsen, J. R., Andersen, M. S., Baalousha, M., & Ocarroll, D. (2015). Association of Arsenic and Phosphorus with Iron Nanoparticles between Streams and Aquifers: Implications for Arsenic Mobility. *Environmental Science and Technology*, *49*(24), 14101–14109. <https://doi.org/10.1021/acs.est.5b03506>
- Harvey, J. W., Böhlke, J. K., Voytek, M. A., Scott, D., & Tobias, C. R. (2013). Hyporheic zone denitrification: Controls on effective reaction depth and contribution to whole-stream mass balance. *Water Resources Research*, *49*(10), 6298–6316.

<https://doi.org/10.1002/wrcr.20492>

- Herzog, S. P., Higgins, C. P., Singha, K., & McCray, J. E. (2018). Performance of Engineered Streambeds for Inducing Hyporheic Transient Storage and Attenuation of Resazurin. *Environmental Science and Technology*, 52(18), 10627–10636. <https://doi.org/10.1021/acs.est.8b01145>
- Hester, E. T., & Doyle, M. W. (2008). In-stream geomorphic structures as drivers of hyporheic exchange. *Water Resources Research*, 44(3). <https://doi.org/10.1029/2006WR005810>
- Hester, E. T., Young, K. I., & Widdowson, M. A. (2013). Mixing of surface and groundwater induced by riverbed dunes: Implications for hyporheic zone definitions and pollutant reactions. *Water Resources Research*, 49(9), 5221–5237. <https://doi.org/10.1002/wrcr.20399>
- Hester, E. T., Young, K. I., & Widdowson, M. A. (2014). Controls on mixing-dependent denitrification in hyporheic zones induced by riverbed dunes: A steady state modeling study. *Water Resources Research*, 50, 9048–9066. <https://doi.org/10.1002/2014WR015424>
- Hester, E. T., Cardenas, M. B., Haggerty, R., & Apte, S. V. (2017). The importance and challenge of hyporheic mixing. *Water Resources Research*, 53, 3565–3575. <https://doi.org/10.1002/2016WR020005>
- Hester, E. T., Eastes, L. E., & Widdowson, M. A. (2019). Effect of Surface Water Stage Fluctuation on Mixing-Dependent Hyporheic Denitrification in Riverbed Dunes. *Water Resources Research*, 55(6), 4668–4687. <https://doi.org/https://doi.org/10.1029/2018WR024198>
- Hinkle, S. R., Bencala, K. E., Wentz, D. A., & Krabbenhoft, D. P. (2014). Mercury and methylmercury dynamics in the hyporheic zone of an Oregon stream. *Water, Air, and Soil Pollution*, 225(1). <https://doi.org/10.1007/s11270-013-1694-y>
- Hochstetler, D. L., Rolle, M., Chiogna, G., Haberer, C. M., Grathwohl, P., & Kitanidis, P. K. (2013). Advances in Water Resources Effects of compound-specific transverse mixing on steady-state reactive plumes : Insights from pore-scale simulations and Darcy-scale experiments. *Advances in Water Resources*, 54, 1–10. <https://doi.org/10.1016/j.advwatres.2012.12.007>
- Hou, Z., Nelson, W. C., Stegen, J. C., Murray, C. J., Arntzen, E., Crump, A. R., et al. (2017). Geochemical and Microbial Community Attributes in Relation to Hyporheic Zone Geological Facies. *Scientific Reports*, 7(1). <https://doi.org/10.1038/s41598-017-12275-w>
- Hynds, P. D., Thomas, M. K., & Pintar, K. D. M. (2014). Contamination of groundwater systems in the US and Canada by enteric pathogens, 1990-2013: A review and pooled-analysis. *PLoS ONE*, 9(5). <https://doi.org/10.1371/journal.pone.0093301>
- Jarvie, H. P., Sharpley, A. N., Scott, J. T., Haggard, B. E., Bowes, M. J., & Massey, L. B. (2012). Within-river phosphorus retention: Accounting for a missing piece in the watershed phosphorus puzzle. *Environmental Science and Technology*, 46(24), 13284–13292. <https://doi.org/dx.doi.org/10.1021/es303562y>
- Kalbus, E., Schmidt, C., Molson, J. W., Reinstorf, F., & Schirmer, M. (2009). Influence of

- aquifer and streambed heterogeneity on the distribution of groundwater discharge. *Hydrology and Earth System Sciences*, 13(1), 69–77. <https://doi.org/10.5194/hess-13-69-2009>
- Kennedy, C. D., Genereux, D. P., Corbett, D. R., & Mitasova, H. (2009). Relationships among groundwater age, denitrification, and the coupled groundwater and nitrogen fluxes through a streambed. *Water Resources Research*, 45(9). <https://doi.org/10.1029/2008WR007400>
- Kessler, A. J., Glud, R. N., Bayani Cardenas, M., Larsen, M., Bourke, M. F., & Cook, P. L. M. (2012). Quantifying denitrification in rippled permeable sands through combined flume experiments and modeling. *Limnology and Oceanography*, 57(4), 1217–1232. <https://doi.org/10.4319/lo.2012.57.4.1217>
- Kitanidis, P. K. (1994). The concept of the Dilution Index. *Water Resources Research*, 30(7), 2011–2026. <https://doi.org/10.1029/94WR00762>
- Landmeyer, J. E., Bradley, P. M., Trego, D. A., Hale, K. G., & Haas II, J. E. (2010). MTBE, TBA, and TAME attenuation in diverse hyporheic zones. *Ground Water*, 48(1), 30–41. <https://doi.org/10.1111/j.1745-6584.2009.00608.x>
- Lapworth, D. J., Baran, N., Stuart, M. E., & Ward, R. S. (2012). Emerging organic contaminants in groundwater: A review of sources, fate and occurrence. *Environmental Pollution*, 163, 287–303. <https://doi.org/10.1016/j.envpol.2011.12.034>
- Lautz, L. K., & Fanelli, R. M. (2008). Seasonal biogeochemical hotspots in the streambed around restoration structures. *Biogeochemistry*, 91(1), 85–104. <https://doi.org/10.1007/s10533-008-9235-2>
- Lautz, Laura K., & Siegel, D. I. (2006). Modeling surface and ground water mixing in the hyporheic zone using MODFLOW and MT3D. *Advances in Water Resources*, 29(11), 1618–1633. <https://doi.org/10.1016/j.advwatres.2005.12.003>
- Li, A., Aubeneau, A. F., Bolster, D., Tank, J. L., & Packman, A. I. (2017). Covariation in patterns of turbulence-driven hyporheic flow and denitrification enhances reach-scale nitrogen removal. *Water Resources Research*, 53(8), 6927–6944. <https://doi.org/10.1002/2016WR019949>
- Lu, C., Kitanidis, P. K., & Luo, J. (2009). Effects of kinetic mass transfer and flow conditions on widening mixing zones in coastal aquifers. *Water Resources Research*, 45(12). <https://doi.org/http://dx.doi.org/10.1029/2008WR007643>
- Mahar, A., Wang, P., Ali, A., Awasthi, M. K., Lahori, A. H., Wang, Q., et al. (2016). Challenges and opportunities in the phytoremediation of heavy metals contaminated soils: A review. *Ecotoxicology and Environmental Safety*, 126, 111–121. <https://doi.org/10.1016/j.ecoenv.2015.12.023>
- Marzadri, A., Tonina, D., Bellin, A., & Valli, A. (2016). Mixing interfaces, fluxes, residence times and redox conditions of the hyporheic zones induced by dune-like bedforms and ambient groundwater flow. *Advances in Water Resources*, 88, 139–151. <https://doi.org/10.1016/j.advwatres.2015.12.014>
- Mermillod-Blondin, F., Winiarski, T., Foulquier, A., Perrissin, A., & Marmonier, P. (2015).

- Links between sediment structures and ecological processes in the hyporheic zone: Ground-penetrating radar as a non-invasive tool to detect subsurface biologically active zones. *Ecohydrology*, 8(4), 626–641. <https://doi.org/10.1002/eco.1530>
- Mulligan, C., Yong, R. N., & Gibbs, B. F. (2001). Remediation Technologies for Metal-Contaminated Soils and Groundwater : An Evaluation. *Engineering Geology*, 60, 193–207. [https://doi.org/10.1016/S0013-7952\(00\)00101-0](https://doi.org/10.1016/S0013-7952(00)00101-0)
- Parker, S. P., Bowden, W. B., Flinn, M. B., Giles, C. D., Arndt, K. A., Beneš, J. P., & Jent, D. G. (2018). Effect of particle size and heterogeneity on sediment biofilm metabolism and nutrient uptake scaled using two approaches. *Ecosphere*, 9(3). <https://doi.org/10.1002/ecs2.2137>
- Perujo, N., Sanchez-Vila, X., Proia, L., & Romaní, A. M. (2017). Interaction between Physical Heterogeneity and Microbial Processes in Subsurface Sediments: A Laboratory-Scale Column Experiment. *Environmental Science and Technology*, 51(11), 6110–6119. <https://doi.org/10.1021/acs.est.6b06506>
- Rasmussen, J. J., McKnight, U. S., Sonne, A. T., Wiberg-Larsen, P., & Bjerg, P. L. (2016). Legacy of a Chemical Factory Site: Contaminated Groundwater Impacts Stream Macroinvertebrates. *Archives of Environmental Contamination and Toxicology*, 70(2), 219–230. <https://doi.org/10.1007/s00244-015-0211-2>
- Robinson, B. A., & Viswanathan, H. S. (2003). Application of the theory of micromixing to groundwater reactive transport models. *Water Resources Research*, 39(11), 1–18. <https://doi.org/10.1029/2003WR002368>
- Robinson, G., Ahmed, A. A., & Hamill, G. A. (2016). Experimental saltwater intrusion in coastal aquifers using automated image analysis: Applications to homogeneous aquifers. *Journal of Hydrology*, 538, 304–313. <https://doi.org/10.1016/j.jhydrol.2016.04.017>
- Roche, K. R., Li, A., Bolster, D., Wagner, G. J., & Packman, A. I. (2019). Effects of Turbulent Hyporheic Mixing on Reach-Scale Transport. *Water Resources Research*, 55(5), 3780–3795. <https://doi.org/10.1029/2018WR023421>
- Rolle, M., Eberhardt, C., Chiogna, G., Cirpka, O. A., & Grathwohl, P. (2009). Enhancement of dilution and transverse reactive mixing in porous media : Experiments and model-based interpretation. *Journal of Contaminant Hydrology*, 110, 130–142. <https://doi.org/10.1016/j.jconhyd.2009.10.003>
- Rolle, M., Chiogna, G., Hochstetler, D. L., & Kitanidis, P. K. (2013a). On the importance of diffusion and compound-specific mixing for groundwater transport : An investigation from pore to field scale. *Journal of Contaminant Hydrology*, 153, 51–68. <https://doi.org/10.1016/j.jconhyd.2013.07.006>
- Rolle, M., Chiogna, G., Hochstetler, D. L., & Kitanidis, P. K. (2013b). On the importance of diffusion and compound-specific mixing for groundwater transport: An investigation from pore to field scale. *Journal of Contaminant Hydrology*, 153, 51–68. <https://doi.org/10.1016/j.jconhyd.2013.07.006>
- Santizo, K. Y., Widdowson, M. A., & Hester, E. T. (2020). Abiotic Mixing-Dependent Reaction

- in a Laboratory Simulated Hyporheic Zone. *Water Resources Research*, 56(9).
<https://doi.org/10.1029/2020WR027090>
- Saup, C. M., Bryant, S. R., Nelson, A. R., Harris, K. D., Sawyer, A. H., Christensen, J. N., et al. (2019). Hyporheic Zone Microbiome Assembly Is Linked to Dynamic Water Mixing Patterns in Snowmelt-Dominated Headwater Catchments. *Journal of Geophysical Research: Biogeosciences*, 124(11), 3269–3280. <https://doi.org/10.1029/2019JG005189>
- Sawyer, A. H., & Cardenas, M. B. (2009). Hyporheic flow and residence time distributions in heterogeneous cross-bed sediment. *Water Resources Research*, 45(8), 1–12.
<https://doi.org/10.1029/2008WR007632>
- Schaper, J. L., Posselt, M., Bouchez, C., Jaeger, A., Nuetzmann, G., Putschew, A., et al. (2019). Fate of Trace Organic Compounds in the Hyporheic Zone: Influence of Retardation, the Benthic Biolayer, and Organic Carbon. *Environmental Science and Technology*, 53(8), 4224–4234. <https://doi.org/10.1021/acs.est.8b06231>
- Sheibley, R. W., Jackman, A. P., Duff, J. H., & Triska, F. J. (2003). Numerical modeling of coupled nitrification-denitrification in sediment perfusion cores from the hyporheic zone of the Shingobee River, MN. *Advances in Water Resources*, 26(9), 977–987.
[https://doi.org/10.1016/S0309-1708\(03\)00088-5](https://doi.org/10.1016/S0309-1708(03)00088-5)
- Shen, G., Yuan, J., & Phanikumar, M. S. (2020). Direct numerical simulations of turbulence and hyporheic mixing near sediment-water interfaces. *Journal of Fluid Mechanics*, 892.
<https://doi.org/10.1017/jfm.2020.173>
- Stegen, J. C., Fredrickson, J. K., Wilkins, M. J., Konopka, A. E., Nelson, W. C., Arntzen, E. V., et al. (2016). Groundwater-surface water mixing shifts ecological assembly processes and stimulates organic carbon turnover. *Nature Communications*, 7, 1–12.
<https://doi.org/10.1038/ncomms11237>
- Stegen, J. C., Johnson, T., Fredrickson, J. K., Wilkins, M. J., Konopka, A. E., Nelson, W. C., et al. (2018). Influences of organic carbon speciation on hyporheic corridor biogeochemistry and microbial ecology. *Nature Communications*, 9(1). <https://doi.org/10.1038/s41467-018-02922-9>
- Su, X., Jim Yeh, T. C., Shu, L., Li, K., Brusseau, M. L., Wang, W., et al. (2020). Scale issues and the effects of heterogeneity on the dune-induced hyporheic mixing. *Journal of Hydrology*, 590. <https://doi.org/10.1016/j.jhydrol.2020.125429>
- Wolke, P., Teitelbaum, Y., Deng, C., Lewandowski, J., & Arnon, S. (2020). Impact of bed form celerity on oxygen dynamics in the hyporheic zone. *Water (Switzerland)*, 12(1), 5–7.
<https://doi.org/10.3390/w12010062>
- Writer, J. H., Barber, L. B., Ryan, J. N., & Bradley, P. M. (2011). Biodegradation and Attenuation of Steroidal Hormones and Alkylphenols by Stream Biofilms and Sediments. *Environmental Science and Technology*, 45, 4370–4376.
- Writer, J. H., Ryan, J. N., & Barber, L. B. (2011). Role of Biofilms in Sorptive Removal of Steroidal Hormones and 4-Nonylphenol Compounds from Streams. *Environmental Science and Technology*, 45, 7275–7283.

- Xiao, F., Simcik, M. F., Halbach, T. R., & Gulliver, J. S. (2015). Perfluorooctane sulfonate (PFOS) and perfluorooctanoate (PFOA) in soils and groundwater of a U.S. metropolitan area: Migration and implications for human exposure. *Water Research*, *72*, 64–74. <https://doi.org/10.1016/j.watres.2014.09.052>
- Ye, Y., Chiogna, G., Cirpka, O. A., Grathwohl, P., & Rolle, M. (2016). Experimental investigation of transverse mixing in porous media under helical flow conditions, *013113*, 1–10. <https://doi.org/10.1103/PhysRevE.94.013113>
- Zarnetske, J. P., Haggerty, R., Wondzell, S. M., & Baker, M. A. (2011). Dynamics of nitrate production and removal as a function of residence time in the hyporheic zone. *Journal of Geophysical Research: Biogeosciences*, *116*(1), 1–12. <https://doi.org/10.1029/2010JG001356>
- Zarnetske, J. P., Haggerty, R., Wondzell, S. M., Bokil, V. A., & González-Pinzón, R. (2012). Coupled transport and reaction kinetics control the nitrate source-sink function of hyporheic zones. *Water Resources Research*, *48*(11), 1–15. <https://doi.org/10.1029/2012WR011894>
- Zarnetske, J. P., Haggerty, R., & Wondzell, S. M. (2015). Coupling multiscale observations to evaluate hyporheic nitrate removal at the reach scale. *Freshwater Science*, *34*(1), 172–186. <https://doi.org/10.1086/680011>
- Zemo, D. A., O'Reilly, K. T., Mohler, R. E., Magaw, R. I., Devine, C. E., Ahn, S., & Tiwary, A. K. (2017). Life cycle of petroleum biodegradation metabolite plumes, and implications for risk management at fuel release sites. *Integrated Environmental Assessment and Management*, *13*(4), 714–727. <https://doi.org/10.1002/ieam.1848>
- Zhang, S., Mao, G., Crittenden, J., Liu, X., & Du, H. (2017). Groundwater remediation from the past to the future: A bibliometric analysis. *Water Research*, *119*, 114–125. <https://doi.org/10.1016/j.watres.2017.01.029>

Chapter 2. Hyporheic transverse mixing zones and dispersivity: laboratory and numerical experiments of hydraulic controls

Erich T. Hester,* Katherine Y. Santizo, Abenezer A. Nida, and Mark A. Widdowson

Key Points

1. Mixing zones in shallow (hyporheic) sediments between advected surface water and groundwater were simulated in a lab and model
2. Mixing zone thickness and dispersion rate increased with rate of surface water intrusion and during transient conditions
3. Peclet number simultaneously increased while dilution index decreased, indicating increases in advection outpaced increases in dispersion

Keywords: hyporheic zone, hyporheic exchange, dispersion, mixing-dependent reactions, mixing-controlled reactions

Status: This manuscript has been submitted to *Journal of Contaminant Hydrology*.

Abstract

Mixing in shallow sediments is important to biogeochemical cycling and contaminant migration and is often used to define the hyporheic zone. Yet knowledge of mixing processes in hyporheic zones is supported by surprisingly few rigorous lab or field observations, and differs from deeper groundwater with enhanced head gradients, sediment heterogeneity, and temporal fluctuations. In a laboratory sediment (sand) tank we photographed a conservative dye to analyze transverse mixing zones between upwelling groundwater and bidirectional hyporheic exchange flows. We then conducted numerical modeling to investigate processes behind observed phenomena and estimate dispersivities. We found mixing zones were thin ($\delta < 5$ cm), consistent with a small, calibrated transverse dispersivity (~ 0.1 mm) and prior lab studies conducted at similar scales. In steady-state experiments and simulations, δ and estimated dispersion coefficients increased with the surface water head drop driving exchange flows. Given relatively constant deeper groundwater heads, increased Δh lead to increased mixing zone length for both steady-state and transient conditions, indicating larger bedforms or weaker gaining conditions enhance subsurface mixing. However, Peclet number and flux-related dilution index simultaneously increased and decreased, respectively, indicating that enhancement of subsurface advection outpaced that of dispersion. In transient experiments and simulations, δ was greater than for steady-state, probably from temporary addition of longitudinal dispersion. δ during transient experiments in the sediment tank exhibited temporal noise, perhaps due to the mixing zone moving past varying patterns of sediment packing. Our results provide basic knowledge of mixing zone behavior in hyporheic zones with implications for hyporheic zone definitions, solute transport, mixing-dependent reaction, and water quality.

2.1 Introduction

Surface water-groundwater interaction is widespread, occurring beneath and adjacent to many types of aquatic and marine water bodies (Winter et al. 1998, Cardenas 2008, Kwon et al. 2014). Bidirectional exchange across the sediment-water interface is typically known as hyporheic exchange in streams and rivers (Stanford and Gaufin 1974, White 1993), but such shallow exchange flows also occur in estuarine and marine sediments (Huettel et al. 1996, Bianchin et al. 2011, Musial et al. 2016). These exchange flows create hyporheic zones where hydrologic, thermal, biologic, and water quality characteristics are different than both surface water and deeper groundwater (Brunke and Gonser 1997, Boulton et al. 1998, Hester and Gooseff 2010). These characteristics make the hyporheic zone more chemically reactive with unique microbial communities (Brunke and Gonser 1997, Lowell et al. 2009), with implications for freshwater aquatic organisms (Baxter and Hauer 2000), nutrient balance (Gomez-Velez et al. 2015), and attenuation of pollutants originating in surface water (Hester et al. 2016) and groundwater (Conant et al. 2004, Hester et al. 2014). Shallow exchange processes similarly affect chemical reactions and biogeochemistry in marine settings (Precht et al. 2004, Cook et al. 2006, Cardenas et al. 2008, Weinstein et al. 2011, Knights et al. 2017).

Common hyporheic zone definitions include where surface water advects through sediment (Thibodeaux and Boyle 1987, Harvey and Wagner 2000) and where surface water and groundwater mix within sediment (Triska et al. 1989, Winter et al. 1998, Bencala 2000). These definitions are related but conceptually distinct (Hester et al. 2013). Here we focus on the latter because it has received less rigorous analysis. Yet mixing is critical because it controls a variety of water quality functions, including concentrations of biogeochemically important elements (Naranjo et al. 2015) and penetration of surface water solutes into the sediment (Kessler et al. 2012). Transverse mixing zones in particular enable mixing-dependent reactions of groundwater pollutants exiting to surface water (Hester et al. 2014, Trauth et al. 2015, Santizo et al. 2020).

Field scale transverse mixing and dispersion studies from the general groundwater literature (Pickens and Grisak 1981) may conflate mixing with spreading caused by differential advection. Similarly, transverse hyporheic dispersion has been modeled, but often with large coefficients that conflate spreading with true mixing (Lautz and Siegel 2006, Hester et al. 2013, Hester et al. 2017 and references therein, Shuai et al. 2017). Most prior field and lab studies that track reactive compounds in shallow sediments suggest medium (> 5 cm) to large (>1 m) hyporheic

mixing zones (Triska et al. 1989, Hedin et al. 1998, Conant et al. 2004, Landmeyer et al. 2010, Freitas et al. 2015, Kaufman et al. 2017), yet have not resolved the specific processes responsible (e.g., mixing vs. reactant flux). Thus, more focused studies that spatially resolve individual hyporheic mixing processes are needed.

Pore scale mixing studies from the general groundwater literature (e.g., Huang et al. 2002, Bijeljic and Blunt 2007, Luo and Cirpka 2011, Rolle et al. 2012) provide useful insights but lack aspects unique to hyporheic sediments such as steep head gradients, high sediment heterogeneity, and rapid head fluctuations (Hester et al. 2017, Bandopadhyay et al. 2018). Some prior pore scale laboratory studies of hyporheic processes have shown thin (thickness < 5 cm) transverse mixing zones (Fox et al. 2016, Kaufman et al. 2017), but mixing was not their focus, and dispersive flux or mixing-dependent reactions were not simulated. More recently, Santizo et al. (2020) conducted a laboratory simulation of pore scale transverse hyporheic mixing, but mixing processes were obscured by mixing-dependent reactions, transient conditions were not included, and numerical simulations were not utilized to interpretation underlying processes. Furthermore, we are unaware of transverse dispersivities determined for hyporheic sediments, either in the field or laboratory, yet they are critical to accurate simulation of hyporheic transport and reaction. Lastly, to our knowledge, prior laboratory or field studies have not linked key mixing metrics such as mixing zone thickness (Abarca and Clement 2009, Robinson et al. 2015) with dilution index (Rolle et al. 2009, Chiogna et al. 2011b, Cirpka et al. 2015) to more fully interpret mixing processes.

Here we used conservative tracers in laboratory and numerical experiments to 1) simulate hyporheic transverse mixing zones, 2) confirm thin (< 5 cm) mixing zones found in the few hyporheic and larger number of general groundwater laboratory conservative tracer mixing studies, 3) determine transverse dispersivities, 4) quantify the effect of varying steady-state and transient hydraulic boundary heads and flows on relative dominance of advection and mixing/dispersion processes, and 5) relate directly measurable mixing metrics (e.g., mixing zone thickness) with theoretical (e.g., flux-related dilution index) mixing metrics. Addressing these objectives will provide insight into how shallow exchange zones function, with implications for mixing-dependent reactions that affect water quality.

2.2 Methods

2.2.1 Laboratory Experiments

2.2.1.1 Sediment Tank and Experimental Treatments

We used a HM 169 Drainage and Seepage Tank from GUNT (Hamburg, Germany) or “sediment tank” to simulate the mixing zone between a hyporheic flow cell (surface water advecting through the sediment due to pressure gradients along the sediment-water interface) and upwelling groundwater (Figure 2.1a). This scenario represents situations where curvilinear transverse mixing zones develop in shallow sediment beneath gaining surface water bodies, for example from dunes in rivers (Thibodeaux and Boyle 1987, Cardenas and Wilson 2007)(Figure 2.1b), in-stream structures in streams (Lautz and Siegel 2006, Hester and Doyle 2008, Azinheira et al. 2014)(Figure 2.1c), and bedforms in marine settings (Huettel et al. 1996, Cardenas et al. 2008).

We used a conservative tracer dye, rhodamine WT, to visualize the mixing zone and focus on mixing of source waters. Clean tap water flowed into the inflow reservoir to simulate surface water inflow (Figure 2.1a). To simulate the upwelling groundwater, it was necessary to modify the GUNT tank by adding the upwelling reservoir at the bottom. The upwelling reservoir was connected to a constant head tank that provided the upwelling source water (Figure 2.1a). We mixed 1-part rhodamine WT liquid dye with 20,000 parts tap water in the constant head tank to visualize groundwater upwelling through the sand. We chose US Silica Ottawa Flint Silica #12 sand for its white color to enhance dye visualization, rounded grains consistent with river settings, and grain size ($d_{50}=0.53$ mm) similar to other hyporheic laboratory studies (Elliott and Brooks 1997, Marion et al. 2002, Packman and MacKay 2003, Packman et al. 2004, Tonina and Buffington 2007). Similar to these prior studies, this sediment is essentially homogeneous as a useful conceptual starting point. We estimated hydraulic conductivity as 6.6×10^{-4} m/s using permeameter tests. We filled the tank with tap water prior to placing the sand to avoid trapping air. We placed the divider 20 cm to the right of the inflow reservoir boundary to both minimize transverse mixing zone formation time and minimize head drop needed to create a flow cell in the sediment. We set the divider depth to 6 cm below the sediment-water interface to eliminate blowout of sand and also keep the mixing zone centered in the tank to avoid boundary effects.

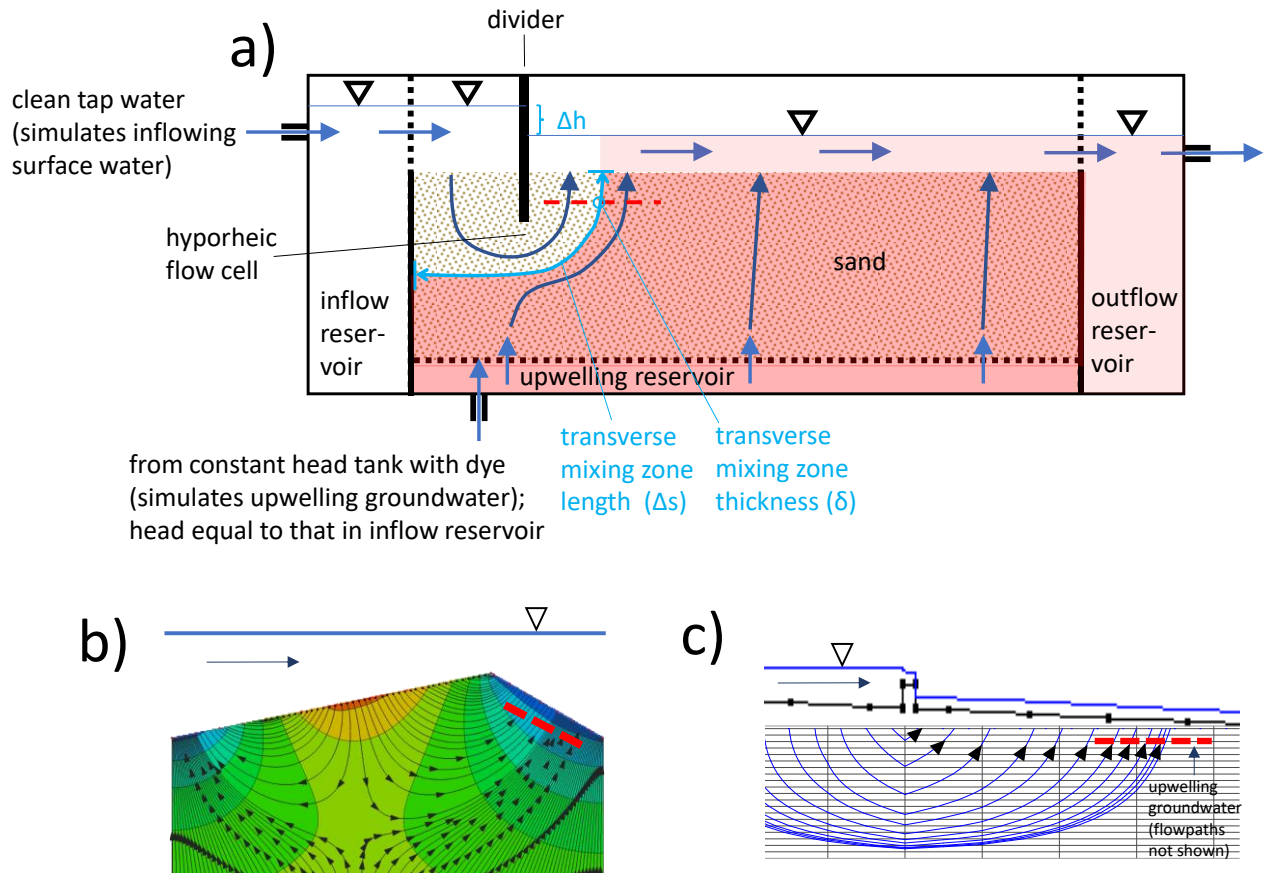


Figure 2.1 a) Schematic (not to scale) of modified Gunt seepage and drainage tank (“sediment tank”). We modified the GUNT tank by adding the upwelling reservoir at the bottom to simulate upwelling groundwater. The upwelling reservoir was connected to an adjustable constant head tank that provided source water to simulate upwelling groundwater. Water levels were controlled in the inflow and outflow reservoirs by adjustable standpipes. Solid black lines are dividers that span the thickness of the tank and prevent flow. Dotted black lines are screens that allow movement of water and dye. The dimensions of the overall sediment tank and just the sand region is 160 cm x 10 cm x 72 cm and 121 cm x 10 cm x 40 cm, respectively (length x width x height). Water flowed through the system as shown by the arrows: there were two water inputs (“surface water” through the inflow reservoir at the left and “groundwater” through the upwelling reservoir at the bottom) and one combined water output (through outflow reservoir at the right). A transverse mixing zone developed along the interface between upwelling groundwater (red portion of sediment in panel a) and hyporheic flow cell (white portion of sediment). Mixing zone size was quantified by mixing zone length (Δs) and thickness (δ). Horizontal dashed red line shows location of δ analyses (4.2 cm beneath sand surface). b) and c) show example hyporheic flowpaths induced by riverbed dunes and in-stream structures, respectively. They show locations (indicated by dashed lines) where hyporheic mixing zones form that are hydraulically similar to those in our experiments (compare panels a, b, and c). For dunes and marine bedforms in particular, our induced flow cell represents one-half of the flow cell (e.g., panel c) where a stagnation point exists at the bottom of the flow cell. In our laboratory setup, this stagnation point exists where the bottom of the hyporheic flow cell meets the barrier between the sand and the inflow reservoir (panel a). Inverted triangles indicate water surface.

We induced a hyporheic flow cell by creating a hydrostatic head drop across the divider (Δh in Figure 2.1). We created Δh by increasing the inflow reservoir head while maintaining a constant head in the outflow reservoir (Table 2.1). This increase in Δh increased the flow rate and hence velocities in the hyporheic flow cell. As Δh increased, we simultaneously increased the head in the constant head tank feeding the upwelling reservoir, but by less than we increased the inflow reservoir head. This allowed the head gradient between the upwelling reservoir and the inflow reservoir to decrease (Table 2.1), which increased the size of the hyporheic flow cell and hence the length of the mixing zone, while simultaneously avoiding direct flow between the two reservoirs.

We varied steady-state Δh among three scenarios, which we refer to as low, medium, and high surface water head drop ($\Delta h=3.5, 5.5, \text{ and } 8.0 \text{ cm}$), respectively. The range of Δh reflects the physical constraints of the equipment, in particular, 3.5 cm is almost the smallest that could induce a coherent hyporheic flow cell while 8.0 was the largest that is possible with this size sediment tank. This range of Δh is consistent with prior field and lab studies of dunes and in-stream structures (Elliott and Brooks 1997, Hester and Doyle 2008, Endreny et al. 2011, Azinheira et al. 2014). We also conducted a transient experiment where we rapidly varied Δh to approximate rapid stage changes such as those from rapid changes in reservoir release rates. To do this, we lowered the inflow reservoir water level, causing Δh to decrease from 8 cm to 0 cm in less than 20 seconds, similar to Kaufman et al. (2017).

Table 2.1. Sediment tank laboratory and simulated boundary heads (see Figure 2.1a for locations).

Surface water head drop (inflow reservoir head minus outflow reservoir head, Δh)	Head in inflow reservoir	Head in outflow reservoir	Head in upwelling reservoir ²	Head in constant head tank	Upwelling reservoir head minus inflow reservoir head	Upwelling reservoir head minus outflow reservoir head
	Observed and Simulated ¹	Observed and Simulated ¹	Simulated ²	Observed		
cm	cm	cm	cm	cm	cm	cm
+3.5	48.0	44.5	48.4	49.4	+0.4	+4.0
+5.5	50.0	44.5	49.2	49.8	-0.8	+4.7
+8.0	52.0	44.0	49.8	50.5	-2.2	+5.8

¹MODFLOW boundaries heads for the inflow and outflow reservoirs were set to values measured in the laboratory experiments.

²From the perspective of MODFLOW, this value is technically for the top side of the screen separating the upwelling reservoir and the sand above. We did not measure head in the upwelling reservoir during the experiments. Instead, we manually adjusted upwelling reservoir heads in MODFLOW until we matched the observed mixing zone position at the downgradient end of the hyporheic flow (i.e., where mixing zone thickness was determined from laboratory observations, see Section 2.1.2). The upwelling reservoir heads differ from heads in the constant head tank due to head loss in the piping between the upwelling reservoir and the constant head tank, as well as in the screen between the upwelling reservoir and the sand. See Section 2.2 for further discussion of model calibration.

2.2.1.2 Image Capture and Data Analysis

We photographed the dye and sand through the glass front of the sediment tank using a Nikon D80 camera placed 1.67 m away, automated by Control My Nikon v4.2, with 75 mm focal length, ISO speed 100, aperture f/10, and shutter speed 1/6 s to maximize photo resolution while maintaining proper exposure. Image resolution was 3872 x 2592 (horizontal x vertical), which corresponded to 0.014 x 0.015 cm (horizontal x vertical) of the sand matrix per pixel. We illuminated the sediment tank diagonally from above using two Genaray Spectro LED 9.0

photographic studio lights, and surrounded the tank, camera, and lights with a black duvetyn fabric enclosure. We acquired images during the steady-state and transient conditions described above, and also before dye was introduced (background). During the steady-state experiments, we took photos well after the sediment tank achieved steady-state transport, which varied between about 30 and 60 minutes, depending on Δh . During the transient experiments, we took photos every 5 seconds from the time the tube was moved until flow cell disappeared.

We converted raw (.nef) images to 8-bit .tiff images using Nikon ViewNX2 software, and used the red channel intensities (0-225, dimensionless) for analysis due to strong response to dye presence. Even with careful control of lighting, some spatial and temporal variation of background light intensity is unavoidable (Castro-Alcala et al. 2012). We corrected spatial variation within each image by dividing the light intensities for each pixel by those from the background image taken without dye tracer using MATLAB (Castro-Alcala et al. 2012). This inverted the intensity scale so that cells with dye had lower rather than higher normalized intensities. We corrected temporal variation among images by scaling the range of intensities in each image from 0.0 to 1.0. Next, we addressed background light intensity noise from sand grains using block processing (Robinson et al. 2015). This replaced pixel values with the averages within larger blocks, and we chose 20x20 pixel (2.8 mm) blocks because these are typically 2-4 sand grains across, which eliminates noise but still maintains maximum spatial resolution.

We calculated transverse mixing zone thickness (δ) as well as transverse dispersion coefficients (D_t), Peclet numbers (Pe) and the flux-related dilution index (E_Q) to understand how dispersion and mixing processes varied among experimental treatments, as well as to conceptually link directly observable mixing metrics with more theoretical ones. Here we describe how we measured δ , and we discuss calculation of D_t , Pe and E_Q in Section 2.4.1. In two dimensions, δ together with mixing zone length (Δs) (Figure 2.1) comprise mixing zone size (Hester et al. 2013). But δ increases in the downgradient direction (Domenico and Schwartz 1998, Huang et al. 2002, Rolle et al. 2012, Van Breukelen and Rolle 2012), such that measurements of δ at the downgradient end of the mixing zone (i.e., dashed horizontal line in Figure 2.1) also account for effects of Δs on mixing zone size. We thus use δ as a surrogate for mixing zone size when looking at the effects of controlling factors. To calculate transverse δ , we linearly interpolated normalized light intensities between adjacent 20-pixel blocks along a series of five vertically adjacent horizontal rows of blocks where the mixing zone is vertical (average of 4.2 cm depth: red dashed line in

Figure 2.1a). We picked this location because a vertical mixing zone simplifies the process of calculating δ from gridded pixels, and because this location is at the downgradient end of the mixing zone, so calculated values of δ represent the cumulative effect of mixing along the length of the mixing zone.

We quantified δ using percentage-based thresholds (Chiogna et al. 2011a, Pool et al. 2014). We determined the spatial distance between 16% and 84% (0.16-0.84) of the maximum light intensity, and repeated the procedure using 10% and 90% (0.10-0.90). The 0.16-0.84 cutoffs are commonly used to delineate 2D plume margins, and can be derived from gaussian plume dispersion theory (Domenico and Schwartz 1998) as we discuss further in Section 2.4.1. The 0.10-0.90 cutoffs are more arbitrary but have been used in the past (Abarca and Clement 2009, Pool et al. 2014), and provide a second set of metrics to confirm that observed trends are not specific to a particular threshold. Regardless, both sets of cutoffs represent the core of the mixing zone rather than the fringe. We chose this approach because the fringe is more difficult to measure given the greater importance of noise in the light intensities.

2.2.2 Numerical Modeling

We constructed a numerical flow and transport model of our laboratory sediment tank experiments using MODFLOW (Harbaugh 2005) and MT3DMS (Zheng and Wang 1999). The model domain was the sand portion of the tank (Figure 2.2). The main purposes of the modeling were to interpret processes behind observed results and calculate transverse dispersivities (α_t) for the hyporheic zone to see if they are consistent with prior values for this scale of groundwater flow. We simulated both our steady-state and transient experimental results.

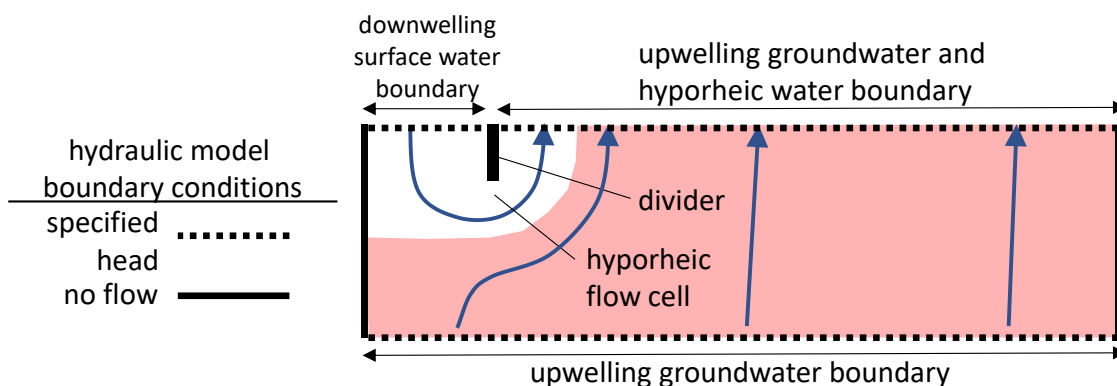


Figure 2.2. Schematic of numerical model of sediment tank flow and transport. Figure not to scale.

2.2.2.1 Flow Model

MODFLOW is a finite-difference groundwater hydraulic code that solves the three-dimensional groundwater flow equation

$$\frac{\partial}{\partial x_i} \left(K_{ii} \frac{\partial h}{\partial x_i} \right) + W = S_s \frac{\partial h}{\partial t} \quad (2.1)$$

where K_{ii} is hydraulic conductivity (L/T) in the direction of respective Cartesian coordinate axes x_i (L), h is the piezometric head (L), W is a water source-sink term (T^{-1}), S_s is specific storage (L^{-1}), and t is time (T). We constructed the 2D computational domain to match the internal dimensions of the sediment tank. To minimize numerical dispersion while also minimizing run times, we systematically reduced a uniform model grid size until modeled δ values no longer changed with further refinement. This resulted in 1.25 mm x 1.25 mm model cells, yielding a total of 304,512 computational cells. The sufficiency of this grid size is consistent with prior modeling studies at similar spatial scales that showed minimal numerical dispersion with larger discretization (Hester et al. 2013, 2014). We used the MODFLOW Preconditioned Conjugate Gradient method to solve Equation (2.1).

We used specified head boundary conditions for the influent boundaries (upwelling groundwater at the bottom, downwelling surface water portion of the hyporheic flow cell at the top left) and the effluent boundary (upwelling groundwater and hyporheic flow cell at the top center and right, Figure 2.2). The remaining perimeter of the model consisted of a no-flow boundary. The hydraulic head values for the two specified head boundaries at the top of the model for the three steady-state model runs were set to those observed in the sediment tank (see Section 2.1.1 including Table 2.1). We then manually adjusted the head at the upwelling groundwater boundary of the steady-state flow model to match the observed position of the tracer front in the transport model (see Table 2.1 and Section 2.2.2). This tracer front matching was done at the downgradient end of the hyporheic flow cell, i.e., at the location where we determined mixing zone thickness from the laboratory data (dashed line in Figure 2.1a).

Once the manual calibration was complete, we varied the upwelling groundwater head (and thus the “inflow ratio” between upwelling and groundwater and downwelling surface water) in a sensitivity analysis to test its influence on mixing zone characteristics. In particular, for each Δh , we varied the upwelling groundwater head from a high value that made the hyporheic flow cell

nearly disappear to a low value that enlarged the hyporheic flow cell as much as possible without inducing edge effects at the bottom boundary. For the transient simulation, a time-varying specified-head condition was applied at the downwelling surface water boundary with constant specified-head maintained at the upwelling groundwater boundary.

K was set to homogeneous at 6.6×10^{-4} m/s per laboratory measurements (Section 2.1.1). S_s was set to homogeneous at 0.0005 m^{-1} , a reasonable value for sand (Domenico and Mifflin 1965), but we also varied this parameter in a sensitivity analysis and found our transient flow simulation to be insensitive.

2.2.2.2 Transport Model and Calibration

MT3DMS is a dissolved solute transport code which utilizes the MODFLOW results to solve the advection, dispersion, and reaction equation in groundwater

$$\frac{\partial(\theta C^k)}{\partial t} = \frac{\partial}{\partial x_i} \left(\theta D_{ij} \frac{\partial C^k}{\partial x_j} \right) - \frac{\partial}{\partial x_i} (\theta v_i C^k) + WC_s^k + \sum R \quad (2.2)$$

where θ is porosity of the porous media (dimensionless), C^k is concentration of dissolved constituent k (ML^{-3}), t is time (T), $x_{i,j}$ is distance along respective Cartesian coordinate axes (L), D_{ij} is the hydrodynamic dispersion coefficient tensor (L^2T^{-1}), v_i is linear pore water velocity (LT^{-1}), C_s^k is the source-sink flux concentration for constituent k (ML^{-3}) and $\sum R$ is the chemical reaction term ($\text{ML}^{-3}\text{T}^{-1}$). We used the MT3DMS Advection Package (Third-Order TVD method) and Dispersion Package with the Generalized Conjugate Gradient Solver to solve Equation (2.2). The Dispersion Package calculates D in each direction using the classic method of Scheidegger (1961), by adding the apparent or bulk molecular diffusion coefficient (D_m , L^2T^{-1}) to the product of v and a dispersivity (α , L). We set D_m to $1.0 \times 10^{-5} \text{ m}^2/\text{d}$ ($1.16 \times 10^{-10} \text{ m}^2/\text{s}$) as a typical or medium value for dissolved solutes in porous media (Freeze and Cherry 1979, Domenico and Schwartz 1998).

Boundary conditions for the MT3DMS model included no-flux conditions coinciding with the no-flow boundaries in MODFLOW. A constant concentration of 100 mg/L was assigned along the upwelling groundwater boundary for convenient data analysis (Figure 2.2). In contrast, the downwelling surface water boundary was 0 mg/L. This concentration differs from the lab experiment but is arbitrary because in our results we report model concentrations normalized to

the maximum. Concentrations along the upper upwelling groundwater and hyporheic water boundary were assigned to specified head cells to equal the tracer concentration in the sediment tank using the MT3DMS Source/Sink Mixing Package. The transport model domain was smaller than the flow model domain (116,543 grid cells) to decrease run times while still including the mixing zone in the simulated domain. This was done by inactivating columns of model cells on the right side of the model domain far away from the mixing zone. This does not change the accuracy of the transport model because as the underlying hydraulics did not change (i.e., the MODFLOW input files were still for the full domain discussed above) and grid resolution of remaining cells did not change.

We manually calibrated the flow model boundary conditions to match the position of mixing zone for the three steady-state scenarios (Section 2.2.1). We also manually calibrated the longitudinal and transverse dispersivity values (1.0 mm and 0.1 mm, respectively) to match the observed mixing zone thickness (δ) for the steady-state $\Delta h = 3.5$ cm scenario. Both calibrations were done at the downgradient end of the mixing zone (dashed line in Figure 2.1a). There were no solute sources/sinks or reactions (i.e., rightmost two terms in Equation (2) = 0).

2.3 Results

2.3.1 Steady State Conditions

Mixing zones in the laboratory appeared quite thin to the eye, as indicated by the sharp change in color (Figure 2.3abc). The steady-state model runs showed mixing zones that also appear thin (Figure 2.3def), although perhaps somewhat thicker than those in the laboratory. We believe any such visual discrepancy is due to the human eye's inability to see relatively low dye concentrations on the left side of the laboratory mixing zones. By contrast, our camera was able to see these lower concentrations, indicated by good agreement between measured and modeled mixing zone thicknesses as discussed more below (Figure 2.4).

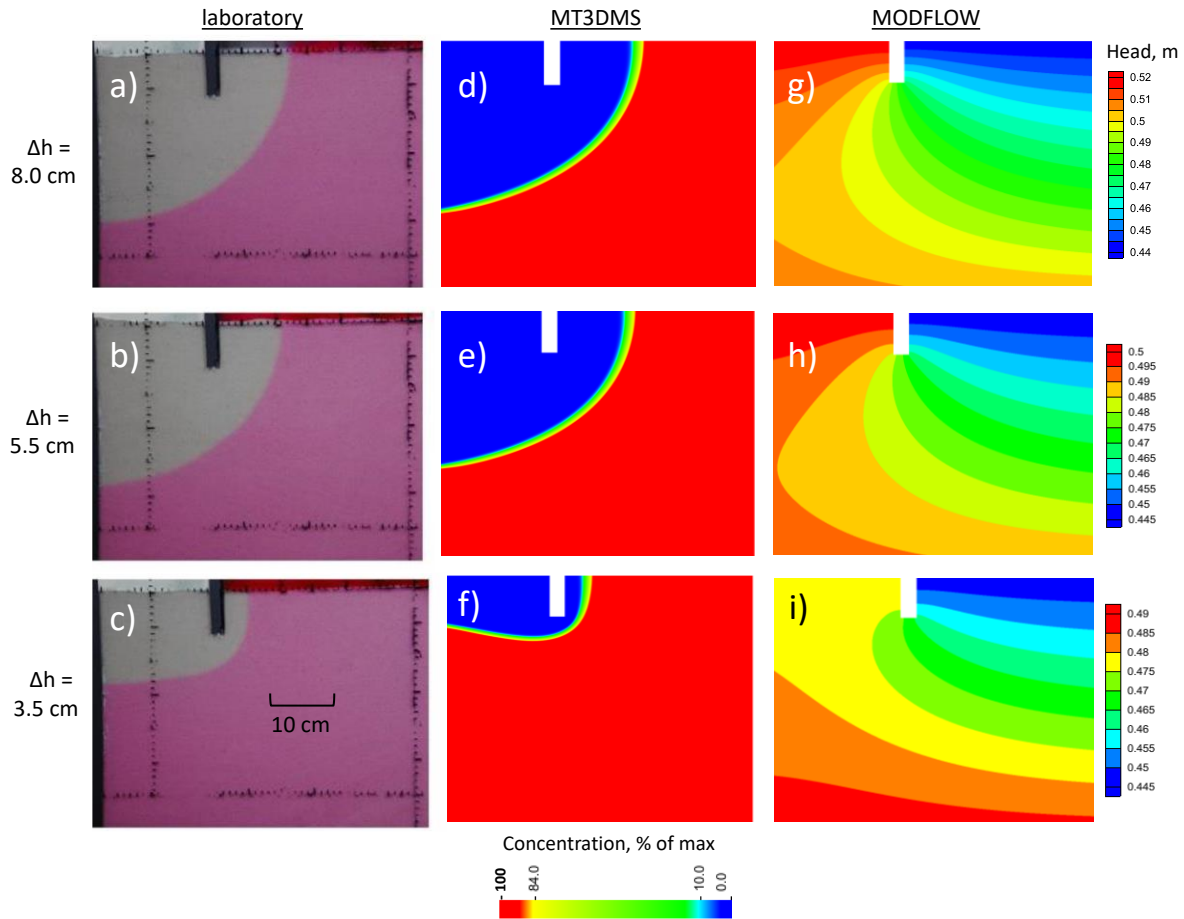


Figure 2.3. Tracer patterns in laboratory sediment tank (a, b, c) and MT3DMS model output (d, e, f) along with hydraulic heads from MODFLOW model (g, h, i) for high surface water head drop ($\Delta h=8.0$ cm, a, d, g), medium surface water head drop ($\Delta h=5.5$ cm, b, e, h), and low head surface water drop ($\Delta h=3.5$ cm, c, f, i) steady-state conditions. Panels do not present full sand box consistent with our focus on that portion of the mixing zone to the right of the divider; for laboratory images (panels a through c) ~ 1 - 2 cm of sand at left side is covered by black electrical tape, and model results (d through i) are similarly cropped. Note that MODFLOW calibration matched observed and simulated mixing zone position at the location where mixing zone thickness was determined (i.e., the downgradient end of hyporheic flow cell to the right of the divider). Thus, model results and observations agree best at that location, and larger deviations elsewhere are likely due to our choice of uniform constant head along the upwelling groundwater boundary, given head likely varied somewhat long this boundary in the laboratory, a variation which we did not measure.

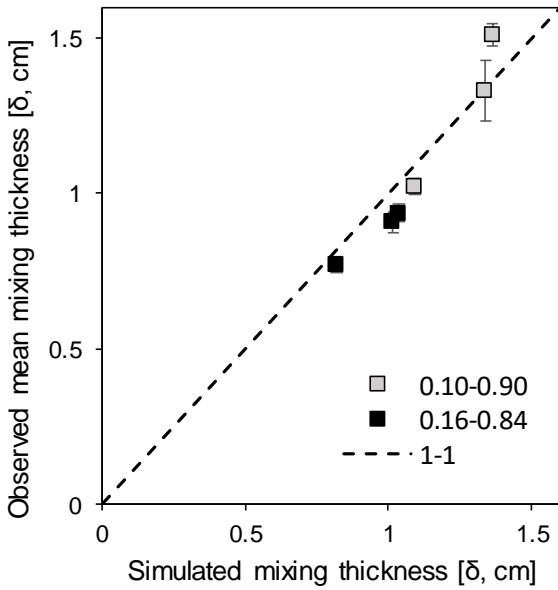


Figure 2.4. Simulated vs. observed mixing zone thickness (δ) for steady-state case. Error bars indicate +/- one standard deviation, where mean and standard deviation are from five rows of 20-pixel blocks centered vertically at 4.2 cm depth.

Mixing zone length (Δs) increased with surface water head drop driving hyporheic exchange (Δh) during the steady-state experiments (Figure 2.5a) because simultaneous variations in upwelling reservoir head were comparatively smaller, with the net effect that head gradient from the upwelling to inflow reservoirs decreased, allowing flow cell size to increase (Figure 2.3). Mixing zone thickness (δ) measured between 1.0 and 1.5 cm for 0.10-0.90 and between 0.8 and 0.9 cm for 0.16-0.84 thresholds (Figure 2.5b). δ increased with Δh and did so more steeply for 0.10-0.90 than 0.16-0.84. Variation in δ measured across the five vertically adjacent horizontal rows of blocks was minimal (standard deviation shown as error bars in Figure 2.5b).

As Δh increased, the trends in the laboratory and model-derived δ values matched each other reasonably well. This match is best for the $\Delta h=3.5$ cm scenario, because the numerical transport model was fit to experimental observations by tuning dispersivity at that Δh . The discrepancy between modeled and simulated δ increased somewhat with Δh . In particular, the difference between δ for 0.10-0.90 and δ for 0.16-0.84 increased more for the laboratory measurements than for the model results (Figure 2.5b). This can be seen when plotting observed

and model values against one another (Figure 2.4), although there is also some systematic bias in the 0.16-0.84 results in that the model slightly over-predicted the lab results in many cases.

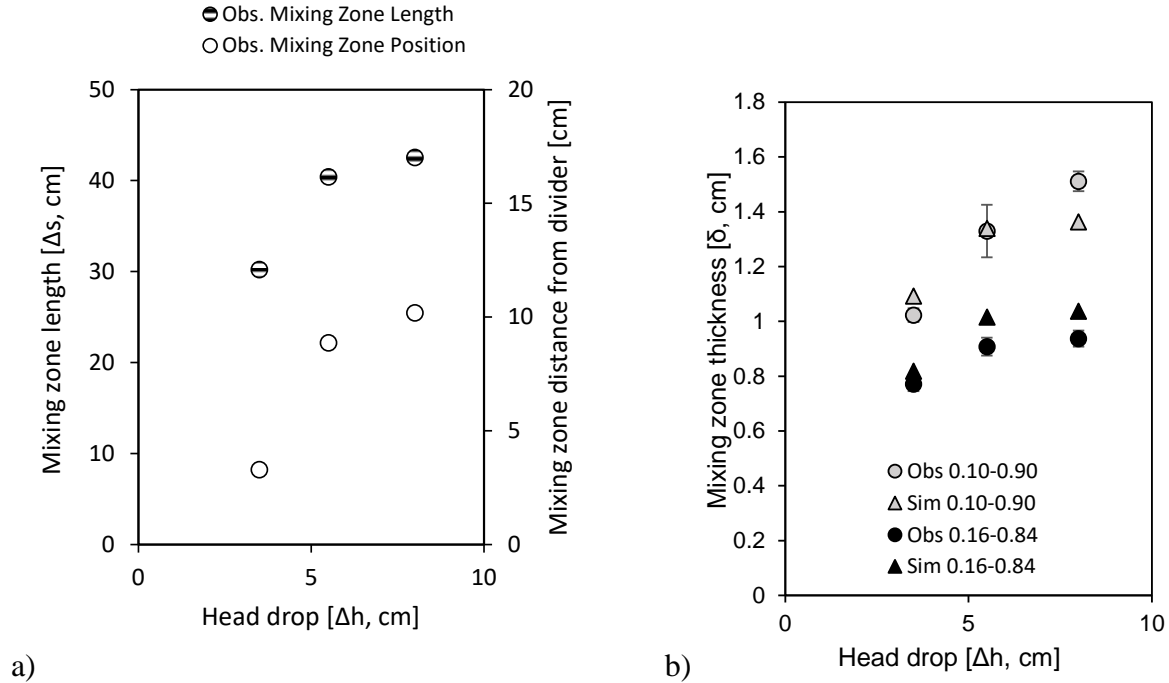


Figure 2.5. Steady-state a) observed mixing zone length (Δs) and position (distance from divider), and b) observed and simulated mixing zone thickness (δ) versus surface water head drop (Δh). In a) mixing zone length is for that portion of mixing zone visible in Figures 2.3abc. In b) we show δ for both 0.10-0.90 and 0.16-0.84 red channel light intensity ranges. Simulated and laboratory values were all taken at same location (i.e., 4.2 cm below the surface of the sand, dashed line in Figure 1). Error bars for δ in panel b) indicate +/- one standard deviation, where mean and standard deviation are from five rows of 20-pixel blocks centered vertically at 4.2 cm depth.

We used MODFLOW ZoneBudget (Harbaugh 1990) to determine steady-state flow rates of water coming into the model through the top boundary (surface water) and the bottom boundary (groundwater). The ratio of upwelling groundwater to downwelling surface water boundary flows was always >1 (Figure 2.6) because of the larger groundwater boundary (Figure 2.2) and to prevent the hyporheic flow cell from getting too large (i.e., mixing zone approaching bottom model boundary). Figure 2.6 shows that a major control on δ in shallow sediments is balance between flows from the surface water and groundwater boundaries. This makes sense because the ratio of

boundary flows controls the size of the hyporheic flow cell, which in turn controls Δs (Figure 2.5a), which in turn controls δ (Figure 2.5b). δ exhibited the greatest sensitivity to the ratio of boundary flows as the balance between groundwater and surface water flows decreased toward unity. Conversely, δ approached asymptotic minimum values as groundwater flow (i.e., strength of upwelling) exceeded surface flow by an order of magnitude and greater.

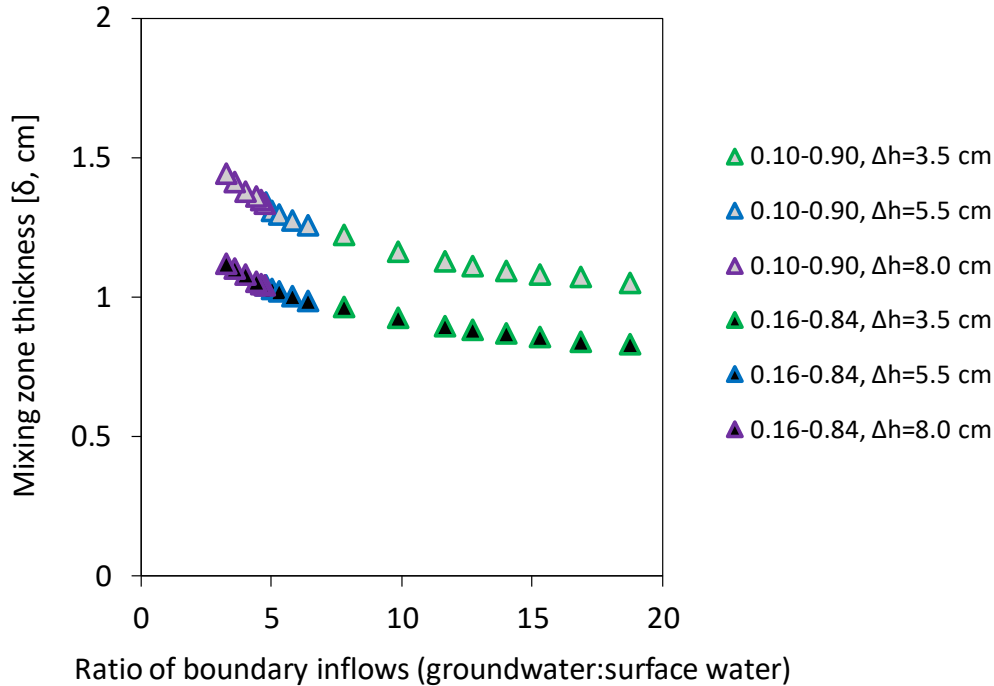


Figure 2.6. Simulated mixing zone thickness (δ) for the steady-state case as a function of the “inflow ratio”, i.e., ratio of water inflows along the bottom boundary (i.e., upwelling groundwater) to water inflows along the top boundary (i.e., downwelling surface water that enters the hyporheic flow cell). Range of points for each surface water head drop (Δh) comes from varying the bottom (upwelling groundwater) specified head and thus upwelling boundary flows in the model.

2.3.2 Transient Conditions

In response to the transient drop in Δh , and the simultaneous corresponding increase in head gradient from the upwelling reservoir to the inflow reservoir, the mixing zone shifted steadily toward the divider (Figure 2.7a), rapidly at first and then slowing down. The simulated and observed trends line up well, indicating that MODFLOW reasonably simulated the transient experiments. As Δh declined, δ initially increased from the steady-state value for the 8.0 cm head

drop (~1 cm) to somewhere between 1.6 and 1.8 cm at ~300 sec for the observed and simulated case (Figure 2.7b). δ then declined to around 0.6 cm at ~1000 sec. Thus, the greatest δ is concurrent with the fastest movement of the mixing zone (compare Figures 2.7a and 2.7b). And the response time in the sediment (~1000 sec) was more than ten times that of the change in surface water head (<20 sec). The MT3DMS model results matched the observations reasonably well both in magnitude of δ and timing of the peak (Figure 2.7b). In addition to this longer time-scale response of δ (~1000 sec, Figure 2.7b), there were shorter-scale fluctuations of δ , on the order of 5-20 seconds (Figure 2.7c). This short-term variability was greater at higher Δh than at lower Δh (Figure 2.7b).

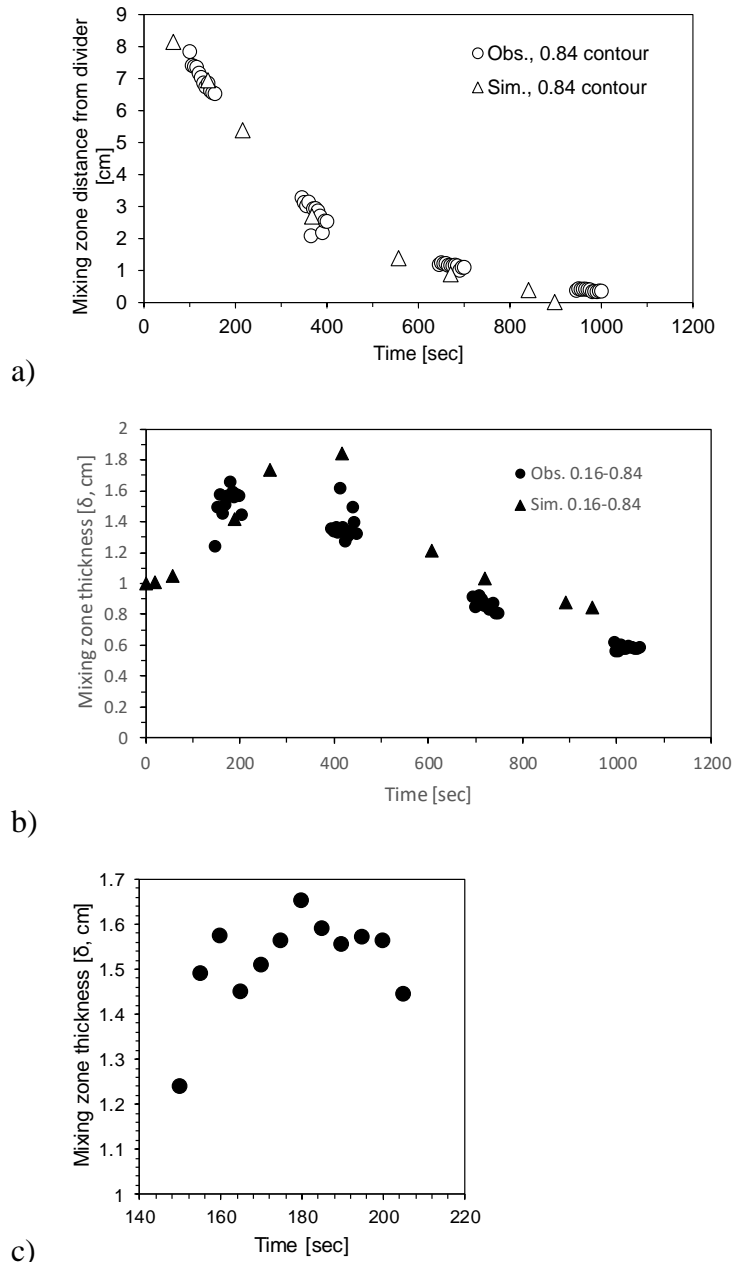


Figure 2.7. Observed and simulated transient mixing zone a) position (distance of 0.84 contour from divider) and b-c) thickness (δ) versus time since sudden head change in inflow reservoir. For b) and c) 0.16-0.84 red channel light intensity ranges are shown. b) shows full experiment duration, and c) shows example subset of full experiment duration with higher temporal resolution. Each laboratory data point is for a 5-second interval across sample periods of 1 minute and is the mean of five 20-pixel block rows centered vertically at 4.2 cm depth, i.e., near the dashed line in Figure 1. Simulated values were taken at same location as laboratory measurements in the sediment tank.

2.4 Discussion and Analysis

2.4.1 Dispersion Coefficient, Peclet Number, and Dilution Index, and Relation to Mixing Zone Thickness

Because an easily observable metric such as mixing zone thickness (δ) is not sufficient by itself to understand variation in transverse mixing in nonuniform flow fields (Rolle et al. 2009), we calculated a series of additional more theoretical transport and mixing parameters to fully quantify and interpret transport processes (Table 2.2). Here in Section 2.4.1, we present the calculations and basic results, including comparing the relatively utility of observable and theoretical mixing metrics. In subsequent sections we then use these metrics to interpret processes occurring in the physical and numerical experiments, including the effect of controlling hydraulics.

We first calculated transverse dispersion coefficients (D_t , m/s) using Santizo et al. (2020)

$$D_t = \frac{\delta_{0.16-0.84}^2 v_{4.2}}{\Delta s_{4.2}} \quad (2.3)$$

where $\delta_{0.16-0.84}$ is observed mixing zone thickness for 0.16-0.84 (Figure 2.5b), $\Delta s_{4.2}$ (m) is distance along the mixing zone visible in the sediment tank to point where δ was observed (i.e., those from Figure 2.5a less the 4.2 cm depth in the sediment at which δ was measured), and $v_{4.2}$ is the porewater velocity along the mixing zone (m/s) from the numerical model also at 4.2 cm depth. We calculated D_t for the downgradient end of the mixing zone (like we did for δ), because that is where our numerical model was calibrated and hence is most accurate (Section 2.2.2), and because doing so quantifies the cumulative mixing processes occurring along the length of mixing zone upgradient i.e. calculates an “apparent” dispersion coefficient (Rahman et al. 2005).

Table 2.2. Transport and mixing parameters, including input parameters for Equations (2.3) -(2.6).

Experimental treatment	Observed mixing zone thickness	Observed length of mixing zone to location of $\delta_{0.16-0.84}$ measurement ¹	Simulated velocity at location of δ measurement at 4.2 cm depth	Transverse dispersion coefficient	Peclet number	Dilution index
Δh	$\delta_{0.16-0.84}$	$\Delta s_{4.2}$	$v_{4.2}$	D_t	Pe	E_Q
cm	cm	cm	m/d	m^2/s	-	m^3/d
3.5	0.77	26.0	35.4	7.97×10^{-8}	1.54×10^3	0.157
5.5	0.91	36.2	37.6	9.02×10^{-8}	1.98×10^3	0.147
8.0	0.94	38.4	43.1	1.04×10^{-7}	2.06×10^3	0.142

¹Distance along the portion of mixing zone visible in the sediment tank (Figures 2.3abc) to point where δ was observed (i.e., those from Figure 2.5a less the 4.2 cm depth in the sediment at which δ was measured).

Next, we calculated the Peclet number (Pe, Bear 1972, Schnoor 1996),

$$Pe = \frac{v_{4.2} \Delta s_{4.2}}{D_t} \quad (2.4)$$

which again is calculated with input values from the downgradient end of the mixing zone. Finally, we calculated the flux-related dilution index E_Q (L^3/T) from the model output using (Rolle et al. 2009)

$$E_Q = \exp \left[- \int_{x_1}^{x_2} p_Q(x, 0, 0) \ln \left(p_Q(x, 0, 0) \right) q(x, 0, 0) dx \right] \quad (2.5)$$

where the limits of integration x_1 and x_2 are the x-coordinates (L) of the top layer model cells immediately to the right of the divider and at the right-hand side of the transport model domain, respectively. q is the upward vertical Darcy velocity across the top of model domain (L/T), and p_Q is calculated by

$$p_Q = \frac{c(x, 0, 0)}{\int_{x_1}^{x_2} c(x, 0, 0) q(x, 0, 0) dx} \quad (2.6)$$

where c is concentration of tracer exiting the top of the model domain (M/L^3).

Pe increased with δ (Figure 2.8), indicating that as advection increasingly dominated over dispersion along the mixing zone, δ simultaneously increased. Thus, both advection and dispersion increased, but advection increased more than dispersion. At the same time as Pe increased, E_Q decreased. This is consistent with advection increasing comparatively more than dispersion. This emphasizes that when quantifying the role of dispersion in transport, a practical and readily observable metric such as mixing zone thickness provides an incomplete picture, and at best can quantify changes to dispersion in isolation but cannot set them in the context of other transport processes such as advection. A more complete picture requires metrics such as Pe and E_Q , which are more challenging to measure in the lab or field, and often require numerical simulations.

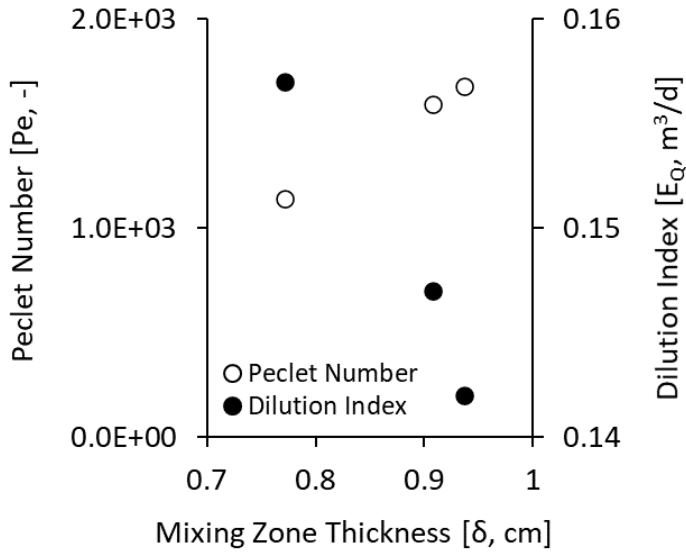


Figure 2.8. Peclet number (Pe) and flux-related dilution index (E_Q) vs. mixing zone thickness (δ).

2.4.2 Magnitude of Hyporheic Transverse Dispersion

Our results showed thin transverse mixing zones ($\delta \approx 1-2$ cm) and advection dominance ($Pe \gg 1$, Table 2.2), consistent with steady-state results from prior hyporheic studies (Sawyer and Cardenas 2009, Jin et al. 2010, Hester et al. 2013), and low opportunity for mixing-dependent reactions (Hester et al. 2014). For example, a numerical model of steady-state conservative tracer transverse mixing based on local dispersion coefficients in a dune-induced hyporheic zone showed the mixing zone occupying 8.2% of the domain, and while δ was not quantified, it appears to be <5 cm for the base case scenario (Figure 2.3 in Hester et al. 2013). Consistent with thin mixing zones, by manually calibrating MT3DMS to our sediment tank data, we determined that the transverse dispersivity (α_t) for our steady-state scenarios was approximately 0.1 mm. This is the first α_t determined from observational data that were explicitly intended to simulate the hyporheic zone, to our knowledge. There are observational data for shallow sediments that quantified longitudinal dispersivity from either laboratory (Chou and Wyseure 2009) or field (Shuai et al. 2017, Liu et al. 2019) settings. And there are many hyporheic studies that have simulated transport including dispersion (e.g., Lutz and Siegel 2006, Qian et al. 2008, Gomez et al. 2012, Hester et al. 2013, Naranjo et al. 2013), but used larger α_t .

However, both the thin mixing zones we observed in the laboratory sediment tank and the magnitude of the corresponding values of α_t from the calibrated transport model are consistent

with the broader range of general groundwater literature. Previous small-scale laboratory studies (longest dimension measuring <1-2 m) of conservative tracer transverse mixing in homogeneous sand have shown mixing zones that appear to range from about 1-4 cm thick (Huang et al. 2002, Bauer et al. 2009, Chiogna et al. 2010, Rolle et al. 2012) with α_t ranging down to ~0.1 mm (e.g., Gaganis et al. 2005), consistent with low mixing (Rolle et al. 2013, Ballarini et al. 2014). Similarly, our value of 0.1 mm is ~19% of our mean grain size (0.53 mm), consistent with percentages previously reported for homogeneous sand (Benekos et al. 2006, Cirpka et al. 2006). Finally, the resulting D_t values (Table 2.2) are consistent with the range of values observed in other laboratory experiments of transverse dispersion of similar scale (Delgado 2006, Rolle et al. 2009, Rolle et al. 2013).

By contrast, field studies of hyporheic or shallow mixing typically show geochemically-defined mixing zones as thicker (Triska et al. 1989, Sawyer et al. 2009), but likely account for additional processes such as spreading, dynamic head boundaries, longitudinal dispersion, and density gradients. Similarly, extensive dispersivity data exist in the general groundwater literature for larger spatial scales. These are often field data, and report α_t (horizontal or vertical) values down to 1.0-10 mm (Gelhar et al. 1992, Zheng and Bennett 2002, Zech et al. 2019), which is still 10-100 times the values we found. Such dispersivities from field data often also account for spreading and thus plume stretching and distortion (i.e., macrodispersivity). In other words, the contrast in α_t values arises due to finer-scale characterization of concentration gradients in the lab relative to typically larger scale field studies (Molz and Widdowson 1988). Field studies generally do not approach the spatial resolution of lab studies, so cannot be directly compared, although a few come close (e.g., Anneser et al. 2008). Thus, even the smaller end of the range of dispersivities from field studies may include some degree of macrodispersivity.

2.4.3 Effect of Hydraulic Controls

Our results show that steady-state mixing zone thickness (δ) increased with the head drop (Δh) driving hyporheic exchange (Figure 2.5b). This makes sense because the simultaneous variations in upwelling reservoir head (Table 2.1) were smaller by comparison, which meant that increased Δh translated to decreased head gradient from the upwelling reservoir to the inflow reservoir, which in turn increased mixing zone length (Δs) (Figure 2.5a), which is known to increase the thickness of a mixing zone at its downgradient end (Domenico and Schwartz 1998,

Huang et al. 2002, Rolle et al. 2012, Van Breukelen and Rolle 2012). This indicates that increasing height of bedforms such as steps, weirs, debris dams, and log dams can lead to thicker mixing zones, assuming relatively constant deeper groundwater heads. On the other hand, variation in deeper groundwater heads by themselves can strongly influence hyporheic flow cell size (Cardenas and Wilson 2007, Hester and Doyle 2008, Azinheira et al. 2014), and hence mixing zone length and thickness. In our experiments, the head gradient between the upwelling reservoir and inflow reservoir was not constant, but rather decreased with increasing Δh (Table 2.1), which in turn increased Δs , and δ . This is consistent with Figure 2.6, which shows that as groundwater upwelling increased relative to flow through the hyporheic flow cell, δ decreased, presumably due to simultaneous decreases in Δs .

D_t also increased with Δh (Figure 2.9a). This makes sense because we calculated D_t as an “apparent” dispersion coefficient from δ measured toward the downgradient end of the mixing zone (Equation (2.3)), meaning it represents mixing that occurred along most of the length of the mixing zone. Our results are thus consistent with Figure 2.11c in Hester et al. (2013) which showed that overall mixing zone size (i.e. Δs multiplied by δ) correlates with transverse dispersive flux across the mixing zone. Increased transverse dispersive flux in turn enhances mixing-dependent reactions. For example, Hester et al. (2019) showed increasing surface water depth lead to increased head gradient between surface water and groundwater that drove hyporheic exchange, increased Δs , and increased mixing-dependent denitrification. Thus, taller bedforms or lesser upwelling or gaining to surface water would lead to enhanced mixing-dependent reactions.

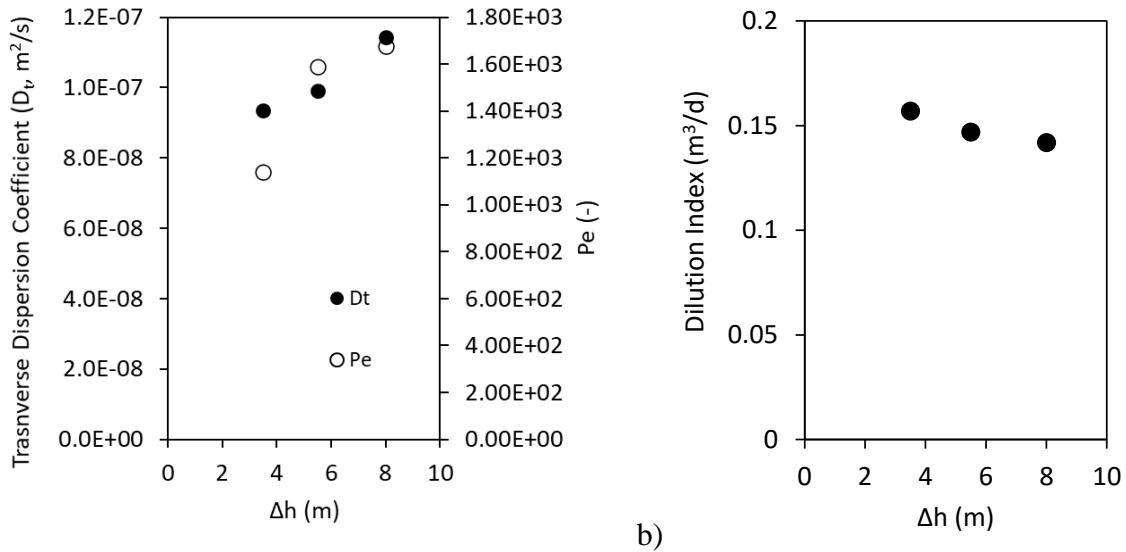


Figure 2.9. a) Transverse dispersion coefficient (D_t), and Peclet number (Pe) vs. head drop (Δh).
b) Flux-related dilution index (E_Q) versus Δh .

Pe also increased with Δh (Figure 2.9a). This indicates that while the dispersion process itself increased; its importance relative to advection decreased. Advection thus increased more with Δh than dispersion, as velocity ($v_{4.2}$) increased (Table 2.2). This may explain why flux-related dilution index (E_Q) simultaneously decreased (Table 2.2, Figure 2.9b). This indicates reduced dilution of the upwelling tracer by adjacent flowpaths that were initially tracer-free. Thus, changes in dispersion and dilution cannot be understood in isolation, but only in the context of simultaneous changes in advection. In sum, increased Δh led to increased v and hence increased dispersion rate (D_t), and while comparatively smaller variations in upwelling reservoir heads (i.e., deeper groundwater heads) meant that increased Δh caused greater Δs and hence δ , yet the increase in v outweighed the increase Δs and thus reduced the time over which that increased dispersion rate can act, leaving advection as the dominant process shown by increased Pe and decreased E_Q .

2.4.4 Effect of Transient Head Variation

During our transient experiments, δ was greater when Δh was greater (i.e., at the beginning of the high to low experiment). This is consistent with our steady-state results in that upwelling reservoir heads were constant during the transient experiment, thus transient decreases in Δh led to simultaneous increases to the head gradient from the upwelling reservoir to the inflow reservoir,

which decreased Δs and therefore δ . Furthermore, δ was greater during changes in Δh than during steady-state conditions (compare Figures 2.5b and 2.7b). This may be due to the temporary presence of longitudinal dispersion as both the flow field and mixing zone adjust to the change in hydraulic boundary conditions. When the dividing line between the hyporheic flow cell and upwelling groundwater contracts upward, an advective front may form between the old location of the dividing line and the new one, and longitudinal dispersion may temporarily occur in that zone. Such advective fronts are temporary and will dissipate as the system comes into a new hydraulic and transport steady-state. Thus, our measurements of δ during this transitory phase may include the effects of both transverse and longitudinal dispersion. In other words, transient conditions increased overall dispersion, even if our data do not sort out the relative contributions of transverse and longitudinal dispersion.

We also observed shorter-term fluctuations in δ (Figure 2.7c). These may be due to the effects of tortuosity (de Anna et al. 2014) on the movement of the dye through spatially-varying patterns of sand grain packing. These short-term fluctuations were greater at greater Δh or greater rate of change in Δh (Figure 2.7b). While no prior lab studies have evaluated these transient dynamics for hyporheic settings to our knowledge, they are consistent with modeling studies which found that transient dynamics enhanced mixing, even in homogeneous sediment (Pool and Dentz 2018). This is also consistent with studies showing tidal oscillations enhance mixing in coastal settings (Pool et al. 2014), although density gradients were also present in that case.

Such increased mixing during transient dynamics would in turn enhance mixing-dependent reactions in shallow and/or hyporheic sediments (Hester et al. 2014, Trauth et al. 2015). Yet reactions have many other controls which could confound such expected trends, for example availability of required reactants or presence of an active microbial community and necessary biogeochemical/redox conditions. For example, Hester et al. (2019) conducted numerical experiments of mixing-dependent denitrification in hyporheic zones with time-varying boundary heads. They found that fluctuating surface water boundary hydraulics increased mixing-dependent reactions, but not as substantially as might be expected from the result of our current study. Thus, in those numerical experiments, other factors may have partially cancelled out the enhancement to mixing from longitudinal dispersion during responses to head changes. One such possible factor includes the requirement that oxygen is depleted before denitrification occurs. Another possible

explanation for the discrepancy is that the head fluctuations in Hester et al. (2019) were slower than in our current experiments.

2.4.5 Limitations and Applications

Calculating mixing metrics directly from light intensities rather than concentrations introduces some error into the process. Studies that have generated light intensity-concentration calibration curves, while often having substantial linear subsections, can be somewhat nonlinear overall (Huang et al. 2002, Castro-Alcala et al. 2012). However, this issue should not affect our major conclusions. Many of our conclusions involve how changes in mixing are caused by changes in hydraulic conditions. Even if the light/concentration calibration curve were nonlinear, these conclusions would not change (e.g., Figures 2.5, 2.6, 2.7, and much of Table 2.2). We recognize that our conclusions involving the magnitude of mixing zone thickness, particularly calculated dispersivities, would be somewhat more sensitive to the shape of the calibration curve. This may be one possible explanation for the modest but systematic overprediction of δ by the model (Figures 2.4, 2.5b). Yet because dispersivities range over several orders of magnitude, the deviations resulting from assuming linear calibration curves would be comparatively minor, and the agreement between our calculated dispersivities and those of prior literature discussed earlier further support their validity.

Our steady-state model simulations with α_t calibrated to the lowest Δh (3.5 cm) did not match the laboratory results as well for the middle and highest Δh (Figure 2.5b). There are a number of possible explanations. For example, the interpolation of blocked concentrations during image processing may introduce error that varies somewhat among different values of Δh . Another possible explanation relates to MT3DMS using the conventional formulation of Scheidegger (1961) to calculate D where α is a function only of porous media characteristics. This view assumes D is a linear function of v under non-inertial or Darcy-flow conditions, and only becomes a non-linear function of v under inertial conditions, i.e. for Reynolds numbers (Re , Equation (2.7)) $> 1-10$ (Bear 1972, Freeze and Cherry 1979). Re is calculated for porous media flow as

$$Re = \frac{\rho v d}{\mu} \quad (2.7)$$

where ρ is density of water (M/L^3), d is a representative pore or particle dimension (L), and μ is dynamic viscosity (M/TL). Yet some recent studies suggest that even under non-inertial conditions α itself varies with v , or D_t otherwise relates nonlinearly to v (Chiogna et al. 2010,

Scheven 2013, Ye et al. 2015). Because our flow conditions were non-inertial ($Re = 0.21-0.26$ using $d=d_{50}$ and assuming $20\text{ }^{\circ}\text{C}$), this is another possible way to explain why our α derived from one Δh did not apply as well to another Δh .

Nevertheless, our use of our α_t determined from our steady-state model calibrations in our transient model did in fact capture the increase in mixing width during the transient conditions (Figure 2.7b). This seems to indicate that using α_t generated from steady-state transport observations in transient transport models generates results that are not particularly inaccurate. Yet clearly any dispersivity data drawn from the literature for use in modeling hyporheic processes must come from field or laboratory studies of similar spatial scale and resolution.

There are many important future directions to pursue. Subsequent studies could expand upon this work by using heterogeneous sediment including preferential flowpaths (Brunke 1999, Cardenas and Zlotnik 2003, Song et al. 2010, Le Borgne et al. 2014, Menichino et al. 2014, Menichino and Hester 2015, Briggs and Hare 2018, Lotts and Hester 2020). Reactions could be added, either abiotic (Santizo et al. 2020) or microbially mediated (Hester et al. 2019). Particulate carbon sources could be added that would form reactive microsites (Sawyer 2015).

More fundamentally, our choice of a 2D analysis, imposed limitations on the possible modes of mixing. The most effective way to enhance transverse mixing in 2D flow fields appears to be flow focusing from spatial heterogeneity of hydraulic conductivity (Werth et al. 2006, Rolle et al. 2009), possibly enhanced by temporal fluctuations (Hester et al. 2017). However, in 3D flow fields, an additional mixing mechanism which is not possible in 2D is helical flows from non-stationary anisotropy which creates twisting streamlines and ultimately greater stretching of solute into thin ribbons or fingers that in turn allow greater opportunity for molecular diffusion to enhance true mixing (Cirpka et al. 2015, Ye et al. 2016). These concepts applied to the hyporheic zone is an important area of future research.

Our results have many potential implications for managing water resources. For example, hydropower operations that create rapid stage shifts may enhance mixing-dependent hyporheic reactions in rivers. Prior studies have shown the significance of such conditions for reactions in bank sediment (Stegen et al. 2016, Shuai et al. 2017), but our results indicate their significance for reactions in bed sediment. Stream and river restoration practices such as in-stream structures and pool-riffle sequences (Anderson et al. 2005, Hester and Doyle 2008, Azinheira et al. 2014) that enhance the length of mixing zones may also enhance such reactions. Finally, fluctuating stage

and velocity from waves or tides may enhance such reactions in coastal settings (Cardenas et al. 2008, Lamontagne et al. 2018, Hester et al. 2019).

2.5 Conclusions

In a laboratory sediment (sand) tank we used a conservative dye to simulate transverse mixing zones between upwelling groundwater and bidirectional (hyporheic) exchange flows. We photographed the experiments and performed image analysis to quantify dye transport and mixing. We then manually calibrated numerical models to the laboratory experiments to investigate processes behind both steady-state and transient observed phenomena and estimate transverse dispersivities. We calculated mixing zone thickness (δ), as it is proportional to transverse dispersive fluxes, and therefore controls biogeochemical zonation and mixing-dependent reactions. We found mixing zones were thin ($\delta < 5$ cm) in the sediment tank, consistent with prior numerical modeling studies of transverse mixing between hyporheic flow cells and upwelling groundwater (e.g., Hester et al. 2013). Calibration of our numerical transport model to sediment tank transport indicated transverse dispersivity values (~ 0.1 mm) smaller than those derived from field studies of deeper groundwater, but consistent with prior lab studies conducted at similar spatial scales.

In both laboratory and modeling results, for both steady-state and transient conditions, increases in the surface water head drop that drives exchange flows (Δh) increased the flow rate and velocities in the induced hyporheic flow cell. At the same time, comparatively smaller variations in head gradients with deeper groundwater meant that increased Δh also led to decreased upward head gradients, leading to increased mixing zone length (Δs) and hence increased δ and dispersion coefficients. Thus, larger bedforms or reduced strength of gaining can enhance subsurface mixing. However, as Δh increased, the Peclet number (Pe) simultaneously increased and the dilution index (E_Q) simultaneously decreased, indicating that advection processes were enhanced even more than dispersion. More generally, Pe increased, and E_Q decreased with increasing δ , indicating that advection increased more than dispersion with increasing δ . This trend emphasizes that readily observable metrics such as δ provide an incomplete picture of the relative importance of mixing. A complete picture requires more theoretical metrics such as Pe and E_Q , which are more challenging to measure in the lab or field, and often require numerical simulations.

δ was greater for transient than steady-state conditions, probably because the change in boundary conditions shifted the location of the flowpath dividing the hyporheic flow cell from upwelling groundwater, which in turn likely added a transient advective front that experienced longitudinal dispersion. δ during transient experiments in the sediment tank exhibited temporal noise, perhaps due to the mixing zone moving past varying patterns of sediment packing. Numerical modeling showed that a major control of δ in shallow sediments is balance between flows from the surface water and groundwater boundaries.

Our results provide basic knowledge of mixing zone behavior in hyporheic sediments, with implications for hyporheic zone definitions, solute transport, reaction, and water quality.

Acknowledgements

We thank the Institute for Critical Technology and Applied Science at Virginia Tech for providing funding for the seepage and drainage tanks. We thank the Edna Bailey Sussman Fund for summer support to A. Nida and K. Santizo. We thank the National Science Foundation under award #1437021 for support to K. Santizo, M. Widdowson, and E. Hester. The opinions expressed are those of the authors and not necessarily those of the NSF. We thank Olaf Cirpka and two anonymous reviewers for helpful comments that greatly improved this manuscript. Data will be published in Hydroshare (www.hydroshare.org), and a link to the data archive will be included here if the manuscript is accepted for publication.

References

- Abarca, E., and T. P. Clement. 2009. A novel approach for characterizing the mixing zone of a saltwater wedge. *Geophysical Research Letters* **36**.
- Anderson, J. K., S. M. Wondzell, M. N. Gooseff, and R. Haggerty. 2005. Patterns in stream longitudinal profiles and implications for hyporheic exchange flow at the H.J. Andrews Experimental Forest, Oregon, USA. *Hydrological Processes* **19**:2931-2949.
- Anneser, B., F. Einsiedl, R. U. Meckenstock, L. Richters, F. Wisotzky, and C. Griebler. 2008. High-resolution monitoring of biogeochemical gradients in a tar oil-contaminated aquifer. *Applied Geochemistry* **23**:1715-1730.
- Azinhaira, D. L., D. T. Scott, W. C. Hession, and E. T. Hester. 2014. Comparison of effects of inset floodplains and hyporheic exchange induced by in-stream structures on solute retention. *Water Resources Research* **50**:6168-6190.
- Ballarini, E., S. Bauer, C. Eberhardt, and C. Beyer. 2014. Evaluation of the Role of Heterogeneities on Transverse Mixing in Bench-Scale Tank Experiments by Numerical Modeling. *Groundwater* **52**:368-377.
- Bandopadhyay, A., P. Davy, and T. Le Borgne. 2018. Shear flows accelerate mixing dynamics in hyporheic zones and hillslopes. *Geophysical Research Letters* **45**:GL079914.
- Bauer, R. D., M. Rolle, P. Kurzinger, P. Grathwohl, R. U. Meckenstock, and C. Griebler. 2009. Two-dimensional flow-through microcosms - Versatile test systems to study biodegradation processes in porous aquifers. *Journal of Hydrology* **369**:284-295.
- Baxter, C. V., and F. R. Hauer. 2000. Geomorphology, hyporheic exchange, and selection of spawning habitat by bull trout (*Salvelinus confluentus*). *Canadian Journal of Fisheries and Aquatic Sciences* **57**:1470-1481.
- Bear, J. 1972. *Dynamics of fluids in porous media*. Dover Publications, Inc., New York, NY.
- Bencala, K. E. 2000. Hyporheic zone hydrological processes. *Hydrological Processes* **14**:2797-2798.
- Benekos, I. D., O. A. Cirpka, and P. K. Kitanidis. 2006. Experimental determination of transverse dispersivity in a helix and a cochlea. *Water Resources Research* **42**:W07406.
- Bianchin, M. S., L. Smith, and R. D. Beckie. 2011. Defining the hyporheic zone in a large tidally influenced river. *Journal of Hydrology* **406**:16-29.
- Bijeljic, B., and M. J. Blunt. 2007. Pore-scale modeling of transverse dispersion in porous media. *Water Resources Research* **43**:W12S11.
- Boulton, A. J., S. Findlay, P. Marmonier, E. H. Stanley, and H. M. Valett. 1998. The functional significance of the hyporheic zone in streams and rivers. *Annual Review of Ecology and Systematics* **29**:59-81.
- Briggs, M. A., and D. K. Hare. 2018. Explicit consideration of preferential groundwater discharges as surface water ecosystem control points. *Hydrological Processes* **32**:2435-2440.

- Brunke, M. 1999. Colmation and depth filtration within streambeds: Retention of particles in hyporheic interstices. *International Review of Hydrobiology* **84**:99-117.
- Brunke, M., and T. Gonser. 1997. The ecological significance of exchange processes between rivers and groundwater. *Freshwater Biology* **37**:1-33.
- Cardenas, M. B. 2008. Surface water-groundwater interface geomorphology leads to scaling of residence times. *Geophysical Research Letters* **35**.
- Cardenas, M. B., P. L. M. Cook, H. S. Jiang, and P. Traykovski. 2008. Constraining denitrification in permeable wave-influenced marine sediment using linked hydrodynamic and biogeochemical modeling. *Earth and Planetary Science Letters* **275**:127-137.
- Cardenas, M. B., and J. L. Wilson. 2007. Thermal regime of dune-covered sediments under gaining and losing water bodies. *Journal of Geophysical Research-Biogeosciences* **112**:G04013.
- Cardenas, M. B., and V. A. Zlotnik. 2003. Three-dimensional model of modern channel bend deposits. *Water Resources Research* **39**:1141.
- Castro-Alcala, E., D. Fernandez-Garcia, J. Carrera, and D. Bolster. 2012. Visualization of Mixing Processes in a Heterogeneous Sand Box Aquifer. *Environmental Science & Technology* **46**:3228-3235.
- Chiogna, G., O. A. Cirpka, P. Grathwohl, and M. Rolle. 2011a. Relevance of local compound-specific transverse dispersion for conservative and reactive mixing in heterogeneous porous media. *Water Resources Research* **47**:15.
- Chiogna, G., O. A. Cirpka, P. Grathwohl, and M. Rolle. 2011b. Transverse mixing of conservative and reactive tracers in porous media: Quantification through the concepts of flux-related and critical dilution indices. *Water Resources Research* **47**.
- Chiogna, G., C. Eberhardt, P. Grathwohl, O. A. Cirpka, and M. Rolle. 2010. Evidence of Compound-Dependent Hydrodynamic and Mechanical Transverse Dispersion by Multitracer Laboratory Experiments. *Environmental Science & Technology* **44**:688-693.
- Chou, P. Y., and G. Wyseure. 2009. Hydrodynamic dispersion characteristics of lateral inflow into a river tested by a laboratory model. *Hydrology and Earth System Sciences* **13**:217-228.
- Cirpka, O. A., G. Chiogna, M. Rolle, and A. Bellin. 2015. Transverse mixing in three-dimensional nonstationary anisotropic heterogeneous porous media. *Water Resources Research* **51**:241-260.
- Cirpka, O. A., A. Olsson, Q. S. Ju, M. A. Rahman, and P. Grathwohl. 2006. Determination of transverse dispersion coefficients from reactive plume lengths. *Ground Water* **44**:212-221.
- Conant, B., J. A. Cherry, and R. W. Gillham. 2004. A PCE groundwater plume discharging to a river: influence of the streambed and near-river zone on contaminant distributions. *Journal of Contaminant Hydrology* **73**:249-279.
- Cook, P. L. M., F. Wenzhoefer, S. Rysgaard, O. S. Galaktionov, F. J. R. Meysman, B. D. Eyre, J. Cornwell, M. Huettel, and R. N. Glud. 2006. Quantification of denitrification in permeable

- sediments: Insights from a two-dimensional simulation analysis and experimental data. *Limnology and Oceanography-Methods* **4**:294-307.
- de Anna, P., M. Dentz, A. Tartakovsky, and T. Le Borgne. 2014. The filamentary structure of mixing fronts and its control on reaction kinetics in porousmedia flows. *Geophysical Research Letters* **41**:4586-4593.
- Delgado, J. M. P. Q. 2006. A critical review of dispersion in packed beds. *Heat and Mass Transfer* **42**:279-310.
- Domenico, P., and F. Schwartz. 1998. *Physical and chemical hydrogeology*. John Wiley and Sons, Inc., New York, NY.
- Domenico, P. A., and M. D. Mifflin. 1965. WATER FROM LOW-PERMEABILITY SEDIMENTS AND LAND SUBSIDENCE. *Water Resources Research* **1**:563-&.
- Elliott, A. H., and N. H. Brooks. 1997. Transfer of nonsorbing solutes to a streambed with bed forms: Laboratory experiments. *Water Resources Research* **33**:137-151.
- Endreny, T., L. Lautz, and D. Siegel. 2011. Hyporheic flow path response to hydraulic jumps at river steps: Hydrostatic model simulations. *Water Resources Research* **47**.
- Fox, A., G. Laube, C. Schmidt, J. H. Fleckenstein, and S. Arnon. 2016. The effect of losing and gaining flow conditions on hyporheic exchange in heterogeneous streambeds. *Water Resources Research* **52**:7460-7477.
- Freeze, R. A., and J. A. Cherry. 1979. *Groundwater*. Prentice-Hall, Inc, Englewood Cliffs, NJ.
- Freitas, J. G., M. O. Rivett, R. S. Roche, M. Durrant, C. Walker, and J. H. Tellam. 2015. Heterogeneous hyporheic zone dechlorination of a TCE groundwater plume discharging to an urban river reach. *Science of the Total Environment* **505**:236-252.
- Gaganis, P., E. D. Skouras, M. A. Theodoropoulou, C. D. Tsakiroglou, and V. N. Burganos. 2005. On the evaluation of dispersion coefficients from visualization experiments in artificial porous media. *Journal of Hydrology* **307**:79-91.
- Gelhar, L. W., C. Welty, and K. R. Rehfeldt. 1992. A critical-review of data on field-scale dispersion in aquifers. *Water Resources Research* **28**:1955-1974.
- Gomez-Velez, J. D., J. Harvey, M. B. Cardenas, and B. Kiel. 2015. Denitrification in the Mississippi River network controlled by flow through river bedforms. *Nature Geoscience* **8**:941-U975.
- Gomez, J. D., J. L. Wilson, and M. B. Cardenas. 2012. Residence time distributions in sinuosity-driven hyporheic zones and their biogeochemical effects. *Water Resources Research* **48**.
- Harbaugh, A. W. 1990. A Computer Program for Calculating Subregional Water Budgets Using Results from the U.S. Geological Survey Modular Three-dimensional Finite-difference Ground-water Flow Model. Open-File Report 90-392. . United States Geological Survey Reston, VA.

- Harbaugh, A. W. 2005. MODFLOW-2005, the U.S. Geological Survey modular ground-water model -- the Ground-Water Flow Process: U.S. Geological Survey Techniques and Methods 6-A16. U.S. Geological Survey, Reston, VA.
- Harvey, J. W., and B. J. Wagner. 2000. Quantifying hydrologic interactions between streams and their subsurface hyporheic zones. Pages 3-44 in J. B. Jones and P. J. Mulholland, editors. Streams and ground waters. Academic Press, San Diego, CA.
- Hedin, L. O., J. C. von Fischer, N. E. Ostrom, B. P. Kennedy, M. G. Brown, and G. P. Robertson. 1998. Thermodynamic constraints on nitrogen transformations and other biogeochemical processes at soil-stream interfaces. *Ecology* **79**:684-703.
- Hester, E. T., M. B. Cardenas, R. Haggerty, and S. V. Apte. 2017. The importance and challenge of hyporheic mixing. *Water Resources Research* **53**:3565-3575.
- Hester, E. T., and M. W. Doyle. 2008. In-stream geomorphic structures as drivers of hyporheic exchange. *Water Resources Research* **44**:W03417.
- Hester, E. T., L. E. Eastes, and M. A. Widdowson. 2019. Effect of Surface Water Stage Variation on Mixing-Dependent Hyporheic Denitrification in Riverbed Dunes. *Water Resources Research* **55**:4668-4687.
- Hester, E. T., and M. N. Gooseff. 2010. Moving Beyond the Banks: Hyporheic Restoration Is Fundamental to Restoring Ecological Services and Functions of Streams. *Environmental Science & Technology* **44**:1521-1525.
- Hester, E. T., B. Hammond, and D. T. Scott. 2016. Effects of inset floodplains and hyporheic exchange induced by in-stream structures on nitrate removal in a headwater stream. *Ecological Engineering* **97**:452-464.
- Hester, E. T., K. I. Young, and M. A. Widdowson. 2013. Mixing of surface and groundwater induced by riverbed dunes: implications for hyporheic zone definitions and pollutant reactions. *Water Resources Research* **49**:5221-5237.
- Hester, E. T., K. I. Young, and M. A. Widdowson. 2014. Controls on mixing-dependent denitrification in hyporheic zones induced by riverbed dunes: A steady state modeling study. *Water Resources Research* **50**:9048-9066.
- Huang, W. E., C. C. Smith, D. N. Lerner, S. F. Thornton, and A. Oram. 2002. Physical modelling of solute transport in porous media: evaluation of an imaging technique using UV excited fluorescent dye. *Water Research* **36**:1843-1853.
- Huettel, M., W. Ziebis, and S. Forster. 1996. Flow-induced uptake of particulate matter in permeable sediments. *Limnology and Oceanography* **41**:309-322.
- Jin, G. Q., H. W. Tang, B. Gibbes, L. Li, and D. A. Barry. 2010. Transport of nonsorbing solutes in a streambed with periodic bedforms. *Advances in Water Resources* **33**:1402-1416.
- Kaufman, M. H., M. B. Cardenas, J. Buttles, A. J. Kessler, and P. L. M. Cook. 2017. Hyporheic hot moments: Dissolved oxygen dynamics in the hyporheic zone in response to surface flow perturbations. *Water Resources Research* **53**:6642-6662.

- Kessler, A. J., R. N. Glud, M. B. Cardenas, M. Larsen, M. F. Bourke, and P. L. M. Cook. 2012. Quantifying denitrification in rippled permeable sands through combined flume experiments and modeling. *Limnology and Oceanography* **57**:1217-1232.
- Knights, D., A. H. Sawyer, R. T. Barnes, C. T. Musial, and S. Bray. 2017. Tidal controls on riverbed denitrification along a tidal freshwater zone. *Water Resources Research* **53**:799-816.
- Kwon, E. Y., G. Kim, F. Primeau, W. S. Moore, H. M. Cho, T. DeVries, J. L. Sarmiento, M. A. Charette, and Y. K. Cho. 2014. Global estimate of submarine groundwater discharge based on an observationally constrained radium isotope model. *Geophysical Research Letters* **41**:8438-8444.
- Lamontagne, S., F. Cosme, A. Minard, and A. Holloway. 2018. Nitrogen attenuation, dilution and recycling in the intertidal hyporheic zone of a subtropical estuary. *Hydrology and Earth System Sciences* **22**:4083-4096.
- Landmeyer, J. E., P. M. Bradley, D. A. Trego, K. G. Hale, and J. E. Haas. 2010. MTBE, TBA, and TAME Attenuation in Diverse Hyporheic Zones. *Ground Water* **48**:30-41.
- Lautz, L. K., and D. I. Siegel. 2006. Modeling surface and ground water mixing in the hyporheic zone using MODFLOW and MT3D. *Advances in Water Resources* **29**:1618-1633.
- Le Borgne, T., T. R. Ginn, and M. Dentz. 2014. Impact of fluid deformation on mixing-induced chemical reactions in heterogeneous flows. *Geophysical Research Letters* **41**:7898-7906.
- Liu, D. S., J. Zhao, W. H. Jeon, and J. Y. Lee. 2019. Solute dynamics across the stream-to-riparian continuum under different flood waves. *Hydrological Processes* **33**:2627-2641.
- Lotts, W. S., and E. T. Hester. 2020. Filling the void: the effect of riverbank soil pipes on transient hyporheic exchange during a peak flow event. *Water Resources Research* **56** e2019WR025959.
- Lowell, J. L., N. Gordon, D. Engstrom, J. A. Stanford, W. E. Holben, and J. E. Gannon. 2009. Habitat Heterogeneity and Associated Microbial Community Structure in a Small-Scale Floodplain Hyporheic Flow Path. *Microbial Ecology* **58**:611-620.
- Luo, J., and O. A. Cirpka. 2011. How well do mean breakthrough curves predict mixing-controlled reactive transport? *Water Resources Research* **47**:W02520
- Marion, A., M. Bellinello, I. Guymer, and A. Packman. 2002. Effect of bed form geometry on the penetration of nonreactive solutes into a streambed. *Water Resources Research* **38**:1209.
- Menichino, G. T., and E. T. Hester. 2015. The effect of macropores on bi-directional hydrologic exchange between a stream channel and riparian groundwater. *Journal of Hydrology* **529**:830-842.
- Menichino, G. T., A. S. Ward, and E. T. Hester. 2014. Macropores as preferential flow paths in meander bends. *Hydrological Processes* **28** 482-495.
- Molz, F. J., and M. A. Widdowson. 1988. Internal inconsistencies in dispersion-dominated models that incorporate chemical and microbial kinetics. *Water Resources Research* **24**:615-619.

- Musial, C. T., A. H. Sawyer, R. T. Barnes, S. Bray, and D. Knights. 2016. Surface water-groundwater exchange dynamics in a tidal freshwater zone. *Hydrological Processes* **30**:739-750.
- Naranjo, R. C., R. G. Niswonger, and C. J. Davis. 2015. Mixing effects on nitrogen and oxygen concentrations and the relationship to mean residence time in a hyporheic zone of a riffle-pool sequence. *Water Resources Research* **51**:7202-7217.
- Naranjo, R. C., G. Pohll, R. G. Niswonger, M. Stone, and A. McKay. 2013. Using heat as a tracer to estimate spatially distributed mean residence times in the hyporheic zone of a riffle-pool sequence. *Water Resources Research* **49**:3697-3711.
- Packman, A., M. Salehin, and M. Zaramella. 2004. Hyporheic exchange with gravel beds: Basic hydrodynamic interactions and bedform-induced advective flows. *Journal of Hydraulic Engineering-Asce* **130**:647-656.
- Packman, A. I., and J. S. MacKay. 2003. Interplay of stream-subsurface exchange, clay particle deposition, and streambed evolution. *Water Resources Research* **39**:1097.
- Pickens, J. F., and G. E. Grisak. 1981. Scale-dependent dispersion in a stratified granular aquifer. *Water Resources Research* **17**:1191-1211.
- Pool, M., and M. Dentz. 2018. Effects of Heterogeneity, Connectivity, and Density Variations on Mixing and Chemical Reactions Under Temporally Fluctuating Flow Conditions and the Formation of Reaction Patterns. *Water Resources Research* **54**:186-204.
- Pool, M., V. E. A. Post, and C. T. Simmons. 2014. Effects of tidal fluctuations on mixing and spreading in coastal aquifers: Homogeneous case. *Water Resources Research* **50**:6910-6926.
- Precht, E., U. Franke, L. Polerecky, and M. Huettel. 2004. Oxygen dynamics in permeable sediments with wave driven pore water exchange. *Limnology and Oceanography* **49**:693-705.
- Qian, Q., V. R. Voller, and H. G. Stefan. 2008. A vertical dispersion model for solute exchange induced by underflow and periodic hyporheic flow in a stream gravel bed. *Water Resources Research* **44**:W07422.
- Rahman, M. A., S. C. Jose, W. Nowak, and O. A. Cirpka. 2005. Experiments on vertical transverse mixing in a large-scale heterogeneous model aquifer. *Journal of Contaminant Hydrology* **80**:130-148.
- Robinson, G., G. A. Hamill, and A. A. Ahmed. 2015. Automated image analysis for experimental investigations of salt water intrusion in coastal aquifers. *Journal of Hydrology* **530**:350-360.
- Rolle, M., G. Chiogna, D. L. Hochstetler, and P. K. Kitanidis. 2013. On the importance of diffusion and compound-specific mixing for groundwater transport: An investigation from pore to field scale. *Journal of Contaminant Hydrology* **153**:51-68.

- Rolle, M., C. Eberhardt, G. Chiogna, O. A. Cirpka, and P. Grathwohl. 2009. Enhancement of dilution and transverse reactive mixing in porous media: Experiments and model-based interpretation. *Journal of Contaminant Hydrology* **110**:130-142.
- Rolle, M., D. Hochstetler, G. Chiogna, P. K. Kitanidis, and P. Grathwohl. 2012. Experimental Investigation and Pore-Scale Modeling Interpretation of Compound-Specific Transverse Dispersion in Porous Media. *Transport in Porous Media* **93**:347-362.
- Santizo, K. Y., M. A. Widdowson, and E. T. Hester. 2020. Abiotic mixing-dependent reaction in a laboratory simulated hyporheic zone. *Water Resources Research*:Accepted.
- Sawyer, A. H. 2015. Enhanced removal of groundwater-borne nitrate in heterogeneous aquatic sediments. *Geophysical Research Letters* **42**:403-410.
- Sawyer, A. H., and M. B. Cardenas. 2009. Hyporheic flow and residence time distributions in heterogeneous cross-bedded sediment. *Water Resources Research* **45**:W08406.
- Sawyer, A. H., M. B. Cardenas, A. Bomar, and M. Mackey. 2009. Impact of dam operations on hyporheic exchange in the riparian zone of a regulated river. *Hydrological Processes* **23**:2129-2137.
- Scheidegger, A. E. 1961. General Theory of Dispersion in Porous Media. *Journal of Geophysical Research* **66**:3273-3278.
- Scheven, U. M. 2013. Pore-Scale Mixing and Transverse Dispersivity of Randomly Packed Monodisperse Spheres. *Physical Review Letters* **110**:214504
- Schnoor, J. L. 1996. *Environmental Modeling*. John Wiley & Sons, Inc., New York, NY.
- Shuai, P., M. B. Cardenas, P. S. K. Knappett, P. C. Bennett, and B. T. Neilson. 2017. Denitrification in the banks of fluctuating rivers: The effects of river stage amplitude, sediment hydraulic conductivity and dispersivity, and ambient groundwater flow. *Water Resources Research* **53**:7951-7967.
- Song, J. X., X. H. Chen, C. Cheng, D. M. Wang, and W. K. Wang. 2010. Variability of streambed vertical hydraulic conductivity with depth along the Elkhorn River, Nebraska, USA. *Chinese Science Bulletin* **55**:992-999.
- Stanford, J. A., and A. R. Gaufin. 1974. Hyporheic communities of two Montana rivers. *Science* **185**:700-702.
- Stegen, J. C., J. K. Fredrickson, M. J. Wilkins, A. E. Konopka, W. C. Nelson, E. V. Arntzen, W. B. Chrisler, R. K. Chu, R. E. Danczak, S. J. Fansler, D. W. Kennedy, C. T. Resch, and M. Tfaily. 2016. Groundwater-surface water mixing shifts ecological assembly processes and stimulates organic carbon turnover. *Nature Communications* **7**.
- Thibodeaux, L. J., and J. D. Boyle. 1987. Bedform-Generated Convective-Transport in Bottom Sediment. *Nature* **325**:341-343.
- Tonina, D., and J. M. Buffington. 2007. Hyporheic exchange in gravel bed rivers with pool-riffle morphology: Laboratory experiments and three-dimensional modeling. *Water Resources Research* **43**:W01421.

- Trauth, N., C. Schmidt, M. Vieweg, S. E. Oswald, and J. H. Fleckenstein. 2015. Hydraulic controls of in-stream gravel bar hyporheic exchange and reactions. *Water Resources Research* **51**:2243-2263.
- Triska, F. J., V. C. Kennedy, R. J. Avanzino, G. W. Zellweger, and K. E. Bencala. 1989. Retention and Transport of Nutrients in a 3rd-Order Stream in Northwestern California - Hyporheic Processes. *Ecology* **70**:1893-1905.
- Van Breukelen, B. M., and M. Rolle. 2012. Transverse Hydrodynamic Dispersion Effects on Isotope Signals in Groundwater Chlorinated Solvents' Plumes. *Environmental Science & Technology* **46**:7700-7708.
- Weinstein, Y., Y. Yechieli, Y. Shalem, W. C. Burnett, P. W. Swarzenski, and B. Herut. 2011. What Is the Role of Fresh Groundwater and Recirculated Seawater in Conveying Nutrients to the Coastal Ocean? *Environmental Science & Technology* **45**:5195-5200.
- Werth, C. J., O. A. Cirpka, and P. Grathwohl. 2006. Enhanced mixing and reaction through flow focusing in heterogeneous porous media. *Water Resources Research* **42**:W12414.
- White, D. S. 1993. Perspectives on defining and delineating hyporheic zones. *Journal of the North American Benthological Society* **12**:61-69.
- Winter, T. C., J. W. Harvey, O. L. Franke, and W. M. Alley. 1998. Ground Water and Surface Water, A Single Resource, Circular 1139. . U.S. Geological Survey, Denver, CO.
- Ye, Y., G. Chiogna, O. Cirpka, P. Grathwohl, and M. Rolle. 2015. Experimental investigation of compound-specific dilution of solute plumes in saturated porous media: 2-D vs. 3-D flow-through systems. *Journal of Contaminant Hydrology* **172**:33-47.
- Ye, Y., G. Chiogna, O. A. Cirpka, P. Grathwohl, and M. Rolle. 2016. Experimental investigation of transverse mixing in porous media under helical flow conditions. *Physical Review E* **94**.
- Zech, A., S. Attinger, A. Bellin, V. Cvetkovic, P. Dietrich, A. Fiori, G. Teutsch, and G. Dagan. 2019. A Critical Analysis of Transverse Dispersivity Field Data. *Groundwater* **57**:632-639.
- Zheng, C., and G. D. Bennett. 2002. *Applied Contaminant Transport Modeling, Second Edition*. John Wiley and Sons, Inc., New York, NY.
- Zheng, C. M., and P. P. Wang. 1999. MT3DMS. A modular three-dimensional multispecies transport model for simulation of advection, dispersion, and chemical reactions of contaminants in groundwater systems. Documentation and User's Guide. Prepared for U.S. Corps of Engineers, Washington, DC 20314-1000.

Chapter 3. Abiotic mixing-dependent reaction in a laboratory simulated hyporheic zone

Authors: Katherine Y. Santizo, Mark A. Widdowson, and Erich T. Hester*

Affiliations: Charles E. Via Jr. Department of Civil and Environmental Engineering, Virginia Tech

Keywords: surface water-groundwater interaction, optode, dispersion, dissolved oxygen

Status: This manuscript was accepted and published in *Water Resources Research*. It is reprinted in this dissertation under license number 5047880480141.

Abstract

Groundwater (GW) contaminants upwelling toward surface water (SW) can attenuate in the hyporheic zone, with dissolved oxygen (DO) frequently controlling the attenuation. In a laboratory mesocosm, we induced downwelling of SW into the sediments to create a hyporheic flow cell (HFC). We added DO to downwelling SW and sodium sulfite (Na_2SO_3) to anoxic upwelling GW to induce an abiotic mixing-dependent reaction along the mixing zone between the HFC and upwelling GW. Using planar optodes and SO_4 measurements, we observed movement of the DO mixing zone (oxic front position), extent of DO mixing (mixing zone thickness), and location of MD reaction (SO_4 peak concentration). Oxic front position and mixing zone thickness were stable during non-reactive control experiments, indicating that dispersion of DO across the mixing zone had come into equilibrium with supply of DO to the mixing zone. By contrast, mixing

zone thickness shrank over time during the reaction experiments, as MD reaction consumed DO in the mixing zone. The decrease in mixing zone thickness for the reaction experiments indicates steeper DO gradients and greater dispersion (transport) limitation, quantified by Damkohler numbers farther above unity. Maximum SO_4 concentrations always occurred further from the center of the HFC (i.e., more toward surrounding upwelling GW) than did the oxic front. In most riverbeds, transport and mixing dynamics are thus superimposed upon existing hydraulic dynamics, with implications for monitoring and attenuation of contaminants.

Plain Language Summary

Groundwater (GW) contaminants approaching surface water (SW) can be removed in shallow sediments (hyporheic zone), with dissolved oxygen (DO) frequently a controlling factor in the removal. These reactions sometimes require mixing of chemicals coming from SW and GW. We simulated such a mixing zone in shallow laboratory sediments, including 1) a non-reactive control experiment where DO coming from SW mixed with water without DO coming from deeper GW, and 2) a non-biological mixing-dependent reaction of sodium sulfite (Na_2SO_3) in GW with DO in surface water (SW) to produce sulfate (SO_4). We found that the concentration patterns for the control experiments were stable over time, but those for the reaction experiments were more dynamic. This was confirmed by differences in location of peak product (SO_4) concentration and that of the current DO mixing zone. Thus, in most riverbeds, transport and mixing dynamics are superimposed upon hydraulic dynamics, with implications for monitoring and attenuation of GW contaminants approaching surface water.

Key Points

1. Hyporheic mixing-dependent reactions are simulated in a laboratory mesocosm and observed with dissolved oxygen planar optode
2. Mixing zone position and thickness varied during reaction experiment but not control; reaction product peak concentration occurred outside mixing zone
3. Even with steady hydraulics, interaction and feedback between reaction and dispersion created dynamic biogeochemical patterns

3.1 Introduction

The hyporheic zone is the riverbed interface where surface water (SW) and groundwater (GW) exchange and mix, enhancing biogeochemical processes in the presence of a diverse and abundant microbial community (Cardenas et al., 2004; Caruso et al., 2017; Sawyer & Cardenas, 2009; Stegen et al., 2016; White, 2006; Zarnetske et al., 2011a). Hyporheic exchange forms hyporheic flow cells (HFC's) in the subsurface that are driven by bedforms (e.g., ripples, dunes, bars, riffles), in-stream structures, meanders and large valley-scale morphology (Azinheira et al., 2014; Elliott & Brooks, 1997; Hester et al., 2014; Kiel & Bayani Cardenas, 2014; Landmeyer et al., 2010; Naranjo et al., 2015). Some of the most important factors controlling exchange and function are sediment hydraulic conductivity, strength of river gaining, and depth of alluvium.

GW contaminants in upwelling flowpaths are known to attenuate in the hyporheic zone even in the absence of attenuation in the upgradient aquifer, reducing impacts to SW quality (Conant et al., 2004; Freitas et al., 2015; Landmeyer et al., 2010; Stuart et al., 2014). Freitas et al. (2015) observed the natural dechlorination of a discharging chloroethene GW plume in an urban streambed. Conant et al. (2004) showed reduction in a tetrachloroethene plume concentration as it approached SW and simultaneous production of daughter products (e.g., dichloroethene). Landmeyer et al. (2010) showed attenuation of fuel-derived contaminants in the hyporheic zone prior to discharging to a river.

Other studies have focused on nutrient dynamics in the hyporheic zone, particularly nitrogen (Azinheira et al., 2014; Gomez-Velez et al., 2015; Harvey et al., 2013a; Hester et al., 2013; Naranjo et al., 2015; Puckett et al., 2008; Sawyer, 2015; Stelzer et al., 2011; Triska et al., 1989; Zarnetske et al., 2011b, 2011a, 2012). Naranjo et al. (2015) conducted a field study showing that hyporheic mixing increased with channel flow rate as more SW cycled through the HFC, and this in turn increased nitrification due to increased downwelling flux of dissolved oxygen (DO) and NH_4 . Zarnetske et al. (2011a) demonstrated that injecting labile DOC in an anoxic HFC enhanced net denitrification. These studies indicate the master role DO plays in reactions that affect contaminants in the hyporheic zone, yet these studies did not fully quantify the relative contributions and interaction of processes such as mixing, dilution, and reaction that may contribute to observed changes in concentration.

3.1.1 Hyporheic Mixing-Dependent Reactions and Their Quantification

Mixing-dependent (i.e. mixing-controlled or mixing-limited) reactions in porous media were first studied in deeper aquifers where transverse mixing and dispersion along the plume fringe is thought to contribute to GW contaminant plume attenuation (Bauer et al., 2008, 2009; Castro-Alcalá et al., 2012; Cirpka et al., 1999; Cirpka & Kitanidis, 2000; Kitanidis, 1994; F. Molz, 2015; F. J. Molz & Widdowson, 1988; Rolle et al., 2009, 2012). Rolle et al. (2009) interpreted 2D tracer and reaction data from a laboratory flow-through tank with a numerical model to show that high permeability zones had a greater influence on mixing than transient flow conditions. Bauer et al. (2008) concluded that toluene biodegradation along the plume fringe in a lab experiment was mixing-dependent due to the steep redox gradient. Molz (2015) cited various field studies of GW plumes in which steep vertical concentration gradients (i.e., thin mixing zone) persisted over relatively large travel distances for reactive GW constituents. Molz and Widdowson (1988) demonstrated local transverse dispersivity values on the order of 1mm or less were required to maintain these gradients. Yet these studies were not conducted in the unique conditions (e.g., steep hydraulic gradients, curvilinear flowpaths) of the hyporheic zone (Hester et al., 2017).

Most studies of hyporheic reactions evaluate non-mixing-dependent reactions in which SW constituents enter the hyporheic zone, undergo transformations, and then return to the SW body (Cardenas et al., 2004, 2008; Dentz et al., 2011; Kalbus et al., 2009; Kessler et al., 2012; Tonina & Bellin, 2008; Zhou et al., 2014). Few studies evaluate mixing-dependent reactions as the mechanism behind observed natural attenuation of GW pollutants that enter the hyporheic zone (Hester et al., 2013, 2014, 2019; Trauth & Fleckenstein, 2017). Contaminant transformations observed in upwelling flowpaths by studies discussed earlier (Conant et al., 2004; Kennedy et al., 2009; Landmeyer et al., 2010; Naranjo et al., 2015) may have been mixing-dependent reactions, but the datasets involved are inconclusive.

Using numerical models with local (rather than macro) dispersivities, Hester et al. (2013) quantified the extent of conservative tracer mixing between upwelling GW contaminants and the HFC at ~10% of upwelling GW, a result influenced by mixing zone length, transverse dispersivity and heterogeneity. Hester et al. (2014) added mixing-dependent and non-mixing-dependent denitrification, showing that mixing-dependent reactions could be significant for upwelling GW nitrate but were often less than non-mixing-dependent reaction of advected SW nitrate. Trauth and Fleckenstein (2017) and Hester et al. (2019) used models to show that mixing-dependent

denitrification increased with SW stage, with implications for storms, seasons, and river hydromodification. Yet to our knowledge, prior studies have not observed mixing-dependent reactions in the laboratory that allow careful 1) control of driving factors and 2) quantification of flow, transport, and reaction processes.

Mixing zone size (e.g., thickness, area) is an important metric of transverse dispersion (Hester et al., 2013) and hence potential for characterizing mixing-dependent reactions. For example, Abarca and Clement (2009) observed mixing-dependent reaction between alkaline freshwater and acidic saltwater in a 2D bench-scale experiment and determined mixing zone thickness defined as 10-90% volumetric fraction of saltwater to be about 1.5 cm. Bauer et al. (2008) also estimated mixing zone thickness between 0 and 1.2 cm with a maximum of over 2.4 cm, however, no concentration range is mentioned. Chiogna et al. (2011) quantified mixing zone as 16-84% of maximum concentrations for a mixing-dependent reaction modeled in a confined aquifer.

While these GW studies provide useful background for mixing-dependent reactions, they cannot be directly applied to reactions in the hyporheic zone due to greater temporal fluctuations in head gradients, greater spatial heterogeneity of hydraulic conductivity, and higher head gradients along the SW boundary that lead to greater porewater velocities, curvilinear flowpaths, and greater shear flow (Bandopadhyay et al., 2018; Hester et al., 2017).

3.1.2 Imaging in Subsurface Experiments

Many of the laboratory studies mentioned above used imaging to aid in observing the mixing processes and quantify mixing zone thickness. Robinson et al. (2016) used a high-speed camera to image salt-intrusion and a light intensity-concentration conversion to calculate mixing zone thickness. Castro-Alcalá et al. (2012) used a similar procedure to image rhodamine concentrations in a heterogeneous aquifer constructed in a laboratory sand box. Bauer et al. (2009) used planar optode strips to observe aerobic biodegradation of a GW toluene plume. Cardenas et al. (2016) used planar optodes to observe the spatial pattern of DO in flume-simulated fish nests with varying SW velocities.

More recently, Kaufman et al. (2017) used planar optodes to explore dynamic behavior of DO distribution in a dune-induced hyporheic zone due to changes in SW velocity. Similarly, Galloway et al. (2019) and Wolke et al. (2020) used planar optode for oxygen dynamics using

stream water and natural stream sediment. Galloway et al. (2019) evaluated oxygen dynamics under unsteady flow with various gaining and losing conditions and evaluated oxygen concentrations with the planar optode to calculate oxygenated areas. Likewise, Wolke et al. (2020) quantify oxygenated areas to determine oxygen dynamics and consumption based on migrating bedforms (i.e., bedform celerity). While these studies have helped understand oxygen dynamics in the hyporheic zone they do not analyze mixing-dependent reactions.

3.1.3 Purpose of Study

We are not aware of prior studies that rigorously evaluated hyporheic mixing-dependent reactions and their controls in a physical experiment, including any which took advantage of the expanded quantification possible with planar optodes. Here we simulated a hyporheic zone in a laboratory mesocosm to understand the evolution of mixing zones and mixing-dependent reactions, particularly those involving DO. Given the role of DO in mediating a wide range of important environmental water quality reactions and the availability of a DO planar optode for imaging, we purposefully chose to design the mixing-dependent reaction experiment to represent oxygen-limited conditions.

Our objectives were to 1) simulate an abiotic DO-consuming hyporheic mixing-dependent reaction in a laboratory mesocosm; 2) quantify the extent of mixing (mixing zone thickness and oxic front) and mixing-dependent reaction using DO planar optodes over time, 3) measure mixing-dependent reaction products and their evolution over time; and 4) evaluate the effect of varying the driving SW head gradient (Δh).

3.2 Materials and Methods

3.2.1 Laboratory Apparatus

We simulated a HFC typical of those induced by in-stream structures (Azinheira et al., 2014; Cardenas et al., 2004; Crispell & Endreny, 2009; Gooseff et al., 2006; Hester et al., 2017; Hester & Doyle, 2008) in a modified GUNT HM-169 drainage and seepage tank (Figure 3.1). These flowpaths are also similar in shape and thus mixing zone characteristics to those induced by ripples and dunes (Cardenas et al., 2004; Elliott & Brooks, 1997; Hester et al., 2013). Since this study is the first physical experiment to simulate mixing-dependent reactions in the hyporheic zone, we intentionally created hydraulics that were steady-state as a useful starting point. To provide a light-controlled environment for imaging of the optode, an enclosure of black duvetyn fabric over a black polyvinyl chloride pipe framework was used.

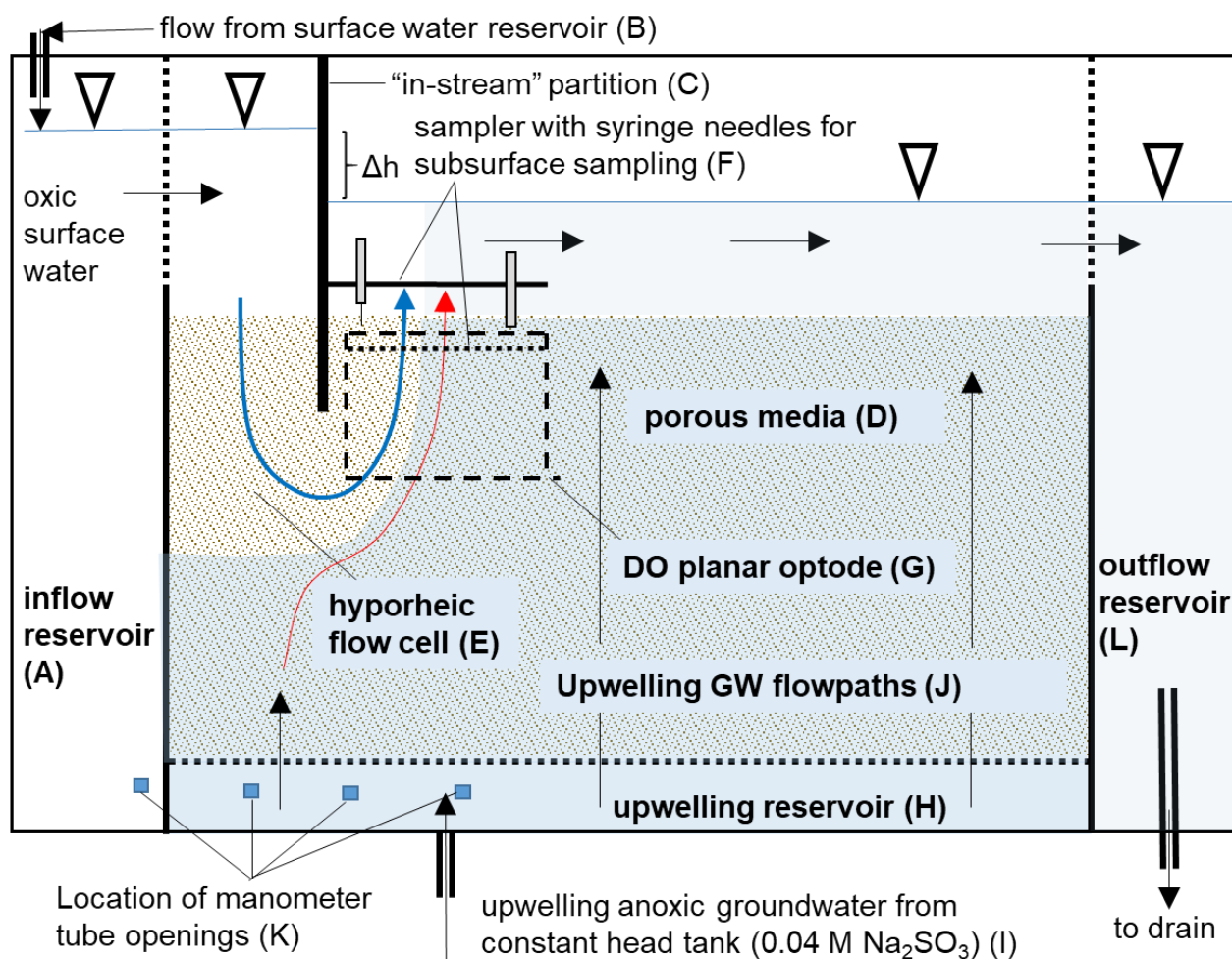


Figure 3.1. Schematic of porous media mesocosm used for laboratory experiments. (A) Inflow oxic reservoir which aids setting up head drop (Δh) and receives oxic water from surface water (SW) reservoir (B). (C) “in-stream” partition in (D) porous media (80 cm x 43 cm x 10 cm) to create (E) hyporheic flow cell (HFC). (F) Plastic sampler (solid black line) added to mesocosm to hold mini-piezometers and syringes used for subsurface head measurements and SO_4 sampling, respectively, which occurred 2-3 cm beneath the sediment-water interface (dotted line). (G) Planar optode used to observe mixing/oxygen concentration (dashed line). (H) Upwelling anoxic reservoir receiving anoxic GW from (I) an Argon-purged upwelling line that was used to create (J) upwelling flowpaths. (K) Built-in mesocosm manometers with measurement locations shown from left to right, (positions 3, 6, 9, and 12 in Figure Appendix B S4). (L) Outflow reservoir that aids in setting up head drop (Δh) and connects to the drain. Solid lines between boundary reservoirs and sand are impermeable partitions, while dotted lines are permeable screens.

We created an HFC within the porous media (Figure 3.1D) using an embedded partition that induced a Δh in the SW (Δh in Figure 3.1). The partition was located 22 cm from the left boundary and penetrated the sediment to a depth of 6.5 cm vertically. The sand was homogeneous Ottawa Flint silica #12 ($d_{50}=0.53$ mm) from US Silica. We estimated hydraulic conductivity (57 m/d) using a constant-head permeameter, and porosity (0.4) by measuring volumes of sediment and porewater (Table 3.1).

The mesocosm contained two source water inflows (i.e., SW and GW), neither of which recirculated, but instead flowed through the mesocosm from their respective sources and then exited to the drain in order to simulate field conditions. Surface water was fed into the inflow reservoir (Figure 3.1A) from an external 45-liter feed tank (Figure 3.1B) through a valve-controlled built-in pump running 1.14 ± 0.12 liters per minute as measured by an inline needle valve flow meter (Table 3.1). Surface water then flowed through the HFC and exited via the outflow reservoir (Figure 3.1L). Groundwater entered via the upwelling reservoir (Figure 3.1H) from an external 40-liter constant head tank that was fed from a 227-liter upwelling GW reservoir by a peristaltic Geotech pump. Groundwater from the upwelling reservoir then flowed through the sand and exited the mesocosm via the SW outflow reservoir. The height of the constant head tank allowed for the flow of upwelling GW to be gravity driven and was set for each Δh such that the heads in the inflow and upwelling reservoirs were similar, in order to prevent direct flow through the sand between those two reservoirs, which in turn would prevent formation of an HFC. An inline upwelling flowmeter (Saim LZT) with a metering valve was inserted in the line connecting the constant head tank and upwelling reservoir and used to maintain a flow rate of 1.15 ± 0.05 liters per minute (Table 3.1) to insure a stable steady-state HFC. The inflow and outflow reservoirs together maintained constant and controllable Δh . The particular values for Δh were chosen based on the physical constraints of the mesocosm and ensuring that the HFC was within the optode boundaries, and are consistent with those measured in field settings (Azinheira et al., 2014; Elliott & Brooks, 1997; Hester & Doyle, 2008).

Built-in manometers (Figure 3.1K) were used to measure heads in the upwelling reservoir (Figure 3.1H). We installed a “sampler” at the top of the porous media used to place mini-piezometers and 1-mL needle syringes for chemical sampling (described in Section 3.2.3 below)

(Figure 3.1F). The sampler was constructed from an acrylonitrile butadiene styrene plastic sheet with placements drilled with equal spacing for precise and repeatable sampling.

Table 3.1. Mixing-dependent reaction experiment set-up values

Temperature (°C)	18-22	18-22
Sediment Hydraulic Conductivity (m/d)	57	57
Sediment Porosity (-)	0.4	0.4
SW Hydraulic Head Drop (cm)	4.5	6.0
Upwelling Inflow Rate (liters per minute)	1.15±0.05	1.15±0.05
Downwelling Inflow Rate (i.e., HFC flow rate, liters per minute)	1.14±0.12	1.14±0.12
Sampling Depth (cm)	2-3	2-3
Sodium Sulfite (Na ₂ SO ₃) Concentration (mol/L)	0.04	0.04

3.2.2 Experiments

A mixing-dependent reaction was designed to occur at the interface of the HFC and the upwelling GW within the porous media (Figure 3.1D&E). Sodium sulfite (Na₂SO₃) from upwelling GW mixed and reacted with DO from SW to form sodium sulfate (Na₂SO₄). This reaction is kinetically favorable and produces a product that is feasible to measure (SO₄). DO was limited exclusively to the SW reservoir (Figure 3.1B). The upwelling GW reservoir was purged with Argon during the full duration of all experiments to remove DO, while Na₂SO₃ was dissolved in the GW constant head tank and reservoir (Figure 3.1I) after DO had been purged, allowing SO₄ to form only where the two source waters mixed in the porous media. This mixing-dependent reaction would not be common in the field but rather was designed to allow us to evaluate the extent of and controls on mixing-dependent reactions and DO dynamics. We intentionally chose an abiotic reaction because it is a simpler starting point for use in the unique conditions of the hyporheic zone. In addition to the abiotic reaction, we conducted control experiments where oxic and anoxic water mixed without Na₂SO₃ to compare non-reactive mixing with mixing-dependent reaction.

Deionized (DI) water was used for all experiments. Thus, GW and SW here refer to the location of water in the reservoirs and not the source of experimental water. DI water in the GW

tank/reservoir was continually deoxygenated with Argon gas throughout the duration of all experiments to minimize Na_2SO_3 reacting with any DO and producing background SO_4 levels. The GW tank/reservoirs were also covered with lids to limit DO diffusion into the reservoir. Once DO levels were below 0.5 mg/L in the GW tank/reservoir, Na_2SO_3 was added at a concentration of 0.04M and upwelled through the system. To maintain a constant upwelling concentration, the GW tank/reservoir was continuously mixed by a 26.4 liters per minute submersible pump and by turbulence induced by the introduction of Argon gas.

HFC's were induced with $\Delta h=4.5$ cm and 6.0 cm. Smaller Δh were attempted but were hard to observe with the planar optode as the HFC was close to the partition boundary and did not provide adequate area for SO_4 sampling. Significantly larger Δh were not possible within the confines of the mesocosm. The values of Δh used in this experiment are similar to those seen in bedforms such as dunes (Elliott & Brooks, 1997; Fox et al., 2014; Harvey et al., 2013b; Marzadri et al., 2016) and in-stream structures (Azinheira et al., 2014). Experimental runs were 60-minutes in duration (after hydraulic steady-state was achieved), with sampling and imaging at 10-minute time steps.

3.2.3 Measurements

We monitored DO in the GW tank/reservoir throughout each experiment using HOBO U26-001 DO meters. We similarly monitored DO in the SW reservoir at the beginning and end of each experiment with a YSI ProPlus. DO distribution was measured in porous media using a planar optode between the sediment and the glass (Figure 3.1G) (Ballarini et al., 2014; Bauer et al., 2009; Cardenas et al., 2016; Galloway et al., 2019; Kaufman et al., 2017; Kessler et al., 2012; Wolke et al., 2020). SO_4 concentration was measured in water samples collected at the sampler (Figure 3.1F). Samples were collected in the vicinity of the mixing zone established between the HFC and upwelling GW (Figure 3.1D&E). Both planar optode images and mixing zone SO_4 samples were taken after a steady state HFC had developed and Na_2SO_3 had been added for the reaction experiment. Steady state HFC conditions were determined by constant head manometer and piezometer measurements (Figures 3.1K and 3.1F, respectively; and Appendix B. Figure S4), and confirmed by stability in optode images (Figure 3.1G). The time at which Na_2SO_3 was added is time zero ($t=0$) for all reaction experiments. In the reaction experiment, the Na_2SO_3 was not added into the reservoirs until the DO reading was below 0.5 mg/L from the purging of oxygen

with Argon, which in turn did not occur until after steady-state hydraulics had been established. In contrast, $t=0$ for control experiments is when the steady state HFC was achieved and upwelling GW was anoxic from Argon purging, again after steady-state hydraulics had been achieved.

Concentrations of SO_4 produced from the Na_2SO_3 mixing and reacting with DO were obtained by collecting 1 mL of sample 2-3 cm below the sediment surface using needle syringes to minimize sediment disturbance. Seven samples were taken along the sampler (Figure 3.1F) during each time step for each experiment. Background SO_4 concentrations from the GW upwelling lines and GW reservoirs were attempted but not reported due to water leaks from the flow line and oxygen leaks through opening the GW reservoir lids. Samples were diluted in 9 mL of DI water, then analyzed using a Hach Sulfate kit and read by a Spectronic 20 spectrophotometer to obtain SO_4 concentrations (Appendix B, Figure S1 and S2).

The planar optode used in the experiments was 22.5 cm by 17.2 cm and placed across the mixing zone (Figure 1G) (Ballarini et al., 2014; Bauer et al., 2009; Cardenas et al., 2016; Frederiksen & Glud, 2006; Glud et al., 1996; Kaufman et al., 2017; Klimant et al., 1997; Larsen et al., 2011; Santner et al., 2015). The planar optode was produced in the laboratory of Dr. R. Glud at the University of Southern Denmark and consisted of a light reactive dye of platinum (II) octaethylporphyrin (PtOEP) and coumarin, a common gain medium that fluoresces, coated onto a plastic sheet.

We used a Canon EOS Rebel T5i DSLR camera to capture the 2D optode color and intensity patterns. The optode was excited using 225 blue LED lights with a peak wavelength of 450 nm evenly spaced in a 28.6 x 28.6 cm lamp head. The light was angled downward at 45° . A f3.5-5.6 lens equipped with a 530 nm long pass Schott filter was used. The camera was additionally modified to ensure that the full color spectrum was captured by removing the factory-installed near infrared blocking filter. The software application Look@RGB (fish-n-chips.de) was used to automate the lighting and camera. Images were taken in triplicate at each time step, averaged by Look@RGB, and split into red, green, and blue channels.

We used the modified Stern-Volmer Equation (Kaufman et al., 2017; Larsen et al., 2011) to make the green-red light intensity ratio versus concentration (calibration) curves (Appendix B, Figure S3 and Table S1 in Appendix B Section 1b) that allowed us to convert light intensities to DO concentrations (Appendix B, Equation S1). Calibration was conducted in the mesocosm tank using Argon gas and Na_2SO_3 in combination to incrementally vary the DO concentrations from

0.0 to 9.0 mg/L. We measured DO concentrations throughout the calibration duration using a YSI ProPlus probe and two HOBO U26-001 DO sensors. To ensure accurate conversion of light intensities to DO concentrations, calibration conditions were identical to experimental conditions, including light angles and intensities. We also determined that optode response varied little (<5%) in the range of 18-22°C, so we kept all mesocosm temperatures in this range.

3.2.4 Data Analysis

MATLAB was used to analyze optode images. A pixel-to-length conversion was employed to show spatial scales of the oxygen distributions/profiles. The images were smoothed by averaging neighboring pixels together in blocks (Castro-Alcalá et al., 2012; Kaufman et al., 2017; Robinson et al., 2015). Block size was 2x2 pixels (0.44mm) because it reduced noise from grain and boundary influences but did not affect the resolution of mixing zone at mm to cm scales.

Mixing zone thickness and position (oxic front position) were determined for each image time step by analyzing planar optode images at rows of pixels located at an average depth of 3.5 cm. Values from three consecutive rows (at depths of 3.45, 3.50, and 3.54 cm) were averaged to minimize the effect of small-scale natural noise resulting from sediment grains. The mixing zone was approximately vertical at this depth, and it closely corresponds in space to the SO₄ sampling. A vertical mixing zone simplified our analysis by allowing us to calculate mixing zone thickness only in the horizontal direction (along a row) rather than diagonally across rows and columns. We normalized DO concentrations in each optode image by dividing DO concentrations in each pixel by the maximum DO concentration in that image to facilitate comparison between the experiments since they had varying starting DO concentrations. The normalized DO profiles at this depth were interpolated to obtain the spatial location of a given percent of maximum concentration. Mixing zone thickness was then calculated as the horizontal distance along the profile between the 16% and 84% normalized DO concentrations. These percentages are one standard deviation from the median in a normal distribution and thus are widely used to define 2D groundwater plume distributions (Abarca & Clement, 2009; Chiogna et al., 2011; Lu et al., 2009; Lu & Luo, 2010; Robinson et al., 2016).

The oxic front and peak SO₄ positions were determined as horizontal distances relative to the partition (Figure 3.1C). The oxic front position was based on the location of the 84% DO

concentration. The peak SO_4 position was the location of the highest measured SO_4 concentration from each time step and not necessarily the overall highest SO_4 concentration for that experiment.

3.3 Results

Consistent with our experimental design, the hydraulics were essentially steady state throughout the duration of each experiment as indicated by constant flow rates (Table 3.1) and constant heads (Appendix B, Figure S4) over time. This allowed us to attribute solute concentration changes over time to transport and reaction dynamics alone which itself may have time-dependency as discussed below.

3.3.1 Sediment DO Distributions (Planar Optode)

Planar optode images show 2D normalized DO concentration fields for the two Δh conditions that capture mixing in both a non-reacting control (mixing between oxic and anoxic water) and the mixing-dependent reaction of Na_2SO_3 and DO (Figure 3.2). Three distinct areas are noted: 1) quarter ellipses of upwelling oxic SW within the HFC (red, orange, yellow), 2) upwelling anoxic GW (deep blue), and 3) mixing zone between SW oxic and GW anoxic zones (greenish band of color gradation). The size of the HFC increased with increasing Δh (compare Figures 2AC with 2BD), consistent with greater downwelling into the subsurface, which in turn lengthens the mixing zone (Hester & Doyle, 2008; Nida, 2015).

Although subtle to the naked eye, the DO concentration distributions are different between control and reaction cases, as verified by image analysis. The intensity of the red coloration within the HFC (i.e., oxic region) is slightly greater for the controls (Figure 3.2AB) than the reaction images (Figure 3.2CD), indicating that maximum DO concentrations decreased proportionally more within the reaction HFC. Estimations of the number of pixels that exceeded 75% DO concentration showed that for $\Delta h=4.5$ cm the control image had about 15% more pixels than the reaction image while for $\Delta h=6.0$ cm the control had 5% more pixels than the reaction image. This effect is greatest near the lower part mixing zone (i.e., deeper in the sediment), indicating that excess Na_2SO_3 in the reaction case may be diffusing far into the HFC at low levels.

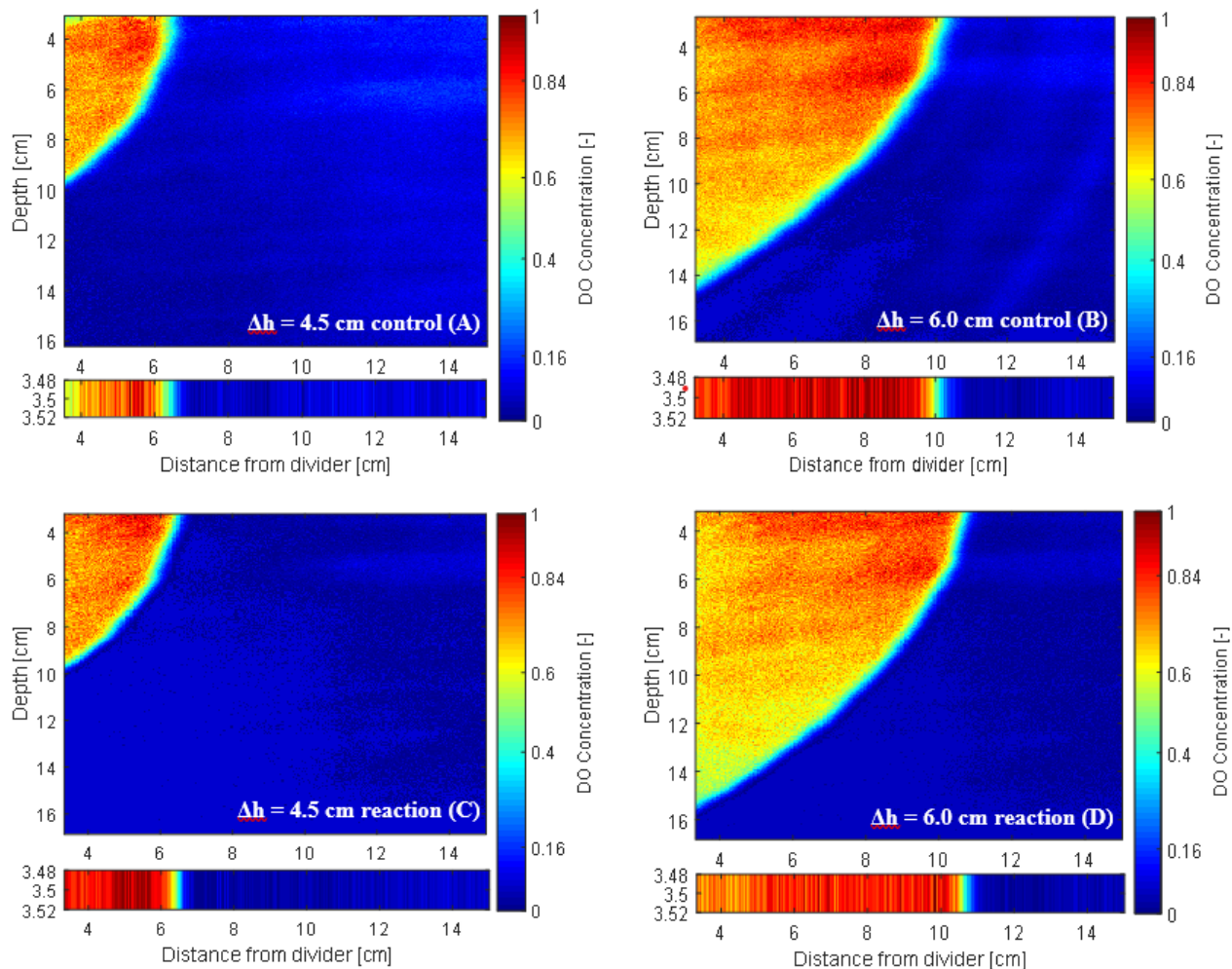


Figure 3.2. Normalized DO spatial distributions from planar optode at $t=60$ minutes for $\Delta h=4.5$ cm (A, C) and 6.0 cm (B, D). (A, B) are controls where no Na_2SO_3 was present; (C, D) are experiments where Na_2SO_3 was introduced and thus SO_4 produced. The pixel row (3.5 cm depth) used for image analysis (Section 3.3.2) is shown below each respective full optode image. Colors represent DO concentrations normalized to initial maximum concentration for each experimental run ($\text{DO}_{\text{max}}=7.8, 7.3, 6.8, 8.2$ mg/L for panels a, b, c, d, respectively), thus colors represent changes in each experiment relative to initial baseline conditions. Variation in maximum DO concentration among experiments does not noticeably impact final DO distribution as shown by similar trends in mixing zone thickness and oxic front (Sections 3.3.2 and 3.3.3). Optodes show some edge effects; colors within a few mm of the optode boundary (we have shown full optode) may not be as accurate, but do not affect oxic front and mixing zone thickness estimates.

3.3.2 Concentration Profiles and Oxidation Fronts

Figure 3.3A shows normalized DO concentration profiles rendered as 1D horizontal slices through the optode images at a depth of 3.5 cm below the sediment surface for the four experimental conditions. Steep DO concentration gradients are noted for each case reflecting a limited effect of transverse dispersion in the horizontal direction. The reactive effect of the Na_2SO_3 is reflected in steeper DO concentration gradients (approximately 3%) compared to those for the control case. The oxidation front is farther to the right for the higher Δh (i.e., $\Delta h=6.0$ cm) consistent with larger HFC.

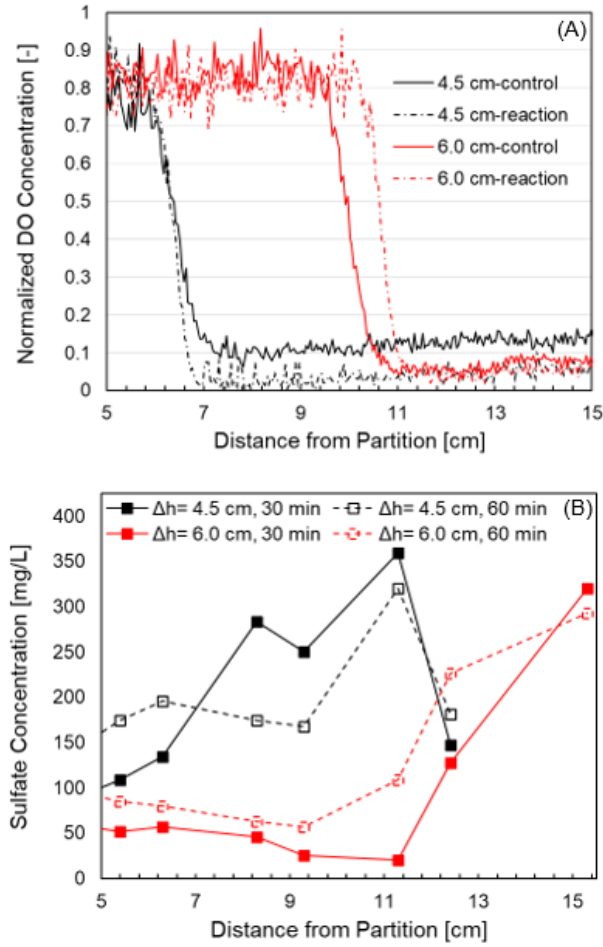


Figure 3.3. Normalized DO (A, reaction and control cases) and SO₄ concentrations (B) versus distance from partition for $\Delta h=4.5$ cm and 6.0 cm. DO data are from a row of optode image pixels at depth=3.5 cm and $t=60$ minutes and normalized per Figure 3.2. DO profiles are shown for only one-time step because those for other times are similar. SO₄ concentration profiles (B) show two times, including that of maximum SO₄ concentration at $t=30$ minutes (359.2 mg/L and 320.0 mg/L for $\Delta h=4.5$ cm and 6.0 cm, respectively), and $t=60$ shown in Figure 3.2 (max SO₄ concentration=320.0 mg/L and 292.5 mg/L, respectively). SO₄ sample locations were unevenly spaced to capture samples within the HFC, in the mixing zone, and outside HFC.

SO₄ concentration profiles are shown in Figure 3.3B for a line of samples collected 2-3 cm below the sediment surface at times of 30 and 60 minutes following the introduction of Na₂SO₃. The position of the SO₄ concentration peaks is to the right of the oxic front in Figure 3 for each

experimental run. This means SO_4 production was occurring further out from the center of the HFC than the location of the oxic front at the time of measurements.

Maximum SO_4 concentrations (359.2 mg/L and 320.0 mg/L for $\Delta h=4.5$ cm and 6.0 cm, respectively) occurred at $t=30$ minutes (Figure 3.3B). Peak SO_4 concentrations had decreased by $t=60$ for both hydraulic conditions. This decrease in max SO_4 concentration occurs concurrently with stabilization of the mixing zone thickness and oxic front position at $t > 30$ min (Figures 3.4-3.5). Differences in the position of the SO_4 peak concentrations reflect differences in Δh .

As Δh increased from 4.5 cm to 6.0 cm in the control and reactive experiments (e.g., Figure 3.2A to 3.2B and 3.2C to 3.2D), the HFC increased in size and thus the mixing zone and oxic front both shifted to the right (Figures 3.3A, 3.4A). For example, the distance between the partition and the 84% concentration contour oxic front increased on average from 5.83 to 9.31 cm for the control experiments (Figure 3.4A). As Δh increased, the distance (i.e., spatial gap) between control and reaction oxic fronts increased (Figure 3.4A, Appendix B Figure S6). The higher Δh would induce higher porewater velocities along the mixing zone, which in turn would allow less time for the system to reach steady-state transport and reaction in the mixing zone. This is consistent with higher maximum SO_4 concentration observed for $\Delta h=4.5$ cm (Figure 3.3B).

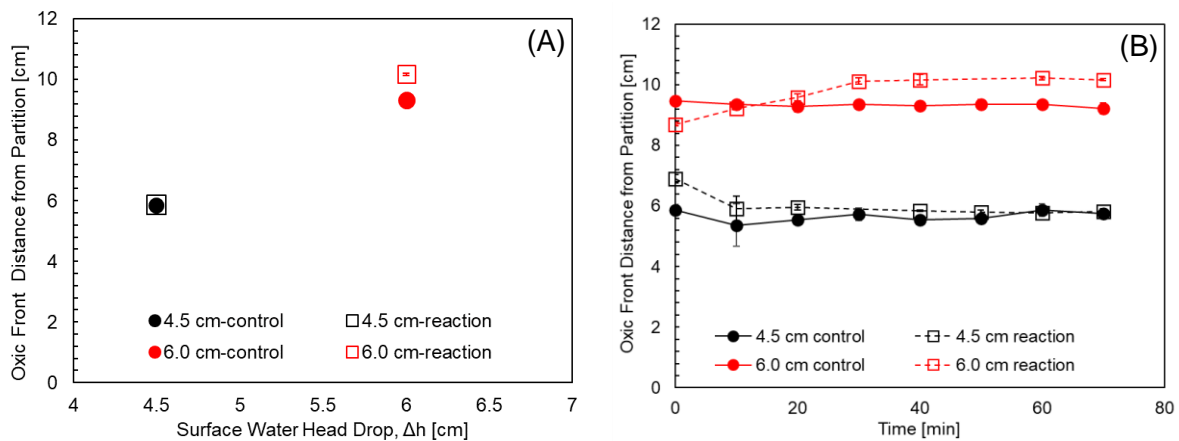


Figure 3.4. Distance from partition to oxic front (84% of peak/normalized DO concentration): (A) versus Δh ; boxes are averages and errors bars are standard deviations across the three depths analyzed (3.45, 3.50, and 3.54 cm) and over the full experimental duration (control) and 30-70 min range (reaction), (B) versus time since steady state hyporheic flow cell (HFC) was observed (control) and since Na_2SO_3 was added (reaction); boxes are averages and errors bars are standard deviations across the three depths analyzed.

Over the course of the control experiments for both Δh , the oxic front moved little in space (Figure 3.4B) and thus is considered steady. By contrast, the oxic front in the $\Delta h=6.0$ cm reactive case moved slightly away (~ 2 cm) from the mesocosm partition (to the right in Figures 3.2-3.3), whereas for $\Delta h=4.5$ cm it moved slightly toward (~ 1 cm) the partition (i.e., to the left in Figures 3.2-3.3). These shifts occur mostly at $t < 30$ minutes because Na_2SO_3 is added at $t=0$, and the system immediately begins to adjust to the reaction taking place. The observed trend may also be explained in part by the differences in advective transport rates between the two Δh . The slower velocities along the mixing front for $\Delta h=4.5$ cm (Table 3.2) allow DO consumption by the SO_4 oxidation to shift the mixing zone and oxic front toward the HFC (to the left in Figures 3.2-3.3). Yet this effect would occur less for $\Delta h=6.0$ cm because higher velocities (Table 3.2) decrease the potential for reactions to occur and thus limit the rate at which the hydraulics and mass transport balance each other as was seen with the lower Δh . Lower potential for reactions would in turn reduce leftward migration of the mixing zone, although we are unsure why the mixing zone actually went as far as to move to the right. This kinetic limitation is indicated by the opposing changes seen in the oxic front from both Δh , where the higher Δh did not shift closer to the partition as the reaction proceeds.

3.3.3 Mixing Zone Thickness

The average mixing zone thickness for the control experiments (Figure 3.5A) are 1.03 cm to 1.06 cm for $\Delta h=4.5$ cm and $\Delta h=6.0$ cm respectively. (Figure 3.5A). This difference in mixing zone thickness is minor for 16-84% concentrations, although the difference is larger for 10-90% (1.71 cm to 2.21 cm, Appendix B Figure S5). These trends are consistent with prior experiments of hyporheic mixing zones (Nida, 2015). The increase in mixing zone thickness may occur because increased Δh leads to longer mixing zone lengths which in turn allow more dispersion to occur along a greater length (Nida, 2015).

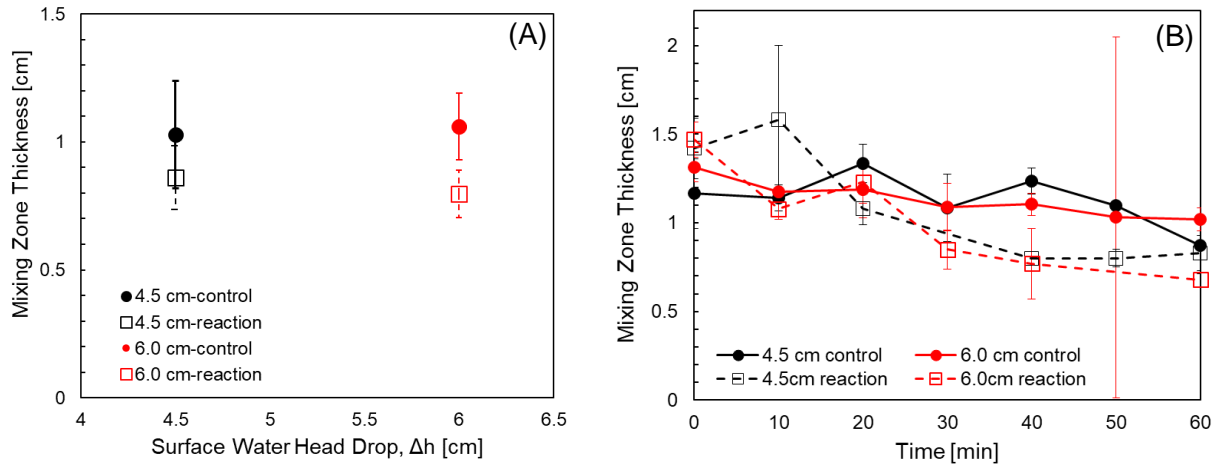


Figure 3.5. Mixing zone thickness (16-84% of peak/normalized DO concentration): (A) versus Δh ; boxes are averages and errors bars are standard deviations across the three depths analyzed (3.45, 3.50, and 3.54 cm) and over the full experimental duration (control) and 30-60 min range (reaction), (B) versus time since steady state hyporheic flow cell (HFC) was observed (control) and since Na_2SO_3 was added (reaction); boxes are averages and errors bars are standard deviations across the three depths analyzed.

Mixing zone thickness was overall greater for the control than the reaction case (Figure 3.5A). We calculated the difference by subtracting the control values from the reaction values; thus, positive means reaction was larger and vice versa for negative values. The values were -0.07 cm and -0.15 cm for $\Delta h = 4.5$ cm and 6.0 cm, respectively. The difference between control and reaction values was caused by the different mechanism taking place during the experiment. During the control experiments, mixing occurs as dispersion determines the gradient between source waters of different oxygen levels (oxic and anoxic). During the reaction experiments, a reaction is superimposed upon the dispersion process. Thus, it is expected that if kinetics rates are faster or equal to dispersion rates (as they are, see dimensionless analysis below in Section 3.4.1) that the mixing zone would shrink (which it did, Figure 3.5b).

Mixing zone thickness did not change substantially over time for the control experiments (Figure 5B), although a decrease was observed from 1.17 cm ($t = 0$ min) to 0.87 cm ($t = 60$ min) for $\Delta h = 4.5$ cm, and 1.31 cm ($t = 0$ min) to 1.02 cm ($t = 60$ min) for $\Delta h = 6.0$ cm. By comparison, mixing zone thickness decreased over time by roughly half for the reaction experiments, from 1.42 cm to

0.83 cm for $\Delta h=4.5$ cm, and from 1.47 cm to 0.68 cm for $\Delta h=6.0$ cm. These values decreased below the corresponding control values as Na_2SO_3 continued to react with DO in the mixing zone. The net effect was mixing zone narrowing; therefore, reaction outweighed any increased dispersion, an indication for high Damkohler numbers (i.e., dispersion limitation, see Section 3.4.1). The rate of decrease in the reaction mixing zone thickness declined with time, with the lower Δh (4.5 cm) stabilizing before the higher Δh (6.0 cm).

3.4 Discussion and Analysis

3.4.1 Relative Dominance of Advection, Dispersion, and Reaction Processes

The relative importance of advection, dispersion, and reaction and processes can be quantified with dimensionless numbers and characteristic timescales. We calculated Peclet (Pe) and Damkohler (Da) numbers (Ahmerkamp et al., 2015; Dykaar & Kitanidis, 1996; Haggerty et al., 2014; Harvey et al., 2013a; Taylor & Guha, 2017; Zarnetske et al., 2012), which first require calculating a dispersion coefficient, D (m^2/s). In this study we focus on transverse mixing across the mixing zone, thus we calculated the transverse dispersion coefficient (D_t , m^2/s). We used the dispersion model equations for conservative advection-dispersion (Hester et al., 2013; Rolle et al., 2013),

$$thickness = \sqrt{\frac{D_t L}{v_p}} \quad (3.1)$$

$$D_t = \frac{thickness^2 v_p}{L} \quad (3.1a)$$

where mixing zone thicknesses (m) are those from the control experiments, v_p is the velocity of porewater movement along the length of the mixing zone (m/s) and L (m) is the length of the mixing zone (Table 3.2). L/v is the residence time of water travelling along the length of the mixing zone, i.e., time available for transverse dispersion to occur. We estimated v_p by applying Darcy's Law to hydraulic head measurements (Appendix B Figure S4) and the bottom of the water column immediately above, together with hydraulic conductivity and porosity from Table 3.1. Thus, these are overestimates for average v_p along the mixing zone flowpath. We estimated L as the length of mixing zone captured by the optode images. These are underestimates but are the

only direct way to measure mixing zone length and capture both the majority of the true length as well as its variation with Δh (Figure 3.2). The underestimate for L and the overestimate for v_p means that calculated values of D_t are overestimates. Calculated values of D_t varied little between the two Δh 's, primarily because increases in L compensated for increases in v_p .

We calculated Pe using the version in Haggerty et al. 2014,

$$Pe = \frac{v_p L}{D_t} \quad (3.2)$$

where L (m) is again the flowpath length along which advection and transverse dispersion operate. The resulting values (Table 3.2) were > 1 , indicating dominance of advection rather than dispersion for both Δh . This is consistent with the thin mixing zones observed (Figures 3.2-3.3), as expected for clean sand porous media (Rolle et al., 2013). Other studies (Ballarini et al., 2014; Haggerty et al., 2014; Rolle et al., 2013; Taylor & Guha, 2017) demonstrate that large Pe numbers indicate solute stretching but low mixing.

We estimated Da based on the approach of Dykaar and Kitanidis (1996) and Taylor and Guha (2017),

$$Da = \lambda L^2 / D_t \quad (3.3)$$

where λ is the kinetic rate of SO_3 oxidation (1/s). We estimated λ from static beaker experiments using the same reactant concentrations in DI water as those used in the mesocosm experiments presented here (Appendix B Section 3a, Figure S7 and Table S2). The resulting Da values were substantially > 1 (Table 3.2), indicating reaction was dispersion-limited, this is consistent with thin mixing zones (Figures 3.2-3.3) and Pe values > 1 . Thus, in our experiments, O_2 and SO_3 advect along the mixing zone, but reaction to SO_4 is limited by minimal dispersion. Because our chosen reaction has inherently fast kinetics, dispersion-limitation is also consistent with declines in mixing zone thickness with time (Figure 3.5B). In particular, because reaction occurred before SO_3 could disperse very far from upwelling groundwater into the hyporheic flow cell, O_2 was consumed only in a narrow band on one side of the mixing zone. This in turn limited the width of the band in which SO_4 production occurred.

Table 3.2. Dimensionless numbers, characteristic process timescales, and related input data

Parameter	$\Delta h = 4.5 \text{ cm}$	$\Delta h = 6.0 \text{ cm}$
$\lambda \text{ (1/s)}$	0.33	0.33
L (m)	0.193	0.261
D_t (m²/s)	9.8×10^{-8}	1.0×10^{-7}
v (cm/min)	1.08	1.41
Mixing Zone Thickness (m)	0.0103	0.0106
Pe (-)	360	610
Da (-)	1.3×10^5	2.2×10^5
Characteristic advection (residence) time along mixing zone (min)	20-30	20-30
Characteristic dispersion time of O₂ across mixing zone¹ (min)	18.0	18.4
Characteristic reaction time of SO₃ ⇌ SO₄ (s)	3.0	3.0

¹At location of mixing zone thickness calculations (3.5 cm beneath sediment-water interface, i.e., “F” in Figure 1).

We also estimated characteristic timescales of relevant processes (Table 3.2). Characteristic advective transport time along the mixing zone was estimated from optode images captured every ten minutes, showing the time elapsed from when SW was switched on to form the hyporheic flow cell (HFC) and when the steady HFC was fully formed. Characteristic times for O₂ reaction and dispersion across the mixing zone were estimated as $\text{thickness}^2/D_t$ and $1/\lambda$, respectively. This is consistent with $Pe > 1$ and thin mixing zones. More importantly, characteristic reaction timescales are substantially lower than either advective or dispersive times, consistent with high Da numbers.

All of this is consistent with the thin mixing zones (~1 cm) in this study and with prior work (Abarca & Clement, 2009; Ballarini et al., 2014; Chiogna et al., 2011; Hester et al., 2014; Marzadri et al., 2016). For example, (Nida, 2015) found mixing zone thickness of roughly 1.0-1.6 cm (10-90% range) in laboratory simulated hyporheic zones whose substrate and hyporheic flow

cell are the same as this study's. Abarca et al. (2009) examined mixing zones in the presence of density gradients in laboratory studies and found mixing zone thicknesses of a few cms with a head drop of 8 cm and porosity of 0.39. Hester et al. (2013, 2014), which has similar head drops and hydraulic conductivity, observed mixing-dependent reactions and found mixing zones (10-90% range) occupying ~10% of the model domain, consistent with thin mixing zone thicknesses. Marzadri et al. (2016) used an analytical model of gaining conditions, and found mixing zone thicknesses from 1-10 cm. This range seen in Marzadri et al. (2016) is larger than the studies mentioned above, due to their wider range of hydraulic conditions. Yet many field studies present data consistent with substantially larger mixing zones (Briggs et al., 2014; Cardenas et al., 2004, 2008; Gomez-Velez et al., 2015; Gooseff et al., 2006; Kasahara & Wondzell, 2003; Malcolm et al., 2005), implying additional conditions or processes further enhance mixing in real rivers (e.g., heterogeneity of sediment texture and microbial abundance that affects residence times and flowpaths). This is an area ripe for future research to understand the interplay between ecology, hydrology, hydraulics, and chemistry on mixing (Hester et al., 2017).

3.4.2 Dynamic Hyporheic Reactive Mixing Zones

The position of the sulfate peak to the right of the oxic front in Figure 3.3 could be explained by the interplay of GW flowpaths and reaction in the mixing zone. At the beginning of each reaction experimental run, steady state hydraulics are established, which sets the location of the boundary between the HFC and upwelling GW, with this boundary further to the right for higher Δh . The mixing zone between oxic and anoxic waters (i.e., oxic front) would then initially set up at this hydraulically induced boundary location (Figure 3.6A). Mixing-dependent Na_2SO_3 oxidation in turn would occur first at this initial mixing zone location, consuming DO and producing SO_4 . DO consumption would then move up the mixing zone/flowpath toward the top of the sand (Figure 3.6B). This process would happen continually, moving the oxic/anoxic mixing zone up and to the left in Figure 3.3, ultimately leading to a measured SO_4 peak toward the top of the sand that is to the right of the oxic front in Figure 3.3 (Figure 3.6C) (i.e., in the anoxic blue area just outside the quarter ellipse in Figure 3.2). This can also be thought of in terms of time, i.e., there is delay between where the oxygen front is and where the highest amount of product is measured, such that it can be thought of as a "trail" of SO_4 that follows the oxic front. Thus, steady-

state hydraulics would set the location for where the mixing-dependent reaction first occurs, but then the reaction would shift the mixing zone as reactants are consumed. We acknowledge that this theory only partially predicts the $\Delta h=6.0$ cm case, where the sulfate peak did form to the right of the late-time mixing zone, but the mixing zone itself did not move left during the period for which we have measurements (Figure 3.4B).

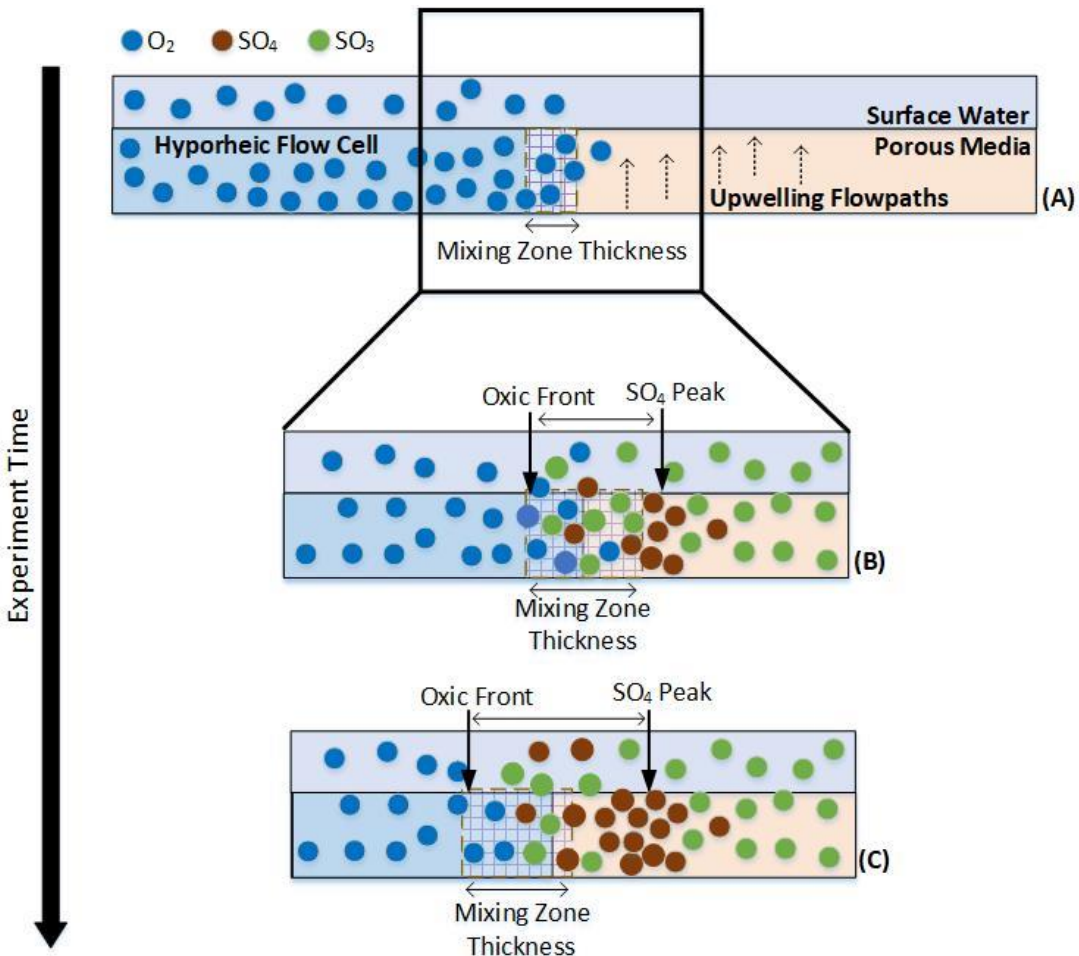


Figure 3.6. Schematic of the SO_3 (green) to SO_4 (maroon) reaction. As the reaction starts, the reaction takes place at the established mixing zone (A), then as the O_2 (blue) gets consumed SO_4 remains at the location of the initial mixing zone boundary (B), and the SO_3 solution moves towards the O_2 front, further separating the oxic front and SO_4 peak (C). Drawings not to scale.

Multiple hyporheic zone studies indicate that increases in SW Δh and transient conditions (e.g., fluctuating SW Δh) can increase mixing-dependent attenuation (Hester et al., 2019;

Newcomer et al., 2018; Shuai et al., 2017). However, these studies did not explore how reactions taking place also influence the mixing zone. Our results show that even with steady-state hydraulics (Figure S4), reactions in the subsurface also influence the mixing zone. In other words, shifts in chemical boundary conditions, in addition to shifts in hydraulic boundary conditions will affect mixing zones. In our study, we saw that steady-state transport (rate of DO dispersion being equal to rate of SO_3 dispersion) was eventually achieved but varied with Δh . These differences in response times to these difference types of boundary shifts make understanding mixing-dependent reactions more complicated.

This has important implications for understanding temporal variations in reactions, and pollutant attenuation in the hyporheic zone as chemical gradients shift, as river stage is always changing due to storms, dam operation, tides, and diel cycles of snowmelt or evapotranspiration (Gomez-Velez et al., 2015; Harvey et al., 2013b; Hester et al., 2019; Knights et al., 2017; Krause et al., 2013; Loheide & Lundquist, 2009; Malzone et al., 2016; Schmadel et al., 2016). Thus, in most rivers, transport and mixing dynamics are superimposed upon hydraulic dynamics, adding to the complexity of interpreting field data and estimating net reaction rates.

3.4.3 Novelty and Limitations of Approach

Our results are the first to observe mixing-dependent reactions under the unique conditions of the hyporheic zone using a controlled physical experiment. We were able to simulate and control an abiotic DO-consuming mixing-dependent reaction, quantify oxic front location and mixing zone thickness in a laboratory mesocosm, and evaluate the effect of driving SW Δh on mixing zones. This allowed careful quantification of hydraulic, transport, and reaction processes which in turn enabled us to recognize the decoupling of the steady-state hydraulically-defined hyporheic flow cell where SW and GW meet from the dynamic movement of the oxic-anoxic mixing zone (i.e., oxic front) due to mixing-dependent oxidation of excess Na_2SO_3 from GW. We were able to perform this quantification for two SW Δh , to also provide insight on how varying hydraulic conditions may influence mixing-dependent reactions and hence mixing zones.

The optode images provided in this study are some of the first shown for hyporheic zone, particularly the first to use planar optodes to analyze and measure oxygen dynamics in a mixing-controlled hyporheic zone reaction. Bauer et al. (2009) and Ballarini et al. (2014) used planar

optodes in their GW studies, however, they did not present the images to illustrate the 2D representation of DO. Kaufman et al. (2017) was the first to use optodes to show spatially explicit DO dynamics in a dune-induced HFC. However, their system was recirculating, and experiments lasted days as opposed to our study which was not recirculating and had a maximum observation time of 2 hours. Wolke et al. (2020) and Galloway et al. (2019) are the first known studies of the hyporheic zone that analyze oxygen data over time with planar optodes to calculate oxygenated area of sediments. These studies provide great insight into subsurface oxygen dynamics, but do not observe mixing-dependent reactions or clearly analyze the reaction kinetics influence on oxygen profiles. This study along with those mentioned here demonstrate a clear delineation between the oxic mixing and anoxic regions.

Na_2SO_3 easily transforms to Na_2SO_4 , thus excess Na_2SO_3 is needed, so we used about 20 times the amount necessary for deoxygenation to ensure the quantification of SO_4 production and ensure abiotic conditions given SO_4 toxicity to microorganisms. The excess Na_2SO_3 added and the instantaneous and irreversible oxidation results in higher concentrations of products measured than for slower and reversible reactions. The excess Na_2SO_3 allowed for a larger amount of SO_3 to be transformed to SO_4 as there is a larger chance for the interaction between the DO and Na_2SO_3 and thus it influences both the mixing zone thickness and peak SO_4 concentration. Yet mixing zone reaction dynamics would likely vary with stoichiometric ratio of SO_3 to O_2 , with lower ratios leading to lower SO_4 concentrations. The stoichiometric ratio could also influence the mixing zone thickness and oxic front location as the reaction was shown to influence these variables, with lower ratios potentially resulting in less shrinking of mixing zone and movement of the oxic front. Therefore, the concentration of the Na_2SO_3 or any groundwater pollutant will impact the mixing zone and chemical fronts.

We calculated mixing zone thickness and measured SO_4 concentrations at an average depth of 3.5 cm because that is at the downgradient end of the mixing zone, where the mixing zone is most developed, and thus is the best metric for overall mixing zone dynamics. The mixing zone is also the most vertical at that location, simplifying calculation of mixing zone dimensions from gridded pixel data. Yet obtaining SO_4 concentrations and mixing zone thickness over multiple depths would expand our understanding of hyporheic mixing dynamics and how they evolve along individual mixing fronts in the hyporheic zone. SO_3 was not measured during the experiments

because SO_3 reacts with any oxygen present making it very difficult to collect samples without contamination. In addition, SO_3 sampling would require withdrawing >1 mL, which would increase disturbance of the mesocosm flow field. Future efforts to collect such measurements could facilitate mass balances of reactants and products.

Obtaining SO_4 measurements across a wider transect (i.e., farther to the right in Figure 3.3B) would ensure the SO_4 peak and plume extent was consistently captured and allow calculation of the mass flow rate exiting the sediment to surface water on both sides of the mixing zone. Understanding the expected relative positions of peak and plume are also important for designing future field studies of hyporheic reactive mixing zones.

Our experimental set up limited both the number and range of Δh that could be observed. The optode placement did not allow for lower Δh , and higher Δh were limited by the inflow pipe in the inflow reservoir. A wider range of Δh in future experiments would allow better characterization of trends versus Δh but would require mesocosm modifications. Furthermore, changing the upwelling flow rate would show how gaining flow rates affect mixing and mixing zone thickness. Future studies could also address response of mixing behavior to transient dynamics in boundary heads.

We acknowledge that syringe sampling could have impacted groundwater flow fields. However, this was minimized by the small sample volume (1 mL translates to a 6.2 mm diameter sphere, which is less than the 1.5 cm spacing between sampling), the upwelling gradient which flushes any perturbation upward away from the mixing zone being studied, and syringe needles which are < 5 mm in diameter and are removed and reinserted within a few minutes. The latter also minimized influence on surface water flow fields especially given Reynold's number below 500 (Chaudry, 2008), see SI Section 3b for details. Laminar surface flow conditions also prevented reactants or products exiting to surface water from circulating back down into the sediments and influencing sample results. Yet, caution is advised to not stir up sediment when inputting and removing the syringe needle which can impact the SO_4 peak location.

Finally, we acknowledge possible artifacts in the planar optode images. For example, in Figure 3.3d, there is unexplained color variation from approximately 0.5 to 0.8 normalized DO concentration between the lower left and upper right portions of the HFC. These two points fall approximately along a hyporheic flow path, and the only possible sources of DO are advection

from the upgradient water column and dispersion from adjacent flowpaths, yet the observed color pattern is not organized along flowpaths, equipotential lines, or dispersion fronts. By contrast, slight variations in color intensity are also visible in the blue upwelling anoxic region, and there is often continuity of these patterns across the mixing zone, consistent with a cause unrelated to flow and transport processes in the sand. For this reason, we believe this particular color pattern to be an artifact of the optode rather than a real trend in DO occurring within the mesocosm. We are not certain the cause of the artifact, but one possibility is mild warping of the optode from the tape that holds the edges of the optode to the glass or leakage of water through the tape to the space between the optode and the glass. Furthermore, this artifact is exacerbated by our normalization to the range of DO concentrations in each individual optode image, rather than to DO saturation. Regardless, our conclusions are built upon measurements of mixing zone thickness and position which are based on large DO differences over short distances measured normal to flowpaths. By contrast, the artifacts described above represent larger scale more subtle effects longitudinally along flowpaths. Thus, we believe that the artifacts do not affect the conclusions of this study.

3.4.4 Application

Since some upwelling GW contaminants require mixing with SW to degrade, this study can aid in informing river management (Graf, 2006; Herzog et al., 2018; Hester et al., 2017; Peralta-Maraver et al., 2018). We demonstrate how hyporheic mixing zones are affected by both SW head conditions and mixing-dependent reactions. SW head controls the advective flowpath length and residence time along the mixing zone (advection timescale), which determines the time available or opportunity for dispersion (dispersion timescale), which in turn determines the opportunity for mixing-dependent reaction. The actual degree of reaction that occurs is then determined by the interaction of this dispersion timescale and kinetic rate of the reaction (reaction timescale). Thus, dispersion and reaction need to be in balance to maximize transformation of mixing-dependent reactions.

Our results show attenuation is a complex system where both hydraulics and kinetics need to be optimized and balanced to maximize attenuation (Bandopadhyay et al., 2017; Dentz et al., 2011). Pollutant attenuation can therefore be enhanced by manipulating residence time distributions (advection timescales) via increasing hyporheic exchange and/or varying hydraulic

conductivity to match the kinetics (reaction timescales) of the desired reaction (Cardenas et al., 2004; Herzog et al., 2018; Sawyer, 2015). In restoration efforts, heterogeneity can be implemented by varying the layering or distribution of different sediments to enhance heterogeneity or create pockets of a different conductivity for specific residence time requirements.

Our study also has implications for pollutant monitoring and documenting attenuation, including monitored natural attenuation (MNA). To accurately quantify the extent of transformation, choice of monitoring location is crucial. In this study, we observed how peak SO_4 production was located at the boundary of the HFC rather than at the oxic front. Yet the oxic front will be more readily observed in the field than the boundary of the HFC, and the oxic front may shift with time even with steady-state hydraulics. We also observed that the SO_4 production zone spans a larger width than the mixing zone, which could be confusing to interpret without the theoretical background provided here. Furthermore, with thin mixing zones, precise placement of monitoring locations is key. Thus, capturing both the mixing-dependent reaction production zone and peak concentrations would indicate the location of mixing and extent of mixing taking place, both crucial for monitoring and enhancing natural attenuation.

In multiple hyporheic zone studies (Conant et al., 2004; Ellis & Rivett, 2007; Freitas et al., 2015; Graham et al., 2017; Landmeyer et al., 2010; Peralta-Maraver et al., 2018; Tonina et al., 2015), measurements are sited within the HFC, yet they do not always indicate how reactions are affecting the position of chemical gradients within hyporheic zone, with implications for monitoring. Knowing how the reaction affects the biogeochemical patterns in the subsurface may be key to evaluating the success of a restoration project.

3.5 Conclusions

Hyporheic zones can naturally attenuate upwelling groundwater (GW) contaminants and may play an important role in maintaining water quality in streams/rivers. In this study, we simulated a mixing-dependent abiotic reaction for the first time in a laboratory hyporheic zone. The experiments maintained steady state hydraulics to focus on transport and kinetics in mixing-dependent reactions. The abiotic reaction of sodium sulfite (Na_2SO_3) and dissolved oxygen (DO) was observed for 60-minutes using a planar optode and multiple SO_4 samples were collected in a mesocosm-simulated hyporheic flow cell. We observed mixing zone thickness, concentration

profiles, and oxic fronts under two driving surface water (SW) head drops (Δh) of 4.5 cm and 6.0 cm. Mixing zone thickness was defined as 16% to 84% of max DO concentration and oxic fronts were the position of 84% of the max.

Under steady state hydraulics, oxic front position and mixing zone thickness were stable during non-reactive control experiments, indicating steady-state transport. By contrast, the mixing-dependent reaction influenced the mixing zone thickness and oxic front over time (Figure 3.4 and 3.5) indicating feedback and interplay between transport and kinetics even under steady-state hydraulics (Figure 3.6). In particular, mixing zone thickness shrank over time during the reactive experiments (Figure 3.5B) as mixing-dependent reaction consumed DO in the mixing zone. The decrease in mixing zone thickness for the reaction experiments (Figure 3.5A) indicates steeper DO gradients and greater dispersion (transport) limitation for the reactive case, quantified by Damkohler (Da) numbers farther above unity. Peak SO_4 concentrations always occurred on the upwelling GW side of the oxic front (to the right in Figure 3.3A), indicating a dynamic process of DO consumption and resulting mixing zone shifts. In addition, SO_4 concentration profiles (Figure 3.3B) demonstrate that the lower Δh of 4.5 cm produced a greater peak SO_4 concentration due to lower porewater velocities and hence greater time for mixing relative to the higher Δh of 6.0 cm. Future studies could extend this work with a rigorous mass balance of SO_4 production and relate that to Δh and residence times.

These results illustrate the importance of understanding the balance of transport and kinetics of mixing-dependent reactions in the hyporheic zone (e.g., quantified by Da) when interpreting contaminant concentrations patterns from field studies (Conant et al., 2004; Freitas et al., 2015; Landmeyer et al., 2010). These dynamics bear further study, including the effect of additional controls such as sediment heterogeneity. Two major constraints of this study were limits on the possible range of Δh due to the size of the mesocosm, and the relatively high reaction kinetic rate we chose to minimize experimental time required given the non-recirculating mesocosm. Yet this is the first study that observes chemical concentrations of a mixing-dependent reaction the hyporheic zone in a physical experiment. In most riverbeds, the transport and mixing dynamics we observed are superimposed upon existing dynamic hydraulic, with implications for attenuation and monitoring of contaminants in the hyporheic zone.

Acknowledgements

We thank the Institute for Critical Technology and Applied Science at Virginia Tech for providing funding for the seepage and drainage tanks. We thank the Edna Bailey Sussman Fund for summer support to K. Santizo. We thank the National Science Foundation under award #1437021 for support to K. Santizo, M. Widdowson, and E. Hester. The opinions expressed are those of the authors and not necessarily those of the NSF. Data will be published in Hydroshare (www.hydroshare.org), and a link to the data archive will be included here if the manuscript is accepted for publication.

References

- Abarca, E., & Clement, T. P. (2009). A novel approach for characterizing the mixing zone of a saltwater wedge. *Geophysical Research Letters*, *36*, 1–5. <https://doi.org/10.1029/2008GL036995>
- Ahmerkamp, S., Winter, C., Janssen, F., Kuypers, M. M. M., & Holtappels, M. (2015). The impact of bedform migration on benthic oxygen fluxes. *Journal of Geophysical Research: Biogeosciences*, *120*(11), 2229–2242. <https://doi.org/10.1002/2015JG003106>
- Azinheira, D. L., Scott, D. T., Hession, W., & Hester, E. T. (2014). Comparison of effects of inset floodplains and hyporheic exchange induced by in-stream structures on solute retention. *Water Resources Research*, *50*, 6168–6190. <https://doi.org/10.1002/2013WR014400>
- Ballarini, E., Bauer, S., Eberhardt, C., & Beyer, C. (2014). Evaluation of the role of heterogeneities on transverse mixing in bench-scale tank experiments by numerical modeling. *Groundwater*, *52*(3), 368–377. <https://doi.org/10.1111/gwat.12066>
- Bandopadhyay, A., Le, T., Méheust, Y., & Dentz, M. (2017). Advances in Water Resources Enhanced reaction kinetics and reactive mixing scale dynamics in mixing fronts under shear flow for arbitrary Damköhler numbers. *Advances in Water Resources*, *100*, 78–95. <https://doi.org/10.1016/j.advwatres.2016.12.008>
- Bandopadhyay, A., Davy, P., & Le Borgne, T. (2018). Shear Flows Accelerate Mixing Dynamics in Hyporheic Zones and Hillslopes. *Geophysical Research Letters*, *45*(21), 11659–11668. <https://doi.org/10.1029/2018GL079914>
- Bauer, R. D., Maloszewski, P., Zhang, Y., Meckenstock, R. U., & Griebler, C. (2008). Mixing-controlled biodegradation in a toluene plume - Results from two-dimensional laboratory experiments. *Journal of Contaminant Hydrology*, *96*(1–4), 150–168. <https://doi.org/10.1016/j.jconhyd.2007.10.008>
- Bauer, R. D., Rolle, M., Kürzinger, P., Grathwohl, P., Meckenstock, R. U., & Griebler, C. (2009). Two-dimensional flow-through microcosms - Versatile test systems to study biodegradation processes in porous aquifers. *Journal of Hydrology*, *369*(3–4), 284–295. <https://doi.org/10.1016/j.jhydrol.2009.02.037>
- Briggs, M. A., Lautz, L. K., & Hare, D. K. (2014). Residence time control on hot moments of net nitrate production and uptake in the hyporheic zone. *Hydrological Processes*, *28*(11), 3741–3751. <https://doi.org/10.1002/hyp.9921>
- Cardenas, M. B., Wilson, J. L., & Zlotnik, V. A. (2004). Impact of heterogeneity, bed forms, and stream curvature on subchannel hyporheic exchange. *Water Resources Research*, *40*(8), 1–14. <https://doi.org/10.1029/2004WR003008>

- Cardenas, M. B., Cook, P. L. M., Jiang, H., & Traykovski, P. (2008). Constraining denitrification in permeable wave-influenced marine sediment using linked hydrodynamic and biogeochemical modeling. *Earth and Planetary Science Letters*, 275(1–2), 127–137. <https://doi.org/10.1016/j.epsl.2008.08.016>
- Cardenas, M. B., Ford, A. E., Kaufman, M. H., Kessler, A. J., & Cook, P. L. M. (2016). Hyporheic flow and dissolved oxygen distribution in fish nests: The effects of open channel velocity, permeability patterns, and groundwater upwelling. *Journal of Geophysical Research: Biogeosciences*, 121(12), 3113–3130. <https://doi.org/10.1002/2016JG003381>
- Caruso, A., Boano, F., Ridolfi, L., Chopp, D. L., & Packman, A. (2017). Biofilm-induced bioclogging produces sharp interfaces in hyporheic flow, redox conditions, and microbial community structure. *Geophysical Research Letters*, 44(10), 4917–4925. <https://doi.org/10.1002/2017GL073651>
- Castro-Alcalá, E., Fernández-García, D., Carrera, J., & Bolster, D. (2012). Visualization of mixing processes in a heterogeneous sand box aquifer. *Environmental Science and Technology*, 46(6), 3228–3235. <https://doi.org/10.1021/es201779p>
- Chaudry, M. H. (2008). *Open Channel Flow* (2nd ed.). New York: Springer US.
- Chiogna, G., Cirpka, O. A., Grathwohl, P., & Rolle, M. (2011). Relevance of local compound-specific transverse dispersion for conservative and reactive mixing in heterogeneous porous media. *Water Resources Research*, 47(7). <https://doi.org/10.1029/2010WR010270>
- Cirpka, O. A., & Kitanidis, P. K. (2000). Characterization of mixing and dilution in heterogeneous aquifers by means of local temporal moments. *Water Resources Research*, 36(5), 1221–1236. <https://doi.org/10.1029/1999WR900354>
- Cirpka, O. A., Frind, E. O., & Helmig, R. (1999). Numerical simulation of biodegradation controlled by transverse mixing. *Journal of Contaminant Hydrology*, 40(2), 159–182. [https://doi.org/10.1016/S0169-7722\(99\)00044-3](https://doi.org/10.1016/S0169-7722(99)00044-3)
- Conant, B., Cherry, J. A., & Gillham, R. W. (2004). A PCE groundwater plume discharging to a river: Influence of the streambed and near-river zone on contaminant distributions. *Journal of Contaminant Hydrology*, 73(1–4), 249–279. <https://doi.org/10.1016/j.jconhyd.2004.04.001>
- Crispell, J. K., & Endreny, T. A. (2009). Hyporheic exchange flow around constructed in-channel structures and implications for restoration design. *Hydrological Processes*, 23, 1158–1168. <https://doi.org/10.1002/hyp.7230>
- Dentz, M., Gouze, P., & Carrera, J. (2011). Effective non-local reaction kinetics for transport in physically and chemically heterogeneous media. *Journal of Contaminant Hydrology*, 120–121, 222–236. <https://doi.org/10.1016/j.jconhyd.2010.06.002>

- Dykaar, B. B., & Kitanidis, P. K. (1996). Macrotransport of a biologically reacting solute through porous media. *Water Resources Research*, 32(2), 307–320. <https://doi.org/10.1029/95WR03241>
- Elliott, A. H., & Brooks, N. H. (1997). Transfer of nonsorbing solutes to a streambed with bed forms: Theory. *Water Resources Research*, 33(1), 123–136.
- Ellis, P. A., & Rivett, M. O. (2007). Assessing the impact of VOC-contaminated groundwater on surface water at the city scale. *Journal of Contaminant Hydrology*, 91(1–2), 107–127. <https://doi.org/10.1016/j.jconhyd.2006.08.015>
- Fox, A., Boano, F., & Arnon, S. (2014). Impact of losing and gaining streamflow conditions on hyporheic exchange fluxes induced by dune-shaped bed forms. *Water Resources Research*, 50, 1895–1907. <https://doi.org/10.1002/2013WR014668>
- Frederiksen, M. S., & Glud, R. N. (2006). Oxygen dynamics in the rhizosphere of *Zostera marina*: A two-dimensional planar optode study. *Limnology and Oceanography*, 51(2), 1072–1083.
- Freitas, J. G., Rivett, M. O., Roche, R. S., Durrant, M., Walker, C., & Tellam, J. H. (2015). Heterogeneous hyporheic zone dechlorination of a TCE groundwater plume discharging to an urban river reach. *Science of the Total Environment*, 505, 236–252. <https://doi.org/10.1016/j.scitotenv.2014.09.083>
- Galloway, J., Fox, A., Lewandowski, J., & Arnon, S. (2019). The effect of unsteady streamflow and stream-groundwater interactions on oxygen consumption in a sandy streambed. *Scientific Reports*, 9(1), 1–11. <https://doi.org/10.1038/s41598-019-56289-y>
- Glud, R. N., Ramsing, N. B., Gundersen, J. K., & Klimant, I. (1996). Planar optodes: a new tool for fine scale measurements of two-dimensional O₂ distribution in benthic communities. *Marine Ecology Progress Series*, 140, 217–226. <https://doi.org/10.3354/meps140217>
- Gomez-Velez, J. D., Harvey, J. W., Cardenas, M. B., & Kiel, B. (2015). Denitrification in the Mississippi River network controlled by flow through river bedforms. *Nature Geoscience*, 8(12), 941–945. <https://doi.org/10.1038/ngeo2567>
- Gooseff, M. N., Anderson, J. K., Wondzell, S. M., LaNier, J., & Haggerty, R. (2006). A modelling study of hyporheic exchange pattern and the sequence, size, and spacing of stream bedforms in mountain stream networks, Oregon, USA. *Hydrological Processes*, 20(11), 2443–2457. <https://doi.org/10.1002/hyp.6349>
- Graf, W. L. (2006). Downstream hydrologic and geomorphic effects of large dams on American rivers. *Geomorphology*, 79(3–4), 336–360. <https://doi.org/10.1016/j.geomorph.2006.06.022>
- Graham, E. B., Crump, A. R., Resch, Charles, T., Fansler, S., Arntzen, E., Kennedy, David W., Fredrickson, J. K., & Stegen, J. C. (2017). Deterministic influences exceed dispersal effects

- on hydrologically-connected microbiomes. *Environmental Microbiology*, 19(4), 1552–1567.
<https://doi.org/10.1111/1462-2920.13720>
- Haggerty, R., Ribot, M., Singer, G. A., Martí, E., Argerich, A., Agell, G., & Battin, T. J. (2014). Ecosystem respiration increases with biofilm growth and bed forms: Flume measurements with resazurin. *Journal of Geophysical Research: Biogeosciences*, 119(12), 2220–2230.
<https://doi.org/10.1002/2013JG002498>
- Harvey, J. W., Böhlke, J. K., Voytek, M. A., Scott, D., & Tobias, C. R. (2013a). Hyporheic zone denitrification: Controls on effective reaction depth and contribution to whole-stream mass balance. *Water Resources Research*, 49(10), 6298–6316.
<https://doi.org/10.1002/wrcr.20492>
- Harvey, J. W., Böhlke, J. K., Voytek, M. A., Scott, D., & Tobias, C. R. (2013b). Hyporheic zone denitrification: Controls on effective reaction depth and contribution to whole-stream mass balance. *Water Resources Research*, 49(10), 6298–6316.
<https://doi.org/10.1002/wrcr.20492>
- Herzog, S. P., Higgins, C. P., Singha, K., & Mccray, J. E. (2018). Performance of Engineered Streambeds for Inducing Hyporheic Transient Storage and Attenuation of Resazurin. *Environmental Science & Technology*, 52, 10627–10636. research-article.
<https://doi.org/10.1021/acs.est.8b01145>
- Hester, E. T., & Doyle, M. W. (2008). In-stream geomorphic structures as drivers of hyporheic exchange. *Water Resources Research*, 44(3). <https://doi.org/10.1029/2006WR005810>
- Hester, E. T., Young, K. I., & Widdowson, M. A. (2013). Mixing of surface and groundwater induced by riverbed dunes: Implications for hyporheic zone definitions and pollutant reactions. *Water Resources Research*, 49(9), 5221–5237.
<https://doi.org/10.1002/wrcr.20399>
- Hester, E. T., Young, K. I., & Widdowson, M. A. (2014). Controls on mixing-dependent denitrification in hyporheic zones induced by riverbed dunes: A steady state modeling study. *Water Resources Research*, 50, 9048–9066. <https://doi.org/10.1002/2014WR015424>
- Hester, E. T., Cardenas, M. B., Haggerty, R., & Apte, S. V. (2017). The importance and challenge of hyporheic mixing. *Water Resources Research*, 53, 3565–3575.
<https://doi.org/10.1002/2016WR020005>
- Hester, E. T., Eastes, L. E., & Widdowson, M. A. (2019). Effect of Surface Water Stage Fluctuation on Mixing-Dependent Hyporheic Denitrification in Riverbed Dunes. *Water Resources Research*, 55(6), 4668–4687.
<https://doi.org/https://doi.org/10.1029/2018WR024198>
- Kalbus, E., Schmidt, C., Molson, J. W., Reinstorf, F., & Schirmer, M. (2009). Influence of

- aquifer and streambed heterogeneity on the distribution of groundwater discharge. *Hydrology and Earth System Sciences*, 13(1), 69–77. <https://doi.org/10.5194/hess-13-69-2009>
- Kasahara, T., & Wondzell, S. M. (2003). Geomorphic controls on hyporheic exchange flow in mountain streams. *Water Resources Research*, 39(1), 1005. <https://doi.org/10.1029/2002wr001386>
- Kaufman, M. H., Cardenas, M. B., Buttles, J., Kessler, A. J., & Cook, P. L. M. (2017). Hyporheic hot moments: Dissolved oxygen dynamics in the hyporheic zone in response to surface flow perturbations. *Water Resources Research*, 53(8), 6642–6662. <https://doi.org/10.1002/2016WR020296>
- Kennedy, C. D., Genereux, D. P., Corbett, D. R., & Mitasova, H. (2009). Relationships among groundwater age, denitrification, and the coupled groundwater and nitrogen fluxes through a streambed. *Water Resources Research*, 45(9). <https://doi.org/10.1029/2008WR007400>
- Kessler, A. J., Glud, R. N., Bayani Cardenas, M., Larsen, M., Bourke, M. F., & Cook, P. L. M. (2012). Quantifying denitrification in rippled permeable sands through combined flume experiments and modeling. *Limnology and Oceanography*, 57(4), 1217–1232. <https://doi.org/10.4319/lo.2012.57.4.1217>
- Kiel, B. A., & Bayani Cardenas, M. (2014). Lateral hyporheic exchange throughout the Mississippi River network. *Nature Geoscience*, 7(6). <https://doi.org/10.1038/ngeo2157>
- Kitanidis, P. K. (1994). The concept of the Dilution Index. *Water Resources Research*, 30(7), 2011–2026. <https://doi.org/10.1029/94WR00762>
- Klimant, I., Kühl, M., Glud, R. N., & Holst, G. (1997). Optical measurement of oxygen and temperature in microscale: strategies and biological applications. *Sensors and Actuators B: Chemical*, 38–39(1–3), 29–37. [https://doi.org/10.1016/S0925-4005\(97\)80168-2](https://doi.org/10.1016/S0925-4005(97)80168-2)
- Knights, D., Sawyer, A. H., Barnes, R. T., Musial, C. T., & Bray, S. (2017). Tidal controls on riverbed denitrification along a tidal freshwater zone. *Water Resources Research*, 53, 799–816. <https://doi.org/10.1002/2016WR019405>
- Krause, S., Tecklenburg, C., Munz, M., & Naden, E. (2013). Streambed nitrogen cycling beyond the hyporheic zone: Flow controls on horizontal patterns and depth distribution of nitrate and dissolved oxygen in the upwelling groundwater of a lowland river. *Journal of Geophysical Research: Biogeosciences*, 118(1), 54–67. <https://doi.org/10.1029/2012JG002122>
- Landmeyer, J. E., Bradley, P. M., Trego, D. A., Hale, K. G., & Haas II, J. E. (2010). MTBE, TBA, and TAME attenuation in diverse hyporheic zones. *Ground Water*, 48(1), 30–41. <https://doi.org/10.1111/j.1745-6584.2009.00608.x>

- Larsen, M., Borisov, S. M., Grunwald, B., Klimant, I., & Glud, R. N. (2011). A simple and inexpensive high-resolution color-ratiometric planar optode imaging approach: Application to oxygen and pH sensing. *Limnology and Oceanography: Methods*, 9, 348–360.
- Loheide, S. P., & Lundquist, J. D. (2009). Snowmelt-induced diel fluxes through the hyporheic zone. *Water Resources Research*, 45(7), 1–9. <https://doi.org/10.1029/2008WR007329>
- Lu, C., & Luo, J. (2010). Dynamics of freshwater-seawater mixing zone development in dual-domain formations. *Water Resources Research*, 46(11). <https://doi.org/http://dx.doi.org/10.1029/2010WR009344>
- Lu, C., Kitanidis, P. K., & Luo, J. (2009). Effects of kinetic mass transfer and flow conditions on widening mixing zones in coastal aquifers. *Water Resources Research*, 45(12). <https://doi.org/http://dx.doi.org/10.1029/2008WR007643>
- Malcolm, I. A., Soulsby, C., Youngson, A. F., & Hannah, D. M. (2005). Catchment-scale controls on groundwater-surface water interactions in the hyporheic zone: Implications for salmon embryo survival. *River Research and Applications*, 21(9), 977–989. <https://doi.org/10.1002/rra.861>
- Malzone, J. M., Anseeuw, S. K., Lowry, C. S., & Allen-King, R. (2016). Temporal Hyporheic Zone Response to Water Table Fluctuations. *Groundwater*, 54(2), 274–285. <https://doi.org/10.1111/gwat.12352>
- Marzadri, A., Tonina, D., Bellin, A., & Valli, A. (2016). Mixing interfaces, fluxes, residence times and redox conditions of the hyporheic zones induced by dune-like bedforms and ambient groundwater flow. *Advances in Water Resources*, 88, 139–151. <https://doi.org/10.1016/j.advwatres.2015.12.014>
- Molz, F. (2015). Advection, dispersion, and confusion. *Groundwater*, 53(3), 348–353. <https://doi.org/10.1111/gwat.12338>
- Molz, F. J., & Widdowson, M. A. (1988). Internal inconsistencies in dispersion-dominated models that incorporate chemical and microbial kinetics. *Water Resources Research*, 24(4), 615–619. <https://doi.org/10.1029/WR024i004p00615>
- Naranjo, R. C., Niswonger, R. G., & Davis, C. J. (2015). Mixing effects on nitrogen and oxygen concentrations and the relationship to mean residence time in a hyporheic zone of a riffle-pool sequence. *Water Resources Research*, 51, 7202–7217. <https://doi.org/10.1002/2014WR016559>.Received
- Newcomer, M. E., Hubbard, S. S., Fleckenstein, J. H., Maier, U., Schmidt, C., Thullner, M., et al. (2018). Influence of Hydrological Perturbations and Riverbed Sediment Characteristics on Hyporheic Zone Respiration of CO₂ and N₂. *Journal of Geophysical Research: Biogeosciences*, 123, 1–21. <https://doi.org/10.1002/2017JG004090>

- Nida, A. (2015). *Investigation of Hydraulic Boundary Conditions Control on Hyporheic Mixing Zone Thickness: A Laboratory Experiment*. Virginia Polytechnic Institute and State University.
- Peralta-Maraver, I., Reiss, J., & Robertson, A. L. (2018). Interplay of hydrology, community ecology and pollutant attenuation in the hyporheic zone. *Science of the Total Environment*, 610–611, 267–275. <https://doi.org/10.1016/j.scitotenv.2017.08.036>
- Puckett, L. J., Zamora, C., Essaid, H., Wilson, J. T., Johnson, H. M., Brayton, M. J., & Vogel, J. R. (2008). Transport and Fate of Nitrate at the Ground-Water/Surface-Water Interface. *Journal of Environment Quality*, 37(3), 1034–1050. <https://doi.org/10.2134/jeq2006.0550>
- Robinson, G., Hamill, G. A., & Ahmed, A. A. (2015). Automated image analysis for experimental investigations of salt water intrusion in coastal aquifers. *Journal of Hydrology*, 530, 350–360. <https://doi.org/10.1016/j.jhydrol.2015.09.046>
- Robinson, G., Ahmed, A. A., & Hamill, G. A. (2016). Experimental saltwater intrusion in coastal aquifers using automated image analysis: Applications to homogeneous aquifers. *Journal of Hydrology*, 538, 304–313. <https://doi.org/10.1016/j.jhydrol.2016.04.017>
- Rolle, M., Eberhardt, C., Chiogna, G., Cirpka, O. A., & Grathwohl, P. (2009). Enhancement of dilution and transverse reactive mixing in porous media : Experiments and model-based interpretation. *Journal of Contaminant Hydrology*, 110, 130–142. <https://doi.org/10.1016/j.jconhyd.2009.10.003>
- Rolle, M., Hochstetler, D., Chiogna, G., Kitanidis, P. K., & Grathwohl, P. (2012). Experimental Investigation and Pore-Scale Modeling Interpretation of Compound-Specific Transverse Dispersion in Porous Media. *Transport in Porous Media*, 93(3), 347–362. <https://doi.org/10.1007/s11242-012-9953-8>
- Rolle, M., Chiogna, G., Hochstetler, D. L., & Kitanidis, P. K. (2013). On the importance of diffusion and compound-specific mixing for groundwater transport : An investigation from pore to field scale. *Journal of Contaminant Hydrology*, 153, 51–68. <https://doi.org/10.1016/j.jconhyd.2013.07.006>
- Santner, J., Larsen, M., Kreuzeder, A., & Glud, R. N. (2015). Two decades of chemical imaging of solutes in sediments and soils - a review. *Analytica Chimica Acta*, 878, 9–42. <https://doi.org/10.1016/j.aca.2015.02.006>
- Sawyer, A. H. (2015). Enhanced removal of groundwater-borne nitrate in heterogeneous aquatic sediments. *Geophysical Research Letters*, 42(2), 403–410. <https://doi.org/10.1002/2014GL062234>
- Sawyer, A. H., & Cardenas, M. B. (2009). Hyporheic flow and residence time distributions in heterogeneous cross-bed sediment. *Water Resources Research*, 45(8), 1–12.

<https://doi.org/10.1029/2008WR007632>

- Schmadel, N. M., Ward, A. S., Lowry, C. S., & Malzone, J. M. (2016). Hyporheic exchange controlled by dynamic hydrologic boundary conditions. *Geophysical Research Letters*, *43*, 4408–4417. <https://doi.org/10.1002/2016GL068286>
- Shuai, P., Cardenas, M. B., Knappett, P. S. K., Bennett, P. C., & Neilson, B. T. (2017). Denitrification in the banks of fluctuating rivers: The effects of river stage amplitude, sediment hydraulic conductivity and dispersivity, and ambient groundwater flow. *Water Resources Research*, *53*, 7951–7967. <https://doi.org/https://doi.org/10.1002/2017WR020610>
- Stegen, J. C., Fredrickson, J. K., Wilkins, M. J., Konopka, A. E., Nelson, W. C., Arntzen, E. V., et al. (2016). Groundwater-surface water mixing shifts ecological assembly processes and stimulates organic carbon turnover. *Nature Communications*, *7*, 1–12. <https://doi.org/10.1038/ncomms11237>
- Stelzer, R. S., Bartsch, L. A., Richardson, W. B., & Strauss, E. A. (2011). The dark side of the hyporheic zone: Depth profiles of nitrogen and its processing in stream sediments. *Freshwater Biology*, *56*(10), 2021–2033. <https://doi.org/10.1111/j.1365-2427.2011.02632.x>
- Stuart, M. E., Lapworth, D. J., Thomas, J., & Edwards, L. (2014). Fingerprinting groundwater pollution in catchments with contrasting contaminant sources using microorganic compounds. *Science of the Total Environment*, *468–469*, 564–577. <https://doi.org/10.1016/j.scitotenv.2013.08.042>
- Taylor, S. W., & Guha, H. (2017). Time and Magnitude of Peak Concentration of Reactive Groundwater Contaminants Discharged to a River, *55*(1), 63–72. <https://doi.org/10.1111/gwat.12478>
- Tonina, D., & Bellin, A. (2008). Effects of pore-scale dispersion, degree of heterogeneity, sampling size, and source volume on the concentration moments of conservative solutes in heterogeneous formations. *Advances in Water Resources*, *31*(2), 339–354. <https://doi.org/10.1016/j.advwatres.2007.08.009>
- Tonina, D., Marzadri, A., & Bellin, A. (2015). Benthic uptake rate due to hyporheic exchange: The effects of streambed morphology for constant and sinusoidally varying nutrient loads. *Water*, *7*(2), 398–419. <https://doi.org/10.3390/w7020398>
- Trauth, N., & Fleckenstein, J. H. (2017). Single discharge events increase reactive efficiency of the hyporheic zone. *Water Resources Research*, *53*(1), 779–798. <https://doi.org/https://doi.org/10.1002/2016WR019488>
- Triska, F. J., Kennedy, V. C., Avanzino, R. J., Zellweger, G. W., & Bencala, K. E. (1989). Retention and transport of nutrients in a third-order stream: channel processes. *Ecology*,

70(6), 1877–1892. <https://doi.org/10.2307/1938119>

White, D. S. (2006). Perspectives on Defining and Delineating Hyporheic Zones. *Journal of the North American Benthological Society*, 12(1), 61–69. <https://doi.org/10.2307/1467686>

Wolke, P., Teitelbaum, Y., Deng, C., Lewandowski, J., & Arnon, S. (2020). Impact of bed form celerity on oxygen dynamics in the hyporheic zone. *Water (Switzerland)*, 12(1), 5–7. <https://doi.org/10.3390/w12010062>

Zarnetske, J. P., Haggerty, R., Wondzell, S. M., & Baker, M. A. (2011a). Dynamics of nitrate production and removal as a function of residence time in the hyporheic zone. *Journal of Geophysical Research: Biogeosciences*, 116(1), 1–12. <https://doi.org/10.1029/2010JG001356>

Zarnetske, J. P., Haggerty, R., Wondzell, S. M., & Baker, M. A. (2011b). Labile dissolved organic carbon supply limits hyporheic denitrification. *Journal of Geophysical Research: Biogeosciences*, 116(4). <https://doi.org/10.1029/2011JG001730>

Zarnetske, J. P., Haggerty, R., Wondzell, S. M., Bokil, V. A., & González-Pinzón, R. (2012). Coupled transport and reaction kinetics control the nitrate source-sink function of hyporheic zones. *Water Resources Research*, 48(11), 1–15. <https://doi.org/10.1029/2012WR011894>

Zhou, Y., Ritzi, R. W., Soltanian, M. R., & Dominic, D. F. (2014). The Influence of Streambed Heterogeneity on Hyporheic Flow in Gravelly Rivers. *Groundwater*, 52(2), 206–216. <https://doi.org/10.1111/gwat.12048>

**Chapter 4. Numerical modeling of an abiotic hyporheic mixing-dependent reaction:
chemical evolution of mixing and reactant production zones**

Authors: Katherine Y. Santizo, Mark A. Widdowson, and Erich T. Hester*

Affiliations: Charles E. Via Jr. Department of Civil and Environmental Engineering, Virginia
Tech

Keywords: surface water-groundwater interaction, mixing zone thickness, production zone
thickness, dispersion, dissolved oxygen

Status: This manuscript is in preparation for journal submission.

Abstract

The hyporheic zone can be defined as where upwelling groundwater mixes with surface water in shallow submerged sediments. Such mixing may allow reactions dependent on chemicals in both source waters (mixing-dependent/mixing-controlled reactions) which can attenuate contaminants along upwelling flowpaths, reducing transport to surface water. This study used MODFLOW/SEAM3D to numerically simulate earlier laboratory observations of mixing zones and mixing-dependent reaction between sodium sulfite (Na_2SO_3) in upwelling groundwater and dissolved oxygen (DO) in downwelling surface water (i.e., hyporheic flow cell) to produce sodium sulfate (Na_2SO_4). This reaction does not occur in nature, but rather acts a surrogate for mixing-dependent reactions, thus allowing evaluation of basic controls. We evaluated how location and thickness of mixing zones and reaction product production zones dynamically respond to variations in 1) hydrologic boundary “inflow ratio” (upwelling groundwater to downwelling surface water that formed the hyporheic flow cell); 2) inflow boundary concentrations of DO, Na_2SO_3 and SO_4 ; and 3) reaction kinetic rate. Sensitivity analysis showed that mixing zones, production zones, and front locations were most sensitive to changes in the inflow ratio and least sensitive to background SO_4 concentrations. Mixing zone thickness for reactive DO calibrated to experimental data was thinner than that for the “DO tracer” (identical source location and concentration as DO but conservative tracer), indicating that as DO is consumed its mixing zone narrows. The SO_4 production zone was consistently larger than the DO mixing zone and located further toward the periphery of the hyporheic flow cell, i.e., where prior reactant consumption occurred. Small changes in mixing/production zone thicknesses were linked to large changes in mass consumed and produced. This study improves understanding of the evolution of hyporheic mixing-dependent reaction zones that occur even under steady state hydraulics, emphasizing their complex controls. It further links practical field metrics such as reactant production widths to their contaminant management implications such as mass consumed.

4.1 Introduction

The hyporheic zone occurs where surface water and groundwater interact below or adjacent to stream and riverbeds. It is a key interface within the river corridor where important chemical reactions occur in the presence of unique biological communities. Mixing along subsurface flowpaths is an important process that influences contaminant attenuation in the hyporheic zone (Bandopadhyay et al., 2018; Hester et al., 2014, 2017; Li et al., 2017). Mixing of source waters is particularly important for upwelling groundwater contaminant plumes which may undergo natural attenuation via mixing-dependent (mixing-controlled) reactions in the hyporheic zone and thus protect surface water (Boano et al., 2018; Conant et al., 2004; Ellis & Rivett, 2007; Freitas et al., 2015; Hester et al., 2014, 2019; Krause et al., 2013; Weatherill et al., 2019).

Controls on natural attenuation of upwelling pollutants in the hyporheic zone have been of growing interest, including how such attenuation may be enhanced. For example, Weatherill et al. (2019) observed that areas where nitrate plumes had already denitrified were more favorable to reductive dechlorination of upwelling chlorinated ethenes due to lowered redox potential. Similarly, Burke et al. (2014) studied temperature-dependent attenuation of micropollutants and showed that the presence of colder surface water allowed for deeper penetration of oxygen-rich water into the subsurface. This in turn aided oxic-dependent attenuation as the mixing of the oxic water and micropollutants enhanced reactions and mass consumption. Finally, Krause et al. (2013) showed the greatest denitrification in upwelling groundwater occurred where low hydraulic conductivity led to higher residence times which allowed for longer mixing times and hence DO depletion. These studies demonstrate that attenuation may be dependent on mixing of solutes that provide ideal location for reactions to occur.

Given the importance of mixing-dependent reactions for natural attenuation of upwelling contaminants in the hyporheic zone, analysis of variables that influence hyporheic mixing processes is an important area of study. Previous studies have shown that key parameters that enhance mixing and therefore mixing-dependent reactions include heterogeneity, transiency, and residence times (Bandopadhyay et al., 2018; Hester et al., 2013, 2014, 2019). For example, Hester et al. (2014) employed a numerical model to study mixing-dependent denitrification in the hyporheic zone and observed that mixing zone thickness was relatively small with values approximately 1 cm. A follow-up study showed that surface water fluctuations increased mixing-dependent reaction of denitrification by roughly 80% (Hester et al., 2019). Su et al. (2020), used a

stochastic approach to determine that surface water velocity and groundwater flux were more influential than heterogeneity at inducing hyporheic mixing.

While these studies show the relative importance of physical parameters on mixing-dependent reactions in the hyporheic zone, the influence of transport variables such as reactant concentrations and kinetic rates have received less attention, as have quantitative analyses of mixing, mass transformation, and mixing locations. Further, many prior studies have focused on the overall influence of controlling parameters but have not carefully evaluated the dynamic evolution of reactive hyporheic mixing zones over time, including how that informs knowledge of process. Finally, the relationship between mixing and attenuation in the hyporheic zone has not been fully explored (Chiogna et al., 2011, 2012; Rolle et al., 2013).

Chiogna et al. (2012) studied how mixing could be quantified using a flux-related dilution index to relate to a reactive plume. They concluded that the flux-related dilution index varied based on the progression of the reaction plume without having to know the location of concentration distributions. However, the flux-related dilution index may be hard to obtain from field and laboratory experiments as it relies on detailed knowledge of location and magnitude of mass fluxes. In comparison, mixing, mixing widths, and location are practical measurements that can be taken in field, laboratory, and modeling experiments. Using these measurements to relate mixing to attenuation can clarify what processes are occurring and therefore what may enhance the attenuation.

In this study, we aim to determine the effects of varying reaction concentrations, kinetic rates, and hydraulic parameters on mixing and mixing-dependent reactions in a model simulated hyporheic zone modeled based on laboratory observations from Chapter 3 (Santizo et al. (2020)). We varied the kinetic rate, initial chemical concentrations, surface water (SW) head drop (Δh), and inflow ratio (ratio between the upwelling GW flow rate and the downwelling SW flow rate, i.e., the amount of gaining). We then quantified the relative influence of these controlling parameters on mixing and reaction production to understand the influence on chemical transformation, reduction, and potential attenuation. Our specific objectives were to (1) simulate mixing-dependent abiotic reaction of sodium sulfite (Na_2SO_3) and dissolved oxygen (DO) to sodium sulfate (Na_2SO_4) observed in laboratory data from Santizo et al. (2020); (2) quantify variation in the location and thickness of both reactant mixing zones and resulting production

zones of mixing-dependent reaction products in response to variations in controlling factors including SW Δh , inflow ratio, reaction kinetic rates, and initial concentrations of DO, SO₃ and SO₄; (3) determine the relative influence of such controlling factors through sensitivity coefficients; and (4) analyze the relationship between mixing and production zone thicknesses and mass consumed/produced.

4.2 Methods

We used MODFLOW to simulate hyporheic flow and SEAM3D to simulate hyporheic transport and mixing-dependent reactions. The model was calibrated to the laboratory experiments of Santizo et al. (2020). A sensitivity analysis was then performed to determine relative effects of controlling factors.

4.2.1 Model Domain and Governing Equations

The model simulated the experimental set-up from Santizo et al. (2020) where a mixing-dependent reaction occurred in shallow submerged sediments between a hyporheic flow cell and upwelling groundwater. The model domain encompassed the sand box and a vertical “in-stream” partition from Santizo et al. (2020) (Figure 4.1a). The model domain was 80 cm by 43 cm by 10 cm with the partition placed 20 cm from the left boundary and to 6 cm depth in the sand.

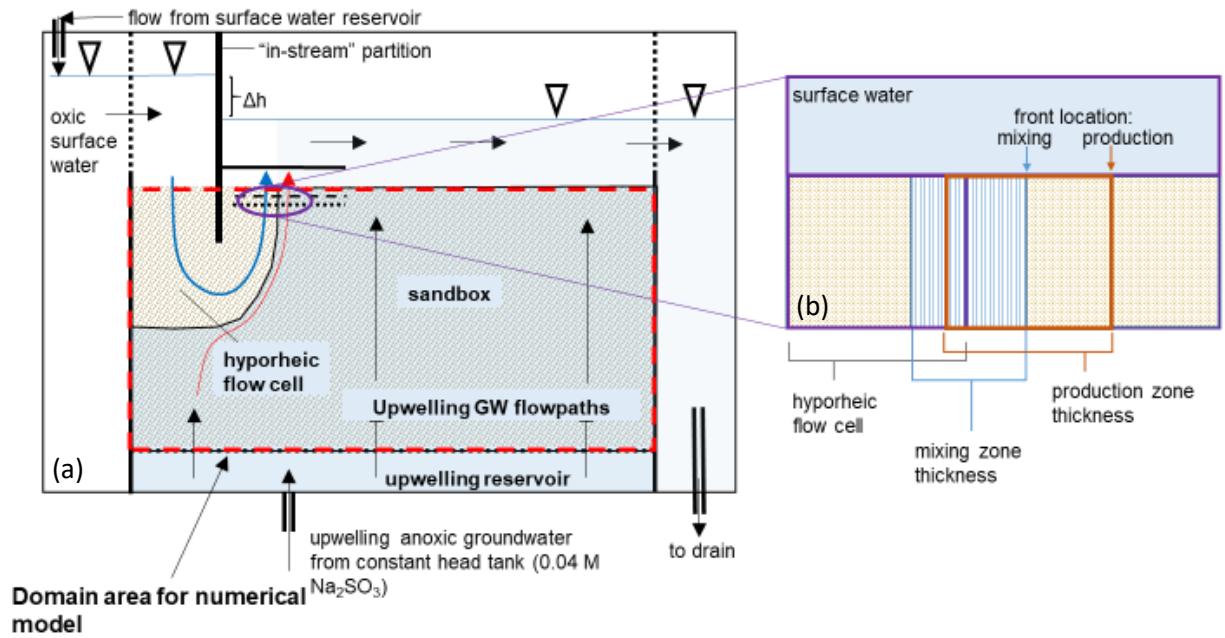


Figure 4.1. (a) Mesocosm set up from laboratory experiments of Santizo et al. (2020) (Chapter 3) showing model domain used in this study (outlined by red dotted line), modified from Santizo et al. (2020). (b) Close-up conceptual schematic of mixing zone thickness, production zone thickness, mixing front location, and production front location metrics relative to one another and hyporheic flow cell (not drawn to scale).

MODFLOW was used to simulate the porewater flow and system hydraulics of the laboratory experiment of Santizo et al. (2020). MODFLOW solves the 3D groundwater equation (equation 4.1)

$$\frac{\partial}{\partial x_i} \left(K_{ii} \frac{\partial h}{\partial x_i} \right) + W = S_s \frac{\partial h}{\partial t} \quad (4.1)$$

using a finite-difference method where K_{ii} is hydraulic conductivity (L/T) in the direction of respective Cartesian coordinate axes x_i (L), h is the piezometric head (L), W is a source-sink term (T^{-1}), S_s is specific storage (L^{-1}), and t is time (T).

SEAM3D (Widdowson et al., 2002) was used to numerically model solute transport and reaction. The reaction in Santizo et al. (2020) was the abiotic mixing-dependent reaction of sodium

sulfite (Na_2SO_3) from GW with dissolved oxygen (DO) from SW to produce sodium sulfate (Na_2SO_4) in the mixing zone. This reaction was chosen by Santizo et al. (2020) for its use of oxygen as its electron acceptor, like many hyporheic reactions, as well as its simple kinetics. SEAM3D simulated the three reactive chemical species plus a “DO tracer” (i.e., conservative tracer entering the model at the same location and concentration as the reactive DO) to compare mixing-dependent reaction to non-reactive mixing.

SEAM3D incorporates the MODFLOW cell-by-cell flow output to solve the advection, dispersion, and reaction equation in groundwater (equation 4.2).

$$\frac{\partial(\theta C^k)}{\partial t} = \frac{\partial}{\partial x_i} \left(\theta D_{ij} \frac{\partial C^k}{\partial x_j} \right) - \frac{\partial}{\partial x_i} (\theta v_i C^k) + W C_s^k + \sum R \quad (4.2)$$

where θ is the porosity (dimensionless), C^k is concentration of dissolved component k (ML^{-3}), t is time (T), x_i, j is distance along respective Cartesian coordinate axes (L), D_{ij} is the hydrodynamic dispersion coefficient tensor (L^2T^{-1}), v_i is linear pore water velocity (LT^{-1}), C_s^k is the source-sink flux concentration for constituent k (ML^{-3}) and $\sum R$ is the chemical reaction term ($\text{ML}^{-3}\text{T}^{-1}$). In this case, the chemical reaction term (equation 4.3) is the abiotic first-order reaction of Na_2SO_3 and DO to Na_2SO_4 which takes the form of:

$$R = \lambda C^{\text{DO}} \quad (4.3)$$

where λ is the reaction kinetic rate with units of inverse time as we have a first order reaction.

The cell grid size for both MODFLOW and SEAM3D was 0.0025 m by 0.0025 m by 0.10 m. Several grid sizes were tested for accuracy in matching observed values and numerical dispersion. The chosen grid size balanced these concerns against run times; larger grid sizes had too much numerical dispersion and run times for smaller grid sizes were too long given minimal improvement in matching observed values. Equations 4.1 and 4.2 are the general 3D case, but in this study, we simulated the mesocosm in 2D.

The model simulated a 3-hr period that matched the experiments. In the experiments, the first two hours were used to ensure enough time had elapsed to fully observe dynamic evolution of transport and reaction zones followed by approach to steady state transport, and the third hour was used for

reaction imaging and sampling. MODFLOW was run in steady-state mode and SEAM3D simulated dynamic transport with a timestep of 5.9×10^{-6} days (0.51 s).

4.2.2 Model Inputs, Calibration, and Outputs

MODFLOW and SEAM3D input parameters were initially determined from the laboratory experimental data of Santizo et al. (2020) and then certain parameters were varied slightly during calibration until the mixing thickness and front location for both Δh matched the laboratory observations (Table 4.1). Here we first lay out the model outputs that were used to evaluate calibration, and then we systematically go through the model inputs themselves. DO mixing zone thickness (Figure 4.1b) was calculated using linear interpolation to estimate locations of the 0.16 and 0.84 normalized concentrations (Marzadri et al., 2016; Santizo et al., 2020) at 3.5 cm depth in the sand (model row 14), and then calculating their spatial separation. This method was also used to determine SO_3 and DO tracer mixing zone thicknesses. SO_4 production zone thicknesses were calculated as the spatial separation between the two 0.16 concentrations on each side of the plume. The mixing front location for all chemical species was taken as the position of the 0.84 concentration, including the location of SO_4 production which used the descending front (right side in Figure 4.1b) again at 3.5 cm depth. We used the 0.84 concentration for mixing front location rather than 0.16 or 0.5 because it represents the end of the bulk concentration providing an “end” location of mixing. Peak location and concentration for SO_4 were also estimated.

The left and right MODFLOW boundaries of the model domain were no-flow. The top and bottom boundaries were constant head boundaries that produced the two different SW head drops (Δh , Figure 4.1a) of 4.5 cm and 6.0 cm from the experiments. The bottom boundary head in MODFLOW and the longitudinal to transverse dispersivity ratio in SEAM3D were not measured in the experiments and were set to match the observed mixing zone front location and thickness, respectively. Kinetic rate, and DO and SO_3 concentrations, were varied in SEAM3D until simulated concentrations to the right of the partition matched the laboratory observations of DO mixing zone thickness and DO concentration profile at 3.5 cm depth (model row 14) for both Δh (4.5 cm and 6.0 cm). Concentration calibration used concentrations normalized by the maximum concentration value found to the right of the partition. Production zone front was not calibrated since the observed values from laboratory experiments did not provide sufficient spatial accuracy.

Table 4.1. Model input parameters used for calibration.

Parameter/Variables	Initial Estimate*	Model Input
Hydraulic conductivity, K (m/d)	57	57
Kinetic rate, λ (1/s)	0.33	0.305
DO concentration (mol/L)	2.3×10^{-4}	2.8×10^{-4}
SO ₃ concentration (mol/L)	0.04	0.04
SO ₄ concentration (mol/L)	0	0
Effective porosity (-)	0.37	0.30
Longitudinal: Transverse Dispersivity Ratio	0.10	0.11
Transverse dispersivity (m)	-	0.00011
Top constant head to the left of the partition (m)	$\Delta h = 0.045 \text{ m: } 0.542$ $\Delta h = 0.060 \text{ m: } 0.557$	$\Delta h = 0.045 \text{ m: } 0.542$ $\Delta h = 0.060 \text{ m: } 0.557$
Top constant head to the right of the partition (m)	0.497	0.497
Bottom constant head (m)	-	$\Delta h = 0.045 \text{ m: } 0.5407$ $\Delta h = 0.060 \text{ m: } 0.544$

*estimates are values from experiments in Santizo et al. (2020). Values are averages from measured values during experiments and benchtop trials.

4.2.3 Sensitivity Analysis and Coefficients

A sensitivity analysis of 26 model runs was conducted in SEAM3D to determine the influence of model input parameters (Table 4.2) on mixing and production zone thickness and front location for Na₂SO₃, DO, SO₄ and tracer DO. In this analysis, the calibrated models were deemed the basecase as they were the scenarios that matched the laboratory experiments.

The inflow ratio, which is the ratio between the upwelling GW flow rate and the downwelling SW flow rate, was varied by adjusting the bottom boundary head, and values below and above those of the basecase were used. The inflow ratio was maintained at values higher than 1.0 since any value below that would indicate a losing condition and a hyporheic flow cell larger

than the model domain. This ratio indicates the degree to which GW inflow exceeds downwelling flow rate for a given SW Δh . The constant head boundaries at the top of the model were not changed to maintain constant Δh .

The upwelling SO_4 concentration was varied to determine if background values influenced mixing and production zone thickness and front location. Lower concentrations were chosen rather than higher concentrations to maintain SO_3 as the excess chemical species, consistent with experimental conditions. The reaction observed is considered instantaneous due to the kinetic rate, however, kinetic rates do vary thus we wanted to observe the impact of a lower and higher kinetic rate on the mixing-dependent reaction.

Table 4.2. Modeling sensitivity analysis parameters. **Bolded** values are basecase (experimental) conditions.

Model Input Parameter	Input Values for Sensitivity Analysis
Surface Water Head Drop (Δh , m)	4.5, 6.0
Inflow Ratio (GW inflow: SW inflow, -)	1.14-3.47 (1.94 , 3.22 for $\Delta h=6.0$ cm and 4.5 cm, respectively)
Downwelling DO Concentration (mol/L)	1.4×10^{-4} , 2.8×10^{-4} , 4.1×10^{-4}
Upwelling SO_4 Concentration (mol/L)	0 , 1.0×10^{-4} , 2.1×10^{-4}
Upwelling SO_3 Concentration (mol/L)	0.01, 0.02, 0.04
Kinetic Rate, λ (1/s)	0.1, 0.305 , 1.0

We calculated sensitivity coefficients to compare the influence of each sensitivity analysis parameter (Table 4.2) on changes in mixing/production zone thickness and front location relative to the basecase. Sensitivity coefficients were calculated for all parameters and time frames using:

$$X_{m,n} = \frac{\partial \hat{y}_m}{\partial a_n/a_n} \approx \frac{\hat{y}_m(a_n + \Delta a_n) - \hat{y}_m(a_n)}{\Delta a_n/a_n} \quad (4.4)$$

where $X_{m,n}$ is the sensitivity coefficient of the dependent variable \hat{y} with respect to the m^{th} parameter at the n^{th} observation point (DO, SO_3 , SO_4 , tracer at basecase), a_n is the parameter value for the basecase, Δa_n is a change in the parameter from the basecase value, and $\hat{y}(a_n)$ and $\hat{y}(a_n +$

Δa_n) are the values of the model-dependent variable obtained for the basecase and for the varied-parameter case, respectively. The values were calculated per parameter changed and per head drop. However, the maximum and minimum value calculated among all timesteps and head drops was used for the comparison of sensitivity coefficients.

4.3 Results

Our results focus on four main outcomes: (1) basecase head and concentration distributions and their match with laboratory experimental observations, (2) temporal trends of mixing zone and reactant production zone thicknesses and front locations for the basecase, (3) zone front locations from model sensitivity analysis compared to the basecase scenarios, and (4) zone thicknesses from model sensitivity analysis compared to the basecase scenarios.

4.3.1 Basecase Head and Concentration Distributions and Match to Laboratory Observations

MODFLOW and SEAM3D head and concentration distributions are shown in Figure 4.2. SEAM3D results show the hyporheic flow cell with high DO concentration (~10 mg/L, red color), upwelling GW below and to the right with low DO concentration (~0 mg/L, blue color), and a thin mixing zone between (0-9 mg/L) (Figure 4.2cdef). The DO “tracer” concentration distributions (Figure 4.2cd) illustrate a larger zone of “mid” concentrations (i.e., greenish colors) between the oxic and anoxic values, whereas in the reactive DO concentration distributions (Figure 4.2ef) this greenish band has narrowed demonstrating the influence of the reaction on the concentration profiles.

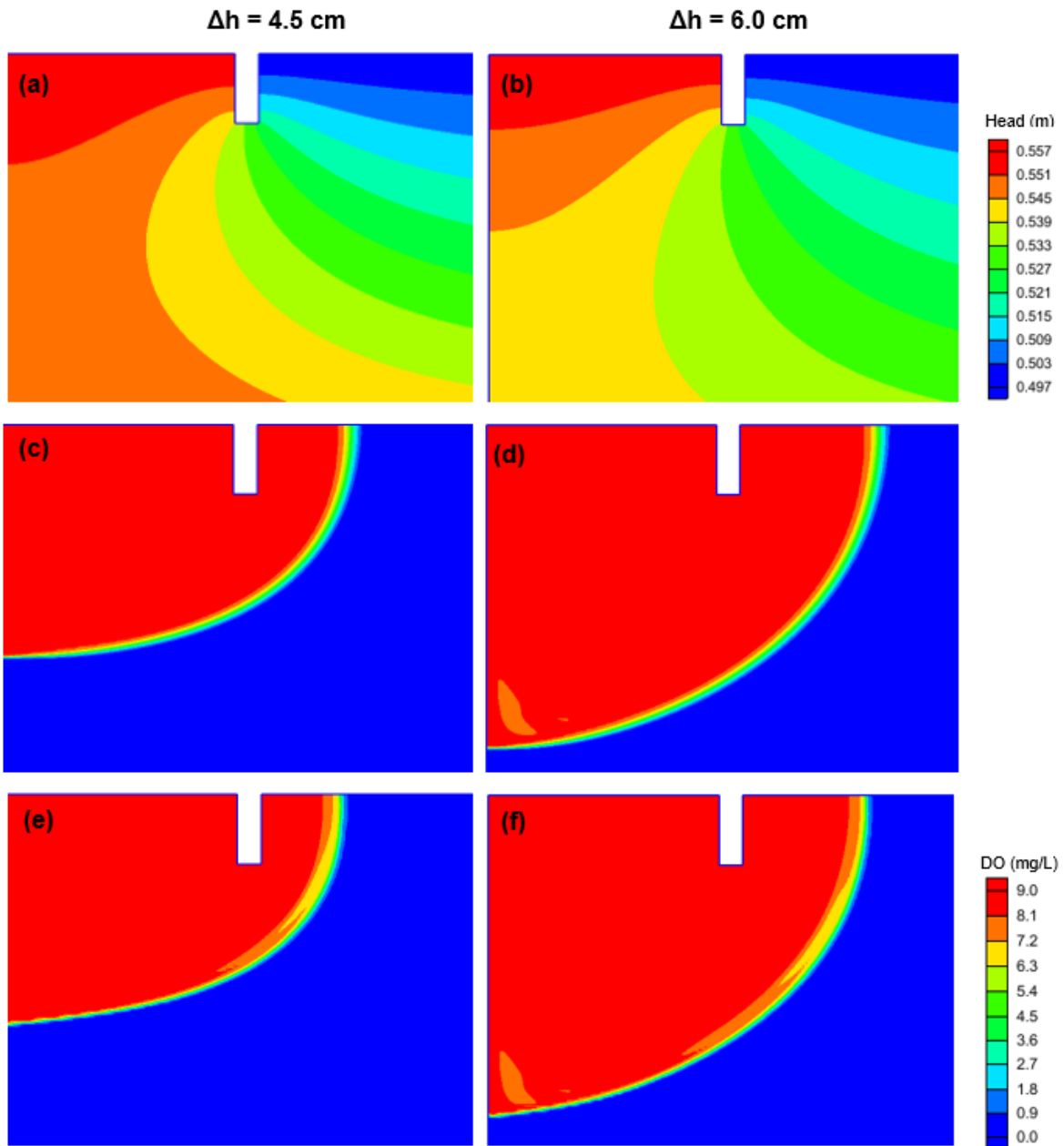


Figure 4.2. MODFLOW head distributions for head drop (Δh) = (a) 4.5 cm and (b) 6.0 cm. Basecase SEAM3D DO “tracer” concentration distributions for Δh = (c) 4.5 cm and (d) 6.0 cm. Basecase SEAM3D reactive DO concentration distributions for Δh = (e) 4.5 cm and (f) 6.0 cm. All images have been cropped to 30 cm (vertical) by 40 cm (horizontal) to provide detail in areas of interest. For comparison, concentration distributions from the laboratory experiments can be found in Figure 3.2 in Chapter 3 (Santizo et al. 2020). Upstream is to the left in each panel, and downstream is to the right.

There was good agreement between model results and laboratory observations (Figure 4.3). The observed and modeled profiles were in good agreement (Figure 4.3a), with the region of normalized DO concentrations of 0.1-0.9 having the best match. DO mixing zone thicknesses and fronts were calculated within this 0.1-0.9 region (i.e., 0.16-0.84) and thus were also in good agreement (Figure 4.3bc).

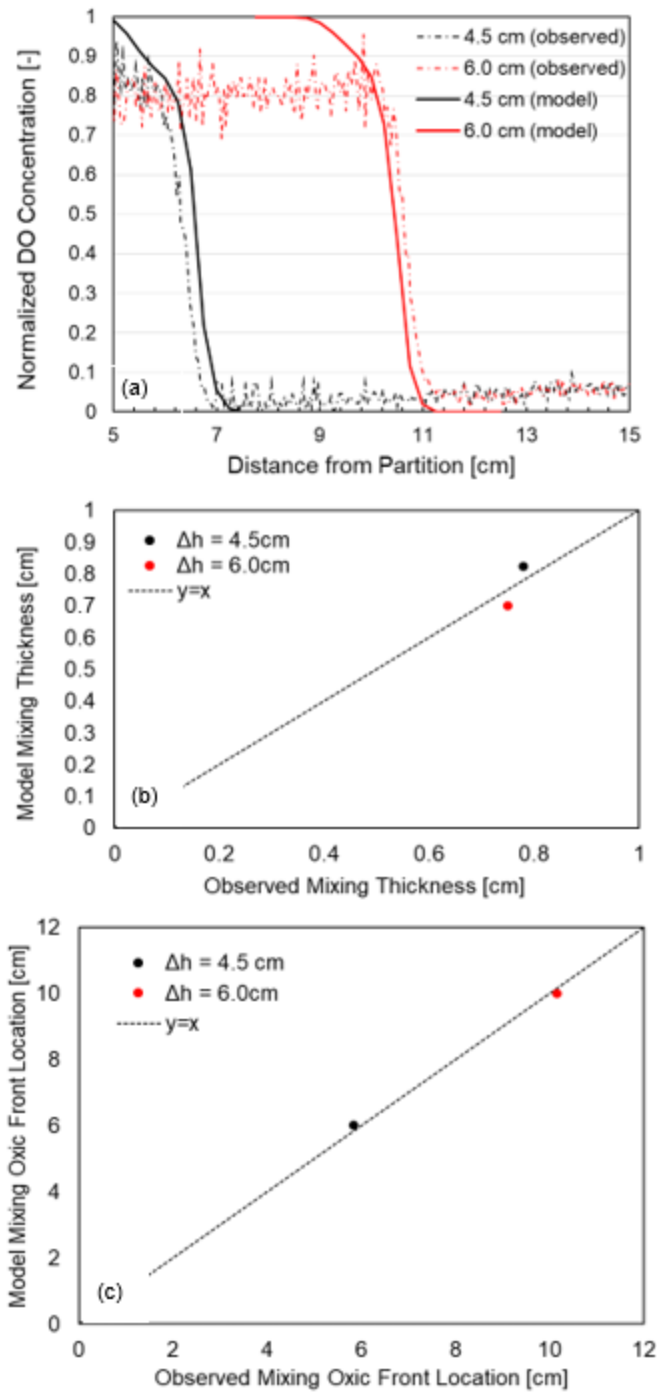


Figure 4.3. Basecase simulated versus observed (a) normalized DO concentration profiles, (b) DO mixing thicknesses, and (c) DO mixing front locations for each head drop (Δh), all at 3.5 cm depth. Upstream is to the left in panel a, and downstream is to the right.

4.3.2 Temporal Trends

Chemical concentration histories revealed dynamic changes in transport and reaction processes despite steady-state hydraulics (Figure 4.4). Both the DO mixing front and SO₄ plume moved upstream with time (to the left in Figure 4.4) as the reaction consumed DO from the downstream side (from the right in Figure 4.4). The concentration profiles for DO (limiting reactant) and SO₄ (reaction product) did not fully overlap. The SO₄ peak was located approximately where DO concentrations went to zero, and thus approximately half of the SO₄ plume was in anoxic conditions.

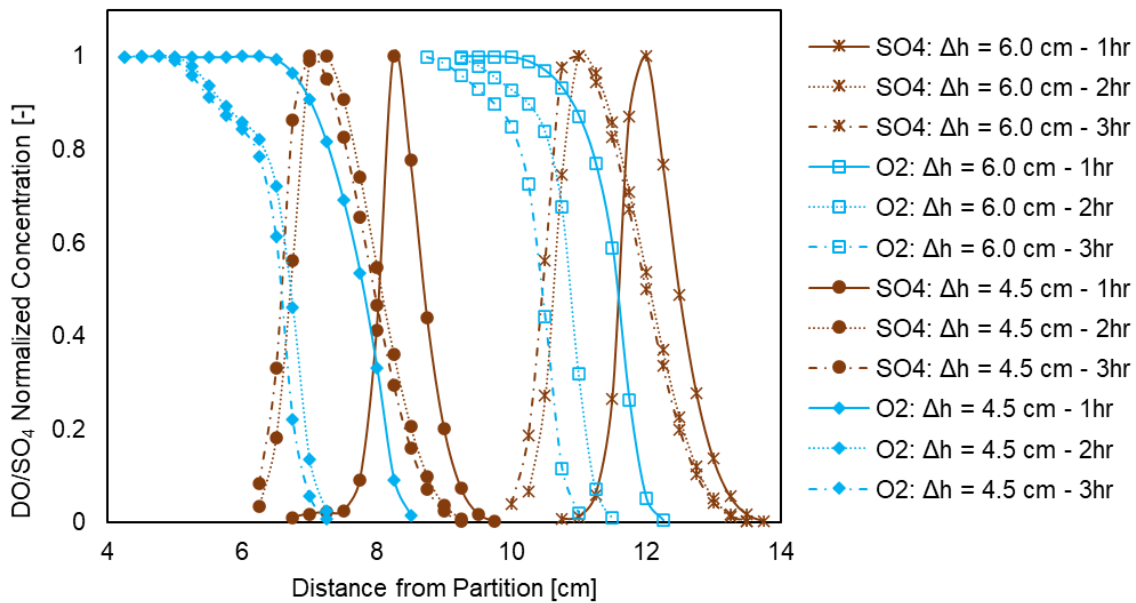


Figure 4.4. Basecase concentration profiles (normalized to maximum concentration) at 3.5 cm depth versus distance to the right of the partition for DO and SO₄ at 1, 2, and 3-hr intervals for each head drop (Δh). Upstream is to the left in the plot, and downstream is to the right.

The SO₄ concentration profiles exhibited a gaussian distribution, as commonly seen in groundwater plumes. The shift upstream with time is seen in both the DO and SO₄. The 2-hr and 3-hr profiles are similar, indicating balance between kinetics and transport was being approached. This match was better (i.e., this transport balance occurred earlier) for the lower Δh of 4.5 cm.

When analyzing mixing/production zone thickness and front location over time for all chemical species, some trends emerge (Figure 4.5). First, the tracer is constant with time consistent

with steady-state hydraulics. Second, the trends for zone thickness and front location vary among chemical species. For example, the DO mixing zone thicknesses for the lower and higher Δh are closer to each other than each respective value to another species at the same Δh . The largest relative change over time for either zone thickness or front location is the increase in SO_4 production zone thickness with time (Figure 4.5b), probably reflecting the large SO_4 production in the system. There is no SO_4 in the system prior to the reaction therefore when SO_4 is produced, the zone thickness quickly increases whereas the already established DO and SO_3 zone thickness changed minimally. The SO_3 change is likely even less so than the DO due to the excess quantity of SO_3 in the system, where SO_3 consumption has less relative effect on zone thickness. The zone front locations changed minimally in all cases regardless of the reaction indicating that hydraulics have a larger influence on the zone front location than reaction kinetics.

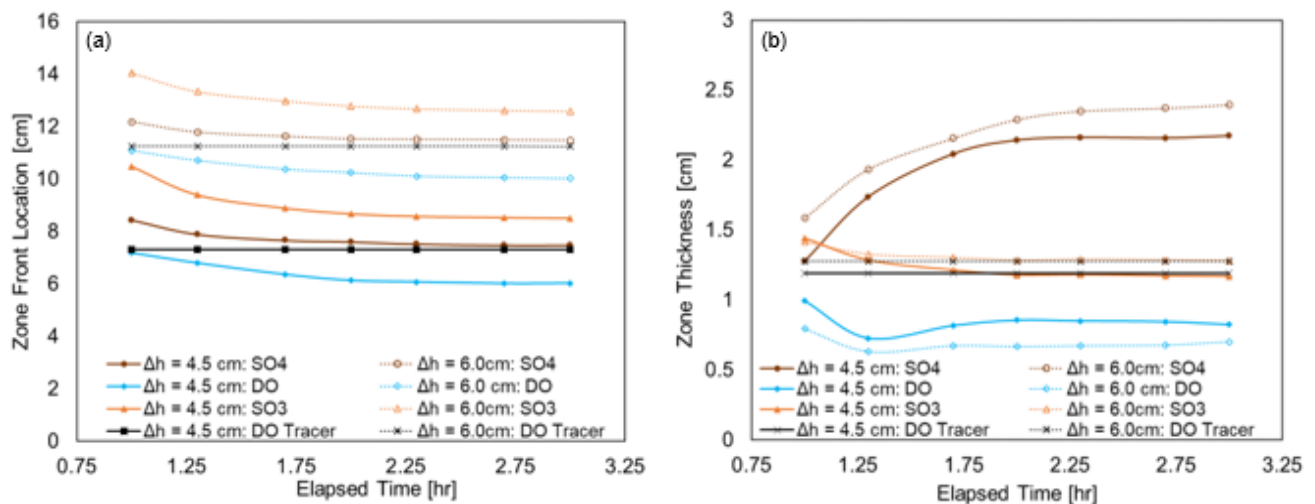


Figure 4.5. Mixing/production zone (a) front location and (b) thickness versus elapsed time for chemical species DO, SO_3 , SO_4 , and DO tracer for both head drops (Δh) basecase scenario.

4.3.3 Mixing and Production Zone Front Location Sensitivity

Sensitivity coefficients relative to the basecase (Table 4.2) were calculated for each model scenario for mixing front and production zone locations (Figure 4.6). Overall, zone front locations were most sensitive to changes in inflow ratios and relatively insensitive to changes in chemical concentration and λ . Exceptions included DO mixing front additionally responding to changes in SO_3 concentration, and SO_4 production zone additionally responding to changes to λ .

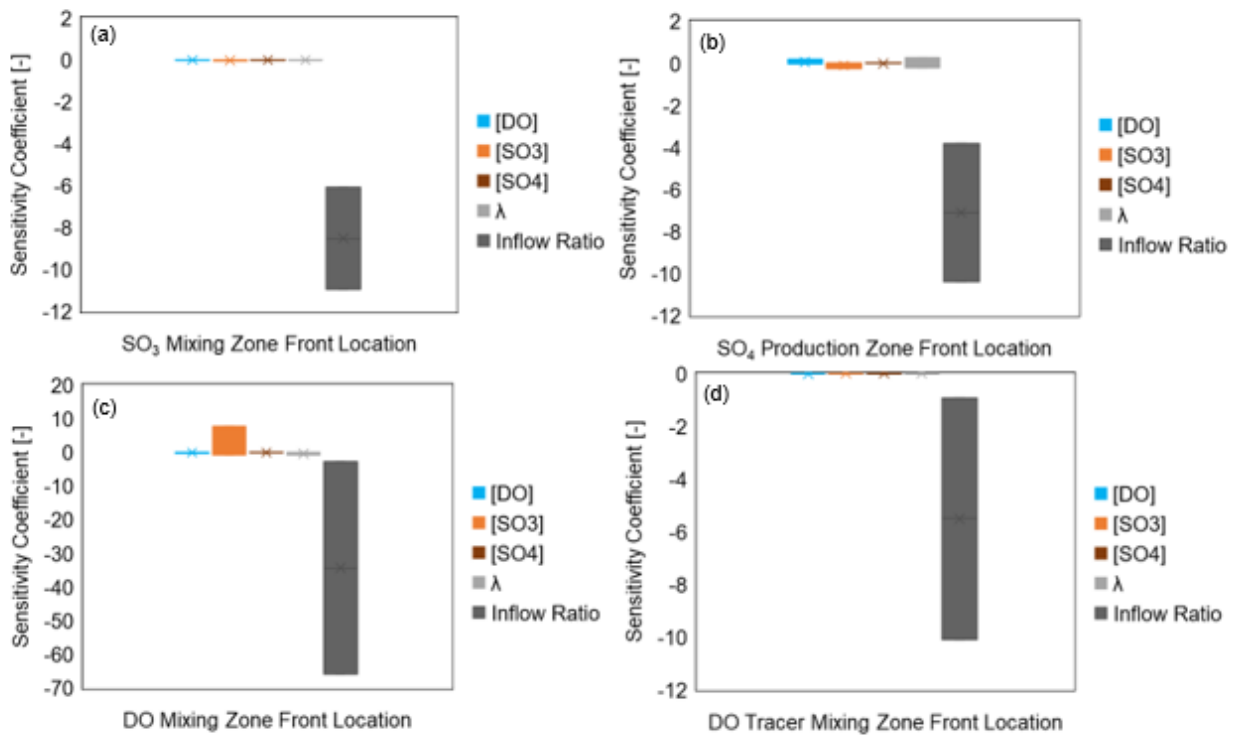


Figure 4.6. Sensitivity coefficients for (a) SO_3 mixing zone front location, (b) SO_4 production zone front location, (c) DO mixing zone front location, and (d) DO tracer mixing zone front location. Bars in each panel encompass all 26 model runs for the given chemical species, and show minimum, mean, and maximum sensitivity coefficient values. Inflow ratio is ratio of GW inflow to SW inflow to model domain. λ is reaction kinetic rate.

Mixing fronts moved upstream (i.e., left in Figure 4.1) with increasing inflow ratio for all chemical species (Figure 4.7). This is consistent with negative sensitivity coefficients (Figure 4.6) and is expected as stronger upwelling/gaining shrinks the hyporheic flow cell. In addition, all chemical species had the same trend with the tracer front position trends falling in line closely with the SO_4 line.

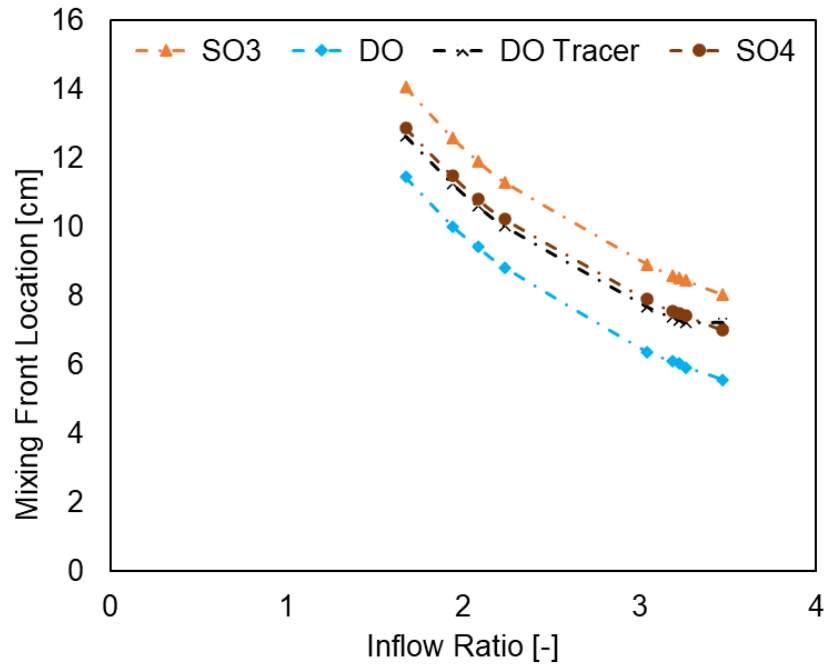


Figure 4.7. Mixing and production zone front locations for all chemical species versus inflow ratio. Inflow ratio is ratio of GW inflow to SW inflow to model domain. Values shown are for basecase (Table 4.2) for last time step ($t = 3.0$ hours).

4.3.4 Mixing and Production Zone Thickness Sensitivity

Sensitivity coefficients indicate that mixing and production zone thicknesses were most sensitive to inflow ratio for all chemical species (Figure 4.8). The next largest sensitivity was to SO_3 concentration for DO and SO_3 mixing zone thickness (Figure 4.8ac), and to λ for SO_4 production zone thickness (Figure 4.8b). DO tracer was only affected by inflow ratio (Figure 4.8d). All mixing and production zone thicknesses were insensitive to concentration of upwelling SO_4 .

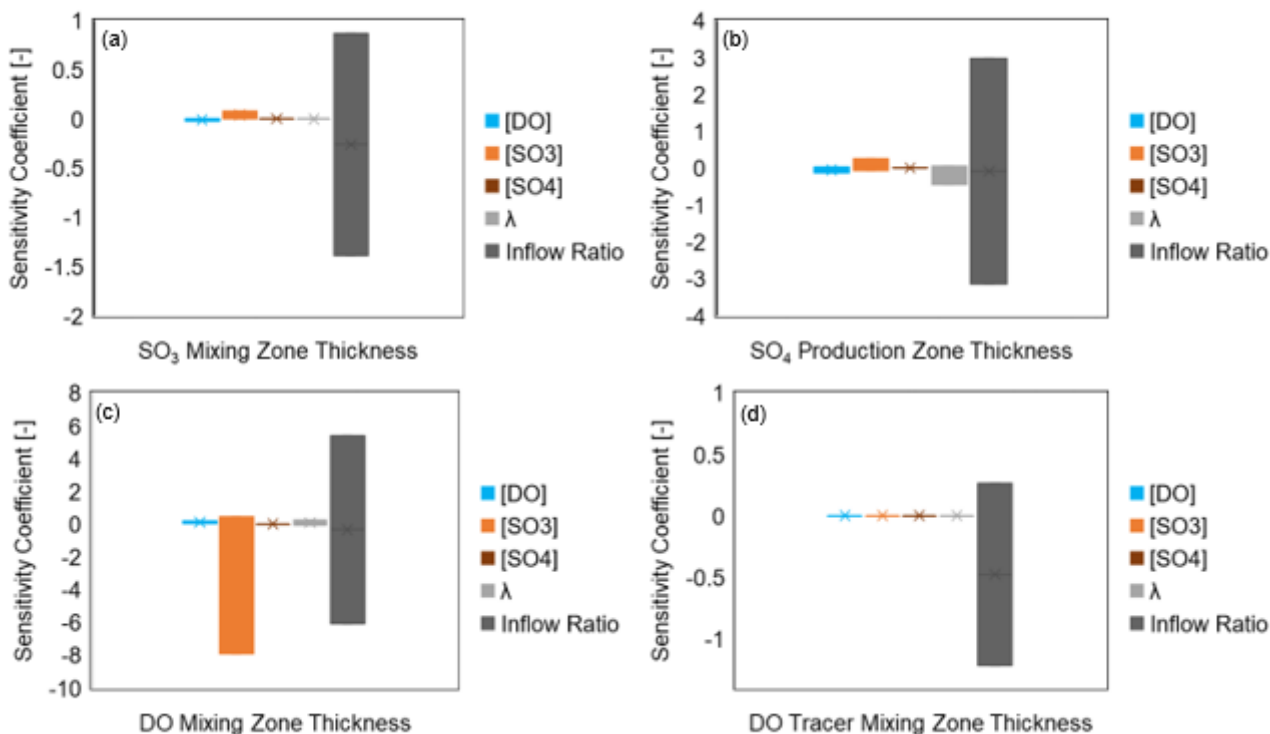


Figure 4.8. Sensitivity coefficients for (a) SO₃ mixing zone thickness, (b) SO₄ production zone thickness, (c) DO mixing zone thickness, and (d) DO tracer mixing zone thickness. Bars in each panel encompass all 26 model runs for the given chemical species, and show minimum, mean, and maximum sensitivity coefficient values. Inflow ratio is ratio of GW inflow to SW inflow to model domain. λ is reaction kinetic rate.

Trends of mixing and production zone thickness versus inflow ratio reveal that the DO trend was opposite that for SO₃, SO₄ and the DO tracer (Figure 4.9). As the mixing zone thickness for DO increased with inflow ratio, the mixing zone thicknesses of SO₃ and DO tracer as well as production thickness of SO₄ all decreased. However, the magnitude of the trend for DO mixing zone thickness was larger than those of SO₃ and DO tracer. The thickness value also differed based on chemical species where SO₄ production thickness was in general double the value of the SO₃ and DO tracer. The smallest mixing zone thickness was for DO, most likely due to DO being a limiting reactant and therefore having sharp concentration gradients. In addition, the SO₃ and DO tracer trends overlapped each other likely due to the fact SO₃ is in such excess that it is not changed by changing inflow ratios. The fact that increasing DO mixing zone thickness corresponded with

decreasing SO_4 production zone thickness may indicate that decreased SO_4 production left more DO in the mixing zone. In other words, the SO_3 reaction consumes DO in such a spatial pattern that it decreases the mixing zone thickness. How the DO mixing zone thickness may be influenced by mass consumption and production is discussed in Section 4.4.2.

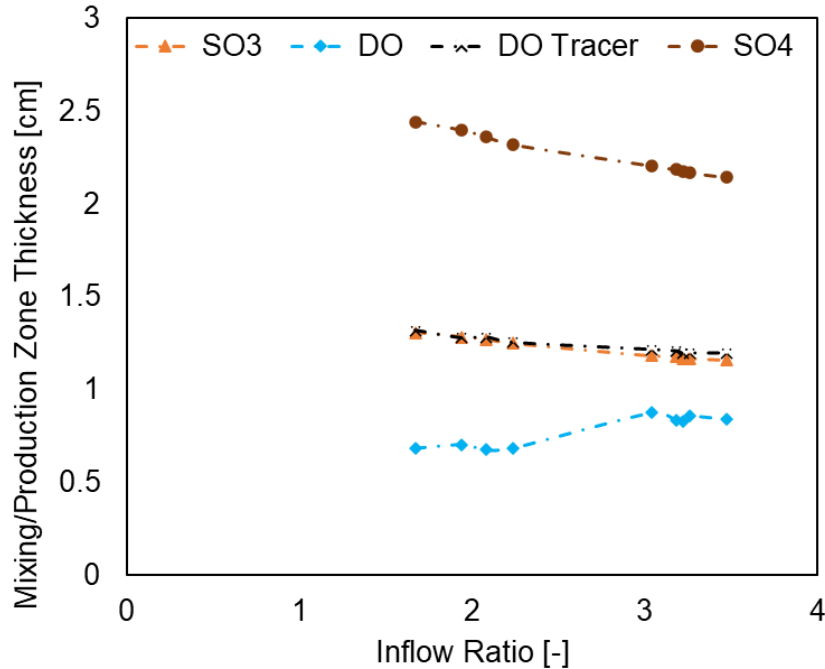


Figure 4.9. Mixing and production zone thickness versus inflow ratio. Inflow ratio is ratio of GW inflow to SW inflow to model domain. Data correspond to the 3-hr time step.

4.4 Discussion and Analysis

4.4.1 Temporal Evolution of Reactive Mixing Zones

Mass consumption and production exhibited temporal dynamics (Figure 4.10). DO consumption began at 0.5-1.0 hours and levelled off at ~1.5 hours (Figure 4.10 a-b). As a result, cumulative consumption increased linearly from ~1.5 hours until the end of the experiment (Figure 4.10a). Mixing zone thickness also leveled off, but perhaps slightly later by (~ 2 hours, Figure 4.5b), confirming that DO mixing zone thickness responded to DO consumption. SO_4 production rate, cumulative production, and production thickness followed very similar trends (Figures 4.10c-d, 4.5b), again confirming that SO_4 production zone thickness responded to SO_4 production itself.

Consumption rate, production rate, and thicknesses thus come into equilibrium over time. Achieving such equilibria likely requires steady-state hydraulics and/or short reaction timescales. We expect this is a general finding that applies to other chemical species/reactions, in particular contaminants and their attenuation in the hyporheic zone.

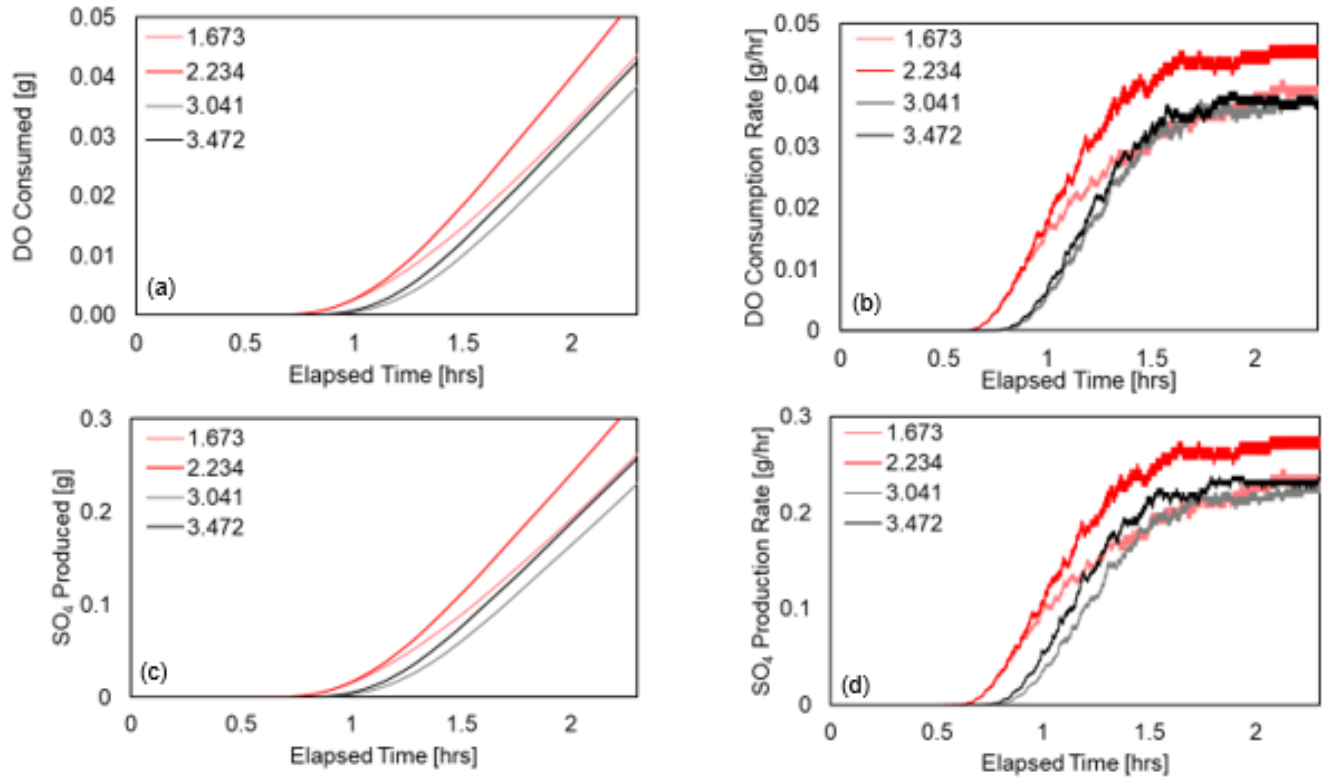


Figure 4.10. (a) Total (cumulative) DO consumed, (b) DO consumption rate, (c) total (cumulative) SO₄ produced and (d) SO₄ production rate versus elapsed time for series of inflow ratios. Inflow ratio is ratio of GW inflow to SW inflow to model domain. The values in (b) and (d) are the slopes of (a) and (c), respectively.

While temporal aspects of abiotic mixing-dependent reactions were explored in our earlier laboratory study (Santizo et al., 2020), simulations in this study allowed more complete analysis of how variations in concentration, kinetic rate, and hydraulics affect mixing and production zones over time (Figures 4.4, 4.5 and 4.10), particularly the relationship between mixing and production zones. For example, this study showed that production zone thickness is larger than mixing zone thickness which was not fully captured in Santizo et al. (2020).

This study further confirms tentative conclusions in Santizo et al. 2020 that even in the presence of steady state hydraulics, transport and reaction processes create dynamic evolution of concentration patterns that influence hyporheic zone processes (Figure 4.4, 4.5 and 4.10). As reactions occur, concentration gradients shift, potentially influencing the extent of surface water-derived oxic zones. This transiency in transport and reaction influences potential for natural attenuation of contaminants and would be further enhanced with unsteady flowrates and sediment heterogeneity. Unsteady hydraulics in either surface water or groundwater would move the mixing zone and potentially enhance mixing with more solutes coming in contact with one another (Hester et al., 2017; Lewandowski et al., 2020). Spatial heterogeneity of grain size distribution, sediment hydraulic conductivity, carbon sources, or microbial populations can create microzones or hotspots which affect residence times and reactant availability (Harvey et al., 2013; Newcomer et al., 2018; Roy Chowdhury et al., 2020). Previous studies (Fox et al., 2016; Galloway et al., 2019; Su et al., 2020; Wolke et al., 2020) have shown how transport transiency and heterogeneity affect hyporheic processes but not specifically mixing-dependent reactions. One exception was Hester et al. (2019), but their model was not calibrated against laboratory data and did not analyze temporal evolution of mixing and reaction zones in detail.

Moreover, DO is a major biogeochemical driver of hyporheic chemistry which is frequently a limiting reactant. The temporal variations in DO concentrations and mixing zones shown here (Figure 4.4) are therefore relevant to understanding how DO concentration profiles are shifted, depleted, and consumed in the hyporheic zone. DO mixing zone thickness (Figure 4.5b) and consumption (Figure 4.10a-b) steadied out with time as the simulations progressed similar to Santizo et al. (2020). These temporal trends indicate potential behavior changes in the system that could influence other redox reactions such of those involving nutrients or metals.

Finally, it is important to note that the location of high DO concentration at a given point in time was not where the most SO_4 production was taking place at that time, but rather reflected the oxic interface as DO is consumed. In other words, the location of the SO_4 production peak at any given time reflected the location where DO was consumed in the past. This has direct relevance to how field measurements are done, particularly how areas of analysis and observation are chosen and used to determine chemical concentrations and reactions taking place (Santizo et al. 2020, Figure 3.6). Therefore, understanding how hyporheic exchange and flowpaths are influenced by the reactions and chemical concentrations may allow more accurate spatial targeting

of chemical gradient characterization. In addition, the fact that the mixing front location stayed fairly constant regardless of kinetic parameters such as concentration and reaction rate (Figure 4.6) is useful in field monitoring in that changing kinetics due to varying conditions such as temperature fluctuations may not require changes in field sampling locations.

4.4.2 Mass Consumption and Production

Mass analysis was completed to determine whether there was a relationship between mass consumed/produced and mixing/production zone thickness. Such relationships could help interpret reaction processes based on more practical system observations such as zone thickness. This analysis was not possible in the original lab study (Chapter 3, Santizo et al. 2020) due to insufficient mass balance data, highlighting the value of this analysis.

The relationships between inflow ratio and the rates of SO_4 mass production and DO mass consumption were complicated (Figure 4.11). There was a weak overall decrease in consumption/production as surface water Δh decreased from 6.0 cm to 4.5 cm. Inflow ratio correspondingly increased, indicating an overall weak trend of decreasing consumption/production with increasing inflow ratio. These trends are consistent with the instantaneous nature of the reaction and the excess of SO_3 which together allow the extra DO advecting in from the SW boundary in lower inflow ratio/higher Δh conditions to fully react despite the shorter residence times along the mixing zone. This illustrates the importance of having matching timescales between transport and kinetics to maximize natural attenuation as the relatively small change in Δh (1.5 cm) produced a molar factor of 1.6 difference in SO_4 produced. The higher DO mass consumption and SO_4 mass production at lower inflow ratios (Figure 4.11) may explain why the DO mixing zone thickness was smaller for the lower inflow ratios than the higher inflow ratios (Figure 4.9).

Along with the overall trend with Δh , there was also a trend within the cluster of inflow ratios corresponding to each Δh . For both the sets of inflow ratios, the consumption and production rates increased with increasing inflow ratio. The increase in rates was most noticeable with the lower Δh that corresponds to the larger Δh of 6.0 cm. Therefore, in the analysis of consumption and production rates, the values were most dependent on the surface water Δh contrary to the zone thickness which was most sensitive to inflow ratio (Figure 4.8).

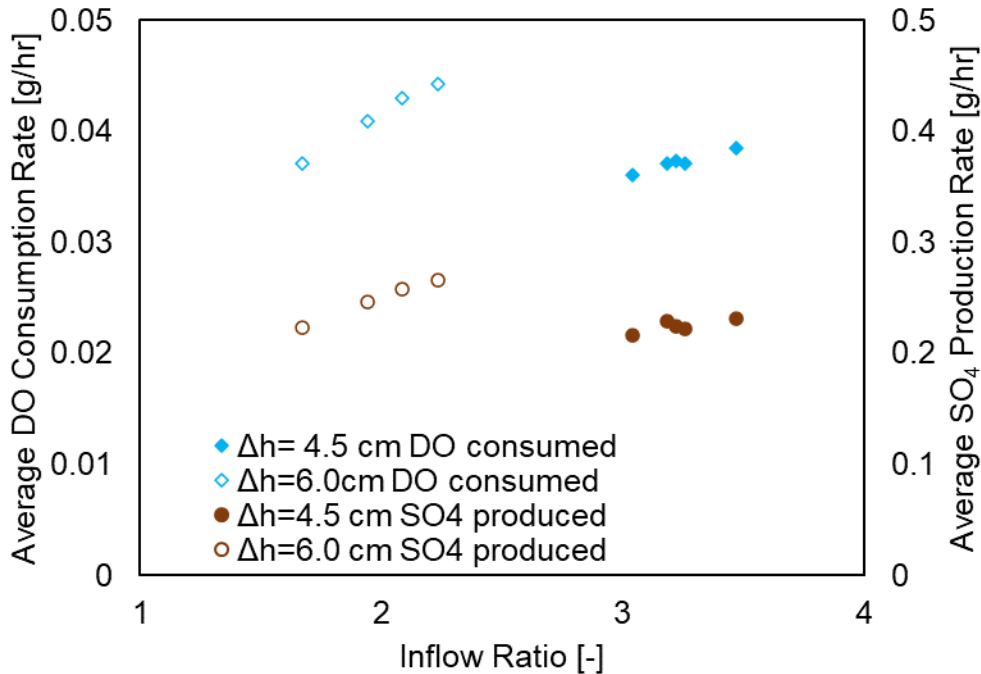


Figure 4.11. Average rate of mass consumed (DO in blue) and produced (SO₄ in maroon) versus inflow ratio. The average rate is between 1.75 to 2.25 hours. Inflow ratio is ratio of GW inflow to SW inflow to model domain. The points in the plot are clustered based on Δh , the lower inflow ratio cluster is for the higher Δh (6.0 cm) and vice-versa. Upwelling flow rates are varied within each cluster which also varies inflow ratio.

Surface water Δh also plays an important role in the relationships between zone thickness and consumption and production rates (Figure 4.12). DO mixing zones were thicker and SO₄ production zones were thinner for lower Δh (black symbols) than for higher Δh (red symbols). This trend corresponds to larger production for higher Δh (lower inflow ratios) despite smaller residence times, thus showing that larger DO consumption corresponds to sharper DO gradients and thus thinner mixing zones. Thus, we hypothesize that reaction rates and therefore reactive consumption control mixing zone thickness. Yet we acknowledge that the opposite may also be true, i.e., that thinner mixing zones allow faster mixing-dependent reaction to occur due to steeper concentration gradients. In end, it is likely that both are occurring simultaneously.

Within the cluster of inflow ratios for each Δh we also see a small trend of increasing average DO consumption rate with increasing average mixing zone thickness (Figure 4.12a). DO

consumption and SO_4 production are of course themselves related (Figure 4.11), with a ~1:6 molar ratio DO consumed to SO_4 produced regardless of inflow ratio as determined through stoichiometric analysis.

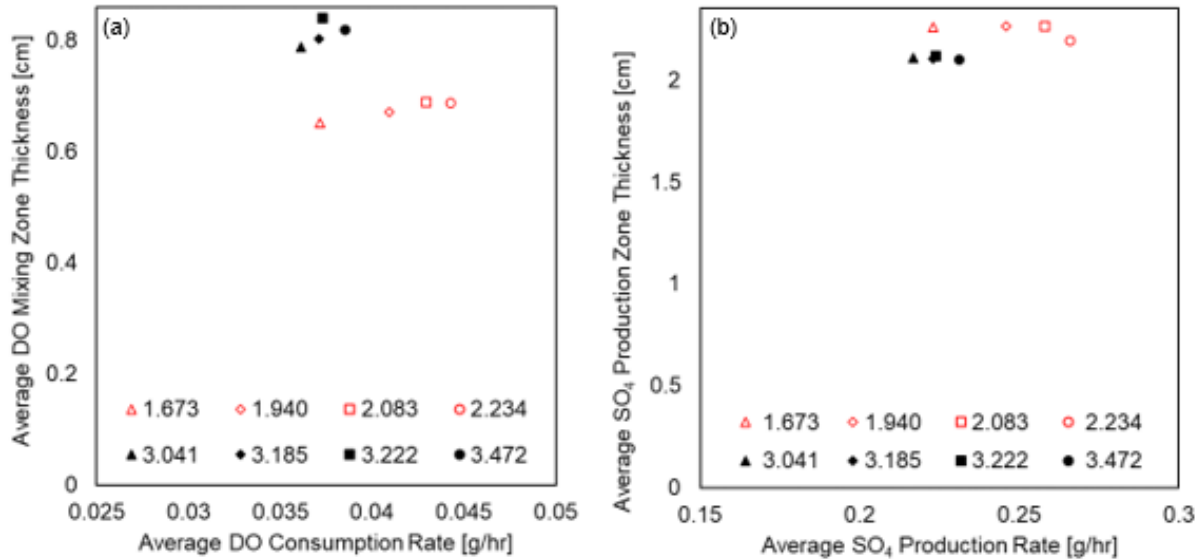


Figure 4.12. (a) Average DO mixing zone thickness versus average DO mass consumption rate and (b) Average SO_4 production zone thickness versus average SO_4 produced for various inflow ratios. Inflow ratio is ratio of GW inflow to SW inflow to model domain. The averages are for 1.75 to 2.25 hours. Data shown in red is for $\Delta h = 6.0$ cm and data in black is for $\Delta h = 4.5$ cm.

4.5 Novelty and Limitations

Our results expand our process-based understanding of transport and reaction processes behind mixing-dependent reaction dynamics observed during steady state hyporheic zone hydraulics. We conceptually link the evolution of mixing-dependent reactions to readily observable mixing zone parameters such as mixing zone thickness and mixing front location. We matched the model to the laboratory observations of DO mixing zone thickness and mixing front location. The model then allowed us to calculate mixing or production zone thickness for SO_3 , SO_4 and a DO tracer which enhances our understanding of how mixing zones differ based on chemical species, concentration gradient, and mass flux. Inflow ratio of groundwater to surface water inflow rate was a key control, leading to improved understanding of how both hydraulic and reaction parameters influence mixing-dependent reaction in the hyporheic zone. This indicates that the balance between upwelling and downwelling flowpaths is crucial to optimize attenuation.

Prior studies focused on hydraulic influences on hyporheic mixing and mixing-dependent reactions, which this study complements through basic insights regarding the influence of reaction kinetics. Chiogna et al. (2012) observed the relationship between mixing and reactions in porous media in ways more specific to deeper aquifers. They quantified mixing on the margins of reactive plumes using flux-related dilution index which aided in interpreting reaction processes. In this study we quantify mixing in the hyporheic flow cell using mixing/production zone thickness and front locations and they gave us insight into how mixing influences reaction processes thus they can also provide useful information on reactions.

This study focused on simulating and interpreting a specific prior laboratory experiment. An important extension of this work would be varying hydraulic conductivity and introducing spatial heterogeneity. We expect a potentially large influence of heterogeneity on flow fields, mixing, and reaction kinetics (Bandopadhyay et al., 2017; Li et al., 2017; Navel et al., 2011; Roy Chowdhury et al., 2020). However, basic relationships among mixing/production zone thickness, fronts, and chemical transformations would likely remain the same due the inflow ratio having the largest influence. Su et al. (2020) showed the largest impact on mixing to be upwelling groundwater rather than heterogeneity, consistent with inflow ratio being a dominant control that emerged from our results.

While the abiotic mixing-dependent reaction evaluated here provides useful insight into mixing/production zone thickness and reaction kinetics, abiotic reactions are simple compared to the complexity of biotically-mediated reactions. For example, our abiotic reaction was instantaneous and first order, which makes it simplistic and ideal for observation. Yet because prior analyses of mixing-dependent reactions and their influence on attenuation in the hyporheic zone are rare, starting from this simple reference point provides fundamental insights and interpretations that build understanding that is useful for future analyses of more complex biotic mixing-dependent reactions. Thus, many of our methods and calculations can be applied to understanding biotic mixing-dependent reactions and natural attenuation in the hyporheic zone.

4.6 Conclusions

Mixing can enhance natural attenuation of groundwater (GW) contaminants in the hyporheic zone as they upwell toward surface water (SW) bodies. Here we numerically simulated prior laboratory experiments in Santizo et al. (2020) of abiotic mixing-dependent reactions of

sodium sulfite (SO_3) in upwelling groundwater and dissolved oxygen (DO) in surface water downwelling into the hyporheic zone to create sodium sulfate (SO_4) in the mixing zone. Hyporheic hydraulics were maintained at two different steady-state conditions (i.e., two SW head drops, Δh , that drove hyporheic exchange) while chemical transport and reaction were simulated for the 3-hr duration of the laboratory experiments. DO, SO_3 , and SO_4 concentrations were varied in a sensitivity analysis. Reaction kinetic rate and groundwater constant head were also varied to determine their influence on mixing-dependent reaction. Extent of mixing-dependent reaction was quantified via mixing/production zone thicknesses (16-84% normalized concentration) and mixing/production zone front locations (84% normalized concentration position).

Results show that under steady state hydraulics, mixing/production zone thickness and front locations varied over time as the reaction progressed (Figure 4.4 and 4.5). A relationship resulted between the DO mixing zone thickness and SO_4 production zone thickness and amount of SO_4 produced (Figure 4.5). The more SO_4 was produced over time the larger the SO_4 production zone thickness while DO mixing zone thickness shrank as DO was simultaneously consumed. Overall, small changes in mixing/production zone thicknesses led to large changes in mass consumed and produced.

In addition, mixing/production zone thickness and mixing/production zone front location were most sensitive to inflow ratio (upwelling GW to downwelling SW, Figure 4.6 and 4.8). However, the sensitivity of inflow ratio on mass produced and consumed was between lower inflow ratios (i.e., $\Delta h = 6.0$ cm) and higher inflow ratios ($\Delta h = 4.5$ cm). As in, all the lower inflow ratios had similar mass production and consumption and the same was true of the higher inflow ratios. Therefore, mass consumption and production were most sensitive to surface water Δh as opposed to inflow ratio.

Overall, this study emphasizes that mixing-dependent reactions in the hyporheic zone depend on matching transport and kinetics. This underlines the complexity of controls on hyporheic zone attenuation, such as inflow ratios, SW Δh , and chemical concentrations, whose variations can either interfere or enhance reactions. This is important for understanding controls on attenuation in the hyporheic zone and their implications for water quality management and ecosystem health.

References

- Bandopadhyay, A., Le Borgne, T., Méheust, Y., & Dentz, M. (2017). Enhanced reaction kinetics and reactive mixing scale dynamics in mixing fronts under shear flow for arbitrary Damköhler numbers. *Advances in Water Resources*, *100*, 78–95. <https://doi.org/10.1016/j.advwatres.2016.12.008>
- Bandopadhyay, A., Davy, P., & Le Borgne, T. (2018). Shear Flows Accelerate Mixing Dynamics in Hyporheic Zones and Hillslopes. *Geophysical Research Letters*, *45*(21), 11659–11668. <https://doi.org/10.1029/2018GL079914>
- Boano, F., Falco, N. De, & Arnon, S. (2018). Advances in Water Resources Modeling chemical gradients in sediments under losing and gaining flow conditions : The GRADIENT code. *Advances in Water Resources*, *112*(November 2017), 72–82. <https://doi.org/10.1016/j.advwatres.2017.12.002>
- Chiogna, G., Cirpka, O. A., Grathwohl, P., & Rolle, M. (2011). Relevance of local compound-specific transverse dispersion for conservative and reactive mixing in heterogeneous porous media. *Water Resources Research*, *47*(7). <https://doi.org/10.1029/2010WR010270>
- Chiogna, G., Hochstetler, D. L., Bellin, A., Kitanidis, P. K., & Rolle, M. (2012). Mixing, entropy and reactive solute transport. *Geophysical Research Letters*, *39*(20), 1–6. <https://doi.org/10.1029/2012GL053295>
- Conant, B., Cherry, J. A., & Gillham, R. W. (2004). A PCE groundwater plume discharging to a river: Influence of the streambed and near-river zone on contaminant distributions. *Journal of Contaminant Hydrology*, *73*(1–4), 249–279. <https://doi.org/10.1016/j.jconhyd.2004.04.001>
- Ellis, P. A., & Rivett, M. O. (2007). Assessing the impact of VOC-contaminated groundwater on surface water at the city scale. *Journal of Contaminant Hydrology*, *91*(1–2), 107–127. <https://doi.org/10.1016/j.jconhyd.2006.08.015>
- Fox, A., Laube, G., Schmidt, C., Fleckenstein, J. H., & Arnon, S. (2016). The effect of losing and gaining flow conditions on hyporheic exchange in heterogeneous streambeds. *Water Resources Research*, *52*, 7460–7477. <https://doi.org/10.1002/2016WR018677>
- Freitas, J. G., Rivett, M. O., Roche, R. S., Durrant, M., Walker, C., & Tellam, J. H. (2015). Heterogeneous hyporheic zone dechlorination of a TCE groundwater plume discharging to an urban river reach. *Science of the Total Environment*, *505*, 236–252. <https://doi.org/10.1016/j.scitotenv.2014.09.083>
- Galloway, J., Fox, A., Lewandowski, J., & Arnon, S. (2019). The effect of unsteady streamflow and stream-groundwater interactions on oxygen consumption in a sandy streambed. *Scientific Reports*, *9*(1), 1–11. <https://doi.org/10.1038/s41598-019-56289-y>

- Harvey, J. W., Böhlke, J. K., Voytek, M. A., Scott, D., & Tobias, C. R. (2013). Hyporheic zone denitrification: Controls on effective reaction depth and contribution to whole-stream mass balance. *Water Resources Research*, *49*(10), 6298–6316.
<https://doi.org/10.1002/wrcr.20492>
- Hester, E. T., Young, K. I., & Widdowson, M. A. (2013). Mixing of surface and groundwater induced by riverbed dunes: Implications for hyporheic zone definitions and pollutant reactions. *Water Resources Research*, *49*(9), 5221–5237.
<https://doi.org/10.1002/wrcr.20399>
- Hester, E. T., Young, K. I., & Widdowson, M. A. (2014). Controls on mixing-dependent denitrification in hyporheic zones induced by riverbed dunes: A steady state modeling study. *Water Resources Research*, *50*, 9048–9066. <https://doi.org/10.1002/2014WR015424>
- Hester, E. T., Cardenas, M. B., Haggerty, R., & Apte, S. V. (2017). The importance and challenge of hyporheic mixing. *Water Resources Research*, *53*, 3565–3575.
<https://doi.org/10.1002/2016WR020005>
- Hester, E. T., Eastes, L. E., & Widdowson, M. A. (2019). Effect of Surface Water Stage Fluctuation on Mixing-Dependent Hyporheic Denitrification in Riverbed Dunes. *Water Resources Research*, *55*(6), 4668–4687.
<https://doi.org/https://doi.org/10.1029/2018WR024198>
- Krause, S., Tecklenburg, C., Munz, M., & Naden, E. (2013). Streambed nitrogen cycling beyond the hyporheic zone: Flow controls on horizontal patterns and depth distribution of nitrate and dissolved oxygen in the upwelling groundwater of a lowland river. *Journal of Geophysical Research: Biogeosciences*, *118*(1), 54–67.
<https://doi.org/10.1029/2012JG002122>
- Lewandowski, J., Meinikmann, K., & Krause, S. (2020, January 1). Groundwater-surface water interactions: Recent advances and interdisciplinary challenges. *Water (Switzerland)*. MDPI AG. <https://doi.org/10.3390/w12010296>
- Li, A., Aubeneau, A. F., Bolster, D., Tank, J. L., & Packman, A. I. (2017). Covariation in patterns of turbulence-driven hyporheic flow and denitrification enhances reach-scale nitrogen removal. *Water Resources Research*, *53*(8), 6927–6944.
<https://doi.org/10.1002/2016WR019949>
- Marzadri, A., Tonina, D., Bellin, A., & Valli, A. (2016). Mixing interfaces, fluxes, residence times and redox conditions of the hyporheic zones induced by dune-like bedforms and ambient groundwater flow. *Advances in Water Resources*, *88*, 139–151.
<https://doi.org/10.1016/j.advwatres.2015.12.014>
- Navel, S., Mermillod-Blondin, F., Montuelle, B., Chauvet, E., Simon, L., & Marmonier, P. (2011). Water-Sediment Exchanges Control Microbial Processes Associated with Leaf

- Litter Degradation in the Hyporheic Zone: A Microcosm Study. *Microbial Ecology*, 61(4), 968–979. <https://doi.org/10.1007/s00248-010-9774-7>
- Newcomer, M. E., Hubbard, S. S., Fleckenstein, J. H., Maier, U., Schmidt, C., Thullner, M., et al. (2018). Influence of Hydrological Perturbations and Riverbed Sediment Characteristics on Hyporheic Zone Respiration of CO₂ and N₂. *Journal of Geophysical Research: Biogeosciences*, 123(3), 902–922. <https://doi.org/10.1002/2017JG004090>
- Rolle, M., Chiogna, G., Hochstetler, D. L., & Kitanidis, P. K. (2013). On the importance of diffusion and compound-specific mixing for groundwater transport: An investigation from pore to field scale. *Journal of Contaminant Hydrology*, 153, 51–68. <https://doi.org/10.1016/j.jconhyd.2013.07.006>
- Roy Chowdhury, S., Zarnetske, J. P., Phanikumar, M. S., Briggs, M. A., Day-Lewis, F. D., & Singha, K. (2020). Formation Criteria for Hyporheic Anoxic Microzones: Assessing Interactions of Hydraulics, Nutrients, and Biofilms. *Water Resources Research*, 56(3), no. <https://doi.org/10.1029/2019WR025971>
- Santizo, K. Y., Widdowson, M. A., & Hester, E. T. (2020). Abiotic Mixing-Dependent Reaction in a Laboratory Simulated Hyporheic Zone. *Water Resources Research*, 56(9). <https://doi.org/10.1029/2020WR027090>
- Su, X., Jim Yeh, T. C., Shu, L., Li, K., Brusseau, M. L., Wang, W., et al. (2020). Scale issues and the effects of heterogeneity on the dune-induced hyporheic mixing. *Journal of Hydrology*, 590. <https://doi.org/10.1016/j.jhydrol.2020.125429>
- Weatherill, J. J., Krause, S., Ullah, S., Cassidy, N. J., Levy, A., Drijfhout, F. P., & Rivett, M. O. (2019). Revealing chlorinated ethene transformation hotspots in a nitrate-impacted hyporheic zone. *Water Research*, 161, 222–231. <https://doi.org/10.1016/j.watres.2019.05.083>
- Widdowson, M. A., Brauner, J. S., Chapelle, F. H., & Bradley, P. M. (2002). *SEAM3D: A numerical Model for Three-Dimensional Solute Transport Coupled to Sequential Electron Acceptor-Based Biological Reactions in Groundwater*. Blacksburg, VA.
- Wolke, P., Teitelbaum, Y., Deng, C., Lewandowski, J., & Arnon, S. (2020). Impact of bed form celerity on oxygen dynamics in the hyporheic zone. *Water (Switzerland)*, 12(1), 5–7. <https://doi.org/10.3390/w12010062>

Chapter 5. Imaging of biotic reactions in the subsurface: Two-dimensional O₂ and CO₂ dynamics of aerobic respiration

Status: This chapter will be prepared for publication.

5.1. Introduction

5.1.1 Relations among Hyporheic Hydrology, Biogeochemistry, and Microbiology

Biogeochemical processes in the subsurface are of great importance to understanding contaminant attenuation in groundwater and shallow submerged sediment. These processes are vital to maintain water quality both for groundwater and surface water. Yet biogeochemical conditions for attenuation and remediation have been observed more extensively in groundwater (Bauer et al., 2009; Molz & Widdowson, 1988; Rolle et al., 2009). Molz et al. (1986) numerically simulated microbial based degradation in porous media, concluding that biodegradation influenced transport as microbial growth changed. Molz and Widdowson (1988) described the need to expand understanding of transport processes in porous media and their relation to properties including biological activity, chemical concentrations, and velocity distributions.

In the decades that followed, studies that observed biogeochemical processes in benthic biolayers and the hyporheic zone were published with more frequency (Hendricks, 1993). Hendricks (1993) was one of the first studies to mention relationships between the hydrology and biology of the hyporheic zone. The author discussed the importance of understanding chemical and biological processes in the hyporheic zone to understand whole-stream ecosystems. Valett et al. (1997) also provided an extensive study on the influences of hydrological changes on the groundwater-surface water ecotone. They attributed differences in nutrient availability to the extent and rate of interaction between groundwater and surface water. In cultivated benthic biofilms, Shanon et al. (2007) observed rates of nitrate uptake and biomass distributions due to substrate geometries and overlying velocities. They determined that both factors had a large influence (up to 10-fold) on nitrate uptake.

More recently, Stegen et al (2016) observed the coupling of groundwater-surface water mixing, microbiology, and biogeochemistry to relate heterotrophic respiration and organic carbon composition. They used various methods from different fields (DNA sequencing, organic carbon

profiling, piezometers, etc.) to connect hyporheic zone processes and microbial ecology. Caruso et al. (2017) modeled biofilms attached to sediment to determine the relationship between microbial growth and permeability, microbial metabolism and pore water fluxes. The authors concluded that bioclogging regulated reactions which were dependent on nutrient fluxes and distribution of microorganisms, sediment, and nutrients.

5.1.2 Advances in Observational Methodology

The studies discussed above show the importance of interdisciplinary approaches to understanding hydrologic, biogeochemical, and microbial dynamics in subsurface and shallow submerged sediment (Caruso et al., 2017; Stegen et al., 2016). Most of these studies used point-measurements, sampling, and numerical modeling. In addition, various visualization techniques have been used for dispersivity coefficient estimations, concentration profiles, mixing processes, and bacterial transport (Abarca & Clement, 2009; Bauer et al., 2009; Castro-Alcalá et al., 2012; Robinson et al., 2016). One visualization technique is planar optodes, which are thin reactive films that provides two-dimensional mapping of chemical concentrations. Optodes have been used to study the subsurface interaction of hydrologic and chemical processes (Galloway et al., 2019; Kaufman et al., 2017; Lehto et al., 2017; Santizo et al., 2020; Wolke et al., 2020). They are able to produce fine scale spatial resolution of concentration distributions by using a quenchable fluorophore that is sensitive to the species of interest.

For example, Kaufman et al. (2017) used DO optodes linked to numerical simulations of DO dynamics in shallow sediments with overlying surface water flow variations. Wolke et al. (2020), Lehto et al. (2017), Galloway et al. (2019) and Santizo et al. (2020) also used DO optodes in shallow submerged sediments to observe chemical mixing dynamics under a variation of hydrological and biogeochemical conditions such as surface water fluctuations, bedform migration, mixing-dependent reactions, and microniches.

Optodes have also been developed for pCO₂ (partial pressure of CO₂ in surface water), pH, and NH₄⁺ (Blossfeld et al., 2013; Borisov et al., 2011; Jiang et al., 2017; Larsen et al., 2011; Santner et al., 2015; Thomas et al., 2017; Zhu & Aller, 2010), but thus far have seen limited use in hydrologic studies. Studies in marine sediments or the rhizosphere have mentioned their application but do not present the 2D chemical profiles in their results. Blossfeld et al. (2013) has

the most extensive images of pH and pCO₂ in a time series in the rhizosphere. Optodes have therefore been underutilized in hydrology, leaving great opportunity to further our understanding of biogeochemical processes in subsurface and shallow submerged environments, particularly where DO is a major driver of chemical processes. For instance, using optodes to couple DO and pCO₂ profiles of aerobic reactions would further the understanding of the relationships between biogeochemical conditions and hydrology showing the relationship between the two chemical profiles and their response based on changing conditions.

5.1.3 Objectives of Chapter

In this chapter we address the use of DO and pCO₂ planar optodes to observe subsurface environments using natural streambed sediment and stream water from the New River near Blacksburg, VA. We used a simple microbially-mediated biotic reaction, aerobic respiration, to determine DO and pCO₂ responses.

We also suggest future optode research that would advance hyporheic zone science. Its feasibility and adaptability in subsurface environments are considered as pCO₂ optode ranges are limited to 0-25%. Since no study to date has shown pCO₂ and DO optode profiles in submerged sediments beneath streams or rivers, we expect that as DO is consumed the pCO₂ produced in aerobic respiration would be shown through changes in the pCO₂ optode signals. Thus, we expect to be able to relate DO and pCO₂ chemical concentrations in aerobic respiration that occur in a simple laboratory tank. Adaptions of these methods along with microbiology and hydrological techniques are discussed.

5.2 Methods

5.2.1 Planar Optodes, Chemical Sensors, and Aquarium Tank

Planar optodes are thin fluorescent films that change fluorescence intensity based on analyte concentrations. The planar optodes used in the previous chapter were made by Ronnie Glud and Morten Larsen at the University of Southern Denmark and used with an independent image capture system. For this chapter, we used planar optodes purchased from a commercial company, PreSens (PreSens Precision Sensing GmbH, Regensburg, Germany), along their own custom-made camera and lighting system. Two different types of planar optodes were purchased,

DO and pCO₂. These have self-adhesive to place them on the front panel of a 10-liter aquarium tank used for experiments. The DO optode was 10 cm x 15 cm whereas the pCO₂ was 10 cm x 10 cm. To capture DO and pCO₂ in close vicinity, the optodes were cut into strips of 10 cm x 1.5 cm and alternated.

All calibration (Section 5.2.6) and batch experiments (Section 5.2.7) were performed in a 10-L aquarium tank (0.31 m long by 0.16 m deep by 0.21 m tall) (Figure 5.1). HOBO DO loggers (Onset Corporation, Bourne, MA) were placed in the back corners of the aquarium tank, and an Eosense CO₂ sensor was placed in the middle of the tank, before conducting calibration (just water, Section 5.2.6) and batch experiments (water and sediment, Sections 5.2.4, 5.2.7).

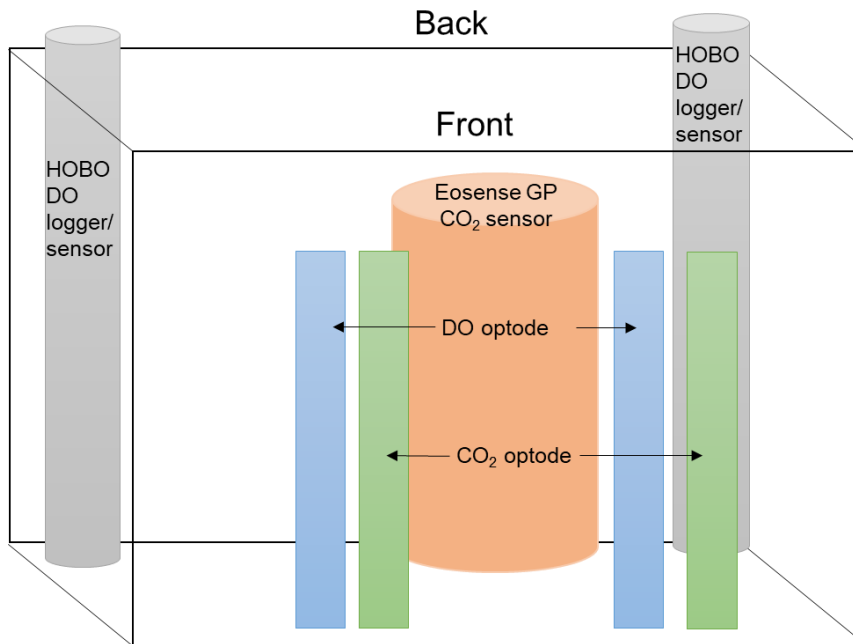


Figure 5.1. Schematic of optodes, HOBO dissolved oxygen (DO) sensor/loggers, and Eosense GP CO₂ sensor set-up in aquarium tank where DO and pCO₂ optode strips are added in pairs to the front for visualization. This shows set up before water or sediment was added for calibration or batch experiments (Sections 5.2.4, 5.2.6, 5.2.7).

Dissolved oxygen (DO) optodes can measure the full range of 0-100% saturation, and measurements (and therefore calibration curves) are temperature dependent. Partial carbon dioxide

(pCO₂) pressure can measure 1-25% pCO₂, and measurements are sensitive to temperature, pH, salinity, and ionic strength. Calibration curves (Section 6.2.6) were generated for four different gas mixtures of varying pCO₂ concentration. Each gas mixture contained the required pCO₂ percentage between 1-25% and was balanced with the inert gas of nitrogen. pCO₂ optodes from Presens require media with ionic strength > 50 mM, therefore the nutrient source utilized (Section 6.2.5) also served to ensure proper ionic strength.

5.2.2 Stern-Volmer Method

The Stern-Volmer method (Stern-Volmer equation, equation 5.1) is used to translate fluorescent intensities to analyte concentrations. The Stern-Volmer method takes advantage of the fluorescence excitation ability where observed excitation is proportional to concentration. An excitation light is used to excite the fluorescent molecule and gives off an energy proportional to an intensity value. However, when a photo chemical reaction occurs, a portion of the fluorescent is quenched (absorbed by the chemical reactant) therefore a relationship develops between quenched/excited intensities and concentrations. Thus, the Stern-Volmer equation was modified to calculate analyte (quenching molecule) concentration (equation 5.2),

$$\frac{R_0}{R} = 1 + \alpha K_{sv} C \quad (5.1)$$

$$C = \frac{R_0 - R}{K_{sv}(R - \alpha R_0)} \quad (5.2)$$

where C is the quenching chemical concentration (%), R/R₀ is the ratio of the intensity of the fluorescent molecule at a specific quenching chemical concentration to that when the quenching chemical concentration is equal to zero (i.e., no quencher present) (dimensionless). K_{sv} and α are constants, the Stern-Volmer quenching constant (1/Molarity) and the non-quenchable fraction of the light signal (dimensionless), respectively.

5.2.3 Camera, Lighting, and Software System

Multiple types of camera and lighting systems have been used for optodes based on type of optode, budget, and resolution needs. In Chapter 3, a DSLR camera was used with the DO

planar optode. A similar set up could have been used with the DO and pCO₂ optodes used for this study, yet we opted to purchase the VisiSens system by PreSens (Figure 6.2) because of its greater ease of use. VisiSens is a camera made by PreSens to use specifically with their optodes and software system VisiSens ScientifiCal. Since the software system and camera were integrated it allowed for easy control of the lights and camera as well as the image analysis. This saved processing time as the calibration curve and concentration conversion were done within the software system. For this specific camera set-up, the most important factors were the gain (signal amplification) and light exposure (amount of light received by film expressed as μS) where both had to be optimized to provide enough signal with the least amount of noise. The exposure for each optode varied while the gain remained the same at a value of 3. Exposure used for pCO₂ was 95,000 μS while for DO it was 170,000 μS . In addition, the software was able to do multispecies capture and therefore could switch between lighting needs for each optode.



Figure 5.2. VisiSens camera and lighting system for DO and pCO₂.

Lighting is specific to each fluorescent molecule in the optodes, and because fluorophores vary among optode types, different optodes require different excitation wavelengths. When using multiple optodes simultaneously e.g., DO and pCO₂, multiple lighting requirements must be met.

Calibration curves to convert intensities to concentrations require not only correct light wavelengths, but also vary with camera and light angle, distance, and exposure time. These variables must be optimized to ensure proper calibration where enough excitation is provided so that the excitation occurs, and the fluorophore quenched. Overexcitation skews the response, leading to difficulty determining a proper intensity ratio. Overexcitation can also result in photodegradation of the fluorophore, thus exposure time and type are crucial to maintaining a stable optode. Over its lifetime (typically 12-36 months), the optode response falters and is deemed unstable as the response does not provide a wide enough range between the concentrations allowing for over and underestimations of concentrations. Therefore, calibration curves must be performed frequently and are recommended with each new experiment. Once the intensity ratio decreases with age (i.e., R_0 and R were reaching similar values), optode accuracy diminishes and the optode must be replaced. Excitation wavelengths and fluorescent molecule used for each analyte (DO and pCO_2) are not provided by the manufacturer, and thus are unknown.

Table 5.1. Lighting and Camera Parameters

Variable	DO optode value	pCO_2 optode value
Camera distance from tank [m]	0.39	0.39
Light Intensity [μS]	170,000	95,000
Gain [-]	3	3
Temperature [$^{\circ}C$]	20-22	20-22
Optode Light Dim	None	None

5.2.4 Sediment and Water Collection

Streambed sediment and stream water were collected from New River at Kentland Farms near Blacksburg, VA (Figure 5.3). Streambed sediment was taken from the top 20 cm near the river's edge. Streambed sediment and stream water were collected during the months of August to November 2020 as needed for each experiment (approximately 8 times). Stream water was taken from the water column close to the location of sediment collection, and water was taken first to minimize sediment in the collected stream water. Stream water was collected in a 20-gallon LDPE container while streambed sediment was collected in a 5-gallon bucket. During stream water and

streambed sediment collection, Collection occurred after a minimum of 24 hours since most recent precipitation, and in the afternoon after maximum surface temperatures had been reached.



Figure 5.3. New River at Kentland Farms near Blacksburg, VA where sediment and water collection took place in late afternoon an average 24 hours before experiments.

5.2.5 Assembly of Water, Sediment, Nutrients, and Carbon Source

As mentioned in Section 5.2.1, a nutrient source was inoculated to stream water and streambed sediment to ensure microbial populations were present during experiments and to maintain ionic strength required for $p\text{CO}_2$ measurements. Usually, a nutrient source is a mixture of salts, however, because the experiment would produce 3-5 liters of water with such salts every few days that required disposal, and because many of the salts are ecotoxic to certain organisms, proper disposal would be difficult to get permitted. Thus, as the nutrient source, we used the salt, potassium dihydrogen phosphate (KH_2PO_4) at concentrations approved by the Virginia Tech Department of Environment Health & Safety for drain disposal (0.08-0.13 M KH_2PO_4). KH_2PO_4 is commonly used as a fertilizer and therefore deemed safe and provides enough of a nutrient source for the microorganisms present in the stream water collected. The KH_2PO_4 was added to stream water rather than the sediment to ensure full and uniform dissolution into the stream water for the experiments. It was added and mixed with a stir bar for approximately an hour. After the

two hours the sediment was added and mixed into the aquarium tank. Glucose ($C_6H_{12}O_6$) was added as the carbon source and electron donor for aerobic respiration by microbes in the subsurface (equation 5.3). Glucose was dissolved stepwise as the streambed sediment was added to the aquarium tank because if not it would result in a highly stratified carbon source as the only way the glucose could get into the streambed sediment would be through dispersion. The streambed sediment was added in 3 steps, and glucose was added at the end of each step. The nutrient and carbon source were added using different methods since the nutrient source would have to be available to all microorganisms present and the ionic strength as to be uniform so that the planar optode response does not vary due to stratification of the nutrient source.



In summary, the steps in order to perform the experiments once optodes were on the tank and had been checked were: (1) Add stream water to aquarium tank, (2) Add KH_2PO_4 and mix, (3) Once KH_2PO_4 fully dissolved and an hour had elapsed, add sediment mixture and glucose stepwise.

It is assumed that DO consumed and pCO_2 produced during the experiments is the result of microbial aerobic respiration. Glucose concentrations measurements during the experiments were attempted, but concentrations were beyond the limits of available instrumentation. A range of glucose concentrations (0.01 M-0.1 M $C_6H_{12}O_6$) were tested in separate bench scale experiments to determine the rate of consumption which in turn allows identification of the ideal concentration for batch experiments in the aquarium tank (see Section 5.2.7 below). However, ultimately, concentrations from the extremes of 0.01-0.10 M $C_6H_{12}O_6$ range were tried as there was enough response in both the DO and pCO_2 . TOC and DOC measurements were attempted but the concentrations used were too large for the instrument and differences in concentration could not be discerned.

5.2.6 Calibration Curves

Calibration curves were constructed to convert light intensities obtained from the photographs of the planar optodes to concentrations of pCO_2 and DO. DO calibration curves were created using a two-step deoxygenation method, argon/nitrogen gas followed by sodium sulfite. The gas was effective at removing the oxygen and the sodium sulfite ensured the water was

maintained anoxic. pCO₂ calibration curves were done with specialized Airgas-purchased gas mixtures. Both calibration curves were done in stream water with nutrient source added (no sediment). The resulting calibration curves were sent to PreSens R&D division to be verified prior to use.

For the DO calibration, DO concentrations were monitored using HOBO DO loggers (Figure 6.1) to ensure a match between the DO logger and planar optode. The DO calibration curve shows that the intensity ratio is high at low DO concentrations and low at high DO concentrations (Figure 6.4, top). The HOBO logger indicated DO concentration in the water column range during the DO calibration from 0-10 mg/L at 20-22°C. The concentration for DO is based on saturation from 0-100% therefore 100% is the maximum (i.e., 10 mg/L) saturation of DO for a specific temperature. However, ratio response has been shown to be consistent over small ranges of temperature (Chapter 3). For the PreSens DO calibration curve, only two points are needed and therefore we use the two extremes (Figure 5.5, top).

For the pCO₂ calibration, four gas mixtures were purchased to obtain an adequate pCO₂ calibration curve: 1.729%, 9.989%, 14.78%, and 24.62% pCO₂. These four concentrations were chosen since the pCO₂ planar optode is able to capture between 1-25% pCO₂ (Figure 5.4, bottom). Gas mixtures were introduced into the 0.08 M KH₂PO₄ water in the aquarium tank using gas lines and left on until a constant pCO₂ signal occurred and was imaged. A Hach CO₂ kit was used in initial studies to determine CO₂ concentration, however, the CO₂ concentration was above the detection limits and once the nutrient salt was added it interfered with the ability to measure CO₂ with the kit even if dilution was possible. Thus, pCO₂ measurements were checked against those from an Eosense GP CO₂ Sensor in the aquarium tank (Figure 5.1). The Eosense GP CO₂ sensor ended up being faulty; however, the pCO₂ calibration curve was verified and approved by PreSens and is thus considered valid.

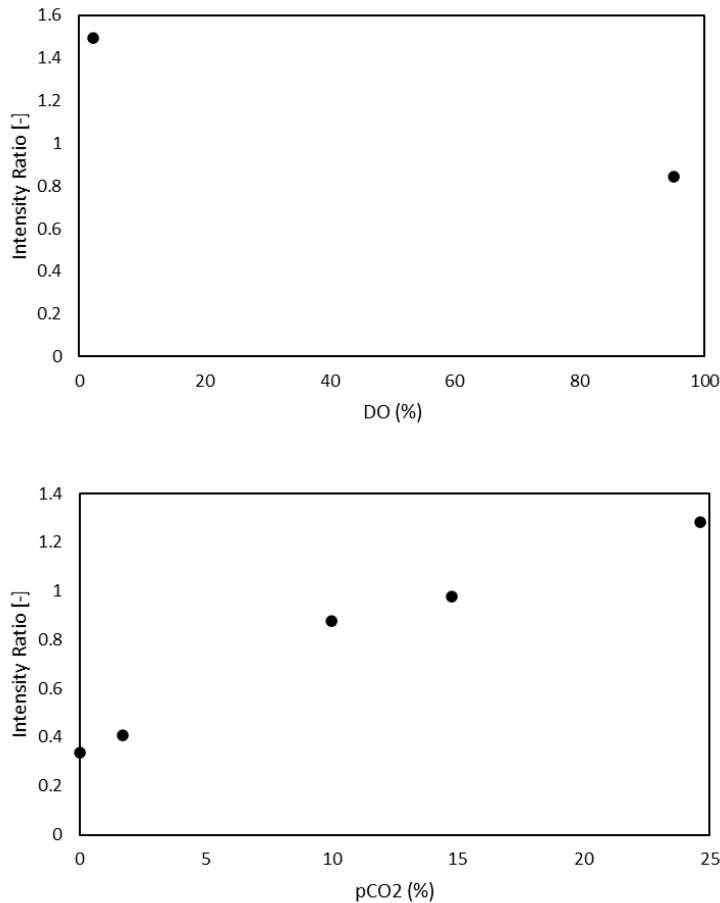


Figure 5.4. Calibration curves for DO (top) and pCO₂ (bottom) obtained from VisiSens ScientifiCal software.

5.2.7 Batch Experiments

Two small batch experiments (trials) were used to observe microbial consumption of DO and glucose (Sections 5.2.4-5.2.5). Batch experiments included 3.0 L of stream water and approximately 5 kg of sediment added at beginning. The tank was static during the experiments, with no inflows or outflows, or other inputs added. The two trials had 0 kg and 2.5 kg of streambed sediment, respectively (Table 5.2). The total sediment for both trials was 5 kg (Figure 5.5), with the remaining sediment being silica sand ($d_{50}=0.53$ mm, US Silica Ottawa Flint Silica #12). Upon collection, the stream water and streambed sediment were taken to the lab to equilibrate to room temperature before commencing the experiments. The sediment was also checked to remove miscellaneous artifacts that were sometimes found such as nails, trash, leaves and twigs.



Figure 5.5. Aquarium tank filled with 1:4 mixture by mass of streambed sediment and silica sand submerged. Planar optodes adhered to front panel and alternated between DO (left) and pCO₂ (right) for each section.

The sediments were thoroughly mixed before the experiments began. The two trials lasted 72 and 18 hours, respectively, from when the full amount of sediment was in the tank (Table 5.2). The time difference was because addition of streambed sediment in Trial 2 hastened DO consumption due to greater microbial biomass.

Sensors and optode strips were arranged as shown in Figure 5.1. Photographs using the camera's set exposure setting (i.e., f-stop and aperture were automatically chosen) and lighting of the appropriate excitation wavelength for pCO₂ and DO were taken consecutively every 20 minutes. Resulting .jpg images were transformed using the VisiSens ScientifiCal software using the calibration curve for each analyte. All experiments were conducted in the dark to reduce photosynthesis and prevent optode photobleaching from natural or artificial light. The only lighting source used during the treatments was the excitation lights used to capture planar optode images. The tank, camera, and lighting system were placed inside a black duvetyn fabric and PVC housing.

Table 5.2. Summary of trial variables for batch experiments

Variable	Trial 1	Trial 2
Stream Water Amount (liters)	3.0	3.0
Streambed Amount (grams)	0	2,500
Silica Sand Amount (grams)	5,000	2,500
C ₆ H ₁₂ O ₆ Concentration (Molar)	0.01	0.10
KH ₂ PO ₄ Concentration (Molar)	0.13	0.08
Experiment Length (hours)	72	18

5.3 Results and Discussion

Trial 1 had no streambed sediment and was fully silica sand submerged in New River stream water with 0.01 M C₆H₁₂O₆ and 0.13 M KH₂PO₄ that was observed for 72 hours. Trial 2 entailed 1:1 streambed sediment: silica sand mixture with 0.1 M C₆H₁₂O₆ and 0.08 M KH₂PO₄ that was observed for 18 hours.

5.3.1 Trial 1: 72-hr DO/pCO₂ Distribution in Silica Sand with 0.01 M C₆H₁₂O₆ and 0.13 M KH₂PO₄

This experimental trial lasted 72 hours because that was necessary to see both a full DO response (Figure 5.6) and a full CO₂ response (Figure 5.7). Both figures show a subset of the experimental duration to best illustrate changes in concentration. The images reveal that noticeable DO depletion began at 4 hours whereas noticeable CO₂ production began at 14 hours after the experiment commenced, indicating a 10-hour lag between the start of O₂ consumption and CO₂ production. DO was fully depleted by 16 hours and maximum CO₂ concentrations are seen at 47 hours. The relatively long duration needed to see a response (compared to Trial 2, see below) may be due to the use of stream water and silica sand. The silica sand was clean and likely contained negligible microorganisms, therefore microorganisms were supplied only from stream water. The time lag likely occurred due to the time required for microorganisms from the stream water to inoculate the silica sand.

In addition, while DO first decreased noticeably at about 4 hours, the rate of DO reduction is slow until 9.7 hours when the DO begins to deplete faster shown by larger amount of red on the optodes. This indicates that at those early hours microbial abundance was not substantial, and once the microbial concentrations increased, respiration correspondingly increased. While both optodes show that the rate of DO reduction increases at 9.7 hours, the rate is not the same at both optodes, with the right-side optode experiencing larger rates than the left-side.

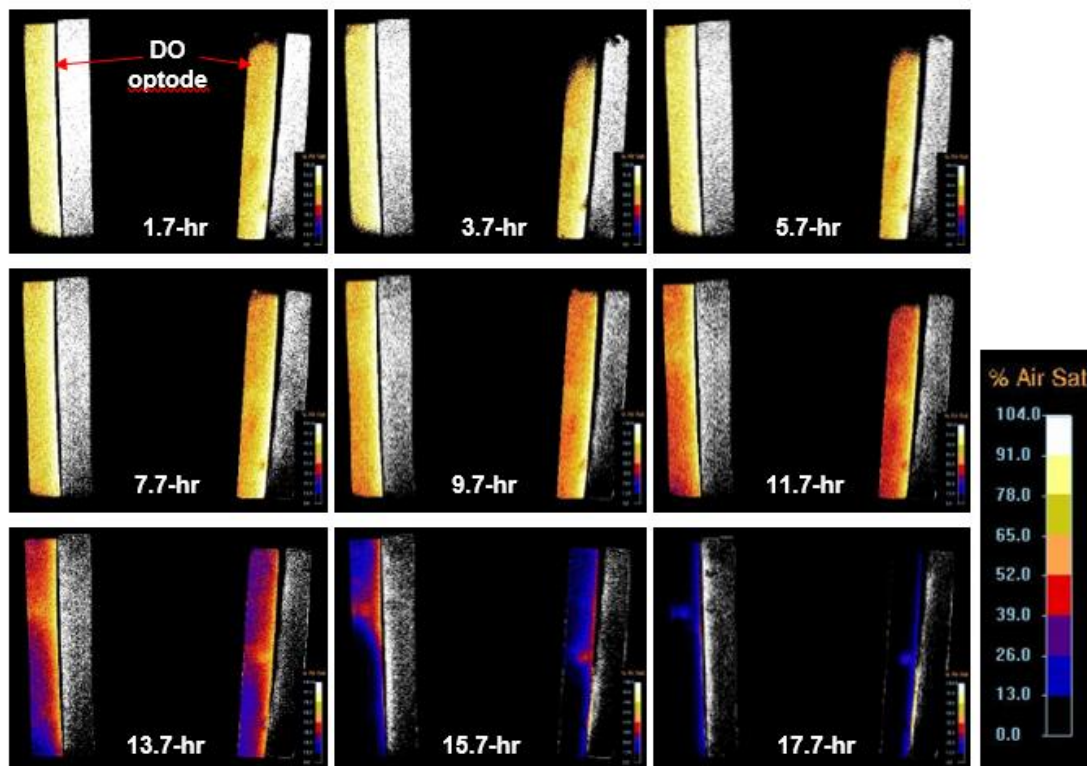


Figure 5.6. Spatial DO concentration distribution (%) shown on DO optodes from 72-hr experiment in silica sand with 0.01 M $C_6H_{12}O_6$ and 0.13 M KH_2PO_4 . Note that pCO_2 optodes are also visible but are shown in black and white because this photograph was taken while the lamp that emitted the correct excitation wavelength for the DO optode was turned on.

Similar to DO, the rate of CO_2 production is low until about 36.3 hours (Figure 5.7). At 36.3 hours CO_2 production occurs throughout the depth of the sediment and across the full optode. The CO_2 distribution is not uniform across the optode, and rather production begins first in the deeper section of the sediment and spreads upward over time. The CO_2 optode range is from 1-25%, meaning that if amounts $> 25\%$ are produced, they will still look like 25%. Therefore, at

time 44.3 hours the right-side optode has reached the 25% threshold while the left-side has not and is able to still show differences. This coincides with the DO reduction being higher on the right side than the left side (Figure 5.6). This shows the heterogeneity of microbial growth and density since the substrate was the homogenous silica sand. The glucose was dissolved into the water and therefore the carbon source was evenly distributed.

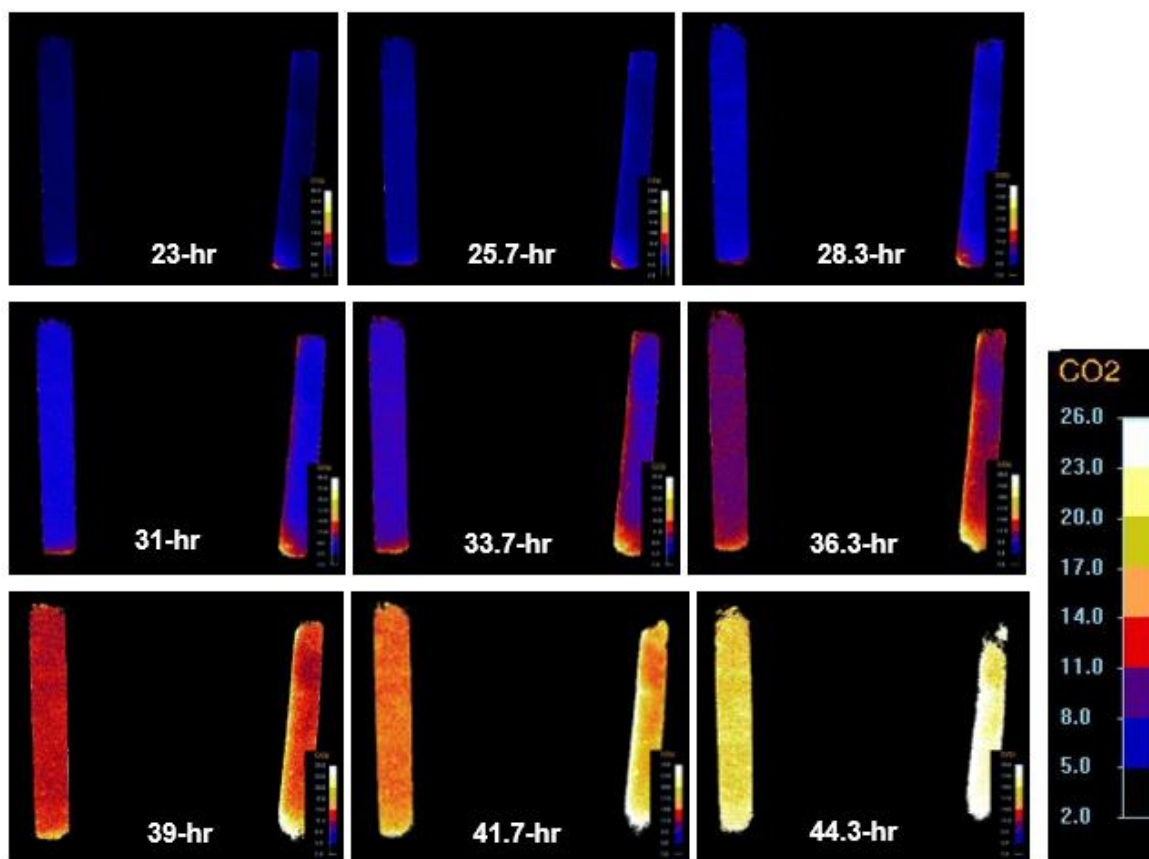


Figure 5.7. Spatial pCO₂ distribution (%) shown on pCO₂ optodes from 72-hr experiment in silica sand with 0.01 M C₆H₁₂O₆ and 0.13 M KH₂PO₄. Note that DO optodes are still present but not visible because this photograph was taken while the lamp that emitted the correct excitation wavelength for the pCO₂ optode was turned on.

5.3.2 Trial 2: 18-hr DO/pCO₂ Distribution in Streambed Sediment and Silica Sand with 0.1 M C₆H₁₂O₆ and 0.08 M KH₂PO₄.

This experiment resulted from the desire to shorten the 72-hr experiment (Trial 1) to under 24-hrs. The desire to shorten the experiments was because we wanted to translate this to flowthrough experiments and decreasing the time would reduce the amount of water, nutrient and glucose needed. In order to achieve a shortened response, streambed sediment was mixed with the silica sand and the glucose increased by a factor of 10 to 0.1 M C₆H₁₂O₆. Figures 5.8 and 5.9 show DO and CO₂ distributions, respectively, for an 18-hr experiment using a 50/50 mixture of streambed sediment and silica sand submerged with 0.1 M C₆H₁₂O₆ and 0.08 M KH₂PO₄. The figures show selected timesteps from the full 18-hr experiment to highlight periods of greatest concentration change.

Figure 5.8 shows that DO concentrations were high up until 10 hours with values above 91%. DO began to noticeably decrease starting at about 11 hours. DO decreased first at intermediate depths and expanded upward and downward from there, yet areas of high DO were still present at the end of the experiment. This greater spatial heterogeneity relative to Trial 1 is likely caused by heterogeneous substrate media and microbial density.

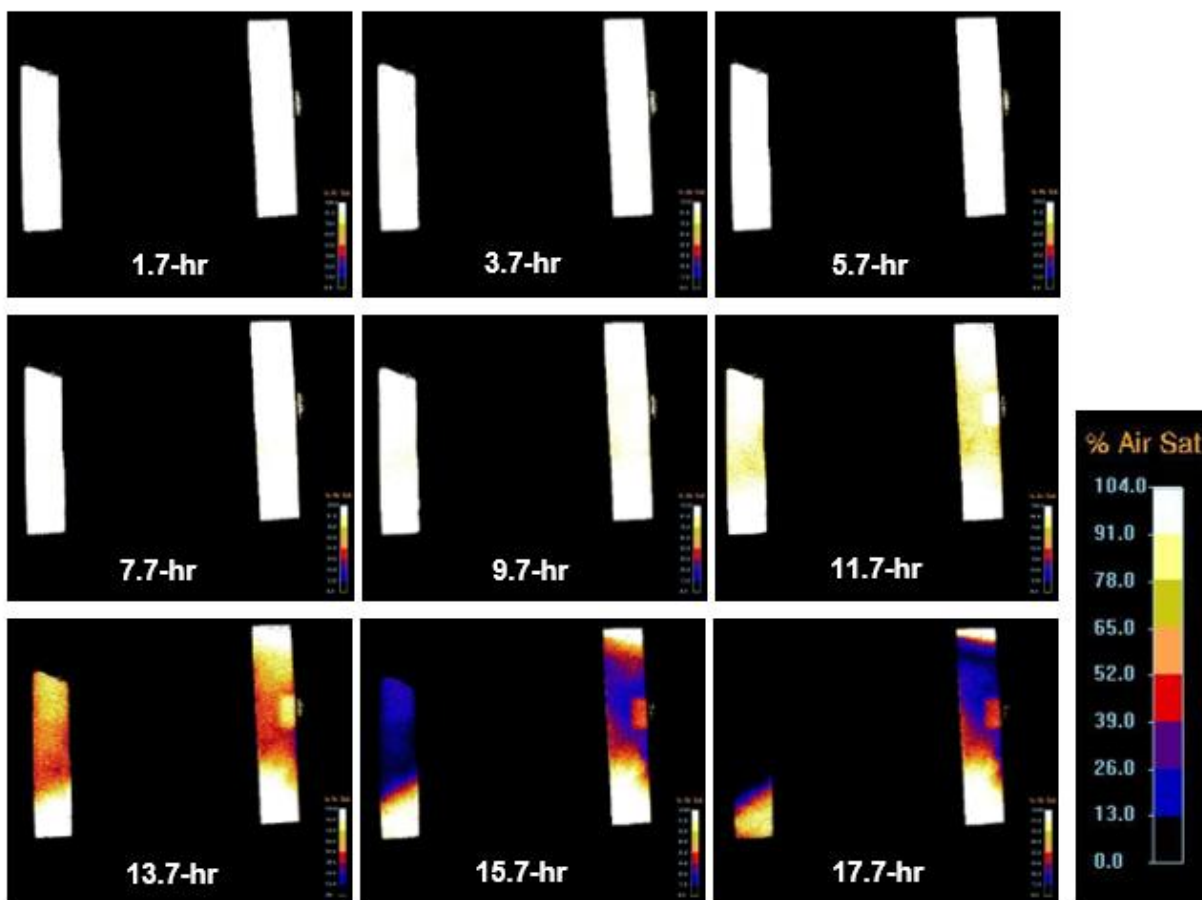


Figure 5.8. Spatial DO optode concentration distribution (%) from 18-hr experiment using 1:1 ratio of streambed sediment to silica sand with 0.10 M $C_6H_{12}O_6$ and 0.08 M KH_2PO_4 . Note that pCO_2 optodes are still present but not visible because this photograph was taken while the lamp that emitted the correct excitation wavelength for the DO optode was turned on.

Similar to Trial 1, DO took over 12 hours for full depletion and large changes of DO began at 11.7 hours. However, while both took the same amount of time to begin substantial depletion, Trial 2 had larger concentrations than Trial 1 (91%+ versus 78-91% DO) therefore microorganisms in this trial depleted more DO in the same amount of time. This indicates that adding streambed sediment (and the microorganisms within) increased the amount of DO reduced. Nonetheless, within the 16-hr timespan, Trial 1 depleted all the DO present while Trial 2 mostly did not. Additionally, the DO reductions over time were more heterogeneous for the streambed sediment. Anoxic/oxic microzones have been found in subsurface studies and therefore it is not unexpected (Briggs et al., 2015; Harvey et al., 2013; Lautz & Fanelli, 2008; Roy Chowdhury et al., 2020).

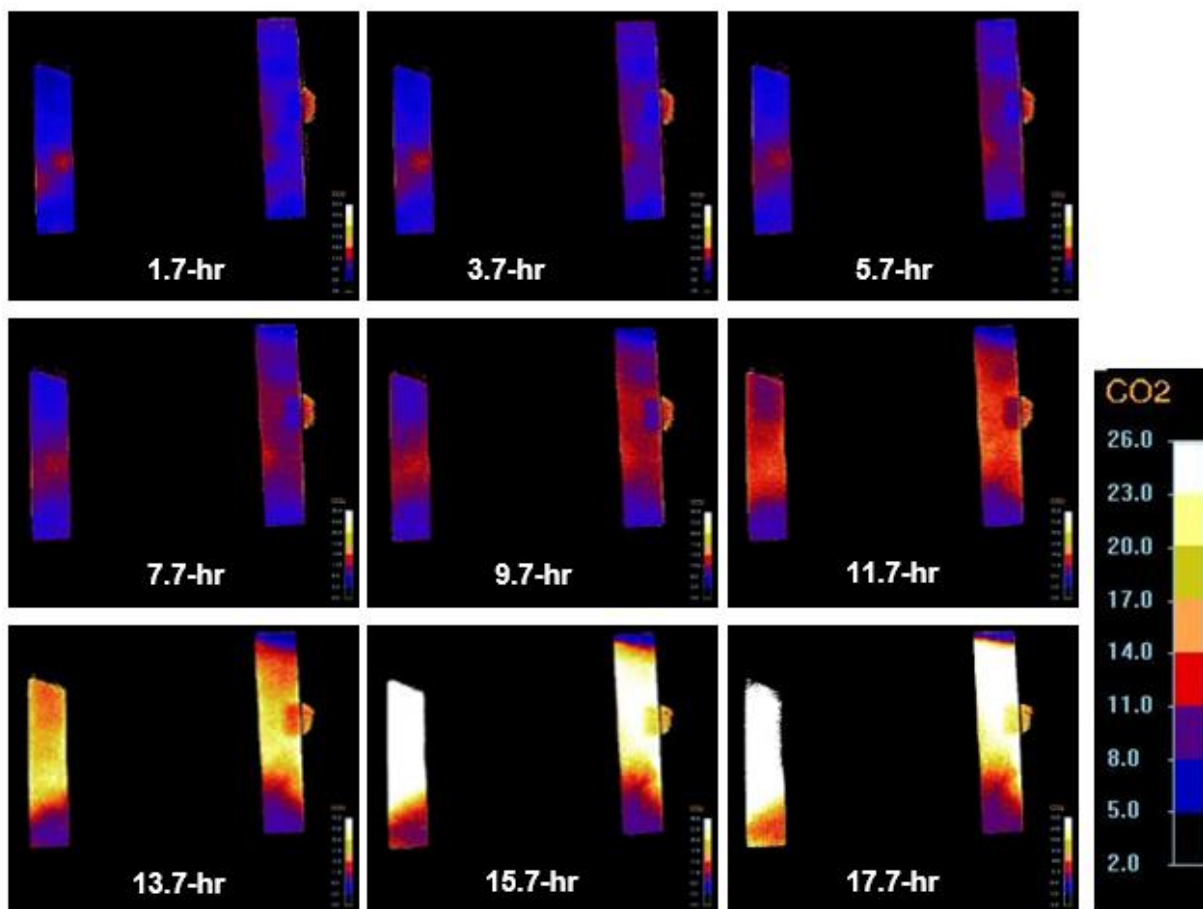


Figure 5.9. pCO₂ distribution (%) shown on pCO₂ optode from 18-hr experiment in 1:1 streambed sediment to silica sand with 0.10 M C₆H₁₂O₆ and 0.08 M KH₂PO₄. Note that DO optodes are still present but not visible because this photograph was taken while the lamp that emitted the correct excitation wavelength for the pCO₂ optode was turned on.

In contrast to Trial 1, CO₂ in Trial 2 is seen at earlier timesteps, yet still coincides with DO consumption. Like for DO consumption, CO₂ production also begins at the center of the optodes and expands outward. The levels and extent of CO₂ production remained low until the DO was reduced. The large number of visual changes for CO₂ which occurred at 11.7 hours matched those at the same time step where DO showed considerable reduction (compare Figures 5.8 and 5.9), in which large amounts of red can be seen indicating larger than 10% pCO₂. Superimposing the two distributions for each timestep during this experiment would show the match between the two analytes. As seen in the last pCO₂ image in Figure 5.9 (17.7 hr), the maximum CO₂ measured coincided with the anoxic section of the DO optode (Figure 5.8) and vice versa with oxic regions.

5.3.3 Comparison of Trials

When trying to understand the observed differences between Trials 1 and 2, the carbon source concentration was increased in the shorter experiment and this larger amount of glucose may have “activated” the microorganisms faster. In addition, the hydraulic conductivity of the sediment was different between the two trials; in particular, the silica sand was coarser than the sediment from the streambed such that the tighter packing of the streambed sediment may create a higher density of microorganisms. In addition, the streambed and stream water both had microorganisms already present, and no inoculation was needed. Thus, more microorganisms were present in the streambed sediment relative to the silica sand since the experiments with just silica sand (i.e., Trial 1) required microorganisms from stream water to inoculate the sediment. As a result, control experiments where one variable is changed at a time or level of complexities are tested would provide insights into the processes or parameters that cause such significant variations.

There could also be differences in biogeochemical processes occurring, given that microorganisms can produce CO₂ in multiple ways during respiration and growth. For example, the lag phase is dependent on initial microbial concentrations, nutrients, and environment conditions such as substrate, temperature, and pH. The microbial biomass, nutrient and carbon source concentration are different between the two trials and therefore both Trials may experience different lag phases. However, fermentation could also explain the large amounts of CO₂ produced in the 72-hr experiment. Anaerobic fermentation takes place in anoxic systems where glucose is the carbon source that gets converted to alcohols and CO₂. Determining whether the CO₂ is produced by aerobic respiration or anaerobic fermentation would be difficult without additional observation methods beyond the optodes, and it is likely that both processes play a role. Chemical analysis would aid in sorting out the relative contributions of these two processes, because alcohol concentrations can be determined via high performance liquid chromatography (HPLC), mass spectrometry (MS), and/or gas chromatography (GC).

While anaerobic fermentation may be worth exploring for these batch experiments that do not have water inflow or outflow, they may not be relevant when observing environments with water exchange or flowpaths as the DO may be replaced. Conducting experiments in batch experiments from stream sediment and water is unrealistic as streams usually have some sort of flow or exchange occurring between the surface water and streambed or subsurface sediment.

Experiments with varying flow rates or hydrological conditions would thus provide valuable information regarding DO/CO₂ dynamics.

5.4 Conclusion and Future Outlook

This chapter presents two-dimensional dissolved oxygen (DO) and carbon dioxide (CO₂) optode concentration distributions from subsurface sediments in batch experiments. The experiments used natural streambed sediment and stream water from New River near Blacksburg, VA. Glucose (C₆H₁₂O₆) and potassium dihydrogen phosphate (KH₂PO₄) were used as carbon and nutrient sources, respectively, to observe aerobic respiration. Two trial experiments were shown, one with streambed sediment and silica sand mixed in equal parts, and one with clean silica sand. The silica sand experiment was 72 hours long as there was a delay in DO and CO₂ signals, while the streambed sediment mixture experiment was 18 hours long. The two trials also varied in terms of nutrient and carbon source concentrations (Table 5.2).

In order to obtain DO and CO₂ concentrations, DO and pCO₂ planar optodes purchased from PreSens were used with the VisiSens System and ScientifiCal software to capture and analyze light intensity images from the planar optodes. Planar optodes use a thin fluorescent film that reacts with different analytes, and the Stern-Volmer equation is then used to relate intensities from the fluorescent films to concentrations of the analytes. As such, calibration curves to relate light intensity to concentration are created for each planar optode and checked to ensure stable optodes over time. The calibration curves are created and developed using ScientifiCal; experiment images are also uploaded to ScientifiCal to transform to concentration and conduct analyses.

Both trials showed clear concentration gradients that formed over time as DO was reduced and CO₂ was produced. DO images showed DO depletion within 12 hours for both experiments. In particular, large gradient shifts occurred at 11.7 hours where the optodes showed consistent decrease of DO. CO₂ optodes also showed clear visualization of CO₂ concentration gradients that form from its production. However, CO₂ distributions did not coincide with DO distributions during the 72-hr experiment. The CO₂ production has a 10-hour delay from the start of DO reduction in the 72-hr experiment. By contrast, in the 18-hr experiment, patterns of CO₂ production and DO consumption did match well. This shows the effect the different substrate and concentrations had on the different experiments.

Additionally, the experiments showed that microbial heterogeneity exists as DO and CO₂ concentrations were not uniformly distributed across the optodes. The silica sand experiments had

less such spatial heterogeneity which is consistent with the homogeneous media used, while the streambed and silica mixture showed more heterogeneity along the optodes where both oxic and anoxic microzones were found. In both cases, however, there were areas of full DO reduction and maximum CO₂ concentrations illustrating the possibility of high activity.

While these experiments show how useful the paired optode system can be in providing insightful information and details into glucose respiration in natural water and sediments it lacks specifics regarding how varying hydrological conditions such as flow rates may impact the respiration. Batch experiments are unrealistic in this way for simulating stream ecosystems and therefore offer only basic information. Yet these results can inform how optodes can be used and adapted to provide more realistic experiment scenarios.

The two experiments differed in sediment texture, as well as nutrient and carbon source concentrations, and their different effects are thus conflated. The streambed sediment showed greater heterogeneity of DO and CO₂ distributions as well as microbial density as more DO was reduced within the same time frame as the experiment with just silica sand. Yet, larger carbon sources could also impact growth rates and thus microbial concentrations which would have impacted the rate at which the DO was reduced, and CO₂ produced. Understanding the effects of the variables and parameters that play a role in respiration is important when observing microbially mediated reactions in subsurface sediments. Therefore, providing controlled scenarios where different variables and parameters are changed one at a time would offer more detailed insight into the processes taking place.

Ultimately, the optodes were able to show changes in concentration over time and space. In addition, they represent some of the first two-dimensional DO and CO₂ optode images produced for natural streambed sediment and stream water. The relationship between these two analytes is important in many environments and crucial when observing water quality. Understanding when, where, and how microbial respiration occurs will aid understanding of contaminant attenuation, refuge for organisms, and stream health, and will allow interdisciplinary and integrated approaches to protecting water quality. Therefore, matching optode images with microbiology and hydrological techniques will more holistically illustrate what processes are occurring in our natural water body systems such as streams and lakes.

References

- Abarca, E., & Clement, T. P. (2009). A novel approach for characterizing the mixing zone of a saltwater wedge. *Geophysical Research Letters*, *36*(6).
<https://doi.org/10.1029/2008GL036995>
- Bauer, R. D., Rolle, M., Kürzinger, P., Grathwohl, P., Meckenstock, R. U., & Griebler, C. (2009). Two-dimensional flow-through microcosms - Versatile test systems to study biodegradation processes in porous aquifers. *Journal of Hydrology*, *369*(3–4), 284–295.
<https://doi.org/10.1016/j.jhydrol.2009.02.037>
- Blossfeld, S., Schreiber, C. M., Liebsch, G., Kuhn, A. J., & Hinsinger, P. (2013). Quantitative imaging of rhizosphere pH and CO₂ dynamics with planar optodes. *Annals of Botany*, *112*(2), 267–276. <https://doi.org/10.1093/aob/mct047>
- Borisov, S. M., Seifner, R., & Klimant, I. (2011). A novel planar optical sensor for simultaneous monitoring of oxygen, carbon dioxide, pH and temperature. *Analytical and Bioanalytical Chemistry*, *400*(8), 2463–2474. <https://doi.org/10.1007/s00216-010-4617-4>
- Briggs, M. A., Day-Lewis, F. D., Zarnetske, J. P., & Harvey, J. W. (2015). A physical explanation for the development of redox microzones in hyporheic flow. *Geophysical Research Letters*, *42*(11), 4402–4410. <https://doi.org/10.1002/2015GL064200>
- Caruso, A., Boano, F., Ridolfi, L., Chopp, D. L., & Packman, A. (2017). Biofilm-induced bioclogging produces sharp interfaces in hyporheic flow, redox conditions, and microbial community structure. *Geophysical Research Letters*, *44*(10), 4917–4925.
<https://doi.org/10.1002/2017GL073651>
- Castro-Alcalá, E., Fernández-García, D., Carrera, J., & Bolster, D. (2012). Visualization of mixing processes in a heterogeneous sand box aquifer. *Environmental Science and Technology*, *46*(6), 3228–3235. <https://doi.org/10.1021/es201779p>
- Galloway, J., Fox, A., Lewandowski, J., & Arnon, S. (2019). The effect of unsteady streamflow and stream-groundwater interactions on oxygen consumption in a sandy streambed. *Scientific Reports*, *9*(1), 1–11. <https://doi.org/10.1038/s41598-019-56289-y>
- Harvey, J. W., Böhlke, J. K., Voytek, M. A., Scott, D., & Tobias, C. R. (2013). Hyporheic zone denitrification: Controls on effective reaction depth and contribution to whole-stream mass balance. *Water Resources Research*, *49*(10), 6298–6316.
<https://doi.org/10.1002/wrcr.20492>
- Hendricks, S. P. (1993). Microbial ecology of the hyporheic zone: a perspective integrating hydrology and biology. *Am. Benthol. Soc.*, *12*(1), 70–78. Retrieved from <http://www.journals.uchicago.edu/t-and-c>
- Jiang, Z., Yu, X., & Hao, Y. (2017). Design and fabrication of a ratiometric planar optode for

- simultaneous imaging of pH and oxygen. *Sensors (Switzerland)*, 17(6).
<https://doi.org/10.3390/s17061316>
- Kaufman, M. H., Cardenas, M. B., Buttles, J., Kessler, A. J., & Cook, P. L. M. (2017). Hyporheic hot moments: Dissolved oxygen dynamics in the hyporheic zone in response to surface flow perturbations. *Water Resources Research*, 53(8), 6642–6662.
<https://doi.org/10.1002/2016WR020296>
- Larsen, M., Borisov, S. M., Grunwald, B., Klimant, I., & Glud, R. N. (2011). A simple and inexpensive high-resolution color-ratiometric planar optode imaging approach: Application to oxygen and pH sensing. *Limnology and Oceanography: Methods*, 9, 348–360.
- Lautz, L. K., & Fanelli, R. M. (2008). Seasonal biogeochemical hotspots in the streambed around restoration structures. *Biogeochemistry*, 91(1), 85–104. <https://doi.org/10.1007/s10533-008-9235-2>
- Lehto, N. J., Larsen, M., Zhang, H., Glud, R. N., & Davison, W. (2017). A mesocosm study of oxygen and trace metal dynamics in sediment microniches of reactive organic material. *Scientific Reports*, (August), 1–12. <https://doi.org/10.1038/s41598-017-10179-3>
- Molz, F. J., & Widdowson, M. A. (1988). Internal inconsistencies in dispersion-dominated models that incorporate chemical and microbial kinetics. *Water Resources Research*, 24(4), 615–619. <https://doi.org/10.1029/WR024i004p00615>
- Robinson, G., Ahmed, A. A., & Hamill, G. A. (2016). Experimental saltwater intrusion in coastal aquifers using automated image analysis: Applications to homogeneous aquifers. *Journal of Hydrology*, 538, 304–313. <https://doi.org/10.1016/j.jhydrol.2016.04.017>
- Rolle, M., Eberhardt, C., Chiogna, G., Cirpka, O. A., & Grathwohl, P. (2009). Enhancement of dilution and transverse reactive mixing in porous media : Experiments and model-based interpretation. *Journal of Contaminant Hydrology*, 110, 130–142.
<https://doi.org/10.1016/j.jconhyd.2009.10.003>
- Roy Chowdhury, S., Zarnetske, J. P., Phanikumar, M. S., Briggs, M. A., Day-Lewis, F. D., & Singha, K. (2020). Formation Criteria for Hyporheic Anoxic Microzones: Assessing Interactions of Hydraulics, Nutrients, and Biofilms. *Water Resources Research*, 56(3), no. <https://doi.org/10.1029/2019WR025971>
- Santizo, K. Y., Widdowson, M. A., & Hester, E. T. (2020). Abiotic Mixing-Dependent Reaction in a Laboratory Simulated Hyporheic Zone. *Water Resources Research*, 56(9).
<https://doi.org/10.1029/2020WR027090>
- Santner, J., Larsen, M., Kreuzeder, A., & Glud, R. N. (2015). Two decades of chemical imaging of solutes in sediments and soils - a review. *Analytica Chimica Acta*. Elsevier B.V.
<https://doi.org/10.1016/j.aca.2015.02.006>

- Stegen, J. C., Fredrickson, J. K., Wilkins, M. J., Konopka, A. E., Nelson, W. C., Arntzen, E. V., et al. (2016). Groundwater-surface water mixing shifts ecological assembly processes and stimulates organic carbon turnover. *Nature Communications*, 7, 1–12. <https://doi.org/10.1038/ncomms11237>
- Thomas, P. J., Atamanchuk, D., Hovdenes, J., & Tengberg, A. (2017). The use of novel optode sensor technologies for monitoring dissolved carbon dioxide and ammonia concentrations under live haul conditions. *Aquacultural Engineering*, 77, 89–96. <https://doi.org/10.1016/j.aquaeng.2017.02.004>
- Wolke, P., Teitelbaum, Y., Deng, C., Lewandowski, J., & Arnon, S. (2020). Impact of bed form celerity on oxygen dynamics in the hyporheic zone. *Water (Switzerland)*, 12(1). <https://doi.org/10.3390/w12010062>
- Zhu, Q., & Aller, R. C. (2010). A rapid response, planar fluorosensor for measuring twodimensional pCO₂ distributions and dynamics in marine sediments. *Limnology and Oceanography: Methods*, 8, 326–336. <https://doi.org/10.4319/lom.2010.8.326>

Chapter 6. Conclusion

6.1 Summary of Research Work

The various research threads presented in this dissertation build on each other to inform understanding of mixing and mixing-dependent reactions in the hyporheic zone. Performing different studies with narrow and controlled objectives allowed us to separate out the controls of mixing and mixing-dependent reactions under different conditions.

In Chapter 2, we observed transverse hyporheic mixing zones with a conservative dye in a laboratory sediment tank. The dye was photographed under steady state and transient surface water head drops that drove exchange across the sediment-water interface. The images were then analyzed to quantify mixing zone thickness. In general, the mixing zone thickness for steady state experiments were thin and increased with increasing surface water head drop. Transient experiments resulted in larger mixing zone thicknesses than those from steady state experiments.

A manually calibrated numerical model of the laboratory experiments was used to replicate the conservative dye transport and estimate transverse dispersivities, mixing zone lengths, Peclet numbers, and dilution indices. These values provide additional insight into mixing processes behind the laboratory observations and demonstrate the importance of calculating mixing zone thickness, transverse dispersivities, and dilution index to provide comprehensive information on mixing. Estimated transverse dispersivity was smaller than reported in the groundwater literature for larger scales, emphasizing the crucial need for determining dispersivities applicable to the smaller spatial scales of the hyporheic zone. Inflow ratios (ratio of upwelling groundwater and downwelling surface water) had a dominant influence with mixing zone thickness decreasing with increasing inflow ratios. Unlike mixing zone thickness, dilution index decreased with increasing surface water head drop. Taken together, these practical and analytical mixing metrics provide differing but complementary information on mixing.

In Chapter 3, we added complexity to mixing by simulating a mixing-dependent abiotic reaction in a laboratory induced hyporheic zone. Planar optodes were used to observe the abiotic reaction of sodium sulfite (Na_2SO_3) and dissolved oxygen (DO) to sodium sulfate (Na_2SO_4). Optode images were analyzed to obtain DO concentration distributions and profiles, mixing zone thicknesses, and oxic front positions under two steady-state surface water head drop conditions of 4.5 cm and 6.0 cm. Image analysis showed that during non-reactive control experiments the mixing

zone thickness and oxic front position stayed stable. This was not the case during the mixing-dependent reaction where oxic fronts shifted and mixing zone thicknesses decreased as DO was consumed. SO_4 concentration profiles showed that peak SO_4 was produced where reactants had already been consumed. This demonstrated that as the reaction progressed, the DO mixing front shifted toward the partition and SO_4 was produced where recent DO consumption had occurred. Similar to Chapter 2, mixing zone thickness increased with increasing surface water head drop both with and without the reaction present. Overall, Chapter 3 shows the importance of transport and kinetics on mixing-dependent reactions in the hyporheic zone.

Chapter 4 extends the results of Chapter 3 by numerically simulating the Chapter 3 laboratory abiotic mixing-dependent reactions. Simulated mixing zone thicknesses and oxic front positions matched well with observed values from Chapter 3. SO_4 production zone thicknesses and production front positions were additional outputs from the model that had not been feasible to measure in the laboratory. Similar to DO, SO_4 production zone fronts moved towards the partition with time. By contrast, production zone thicknesses showed the opposite trend from DO, i.e., increasing with time. To quantify the influence of hydrologic and kinetic parameters on mixing-dependent reaction, inflow ratios (the flow ratio between upwelling groundwater and downwelling surface water) as well as DO, SO_3 , and SO_4 concentrations were varied in a sensitivity analysis. Inflow ratio showed the greatest influence and was therefore a key driver of DO mass consumed and SO_4 mass produced.

In this analysis, we were also able to look at mass balances between the reactants and products and compare them to zone thickness and front position. The more SO_4 was produced over time the larger the SO_4 production zone thickness, while DO mixing zone thickness shrank as DO was simultaneously consumed. For small changes in zone thickness, large amounts of mass consumption and production occurred. Thus, zone thickness has potential as a practical indicator of consumption and production in lab or field settings. Similar to mixing and production zone thickness, reaction mass was sensitive to inflow ratio. All the lower inflow ratios had similar mass production and consumption and the same was true of the higher inflow ratios. Variations of controls on hyporheic zone attenuation, such as inflow ratios and chemical concentrations, are complex and can interfere and/or enhance reactions with implications for water quality management and ecosystem health.

Among chapters 2-4 we analyze dimensionless numbers to characterize dominant characteristics within our domain. In specific, the Peclet (Pe) and Damkohler (Da) number were used to determine hydraulic and kinetic properties. All chapters have Pe numbers show that the domain was advection dominant with dispersion limited due to the high Pe values. While the Pe values were all high there was a range and magnitude difference among the values in the studies. This is likely due to the differences in calculating the value. In Chapter 2 the mixing length and thickness are calculated at a depth of 4.2 cm and across the full hyporheic flow cell. Chapter 4 differs in the depth of calculation as it follows Chapter 3's analysis which was measured at 3.5 cm in depth. The biggest difference among the chapters is among Chapter 3 where the mixing length is truncated due to the limitation with the images that were taken. Chapter 3 is where we see the largest difference in values indicating that the full mixing length is needed to appropriately compare the values among all the chapters.

Chapter 5 presents two trials of DO and carbon dioxide (CO₂) optodes in batch experiments of submerged sediments. The objective of Chapter 5 was to determine the feasibility of using a coupled DO-CO₂ optode system to provide basic understanding of coupled DO-CO₂ patterns and processes to build toward future understanding of hyporheic zone biogeochemical and microbial function. The experiments used natural streambed sediment and stream water from New River near Blacksburg, VA as well as silica sand. Glucose (C₆H₁₂O₆) and potassium dihydrogen phosphate (KH₂PO₄) were used as carbon and nutrient sources, respectively, to observe aerobic respiration in 72-hour and 18-hour long trials. Trial times were different due to differences in glucose and potassium dihydrogen phosphate concentrations. Both trials showed clear spatial concentration gradients that formed over time as DO was reduced and CO₂ was produced. In addition, the effect of different substrate and concentrations were also seen in the optode images. However, there were areas of full DO reduction and maximum CO₂ concentrations in both trials illustrating the possibility of high activity. Additionally, the trials showed microbial heterogeneity as DO and CO₂ concentrations were not uniformly distributed across the optodes.

It is important to note the distinction between Chapter 3,4 and Chapter 5 in its reaction kinetics. We expect some of the conclusions from the abiotic reaction in Chapter 3 and 4 regarding mixing zone thickness and mass production/consumption to be applicable to biotic reactions like that of Chapter 5. However, the profiles may not look the same as reaction times are highly different. The reaction time for the abiotic reaction explored is seconds while for the biotic reaction

it may be minutes to hours. Thus, the mixing may look different due to the extend reaction times. Nevertheless, the current studies are not directly comparable due to biotic reaction in Chapter 5 taking place in a batch system with no flow. When the biotic reaction is transferred to the hyporheic zone we may see changes in the reaction response time as there would be more controlling factors (i.e., pore scale velocities, hydraulic conductivity, surface water Δh) therefore potentially introducing additional mixing dynamics as microorganisms alter the mixing zones. Thus, we expect that while the trends may be similar the timescales would be longer.

These preliminary trials show the feasibility and value of the coupled optode system in detailing microbial processes. Ultimately, the optodes were able to show changes in concentration over time and space. In addition, they represent some of the first two-dimensional DO and CO₂ optode images produced for natural streambed sediment and stream water.

6.2 Engineering Significance and Implications

This dissertation provides fundamental insights into mixing processes in the hyporheic zone. Mixing processes have been extensively studied for deeper groundwater contaminant attenuation and ways to enhance mixing has been a key concern (Cirpka et al., 2015; Werth et al., 2006; Ye et al., 2016). Therefore, understanding mixing processes is instrumental to enhancing attenuation and maintaining ecosystem health. More recently, mixing in the hyporheic zone has also been an area of growing research interest due to its biogeochemical importance (Cardenas et al., 2004; Hester et al., 2014, 2017; Lewandowski et al., 2019, 2020; Li et al., 2017).

Upwelling groundwater contaminants traversing the hyporheic zone undergo attenuation as mixing of reactants occurs (Conant et al., 2004; Ellis & Rivett, 2007; Hester et al., 2013). This process is somewhat similar to mixing on the fringes of a groundwater plume as it moves along an aquifer transect (Bauer et al., 2009; Liu et al., 2014; Werth et al., 2006; Ye et al., 2015). Therefore, in Chapter 2 we explore mixing due to a conservative dye in the hyporheic zone and most importantly verify thin mixing zones and relate mixing zone thickness to a groundwater parameter of dilution index. This relationship had not yet been shown in either groundwater or hyporheic zone literature. This comparison illustrates the complementary nature of practical visual parameters on the one hand versus analytically derived parameters on the other, which together provides more holistic description of mixing. Neither parameter wholly describes mixing zones

and therefore both together better informs remediation, restoration, and attenuation in the hyporheic zone.

Explicitly observing mixing and kinetics, Chapter 3 focuses on a mixing-dependent reaction (Santizo et al., 2020). While the reaction is abiotic and performed under steady-state hydraulics and homogeneous sediment, this was one of the first studies that looked at controls for mixing-dependent reactions in the hyporheic zone using two-dimensional visualization techniques (Cardenas et al., 2016; Galloway et al., 2019; Kaufman et al., 2017; Wolke et al., 2020). This study provides basic information on how reactions influence mixing and most importantly it shows that reaction dynamics changed the mixing zone thickness and mixing zone front location over time, illustrating that even with steady-state and homogeneous conditions, dynamic progression of transport and reactions are seen. This directly impacts attenuation potential and characterization of chemical concentrations. In the field, transient hydraulics and heterogeneous sediment is the norm, and these added complexities would further enhance the dynamics evolution of mixing zone front locations and mixing zone thicknesses, potentially further enhancing chemical transformations. Yet capturing this full range of dynamics would be challenging in the field, both in terms of spatial and temporal resolution of monitoring efforts. The extent of attenuation could be easily truncated if the reaction dynamics are not considered.

Chapter 3 provided insight into reaction dynamics but did not relate these to production zone thicknesses or mass balance. Thus, Chapter 4 addresses the relationship between reaction dynamics, mixing-dependent reactions, and mass consumption/production. In addition, sensitivity to reaction kinetic and hydraulic parameters were measured. It demonstrated that small changes in the flow balance changed the amount of mass consumed and produced, and that mass trends can be inferred from zone thickness trends. This is a practical insight that is useful infer mass changes in the system from simply observations, which could further provide insights into attenuation for laboratory and field studies.

Ultimately, Chapters 2-4 illuminate the relationships between mixing and its controls. Each chapter builds on the previous in levels of complexity to show the importance of mixing for attenuation and water quality efforts in the hyporheic zone. These studies could be used to provide guidance to management decisions for river management and mitigating groundwater contaminants.

For example, because inflow ratios were a dominant factor in all chapters, this might be leveraged to control and enhance mixing in highly impaired rivers. Many rivers across the U.S. have substantial flow management which could be adapted to optimize flow and attenuation to improve water quality and remove rivers from impaired lists. Weirs, dams, and other in-stream structures have long been used as flow control features in rivers and therefore adapting their use, placement, and flow-release timing to enhance mixing and attenuation could be studied and implemented. Many times, these decisions are made with one goal in mind e.g., flow control. However, processes do not occur in a vacuum and flow control has impacts on biogeochemical processes, thus optimizing both would have enhanced benefits relative to single purpose design or management. Adapting and implementing such changes would also enhance recognition of the hyporheic zone as a location for attenuation and efforts to enhance attenuation by government agencies either through regulations or acts. As such, remediation efforts that have traditionally focused on deeper groundwater can also be applied to the hyporheic zone.

Lastly, the information provided in Chapter 4 regarding mass production and consumption in relation to mixing zone front locations and thickness could be an important tool in monitored natural attenuation (MNA). In MNA, understanding where to make observations regarding contaminant concentrations is crucial thus having knowledge on the location and mixing dynamics would aid in successful attenuation. In addition, providing the relationship between timescales and its controls would improve MNA as favorable conditions for the reaction of interest may be implemented. Having the practical measurement (zone thickness) and relating it to the concentration changes as done in Chapter 4 could provide an opportunity for MNA evaluation.

The last chapter, Chapter 5, can be thought of a preliminary study that explored the potential of coupling planar optodes for imaging biotic mixing-dependent reactions in the hyporheic zone. The images of CO₂ and DO are some of the first from subsurface studies measuring microbial respiration from streambed sediments. Implementing this coupled optode technique could offer relationships on respiration and dynamics by providing two-dimensional profiles with chemical spatial distributions. Numerical models and field experiments have shown the importance of microbial respiration for attenuation and most recently the interplay between mixing, microbial communities, and attenuation.

6.3 Future Work

There are many avenues these studies can take to further understanding of hyporheic processes relating to mixing and attenuation. Each chapter is addressed separately by expanding on the future work already stated in each chapter.

Chapter 2 used homogeneous sediment and therefore the next logical step would be to address mixing in heterogeneous sediment and determine the relationships that evolve from heterogeneity. Flux-related dilution indices have been applied to heterogeneous aquifers and therefore can also be used in hyporheic settings (Ballarini et al., 2014; Chiogna et al., 2012; Rolle et al., 2013). In addition, three-dimensional model domains could allow observation of additional flow patterns such as helical flows (Ye et al., 2016). Lastly, adding mixing-dependent reactions and using groundwater analytical parameters such as critical dilution index could inform the relationship between mixing zone thickness and dilution indices under reactive conditions.

Chapter 3 could be extended with transient head boundaries to determine how they affect the transport and kinetics dynamics already observed (Bottacin-Busolin, 2019; Hester et al., 2019). Observing different reactions such as microbially mediated, precipitation or decomposition reactions with varying kinetic rates could also inform how mixing dynamics change due to a range of kinetic rates. Ultimately, this will allow the ability to properly sample and map concentration profiles in the laboratory and field and thus help determine relationships between mixing zones, consumption, and production. To accomplish these goals, more robust sampling and chemical analysis procedures in laboratory and field settings are needed.

Similar to Chapter 2 and 3, Chapter 4 would benefit from heterogeneity analysis and transient head conditions. Extending the numerical model to a wider range of surface water head drops, inflow ratios, and reactions observed would help expand the trends and connections found in the study. Using larger and smaller head drops to expand from the two values observed would help determine the limits of mixing-dependent reactions as faster velocities may impede reaction completion. Using a wider range of inflow ratios would help determine the relationships between mass changes and mixing/production zone thickness and front positions. Lastly, using different reactions that use DO as the electron acceptor such as degradation of halogenated hydrocarbons and fuel-derived compounds can inform what influence the reaction order may have on mixing dynamics. Implementing biotic mixing-dependent reactions allows for comparison on the effects

of the types of reactions as attenuation depends on both abiotic and biotic reactions in the hyporheic zone.

Finally, considering the optodes tested in Chapter 5, implementing larger scale experiments in laboratory flumes with circulating or non-circulating flow conditions will more realistically simulate processes in hyporheic zones. In addition, having controlled scenarios to test different variables (nutrient, carbon and DO concentrations; ratio of sediment mixture) would provide detailed insight into mixing processes. In addition, using microbiology techniques in tandem can inform of microorganisms involved and their response to mixing. The coupled optode system shows great promise to expand our understanding of biogeochemical processes that occur in the hyporheic zone with greater spatial resolution.

References

- Ballarini, E., Bauer, S., Eberhardt, C., & Beyer, C. (2014). Evaluation of the role of heterogeneities on transverse mixing in bench-scale tank experiments by numerical modeling. *Groundwater*, 52(3), 368–377. <https://doi.org/10.1111/gwat.12066>
- Bauer, R. D., Rolle, M., Kürzinger, P., Grathwohl, P., Meckenstock, R. U., & Griebler, C. (2009). Two-dimensional flow-through microcosms - Versatile test systems to study biodegradation processes in porous aquifers. *Journal of Hydrology*, 369(3–4), 284–295. <https://doi.org/10.1016/j.jhydrol.2009.02.037>
- Bottacin-Busolin, A. (2019). Modeling the Effect of Hyporheic Mixing on Stream Solute Transport. *Water Resources Research*, 55(11), 9995–10011. <https://doi.org/10.1029/2019WR025697>
- Cardenas, M. B., Wilson, J. L., & Zlotnik, V. A. (2004). Impact of heterogeneity, bed forms, and stream curvature on subchannel hyporheic exchange. *Water Resources Research*, 40(8), 1–14. <https://doi.org/10.1029/2004WR003008>
- Cardenas, M. B., Ford, A. E., Kaufman, M. H., Kessler, A. J., & Cook, P. L. M. (2016). Hyporheic flow and dissolved oxygen distribution in fish nests: The effects of open channel velocity, permeability patterns, and groundwater upwelling. *Journal of Geophysical Research: Biogeosciences*, 121(12), 3113–3130. <https://doi.org/10.1002/2016JG003381>
- Chiogna, G., Hochstetler, D. L., Bellin, A., Kitanidis, P. K., & Rolle, M. (2012). Mixing, entropy and reactive solute transport. *Geophysical Research Letters*, 39(20), 1–6. <https://doi.org/10.1029/2012GL053295>
- Cirpka, O. A., Chiogna, G., Rolle, M., & Bellin, A. (2015). Transverse mixing in three-dimensional nonstationary anisotropic heterogeneous porous media. *Water Resources Research*, 51(1), 241–260. <https://doi.org/10.1002/2014WR015331>
- Conant, B., Cherry, J. A., & Gillham, R. W. (2004). A PCE groundwater plume discharging to a river: Influence of the streambed and near-river zone on contaminant distributions. *Journal of Contaminant Hydrology*, 73(1–4), 249–279. <https://doi.org/10.1016/j.jconhyd.2004.04.001>
- Ellis, P. A., & Rivett, M. O. (2007). Assessing the impact of VOC-contaminated groundwater on surface water at the city scale. *Journal of Contaminant Hydrology*, 91(1–2), 107–127. <https://doi.org/10.1016/j.jconhyd.2006.08.015>
- Galloway, J., Fox, A., Lewandowski, J., & Arnon, S. (2019). The effect of unsteady streamflow and stream-groundwater interactions on oxygen consumption in a sandy streambed. *Scientific Reports*, 9(1). <https://doi.org/10.1038/s41598-019-56289-y>
- Hester, E. T., Young, K. I., & Widdowson, M. A. (2013). Mixing of surface and groundwater induced by riverbed dunes: Implications for hyporheic zone definitions and pollutant reactions. *Water Resources Research*, 49(9), 5221–5237. <https://doi.org/10.1002/wrcr.20399>
- Hester, E. T., Young, K. I., & Widdowson, M. A. (2014). Controls on mixing-dependent denitrification in hyporheic zones induced by riverbed dunes: A steady state modeling

- study. *Water Resources Research*, 50, 9048–9066. <https://doi.org/10.1002/2014WR015424>
- Hester, E. T., Cardenas, M. B., Haggerty, R., & Apte, S. V. (2017). The importance and challenge of hyporheic mixing. *Water Resources Research*, 53, 3565–3575. <https://doi.org/10.1002/2016WR020005>
- Hester, E. T., Eastes, L. E., & Widdowson, M. A. (2019). Effect of Surface Water Stage Fluctuation on Mixing-Dependent Hyporheic Denitrification in Riverbed Dunes. *Water Resources Research*, 55(6), 4668–4687. <https://doi.org/https://doi.org/10.1029/2018WR024198>
- Kaufman, M. H., Cardenas, M. B., Buttles, J., Kessler, A. J., & Cook, P. L. M. (2017). Hyporheic hot moments: Dissolved oxygen dynamics in the hyporheic zone in response to surface flow perturbations. *Water Resources Research*, 53(8), 6642–6662. <https://doi.org/10.1002/2016WR020296>
- Lewandowski, J., Arnon, S., Banks, E., Batelaan, O., Betterle, A., Broecker, T., et al. (2019). Is the hyporheic zone relevant beyond the scientific community? *Water (Switzerland)*, 11(11). <https://doi.org/10.3390/w11112230>
- Lewandowski, J., Meinikmann, K., & Krause, S. (2020, January 1). Groundwater-surface water interactions: Recent advances and interdisciplinary challenges. *Water (Switzerland)*. MDPI AG. <https://doi.org/10.3390/w12010296>
- Li, A., Aubeneau, A. F., Bolster, D., Tank, J. L., & Packman, A. I. (2017). Covariation in patterns of turbulence-driven hyporheic flow and denitrification enhances reach-scale nitrogen removal. *Water Resources Research*, 53(8), 6927–6944. <https://doi.org/10.1002/2016WR019949>
- Liu, Y., Illangasekare, T. H., & Kitanidis, P. K. (2014). Long-term mass transfer and mixing-controlled reactions of a DNAPL plume from persistent residuals. *Journal of Contaminant Hydrology*, 157, 11–24. <https://doi.org/10.1016/j.jconhyd.2013.10.008>
- Rolle, M., Chiogna, G., Hochstetler, D. L., & Kitanidis, P. K. (2013). On the importance of diffusion and compound-specific mixing for groundwater transport: An investigation from pore to field scale. *Journal of Contaminant Hydrology*, 153, 51–68. <https://doi.org/10.1016/j.jconhyd.2013.07.006>
- Santizo, K. Y., Widdowson, M. A., & Hester, E. T. (2020). Abiotic Mixing-Dependent Reaction in a Laboratory Simulated Hyporheic Zone. *Water Resources Research*, 56(9). <https://doi.org/10.1029/2020WR027090>
- Werth, C. J., Cirpka, O. A., & Grathwohl, P. (2006). Enhanced mixing and reaction through flow focusing in heterogeneous porous media. *Water Resources Research*, 42(12). <https://doi.org/10.1029/2005WR004511>
- Wolke, P., Teitelbaum, Y., Deng, C., Lewandowski, J., & Arnon, S. (2020). Impact of bed form celerity on oxygen dynamics in the hyporheic zone. *Water (Switzerland)*, 12(1), 5–7. <https://doi.org/10.3390/w12010062>
- Ye, Y., Chiogna, G., Cirpka, O. A., Grathwohl, P., & Rolle, M. (2015). Enhancement of plume dilution in two-dimensional and three-dimensional porous media by flow focusing in high-

permeability inclusions. *Water Resources Research*, 51, 5582–5602.
<https://doi.org/10.1002/2015WR016962>

Ye, Y., Chiogna, G., Cirpka, O. A., Grathwohl, P., & Rolle, M. (2016). Experimental investigation of transverse mixing in porous media under helical flow conditions, *013113*, 1–10. <https://doi.org/10.1103/PhysRevE.94.013113>

Appendix A. Steady-State MATLAB Codes for Chapter 2: Hyporheic transverse mixing zones and dispersivity

Contents for High Head Drop: Steady State

- 1. Importing Data
- 2. First Normalization
- 3. Block Processing
- 4. Second Normalization
- 5. Interpolation and Mixing Zone Width Calculation

%High Drop steady state analysis

%Analysis performed in this script:

- % 1. Import of data (i.e., images) to be analyzed (background and experimental images)
- % 2. Normalization (converting images to ratios between experimental and background images)
- % 3. Block processing (averaging images into blocks for further processing)
- % 4. Second normalization (normalize intensities found in each image by color channel)

clear; clc; close all

%created by: Abenezer Nida (2014/2015) edited by: Katherine Santizo (2017/2018)

1. Importing Data

%importing data--Background

%This imports all ten background images that will be used for the first normalization. You can conversely load the folder and then call upon the images but the directory will have to match regardless of who is using the script. As long as the images do not get renamed there will be no issue importing them onto MATLAB when the folder is in MATLAB's pathway.

```
B1 = double(importdata('006953.tif'));
B2= double(importdata('006959.tif'));
B3= double(importdata('006965.tif'));
B4= double(importdata('006971.tif'));
B5= double(importdata('006977.tif'));
B6= double(importdata('006983.tif'));
B7= double(importdata('006989.tif'));
B8= double(importdata('006995.tif'));
B9= double(importdata('007001.tif'));
B10= double(importdata('007007.tif'));
```

%importdata is the built-in function that MATLAB uses to open an image as a Matrix. double allows for the image values to have double precision.

%The first normalization just takes into account background differences that could have happened. Thus, the background image is divided by the

```
%experiment concentration image.
```

```
%importing data--Experimental High drop runs
```

```
%This does the same procedure as the background images (see above)
```

```
C1 = double(importdata('007313.tif'));  
C2= double(importdata('007319.tif'));  
C3= double(importdata('007325.tif'));  
C4= double(importdata('007331.tif'));  
C5= double(importdata('007337.tif'));  
C6= double(importdata('007343.tif'));  
C7= double(importdata('007349.tif'));  
C8= double(importdata('007355.tif'));  
C9= double(importdata('007361.tif'));  
C10= double(importdata('007367.tif'));
```

```
% Now that we have all the images we need, we can start working on  
% normalizing. Begin by combining the images into one large file. Can do  
% this by using imlincomb which stands for image linear combination.
```

2. First Normalization

```
k = 0.1; %this is the factor that will be used throughout the linear  
%combination because we are working with ten images. In linear  
%combinations, the value in front of the image file is usually (1/n) where  
%n is the number of images that will be combined.
```

```
%BGH stands for background high drop
```

```
BGH = imlincomb(k,B1,k,B2,k,B3,k,B4,k ,B5,k,B6,k,B7,k,B8,k,B9,k,B10);
```

```
%ECH = experimental concentration high drop
```

```
ECH= imlincomb(k,C1,k,C2,k,C3,k,C4,k,C5,k,C6,k,C7,k,C8,k,C9,k,C10);
```

```
%Now for the normalization which asks to divide the images from BGH by ECH.
```

```
%There are multiple ways to carry such task out. Can do BGH ./ ECH but will
```

```
%use imdivide since that is the image processing tool to divide out
```

```
%images.
```

```
%FNH= first normalization of high head drop. Ratio of background and experimental images.
```

```
FNH = double(imdivide(BGH,ECH));
```

```
%Process filter to ensure reals numbers are only being dealt with. Since
```

```
%the first normalization is a ratio all numbers results should be between 0
```

```
%and 1. isinf=infinite values found in matrices; isnan=undefined value
```

```
%found in matrices.
```

```
for i = 1:2592 % i,j,m %i,j,m must match the matrix size of FNH.
```

```
for j = 1:3872
```

```
for m = 1:3
```

```
if isinf(FNH(i,j,m))
```

```
FNH(i,j,m) = 1;
```

```
elseif isnan(FNH(i,j,m))
```

```
FNH(i,j,m) = 0;
```

```
elseif FNH(i,j,m)>= 1
```

```
FNH(i,j,m)= 1;
```

```
elseif FNH(i,j,m)<=0
```

```

FNH(i,j,m)=0;
end
    end
end
end

```

3. Block Processing

%BLOCK PROCESSING: averages images in blocks of desired size. It creates a uniform size block for further processing. It divides the image for easier processing. Blockproc is the MATLAB built in function to block process images. To reduce noise median filter can be used in this step.

```

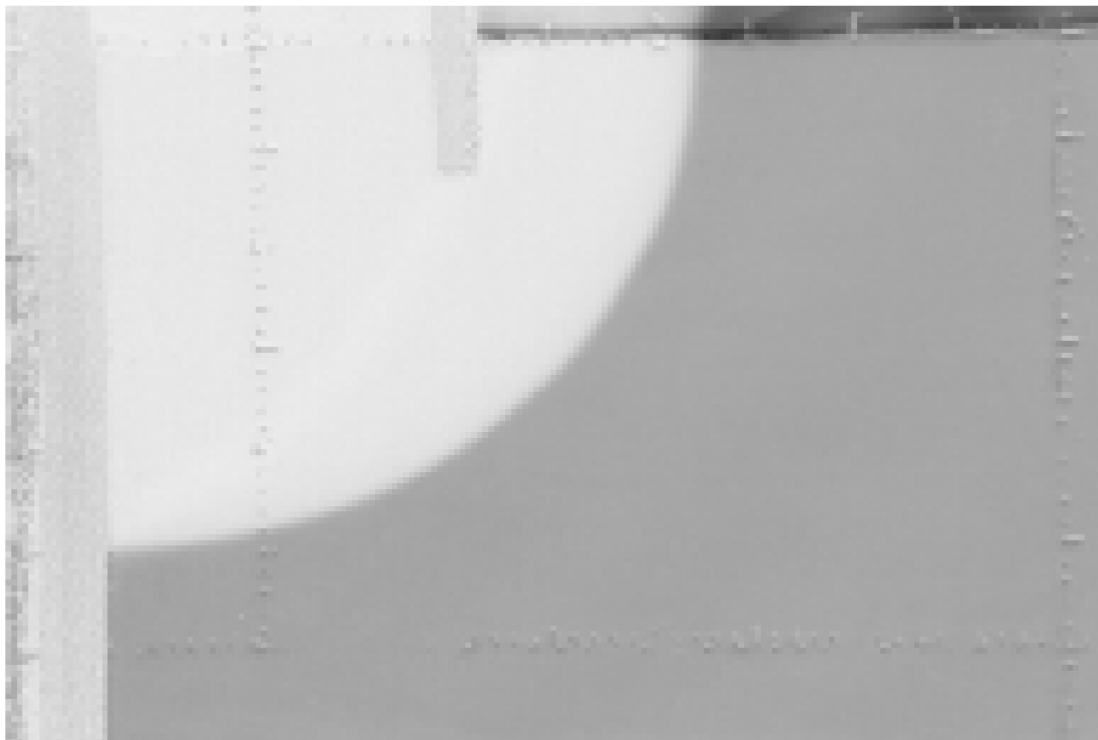
%these first two lines are included to create a block processing function
%that the blockproc can then read. It tells it what kind of data it is processing
%block_struct.data is specifically used for matrices of block data which an image is.
fun = @(block_struct) ...
mean2(block_struct.data) * ones(size(block_struct.data));
bl=20;

```

```

%Block processing for all three matrices from first normalization
%(based on the three intensity channels, RGB where R=1, G=2 and B=3 in MATLAB)
BPH(:,:,1) = blockproc(FNH(:,:,1),[bl bl],fun);%BPH=block processing of high head drop
%BPH(:,:,2) = blockproc(FNH(:,:,2),[10 10],fun); %The G and B channels
%could be omitted since we will only be working the red channel.
%BPH(:,:,3) = blockproc(FNH(:,:,3),[10 10],fun);
figure (1)% displays figure to verify that image frame has been normalized and block processed
imshow (BPH);

```



4. Second Normalization

The second normalization focuses on correcting intensity differences that may occur due to changes in exposure. Once again, the normalization is a ratio between 0 and 1. With it being set for 0 to be the highest dye concentration and 1 lowest dye concentration (i.e. no dye).

```
for a=260:bl:340 %a is a check of the BPH along a set of rows, Abenezzer decided to do calculations
    %off Row 300 so this gives a +/-20 rows for analysis. The range can
    %vary based on needs. Recall the block process so 280-300 are the same
    %value.
    b=1900:bl:3300;
```

```
figure(2)
plot(BPH(a,b,1)); %SNH1 is second normalization of high drop (1st figure)
%1700:3500 is the columns of interest, based on the hyporheic flow cell and
%figure (1)
hold on %hold on allows for a figure to be built on based on multiple plots that are
%wanted to be placed in a figure together
xlabel({'Column#','(Row:280-320 Col: 1700-3500)'},'fontsize',12,'fontweight','bold');
ylabel({'Normalized Intensity, I_N [-]'},'fontsize',12,'fontweight','bold');
set(gca,'XMinorTick','on','YMinorTick','on');
set(gca,'fontweight','bold','fontsize',10);
% title({'High Drop Steady State Experiment','Normalized Intensity Profiles'},...
% 'fontweight','bold','fontsize',14);
end
```

```
b=260:bl:340; %matching the rows that will be analyzed. To build a matrix of each row.
c=1900:bl:3300; %columns of interest
BPHN=BPH(b,c); %41 by 1801 matrix with section of interest.
```

```
%Normalization calculation
%finding the maximum value in both dyed and undyed parts
UndyedValueHigh= max(BPHN(:,:)); %The undyed section of the image has the highest
%and thus will have the highest value in the matrix of observation. Finding
%the max for each row using the max function means the matrix must be
%transposed as the max function takes maximum value from each column.
UndyedValueHigh = UndyedValueHigh'; %This retransposes the matrix to present
%maximums for each row as a 41 by 1 matrix
DyedValueHigh= max(BPHN(:,51:71));
DyedValueHigh=DyedValueHigh';
```

```
for i=1:length(b) %i,j must match the matrix size of BPHN
    for j=1:length(c)
        if (BPHN(i,j))>=(UndyedValueHigh(i)-(UndyedValueHigh(i)*0.01))
            BPHN(i,j) = UndyedValueHigh(i);
        elseif (BPHN(i,j))<= (DyedValueHigh(i)-(DyedValueHigh(i)*0.01))
            BPHN(i,j) = DyedValueHigh(i);
        end
    end
end
% UndyedValueHigh= mean(BPH(300,2075,1),2); % Values for mean were decided by Abenezzer
% %thus understanding is limited. Undyed value is sand with no dye. This
% does not make sense as there is no mean to a single value. The value high
```

```

% was a single value taken from row 300,column 2075.

% DyedValueHigh=mean(BPH(300,2625,1),2); %area with dye
% BPH(300,1700:2100,1)=UndyedValueHigh; %Why/how were these decided? 2100, 2600
% BPH(300,2600:3500,1)=DyedValueHigh;
% DbNormalizedBlcproc50High=BPH;

% for i = 1:1:5 % i,j, %i,j must match the matrix size of BPHN.
%   for j = 1:91
%     if (BPHN(i,j))>= (UndyedValueHigh(i)-(UndyedValueHigh(i)*0.04))
%       BPHN(i,j) = UndyedValueHigh(i);
%     elseif (BPHN(i,j))<= (DyedValueLow(i)-(DyedValueLow(i)*0.01))
%       BPHN(i,j) = DyedValueLow(i);
%     end
%   end
% end

%%%JUST NORMALIZE BASED ON HIGH NO NEED FOR SMOOTHING VARIATION LOOP

%In this for loop, in every cell along the row of interest it calculates
%the double normalized intensity so that the maximum is at 1 and minimum at
%zero

DbNormalizedBlcproc10High=1-((UndyedValueHigh-BPHN)./(UndyedValueHigh-DyedValueHigh));
Horizontal_axis=0+(200*0.014):(bl*0.014):25.2-(200*0.014);

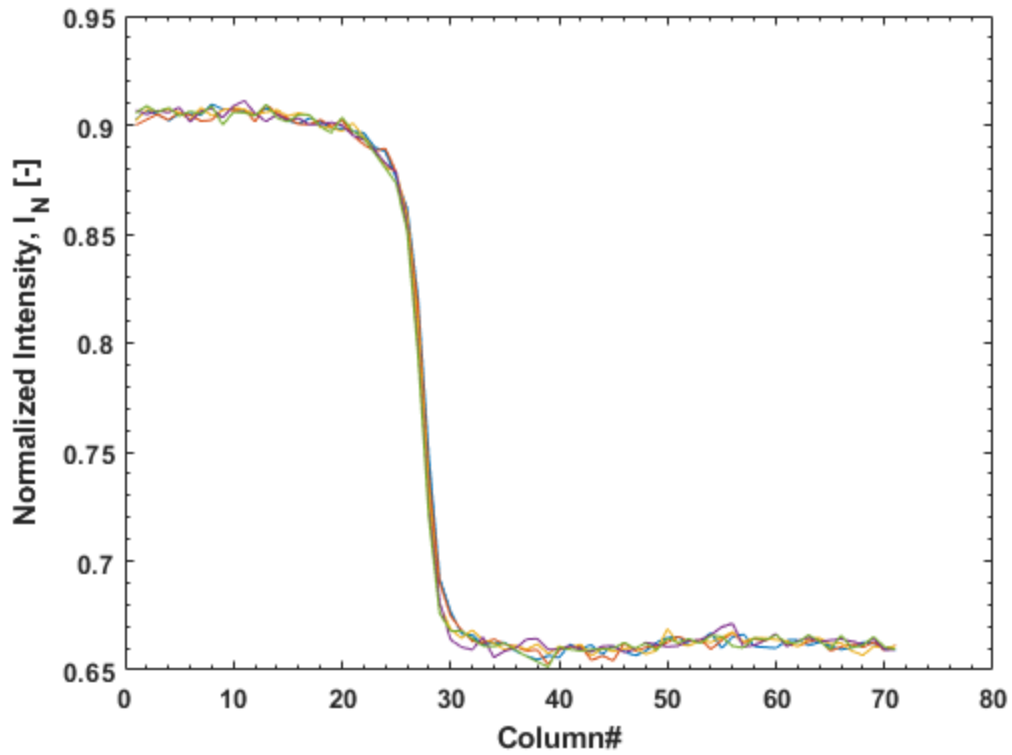
for v=1:length(b)
    for w=1:length(c)
if DbNormalizedBlcproc10High(v,w)<=0
    DbNormalizedBlcproc10High(v,w)=0;
end
    end
end

for v=1:length(b)

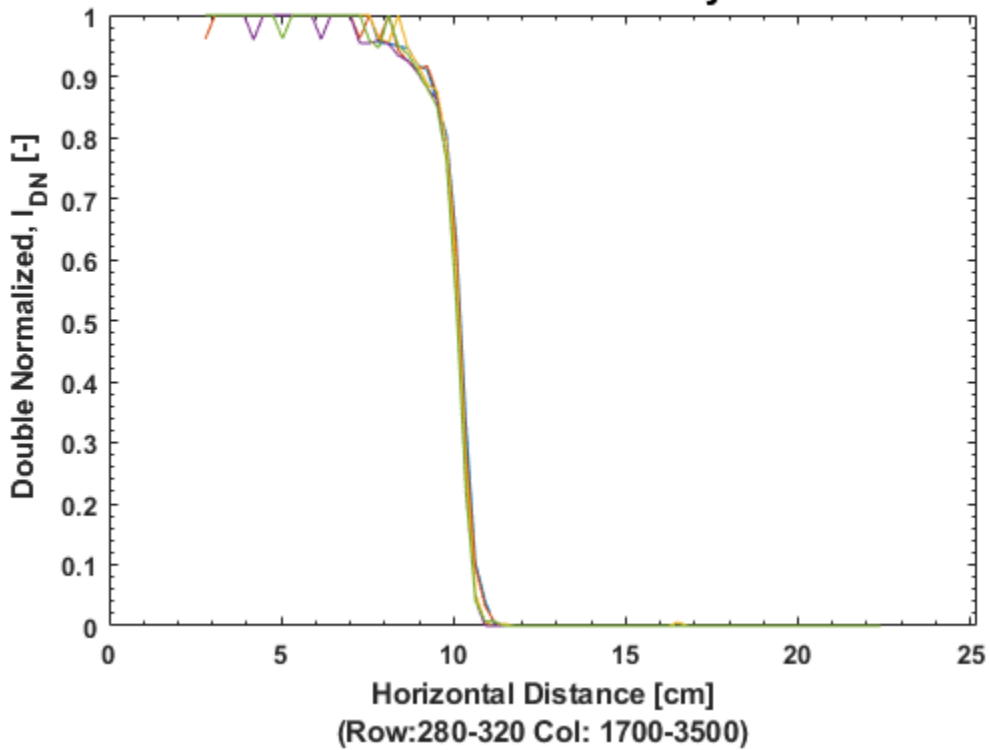
figure(3);
plot(Horizontal_axis,DbNormalizedBlcproc10High(v,1:length(c)));
hold on
xlabel({'Horizontal Distance [cm]',(Row:280-320 Col: 1700-3500)'),'fontsize',12,'fontweight','bold');
ylabel(' Double Normalized, I_D_N [-]','fontsize',12,'fontweight','bold');
set(gca,'XMinorTick','on','YMinorTick','on');
set(gca,'fontweight','bold','fontsize',10);
axis([0 25.2 0 1.0]);
title({'High Drop Steady State Experiment',' Double Normalized Intensity Profiles'},...
'fontweight','bold','fontsize',14);

end

```



**High Drop Steady State Experiment
Double Normalized Intensity Profiles**



5. Interpolation and Mixing Zone Width Calculation

%cannot do loop for this because the unique formula provides different
%lengths for each row in analysis therefore cannot set a specific size for
%the an output matrix

```
[x1, index] = unique(DbNormalizedBlcproc10High(1,:),'stable'); %row1 from Db..  
y90_1 = interp1(x1, Horizontal_axis(18:31), 0.90); y10_1 = interp1(x1, Horizontal_axis(18:31), 0.10);  
[x2, index] = unique(DbNormalizedBlcproc10High(2,:),'stable'); %row2 from Db..  
y90_2 = interp1(x2, Horizontal_axis(17:32), 0.90); y10_2 = interp1(x2, Horizontal_axis(17:32), 0.10);  
[x3, index] = unique(DbNormalizedBlcproc10High(3,:),'stable'); %row3 from Db..  
y90_3 = interp1(x3, Horizontal_axis(19:33), 0.90); y10_3 = interp1(x3, Horizontal_axis(19:33), 0.10);  
[x4, index] = unique(DbNormalizedBlcproc10High(4,:),'stable'); %row4 from Db..  
y90_4 = interp1(x4, Horizontal_axis(14:30), 0.90); y10_4 = interp1(x4, Horizontal_axis(14:30), 0.10);  
[x5, index] = unique(DbNormalizedBlcproc10High(5,:),'stable'); %row5 from Db..  
y90_5 = interp1(x5, Horizontal_axis(17:32), 0.90); y10_5 = interp1(x5, Horizontal_axis(17:32), 0.10);
```

```
MZW_10_90 = [y10_1-y90_1 ; y10_2-y90_2; y10_3-y90_3 ; y10_4-y90_4 ; y10_5-y90_5];
```

```
MZW_10_90_avg = mean(MZW_10_90);  
MZW_10_90_std = std(MZW_10_90);  
CV = 100*(MZW_10_90_std / MZW_10_90_avg);
```

```
formatSpec = 'The average mixing zone width for the low head drop is %3.2f cm with standard deviation of %3.2f  
cm and coefficient of variation of %2.1f percent\n';
```

```
fprintf(formatSpec,MZW_10_90_avg,MZW_10_90_std,CV)
```

```
The average mixing zone width for the low head drop is 1.47 cm with standard deviation of 0.07 cm and coefficient  
of variation of 4.6 percent
```

Contents for Mid Head Drop: Steady State

- **1. Importing Data**
- **2. First Normalization**
- **3. Block Processing**
- **4. Second Normalization**
- **5. Interpolation and Mixing Zone Width Calculation**

```
%Mid Head Drop steady state analysis
```

```
%Analysis performed in this script:
```

```
%1. Import of data (i.e. images) to be analyzed (background and
```

```
%experimental images)
```

```
%2. Normalization (converting images to ratios between experimental
```

```
%and background images)
```

```
%3. Block processing (averaging images into blocks for further
```

```
%processing)
```

```
%4. Second normalization (normalize intensities found in each image
```

```
%by color channel)
```

```
%5. Mixing thickness calculations (Calculate dyed and undyed mixing)
```

```
clear; clc; close all
```

1. Importing Data

```
%importing data--Background
```

```
% This imports all ten background image that will be used for the first  
% normalization. You can conversely load the folder and then call upon  
% the images but the directory will have to match regardless of who is  
% using the script. As long as the images do not get renamed there will  
% be no issue importing them onto MATLAB when the folder is in MATLAB's  
% pathway.
```

```
B1 = double(importdata('005981.tif'));  
B2= double(importdata('005987.tif'));  
B3= double(importdata('005993.tif'));  
B4= double(importdata('005999.tif'));  
B5= double(importdata('006005.tif'));  
B6= double(importdata('006011.tif'));  
B7= double(importdata('006017.tif'));  
B8= double(importdata('006023.tif'));  
B9= double(importdata('006029.tif'));  
B10= double(importdata('006035.tif'));
```

```
%importdata is the built in function that MATLAB uses to open an image as a  
%Matrix. double allows for the image values to have double precision.
```

```
%The first normalization just takes into account background differences  
%that could have happened. Thus the background image is divided by the  
%experiment concentration image.
```

```
%importing data--Experimentalmid head drop runs
```

```
% This does the same procedure as the background images.
```

```
C1 = double(importdata('006338.tif'));  
C2= double(importdata('006344.tif'));  
C3= double(importdata('006350.tif'));  
C4= double(importdata('006356.tif'));  
C5= double(importdata('006362.tif'));  
C6= double(importdata('006368.tif'));  
C7= double(importdata('006374.tif'));  
C8= double(importdata('006380.tif'));  
C9= double(importdata('006386.tif'));  
C10= double(importdata('006392.tif'));
```

```
% Now that we have all the images we need we can start working on  
% normalizing. Begin by combining the images into one large file. Can do  
% this by using imlincomb which stands for image linear combination.
```

2. First Normalization

```
%BGH stands for background high drop
```

```
k = 0.1; %this is the factor that will be used throughout the linear
```

```
%combination because we are working with ten images. In linear
```

```
%combinations, the value in front of the image file is usually (1/n) where
```

```
%n is the number of images that will be combined.
```

```

BGH = imlincomb(k,B1,k,B2,k,B3,k,B4,k ,B5,k,B6,k,B7,k,B8,k,B9,k,B10);
%ECH = experimental concentration high drop
ECH= imlincomb(k,C1,k,C2,k,C3,k,C4,k,C5,k,C6,k,C7,k,C8,k,C9,k,C10);

%Now for the normalization which asks to divide the images from BGH by ECH.

%There are multiple ways to carry such task out. Can do BGH ./ ECH but will
%use imdivide since that is the image processing tool to divide out
%images.

%FNH= first normalization of mid head drop. Ratio of background and experimental images.
FNH = double(imdivide(BGH,ECH));

%Process filter to ensure real numbers are only being dealt with. Since
%the first normalization is a ratio all numbers results should be between 0
%and 1. isinf=infinite values found in matrices; isnan=undefined value
%found in matrices.

for i = 1:2592 % i, j, m
    for j = 1:3872
        for m = 1:3
            if isinf(FNH(i,j,m))
                FNH(i,j,m) = 1;
            elseif isnan(FNH(i,j,m))
                FNH(i,j,m) = 0;
            elseif FNH(i,j,m)>= 1
                FNH(i,j,m)= 1;
            end
        end
    end
end

3. Block Processing

%BLOCK PROCESSING: averages images in blocks of desired size. It creates a
%uniform size block for further processing. It divides the image for easier
%processing. Blockproc is the MATLAB built in function to block process
%images. To reduce noise median filter can be used in this step.

%these first two lines are included to create a block processing function
%that the blockproc can then read. It tells it what kind of data it is processing
%block_struct.data is specifically used for matrices of block data which an image is.
fun = @(block_struct) ...
mean2(block_struct.data) * ones(size(block_struct.data));
bl=20;

%Block processing for all three matrices from first normalization
%(based on the three intensity channels, RGB where R=1, G=2 and B=3 in MATLAB)
BPH(:,:,1) = blockproc(FNH(:,:,1),[bl bl],fun);%BPH=block processing of high head drop
%BPH(:,:,2) = blockproc(FNH(:,:,2),[10 10],fun); %The G and B channels
%could be omitted since we will only be working the red channel.
%BPH(:,:,3) = blockproc(FNH(:,:,3),[10 10],fun);
figure (1)% displays figure to verify that image frame has been normalized and block processed
imshow (BPH);

```



4. Second Normalization

The second normalization focuses on correcting intensity differences that may occur due to changes in exposure. Once again the normalization is a ratio between 0 and 1. With it being set for 0 to be the highest dye concentration and 1 lowest dye concentration (i.e. no dye).

```
for a=260:bl:340 %a is a check of the BPH along a set of rows, Abenezer decided to do calculations
    %off Row 300 so this gives a +/-20 rows for analysis. The range can
    %vary based on needs. Recall the block process so 280-300 are the same
    %value.
    b=1900:bl:3300;
```

```
figure(2)
plot(BPH(a,b,1)); %SNH1 is second normalization of mid drop (1st figure)
%1700:3500 is the columns of interest, based on the hyporheic flow cell and
%figure (1)
hold on %hold on allows for a figure to be built on based on multiple plots that are
%wanted to be placed in a figure together
xlabel({'Column#','(Row:280-320 Col: 1700-3500)'},'fontsize',12,'fontweight','bold');
ylabel({'Normalized Intensity, I_N [-]'},'fontsize',12,'fontweight','bold');
set(gca,'XMinorTick','on','YMinorTick','on');
set(gca,'fontweight','bold','fontsize',10);
% title({'Mid Drop Steady State Experiment','Normalized Intensity Profiles'},...
% 'fontweight','bold','fontsize',14);
end
```

```

b=260:bl:340; %matching the rows that will be analyzed. To build a matrix of each row.
c=1900:bl:3300; %columns of interest
BPHN=BPH(b,c); %41 by 1801 matrix with section of interest.

%Normalization calculation
%finding the maximum value in both dyed and undyed parts
UndyedValueHigh= max(BPHN'); %The undyed section of the image has the highest
%and thus will have the highest value in the matrix of observation. Finding
%the max for each row using the max function means the matrix must be
%transposed as the max function takes maximum value from each column.
UndyedValueHigh = UndyedValueHigh'; %This retransposes the matrix to present
%maximums for each row as a 41 by 1 matrix
DyedValueHigh= max(BPHN(:,51:71));
DyedValueHigh=DyedValueHigh';

for i=1:1:length(b) %i,j must match the matrix size of BPHN
    for j=1:length(c)
        if (BPHN(i,j))>=(UndyedValueHigh(i)-(UndyedValueHigh(i)*0.01))
            BPHN(i,j) = UndyedValueHigh(i);
        elseif (BPHN(i,j))<= (DyedValueHigh(i)-(DyedValueHigh(i)*0.01))
            BPHN(i,j) = DyedValueHigh(i);
        end
    end
end

%In this for loop, in every cell along the row of interest it calculates
%the double normalized intensity so that the maximum is at 1 and minimum at
%zero

DbNormalizedBlcproc10Mid=1-((UndyedValueHigh-BPHN)./(UndyedValueHigh-DyedValueHigh));
Horizontal_axis=0+(200*0.014):(bl*0.014):25.2-(200*0.014);

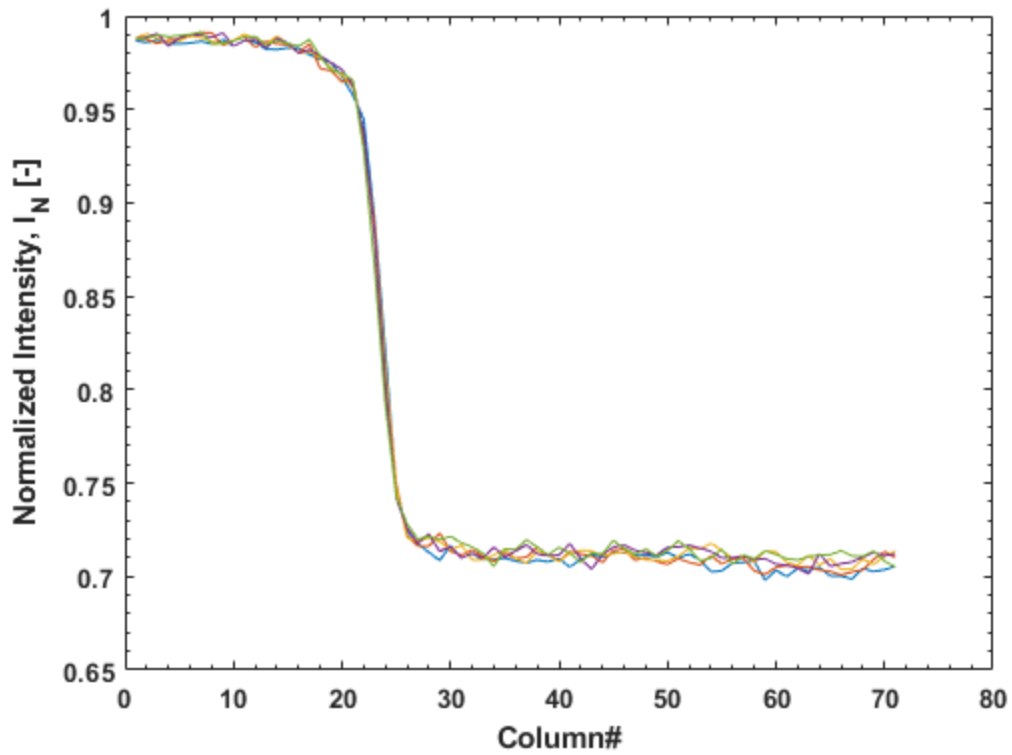
for v=1:length(b)
    for w=1:length(c)
if DbNormalizedBlcproc10Mid(v,w)<=0
        DbNormalizedBlcproc10Mid(v,w)=0;
    end
    end
end

for v=1:length(b)

figure(3);
plot(Horizontal_axis,DbNormalizedBlcproc10Mid(v,1:length(c)));
hold on
xlabel({'Horizontal Distance [cm]',(Row:280-320 Col: 1700-3500)},'fontsize',12,'fontweight','bold');
ylabel(' Double Normalized, I_D_N [-]','fontsize',12,'fontweight','bold');
set(gca,'XMinorTick','on','YMinorTick','on');
set(gca,'fontweight','bold','fontsize',10);
axis([0 25.2 0 1.0]);
title({'Mid Drop Steady State Experiment', ' Double Normalized Intensity Profiles'},...
'fontweight','bold','fontsize',14);

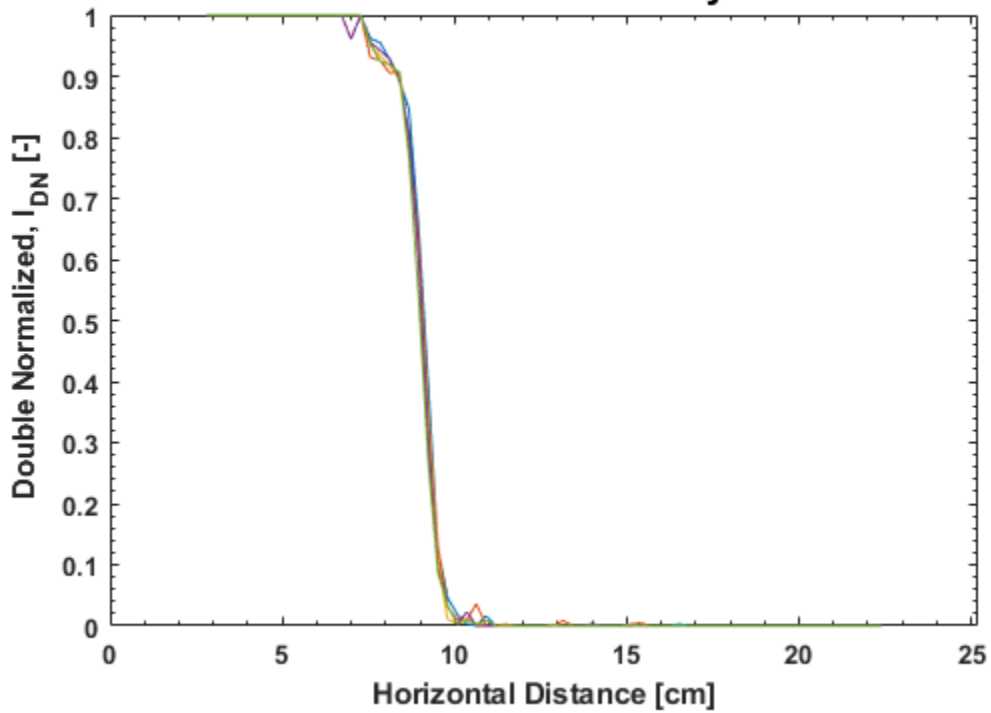
end

```



(Row:280-320 Col: 1700-3500)

Mid Drop Steady State Experiment Double Normalized Intensity Profiles



(Row:280-320 Col: 1700-3500)

5. Interpolation and Mixing Zone Width Calculation

```
%cannot do loop for this because the unique formula provides different  
%lengths for each row in analysis therefore cannot set a specific size for  
%the an output matrix
```

```
[x1, index] = unique(DbNormalizedBlcproc10Mid(1,:), 'stable'); %row1 from Db..  
y90_1 = interp1(x1, Horizontal_axis(17:34), 0.90); y10_1 = interp1(x1, Horizontal_axis(17:34), 0.10);  
[x2, index] = unique(DbNormalizedBlcproc10Mid(2,:), 'stable'); %row2 from Db..  
y90_2 = interp1(x2, Horizontal_axis(16:36), 0.90); y10_2 = interp1(x2, Horizontal_axis(16:36), 0.10);  
[x3, index] = unique(DbNormalizedBlcproc10Mid(3,:), 'stable'); %row3 from Db..  
y90_3 = interp1(x3, Horizontal_axis(16:30), 0.90); y10_3 = interp1(x3, Horizontal_axis(16:30), 0.10);  
[x4, index] = unique(DbNormalizedBlcproc10Mid(4,:), 'stable'); %row4 from Db..  
y90_4 = interp1(x4, Horizontal_axis(16:32), 0.90); y10_4 = interp1(x4, Horizontal_axis(16:32), 0.10);  
[x5, index] = unique(DbNormalizedBlcproc10Mid(5,:), 'stable'); %row5 from Db..  
y90_5 = interp1(x5, Horizontal_axis(17:33), 0.90); y10_5 = interp1(x5, Horizontal_axis(17:33), 0.10);
```

```
MZW_10_90 = [y10_1-y90_1 ; y10_2-y90_2; y10_3-y90_3 ; y10_4-y90_4 ; y10_5-y90_5];
```

```
MZW_10_90_avg = mean(MZW_10_90);  
MZW_10_90_std = std(MZW_10_90);  
CV = 100*(MZW_10_90_std / MZW_10_90_avg);
```

```
formatSpec = 'The average mixing zone width for the low head drop is %3.2f cm with standard deviation of %3.2f  
cm and coefficient of variation of %2.1f percent\n';
```

```
fprintf(formatSpec, MZW_10_90_avg, MZW_10_90_std, CV)
```

```
The average mixing zone width for the low head drop is 1.30 cm with standard deviation of 0.26 cm and coefficient  
of variation of 19.8 percent
```

Contents for Low Head Drop: Steady State

- **1. Importing Data**
- **2. First Normalization**
- **3. Block Processing**
- **4. Second Normalization**
- **5. Interpolation and Mixing Zone Width Calculation**

```
%Low Drop steady state analysis
```

```
%Analysis performed in this script:
```

```
%1. Import of data (i.e. images) to be analyzed (background and  
%experimental images)
```

```
%2. Normalization (converting images to ratios between experimental  
%and background images)
```

```
%3. Block processing (averaging images into blocks for further  
%processing)
```

```
%4. Second normalization (normalize intensities found in each image  
%by color channel)
```

```
%5. Mixing thickness calculations (Calculate dyed and undyed mixing)
```

```
clear; clc; close all
```

1. Importing Data

%importing data--Background

%This imports all ten background images that will be used for the first
%normalization. You can conversely load the folder and then call upon
%the images but the directory will have to match regardless of who is
%using the script. As long as the images do not get renamed there will
%be no issue importing them onto MATLAB when the folder is in MATLAB's
%pathway.

```
B1 = double(importdata('006398.tif'));
B2= double(importdata('006404.tif'));
B3= double(importdata('006410.tif'));
B4= double(importdata('006416.tif'));
B5= double(importdata('006422.tif'));
B6= double(importdata('006428.tif'));
B7= double(importdata('006434.tif'));
B8= double(importdata('006440.tif'));
B9= double(importdata('006446.tif'));
B10= double(importdata('006452.tif'));
```

%importdata is the built in function that MATLAB uses to open an image as a
%Matrix. double allows for the image values to have double precision.

%The first normalization just takes into account background differences
%that could have happened. Thus the background image is divided by the
%experiment concentration image.

%importing data--Experimental low drop runs

%This does the same procedure as the background images.

```
C1 = double(importdata('006893.tif'));
C2= double(importdata('006899.tif'));
C3= double(importdata('006905.tif'));
C4= double(importdata('006911.tif'));
C5= double(importdata('006917.tif'));
C6= double(importdata('006923.tif'));
C7= double(importdata('006929.tif'));
C8= double(importdata('006935.tif'));
C9= double(importdata('006941.tif'));
C10= double(importdata('006947.tif'));
```

% Now that we have all the images we need we can start working on
% normalizing. Begin by combining the images into one large file. Can do
% this by using imlincomb which stands for image linear combination.

2. First Normalization

%BGH stands for background low drop

k = 0.1; %this is the factor that will be used throughout the linear

%combination because we are working with ten images. In linear

%combinations, the value in front of the image file is usually (1/n) where

%n is the number of images that will be combined.

```
BGH = imlincomb(k,B1,k,B2,k,B3,k,B4,k ,B5,k,B6,k,B7,k,B8,k,B9,k,B10);
```

%ECH = experimental concentration low drop

```

ECH= imlincomb(k,C1,k,C2,k,C3,k,C4,k,C5,k,C6,k,C7,k,C8,k,C9,k,C10);

%Now for the normalization which asks to divide the images from BGH by ECH.

%There are multiple ways to carry such task out. Can do BGH ./ ECH but will
%use imdivide since that is the image processing tool to divide out
%images.

%FNH= first normalization of low head drop. Ratio of background and experimental images.
FNH = double(imdivide(BGH,ECH));

%Process filter to ensure reals numbers are only being dealt with. Since
%the first normalization is a ratio all numbers results should be between 0
%and 1. isinf=infinite values found in matrices; isnan=undefined value
%found in matrices.

for i = 1:2592 % i, j, m
    for j = 1:3872
        for m = 1:3
            if isinf(FNH(i,j,m))
                FNH(i,j,m) = 1;
            elseif isnan(FNH(i,j,m))
                FNH(i,j,m) = 0;
            elseif FNH(i,j,m)>= 1
                FNH(i,j,m)= 1;
            end
        end
    end
end
end
end

```

3. Block Processing

```

%BLOCK PROCESSING: averages images in blocks of desired size. It creates a
%uniform size block for further processing. It divides the image for easier
%processing. Blockproc is the MATLAB built in function to block process
%images. To reduce noise median filter can be used in this step.

%these first two lines are included to create a block processing function
%that the blockproc can than read. It tells it what kind of data it is processing
%block_struct.data is specifically used for matrices of block data which an image is.

% %Block processing for all three matrices from first normalization
% %(based on the three intensity channels, RGB where R=1, G=2 and B=3 in MATLAB)

fun = @(block_struct) ...
mean2(block_struct.data) * ones(size(block_struct.data));
bl=20;

%Block processing for all three matrices from first normalization
%(based on the three intensity channels, RGB where R=1, G=2 and B=3 in MATLAB)
BPH(:,:,1) = blockproc(FNH(:,:,1),[bl bl],fun);%BPH=block processing of high head drop
%BPH(:,:,2) = blockproc(FNH(:,:,2),[10 10],fun); %The G and B channels
%could be omitted since we will only be working the red channel.
%BPH(:,:,3) = blockproc(FNH(:,:,3),[10 10],fun);
figure (1)% displays figure to verify that image frame has been normalized and block processed

```

imshow (BPH);



4. Second Normalization

The second normalization focuses on correcting intensity differences that may occur due to changes in exposure. Once again the normalization is a ratio between 0 and 1. With it being set for 0 to be the highest dye concentration and 1 lowest dye concentration (i.e. no dye).

```
for a=260:bl:340 %a is a check of the BPH along a set of rows, Abenezer decided to do calculations
    %off Row 300 so this gives a +/-20 rows for analysis. The range can
    %vary based on needs. Recall the block process so 280-290 are the same
    %value. 280,290,300, 310, 320 are going to be processes only.
    b=1900:bl:3300; %full area starting from divider
```

```
figure(2)
plot(BPH(a,b,1)); %SNH1 is second normalization of high drop (1st figure)
%1700:3500 is the columns of interest, based on the hyporheic flow cell and
%figure (1)
hold on %hold on allows for a figure to be built on based on multiple plots that are
%wanted to be placed in a figure together
xlabel({'Column#','(Row:280-320 Col: 1700-3500)'},'fontsize',12,'fontweight','bold');
ylabel({'Normalized Intensity, I_N [-1]'},'fontsize',12,'fontweight','bold');
set(gca,'XMinorTick','on','YMinorTick','on');
set(gca,'fontweight','bold','fontsize',10);
% title({'Low Drop Steady State Experiment','Normalized Intensity Profiles'},...
% 'fontweight','bold','fontsize',14);
end
```

```

b=260:bl:340; %matching the rows that will be analyzed. To build a matrix of each row.
c=1900:bl:3300; %columns of interest
BPHN=BPH(b,c); %41 by 1801 matrix with section of interest.

%Normalization calculation
%finding the maximum value in both dyed and undyed parts
UndyedValueHigh= max(BPHN'); %The undyed section of the image has the highest
%and thus will have the highest value in the matrix of observation. Finding
%the max for each row using the max function means the matrix must be
%transposed as the max function takes maximum value from each column.
UndyedValueHigh = UndyedValueHigh'; %This retransposes the matrix to present
%maximums for each row as a 41 by 1 matrix
DyedValueHigh= max(BPHN(:,51:71));
DyedValueHigh=DyedValueHigh';

for i=1:length(b) %i,j must match the matrix size of BPHN
    for j=1:length(c)
        if (BPHN(i,j))>=(UndyedValueHigh(i)-(UndyedValueHigh(i)*0.01))
            BPHN(i,j) = UndyedValueHigh(i);
        elseif (BPHN(i,j))<= (DyedValueHigh(i)-(DyedValueHigh(i)*0.01))
            BPHN(i,j) = DyedValueHigh(i);
        end
    end
end

DbNormalizedBlcproc10Low=1-((UndyedValueHigh-BPHN)./(UndyedValueHigh-DyedValueHigh));
Horizontal_axis=0+(200*0.014):(bl*0.014):25.2-(200*0.014);

%In this for loop, in every cell along the row of interest it calculates
%the double normalized intensity so that the maximum is at 1 and minimum at
%zero

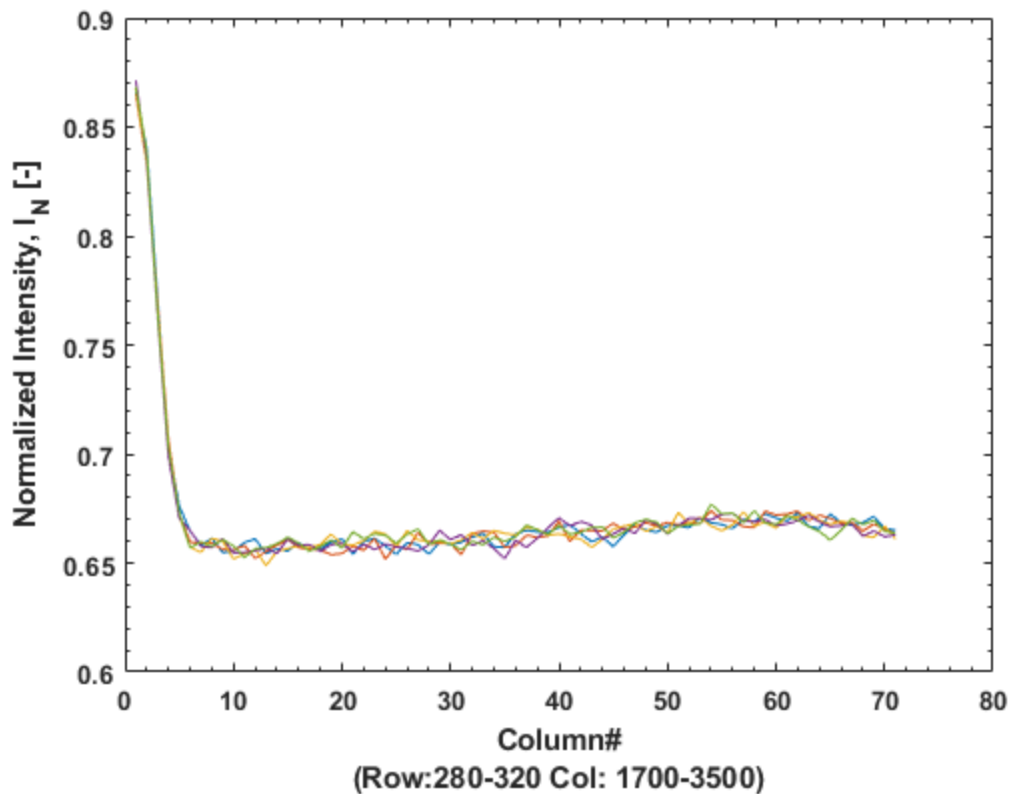
for v=1:length(b)
    for w=1:length(c)
        if DbNormalizedBlcproc10Low(v,w)<=0
            DbNormalizedBlcproc10Low(v,w)=0;
        end
    end
end

for v=1:length(b)

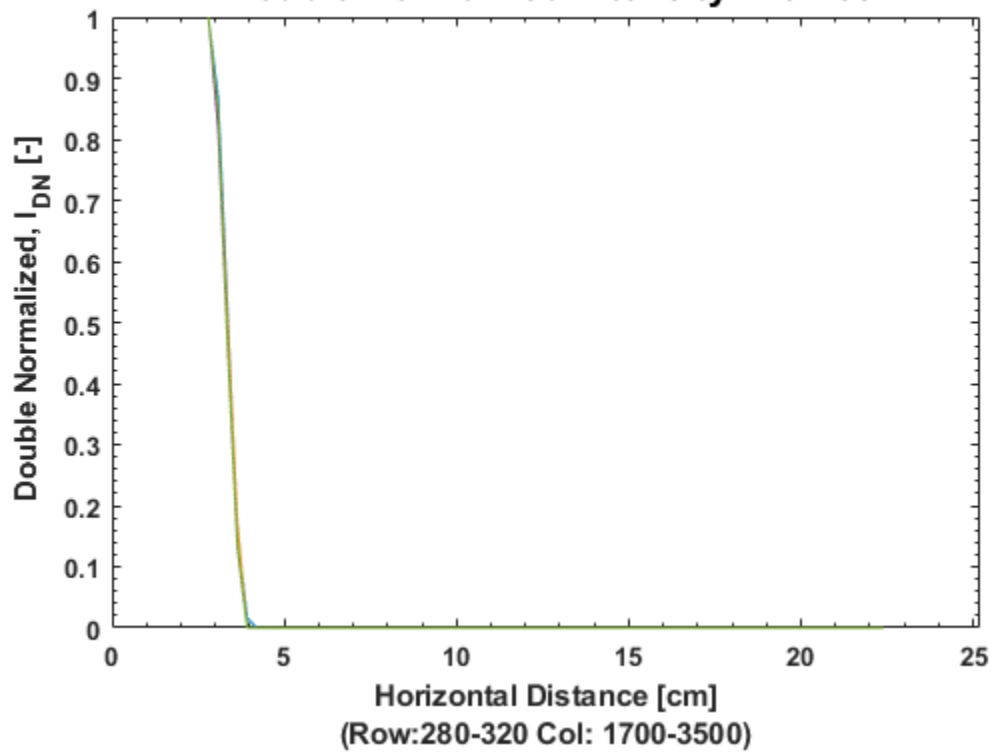
figure(3);
plot(Horizontal_axis,DbNormalizedBlcproc10Low(v,1:length(c)));
hold on
xlabel({'Horizontal Distance [cm]',(Row:280-320 Col: 1700-3500)},'fontsize',12,'fontweight','bold');
ylabel(' Double Normalized, I_D_N [-]','fontsize',12,'fontweight','bold');
set(gca,'XMinorTick','on','YMinorTick','on');
set(gca,'fontweight','bold','fontsize',10);
axis([0 25.2 0 1.0]);
title({'Low Drop Steady State Experiment', ' Double Normalized Intensity Profiles'},...
'fontweight','bold','fontsize',14);

end

```



**Low Drop Steady State Experiment
Double Normalized Intensity Profiles**



5. Interpolation and Mixing Zone Width Calculation

%cannot do loop for this because the unique formula provides different
%lengths for each row in analysis therefore cannot set a specific size for
%the an output matrix

```
[x1, index] = unique(DbNormalizedBlcproc10Low(1,:), 'stable'); %row1 from Db..  
y90_1 = interp1(x1, Horizontal_axis(1:6), 0.90); y10_1 = interp1(x1, Horizontal_axis(1:6), 0.10);  
[x2, index] = unique(DbNormalizedBlcproc10Low(2,:), 'stable'); %row2 from Db..  
y90_2 = interp1(x2, Horizontal_axis(1:5), 0.90); y10_2 = interp1(x2, Horizontal_axis(1:5), 0.10);  
[x3, index] = unique(DbNormalizedBlcproc10Low(3,:), 'stable'); %row3 from Db..  
y90_3 = interp1(x3, Horizontal_axis(1:5), 0.90); y10_3 = interp1(x3, Horizontal_axis(1:5), 0.10);  
[x4, index] = unique(DbNormalizedBlcproc10Low(4,:), 'stable'); %row4 from Db..  
y90_4 = interp1(x4, Horizontal_axis(1:5), 0.90); y10_4 = interp1(x4, Horizontal_axis(1:5), 0.10);  
[x5, index] = unique(DbNormalizedBlcproc10Low(5,:), 'stable'); %row5 from Db..  
y90_5 = interp1(x5, Horizontal_axis(1:5), 0.90); y10_5 = interp1(x5, Horizontal_axis(1:5), 0.10);
```

```
MZW_10_90 = [y10_1-y90_1 ; y10_2-y90_2; y10_3-y90_3 ; y10_4-y90_4 ; y10_5-y90_5];
```

```
MZW_10_90_avg = mean(MZW_10_90);  
MZW_10_90_std = std(MZW_10_90);  
CV = 100*(MZW_10_90_std / MZW_10_90_avg);
```

```
formatSpec = 'The average mixing zone width for the low head drop is %3.2f cm with standard deviation of %3.2f  
cm and coefficient of variation of %2.1f percent\n';
```

```
fprintf(formatSpec, MZW_10_90_avg, MZW_10_90_std, CV)
```

```
The average mixing zone width for the low head drop is 0.76 cm with standard deviation of 0.02 cm and coefficient  
of variation of 3.3 percent
```

Appendix B. Supporting Information on Chapter 3 publication

The supporting information content here is part of the manuscript accepted and published in *Water Resources Research*. It is reprinted in this dissertation under license number 5047880480141.

Supporting Information

Abiotic mixing-dependent reaction in a laboratory simulated hyporheic zone

Katherine Y. Santizo, Mark A. Widdowson, and Erich T. Hester,

Charles E. Via Jr. Department of Civil and Environmental Engineering, Virginia Tech

Corresponding author: ehester@vt.edu

This supporting document contains three sections: (1) calibration data for sulfate (SO_4) spectrophotometer and dissolved oxygen (DO) optode results, (2) supplemental figures that extend the results in the main manuscript, and (3) details of estimating transport parameters from laboratory data.

B.1 Calibration Information

B.1a. Sulfate Spectrophotometer Calibration

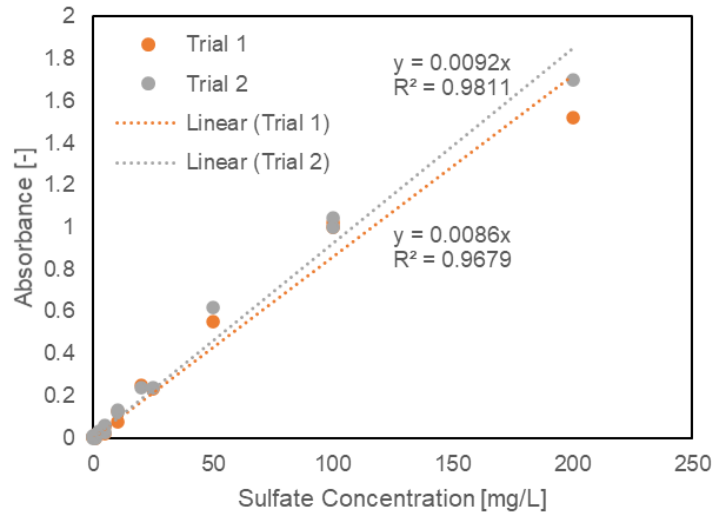


Figure S1. Absorbance versus SO_4 concentration calibration curve for SO_4 concentration measurements in mesocosm. Linear trendlines are shown with equation next to each line. The average slope was used to transform absorbance values to concentration values seen in Figure 3b.

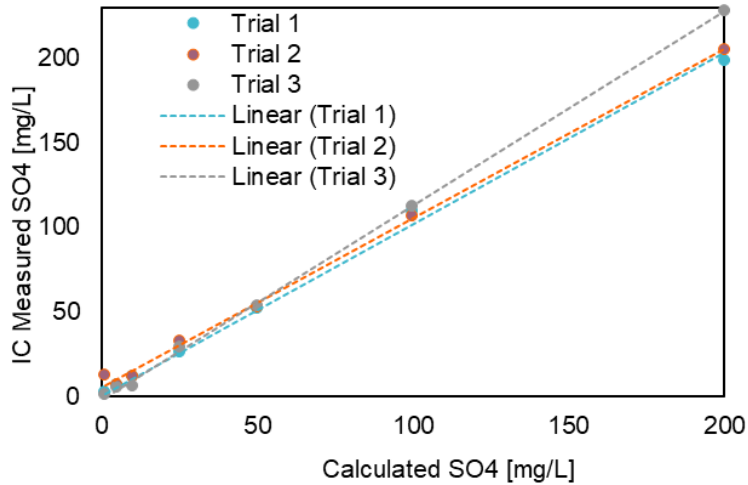


Figure S2. Ion chromatography (IC) measured SO_4 vs calculated SO_4 via spectrophotometer. The linear trend fit shows that the calculated SO_4 matches well with the IC measured SO_4 .

B.1b. Dissolved Oxygen (DO) Planar Optode Calibration

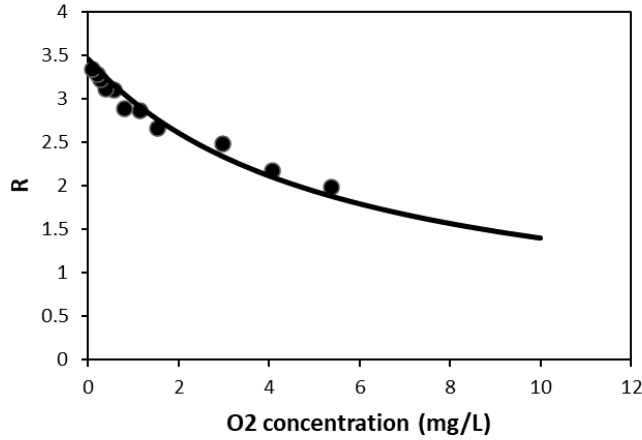


Figure S3. DO optode calibration curve using Argon to remove DO from water in mesocosm. $R^2=0.98$ (Table S2).

From Figure S3 we were able to obtain the parameters needed for the Stern-Volmer Equation (Equation S1, (Larsen et al., 2011)) to transform image ratio values (Equation S2) to concentration values. The values obtained from the curve are shown in Table S1.

$$C = \frac{R_0 - R}{K_{Sv}(R - \alpha R_0)} \quad (\text{Equation S1})$$

$$R = \frac{\text{Red Channel} - \text{Green Channel}}{\text{Green Channel}} \quad (\text{Equation S2})$$

The parameters used for the transformation are the ratio of the image when DO is depleted (R_0 , i.e. DO=0 mg/L), the ratio of red to green light for a given DO concentration (R), the Stern-Volmer quenching constant (K_{sv}), and the non-quenchable fraction of the light signal (α).

Table S1. Calculated parameters (Equation 1) from optode calibration curve in Figure S4. Obtained by curve fit of DO as mg/L.

Parameter from Equation 1	Estimated Value
α [-]	0.08
K_{Sv} [1/M]	0.182
R_0 [-]	3.45
r^2	0.9781

B.2 Supplemental Results

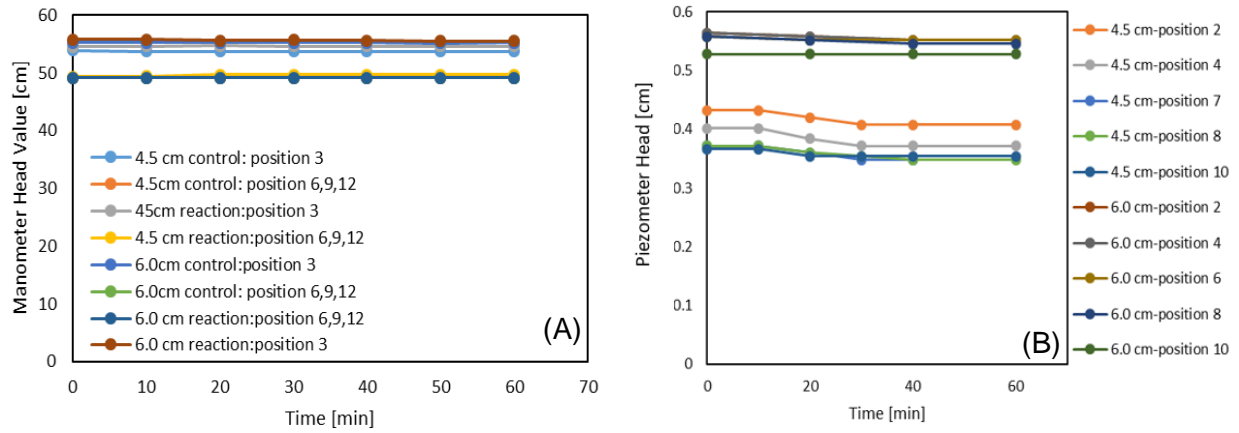


Figure S4. (A) Manometer heads (cm) from mesocosm (Figure 1K) over time for both control and reaction experiments. Taken at four different positions: position 3 is outside of the sandbox located within the inflow reservoir (Figure 1A), position 6, 9, and 12 are below the porous media (Figure 1D) in the upwelling reservoir (Figure 1H). (B) Piezometer heads (cm) at 2-3 cm depth for reaction experiments, taken at five different locations across the sampler (Figure 1F). Time on the x-axis is duration since a steady state hyporheic flow cell was observed (control) and when NaSO_3 was added (reactive).

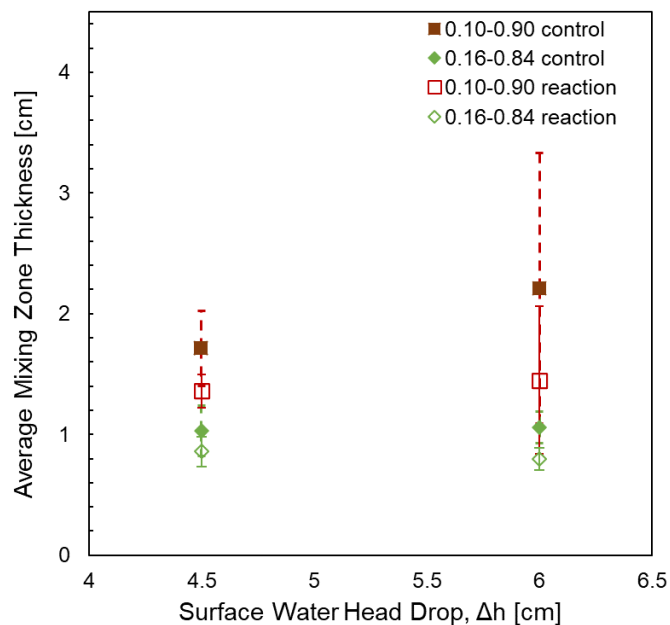


Figure S5. Average mixing zone thickness versus head drop for two concentration ranges (0.16-0.84 and 0.10-0.90). Values are averaged over three rows and error bars represent standard deviation.

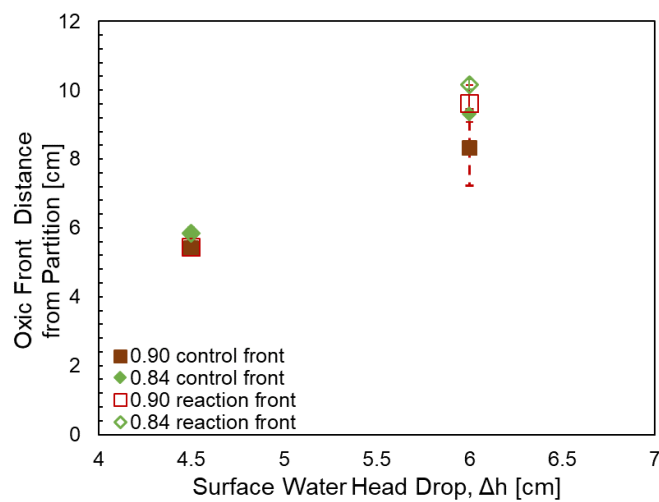


Figure S6. Average oxidic front distance from partition versus head drop for two concentration values (0.84 and 0.90). Values are averaged over three rows and error bars represent standard deviation.

B.3 Parameter Estimations and Dimensionless Numbers

B.3a. Values calculated from experiment

Reaction rate: $\lambda = 0.33/\text{sec}$

This parameter came from bench top experiments in DI water with NaSO_3 added at time zero. A YSI ProPlus meter was used to measure DO with 1 second recording interval.

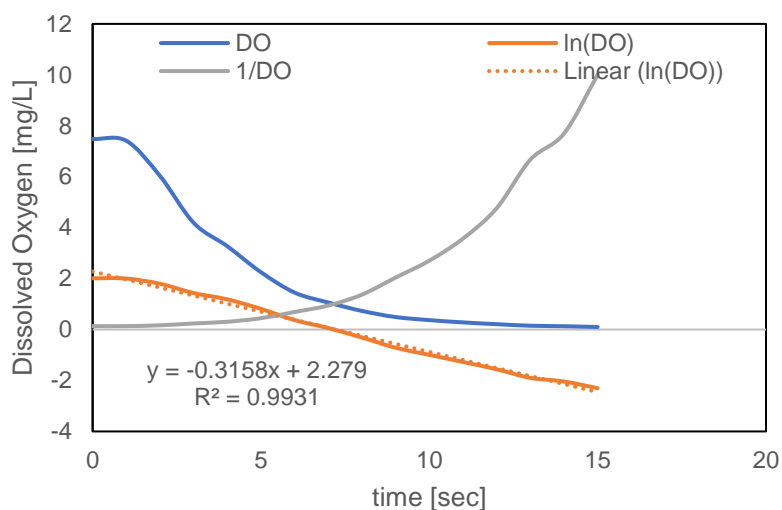


Figure S7. DO versus time for resulting reaction of NaSO_3 and DO in water with first and second order fits. Resulting DO rate coefficients are found in Table S2, the values were averaged for the resulting reaction rate value found in Table 1.

Table S2. First-order fitting of DO kinetics in reaction of NaSO_3 and DO.

Trial	DO Rate Coef. [1/sec]	DO R^2
1	0.340	0.989
2	0.313	0.976
3	0.340	0.990
4	0.316	0.993

Porosity: $n = 0.4$

This parameter came from bench top experiments with the same silica sand used in the mesocosm and DI water, based on volumetric calculations.

Average porewater velocity (v_p):

$\Delta h = 4.5$ cm: 1.08 ± 0.07 cm/min

$\Delta h = 6.0$ cm: 1.41 ± 0.08 cm/min

The porewater velocity calculations come from head values in Figure S4, hydraulic conductivity from a permeameter using the same silica and used in the mesocosm (57 m/d), and porosity from above.

Characteristic transport time across the cell: 20-30 min

Characteristic transport time across the cell was estimated from optode images. Optode images were captured every ten minutes from the beginning of the experiments (i.e. before steady state developed). Thus, the value comes from the oxic hyporheic flow cell development as it reached steady state.

Characteristic dispersion time for O_2 across the mixing zone:

$\Delta h = 4.5$ cm: 18.0 min

$\Delta h = 6.0$ cm: 18.4 min

Estimated as $\text{thickness}^2/D_t$ from characteristic dispersion with solute mass

Characteristic reaction time: 3 sec

Characteristic reaction time is estimated as $1/\lambda$ for first order reactions.

Transverse dispersion coefficient estimation based on advection-dispersion equations, using control experiments (Hester et al., 2013; Rolle et al., 2013):

$$thickness = \sqrt{\frac{D_t x}{v_p}}$$

D_t is transverse dispersion coefficient, x is the mixing zone length, v_p is the porewater velocity, thickness is the mixing zone width (average values from control experiments).

$$D_t = \frac{thickness^2 v_p}{x}$$

$$D_{t,4.5} = \frac{(1.03 \text{ cm})^2 \cdot 1.08 \text{ cm/min}}{19.3 \text{ cm}}$$

$$D_{t,6.0} = \frac{(1.06 \text{ cm})^2 \cdot 1.41 \text{ cm/min}}{26.1 \text{ cm}}$$

$$D_{t,4.5} = 0.059 \text{ cm}^2/\text{min} = 9.8 \times 10^{-8} \text{ m}^2/\text{sec}$$

$$D_{t,6.0} = 0.061 \text{ cm}^2/\text{min} = 1.0 \times 10^{-7} \text{ m}^2/\text{sec}$$

B.3b. Dimensionless number calculations

In open channel flow, laminar flow exists for Reynolds number (Re) < 500 , while turbulent flow exists for $Re > 2000$. For flow in the rectangular channel in our experimental mesocosm above the sediment-water interface (flow toward the right in Figure 1 of the main manuscript) (Chaudry, 2008):

$$Re = \frac{4 R v}{\nu}$$

where R is hydraulic radius ($= A/P_w$, m), A is the cross sectional flow area of the channel (27 cm^2) and P_w is the wetted perimeter (15.4 cm), v is the average water velocity in the channel (m/s) calculated by dividing total flow in channel (Table 1, upwelling inflow rate only because area of interest is “upstream” end of channel, i.e. left side in Figure 1) by A , and ν is kinematic viscosity ($1 \times 10^{-6} \text{ m}^2/\text{s}$ at 20°C).

$$Re = \frac{4 \cdot 0.0175 \text{ m} \cdot 0.007 \text{ m/s}}{1.0 \times 10^{-6} \text{ m}^2/\text{s}}$$

$$Re = 490$$

Peclet number to describe advection versus dispersion dominance (Haggerty et al., 2014). Values greater than one indicate advection dominance while values less than one indicate dispersion dominance.

$$Pe = \frac{v_p L}{D_t}$$

$$Pe_{4.5} = \frac{0.00018 \frac{\text{m}}{\text{s}} \cdot 0.193 \text{ m}}{9.8 \times 10^{-8} \text{ m}^2/\text{s}}$$

$$Pe_{6.0} = \frac{0.000235 \frac{\text{m}}{\text{s}} \cdot 0.261 \text{ m}}{1.0 \times 10^{-7} \text{ m}^2/\text{s}}$$

$$Pe_{4.5} = 354.5$$

$$Pe_{6.0} = 613.4$$

Damkohler number describes kinetic versus dispersion limitation (Kaufman et al., 2017; Rolle et al., 2013). A Damkohler number greater than one indicates a dispersion limited reaction, whereas a value less than one indicates a kinetic limited reaction.

$$Da = \frac{\lambda L^2}{D_t}$$

$$Da_{t,4.5} = \frac{0.33 \cdot 0.193^2}{9.8 \times 10^{-8}}$$

$$Da_{t,6.0} = \frac{0.33 \cdot 0.261^2}{1.0 \times 10^{-7}}$$

$$Da_{t,4.5} = 125,430$$

$$Da_{t,6.0} = 224,799$$

References

- Chaudry, M. H. (2008). *Open Channel Flow* (2nd ed.). New York: Springer US.
- Haggerty, R., Ribot, M., Singer, G. A., Martí, E., Argerich, A., Agell, G., & Battin, T. J. (2014). Ecosystem respiration increases with biofilm growth and bed forms: Flume measurements with resazurin. *Journal of Geophysical Research: Biogeosciences*, *119*(12), 2220–2230. <https://doi.org/10.1002/2013JG002498>
- Hester, E. T., Young, K. I., & Widdowson, M. A. (2013). Mixing of surface and groundwater induced by riverbed dunes: Implications for hyporheic zone definitions and pollutant reactions. *Water Resources Research*, *49*(9), 5221–5237. <https://doi.org/10.1002/wrcr.20399>
- Kaufman, M. H., Cardenas, M. B., Buttle, J., Kessler, A. J., & Cook, P. L. M. (2017). Hyporheic hot moments: Dissolved oxygen dynamics in the hyporheic zone in response to surface flow perturbations. *Water Resources Research*, *53*(8), 6642–6662. <https://doi.org/10.1002/2016WR020296>
- Larsen, M., Borisov, S. M., Grunwald, B., Klimant, I., & Glud, R. N. (2011). A simple and inexpensive high-resolution color-ratiometric planar optode imaging approach: Application to oxygen and pH sensing. *Limnology and Oceanography: Methods*, *9*, 348–360.
- Rolle, M., Chiogna, G., Hochstetler, D. L., & Kitanidis, P. K. (2013). On the importance of diffusion and compound-specific mixing for groundwater transport: An investigation from pore to field scale. *Journal of Contaminant Hydrology*, *153*, 51–68. <https://doi.org/10.1016/j.jconhyd.2013.07.006>

Appendix C. MATLAB codes for analysis of laboratory simulated mixing-dependent abiotic reaction

Controls: Fall 2018, head drop: 6.0cm

```
clear; clc; close all
```

```
%row and column used for cropping images so only optode visible for
```

```
%analysis
```

```
row=450:1300;
```

```
column=700:2020;
```

```
%Using Stern-Volmer equation, only need to use green and red channels
```

```
%Stern-Volmer equation--modified:  $C = (R_0 - R) / (K_{sv} * (R - \alpha * R_0))$  where  $R = (Red - Green) / Green$ 
```

```
%R0 is the Ratio when DO=0 mg/L, Ksv is the Stern-Volmer quenching constant, and alpha is the non-quenchable fraction of the light signal
```

```
%images are from Look@RGB software
```

```
%Ratio of red and green channel (R) for concentration calculation
```

```
%time -10 min
```

```
Red1 = double(imread('control60_0000_S0001_I0002_R.tif'));
```

```
Green1 = double(imread('control60_0000_S0001_I0002_G.tif'));
```

```
Ratio1 = (Red1(row,column)-Green1(row,column))./(Green1(row,column));
```

```
%time 0 min
```

```
Red2 = double(imread('control60_0000_S0002_I0002_R.tif'));
```

```
Green2 = double(imread('control60_0000_S0002_I0002_G.tif'));
```

```
Ratio2 = (Red2(row,column)-Green2(row,column))./(Green2(row,column));
```

```
%time 10 min
```

```
Red3 = double(imread('control60_0000_S0003_I0002_R.tif'));
```

```
Green3 = double(imread('control60_0000_S0003_I0002_G.tif'));
```

```
Ratio3 = (Red3(row,column)-Green3(row,column))./(Green3(row,column));
```

```
%time 20 min
```

```
Red4 = double(imread('control60_0000_S0004_I0002_R.tif'));
```

```
Green4 = double(imread('control60_0000_S0004_I0002_G.tif'));
```

```
Ratio4 = (Red4(row,column)-Green4(row,column))./(Green4(row,column));
```

```
%time 30 min
```

```
Red5 = double(imread('control60_0000_S0005_I0002_R.tif'));
```

```
Green5 = double(imread('control60_0000_S0005_I0002_G.tif'));
```

```
Ratio5 = (Red5(row,column)-Green5(row,column))./(Green5(row,column));
```

```
%time 40 min
```

```
Red6 = double(imread('control60_0000_S0006_I0002_R.tif'));
```

```
Green6 = double(imread('control60_0000_S0006_I0002_G.tif'));
```

```
Ratio6 = (Red6(row,column)-Green6(row,column))./(Green6(row,column));
```

```
%time 50 min
```

```
Red7 = double(imread('control60_0000_S0007_I0002_R.tif'));
```

```
Green7 = double(imread('control60_0000_S0007_I0002_G.tif'));
```

```
Ratio7 = (Red7(row,column)-Green7(row,column))./(Green7(row,column));
```

```

%Time 60 min
Red8 = double(imread('control60_0000_S0008_I0002_R.tif'));
Green8 = double(imread('control60_0000_S0008_I0002_G.tif'));
Ratio8 = (Red8(row,column)-Green8(row,column))./(Green8(row,column));

%time 70 min
Red9 = double(imread('control60_0000_S0009_I0002_R.tif'));
Green9 = double(imread('control60_0000_S0009_I0002_G.tif'));
Ratio9 = (Red9(row,column)-Green9(row,column))./(Green9(row,column));

%time 80 min
Red10 = double(imread('control60_0000_S0010_I0002_R.tif'));
Green10 = double(imread('control60_0000_S0010_I0002_G.tif'));
Ratio10 = (Red10(row,column)-Green10(row,column))./(Green10(row,column));

%Ro, K and alpha from calibration curve for conc. conversion
Ro=3.45; K=0.182; alpha= 0.08;

%concentration conversion
conc1= (Ro-Ratio1)./(K.*(Ratio1-(Ro*alpha)));
conc2= (Ro-Ratio2)./(K.*(Ratio2-(Ro*alpha)));
conc3= (Ro-Ratio3)./(K.*(Ratio3-(Ro*alpha)));
conc4= (Ro-Ratio4)./(K.*(Ratio4-(Ro*alpha)));
conc5= (Ro-Ratio5)./(K.*(Ratio5-(Ro*alpha)));
conc6= (Ro-Ratio6)./(K.*(Ratio6-(Ro*alpha)));
conc7= (Ro-Ratio7)./(K.*(Ratio7-(Ro*alpha)));
conc8= (Ro-Ratio8)./(K.*(Ratio8-(Ro*alpha)));
conc9= (Ro-Ratio9)./(K.*(Ratio9-(Ro*alpha)));
conc10= (Ro-Ratio10)./(K.*(Ratio10-(Ro*alpha)));

%function used to set up block images below, based on means of pixels that
%are grouped and replaced
fun = @(block_struct) ...
mean2(block_struct.data) * ones(size(block_struct.data));
bl=2;%block size

bc1 = blockproc(conc1, [bl bl], fun);
bc2 = blockproc(conc2, [bl bl], fun);
bc3 = blockproc(conc3, [bl bl], fun);
bc4 = blockproc(conc4, [bl bl], fun);
bc5 = blockproc(conc5, [bl bl], fun);
bc6 = blockproc(conc6, [bl bl], fun);
bc7 = blockproc(conc7, [bl bl], fun);
bc8 = blockproc(conc8, [bl bl], fun);
bc9 = blockproc(conc9, [bl bl], fun);
bc10 = blockproc(conc10, [bl bl], fun);

%for loop to set up bounds for DO
for i=1:length(row)
    for j=1:length(column)

        if bc1(i,j)>=8.5
            bc1(i,j)= 8.4;

```

```

elseif bc1(i,j)<0
    bc1(i,j)= 0.5;
end

if bc2(i,j)>=8.5
    bc2(i,j)= 8.4;
elseif bc2(i,j)<0
    bc2(i,j)= 0.5;
end

if bc3(i,j)>=8.5
    bc3(i,j)= 8.4;
elseif bc3(i,j)<0
    bc3(i,j)= 0.5;
end

if bc4(i,j)>=8.5
    bc4(i,j)= 8.4;
elseif bc4(i,j)<0
    bc4(i,j)= 0.5;
end

if bc5(i,j)>=8.5
    bc5(i,j)= 8.4;
elseif bc5(i,j)<0
    bc5(i,j)= 0.5;
end

if bc6(i,j)>=8.5
    bc6(i,j)= 8.4;
elseif bc6(i,j)<0
    bc6(i,j)= 0.5;
end

if bc7(i,j)>=8.5
    bc7(i,j)= 8.4;
elseif bc7(i,j)<0
    bc7(i,j)= 0.5;
end

if bc8(i,j)>=8.5
    bc8(i,j)= 8.4;
elseif bc8(i,j)<0
    bc8(i,j)= 0.5;
end

if bc9(i,j)>=8.5
    bc9(i,j)= 8.4;
elseif bc9(i,j)<0
    bc9(i,j)= 0.5;
end

if bc10(i,j)>=8.5
    bc10(i,j)= 8.4;
elseif bc10(i,j)<0
    bc10(i,j)= 0.5;
end

```

```

end

end

end

%conversion from pixel to cm lengths for optodes, based on manual length measurements of planar optodes
h_axis=2.2:(bl*0.0218):31; %Need to change this if changing amount of rows/columns are changed at beginning of
code
v_axis=2.7:(bl*0.0221):21.5;

%Concentration maximum within optode for normalization
cmax1=max(bc1(:));cmax2=max(bc2(:));cmax3=max(bc3(:));cmax4=max(bc4(:));
cmax5=max(bc5(:));cmax6=max(bc6(:));cmax7=max(bc7(:));cmax8=max(bc8(:));cmax9=max(bc9(:));
cmax10=max(bc10(:));

a=1:bl:851; %Need to change this if changing amount of rows/columns at the beginning of code
b=1:bl:1321;

%normalization of concentration profiles
rc1 = bc1(a,b)./cmax1;rc2 = bc2(a,b)./cmax2;rc3 = bc3(a,b)./cmax3;rc4 = bc4(a,b)./cmax4;
rc5 = bc5(a,b)./cmax5;rc6 = bc6(a,b)./cmax6;rc7 = bc7(a,b)./cmax7;rc8 = bc8(a,b)./cmax8;rc9 = bc9(a,b)./cmax9;
rc10 = bc10(a,b)./cmax10;

%Figure set up of concentration profiles
figure;imagesc(h_axis, v_axis,rc1)
colormap (jet); c=colorbar;
c.Label.String='DO Concentration [-]'; caxis([0.0 1.0]); c.Label.FontSize =14;
xlabel('Distance from divider [cm]', 'FontSize',14); ylabel('Depth [cm]', 'FontSize',14)
figure;imagesc(h_axis, v_axis,rc2)
colormap (jet); c=colorbar;
c.Label.String='DO Concentration [-]'; caxis([0.0 1.0]); c.Label.FontSize =14;
xlabel('Distance from divider [cm]', 'FontSize',14); ylabel('Depth [cm]', 'FontSize',14)
figure;imagesc(h_axis,v_axis,rc3)
colormap (jet); c=colorbar;
c.Label.String='DO Concentration [-]'; caxis([0.0 1.0]); c.Label.FontSize =14;
xlabel('Distance from divider [cm]', 'FontSize',14); ylabel('Depth [cm]', 'FontSize',14)
figure;imagesc(h_axis, v_axis,rc4)
colormap (jet); c=colorbar;
c.Label.String='DO Concentration [-]'; caxis([0.0 1.0]); c.Label.FontSize =14;
xlabel('Distance from divider [cm]', 'FontSize',14); ylabel('Depth [cm]', 'FontSize',14)
figure;imagesc(h_axis, v_axis,rc5)
colormap (jet); c=colorbar;
c.Label.String='DO Concentration [-]'; caxis([0.0 1.0]); c.Label.FontSize =14;
xlabel('Distance from divider [cm]', 'FontSize',14); ylabel('Depth [cm]', 'FontSize',14)
figure;imagesc(h_axis,v_axis,rc6)
colormap (jet); c=colorbar;
c.Label.String='DO Concentration [-]'; caxis([0.0 1.0]); c.Label.FontSize =14;
xlabel('Distance from divider [cm]', 'FontSize',14); ylabel('Depth [cm]', 'FontSize',14)
figure;imagesc(h_axis,v_axis,rc7)
colormap (jet); c=colorbar;
c.Label.String='DO Concentration [-]'; caxis([0.0 1.0]); c.Label.FontSize =14;
xlabel('Distance from divider [cm]', 'FontSize',14); ylabel('Depth [cm]', 'FontSize',14)
figure;imagesc(h_axis,v_axis,rc8)
colormap (jet); c=colorbar;
c.Label.String='DO Concentration [-]'; caxis([0.0 1.0]); c.Label.FontSize =14;

```

```

xlabel('Distance from divider [cm]',FontSize,14); ylabel('Depth [cm]',FontSize,14)
figure;imagesc(h_axis,v_axis,rc9)
colormap (jet); c=colorbar;
c.Label.String='DO Concentration [-]'; caxis([0.0 1.0]); c.Label.FontSize =14;
xlabel('Distance from divider [cm]',FontSize,14); ylabel('Depth [cm]',FontSize,14)
figure;imagesc(h_axis,v_axis,rc10)
colormap (jet); c=colorbar;
c.Label.String='DO Concentration [-]'; caxis([0.0 1.0]); c.Label.FontSize =14;
xlabel('Distance from divider [cm]',FontSize,14); ylabel('Depth [cm]',FontSize,14)

```

%Plot set-up for images in manuscript, edited manually in MATLAB editor

```

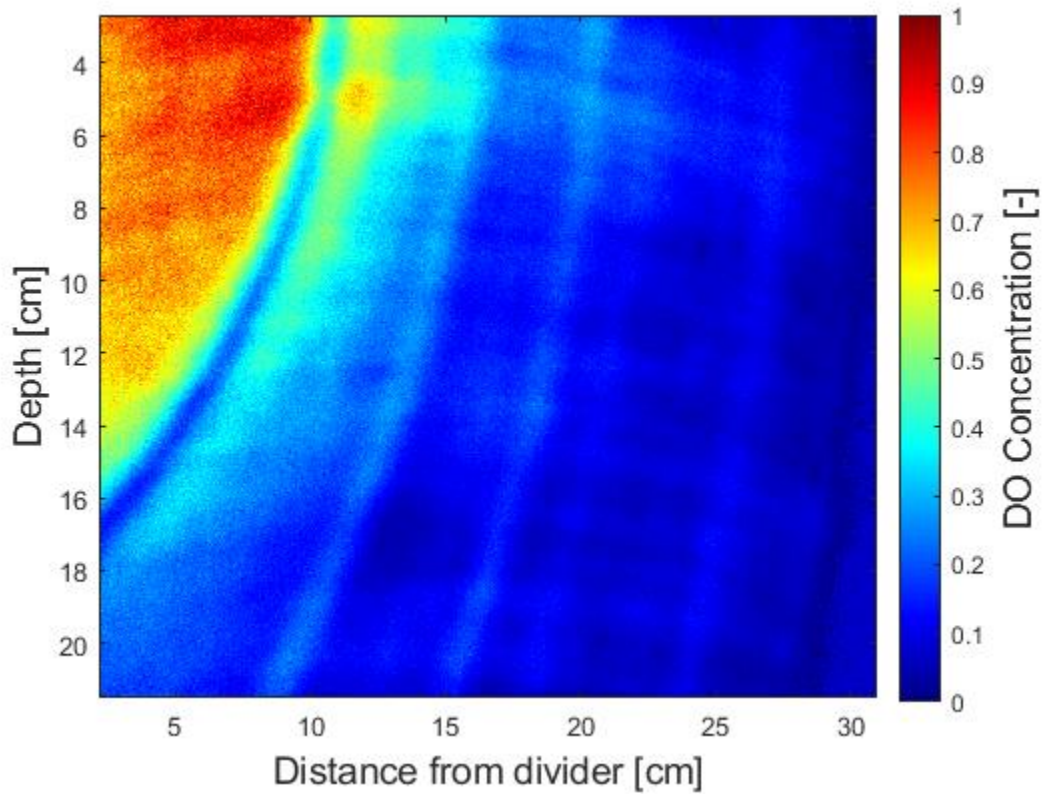
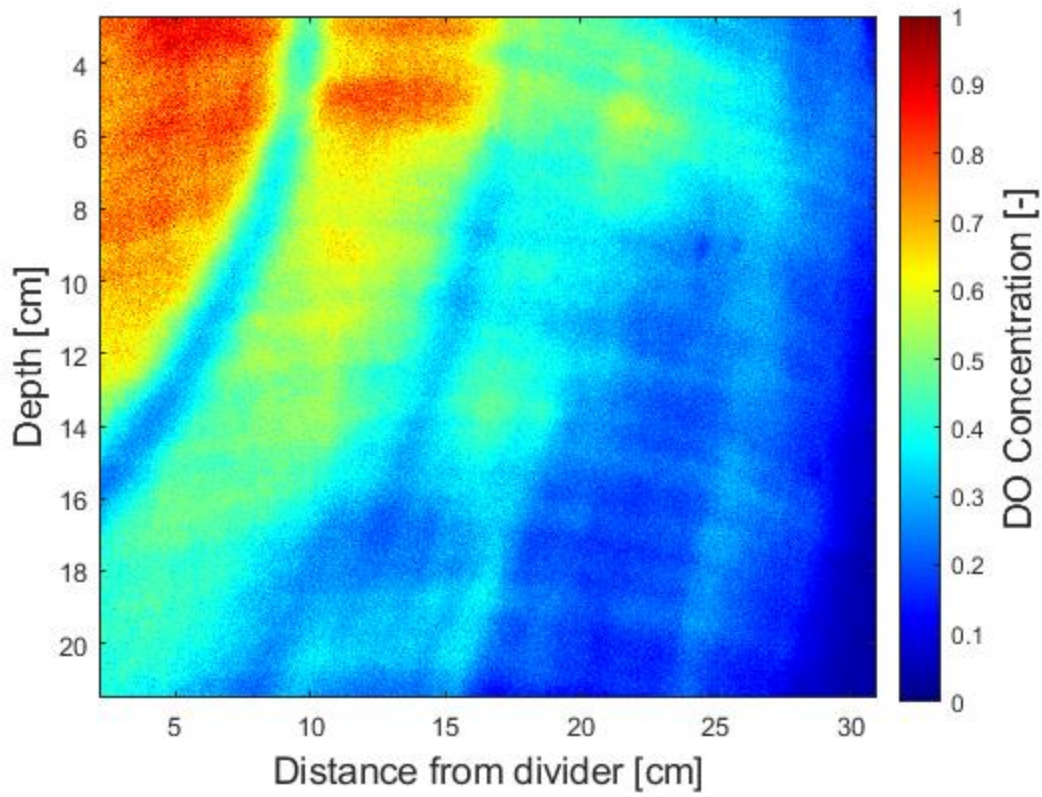
subplot(2,1,1);
imagesc(h_axis(24:295),v_axis(1:322),rc8(1:322,24:295))
colormap (jet); c=colorbar;
c.Label.String='DO Concentration [-]'; caxis([0.0 1.0]); c.Label.FontSize =14;
ylabel('Depth [cm]',FontSize,14)

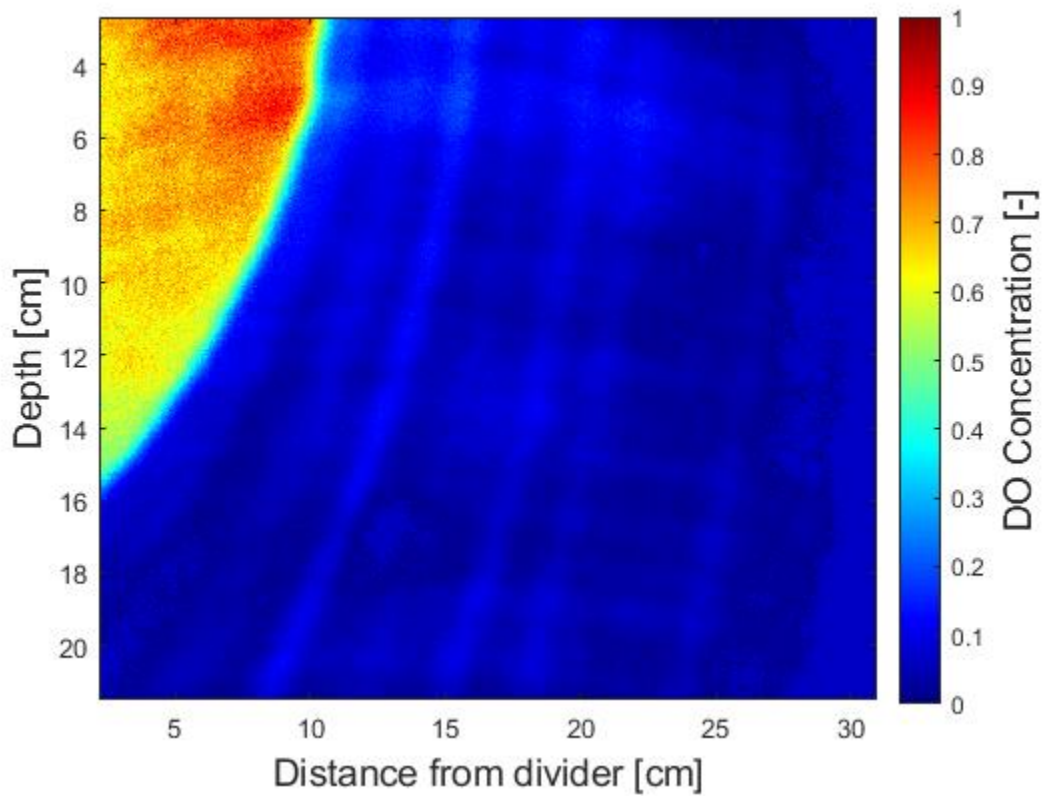
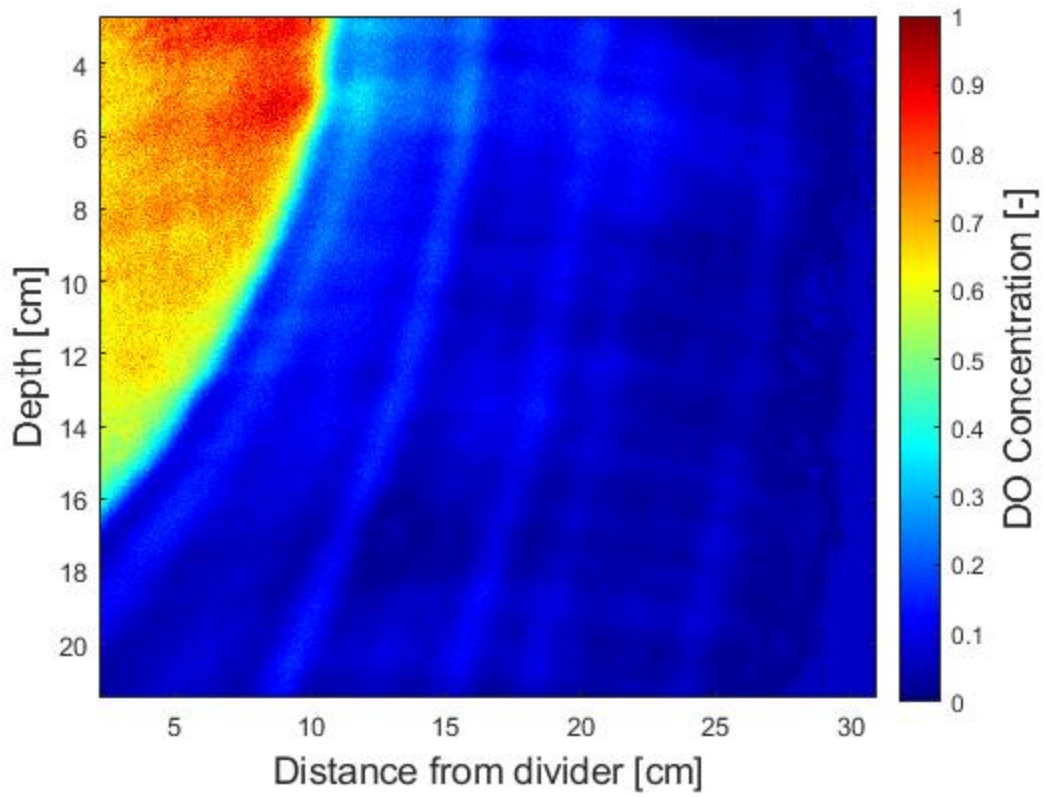
```

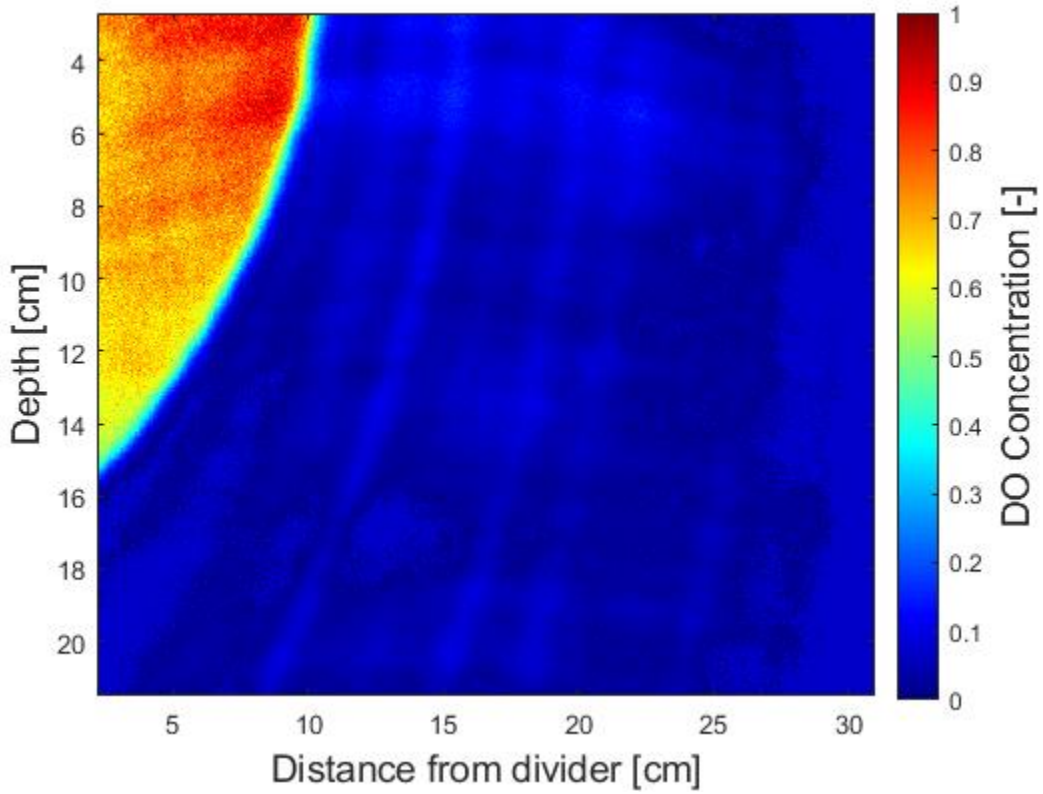
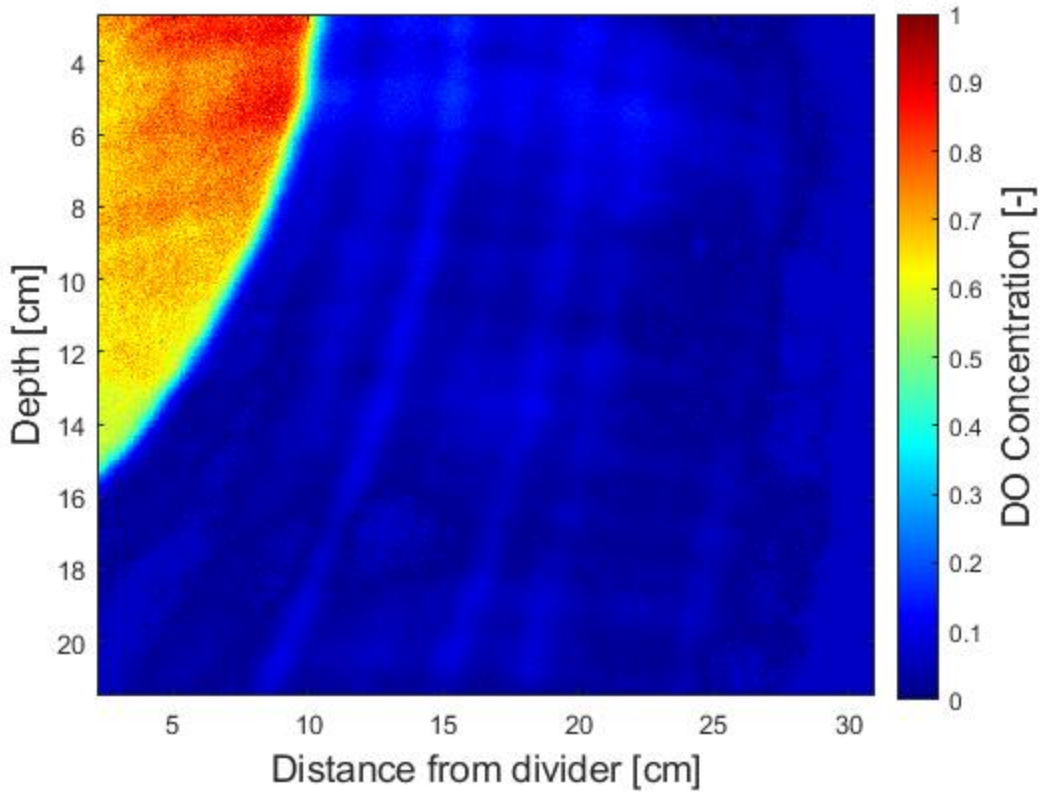
```

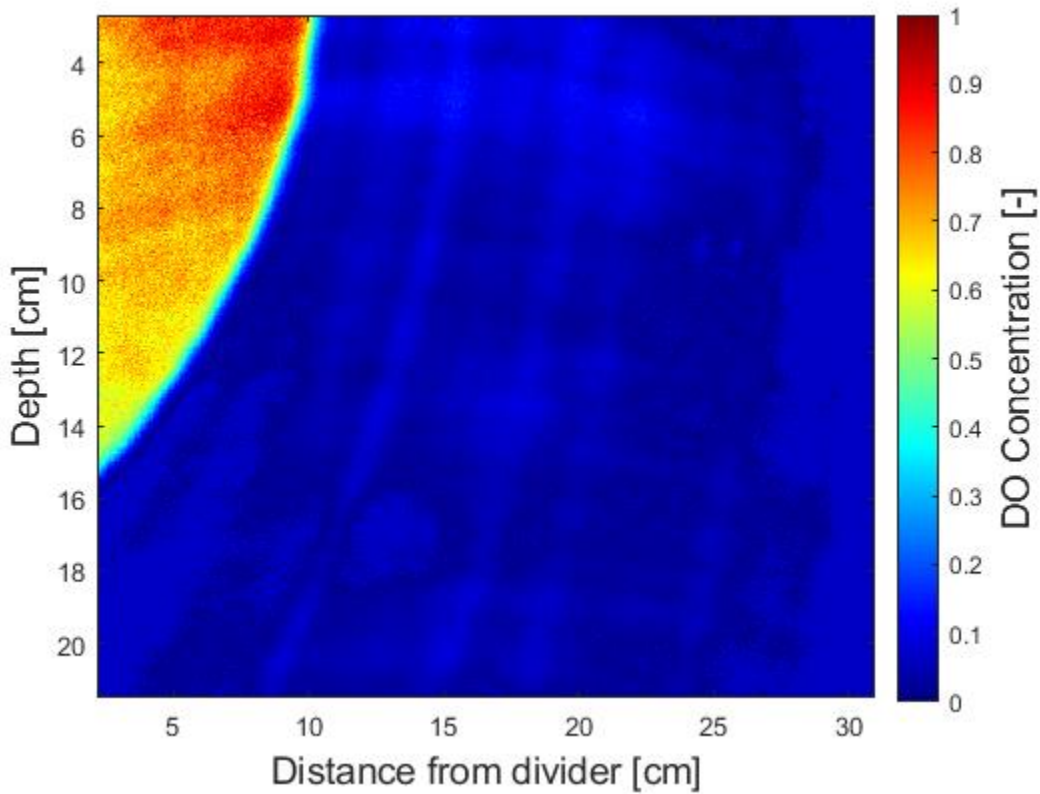
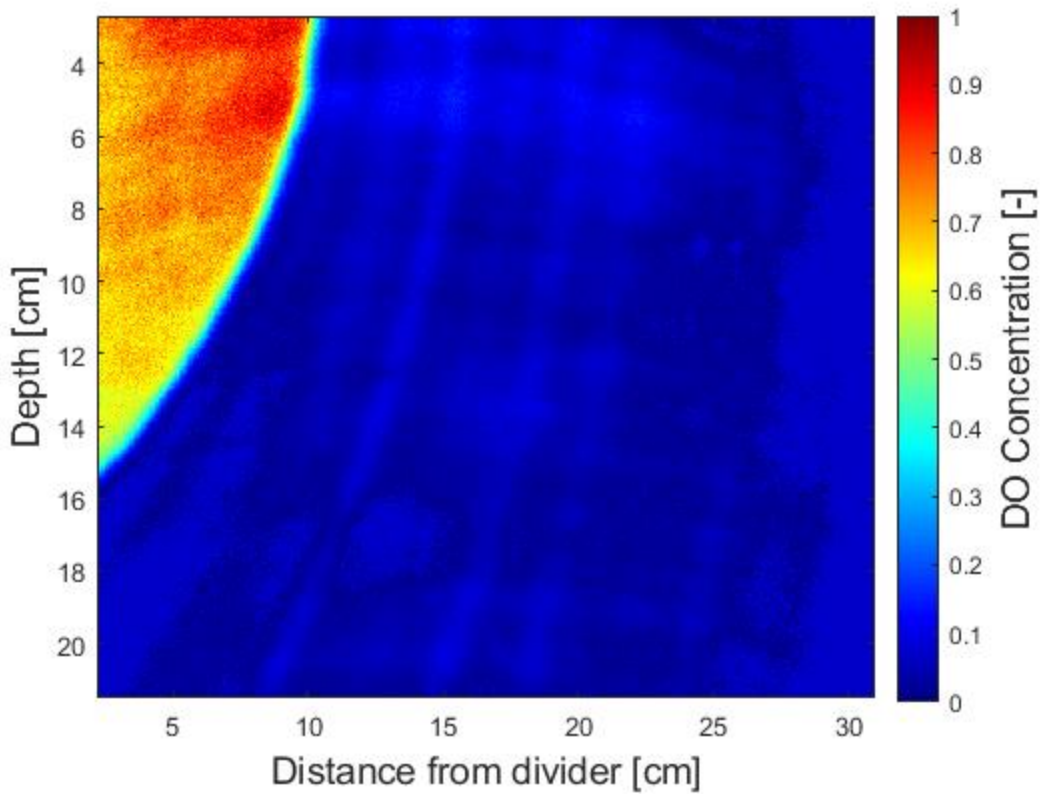
subplot(2,1,2);
imagesc(h_axis(24:295),3.48:3.52,rc8(19,24:295))
xlabel('Distance from divider [cm]',FontSize,14);

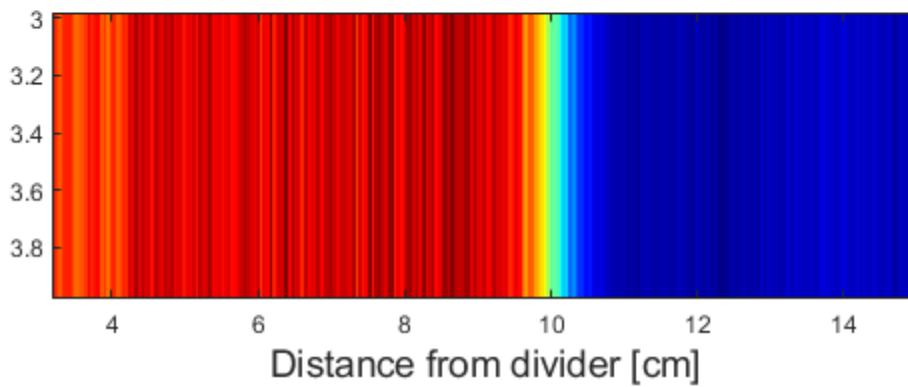
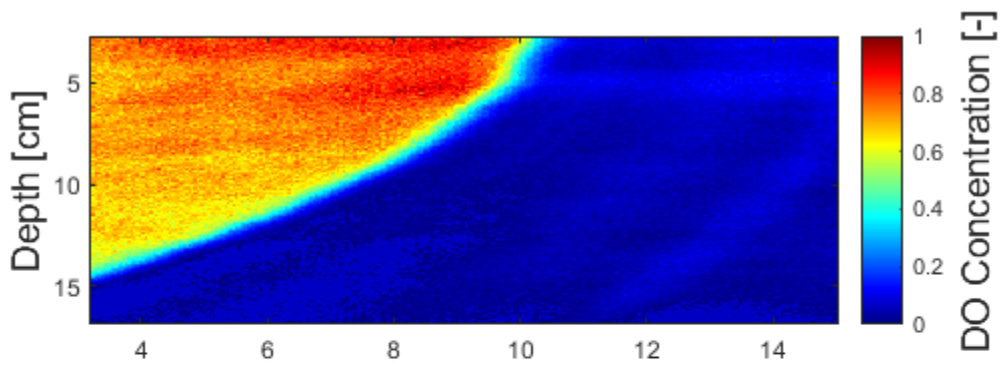
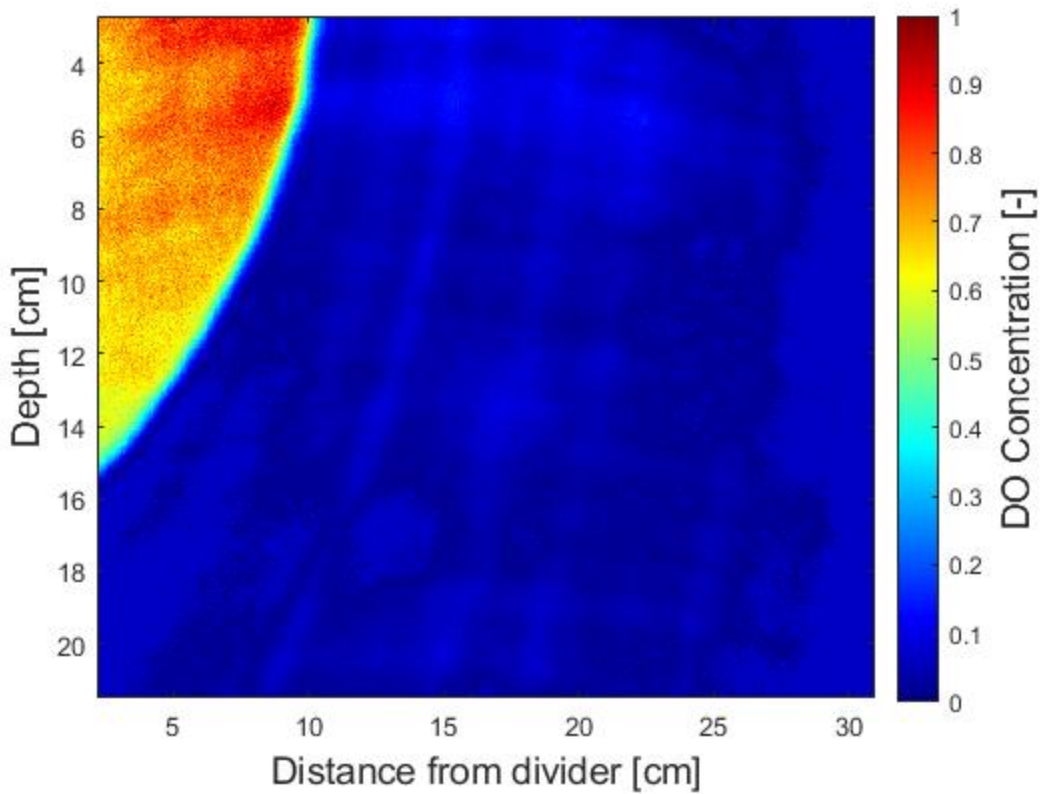
```











Abiotic Reaction: Fall 2018, head drop: 6.0cm

clear; clc; close all

%row and column used for cropping images so only optode visible for

%analysis

row=440:1300;

column=600:1960;

%Using Stern-Volmer equation, only need to use green and red channels

%Stern-Volmer equation--modified: $C = (R0-R)/(Ksv*(R-(\alpha*R0)))$ where $R = (Red-Green)/Green$

%R0 is the Ratio when DO=0 mg/L, Ksv is the Stern-Volmer quenching constant, and alpha is the non-quenchable fraction of the light signal

%images are from Look@RGB software

%Ratio of red and green channel (R) for concentration calculation

%time -10 min

Red1 = double(imread('60min_6.0_0000_S0001_I0001_R.tif'));

Green1 = double(imread('60min_6.0_0000_S0001_I0001_G.tif'));

Ratio1 = (Red1(row,column)-Green1(row,column))./(Green1(row,column));

%time 0 min

Red2 = double(imread('60min_6.0_0000_S0002_I0001_R.tif'));

Green2 = double(imread('60min_6.0_0000_S0002_I0001_G.tif'));

Ratio2 = (Red2(row,column)-Green2(row,column))./(Green2(row,column));

%time 10 min

Red3 = double(imread('60min_6.0_0000_S0003_I0001_R.tif'));

Green3 = double(imread('60min_6.0_0000_S0003_I0001_G.tif'));

Ratio3 = (Red3(row,column)-Green3(row,column))./(Green3(row,column));

%time 20 min

Red4 = double(imread('60min_6.0_0000_S0004_I0001_R.tif'));

Green4 = double(imread('60min_6.0_0000_S0004_I0001_G.tif'));

Ratio4 = (Red4(row,column)-Green4(row,column))./(Green4(row,column));

%time 30 min

Red5 = double(imread('60min_6.0_0000_S0005_I0001_R.tif'));

Green5 = double(imread('60min_6.0_0000_S0005_I0001_G.tif'));

Ratio5 = (Red5(row,column)-Green5(row,column))./(Green5(row,column));

%time 40 min

Red6 = double(imread('60min_6.0_0000_S0006_I0001_R.tif'));

Green6 = double(imread('60min_6.0_0000_S0006_I0001_G.tif'));

Ratio6 = (Red6(row,column)-Green6(row,column))./(Green6(row,column));

%time 50 min

Red7 = double(imread('60min_6.0_0000_S0007_I0001_R.tif'));

Green7 = double(imread('60min_6.0_0000_S0007_I0001_G.tif'));

Ratio7 = (Red7(row,column)-Green7(row,column))./(Green7(row,column));

%time 60 min

Red8 = double(imread('60min_6.0_0000_S0008_I0001_R.tif'));

Green8 = double(imread('60min_6.0_0000_S0008_I0001_G.tif'));

Ratio8 = (Red8(row,column)-Green8(row,column))./(Green8(row,column));

%time 70 min

```

Red9 = double(imread('60min_6.0_0000_S0009_I0001_R.tif'));
Green9 = double(imread('60min_6.0_0000_S0009_I0001_G.tif'));
Ratio9 = (Red9(row,column)-Green9(row,column))./(Green9(row,column));

%time 80 min
Red10 = double(imread('60min_6.0_0000_S0010_I0001_R.tif'));
Green10 = double(imread('60min_6.0_0000_S0010_I0001_G.tif'));
Ratio10 = (Red10(row,column)-Green10(row,column))./(Green10(row,column));

%Ro, K and alpha from calibration curve for conc. conversion
Ro=3.45; K=0.182; alpha= 0.08;
%Concentration conversion
conc1=(Ro-Ratio1)./(K.*(Ratio1-(Ro*alpha)));
conc2=(Ro-Ratio2)./(K.*(Ratio2-(Ro*alpha)));
conc3=(Ro-Ratio3)./(K.*(Ratio3-(Ro*alpha)));
conc4=(Ro-Ratio4)./(K.*(Ratio4-(Ro*alpha)));
conc5=(Ro-Ratio5)./(K.*(Ratio5-(Ro*alpha)));
conc6=(Ro-Ratio6)./(K.*(Ratio6-(Ro*alpha)));
conc7=(Ro-Ratio7)./(K.*(Ratio7-(Ro*alpha)));
conc8=(Ro-Ratio8)./(K.*(Ratio8-(Ro*alpha)));
conc9=(Ro-Ratio9)./(K.*(Ratio9-(Ro*alpha)));
conc10=(Ro-Ratio10)./(K.*(Ratio10-(Ro*alpha)));

%function used to set up block images below, based on means of pixels that
%are grouped and replaced
fun = @(block_struct) ...
mean2(block_struct.data) * ones(size(block_struct.data));
bl=2; %block size

bc1 = blockproc(conc1, [bl bl], fun);
bc2 = blockproc(conc2, [bl bl], fun);
bc3 = blockproc(conc3, [bl bl], fun);
bc4 = blockproc(conc4, [bl bl], fun);
bc5 = blockproc(conc5, [bl bl], fun);
bc6 = blockproc(conc6, [bl bl], fun);
bc7 = blockproc(conc7, [bl bl], fun);
bc8 = blockproc(conc8, [bl bl], fun);
bc9 = blockproc(conc9, [bl bl], fun);
bc10 = blockproc(conc10, [bl bl], fun);

%for loop to set up bounds of DO conc.
for i=1:length(row)
    for j=1:length(column)

        if bc1(i,j)>=8.5
            bc1(i,j)= 8.4;
        elseif bc1(i,j)<0
            bc1(i,j)= 0.5;
        end

        if bc2(i,j)>=8.5
            bc2(i,j)= 8.4;
        elseif bc2(i,j)<0
            bc2(i,j)= 0.5;
        end
    end
end

```

```
    if bc3(i,j)>=8.5
        bc3(i,j)= 8.4;
    elseif bc3(i,j)<0
        bc3(i,j)= 0.5;
    end
```

```
    if bc4(i,j)>=8.5
        bc4(i,j)= 8.4;
    elseif bc4(i,j)<0
        bc4(i,j)= 0.5;
    end
```

```
    if bc5(i,j)>=8.5
        bc5(i,j)= 8.4;
    elseif bc5(i,j)<0
        bc5(i,j)= 0.5;
    end
```

```
    if bc6(i,j)>=8.5
        bc6(i,j)= 8.4;
    elseif bc6(i,j)<0
        bc6(i,j)= 0.5;
    end
```

```
    if bc7(i,j)>=8.5
        bc7(i,j)= 8.4;
    elseif bc7(i,j)<0
        bc7(i,j)= 0.5;
    end
```

```
    if bc8(i,j)>=8.5
        bc8(i,j)= 8.4;
    elseif bc8(i,j)<0
        bc8(i,j)= 0.5;
    end
```

```
    if bc9(i,j)>=8.5
        bc9(i,j)= 8.4;
    elseif bc9(i,j)<0
        bc9(i,j)= 0.5;
    end
```

```
    if bc10(i,j)>=8.5
        bc10(i,j)= 8.4;
    elseif bc10(i,j)<0
        bc10(i,j)= 0.5;
    end
```

```
end
end
```

```
%Concentration maximum within optode for normalization
cmax1=max(bc1(:));cmax2=max(bc2(:));cmax3=max(bc3(:));cmax4=max(bc4(:));
cmax5=max(bc5(:));cmax6=max(bc6(:));cmax7=max(bc7(:));cmax8=max(bc8(:));cmax9=max(bc9(:));
```

```

cmax10=max(bc10(:));

%conversion from pixels to cm lengths for optodes, based on manual length
%measurements of planar optodes
a=1:bl:861; %Need to change this if changing amount of rows/columns
b=1:bl:1361;
h_axis=2.4:(bl*(29/1395)):30.7; %Need to change this if changing amount of rows/columns
v_axis=3.2:(bl*(19.5/920)):21.5;

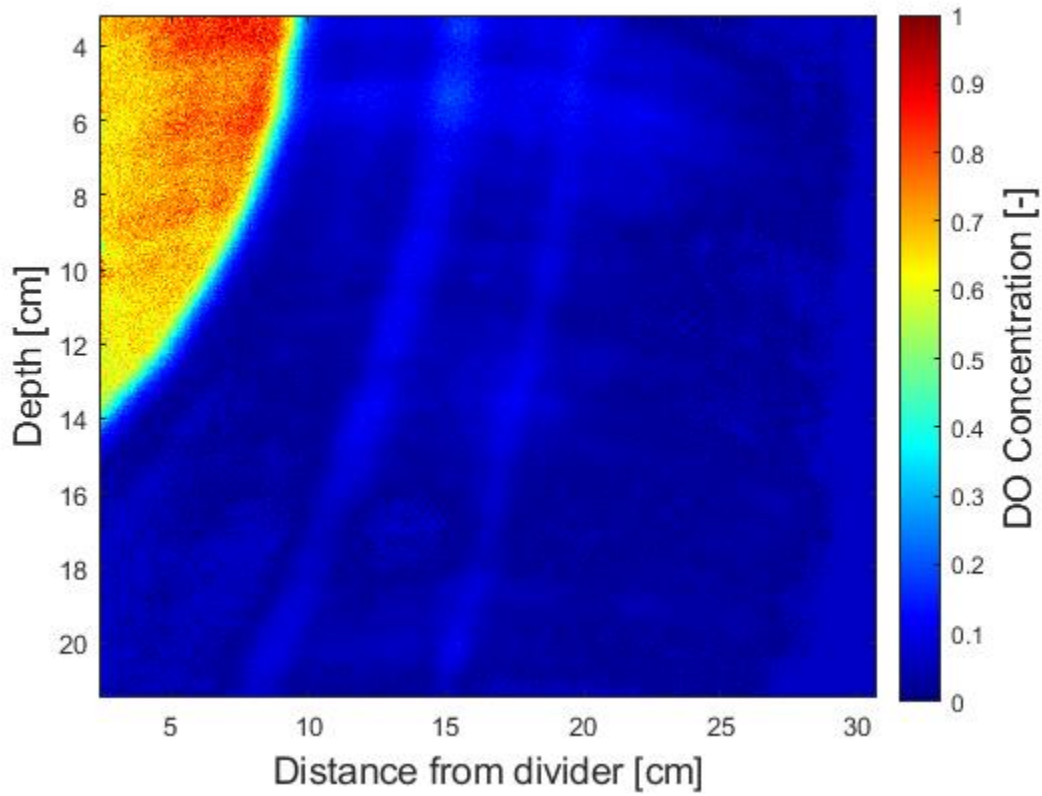
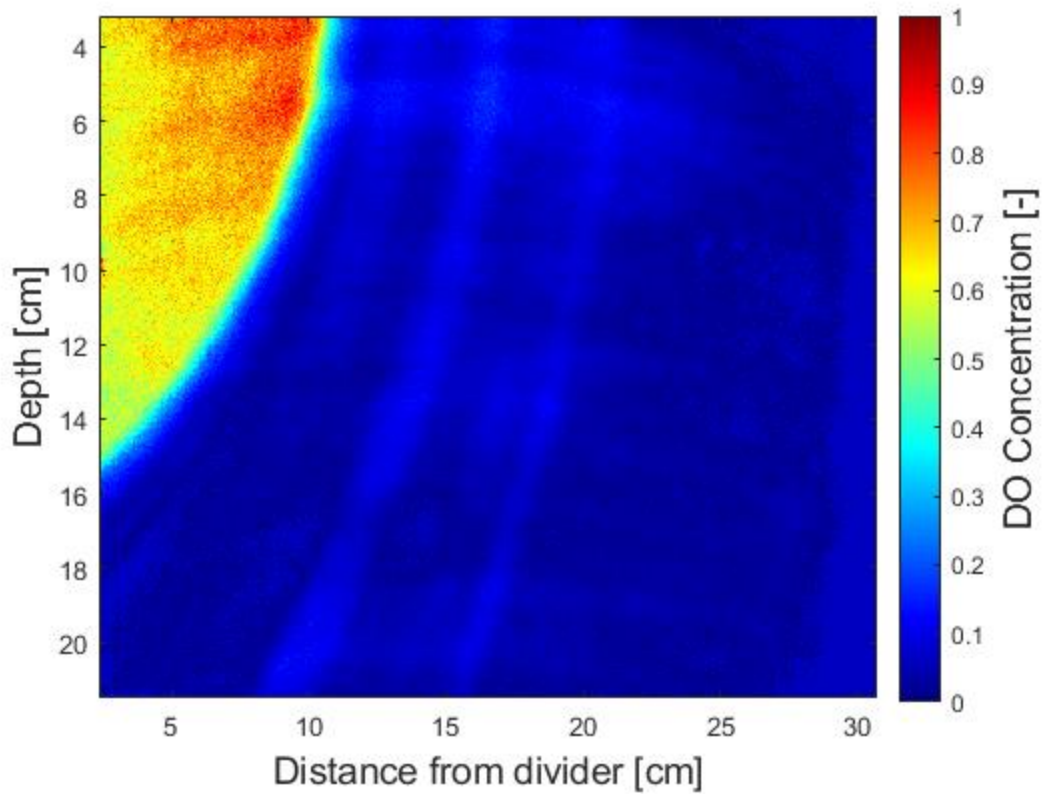
%normalization of concentration profiles
rc1 = bc1(a,b)./cmax1;rc2 = bc2(a,b)./cmax2;rc3 = bc3(a,b)./cmax3;rc4 = bc4(a,b)./cmax4;
rc5 = bc5(a,b)./cmax5;rc6 = bc6(a,b)./cmax6;rc7 = bc7(a,b)./cmax7;rc8 = bc8(a,b)./cmax8;rc9 = bc9(a,b)./cmax9;
rc10 = bc10(a,b)./cmax10;

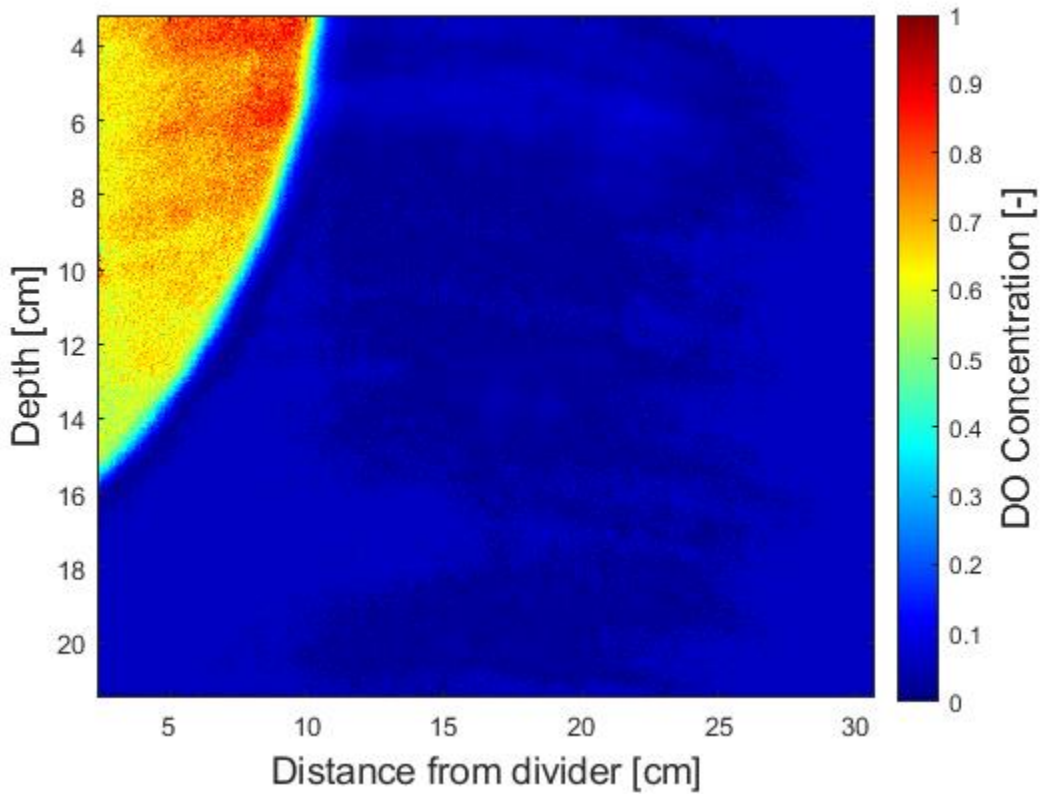
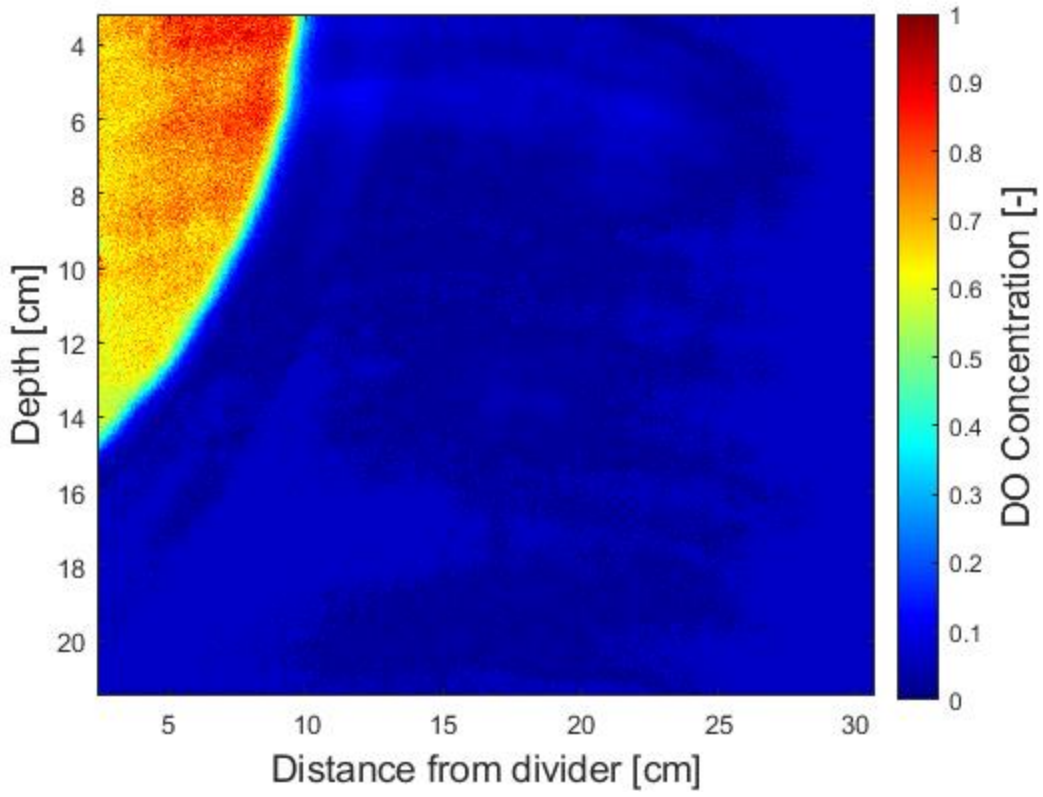
%figure set up of concentration profiles
figure;imagesc(h_axis, v_axis,rc1)
colormap (jet); c=colorbar;
c.Label.String='DO Concentration [-]'; caxis([0.0 1.0]); c.Label.FontSize =14;
xlabel('Distance from divider [cm]',FontSize,14); ylabel('Depth [cm]',FontSize,14)
figure;imagesc(h_axis, v_axis,rc2)
colormap (jet); c=colorbar;
c.Label.String='DO Concentration [-]'; caxis([0.0 1.0]); c.Label.FontSize =14;
xlabel('Distance from divider [cm]',FontSize,14); ylabel('Depth [cm]',FontSize,14)
figure;imagesc(h_axis,v_axis,rc3)
colormap (jet); c=colorbar;
c.Label.String='DO Concentration [-]'; caxis([0.0 1.0]); c.Label.FontSize =14;
xlabel('Distance from divider [cm]',FontSize,14); ylabel('Depth [cm]',FontSize,14)
figure;imagesc(h_axis, v_axis,rc4)
colormap (jet); c=colorbar;
c.Label.String='DO Concentration [-]'; caxis([0.0 1.0]); c.Label.FontSize =14;
xlabel('Distance from divider [cm]',FontSize,14); ylabel('Depth [cm]',FontSize,14)
figure;imagesc(h_axis, v_axis,rc5)
colormap (jet); c=colorbar;
c.Label.String='DO Concentration [-]'; caxis([0.0 1.0]); c.Label.FontSize =14;
xlabel('Distance from divider [cm]',FontSize,14); ylabel('Depth [cm]',FontSize,14)
figure;imagesc(h_axis,v_axis,rc6)
colormap (jet); c=colorbar;
c.Label.String='DO Concentration [-]'; caxis([0.0 1.0]); c.Label.FontSize =14;
xlabel('Distance from divider [cm]',FontSize,14); ylabel('Depth [cm]',FontSize,14)
figure;imagesc(h_axis,v_axis,rc7)
colormap (jet); c=colorbar;
c.Label.String='DO Concentration [-]'; caxis([0.0 1.0]); c.Label.FontSize =14;
xlabel('Distance from divider [cm]',FontSize,14); ylabel('Depth [cm]',FontSize,14)
figure;imagesc(h_axis,v_axis,rc8)
colormap (jet); c=colorbar;
c.Label.String='DO Concentration [-]'; caxis([0.0 1.0]); c.Label.FontSize =14;
xlabel('Distance from divider [cm]',FontSize,14); ylabel('Depth [cm]',FontSize,14)
figure;imagesc(h_axis,v_axis,rc9);
colormap (jet); c=colorbar;
c.Label.String='DO Concentration [-]'; caxis([0.0 1.0]); c.Label.FontSize =14;
xlabel('Distance from divider [cm]',FontSize,14); ylabel('Depth [cm]',FontSize,14)
figure;imagesc(h_axis,v_axis,rc10)
colormap (jet); c=colorbar;
c.Label.String='DO Concentration [-]'; caxis([0.0 1.0]); c.Label.FontSize =14;
xlabel('Distance from divider [cm]',FontSize,14); ylabel('Depth [cm]',FontSize,14)

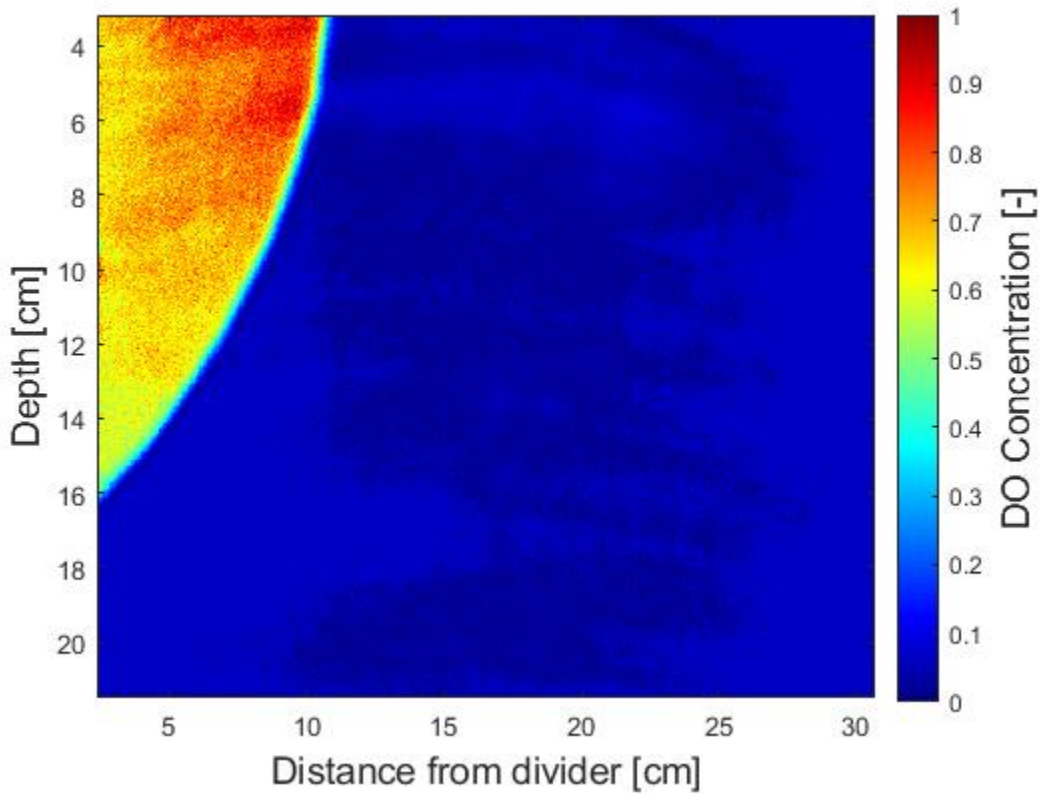
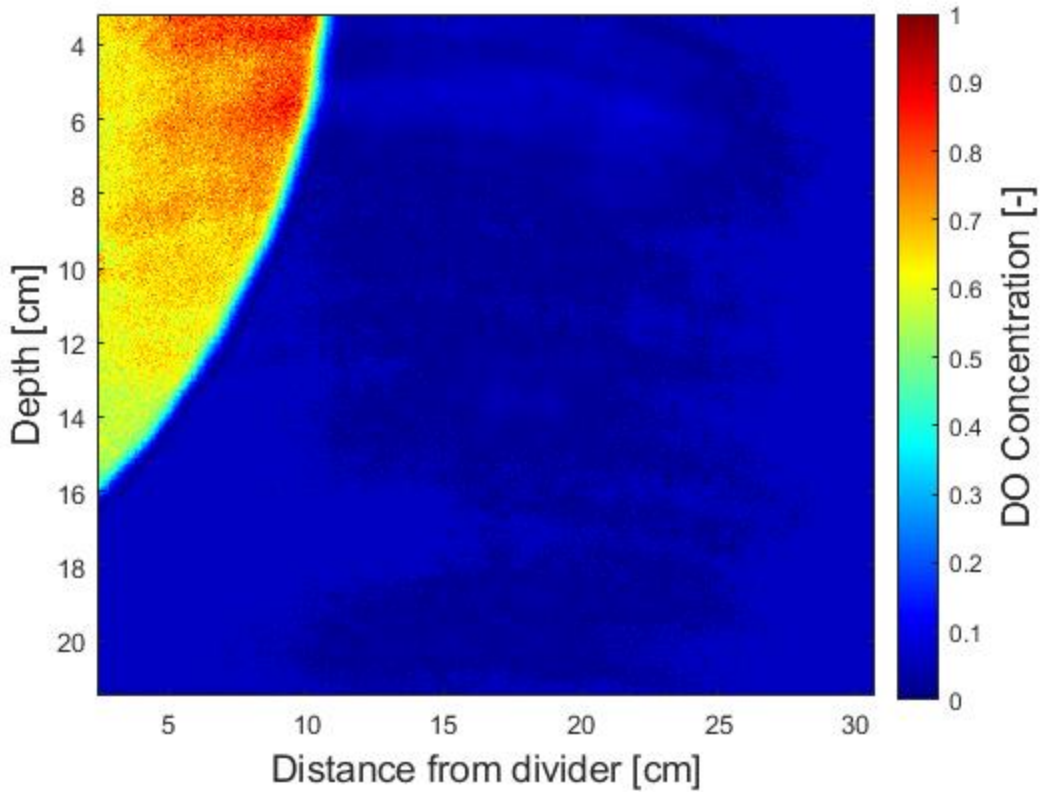
```

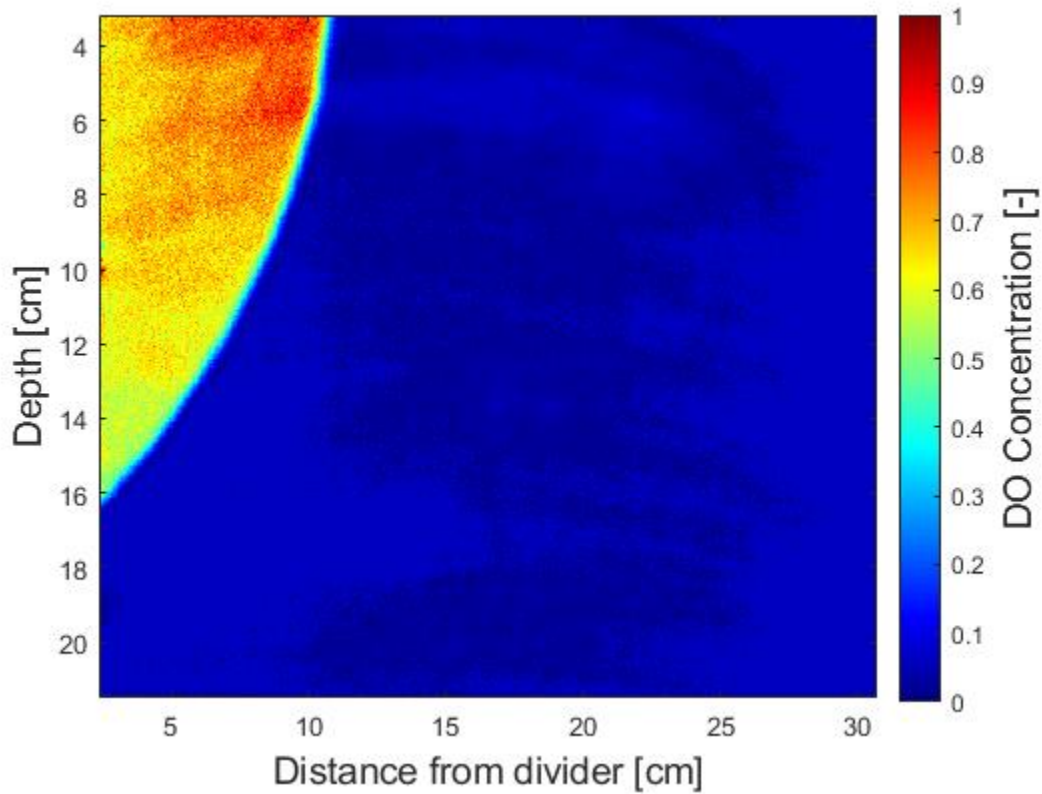
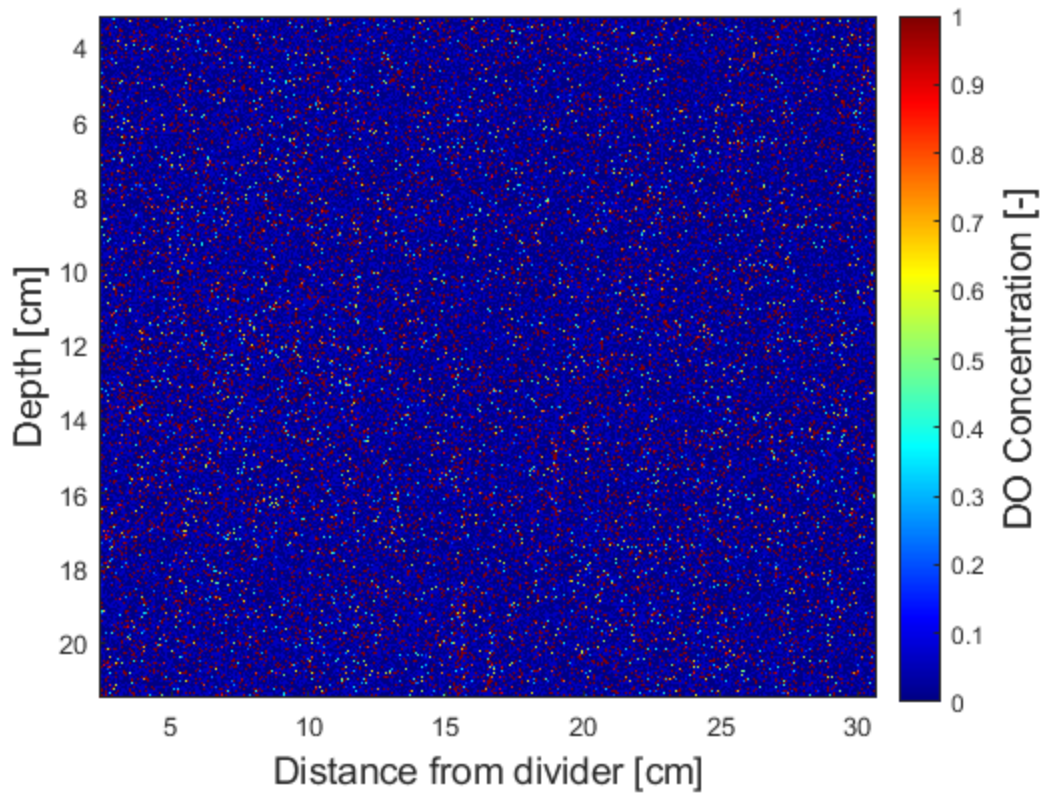
```
%Plot set-up for image in manuscript, edited manually in MATLAB editor
subplot(2,1,1);
imagesc(h_axis(24:304),v_axis(1:322),rc8(1:322,24:304))
colormap (jet); c=colorbar;
c.Label.String='DO Concentration [-]'; caxis([0.0 1.0]); c.Label.FontSize =14;
ylabel('Depth [cm]',FontSize,14)

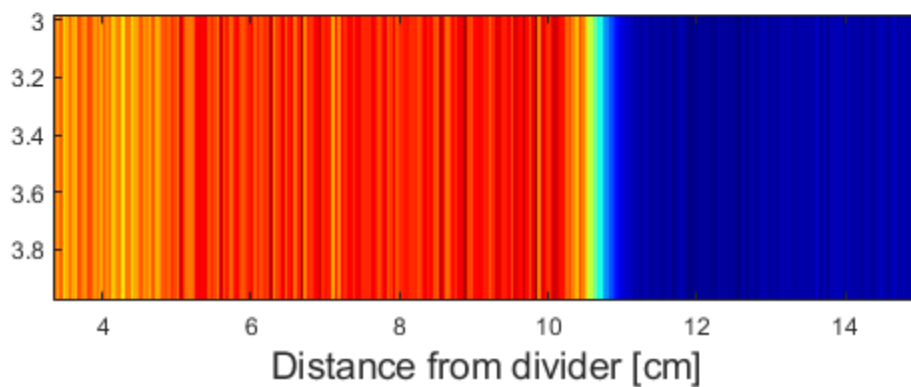
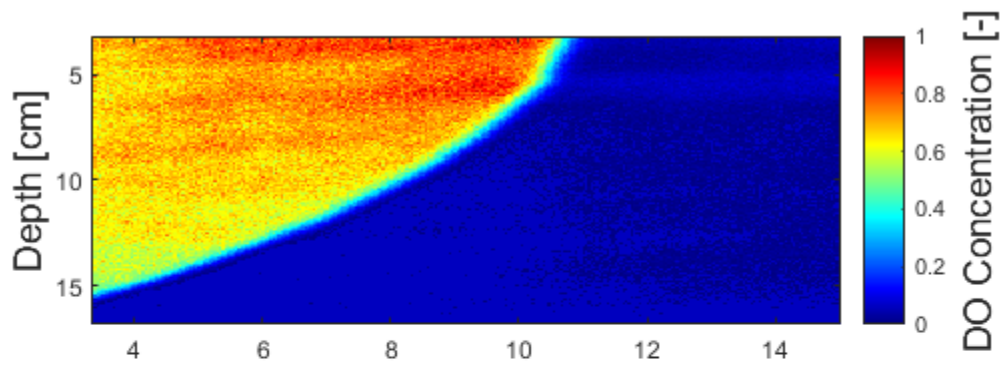
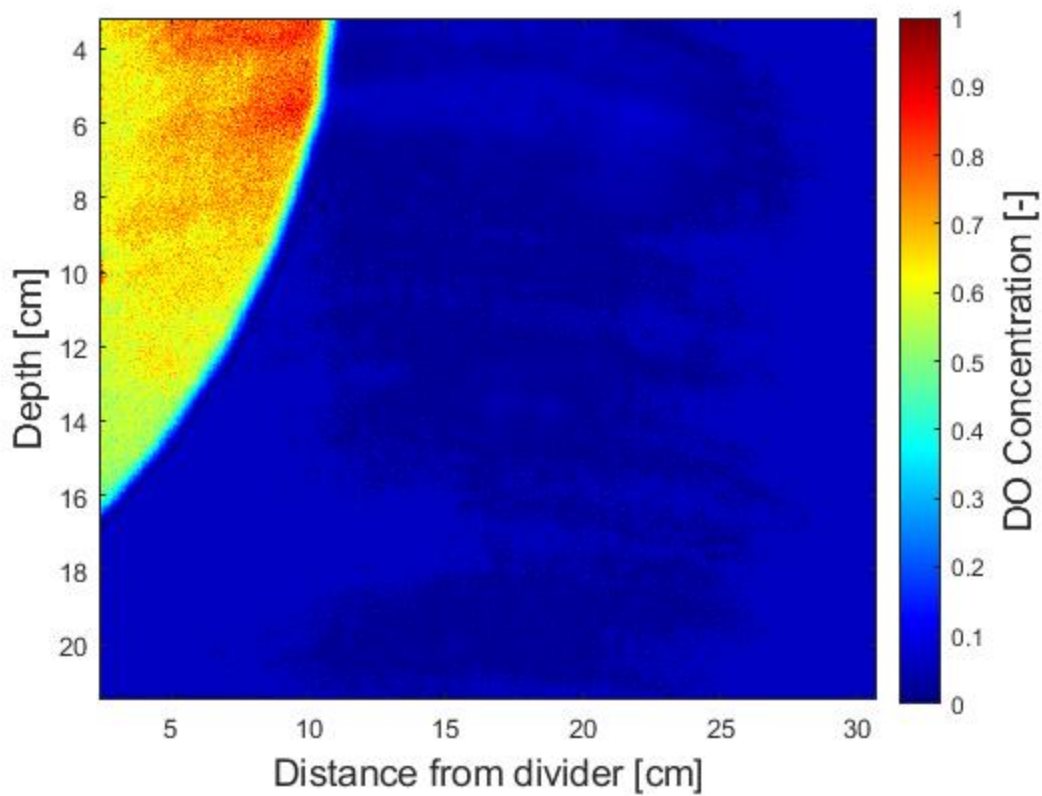
subplot(2,1,2);
imagesc(h_axis(24:304),3.48:3.52,rc8(8,24:304))
xlabel('Distance from divider [cm]',FontSize,14);
```











Controls: Fall 2018, head drop: 4.5cm

clear; clc; close all

%row and column used for cropping images so only optode visible for

%analysis

row=400:1300;

column=600:1950;

%Using Stern-Volmer equation, only need to use green and red channels

%Stern-Volmer equation--modified: $C = (R_0 - R) / (K_{sv} * (R - (\alpha * R_0)))$ where $R = (Red - Green) / Green$

% R_0 is the Ratio when $DO = 0$ mg/L, K_{sv} is the Stern-Volmer quenching constant, and α is the non-quenchable fraction of the light signal

%images are from Look@RGB software

%Ratio of red and green channel (R) for concentration calculation

%time -10 min

Red1 = double(imread('control_4.5cm_0000_S0001_I0001_R.tif'));

Green1 = double(imread('control_4.5cm_0000_S0001_I0001_G.tif'));

Ratio1 = (Red1(row,column)-Green1(row,column))./Green1(row,column);

%time 0 min

Red2 = double(imread('control_4.5cm_0000_S0002_I0001_R.tif'));

Green2 = double(imread('control_4.5cm_0000_S0002_I0001_G.tif'));

Ratio2 = (Red2(row,column)-Green2(row,column))./Green2(row,column);

%time 10 min

Red3 = double(imread('control_4.5cm_0000_S0003_I0001_R.tif'));

Green3 = double(imread('control_4.5cm_0000_S0003_I0001_G.tif'));

Ratio3 = (Red3(row,column)-Green3(row,column))./Green3(row,column);

%time 20 min

Red4 = double(imread('control_4.5cm_0000_S0004_I0001_R.tif'));

Green4 = double(imread('control_4.5cm_0000_S0004_I0001_G.tif'));

Ratio4 = (Red4(row,column)-Green4(row,column))./Green4(row,column);

%time 30 min

Red5 = double(imread('control_4.5cm_0000_S0005_I0001_R.tif'));

Green5 = double(imread('control_4.5cm_0000_S0005_I0001_G.tif'));

Ratio5 = (Red5(row,column)-Green5(row,column))./Green5(row,column);

%time 40 min

Red6 = double(imread('control_4.5cm_0000_S0006_I0001_R.tif'));

Green6 = double(imread('control_4.5cm_0000_S0006_I0001_G.tif'));

Ratio6 = (Red6(row,column)-Green6(row,column))./Green6(row,column);

%time 50 min

Red7 = double(imread('control_4.5cm_0000_S0007_I0001_R.tif'));

Green7 = double(imread('control_4.5cm_0000_S0007_I0001_G.tif'));

Ratio7 = (Red7(row,column)-Green7(row,column))./Green7(row,column);

%time 60 min

Red8 = double(imread('control_4.5cm_0000_S0008_I0001_R.tif'));

Green8 = double(imread('control_4.5cm_0000_S0008_I0001_G.tif'));

Ratio8 = (Red8(row,column)-Green8(row,column))./Green8(row,column);

%time 70 min

```

Red9 = double(imread('control_4.5cm_0000_S0009_I0001_R.tif'));
Green9 = double(imread('control_4.5cm_0000_S0009_I0001_G.tif'));
Ratio9 = (Red9(row,column)-Green9(row,column))./(Green9(row,column));

%time 80 min
Red10 = double(imread('control_4.5cm_0000_S0010_I0001_R.tif'));
Green10 = double(imread('control_4.5cm_0000_S0010_I0001_G.tif'));
Ratio10 = (Red10(row,column)-Green10(row,column))./(Green10(row,column));

%Ro, K and alpha from calibration curve for conc. conversion
Ro= 3.45; K=0.182; alpha=0.08;
%Concentration conversion
conc1= (Ro-Ratio1)./(K.*(Ratio1-(Ro*alpha)));
conc2= (Ro-Ratio2)./(K.*(Ratio2-(Ro*alpha)));
conc3= (Ro-Ratio3)./(K.*(Ratio3-(Ro*alpha)));
conc4= (Ro-Ratio4)./(K.*(Ratio4-(Ro*alpha)));
conc5= (Ro-Ratio5)./(K.*(Ratio5-(Ro*alpha)));
conc6= (Ro-Ratio6)./(K.*(Ratio6-(Ro*alpha)));
conc7= (Ro-Ratio7)./(K.*(Ratio7-(Ro*alpha)));
conc8= (Ro-Ratio8)./(K.*(Ratio8-(Ro*alpha)));
conc9= (Ro-Ratio9)./(K.*(Ratio9-(Ro*alpha)));
conc10= (Ro-Ratio10)./(K.*(Ratio10-(Ro*alpha)));

%function used to set up block images below, based on means of pixels that
%are grouped and replaced
fun = @(block_struct) ...
mean2(block_struct.data) * ones(size(block_struct.data));
bl=2; %block size

bc1 = blockproc(conc1, [bl bl], fun);
bc2 = blockproc(conc2, [bl bl], fun);
bc3 = blockproc(conc3, [bl bl], fun);
bc4 = blockproc(conc4, [bl bl], fun);
bc5 = blockproc(conc5, [bl bl], fun);
bc6 = blockproc(conc6, [bl bl], fun);
bc7 = blockproc(conc7, [bl bl], fun);
bc8 = blockproc(conc8, [bl bl], fun);
bc9 = blockproc(conc9, [bl bl], fun);
bc10 = blockproc(conc10, [bl bl], fun);

%for loop to set up bounds of DO conc.
for i=1:length(row)
    for j=1:length(column)

        if bc1(i,j)>=8.5
            bc1(i,j)= 8.4;
        elseif bc1(i,j)<0
            bc1(i,j)= 0.5;
        end

        if bc2(i,j)>=8.5
            bc2(i,j)= 8.4;
        elseif bc2(i,j)<0
            bc2(i,j)= 0.5;

```

```

end

if bc3(i,j)>=8.5
bc3(i,j)= 8.4;
elseif bc3(i,j)<0
bc3(i,j)= 0.5;
end

if bc4(i,j)>=8.5
bc4(i,j)= 8.4;
elseif bc4(i,j)<0
bc4(i,j)= 0.5;
end

if bc5(i,j)>=8.5
bc5(i,j)= 8.4;
elseif bc5(i,j)<0
bc5(i,j)= 0.5;
end

if bc6(i,j)>=8.5
bc6(i,j)= 8.4;
elseif bc6(i,j)<0
bc6(i,j)= 0.5;
end

if bc7(i,j)>=8.5
bc7(i,j)= 8.4;
elseif bc7(i,j)<0
bc7(i,j)= 0.5;
end

if bc8(i,j)>=8.5
bc8(i,j)= 8.4;
elseif bc8(i,j)<0
bc8(i,j)= 0.5;
end

if bc9(i,j)>=8.5
bc9(i,j)= 8.4;
elseif bc9(i,j)<0
bc9(i,j)= 0.5;
end

if bc10(i,j)>=8.5
bc10(i,j)= 8.4;
elseif bc10(i,j)<0
bc10(i,j)= 0.5;
end

end
end

```

```

%Concentration maximum within optode for normalization
cmax1=max(bc1(:));cmax2=max(bc2(:));cmax3=max(bc3(:));cmax4=max(bc4(:));
cmax5=max(bc5(:));cmax6=max(bc6(:));cmax7=max(bc7(:));cmax8=max(bc8(:));cmax9=max(bc9(:));

```

```

cmax10=max(bc10(:));

%conversion from pixels to cm lengths for optodes, based on manual length
%measurements of planar optodes
a=1:bl:901; %Need to change this if changing amount of rows/columns
b=1:bl:1351;
h_axis =2.6:(bl*0.0210):31; %Need to change this if changing amount of rows/columns
v_axis=3.1:(bl*0.0204):21.5;

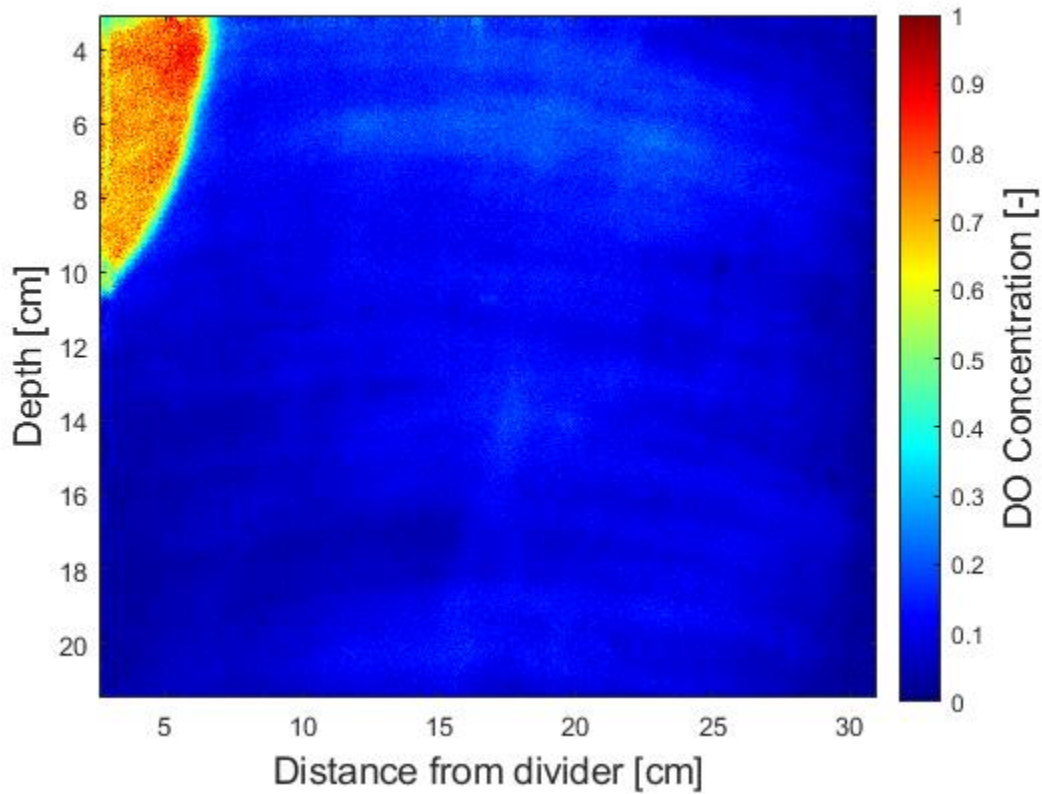
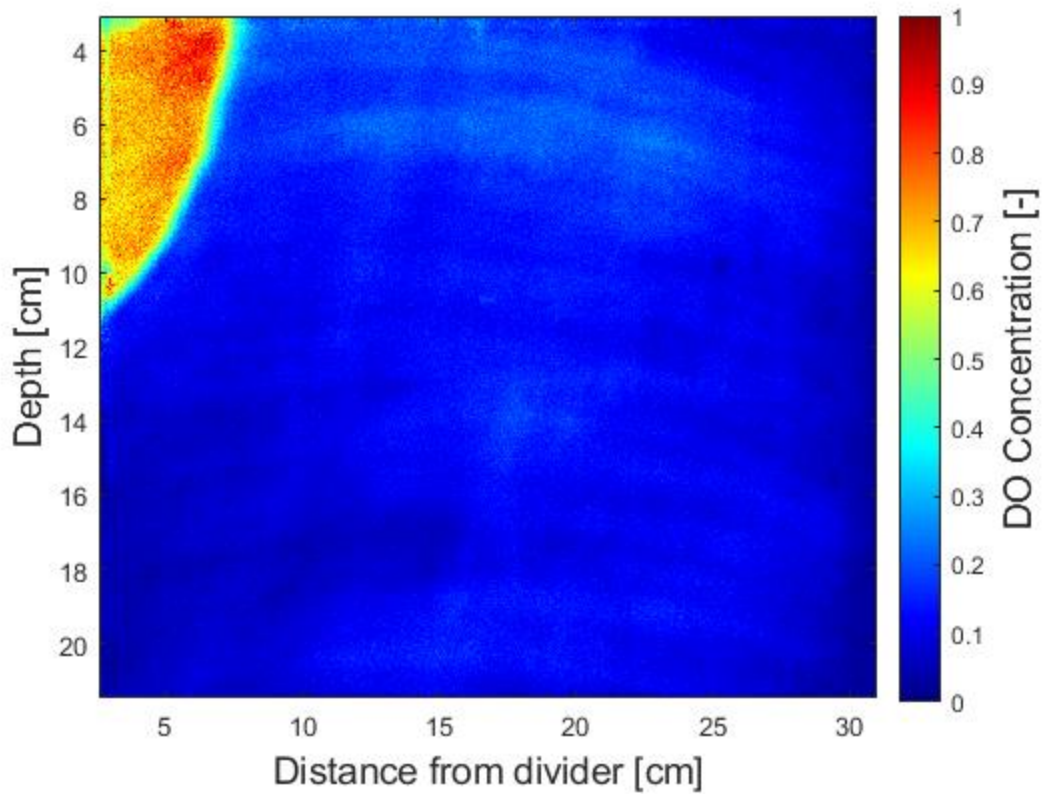
%normalization of concentration profiles
rc1 = bc1(a,b)./cmax1;rc2 = bc2(a,b)./cmax2;rc3 = bc3(a,b)./cmax3;rc4 = bc4(a,b)./cmax4;
rc5 = bc5(a,b)./cmax5;rc6 = bc6(a,b)./cmax6;rc7 = bc7(a,b)./cmax7;rc8 = bc8(a,b)./cmax8;rc9 = bc9(a,b)./cmax9;
rc10 = bc10(a,b)./cmax10;

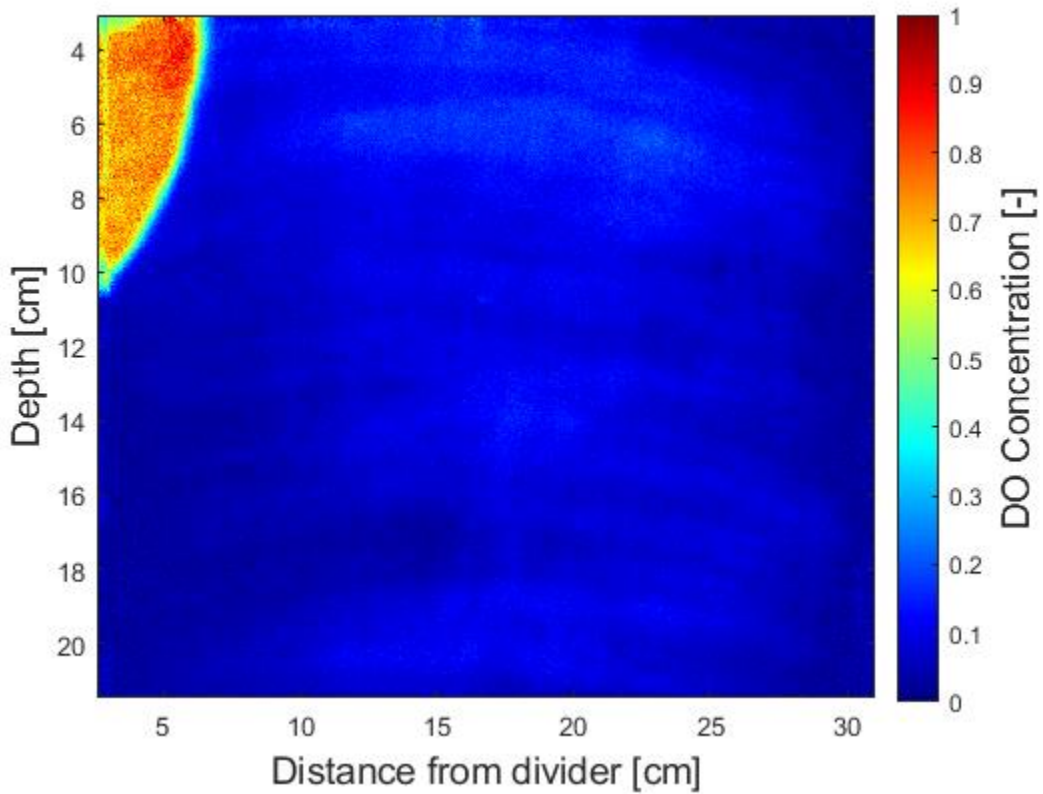
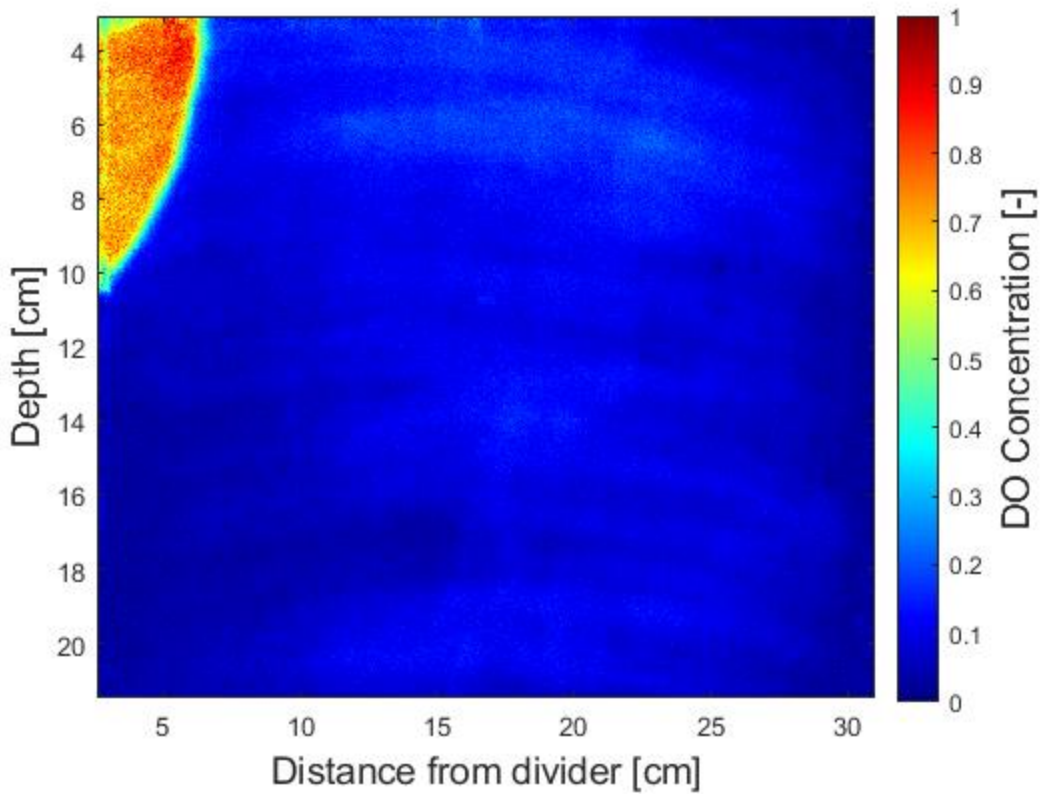
%figures set up of concentration profiles
figure;imagesc(h_axis, v_axis,rc1)
colormap (jet); c=colorbar;
c.Label.String='DO Concentration [-]'; caxis([0.0 1.0]); c.Label.FontSize =14;
xlabel('Distance from divider [cm]',FontSize,14); ylabel('Depth [cm]',FontSize,14)
figure;imagesc(h_axis, v_axis,rc2)
colormap (jet); c=colorbar;
c.Label.String='DO Concentration [-]'; caxis([0.0 1.0]); c.Label.FontSize =14;
xlabel('Distance from divider [cm]',FontSize,14); ylabel('Depth [cm]',FontSize,14)
figure;imagesc(h_axis,v_axis,rc3)
colormap (jet); c=colorbar;
c.Label.String='DO Concentration [-]'; caxis([0.0 1.0]); c.Label.FontSize =14;
xlabel('Distance from divider [cm]',FontSize,14); ylabel('Depth [cm]',FontSize,14)
figure;imagesc(h_axis, v_axis,rc4)
colormap (jet); c=colorbar;
c.Label.String='DO Concentration [-]'; caxis([0.0 1.0]); c.Label.FontSize =14;
xlabel('Distance from divider [cm]',FontSize,14); ylabel('Depth [cm]',FontSize,14)
figure;imagesc(h_axis, v_axis,rc5)
colormap (jet); c=colorbar;
c.Label.String='DO Concentration [-]'; caxis([0.0 1.0]); c.Label.FontSize =14;
xlabel('Distance from divider [cm]',FontSize,14); ylabel('Depth [cm]',FontSize,14)
figure;imagesc(h_axis,v_axis,rc6)
colormap (jet); c=colorbar;
c.Label.String='DO Concentration [-]'; caxis([0.0 1.0]); c.Label.FontSize =14;
xlabel('Distance from divider [cm]',FontSize,14); ylabel('Depth [cm]',FontSize,14)
figure;imagesc(h_axis,v_axis,rc7)
colormap (jet); c=colorbar;
c.Label.String='DO Concentration [-]'; caxis([0.0 1.0]); c.Label.FontSize =14;
xlabel('Distance from divider [cm]',FontSize,14); ylabel('Depth [cm]',FontSize,14)
figure;imagesc(h_axis,v_axis,rc8)
colormap (jet); c=colorbar;
c.Label.String='DO Concentration [-]'; caxis([0.0 1.0]); c.Label.FontSize =14;
xlabel('Distance from divider [cm]',FontSize,14); ylabel('Depth [cm]',FontSize,14)
figure;imagesc(h_axis,v_axis,rc9)
colormap (jet); c=colorbar;
c.Label.String='DO Concentration [-]'; caxis([0.0 1.0]); c.Label.FontSize =14;
xlabel('Distance from divider [cm]',FontSize,14); ylabel('Depth [cm]',FontSize,14)
figure;imagesc(h_axis,v_axis,rc10)
colormap (jet); c=colorbar;
c.Label.String='DO Concentration [-]'; caxis([0.0 1.0]); c.Label.FontSize =14;
xlabel('Distance from divider [cm]',FontSize,14); ylabel('Depth [cm]',FontSize,14)

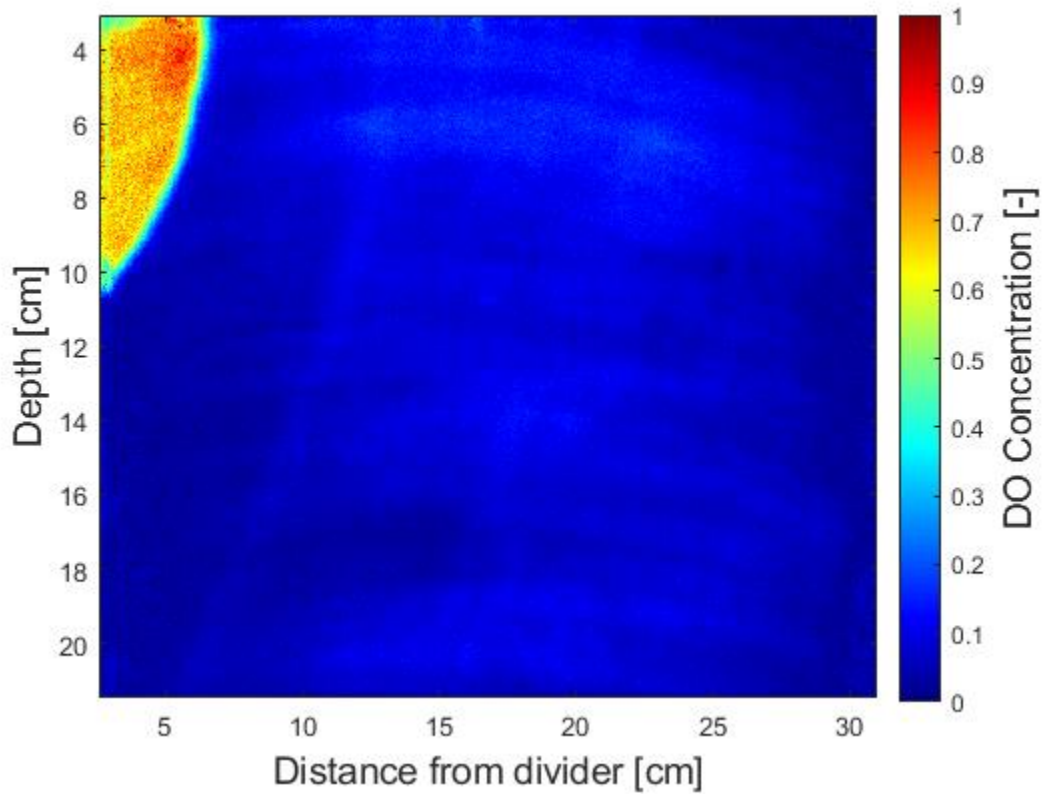
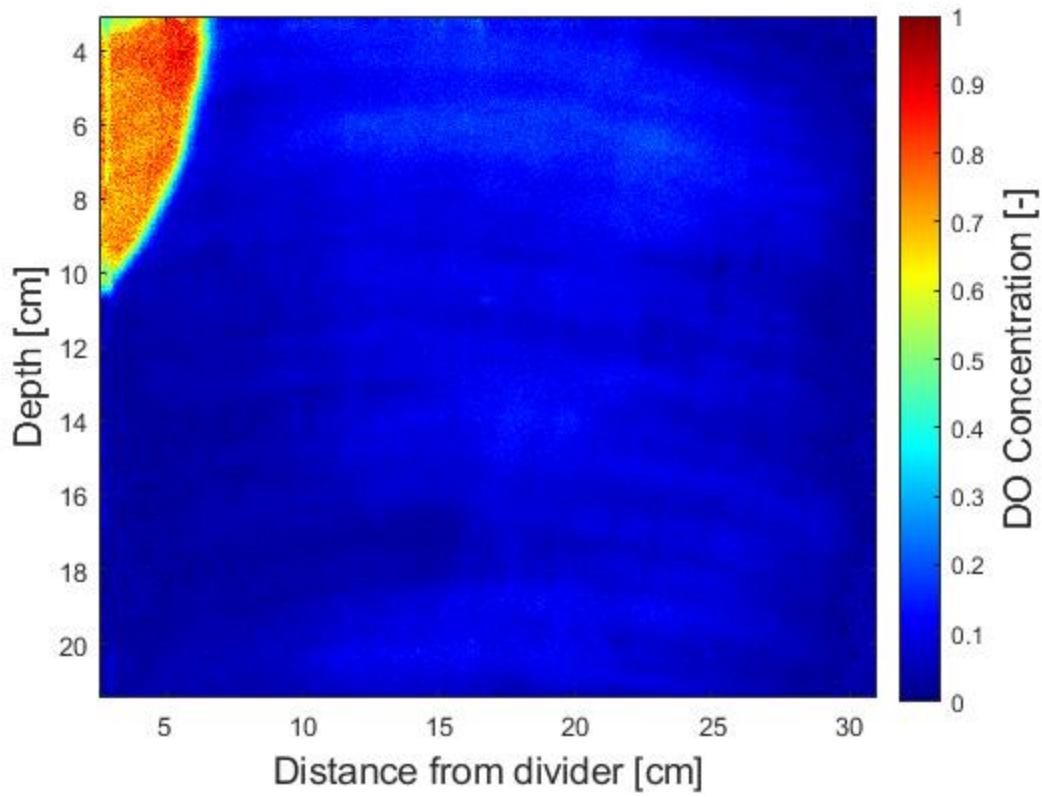
```

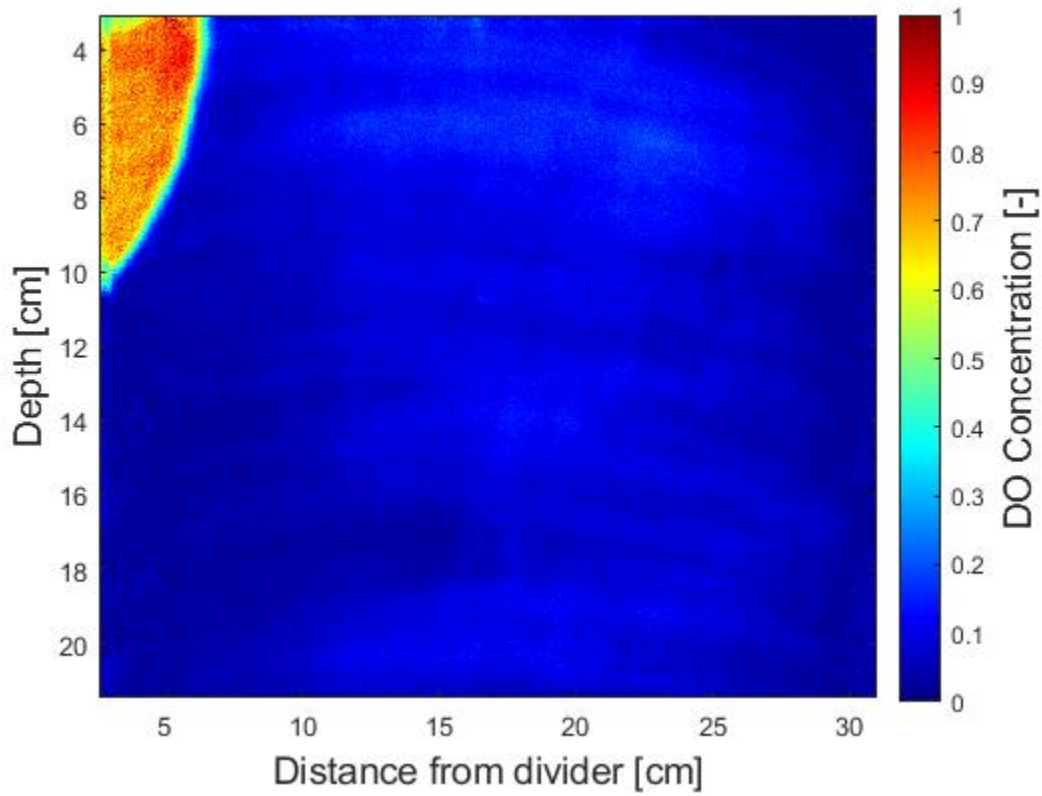
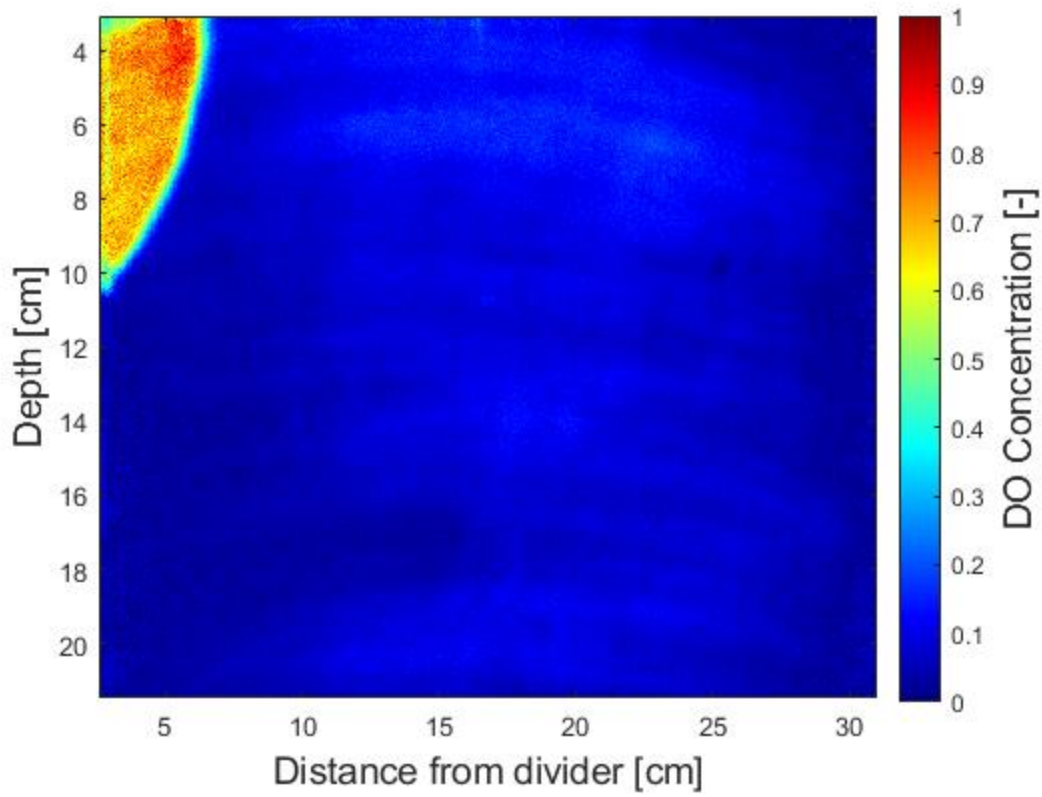
```
%Plot set-up for image in manuscript, edited manually in MATLAB editor
subplot(2,1,1);
imagesc(h_axis(24:296),v_axis(1:322),rc8(1:322,24:296))
colormap (jet); c=colorbar;
c.Label.String='DO Concentration [-]'; caxis([0.0 1.0]); c.Label.FontSize =14;
ylabel('Depth [cm]',FontSize,14)

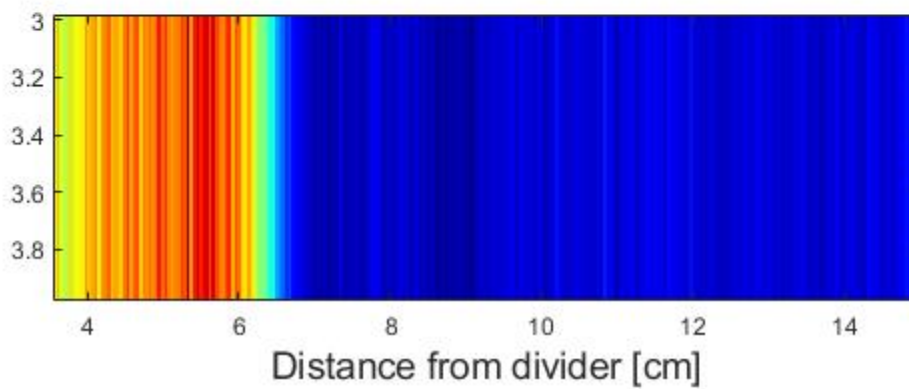
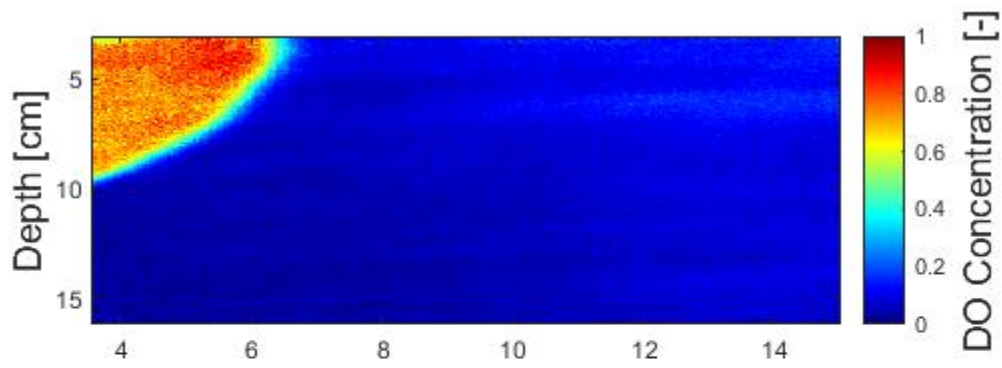
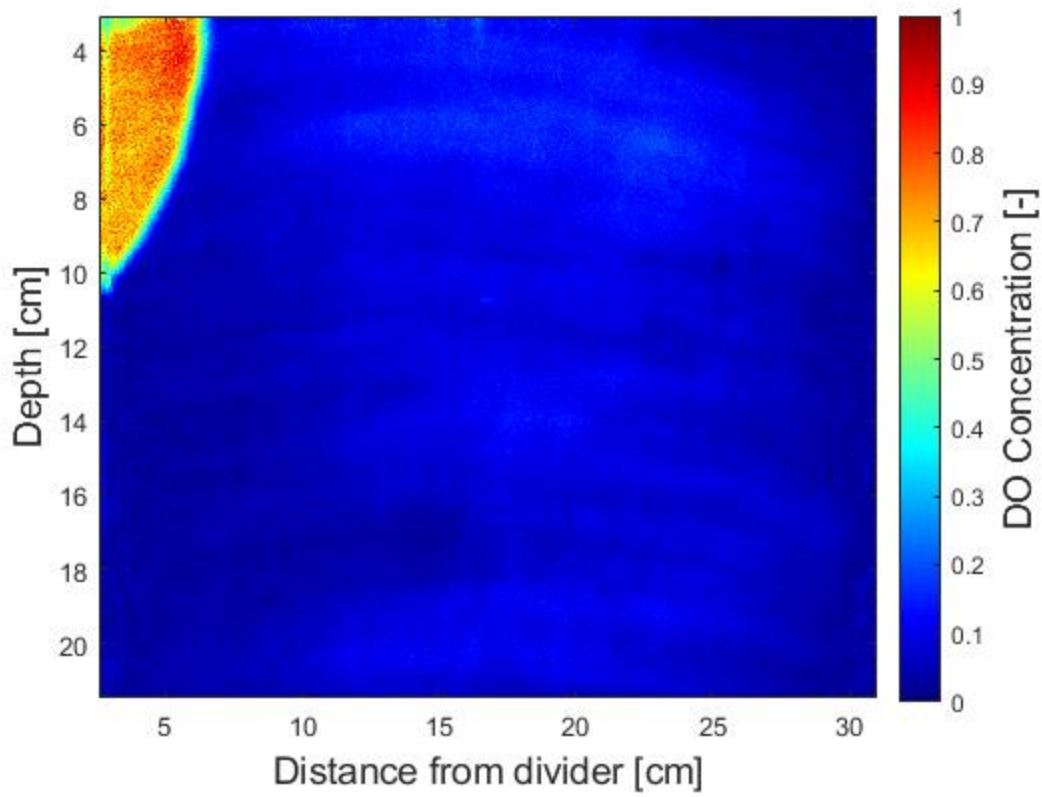
subplot(2,1,2);
imagesc(h_axis(24:296),3.48:3.52,rc8(8,24:296))
xlabel('Distance from divider [cm]',FontSize,14);
```











Abiotic Reaction: Fall 2018, head drop: 4.5cm

clear; clc; close all

%row and column used for cropping images so only optode visible for

%analysis

row=440:1300;

column=600:1960;

%Using Stern-Volmer equation, only need to use green and red channels

%Stern-Volmer equation--modified: $C = (R0-R)/(Ksv*(R-(\alpha*R0)))$ where $R = (Red-Green)/Green$

%R0 is the Ratio when DO=0 mg/L, Ksv is the Stern-Volmer quenching constant, and alpha is the non-quenchable fraction of the light signal

%images are from Look@RGB software

%Ratio of red and green channel (R) for concentration calculation

%time -10 min

Red1 = double(imread('60min_4.5_0000_S0001_I0001_R.tif'));

Green1 = double(imread('60min_4.5_0000_S0001_I0001_G.tif'));

Ratio1 = (Red1(row,column)-Green1(row,column))./(Green1(row,column));

%time 0 min

Red2 = double(imread('60min_4.5_0000_S0002_I0001_R.tif'));

Green2 = double(imread('60min_4.5_0000_S0002_I0001_G.tif'));

Ratio2 = (Red2(row,column)-Green2(row,column))./(Green2(row,column));

%time 10 min

Red3 = double(imread('60min_4.5_0000_S0003_I0001_R.tif'));

Green3 = double(imread('60min_4.5_0000_S0003_I0001_G.tif'));

Ratio3 = (Red3(row,column)-Green3(row,column))./(Green3(row,column));

%time 20 min

Red4 = double(imread('60min_4.5_0000_S0004_I0001_R.tif'));

Green4 = double(imread('60min_4.5_0000_S0004_I0001_G.tif'));

Ratio4 = (Red4(row,column)-Green4(row,column))./(Green4(row,column));

%time 30 min

Red5 = double(imread('60min_4.5_0000_S0005_I0001_R.tif'));

Green5 = double(imread('60min_4.5_0000_S0005_I0001_G.tif'));

Ratio5 = (Red5(row,column)-Green5(row,column))./(Green5(row,column));

%time 40 min

Red6 = double(imread('60min_4.5_0000_S0006_I0001_R.tif'));

Green6 = double(imread('60min_4.5_0000_S0006_I0001_G.tif'));

Ratio6 = (Red6(row,column)-Green6(row,column))./(Green6(row,column));

%time 50 min

Red7 = double(imread('60min_4.5_0000_S0007_I0001_R.tif'));

Green7 = double(imread('60min_4.5_0000_S0007_I0001_G.tif'));

Ratio7 = (Red7(row,column)-Green7(row,column))./(Green7(row,column));

%time 60 min

Red8 = double(imread('60min_4.5_0000_S0008_I0001_R.tif'));

Green8 = double(imread('60min_4.5_0000_S0008_I0001_G.tif'));

Ratio8 = (Red8(row,column)-Green8(row,column))./(Green8(row,column));

```

%time 70 min
Red9 = double(imread('60min_4.5_0000_S0009_I0001_R.tif'));
Green9 = double(imread('60min_4.5_0000_S0009_I0001_G.tif'));
Ratio9 = (Red9(row,column)-Green9(row,column))./(Green9(row,column));

%time 80 min
Red10 = double(imread('60min_4.5_0000_S0010_I0001_R.tif'));
Green10 = double(imread('60min_4.5_0000_S0010_I0001_G.tif'));
Ratio10 = (Red10(row,column)-Green10(row,column))./(Green10(row,column));

%Ro, K and alpha from calibration curve for conc. conversion
Ro=3.45; K=0.182; alpha= 0.08;

%Concentration conversion
conc1= (Ro-Ratio1)./(K.*(Ratio1-(Ro*alpha)));
conc2= (Ro-Ratio2)./(K.*(Ratio2-(Ro*alpha)));
conc3= (Ro-Ratio3)./(K.*(Ratio3-(Ro*alpha)));
conc4= (Ro-Ratio4)./(K.*(Ratio4-(Ro*alpha)));
conc5= (Ro-Ratio5)./(K.*(Ratio5-(Ro*alpha)));
conc6= (Ro-Ratio6)./(K.*(Ratio6-(Ro*alpha)));
conc7= (Ro-Ratio7)./(K.*(Ratio7-(Ro*alpha)));
conc8= (Ro-Ratio8)./(K.*(Ratio8-(Ro*alpha)));
conc9= (Ro-Ratio9)./(K.*(Ratio9-(Ro*alpha)));
conc10= (Ro-Ratio10)./(K.*(Ratio10-(Ro*alpha)));

%function used to set up block images below, based on means of pixels that
%are grouped and replaced
fun = @(block_struct) ...
mean2(block_struct.data) * ones(size(block_struct.data));
bl=2; %block size

bc1 = blockproc(conc1, [bl bl], fun);
bc2 = blockproc(conc2, [bl bl], fun);
bc3 = blockproc(conc3, [bl bl], fun);
bc4 = blockproc(conc4, [bl bl], fun);
bc5 = blockproc(conc5, [bl bl], fun);
bc6 = blockproc(conc6, [bl bl], fun);
bc7 = blockproc(conc7, [bl bl], fun);
bc8 = blockproc(conc8, [bl bl], fun);
bc9 = blockproc(conc9, [bl bl], fun);
bc10 = blockproc(conc10, [bl bl], fun);

%for loop to set up bounds of DO conc.
for i=1:length(row)
    for j=1:length(column)

        if bc1(i,j)>=8.5
            bc1(i,j)= 8.4;
        elseif bc1(i,j)<0
            bc1(i,j)= 0.5;
        end
    end
end

```

```
if bc2(i,j)>=8.5
  bc2(i,j)= 8.4;
elseif bc2(i,j)<0
  bc2(i,j)= 0.5;
end
```

```
if bc3(i,j)>=8.5
  bc3(i,j)= 8.4;
elseif bc3(i,j)<0
  bc3(i,j)= 0.5;
end
```

```
if bc4(i,j)>=8.5
  bc4(i,j)= 8.4;
elseif bc4(i,j)<0
  bc4(i,j)= 0.5;
end
```

```
if bc5(i,j)>=8.5
  bc5(i,j)= 8.4;
elseif bc5(i,j)<0
  bc5(i,j)= 0.5;
end
```

```
if bc6(i,j)>=8.5
  bc6(i,j)= 8.4;
elseif bc6(i,j)<0
  bc6(i,j)= 0.5;
end
```

```
if bc7(i,j)>=8.5
  bc7(i,j)= 8.4;
elseif bc7(i,j)<0
  bc7(i,j)= 0.5;
end
```

```
if bc8(i,j)>=8.5
  bc8(i,j)= 8.4;
elseif bc8(i,j)<0
  bc8(i,j)= 0.5;
end
```

```
if bc9(i,j)>=8.5
  bc9(i,j)= 8.4;
elseif bc9(i,j)<0
  bc9(i,j)= 0.5;
end
```

```
if bc10(i,j)>=8.5
  bc10(i,j)= 8.4;
elseif bc10(i,j)<0
  bc10(i,j)= 0.5;
end
```

end

end

```
%Concentration maximum within optode for normalization
cmax1=max(bc1(:));cmax2=max(bc2(:));cmax3=max(bc3(:));cmax4=max(bc4(:));
cmax5=max(bc5(:));cmax6=max(bc6(:));cmax7=max(bc7(:));cmax8=max(bc8(:));cmax9=max(bc9(:));
cmax10=max(bc10(:));

%conversion from pixels to cm lengths for optodes, based on manual length
%measurements of planar optodes
a=1:bl:861; %Need to change this if changing amount of rows/columns
b=1:bl:1361;
h_axis=2.4:(bl*(28.3/1361)):30.7; %Need to change this if changing amount of rows/columns
v_axis=3.2:(bl*(18.3/861)):21.5;

%normalization of concentration profiles
rc1 = bc1(a,b)./cmax1;rc2 = bc2(a,b)./cmax2;rc3 = bc3(a,b)./cmax3;rc4 = bc4(a,b)./cmax4;
rc5 = bc5(a,b)./cmax5;rc6 = bc6(a,b)./cmax6;rc7 = bc7(a,b)./cmax7;rc8 = bc8(a,b)./cmax8;rc9 = bc9(a,b)./cmax9;
rc10 = bc10(a,b)./cmax10;

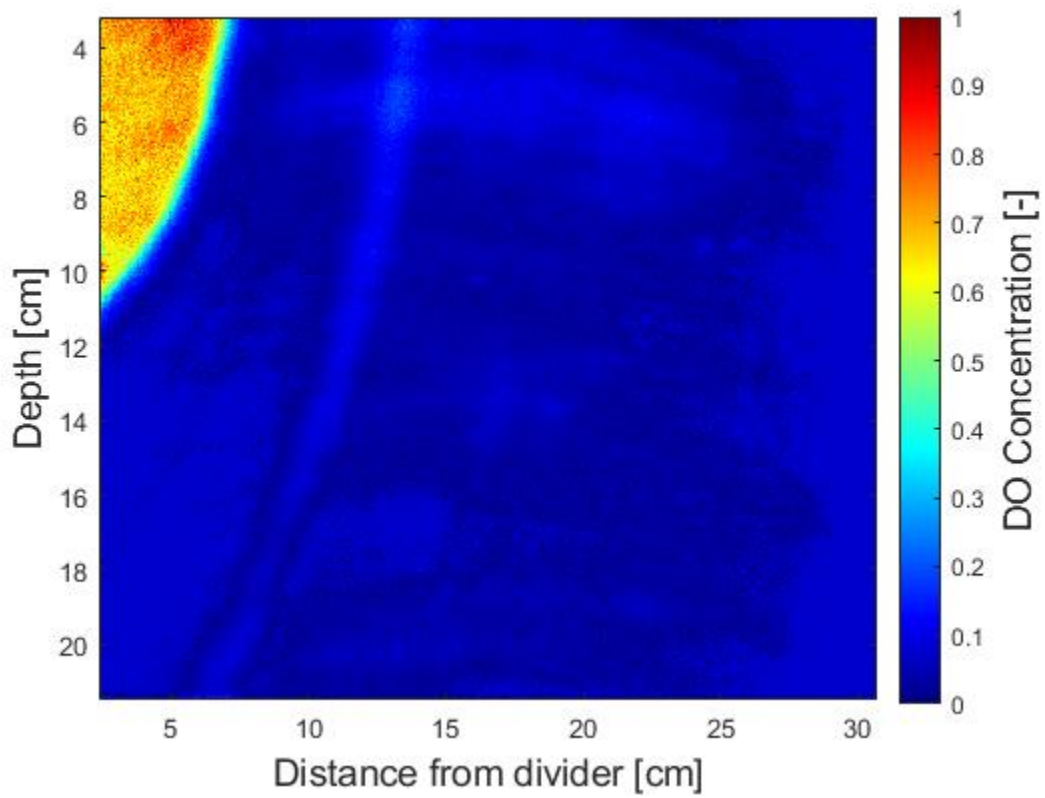
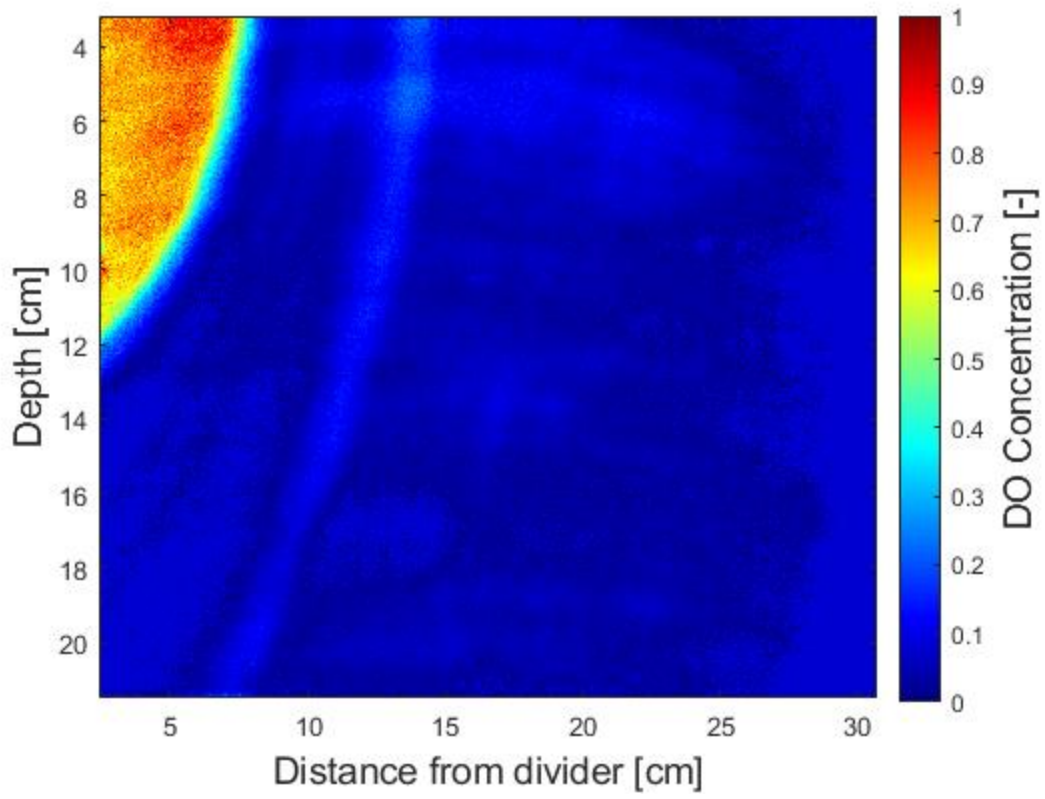
%figures set up of concentration profiles
figure;imagesc(h_axis, v_axis,rc1)
colorbar (jet); c=colorbar;
c.Label.String='DO Concentration [-]'; caxis([0.0 1.0]); c.Label.FontSize =14;
xlabel('Distance from divider [cm]',FontSize,14); ylabel('Depth [cm]',FontSize,14)
figure;imagesc(h_axis, v_axis,rc2)
colorbar (jet); c=colorbar;
c.Label.String='DO Concentration [-]'; caxis([0.0 1.0]); c.Label.FontSize =14;
xlabel('Distance from divider [cm]',FontSize,14); ylabel('Depth [cm]',FontSize,14)
figure;imagesc(h_axis,v_axis,rc3)
colorbar (jet); c=colorbar;
c.Label.String='DO Concentration [-]'; caxis([0.0 1.0]); c.Label.FontSize =14;
xlabel('Distance from divider [cm]',FontSize,14); ylabel('Depth [cm]',FontSize,14)
figure;imagesc(h_axis, v_axis,rc4)
colorbar (jet); c=colorbar;
c.Label.String='DO Concentration [-]'; caxis([0.0 1.0]); c.Label.FontSize =14;
xlabel('Distance from divider [cm]',FontSize,14); ylabel('Depth [cm]',FontSize,14)
figure;imagesc(h_axis, v_axis,rc5)
colorbar (jet); c=colorbar;
c.Label.String='DO Concentration [-]'; caxis([0.0 1.0]); c.Label.FontSize =14;
xlabel('Distance from divider [cm]',FontSize,14); ylabel('Depth [cm]',FontSize,14)
figure;imagesc(h_axis,v_axis,rc6)
colorbar (jet); c=colorbar;
c.Label.String='DO Concentration [-]'; caxis([0.0 1.0]); c.Label.FontSize =14;
xlabel('Distance from divider [cm]',FontSize,14); ylabel('Depth [cm]',FontSize,14)
figure;imagesc(h_axis,v_axis,rc7)
colorbar (jet); c=colorbar;
c.Label.String='DO Concentration [-]'; caxis([0.0 1.0]); c.Label.FontSize =14;
xlabel('Distance from divider [cm]',FontSize,14); ylabel('Depth [cm]',FontSize,14)
figure;imagesc(h_axis,v_axis,rc8)
colorbar (jet); c=colorbar;
c.Label.String='DO Concentration [-]'; caxis([0.0 1.0]); c.Label.FontSize =14;
xlabel('Distance from divider [cm]',FontSize,14); ylabel('Depth [cm]',FontSize,14)
figure;imagesc(h_axis,v_axis,rc9)
colorbar (jet); c=colorbar;
c.Label.String='DO Concentration [-]'; caxis([0.0 1.0]); c.Label.FontSize =14;
```

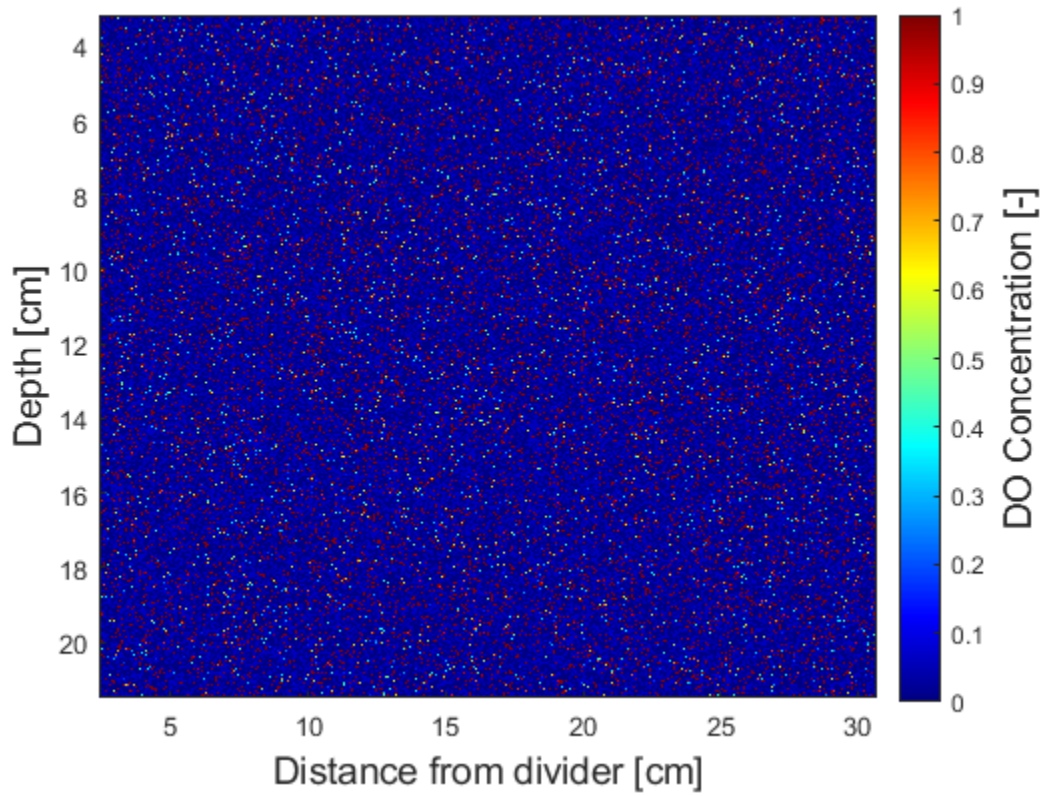
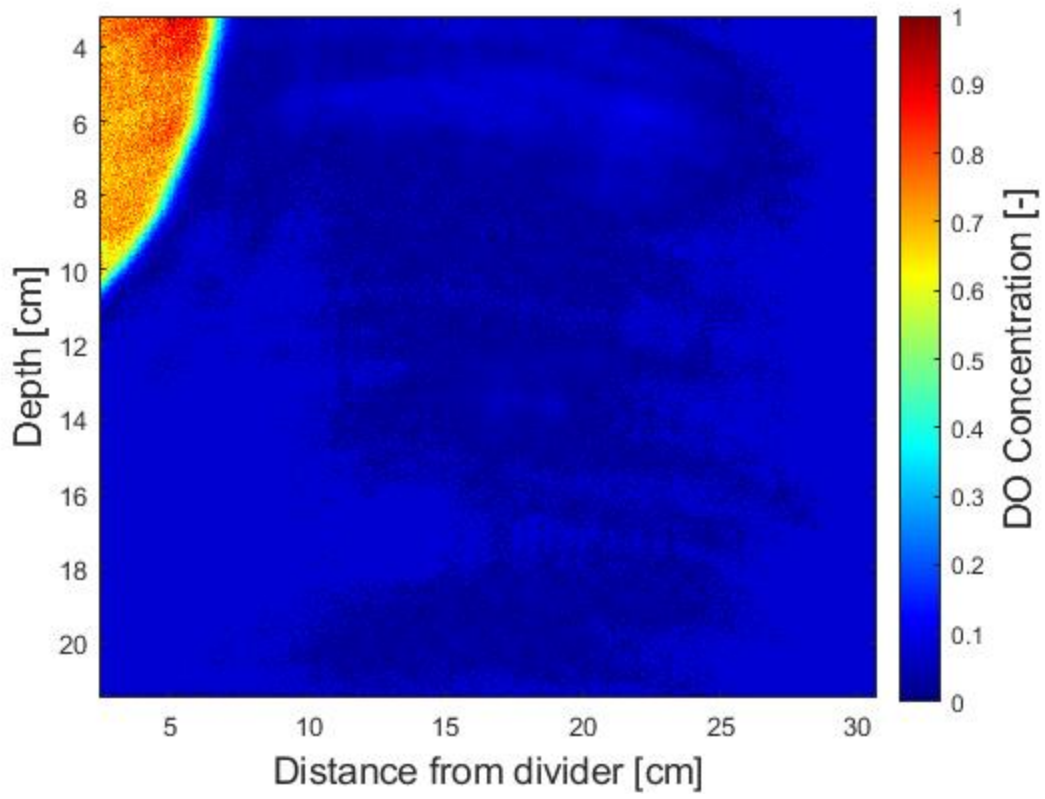
```
xlabel('Distance from divider [cm]',FontSize,14); ylabel('Depth [cm]',FontSize,14)
figure;imagesc(h_axis,v_axis,rc10)
colormap (jet); c=colorbar;
c.Label.String='DO Concentration [-]'; caxis([0.0 1.0]); c.Label.FontSize =14;
xlabel('Distance from divider [cm]',FontSize,14); ylabel('Depth [cm]',FontSize,14)
```

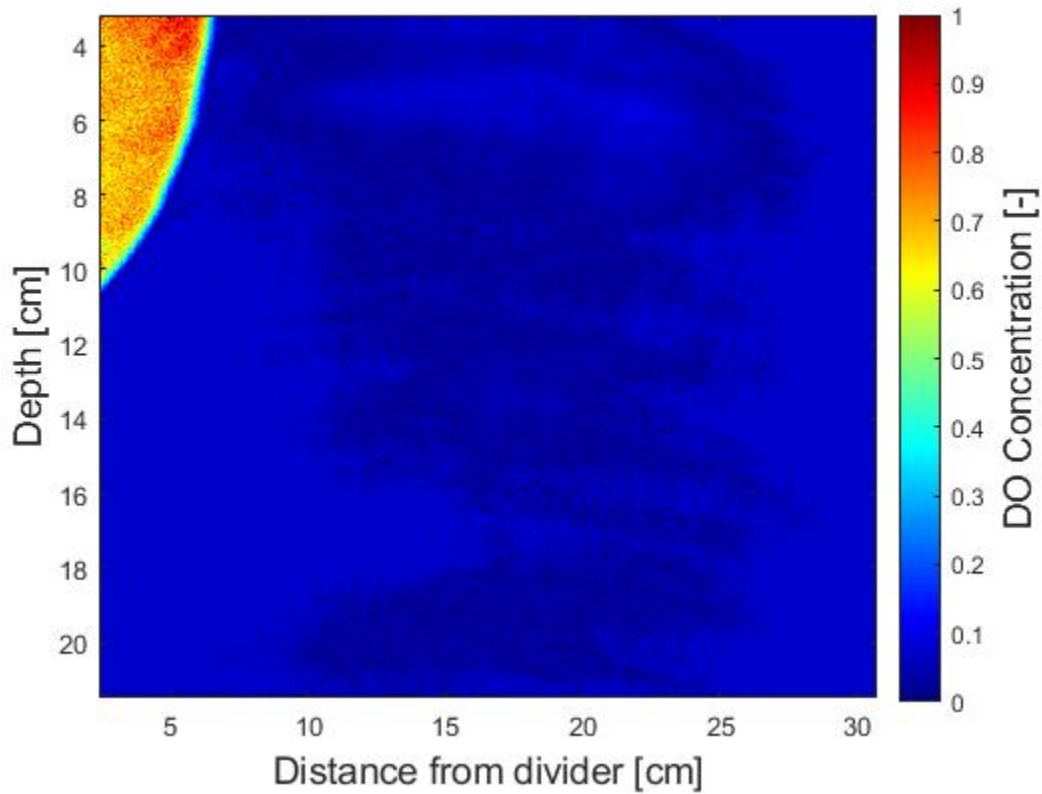
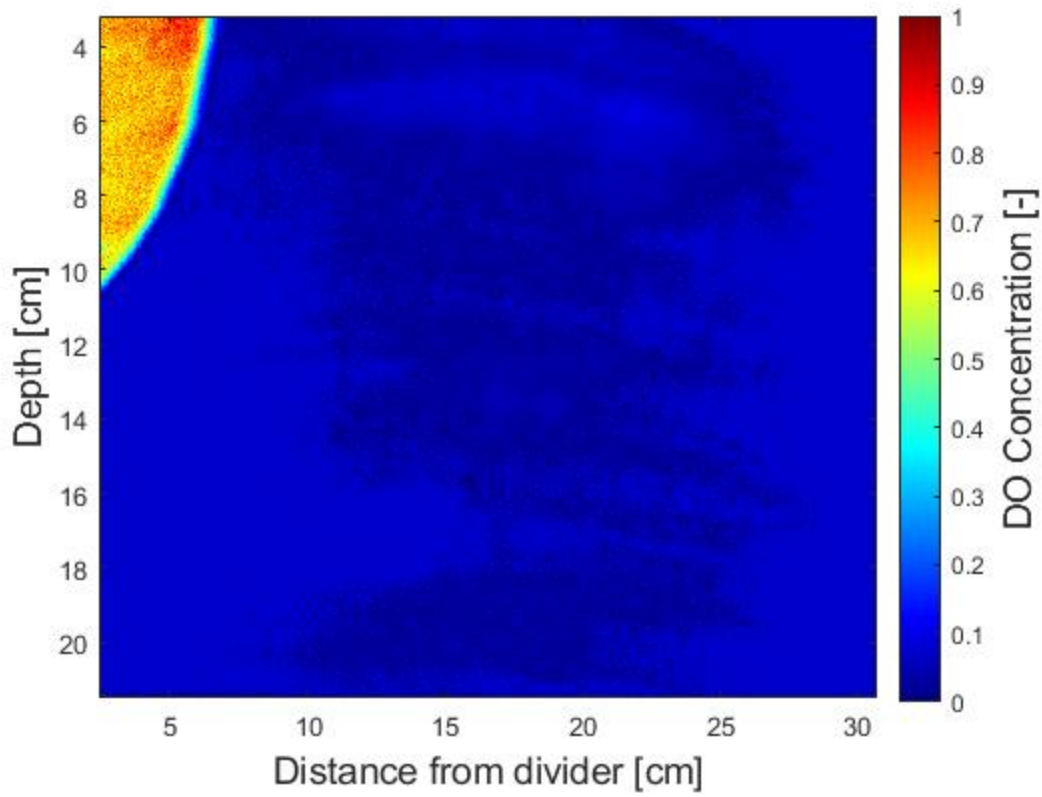
%Plot set-up for image in manuscript, edited manually in MATLAB editor

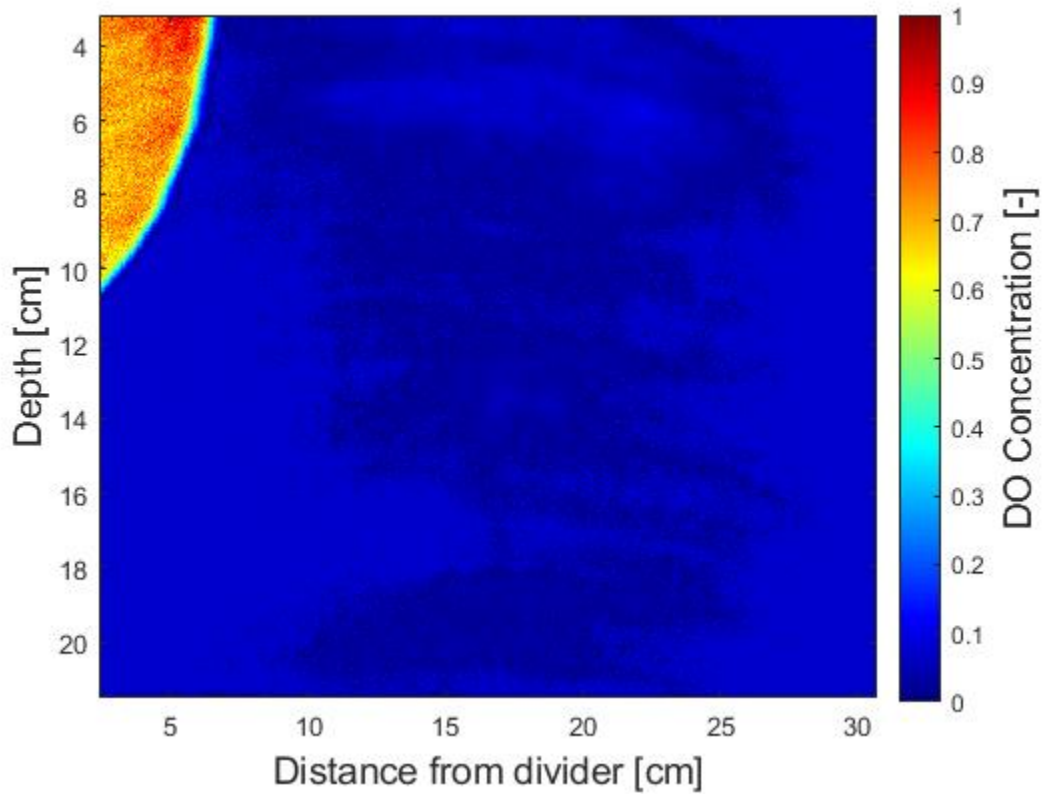
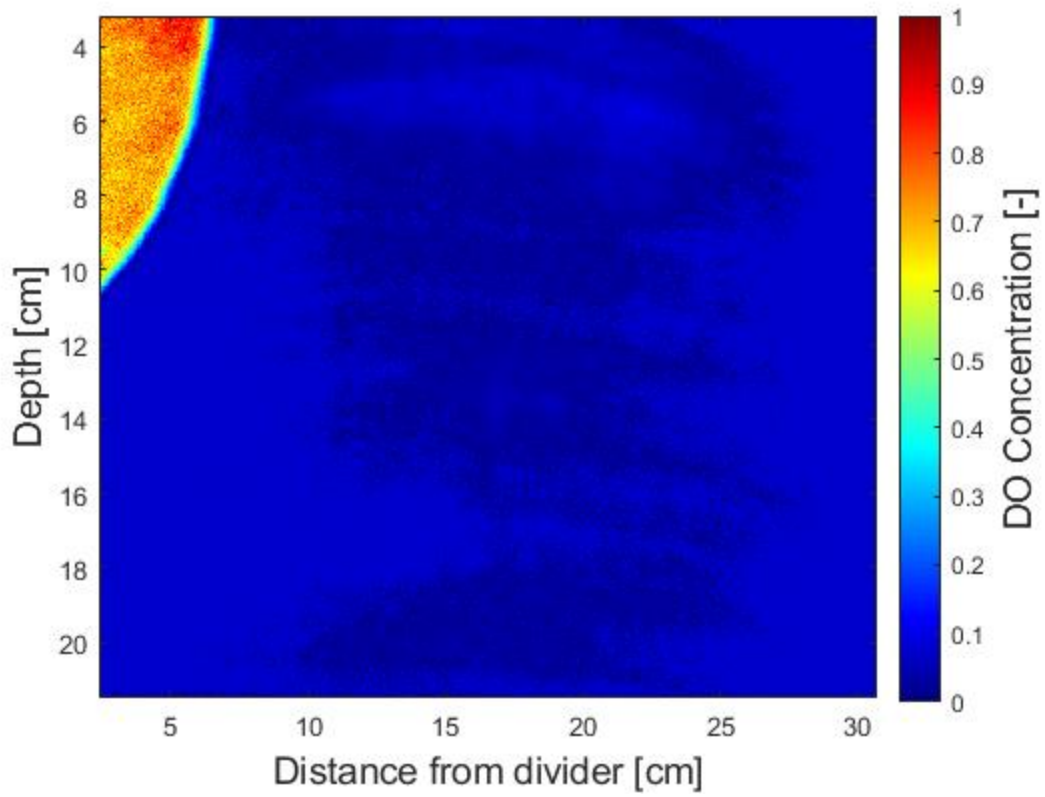
```
subplot(2,1,1);
imagesc(h_axis(24:304),v_axis(1:322),rc8(1:322,24:304))
colormap (jet); c=colorbar;
c.Label.String='DO Concentration [-]'; caxis([0.0 1.0]); c.Label.FontSize =14;
ylabel('Depth [cm]',FontSize,14)
```

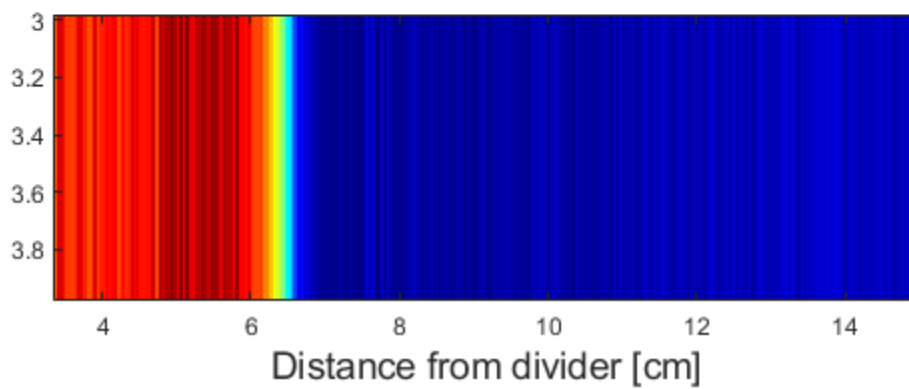
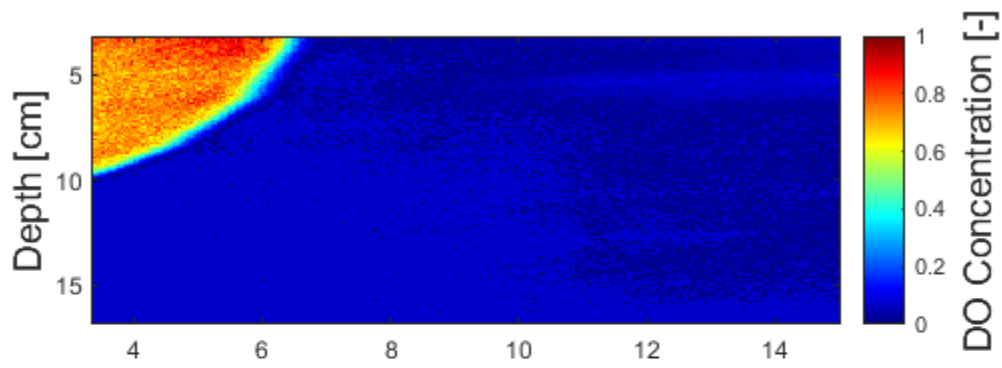
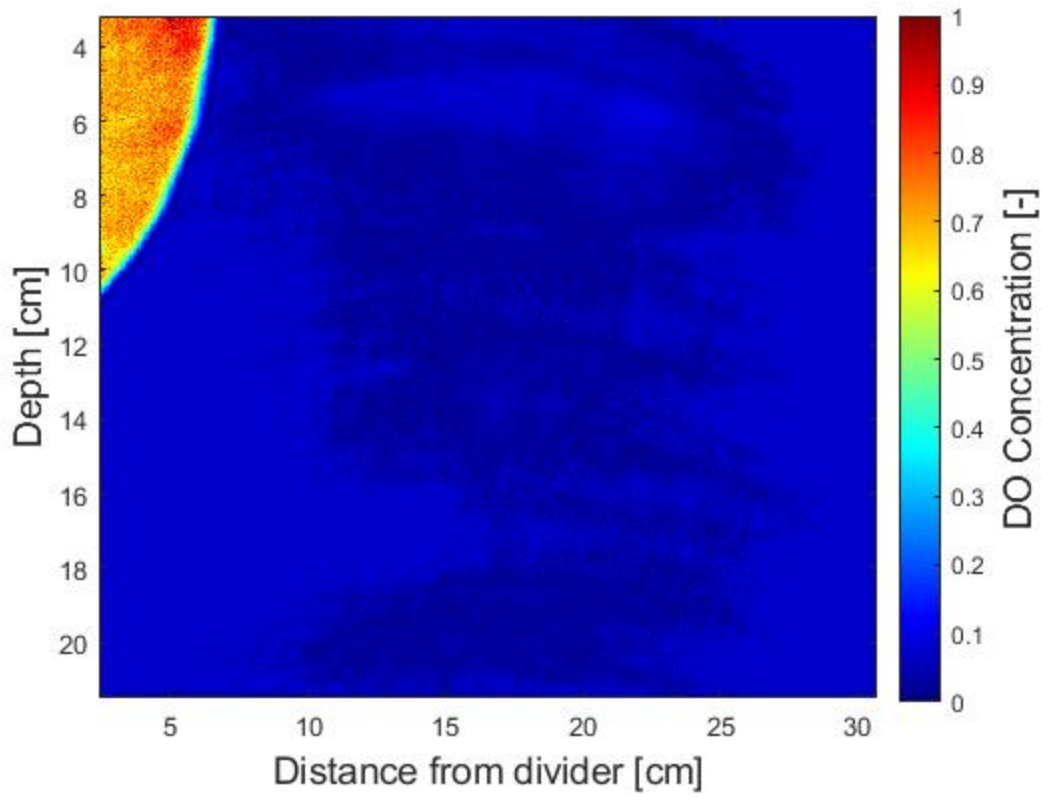
```
subplot(2,1,2);
imagesc(h_axis(24:304),3.48:3.52,rc8(8,24:304))
xlabel('Distance from divider [cm]',FontSize,14);
```











Appendix D. Microbial Growth/Respiration in Abiotic Experiments

Work was performed Summer 2017 with help from Multicultural Academic Opportunities Program Research Experience for Undergraduates (MAOP REU) student Ridi Barua to test microbial growth kinetics/growth/feasibility.

Experimental Method:

Quantify Dissolved Oxygen (DO) Respiration under a Range of Conditions

Sodium Sulfit	Blank Solution	Dextrose
<ul style="list-style-type: none">• A positive control• Depletes oxygen	<ul style="list-style-type: none">• Nothing is added• Used as control	<ul style="list-style-type: none">• A carbon source• Food for microbes

7

Materials

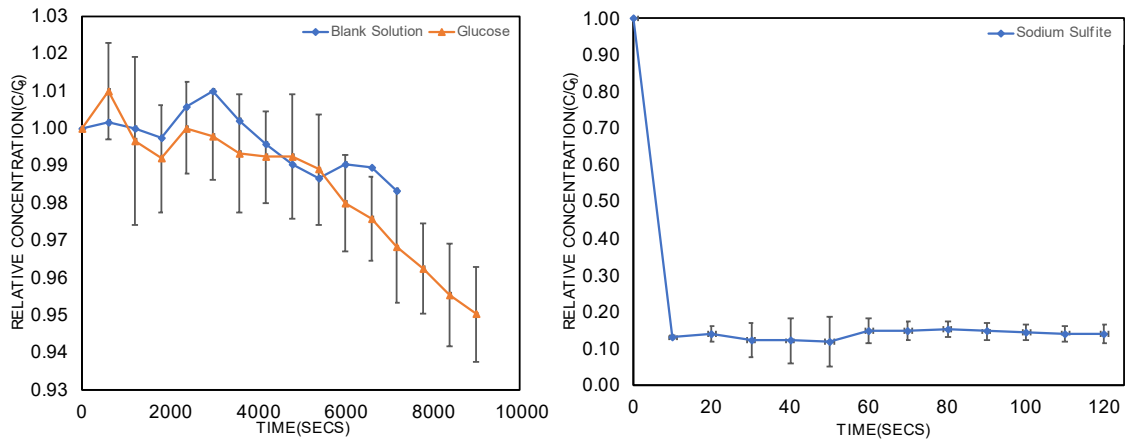
- Dissolved Oxygen Meter
- Dissolved Oxygen Probe
- 300mL BOD bottle
- Sand samples
- Stir plate and stir bar inside the sand sample



Oxygen Uptake experiment: Ridi Barua⁴

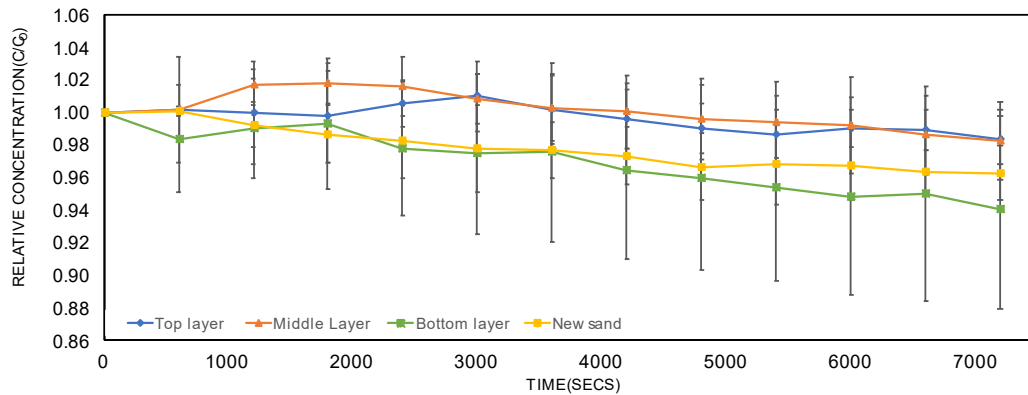
8

Results: Sand Sample from Mesocosm (Top Layer)



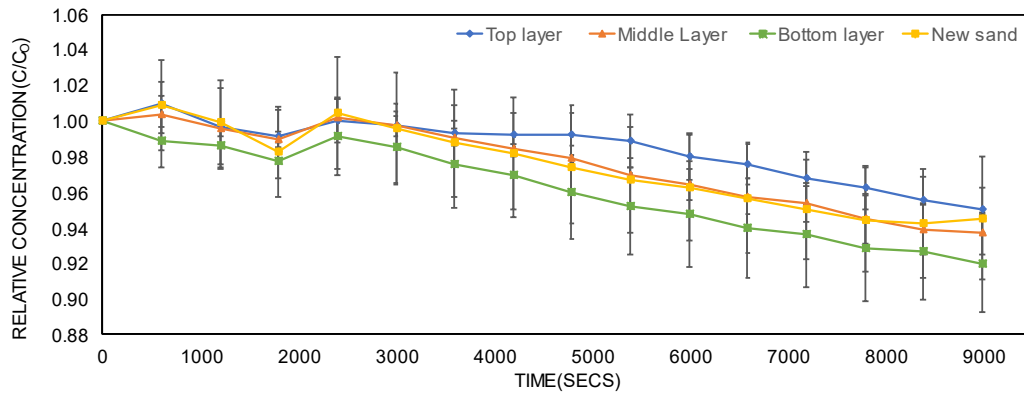
9

Results: Blank Solution



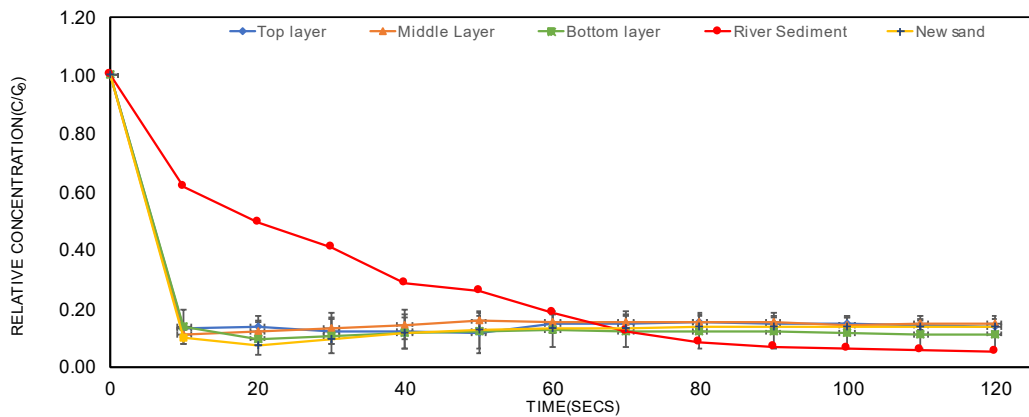
10

Results: Glucose



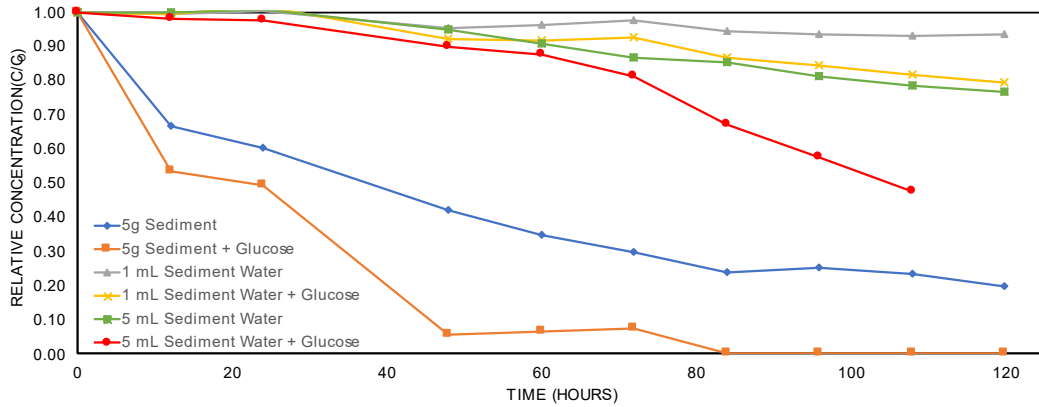
11

Results: Sodium Sulfite & River Sediment



12

Results: Sediment Sample



13

Average Dissolved Oxygen (DO) Respiration

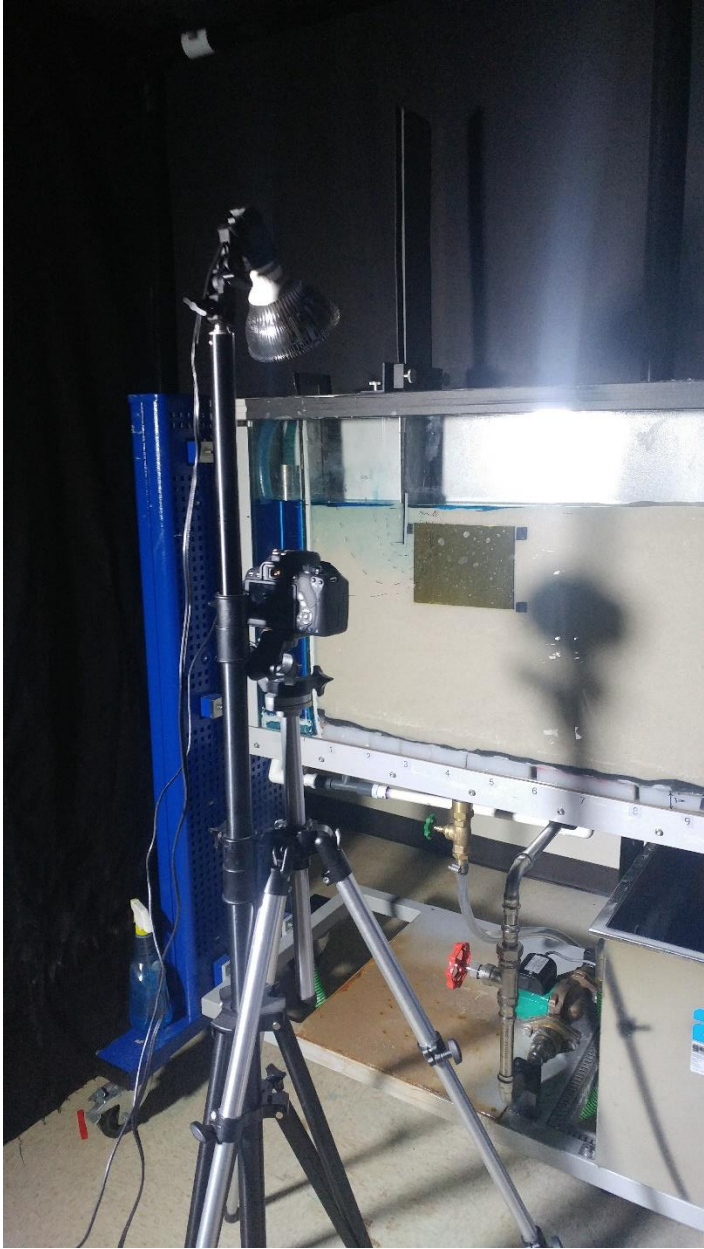
Samples	Experiments of DO Consumption	
	Blank (mg)	Dextrose (mg)
Top	0.04	0.10
Middle	0.04	0.07
Bottom	0.12	0.16
New Sand	0.07	0.10
5g of stream sediment	1.30	1.42
1mL of stream water	0.13	0.39
5mL of stream water	0.44	1.24

14

Appendix E. Additional set-up images for laboratory simulated mixing-dependent abiotic reaction







Appendix F. Trials of Microbial Respiration for Biotic Experiments

Work was performed Spring 2018 with help from Honors student Adrianna Weber to test microbial activity from different sites and conditions.

Procedure - Sites

- New River
- Strouble's Creek:
 - Webb Branch
 - Horse Farm



Procedure – Dissolved Oxygen (D.O.) experiments

- Trials:
 - 1) 10 g New River with 10 g Dextrose
 - 2) 10 g Webb Branch with 10 g Dextrose
 - 3) 10 g Horse Farm with 10 g Dextrose
 - 4) Varying Concentrations of Horse Farm
 - No clean sediment
 - No stream sediment
 - 1-1
 - 1-4
 - 3-4
 - Varying Dextrose Amounts – 1 gram and 2.5 grams

Procedure – Dissolved Oxygen (D.O.) experiments

- Bench Beaker Experiments
 - D.O. Meter and D.O. Probe
 - 300 mL Distilled Water
 - Stir Plate



Procedure – Total Organic Carbon (TOC) Analyzer

- Trials:
 - Undiluted
 - 1-10 Dilution
 - 1-10 Dilution and Filtered (.45 μm)
- Collected Samples Every 15 Minutes
 - Set in instrument for analysis

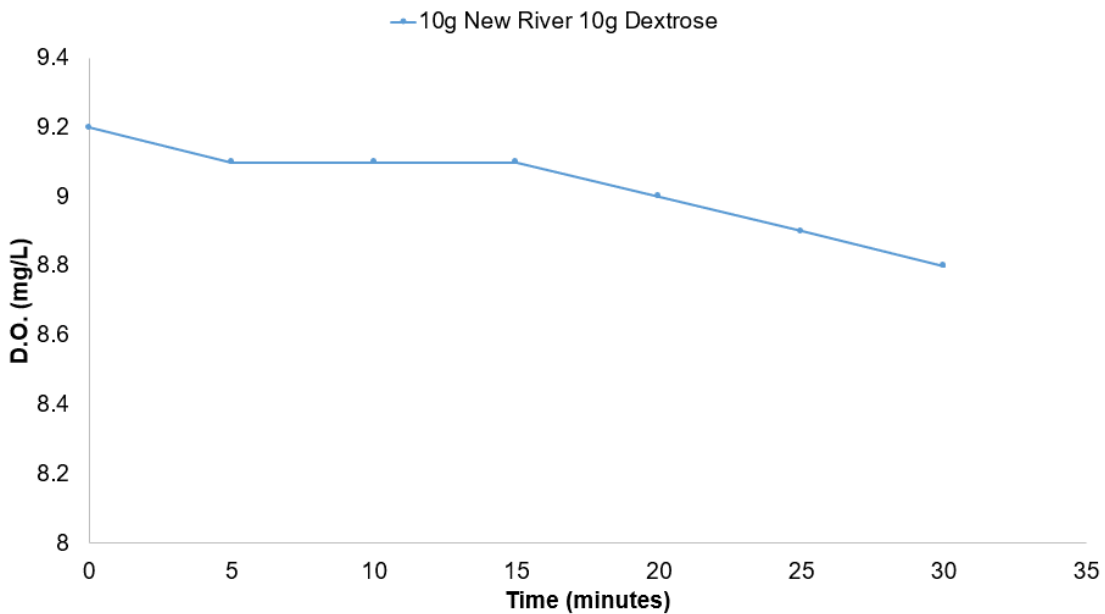


Figure 1: Plot of Time Versus D.O. for 10 g of New River Sediment and 10 g of Dextrose

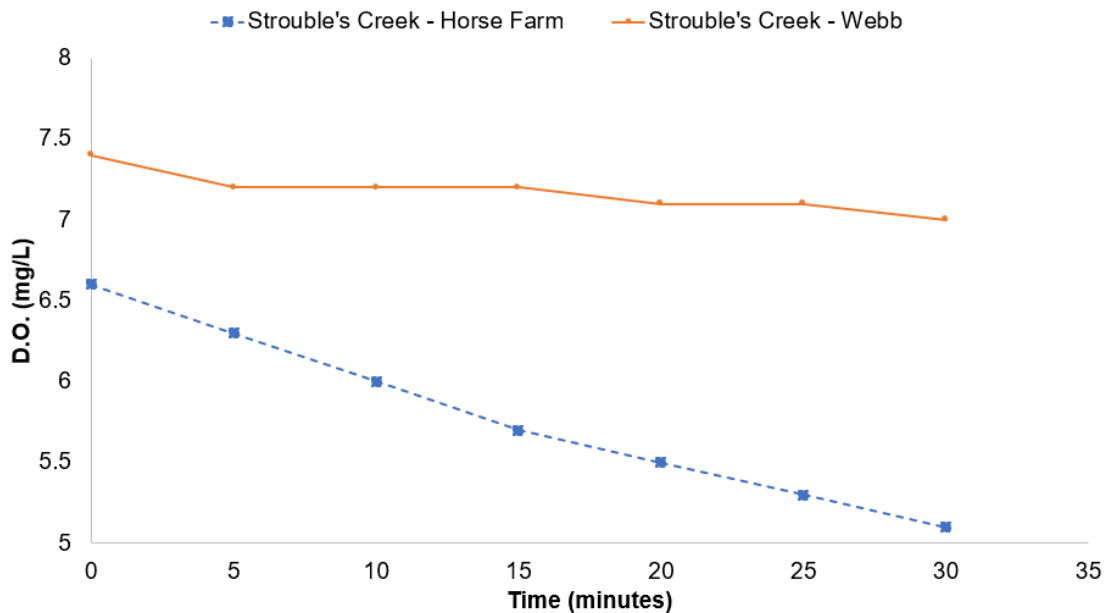


Figure 2: Plot of Time Versus D.O. for 10 g of Strouble's Creek Sediment and 10 g of Dextrose

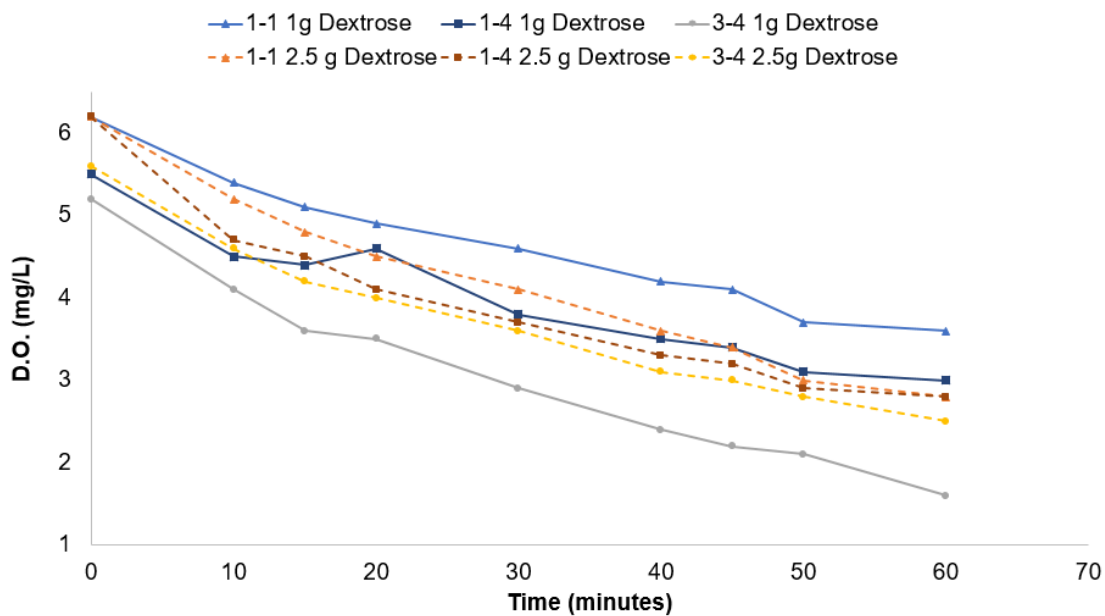


Figure 3: Plot of Time Versus D.O. for Strouble's Creek – Horse Farm with 1 g and 2.5 g of Dextrose

Table 1: Differential Filtered TOC of 1 g Dextrose

Time (Minutes)	Differential TOC				
	10 g Horse Farm	10 g Clean Sand	1-1	1-4	3-4
Dextrose Control	939.3	1258.0	1422.0	1258.0	1422.0
15	+398.7	+13.0	-9.0	+175.0	-210.0
30	-23.0	+105.0	-110.0	-62.0	+34.0
45	+51.0	----	+3.0	+265.0	+96.0
60	-35.0	-9.0	+14.0	+220.0	-90.0

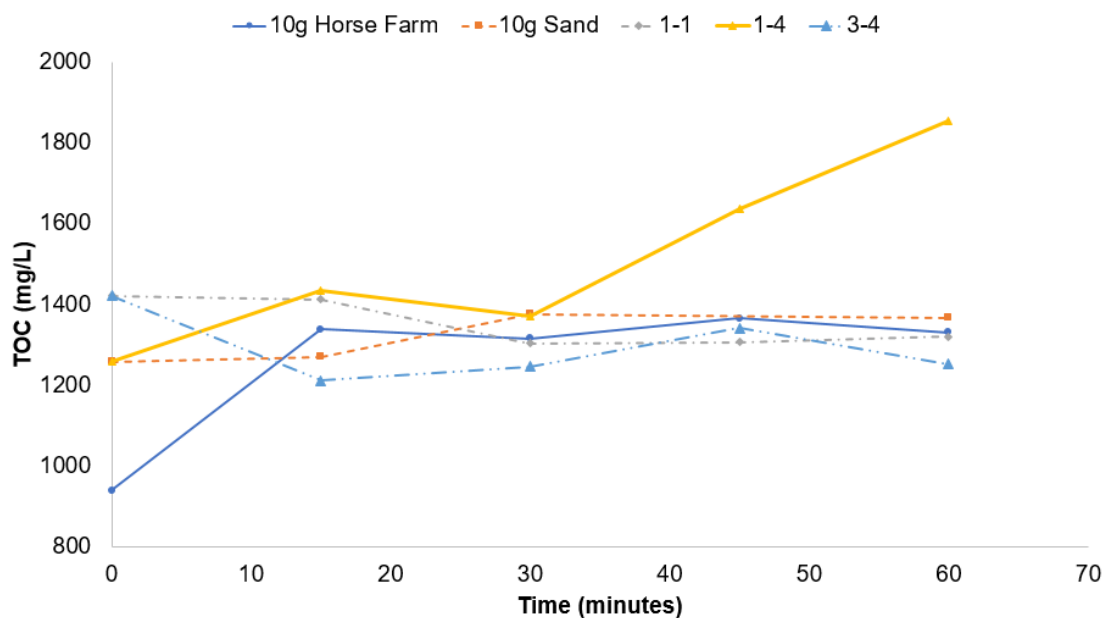


Figure 4: Plot of Time Versus Filtered TOC for 1 g of Dextrose

Table 2: Differential Filtered TOC of 2.5 g Dextrose

Time (Minutes)	Differential TOC				
	10 g Horse Farm	10 g Clean Sand	1-1	1-4	3-4
Dextrose Control	1147.0	2881.0	2766.0	2881.0	2766.0
15	+2329.0	+131.0	+331.0	+359.0	+354.0
30	-338.0	-14.0	+35.0	-91.0	+16.0
45	+10.0	+62.0	+39.0	-279.0	+107.0
60	+102.0	+53.0	-52.0	-67.0	+166.0

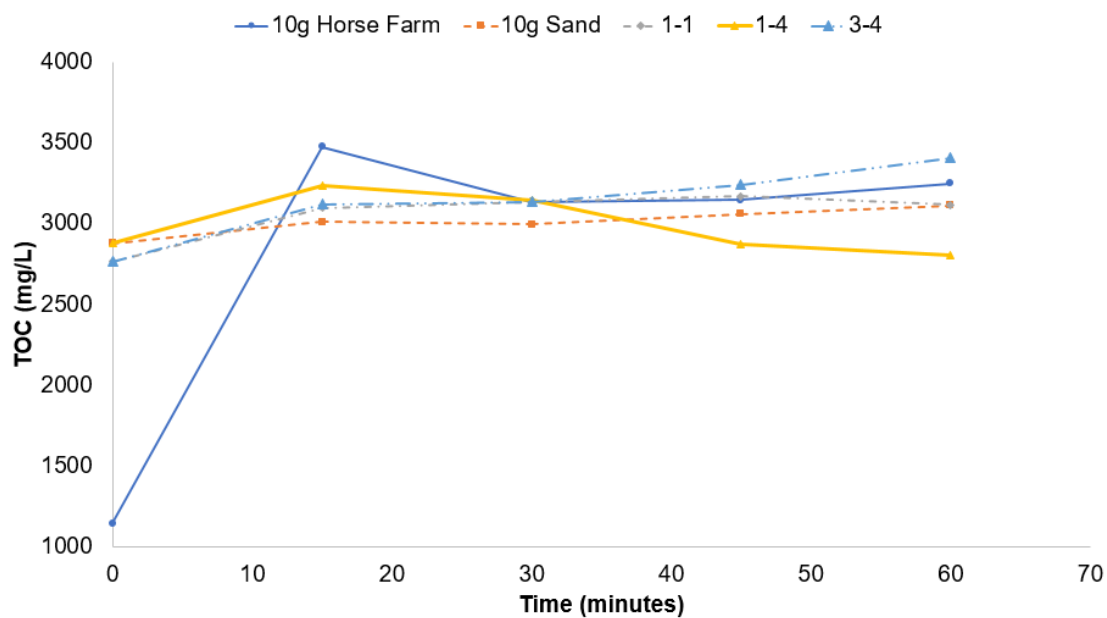


Figure 5: Plot of Time Versus Filtered TOC for 2.5 grams Dextrose

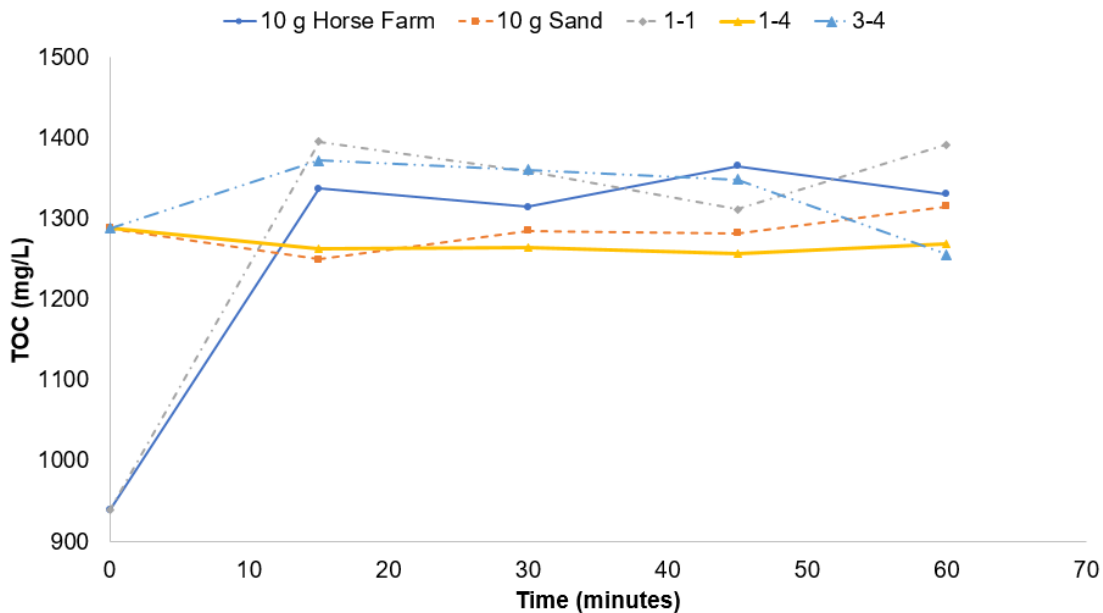


Figure 6: Plot of Time Versus Unfiltered TOC for 1 grams Dextrose

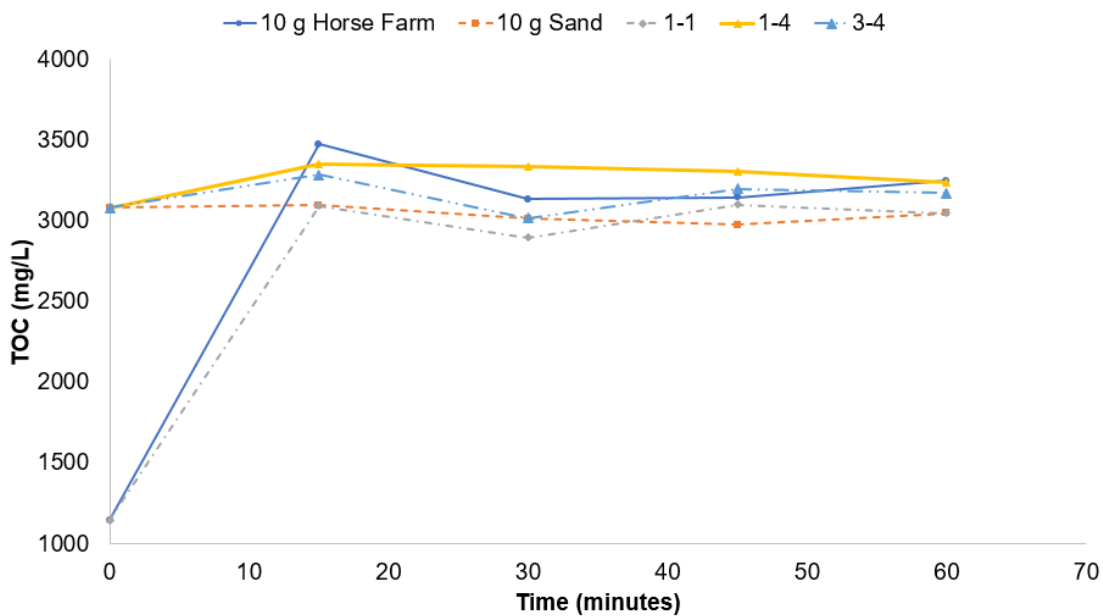


Figure 7: Plot of Time Versus Unfiltered TOC for 2.5 grams Dextrose

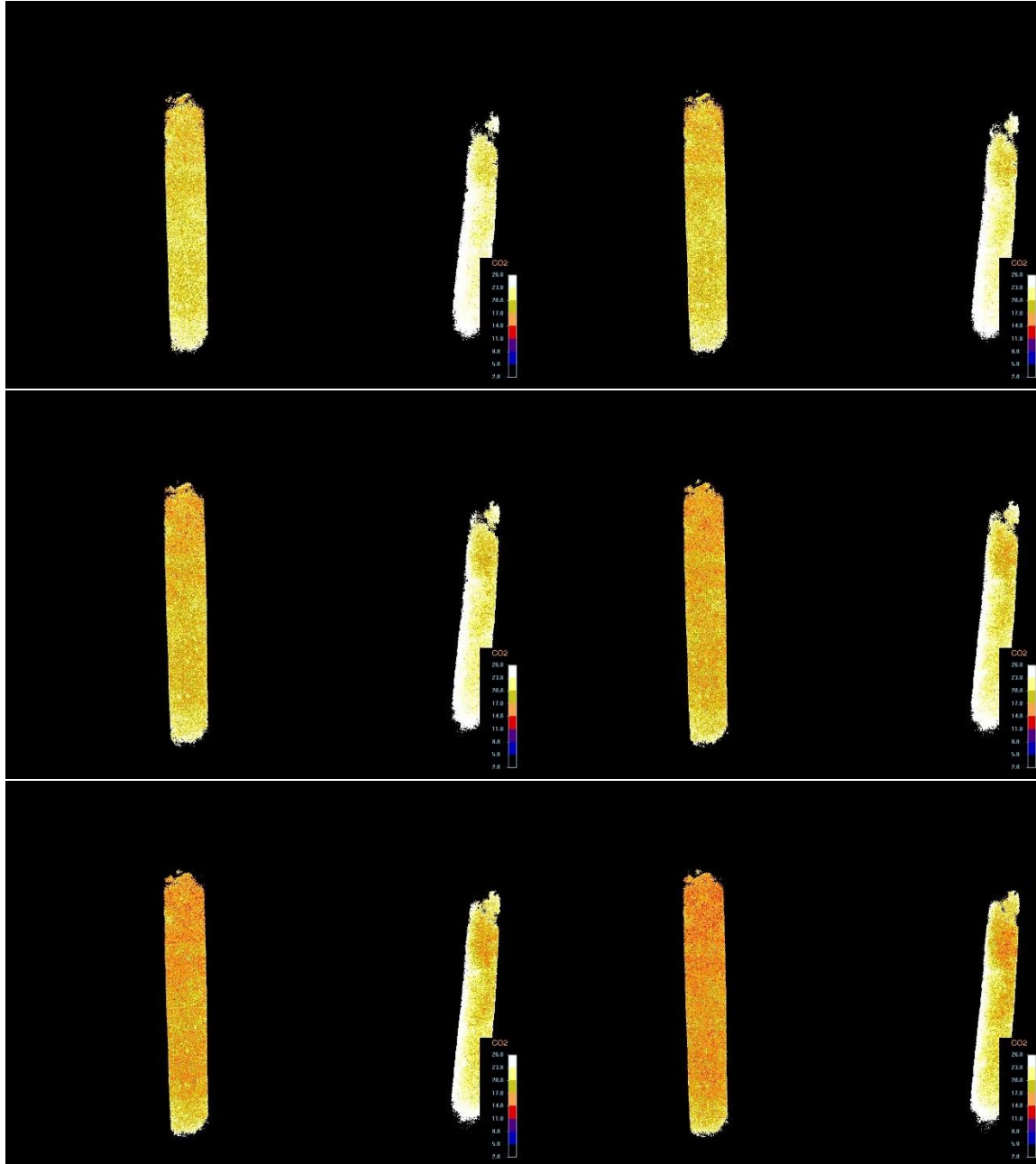
Results and Conclusions

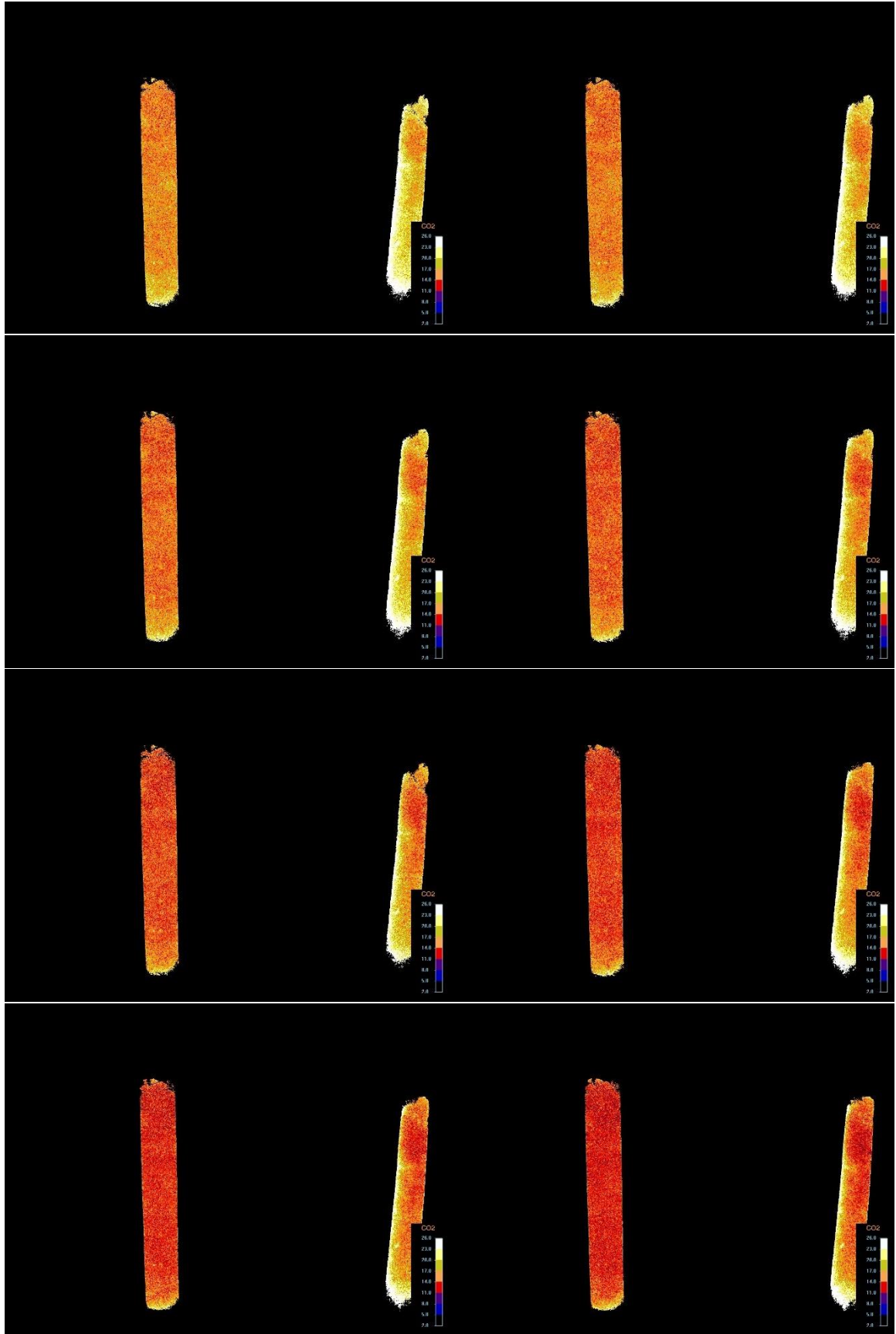
- Turbid Water required filtration to obtain TOC values from dextrose only
 - TOC analyzer not sensitive enough to detect changes in DO from samples due to dilution and high dextrose concentrations
- DO reduced in all experiments
 - NO anoxia formed –DO did not drop below 2 mg/L
 - Horse Farm water and sediment most active with largest reduction of DO
- Butyric Acid formed during experiments

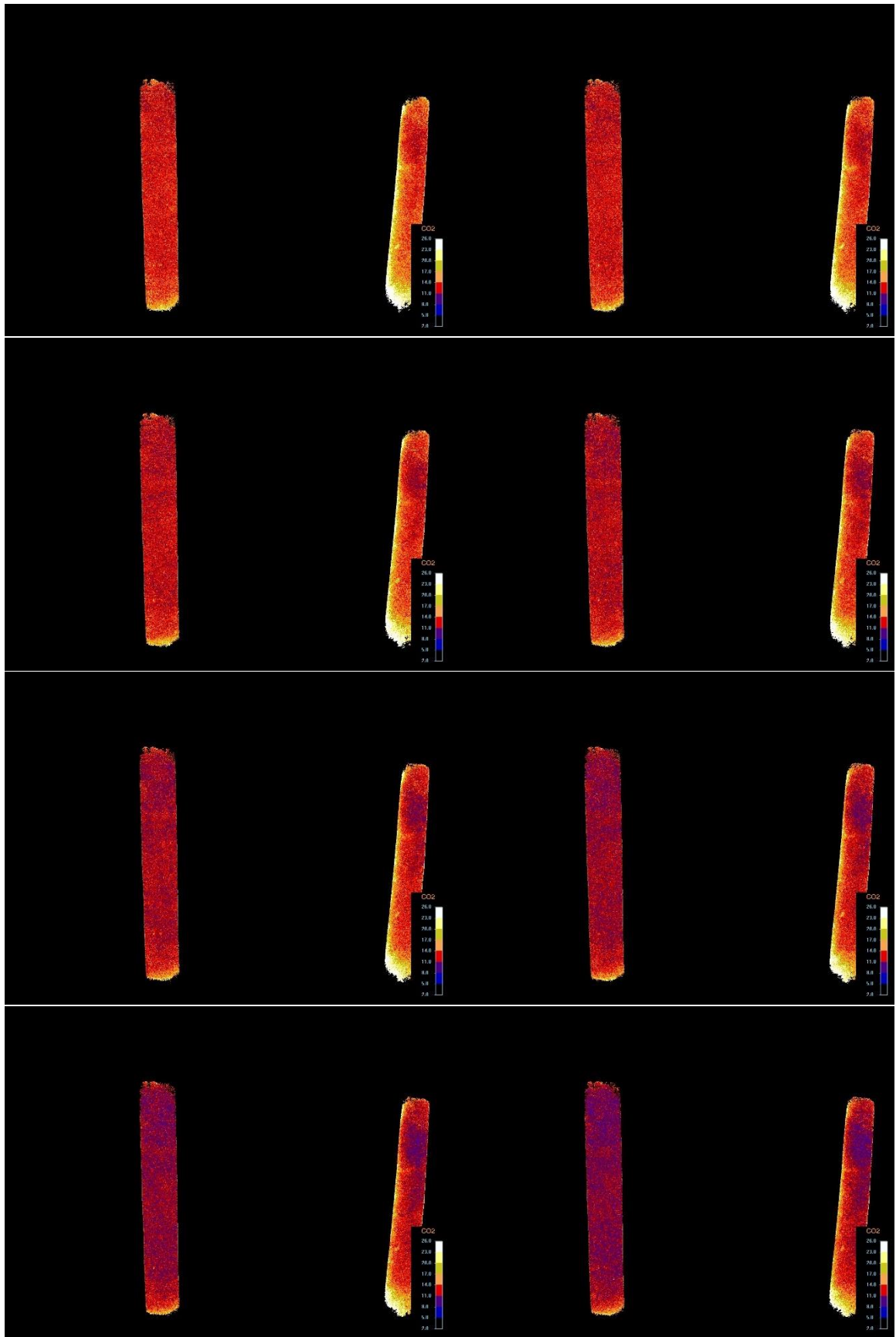
Appendix G. Set of Images from Biotic Experiments in Chapter 5

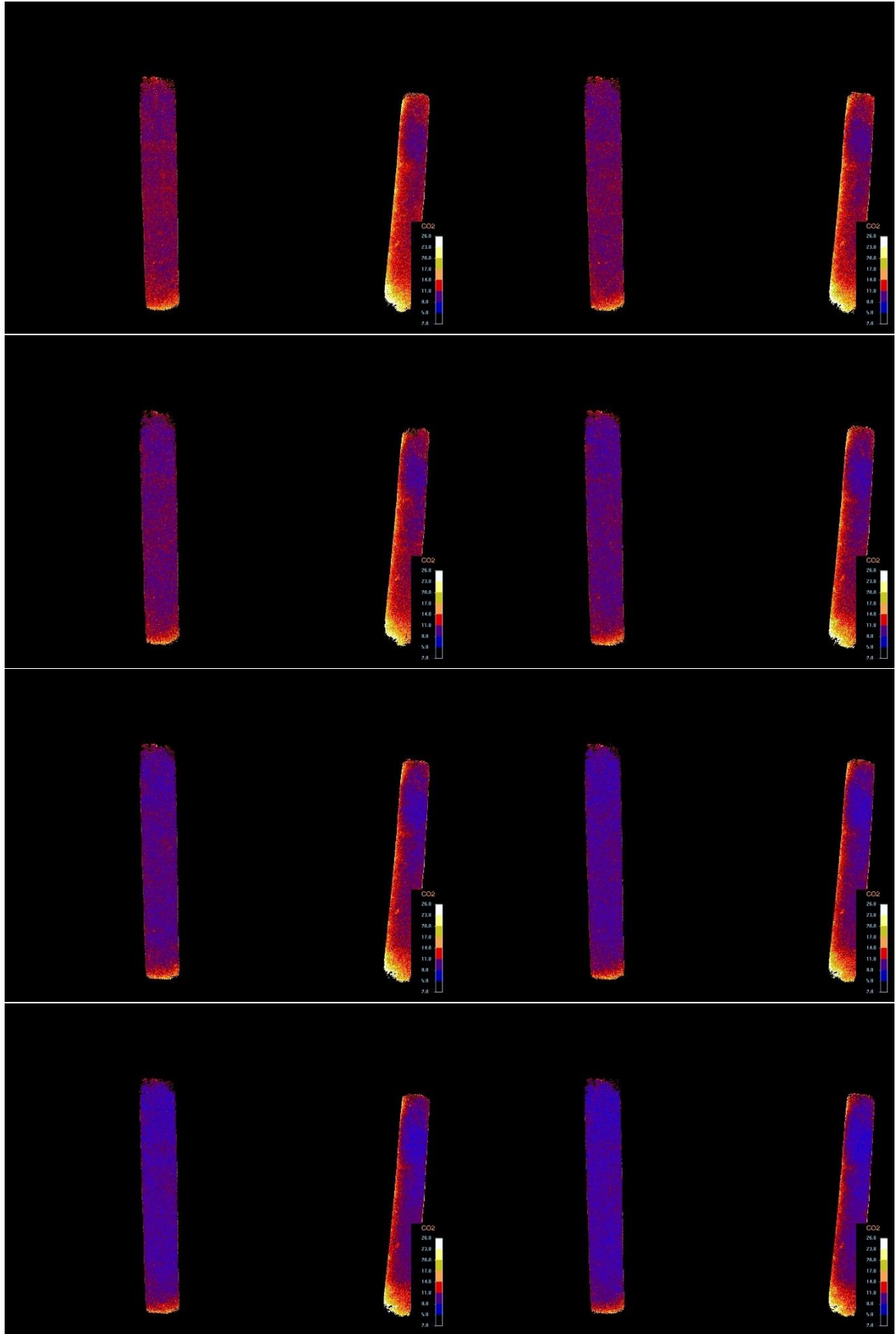
The images shown here correspond to Trial 1 and 2 and the timespan shown for the figures showing DO and CO₂ profiles (Figures 5.6-5.9)

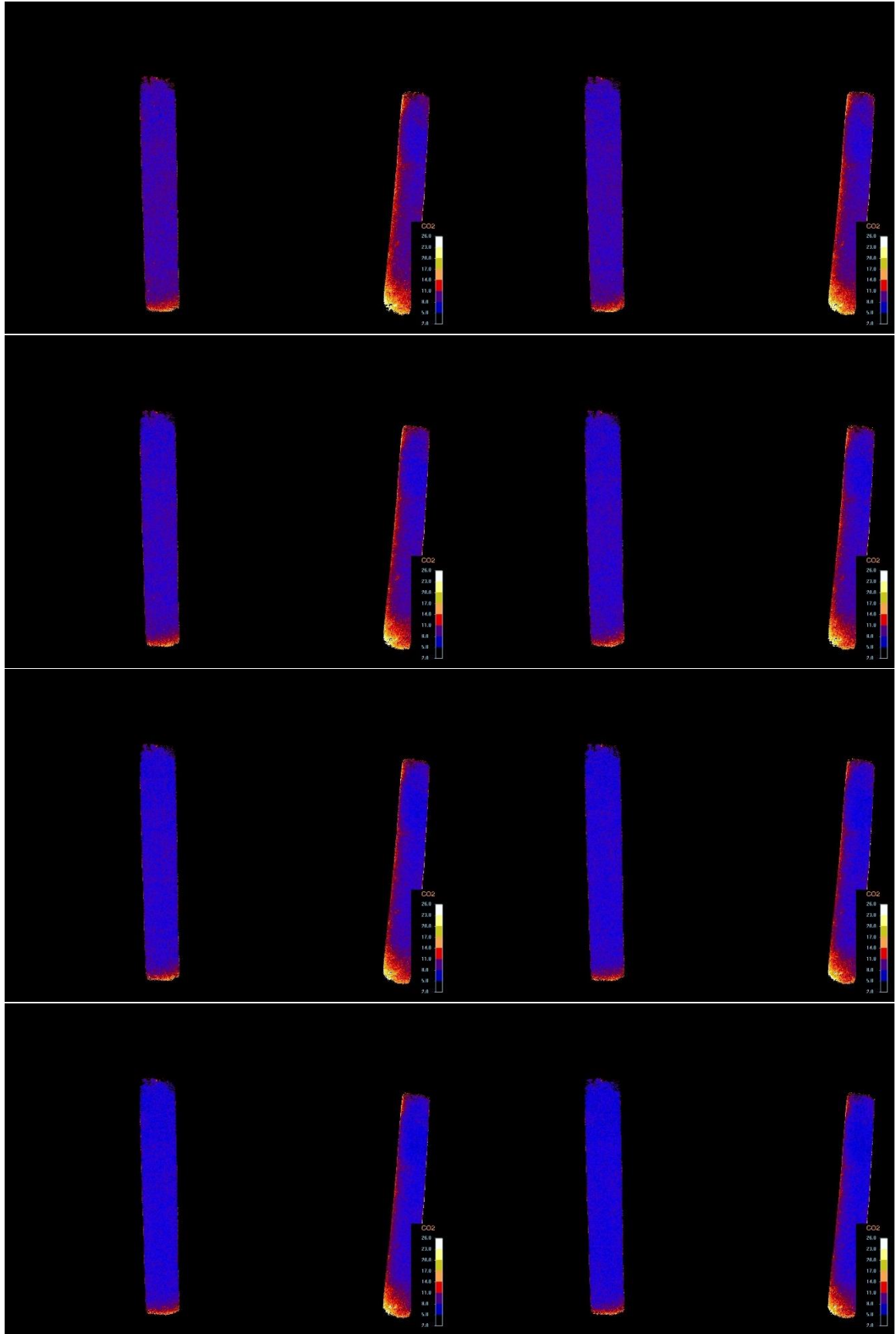
Trial 1: CO₂ time 23-45 hours from 72-hr experiment in 20 min increments

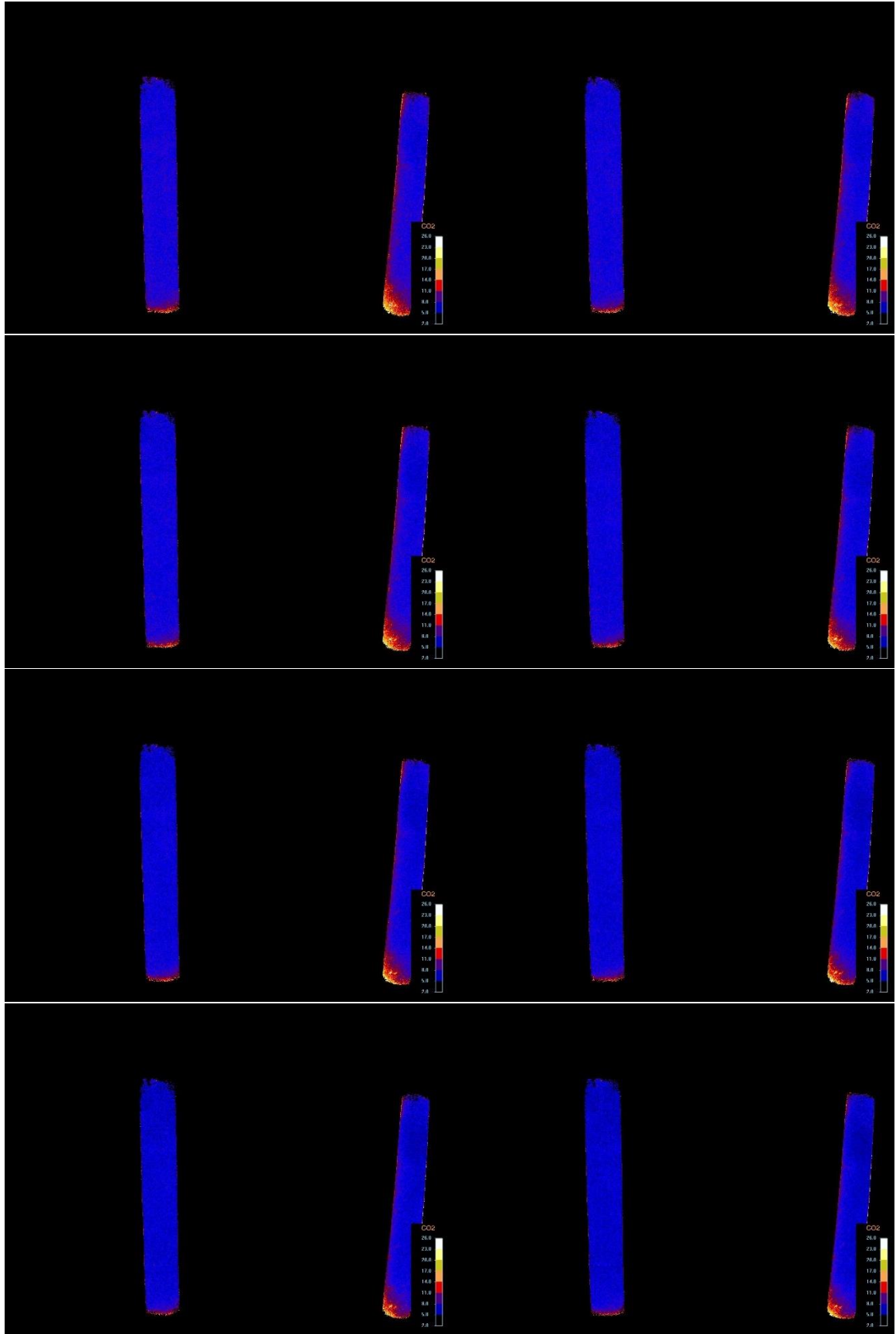


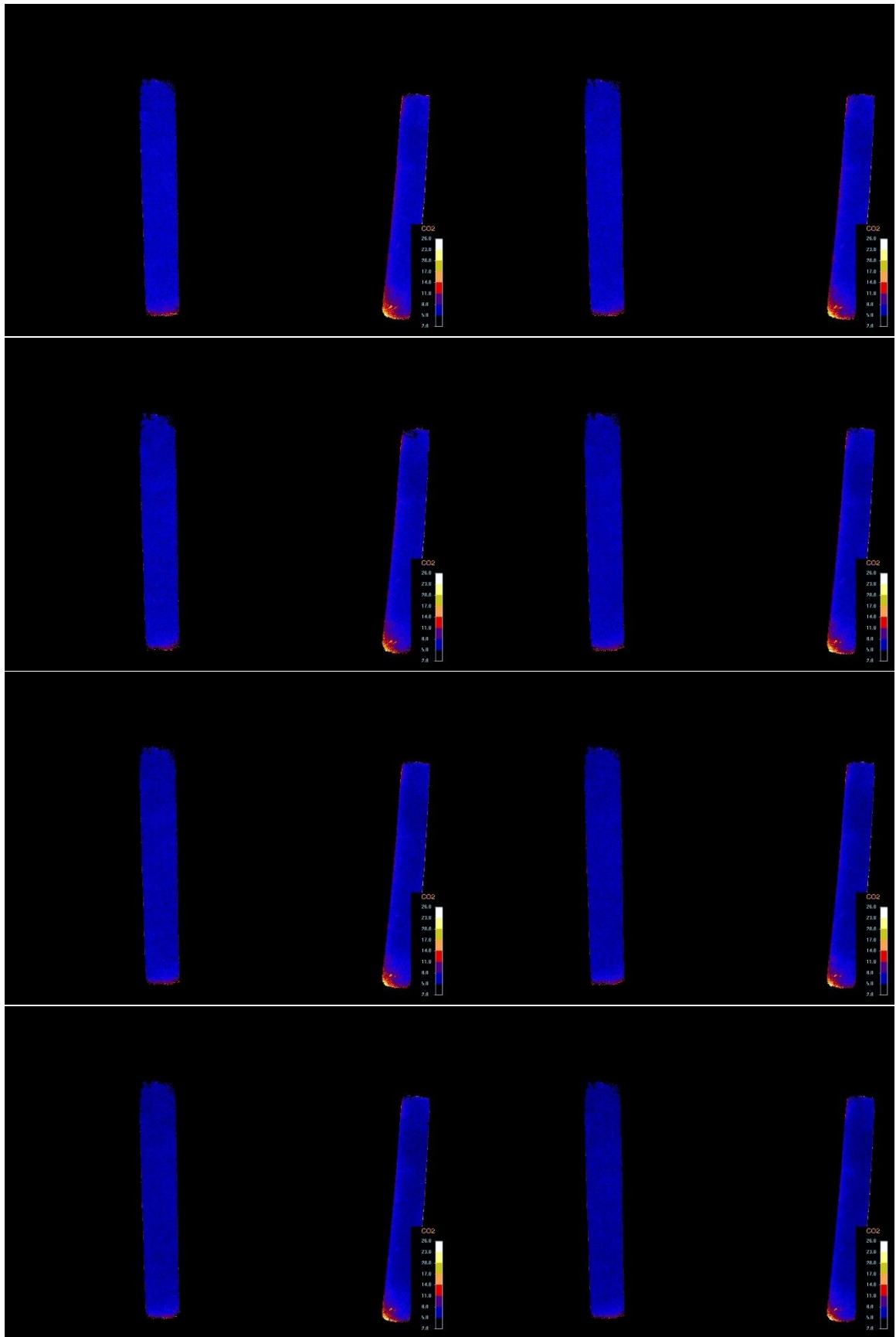


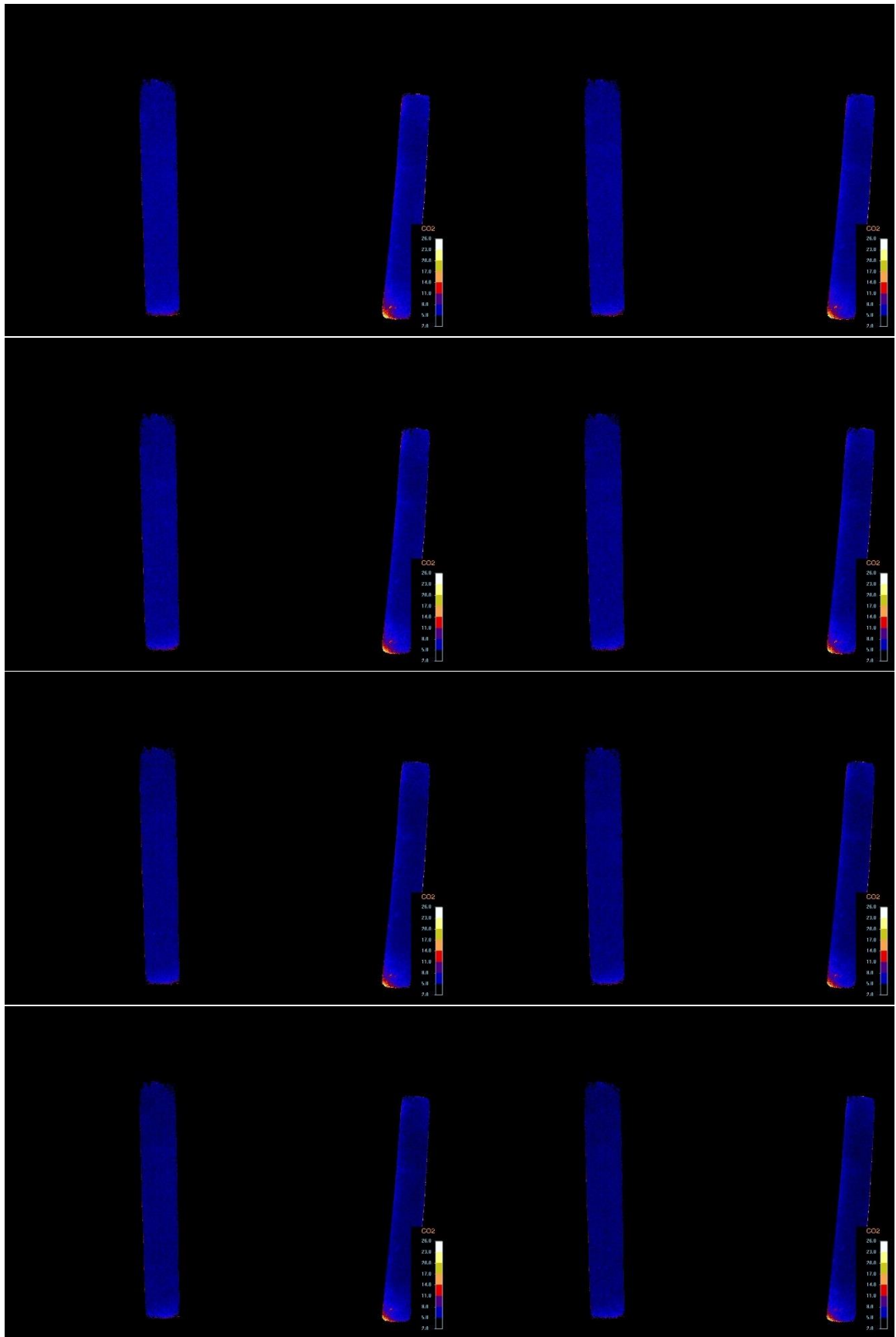


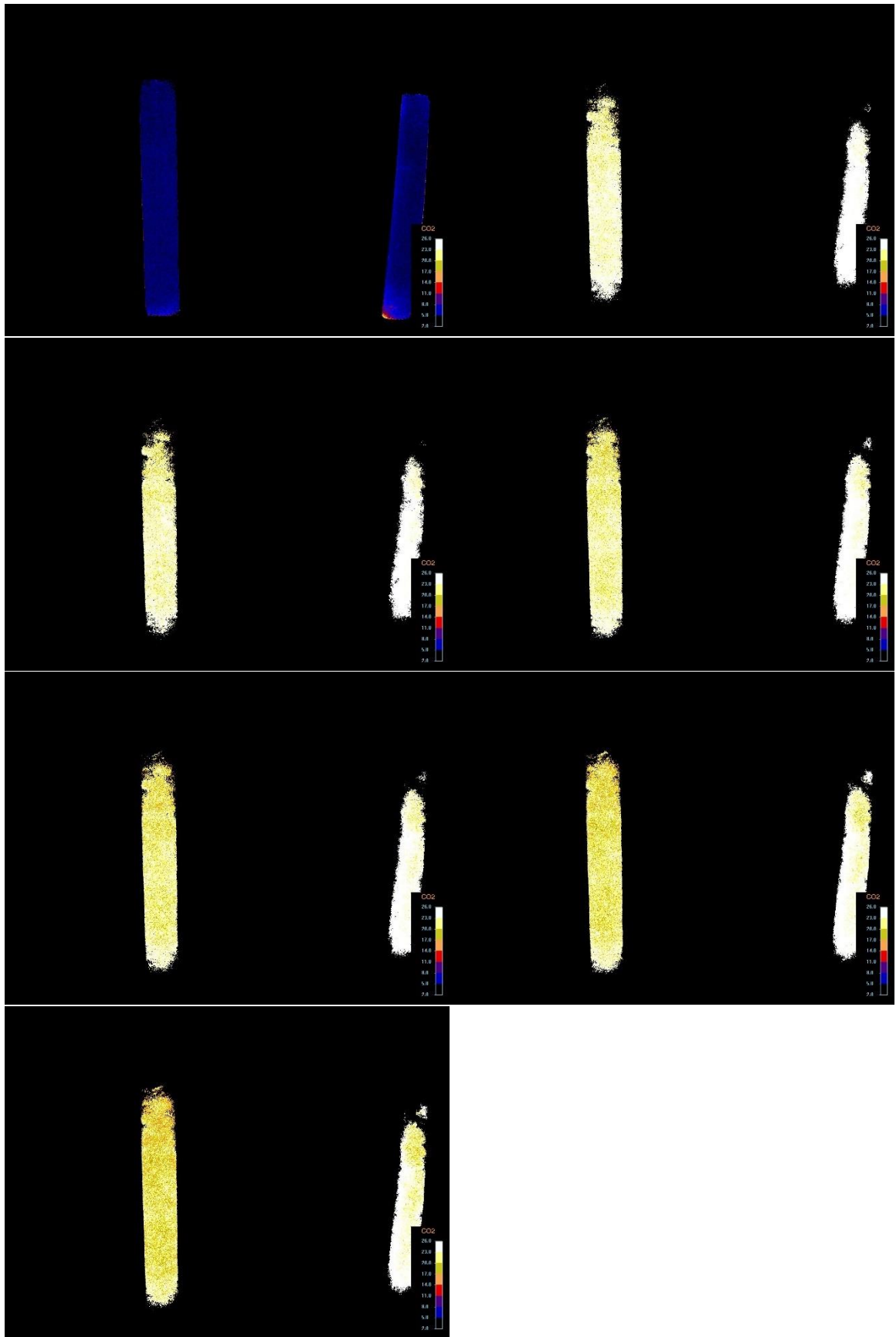




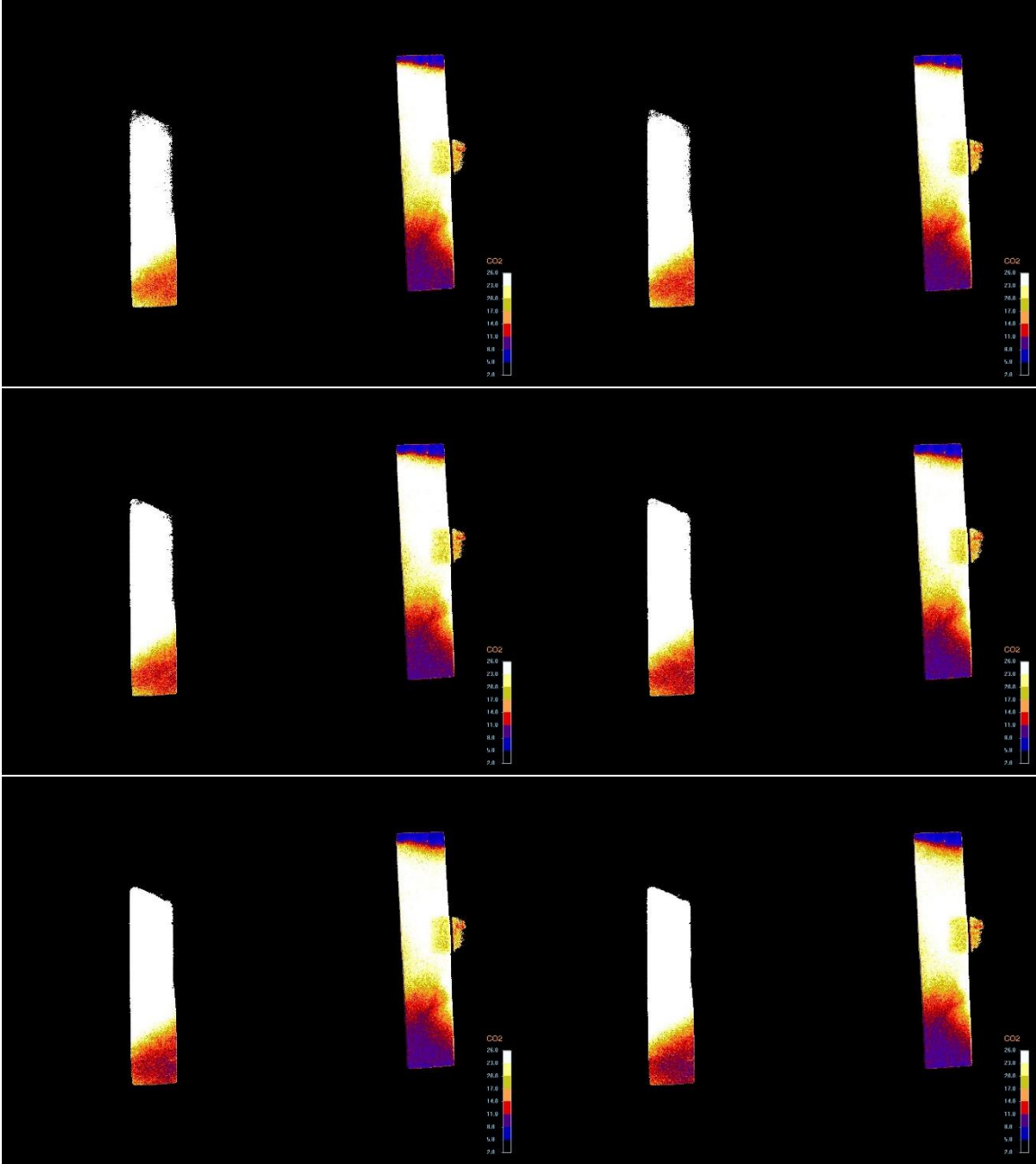


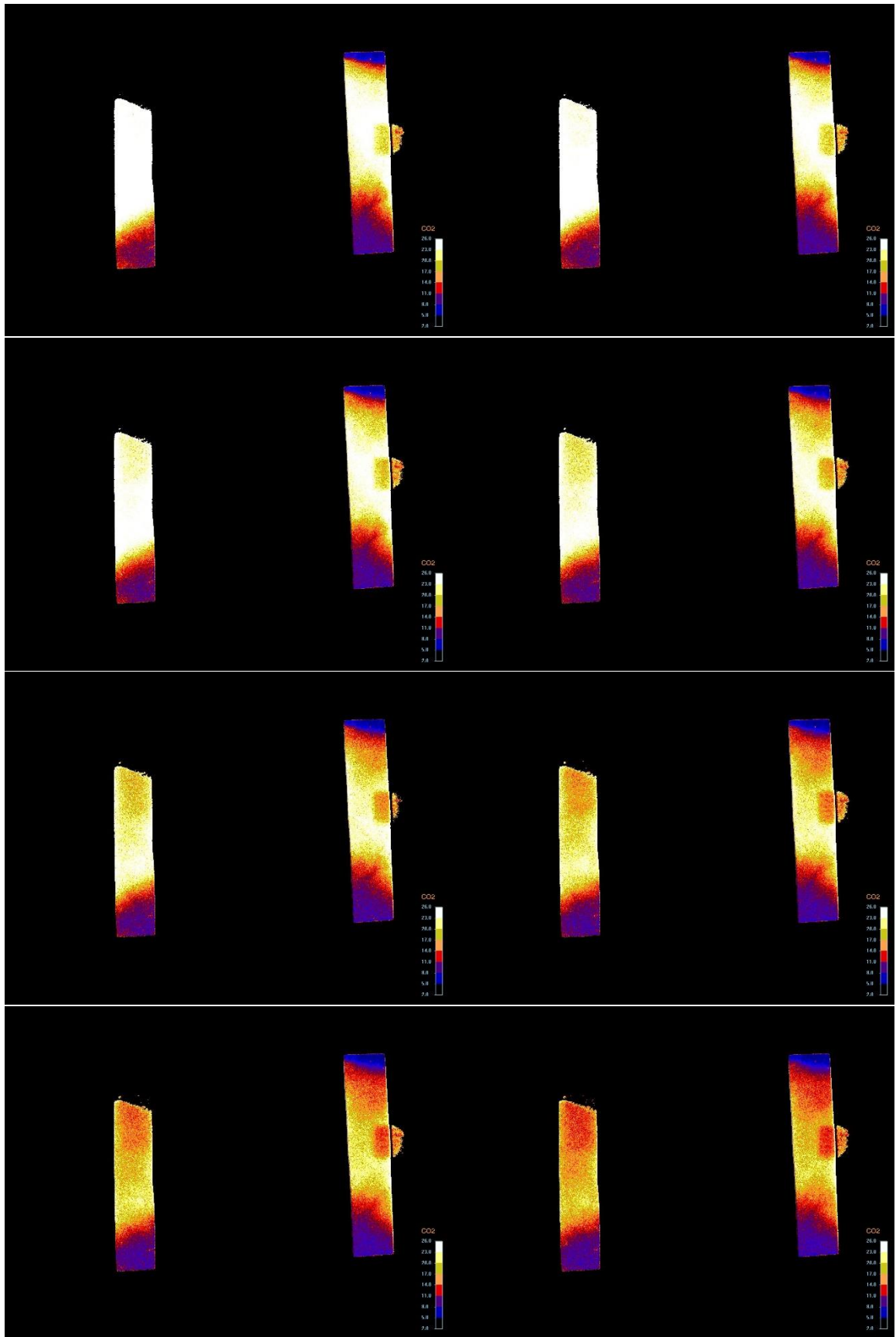


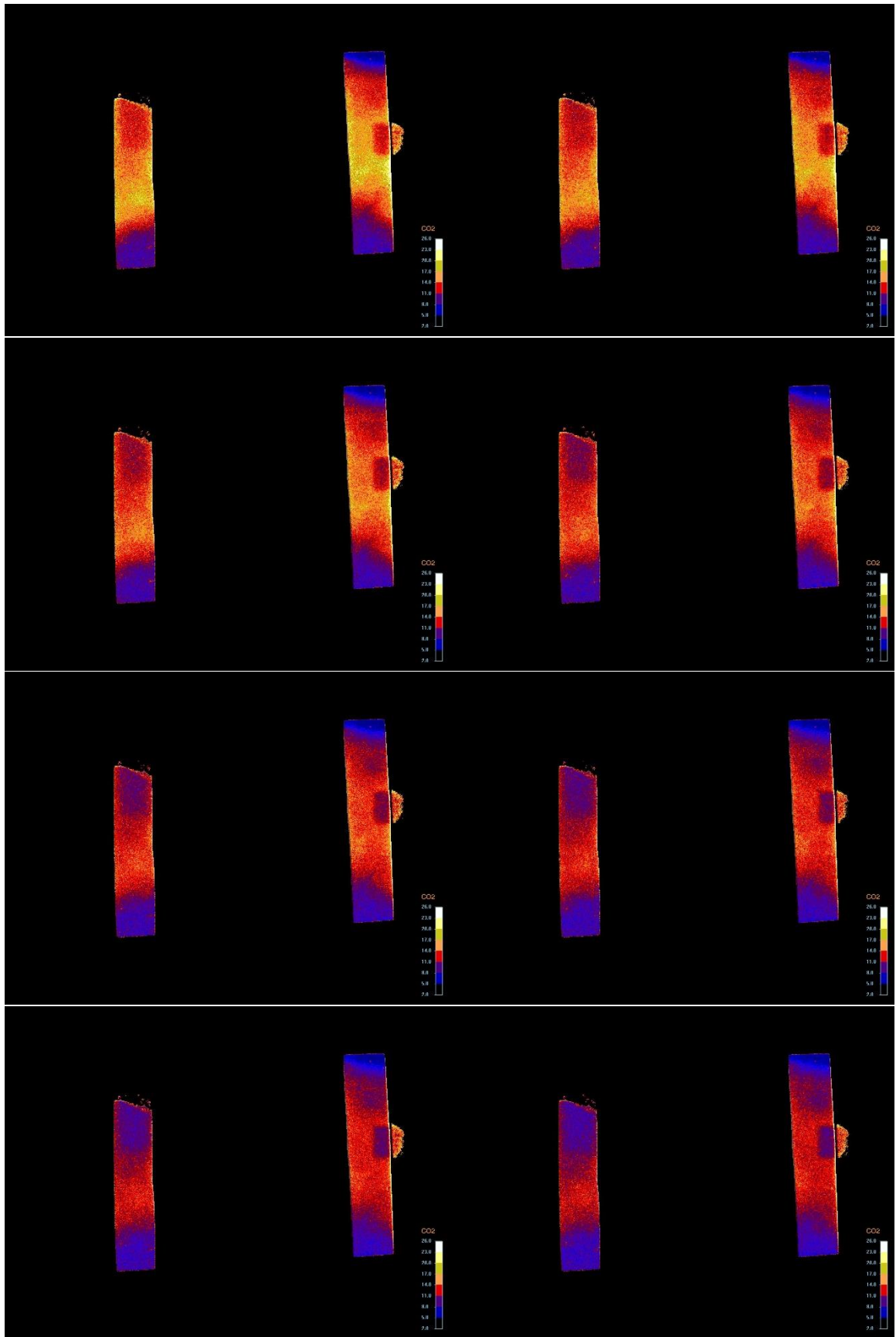


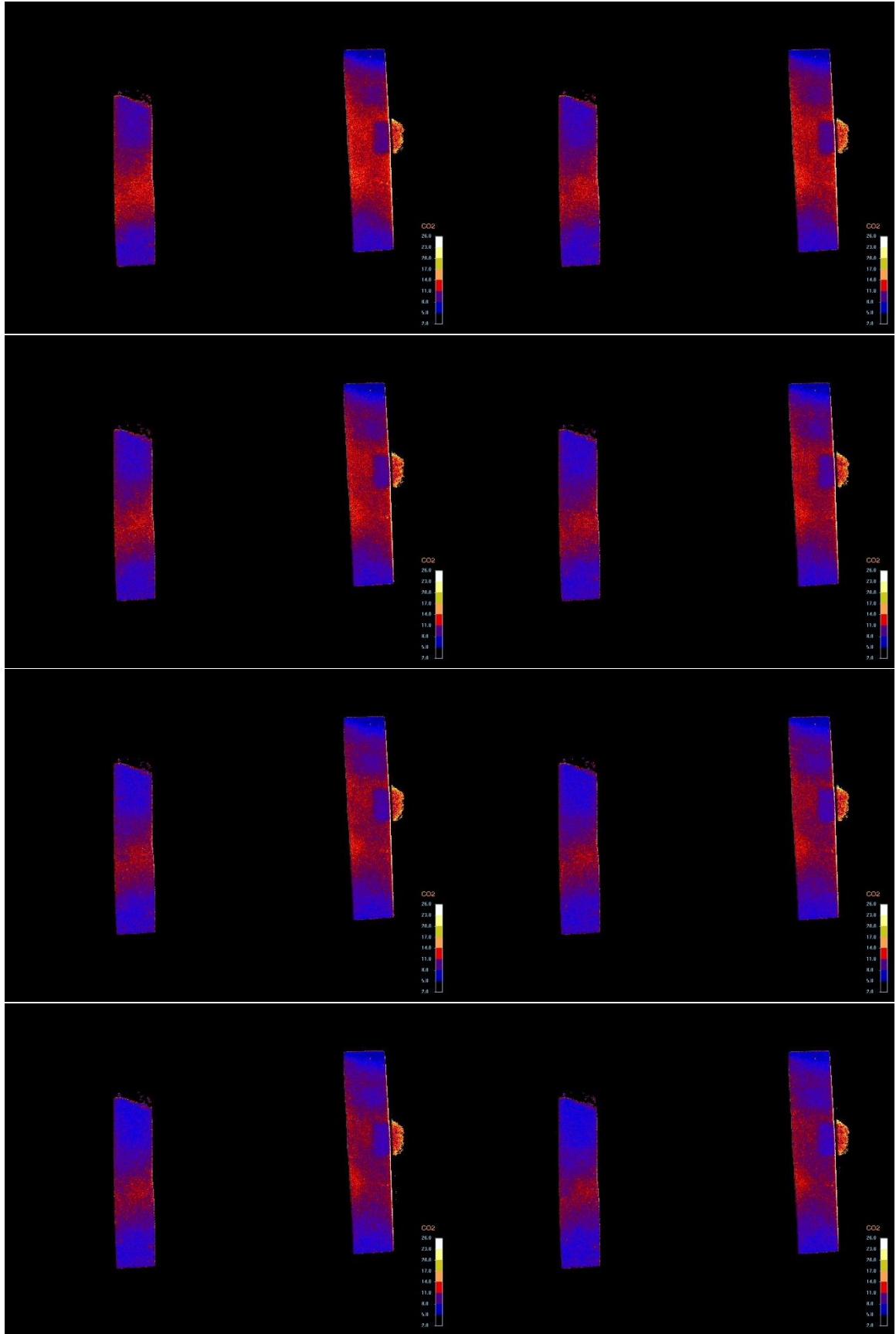


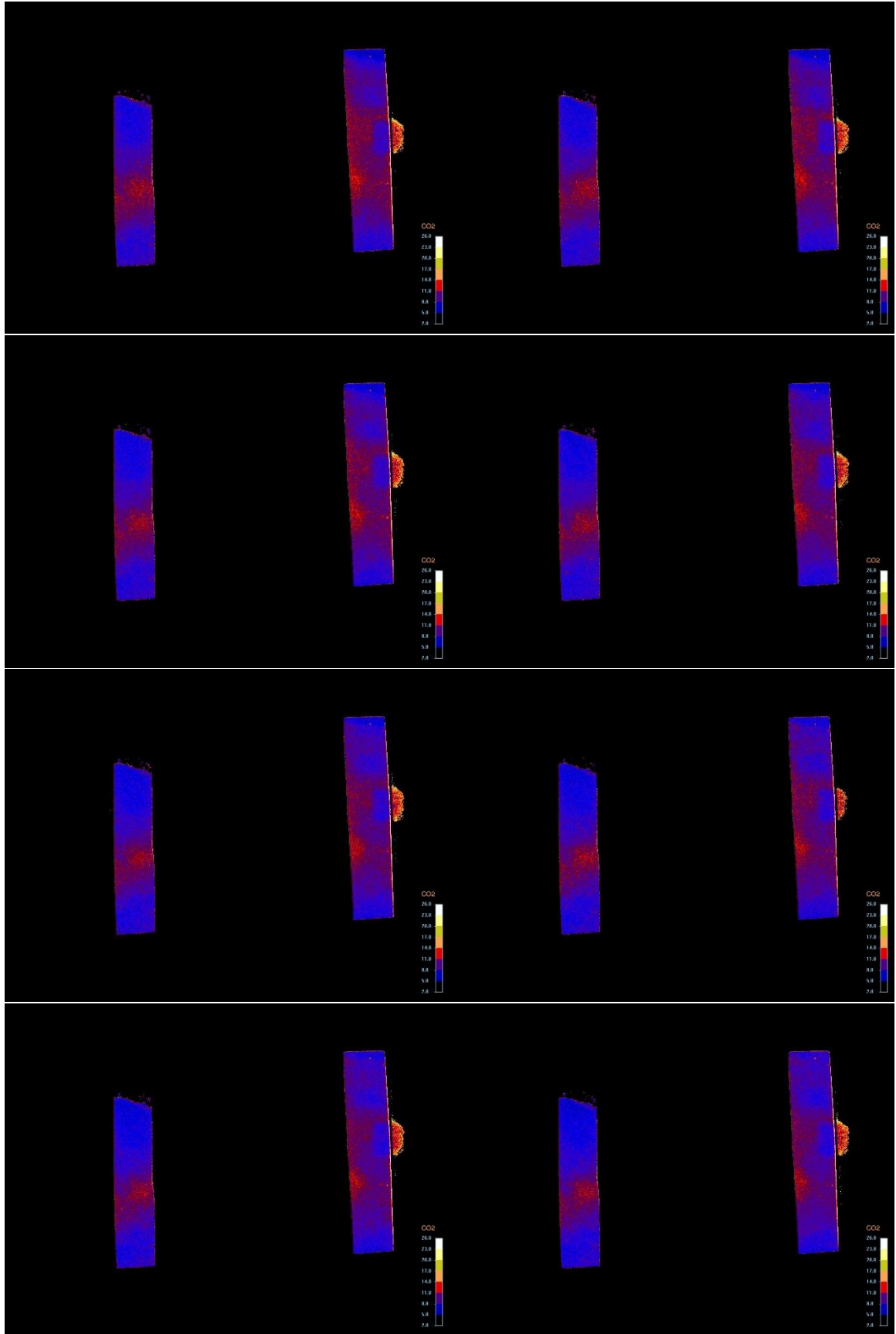
Trial 2: CO₂ time 0-18 hours from 18-hr experiment in 20 min increments

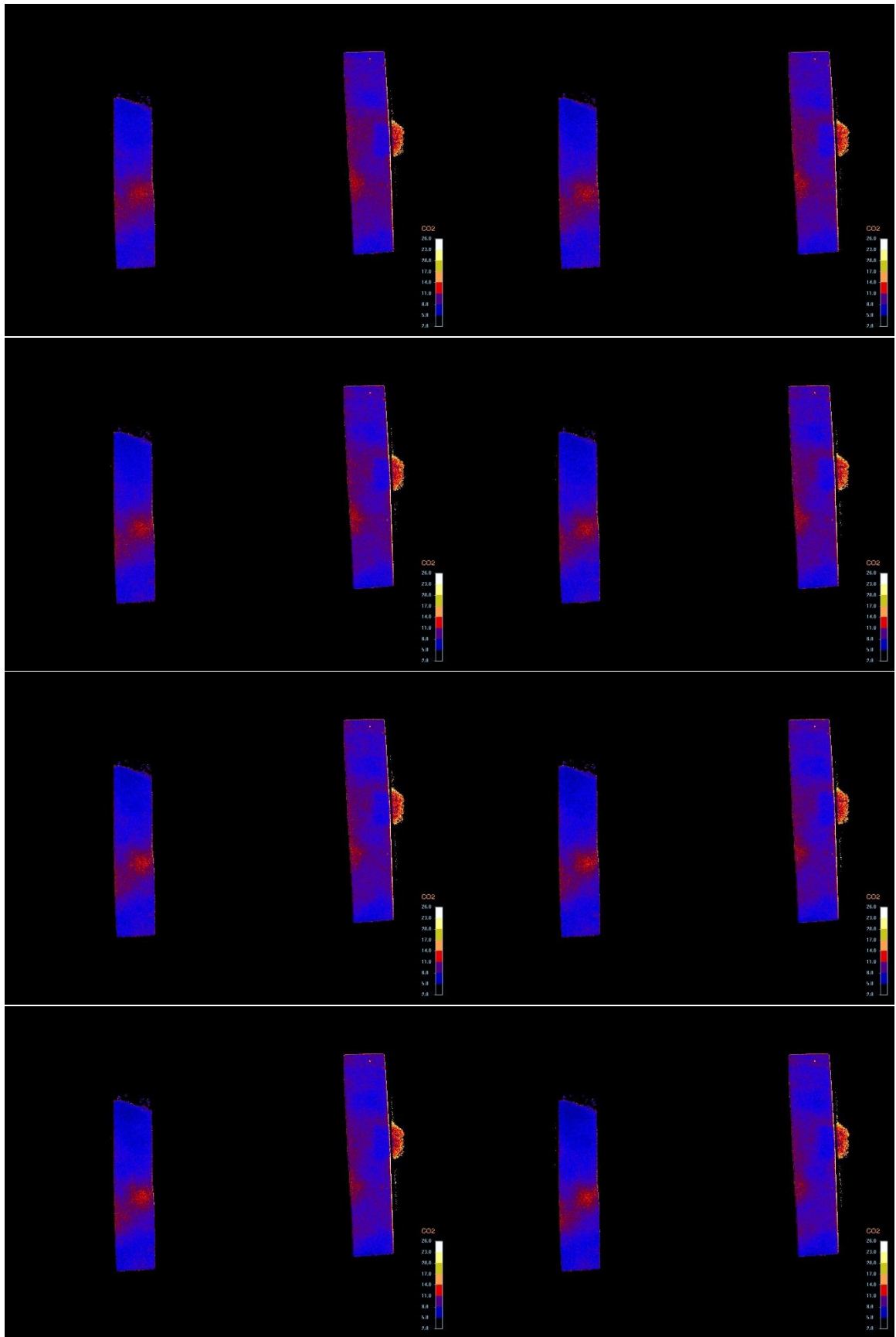


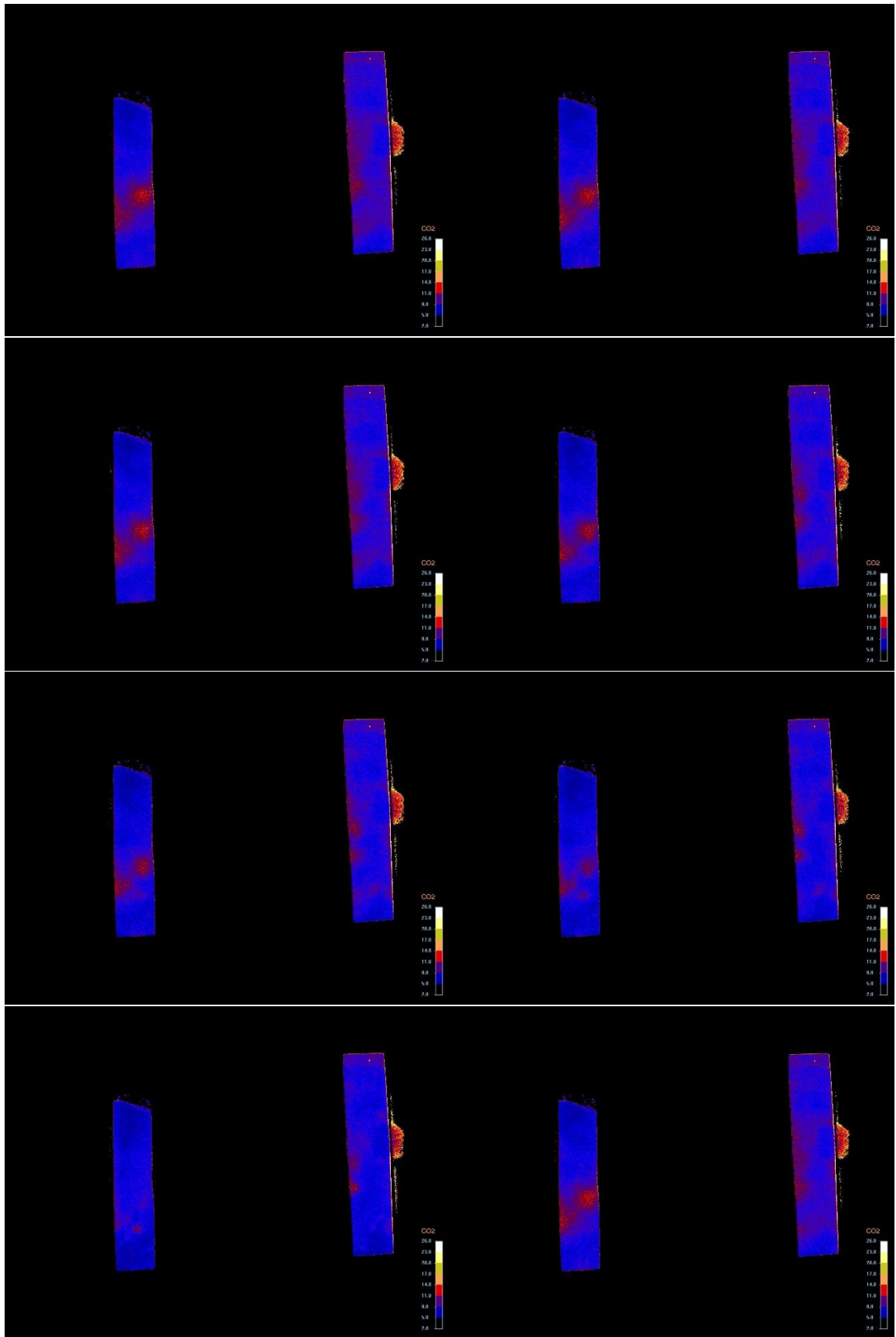




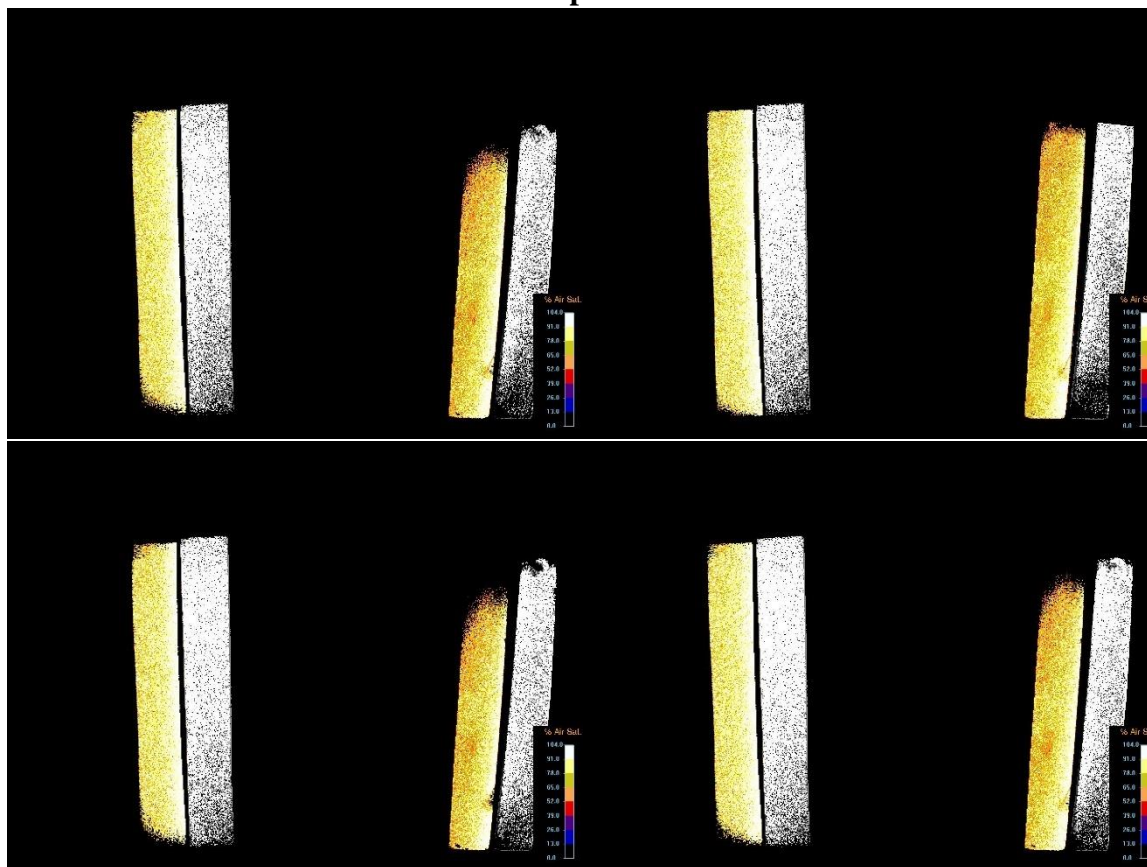


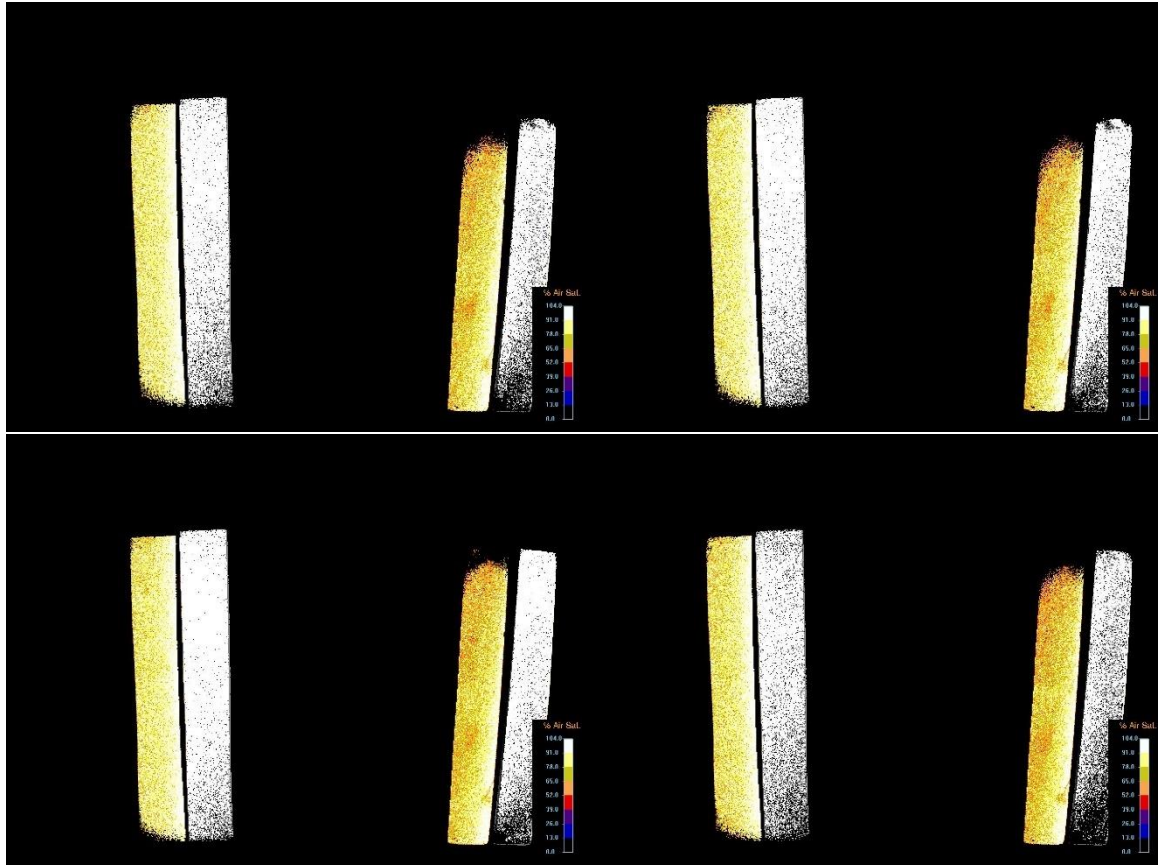


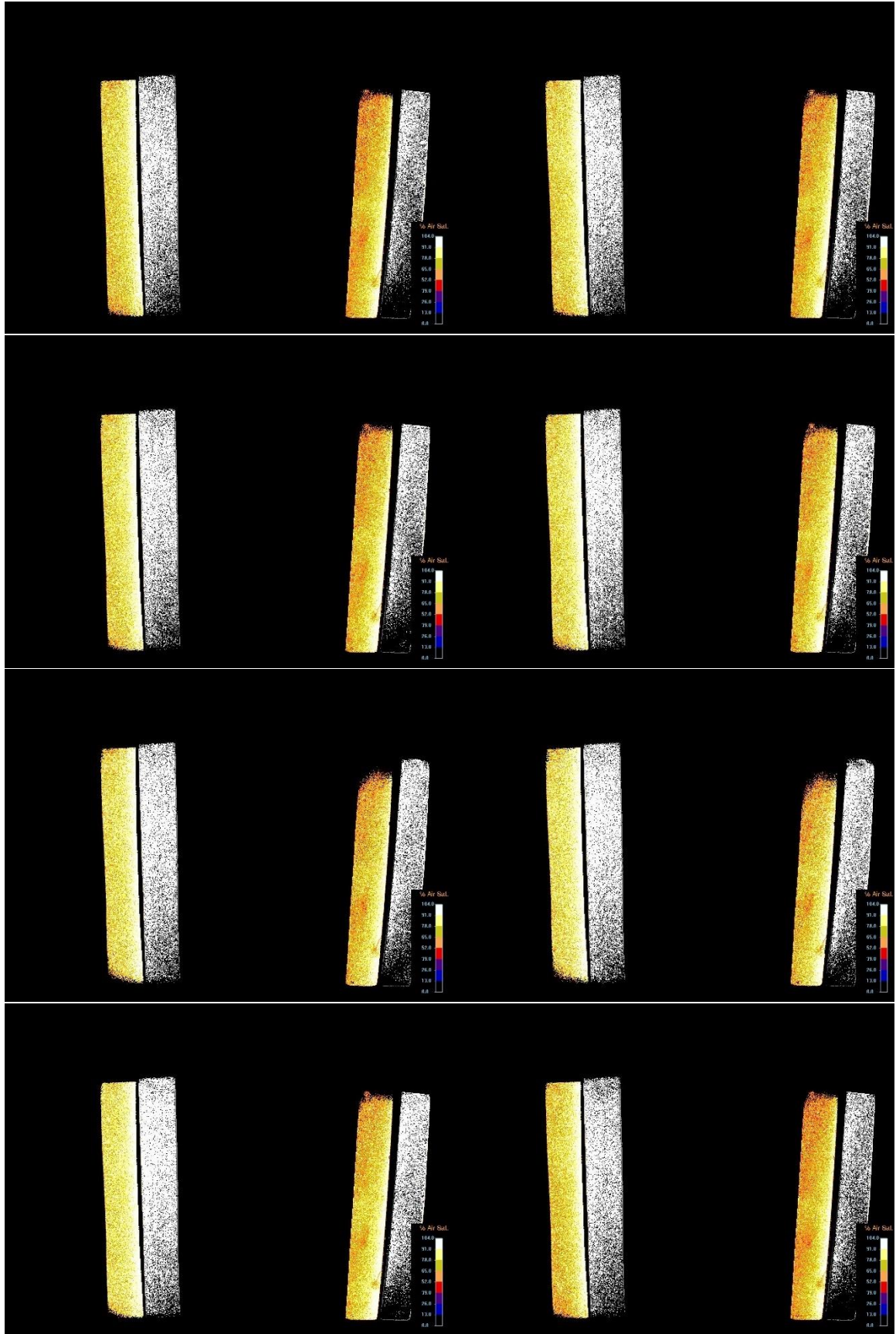


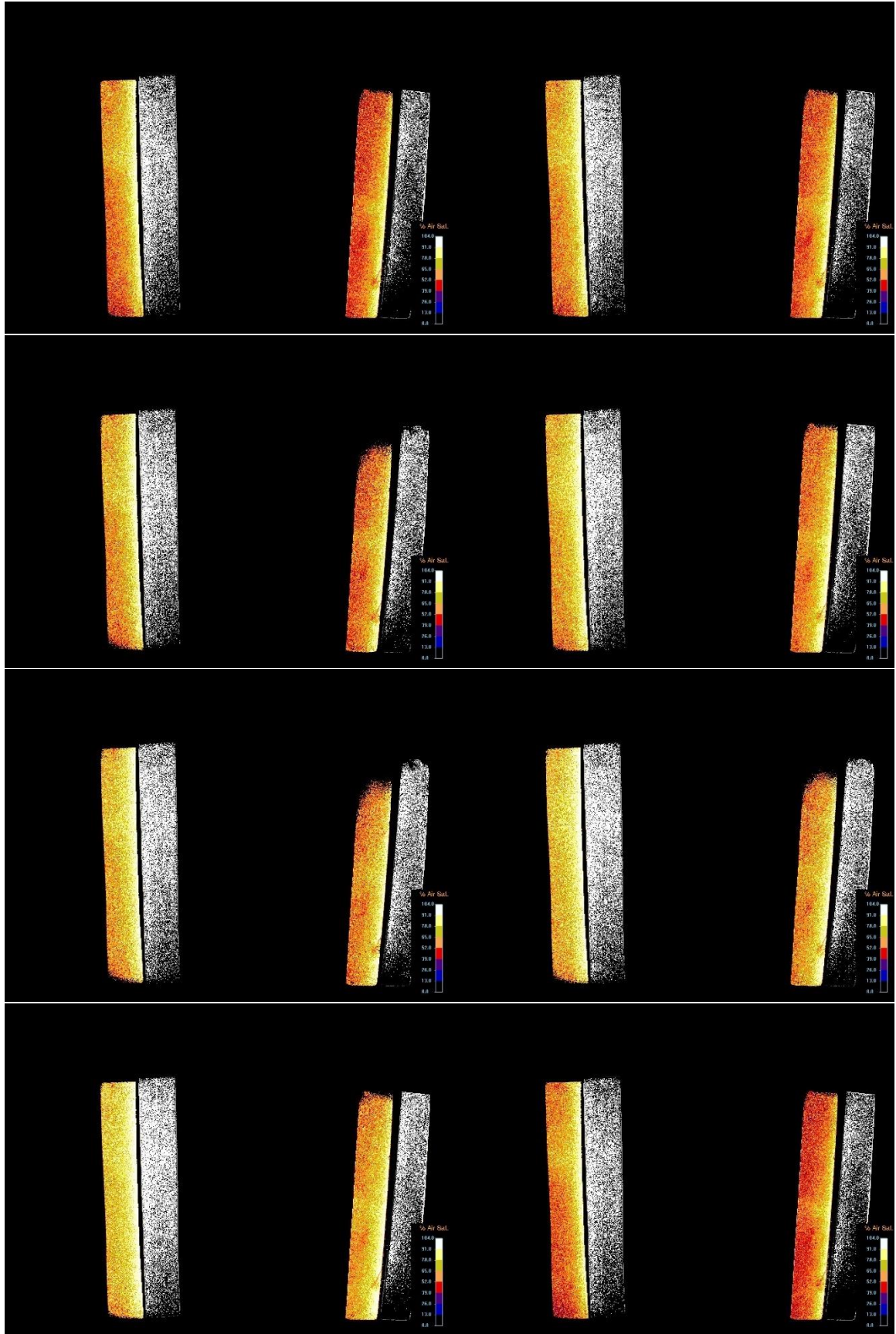


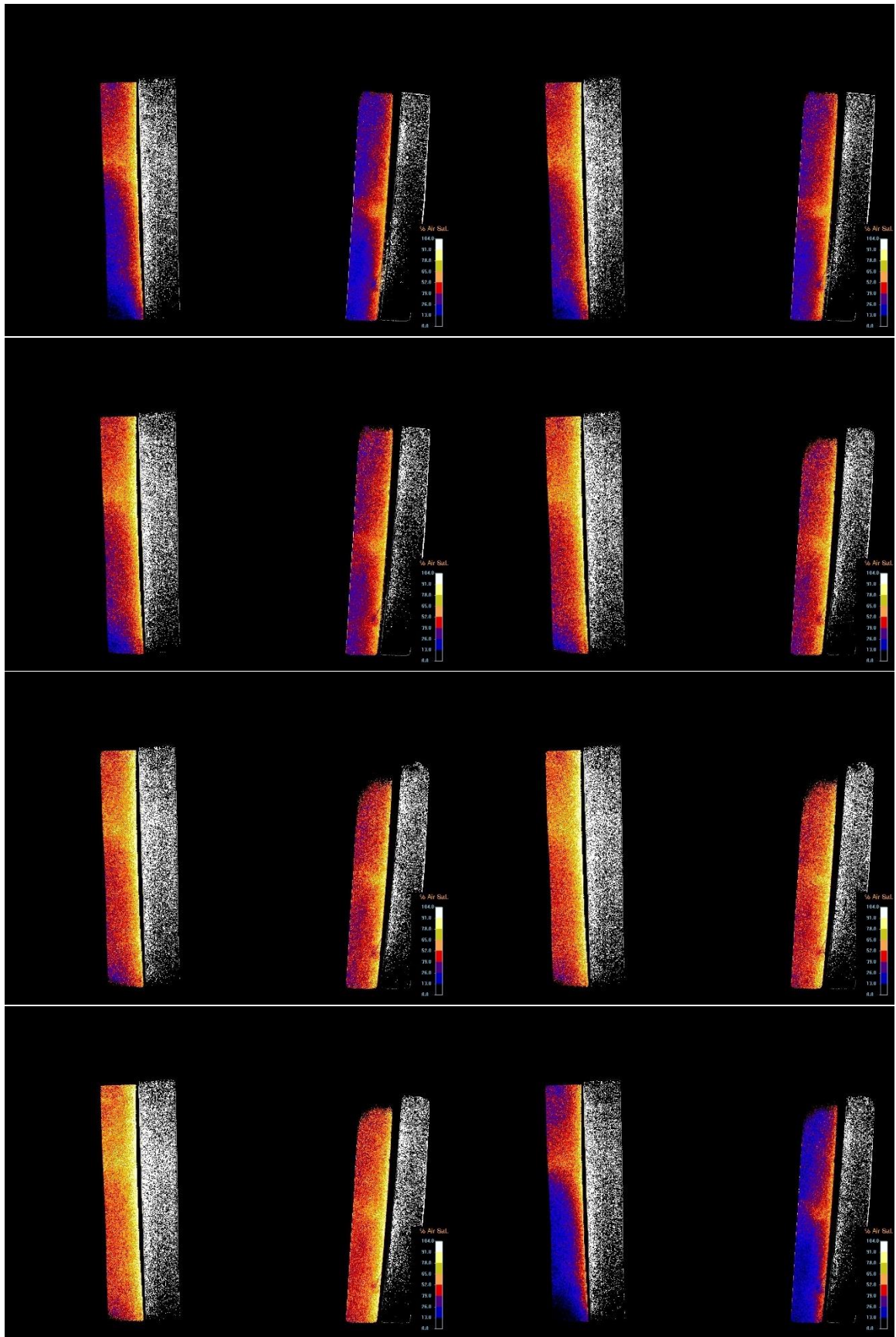
Trial 1: O₂ time 0-18 hours from 72-hr experiment in 20 min increments

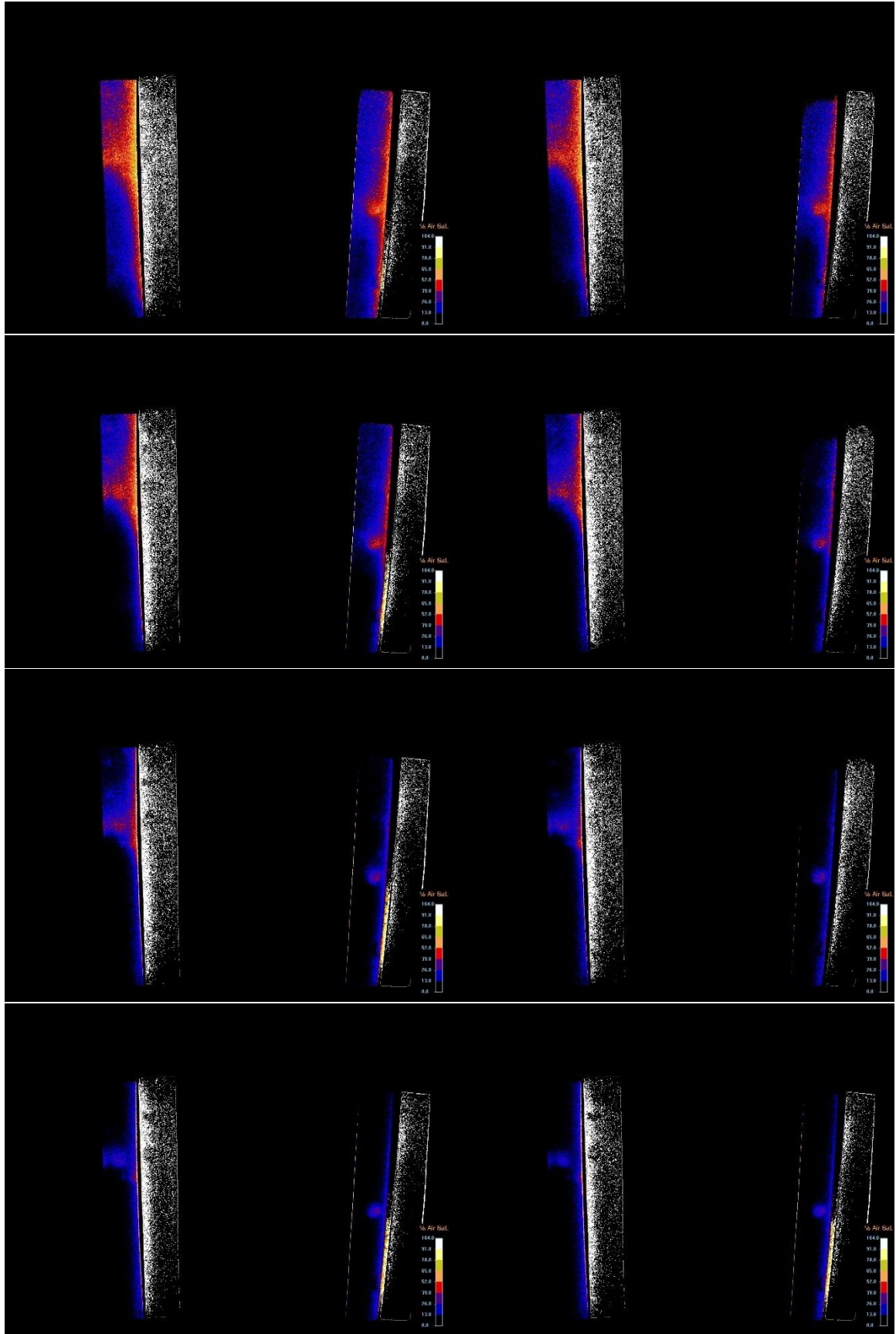


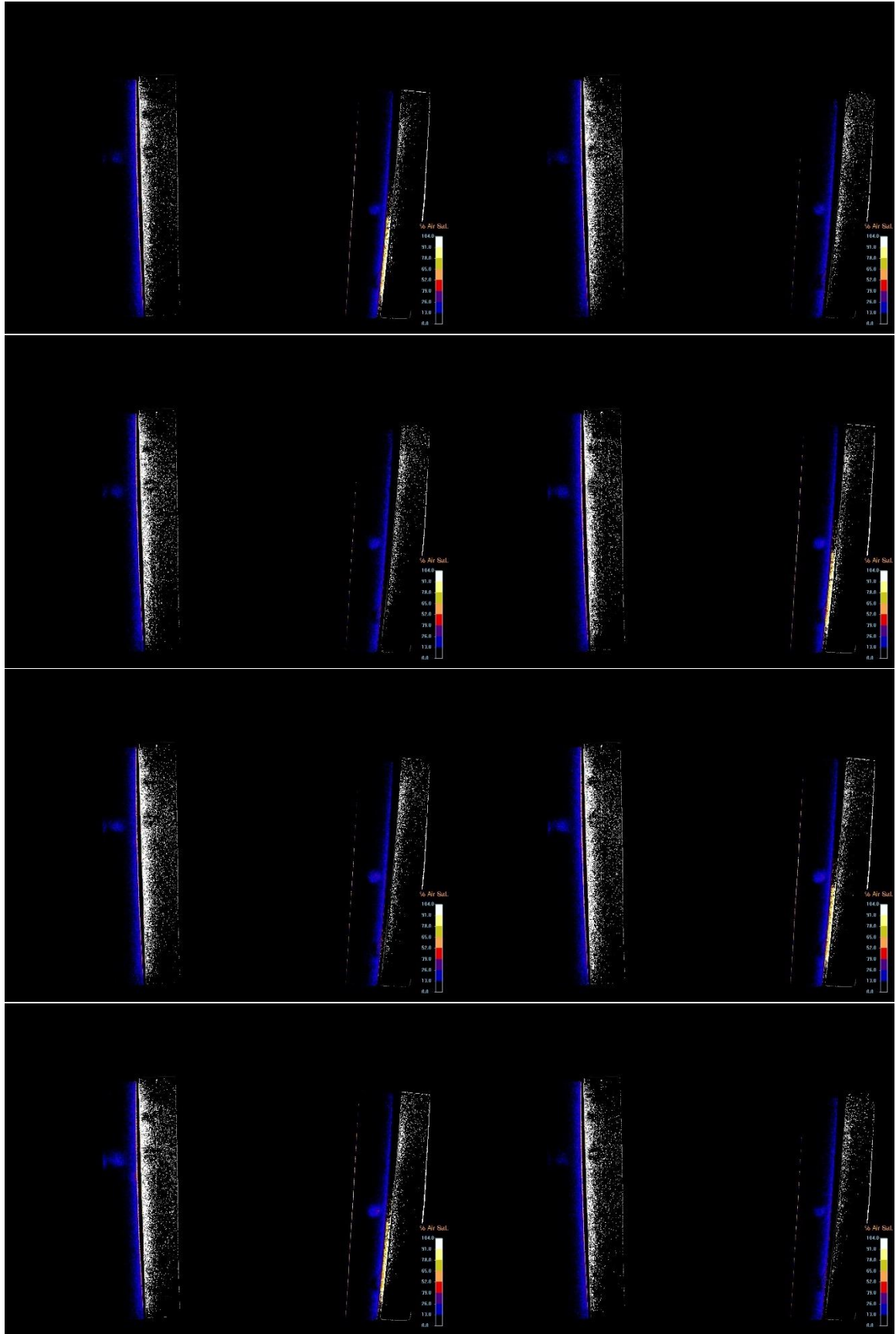


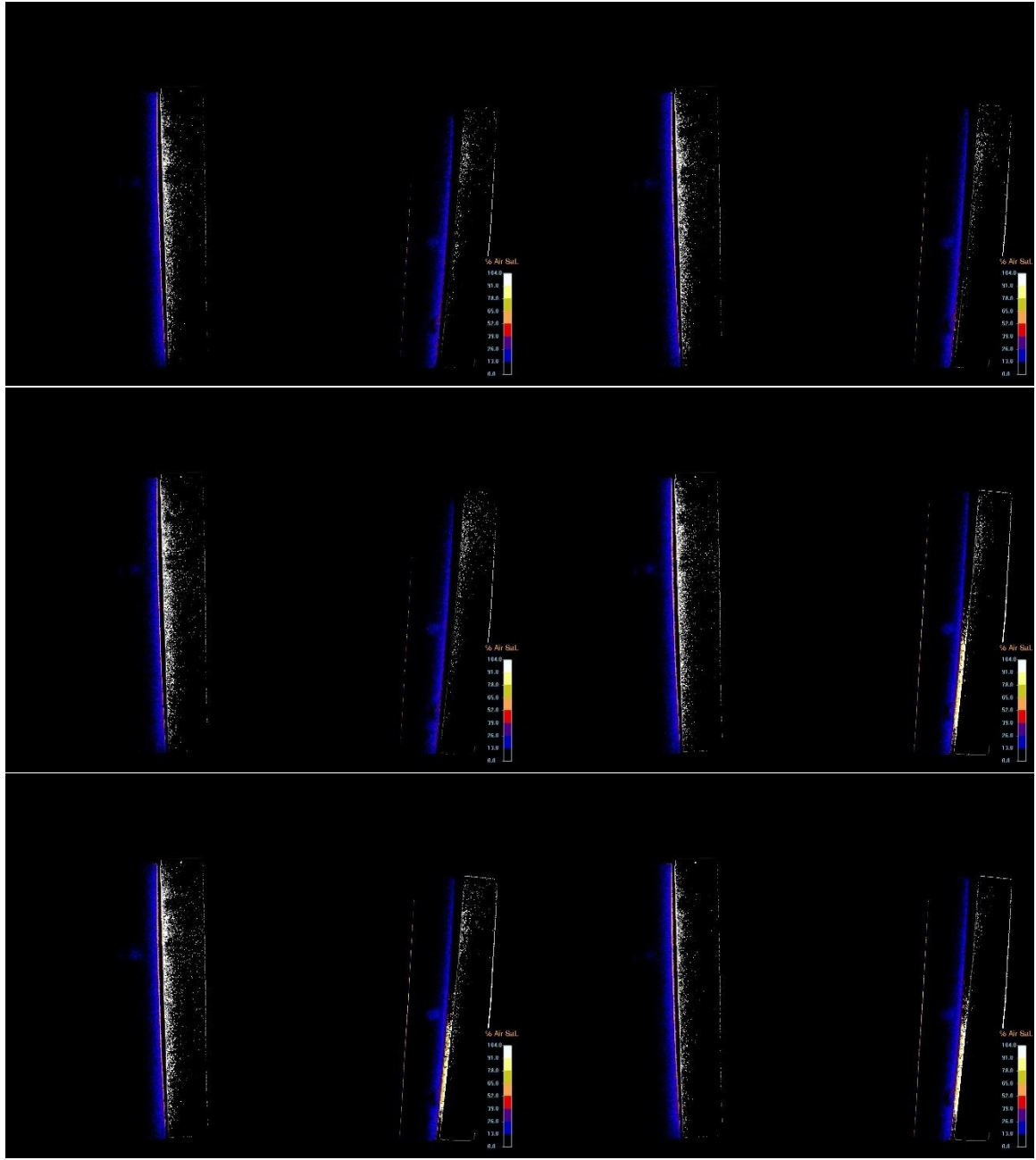




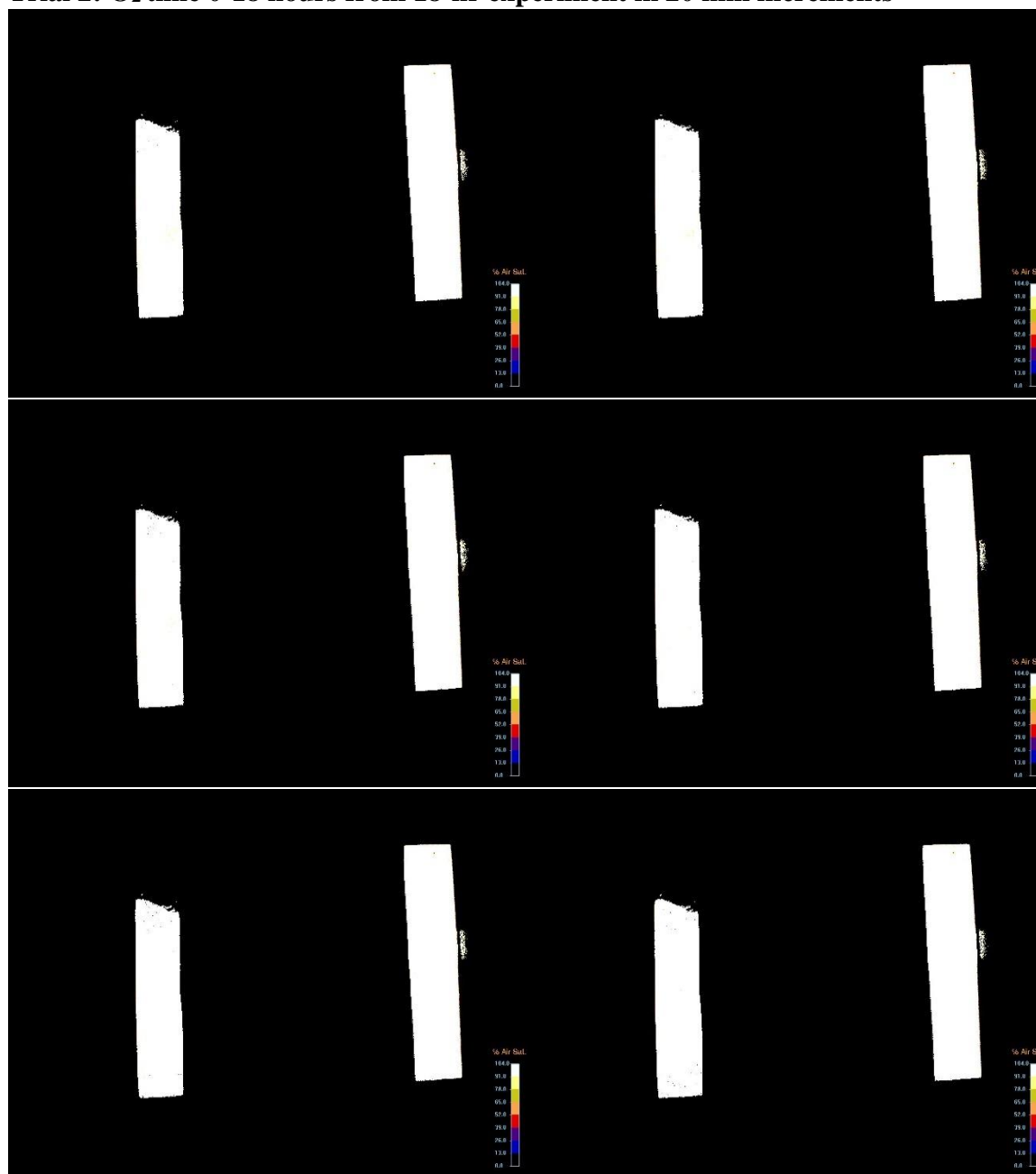


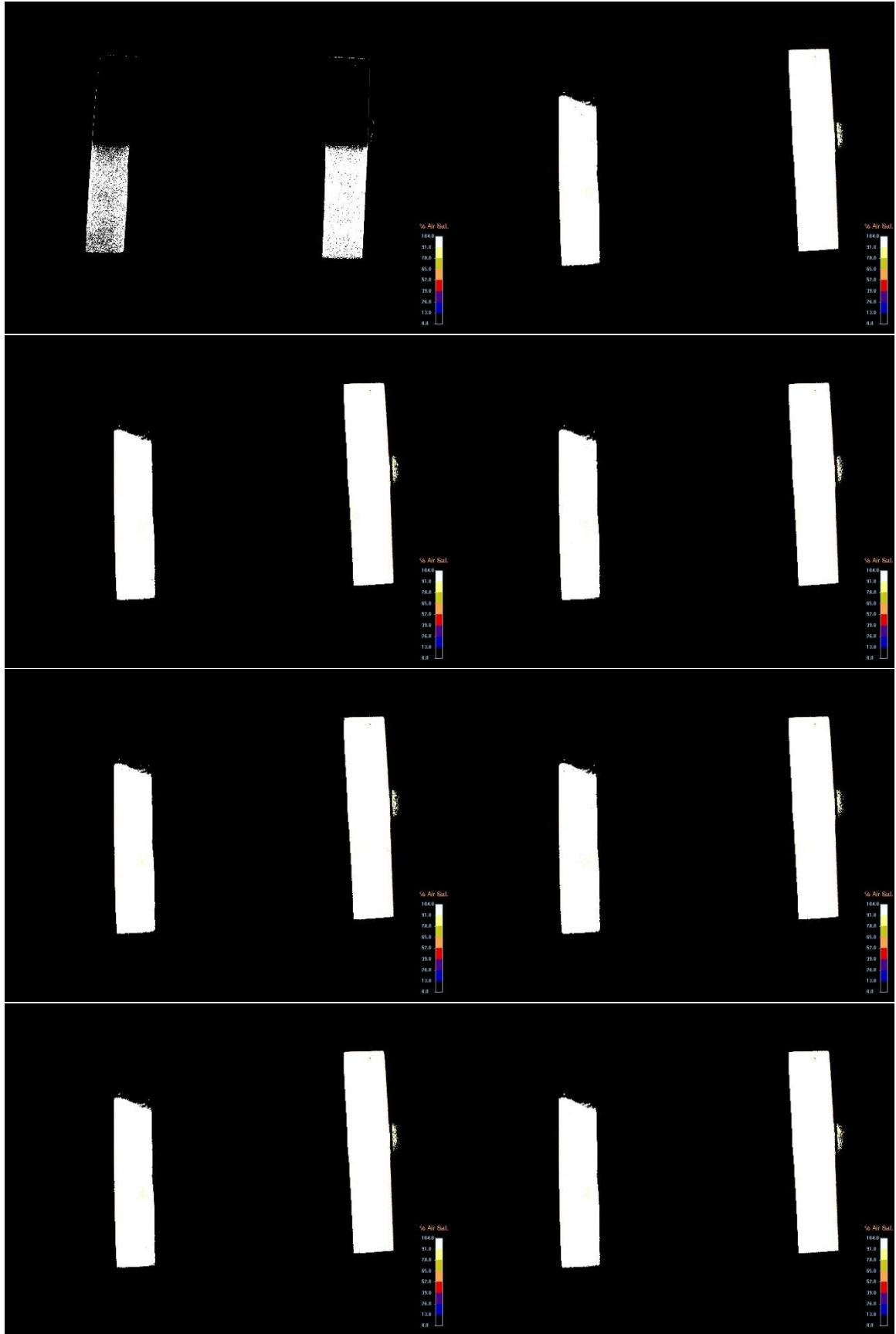


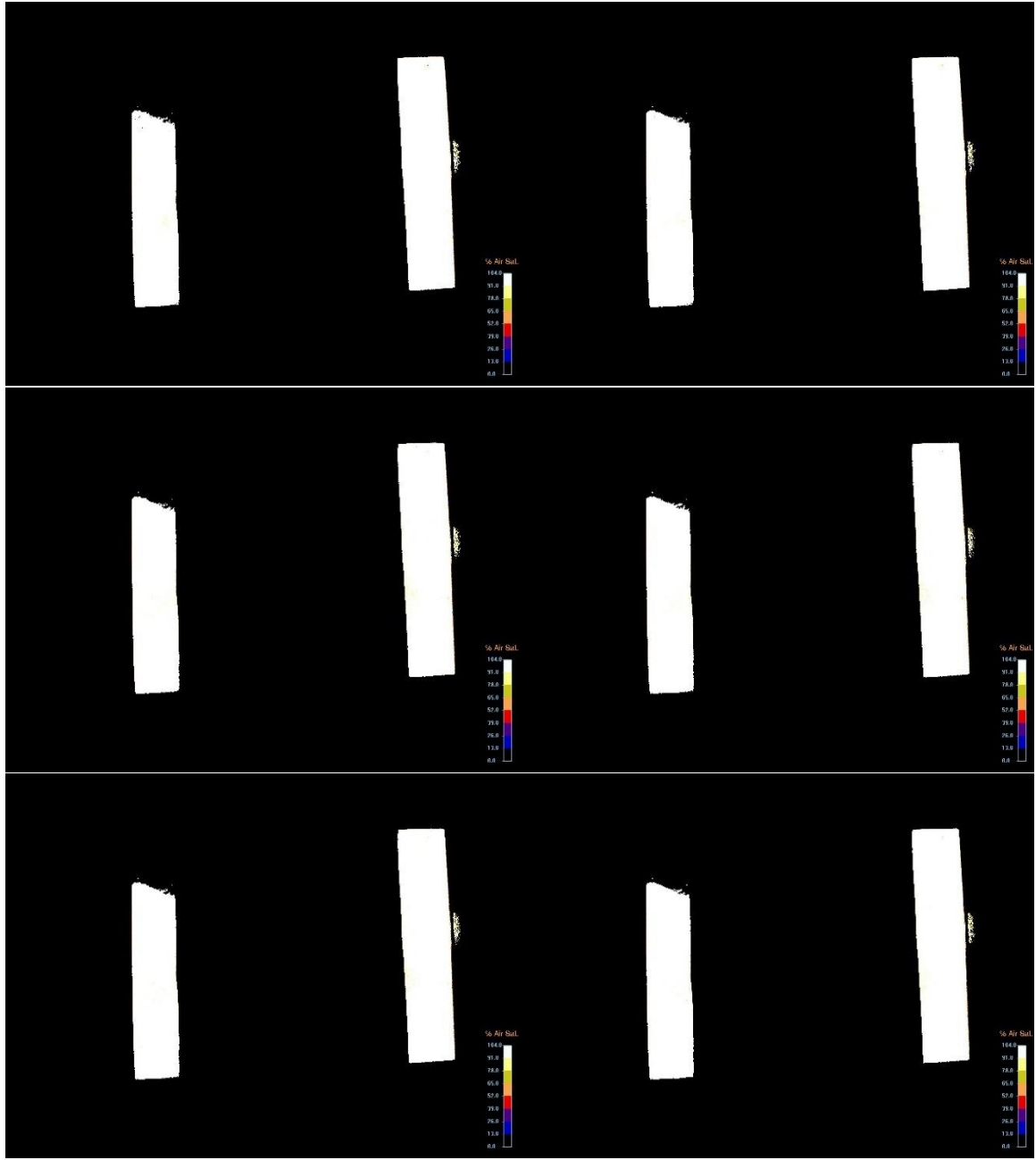


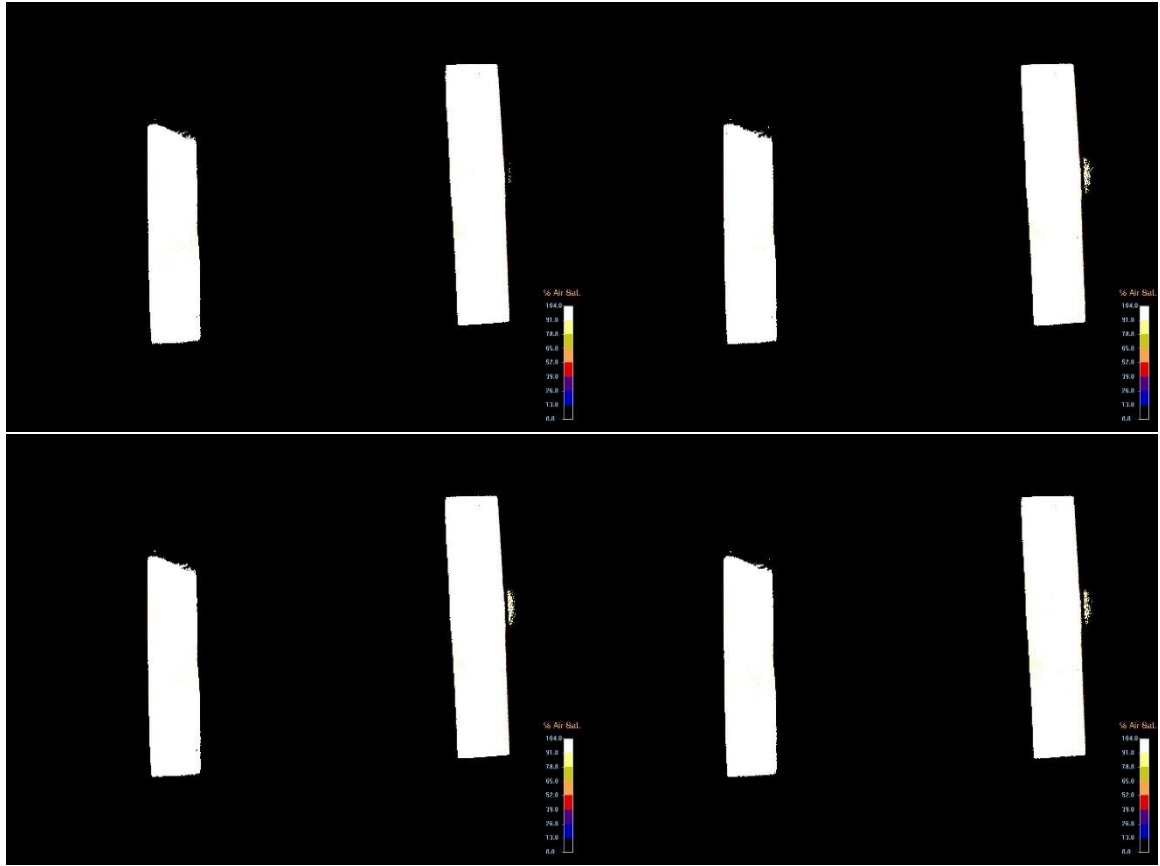


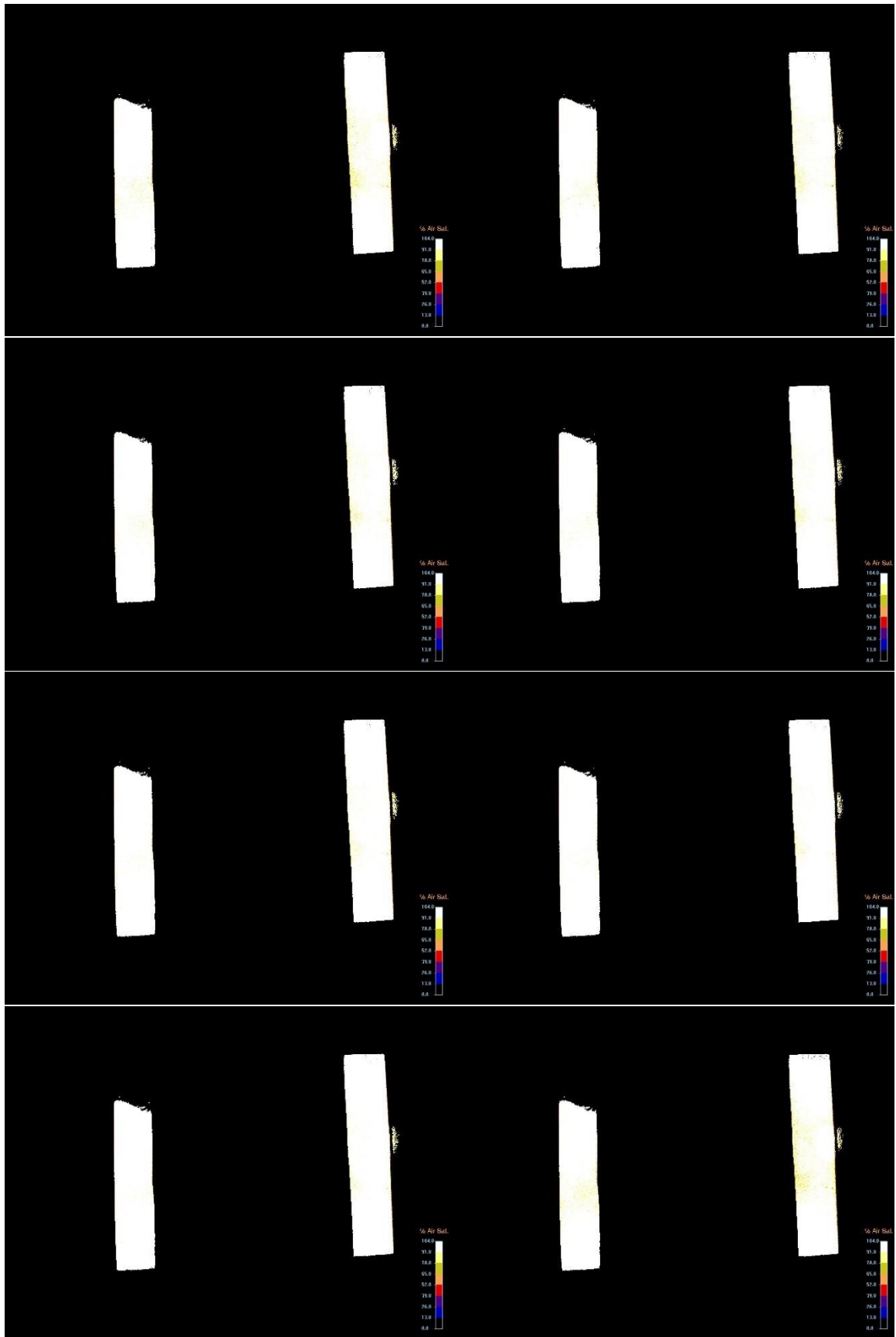
Trial 2: O₂ time 0-18 hours from 18-hr experiment in 20 min increments

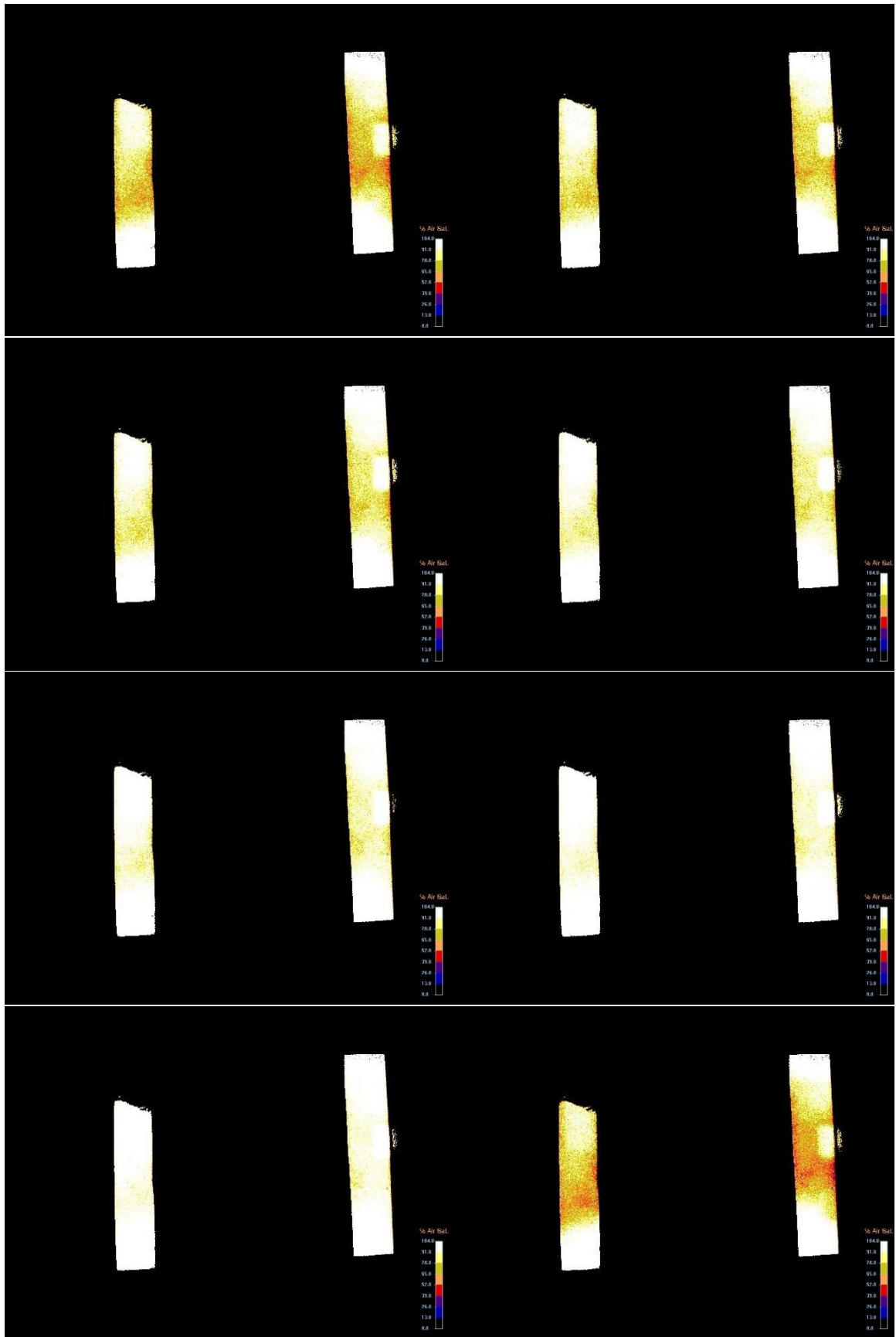


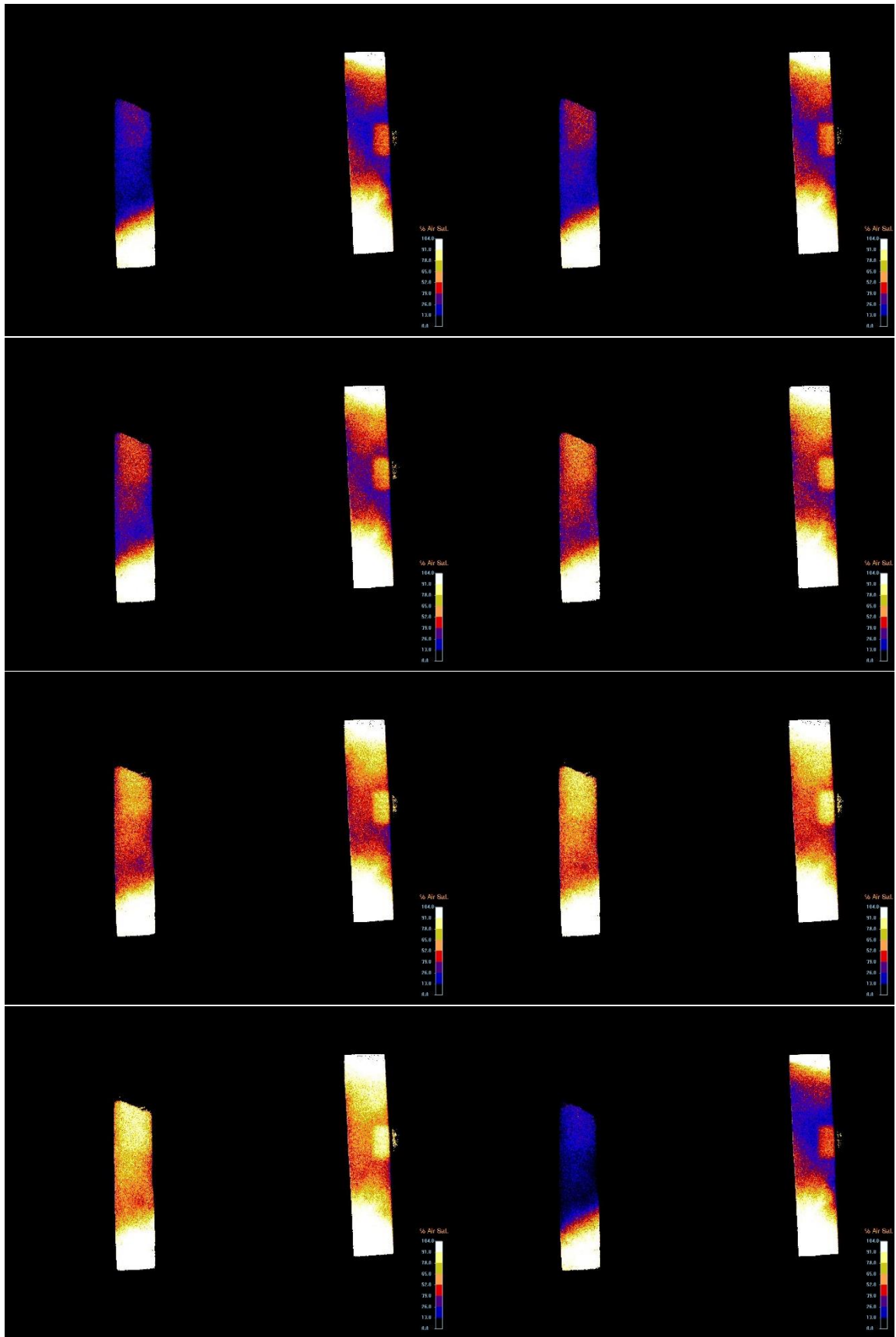


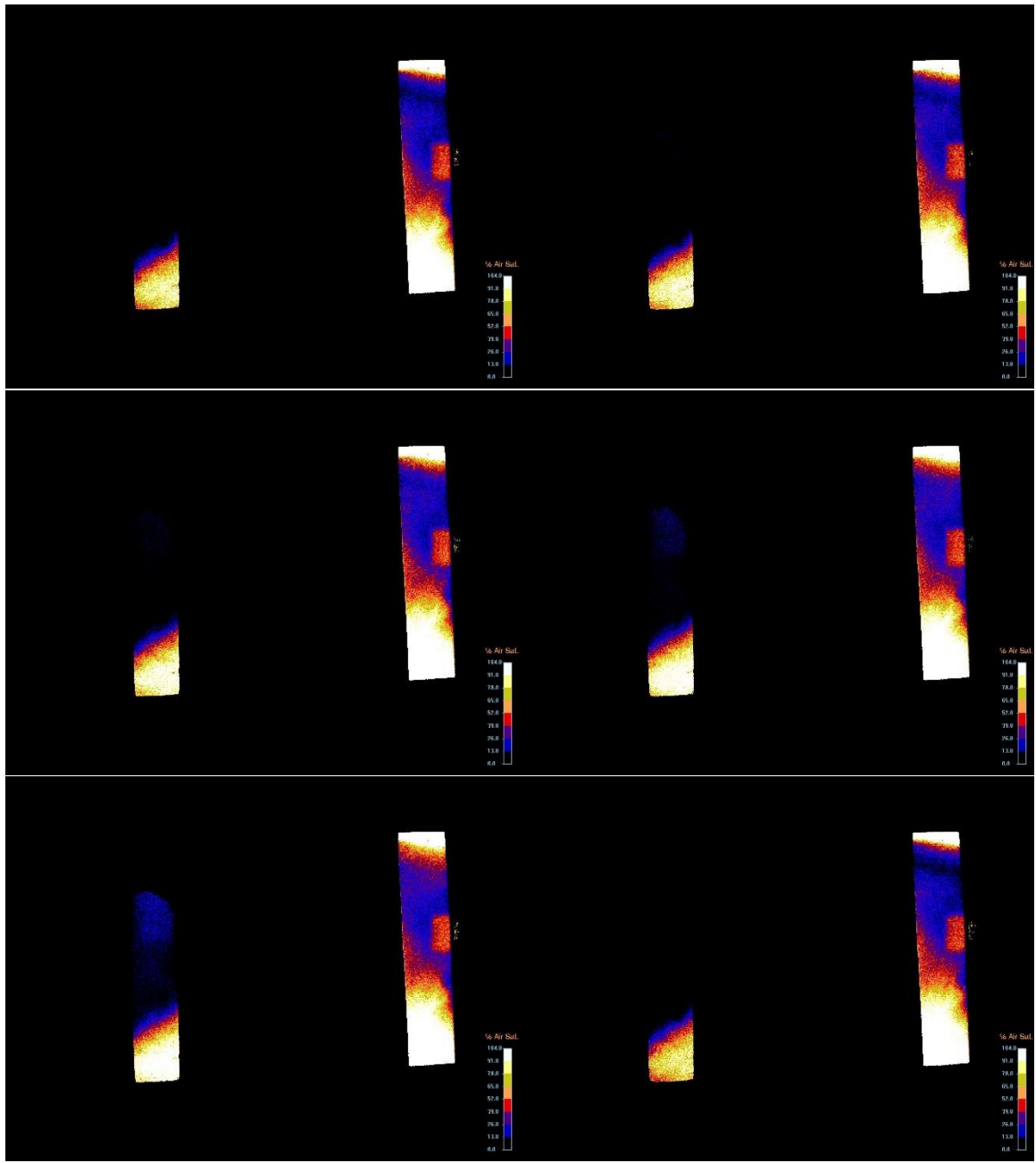












Appendix H. Preliminary Research for Experiments using Resazurin REU Student Report: Summer 2016

Natural Attenuation Of Groundwater Contaminant Plumes in The Hyporheic Zone

Aubrey McCutchan*, Katherine Santizo**, Dr. Erich Hester***, Dr. Mark Widdowson***

**NSF-REU fellow, Virginia Tech (Home Institution: Civil and Environmental Engineering, Oklahoma State University)*

***Ph.D. Student, Department of Civil and Environmental Engineering, Virginia Tech*

****Department of Civil and Environmental Engineering, Virginia Tech*

Abstract

This study looked at the reaction of resazurin to resorufin used for laboratory simulations of the hyporheic zone, a zone where groundwater and surface water mix in areas such as a riverbed. Little is understood about the rate which pollutants are remediated in this zone and the controlling factors. To establish a method for studying this topic we studied the resazurin to resorufin reaction to be used as a reactive tracer. In this reaction dissolved oxygen (DO) is consumed as well as a charged oxygen atom on the resazurin by sodium sulfite and this transforms the solution from dark blue to pink. This reaction will also be used to mimic attenuation of contaminants during naturally occurring reactions. To study the reaction, we measured the rate of DO consumption as well as the time for the solution to change color. Additionally, we used a permeameter to record the time difference of color change when the reaction occurs in sediment and if it is visible enough to be used as a tracer. Next, we also preformed tests on samples using a spectrofluorometer to understand intensity of color versus concentration during the reaction. Lastly, these results were used in computer models to mimic the hyporheic zone. These numerical models will be used to understand flow paths and chemical concentrations of DO and sodium sulfite throughout an experimental tank.

Keywords: hyporheic zone, resazurin, dissolved oxygen, numerical models

1. Introduction

The hyporheic zone is a region where surface water and groundwater mix. This zone would likely occur in a place such as a river bottom where surface water is flowing, and upwelling groundwater can combine with it in the sediment. Surface water flows into the ground due to natural phenomenon such as a barrier¹. The two water sources often have varying properties such that when they mix, can cause chemical reactions to occur which could break down pollutants otherwise known as mixing-dependent reactions^{2, 3}. Mixing-dependent reactions are reactions that can only occur when two solutions mix with each other. The different chemical compositions will allow for a chemical in one of the solutions to react with a chemical in the other solution when they mix. For example, groundwater is unlikely to have dissolved oxygen while the surface water will. Specific pollutants in the groundwater could possibly react with dissolved oxygen in surface water when the two water sources mix in the hyporheic zone⁷. Moreover, bacteria and other microorganisms reside here and can provide a way for pollutants to be naturally remediated in a river or stream⁴. In this case pollutants can be transformed by bacteria into a different compound which may be less toxic or not at all. In addition, the zone can even act as a sink for pollutants like heavy metals keeping it from the stream or river^{5, 7}. However, in certain cases such as with methylmercury, the problem with this toxic compound can be intensified which is significant because methylmercury can be passed on in the food chain and accumulate over time⁶. Overall, the hyporheic zone needs to be studied more to understand all

the processes that occur in this zone and how effective in treating pollutants it is or any negative side effects from a reaction that may occur here.

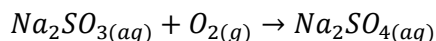
The problem we work to solve in this study is to quantify the amount of which a pollutant can be remediated in mixing-dependent reactions in the hyporheic zone as there is not very many data on this topic⁷. Our method for accomplishing this problem was to first find an abiotic reaction to simulate mixing-dependent hyporheic reactions in the lab that could mimic those that might realistically happen in the field. Furthermore, in this study only a chemical process—the resazurin to resorufin—is investigated compared to a different type of process that could take place in the hyporheic zone such as one by bacteria⁸. Next, data from the reaction was used in computer models to predict concentrations of dissolved oxygen in a large experimental tank (mesocosm) among other variables by the software such as flow paths of the solutions while in the tank. Lastly, using optodes and samples taken from the mesocosm the models will be confirmed in future laboratory experiments. These models in later studies could possibly be used for other chemical or microbial processes that occur in the hyporheic zone.

2. Research Methods and Experiment Setup

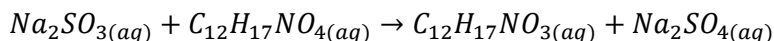
2.1 Resazurin to Resorufin Reaction Using Sodium Sulfite

To determine the reaction properties including time for dissolved oxygen consumption and for the solution to turn color from dark blue to pink, we set up a simple beaker reaction. The reactants used were resazurin (Acros Organics), sodium sulfite (certified ACS Fisher Scientific, 98%), and cobalt chloride (certified ACS Fisher Scientific, 99.2%).

The reaction has two parts as follows:



Here sodium sulfite consumes DO producing sulfate.



In this chemical reaction the sodium sulfite consumes an unstable oxygen off of the resazurin transforming it into resorufin, while also producing more sulfate.

For the beaker test 1.5 mL of resazurin from a stock solution of 0.5 g/L were used. The resazurin stocks along with the solutions made were kept in a cold room and out of light to keep the chemical from undergoing photochemical decay⁹. Then 148.5 mL of either tap or distilled water was added for the overall 150 ml solution to get a resazurin concentration of 5 mg/L. A stir plate continually mixed the solution throughout the reaction. A YSI Pro-Plus probe was used to begin measuring dissolved oxygen (mg/L) to get initial DO. Stock solutions of cobalt chloride at 0.001 M and sodium sulfite at 0.1 M were also made. Recording was then started at every one second for dissolved oxygen of the solution followed by 20 mL each of the sodium sulfite and cobalt chloride solution¹⁰. The DO continued to be recording until it neared zero and this data was analyzed to get reaction rates. Furthermore, the time for the solution to turn from blue to pink was also noted for each experiment, although this is partially variable because of the different shades of pink based off of resorufin concentration. The spectrofluorometer data are clearer on intensity of color versus concentration of both the resazurin and resorufin then what can be easily observed. This reaction was run multiple times to ensure accurate results.

2.2 Resazurin to Resorufin Reaction Without Cobalt Chloride

We also ran the resazurin to resorufin reaction with sodium sulfite but without the catalyst cobalt chloride that is meant to speed up the reaction. The reason this test was run is because using cobalt chloride as well as the other reactants adds to the waste of large experiments and past research has shown cobalt chloride to be a probable carcinogen¹¹. Cobalt chloride also interferes with the spectrofluorometer reading

of the resazurin and resorufin mostly likely due to its slight blue hue. If it can be determined cobalt chloride does need to be used this is the best outcome for the project and future studies that will use this reaction. The experiment was the same as detailed above, but only 20 ml of sodium sulfite was added to the 150 ml solution. Tests were also run on simply 150 ml of tap or distilled water with 20 ml sodium sulfite being added. The rate of DO consumption was recorded to compare reactions rates to the resazurin to resorufin tests.

2.3 Permeameter Tests

A permeameter is a device that measures the ability of sediment to allow liquid to pass through. By controlling the hydraulic head on the device, we can have liquid pass through it at a specific flow rate. The permeameter first had water run through it continuously for at least 3 days to ensure the sand settled and that all the air was pushed out of the column. Additionally, the sand used for the permeameter was also the same type of sand to be used in the large mesocosm experiments to eliminate sand type from being a variable in the experiments (DO-50 white sand with an average diameter of 0.53 mm). Multiple tests with tap water running through the device were then run to find the right hydraulic head for a flow rate that would allow enough time for the resazurin to resorufin reaction to occur and to ensure the permeameter was giving steady readings. Once the flow rate was deemed constant a solution of resazurin at 5 mg/L was ran through the permeameter immediately followed by a solution of 1:1 mix of cobalt chloride (0.001 M) and sodium sulfite (0.1 M). Where these two solutions met is where the resazurin should start to transform into resorufin and pink should be seen in the sediment. This process will not only show that this reaction could most likely be replicated in the mesocosm experiments, but that the blue and pink colors can actually be seen in the sediment so photographs of the tracer can help calibrate computer models of the mesocosm.

2.4 Spectrofluorometer Tests

The spectrofluorometer (FluoroMax®-4 Spectrofluorometer, Horiba Scientific) was used to measure the light intensity emitted by resazurin and resorufin during the reaction. These values will be used to get concentration from samples during mesocosm experiments to see if the data matched the concentration we would expect based off of the computer models. This also shows how intensity can be matched to concentration when using a similar method to get concentration of resazurin in the mesocosm by analyzing pictures from a camera. The camera will have a fairly similar calibration process as detailed below, but still separate than the process done with the spectrofluorometer.

First, using a UV spectrophotometer (UV-1800, Shimadzu), the excitation wavelengths for both resazurin and resorufin were determined. The samples used for this were from 1 mg/L to 5 mg/L of both resazurin and resorufin to confirm different concentrations would have the same excitation wavelength. Once the excitation wavelength was known the emission was found using single point tests on the spectrofluorometer. Now to know intensity per concentration calibration curves had to be determined. We measured resazurin at 8, 16, 24, 32, 40 μ L for 1, 2, 3, 4, 5 mg/L solutions respectively at a total 4 mL each (cuvettes hold up to 4mL). The dilution to get to 4 ml was half DI water (1.992-1.960 mL) and 1.5 mL sodium sulfite (0.1 M). Using an excitation of 607.5 nm and 675 nm for emission, the intensity of each solution was recorded to get the calibration curves. Once calibration curves were established a resazurin to resorufin reaction was then performed (one without cobalt chloride) as outlined in Section 2.1. Samples were taken every 1-minute for 40 minutes and then additionally every 5 minutes at 55 minutes until 80 minutes had passed. This is approximately how long it takes to see a full color change using this particular solution. Samples were run in the spectrofluorometer to get the intensity at each time reading. Using the calibration curves, we can determine intensity versus concentration to use for mesocosm models.

2.5 Ion Chromatography

Preliminary results indicated that the time for the solution of resazurin to resorufin reaction to turn from blue to pink took longer when tap water was used instead of distilled water. Although it is not completely clear why this occurs, one hypothesis is that perhaps sulfate or other compounds in tap water are interfering with resorufin production. Furthermore, the theoretical amount of sulfate produced using stoichiometry is much higher based off of preliminary data when using ion chromatography to measure the sulfate production. Using ion chromatography, we can determine the differences in sulfate production when tap water is used compared to distilled water. We used an Ion Chromatography System (Thermo Scientific), and the samples had no headspace to keep the sulfite from reacting with oxygen preventing additional sulfate production after the initial reaction had occurred. The samples were also kept refrigerated as a precaution.

2.6 Future Mesocosm Experiments

This mesocosm (HM 169, Gunt Hamburg) has been altered to obtain desired residence times based off of how long the reaction will take to occur. Dimensions of the mesocosm are used in the numerical models of the hydraulic head throughout the tank.

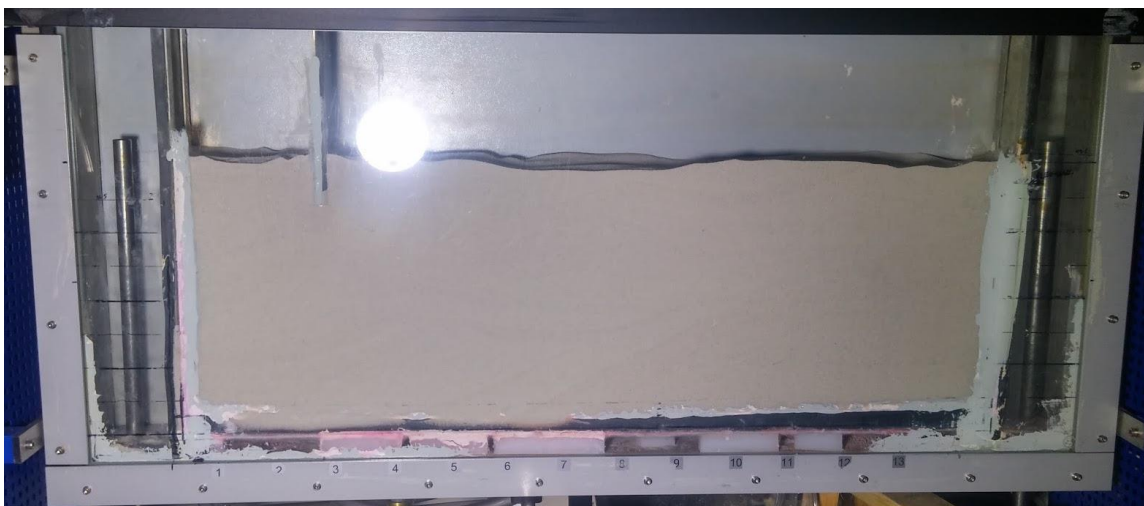


**Photo 1. Picture of the mesocosm that will be used in experiments.
(Katherine Santizo, 06/02/2016)**

The planar optodes to be used in later experiments were provided by Dr. Glud and Dr. Larsen at the University of Southern Denmark¹². Blue LED lights, and computer software (Look@RGB, Fish N' Chips) are also needed for analyzing the data from the optodes. The optodes will confirm DO concentrations predicted by the computer models. Syringes (Sigma Aldrich) will be used to draw samples for sulfate concentration.

2.7 Numerical Models

The softwares used were MODFLOW and SEAM3D. They were used to come up with models of hydraulic head throughout the mesocosm and concentrations of chemicals at different locations at steady state. MODFLOW used the dimensions of the mesocosm while the SEAM3D models were a combination of the hydraulic head information from MODFLOW, and the reaction rate of dissolved oxygen

consumption. Images of the mesocosm using the optodes and samples from the mesocosm will be used to verify the models or indicate needed adjustments.

3. Results and Discussion

3.1 Reaction Rates for Dissolved Oxygen Consumption

Shown below in Figure 1 is raw data of dissolved oxygen versus time when using distilled water, the reactant sodium sulfite, and with the addition of cobalt chloride. The reaction time for resazurin to resorufin reaction to deplete the dissolved oxygen in the water occurs in about 12 seconds. A similar reaction time was also shown during tests using tap water and another run without the addition of the catalyst cobalt chloride. Shown in Figure 2 and 3 respectively is the natural log of the DO versus time and 1 divided by DO versus time. Based off of the three graphs you can determine what order reaction it is. The graph with the most linear slope determines this. Concentration versus time indicates a zeroth order reactions. The natural log of concentration versus time indicates first order. 1/concentration versus time indicates a second order reaction. The natural log of DO graph has the most linear slope and indicates the resazurin to resorufin reaction is a first order reaction. The rate coefficient as shown on Figure 2 is 0.2845 s^{-1} . This rate coefficient along with type of reaction (first order) is used in the computer models to show the concentration of dissolved oxygen at steady state in the mesocosm.

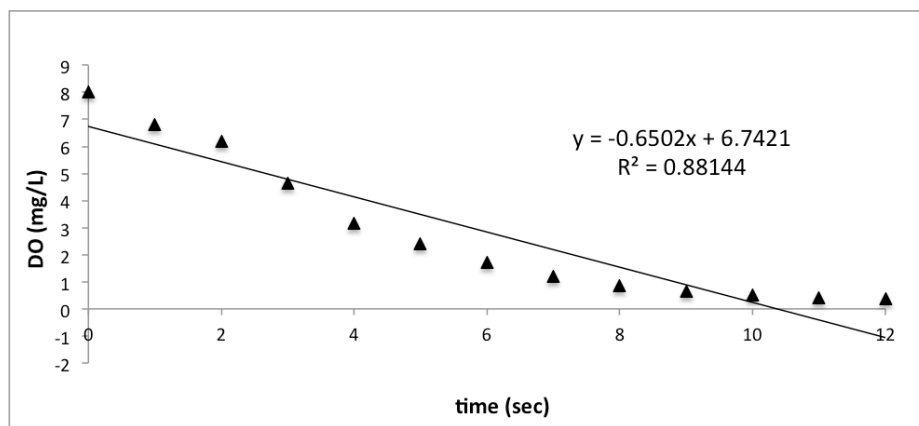


Figure 1. Raw data from YSI ProPlus of DO vs time.

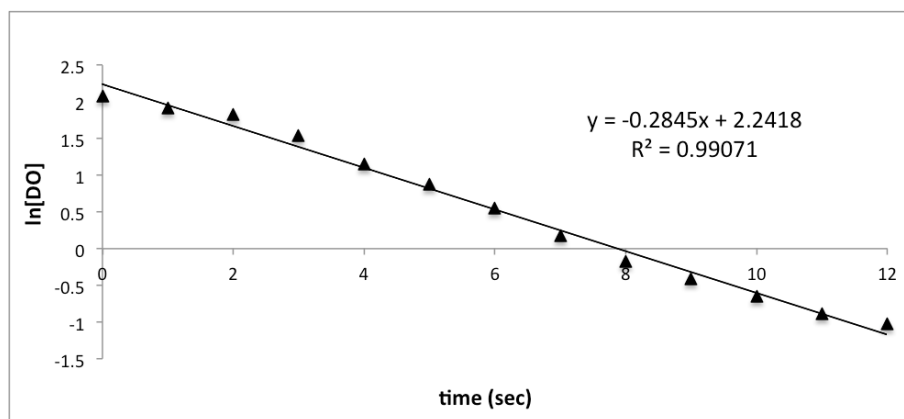


Figure 2. Natural log of DO vs time.

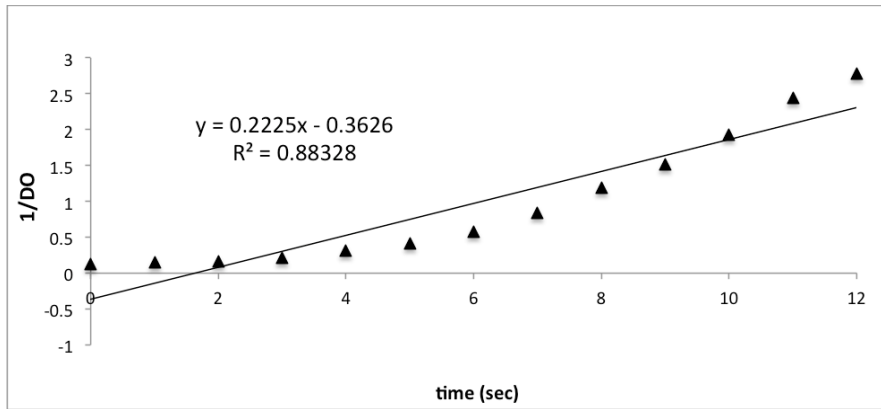
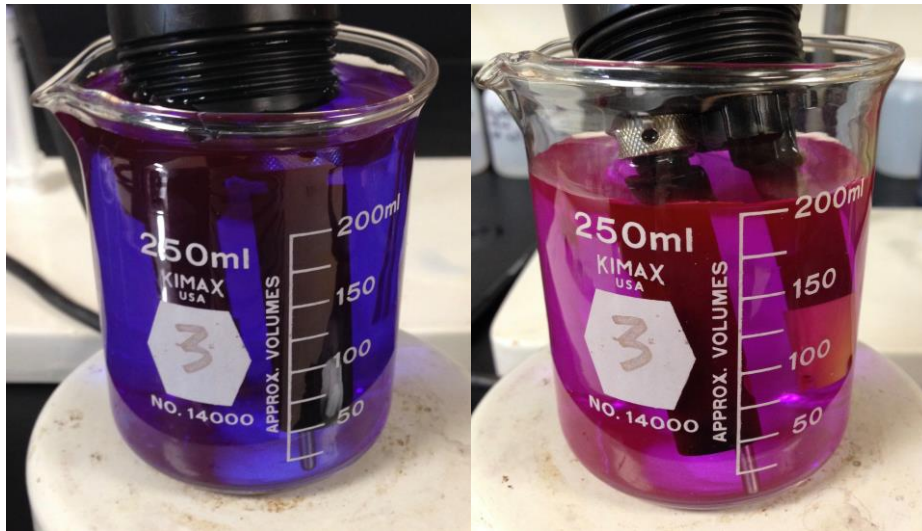


Figure 3. 1/DO vs time.

3.2 Color Change

Although the time for almost complete dissolved oxygen consumption by sodium sulfite is less than fifteen seconds, it takes about 35-40 minutes for the resazurin to be converted sufficiently to resorufin to make a complete color change (Photos 3-4). Additional results from the reaction without using cobalt chloride and a distilled water solution indicate the time to take slightly longer at about 45 minutes to 1 hour. However, when doing this same test with tap the solution never makes a full color change. This needs to be investigated further to know if tap water can be used in the large mesocosm experiments without using cobalt chloride.



Time = 0 min

Time = 35 min

Photo 2 and 3. (Aubrey McCutchan, 06/01/2016)

3.3 Permeameter Results

The results as shown in Photos 4 and 5 demonstrate the resazurin to resorufin reaction will be useful as a tracer reaction in the mesocosm because there is a noticeable pink hue that can be seen in the sediment column. Furthermore, the color change happened in about 12 minutes, which is much faster than the time observed in beaker experiments. This result indicates that when mesocosm results are performed the reactions could take a shorter amount of time to occur than expected and the models will need to be adjusted accordingly. Moreover, when the reaction takes place sodium sulfite consumes the dissolved oxygen first

and because the beaker experiments are open, reoxygenation is occurring. In sediment experiments the solution is not open to the air; therefore, the sodium sulfite reactant will not be continually consuming DO and will produce resorufin from resazurin much more quickly. This would result in the faster color change that we observed.



Resorufin
production
seen (pink
hue).

Before reactants are added. Reaction inside of the column.
Time = 0 min Time = 12 min

Photo 4 and 5. (Aubrey McCutchan, 06/09/2016)

Towards the bottom of the columns note the darker color seen is not the blue resazurin solution but precipitate of the cobalt chloride from sodium sulfite and cobalt chloride mixing. This is another reason to avoid using cobalt chloride in the reaction because the precipitate sticks onto the sand and would most likely interfere with pictures trying to determine resazurin concentration later on.

3.3 Spectrofluorometer Results

Figures 4 through 6 show the results for the calibration curve, intensity versus time during the reaction, and concentration versus time using the calibration curve equation $y = 12491x + 17321$ where y is the intensity and x is the concentration. Only resazurin values are shown as the resorufin data, although recorded, is not expected to be as accurate because the excitation and emission wavelengths of resorufin to use for the spectrofluorometer were not coming out precisely enough. The data shown will be used for samples taken from future mesocosm experiments to determine the concentration of resazurin.

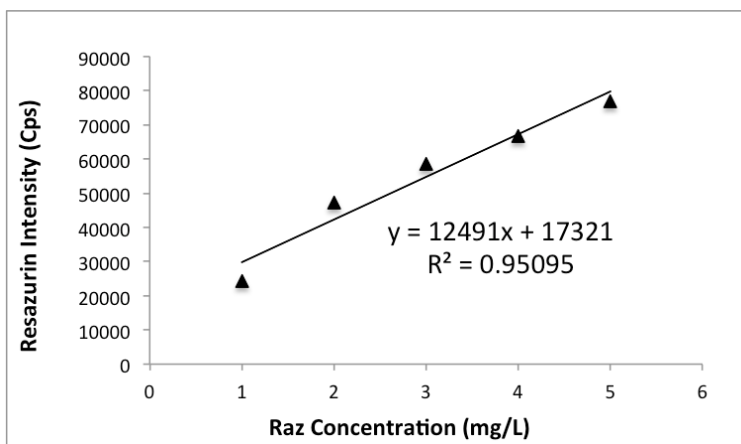


Figure 4. Resazurin calibration curve. Raw data from spectrofluorometer of intensity vs concentration.

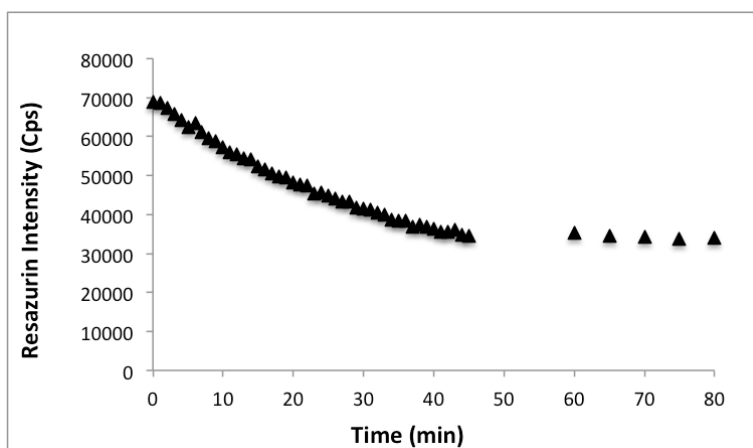


Figure 5. Resazurin intensity curves. Raw data from spectrofluorometer of intensity vs time.

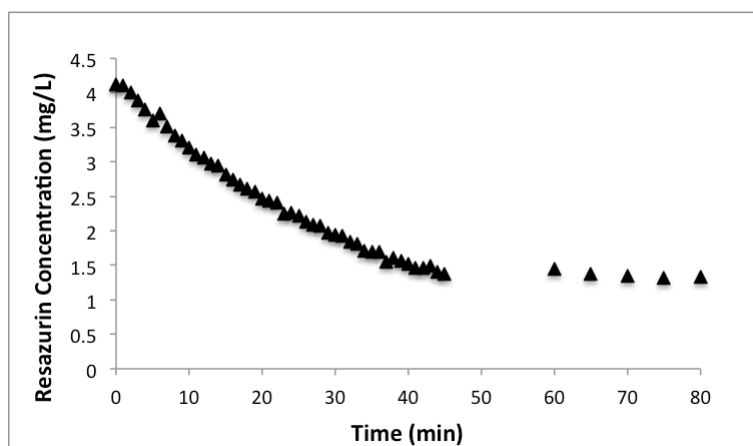


Figure 6. Resazurin concentration curve. Graph using resazurin calibration and intensity curves to show resazurin concentration vs time during the reaction.

3.4 Numerical Models

The three figures below are models of the mesocosm showing the hydraulic head distribution, and the dissolved oxygen and sodium sulfite concentrations at steady state. In these models red indicates a higher value while blue represents lower values.

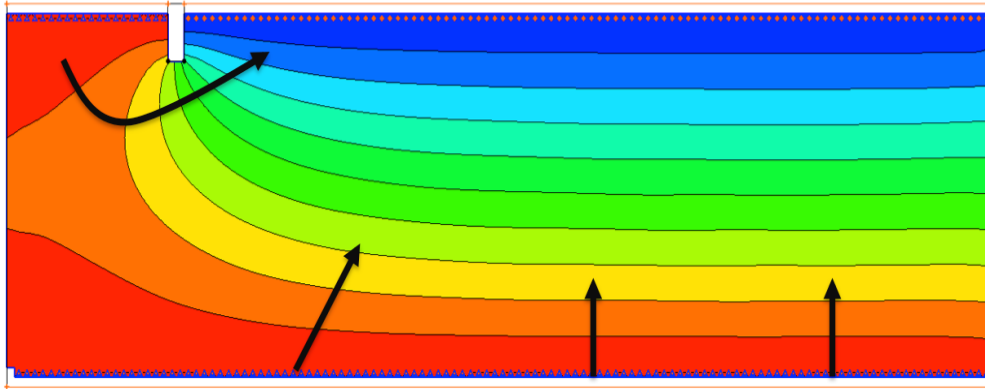


Figure 7. Hydraulic head distribution of the mesocosm using MODFLOW.

As indicated by the arrows on Figure 7 this model shows the flow paths of the solutions inside the tank.

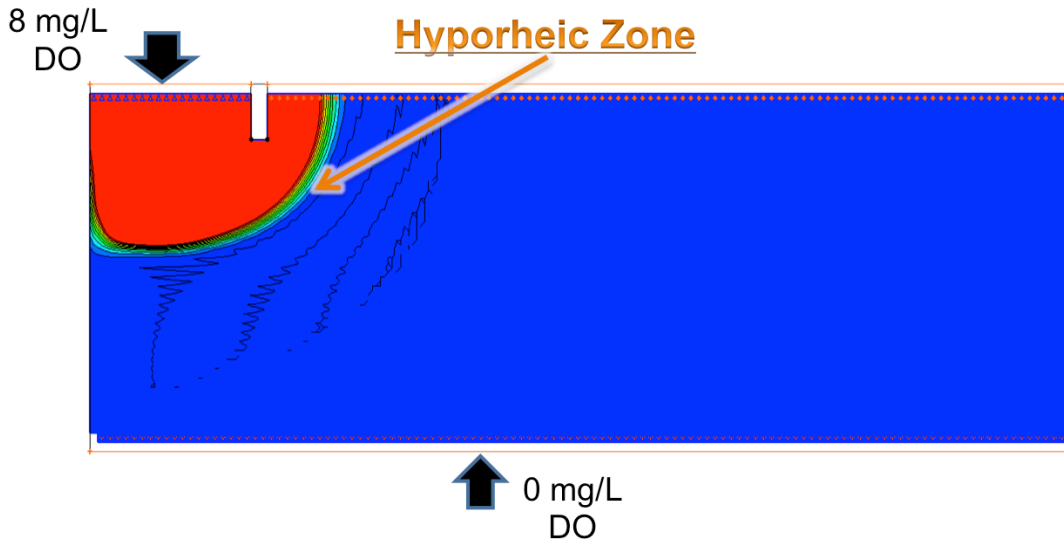


Figure 8. Dissolved oxygen concentration in the mesocosm at steady state using SEAM3D.

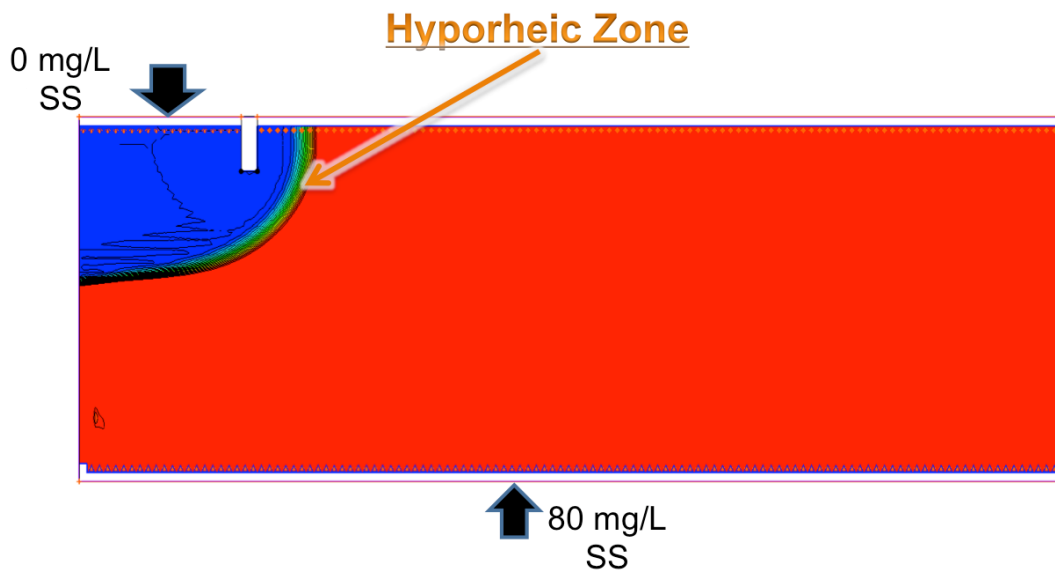


Figure 9. Sodium sulfite concentration in the mesocosm at steady state using SEAM3D.

Figures 8 and 9 show the concentration of two of the main components in the resazurin to resorufin reaction. Upwelling water coming in at the bottom of the tank will mimic groundwater. This source will have no dissolved oxygen but will have a sodium sulfite concentration of 80 mg/L. The water flowing in from the top left corner will act as surface water being pushed into the sediment, therefore mixing with the groundwater to create a hyporheic zone as labeled in the models. This source will have a dissolved oxygen concentration but no sodium sulfite. Additionally, in Figure 8 and 9 the hyporheic zone is labeled. Based off of data used for the numerical model this is where we expect the laboratory simulated hyporheic zone to occur. The small multicolored band in each figure represents varying high to low concentrations of dissolved oxygen or sodium sulfite.

3.5 Ion Chromatography – Preliminary Results

Data from the ion chromatography tests have not provided meaningful results and more testing is needed. Data showed sulfate production was still much higher than the values we should have received based off of stoichiometry calculations.

4. Conclusion

Altogether, this project has made significant progress in determining a method to quantify the amount of which a pollutant can be naturally attenuated in the hyporheic zone. As shown by the data additional testing is still needed to see if the resazurin to resorufin reaction will work in experiments as a reactive tracer for our purposes. Although by the results in this paper, specifically the permeameter data, it can be hypothesized that the reaction will work as a tracer for large laboratory experiments. Furthermore, we have established a reaction rate for dissolved oxygen consumption during the resazurin to resorufin reaction. Moreover, tests on the spectrofluorometer have helped us determine kinetic parameters for the reaction. Through the spectrofluorometer work we can now also estimate resazurin concentration using intensity of samples taken during mesocosm experiments. In future experiments this data and methodology will be used to verify numerical computer models and to make adjustments to them. Later a bacterial component to the mesocosm will be added to understand bacterial remediation that occurs in the hyporheic zone.

5. Acknowledgements

I would like to thank my faculty mentors Dr. Erich Hester and Dr. Mark Widdowson for the all the help and guidance they have given me during my time in the REU program. I would like to give a special thanks to my graduate mentor Katherine Santizo for all the support and direction she has given me in the project. I would also like to thank Dr. Lohani, the coordinator of the REU program, for his dedication to the program and for making sure the REU scholars got the most out of our experience.

We acknowledge the support of the National Science Foundation through NSF/REU Site Grant EEC-1359051 and NSF-Environmental Engineering Award 1437021. Any opinions, findings, and conclusions or recommendations expressed in this paper are those of the author(s) and do not necessarily reflect the views of the National Science Foundation.

References

1. Boulton, A., Findlay, S., & Marmonier, P. (1998). The functional significance of the hyporheic zone in streams and rivers. *Annual Review of Ecology and Systematics*, 29(1998), 59–81. doi:10.1146/annurev.ecolsys.29.1.59
2. Landmeyer, J. E., Bradley, P. M., Trego, D. A., Hale, K. G., & Haas, J. E. (2010). MTBE, TBA, and TAME attenuation in diverse hyporheic zones. *Ground Water*, 48(1), 30–41. doi:10.1111/j.1745-6584.2009.00608.x
3. Stegen, J. C., Fredrickson, J. K., Wilkins, M. J., Konopka, A. E., Nelson, W. C., Arntzen, E. V., ... Tfaily, M. (2016). Groundwater–surface water mixing shifts ecological assembly processes and stimulates organic carbon turnover. *Nature Communications*, 7, 11237. doi:10.1038/ncomms11237
4. Pinay, G., O’Keefe, T. C., Edwards, R. T., & Naiman, R. J. (2009). Nitrate removal in the hyporheic zone of a salmon river in Alaska. *River Research and Applications*, 25(4), 367–375. doi:10.1002/rra.1164
5. Gandy, C. J., Smith, J. W. N., & Jarvis, A. P. (2007). Attenuation of mining-derived pollutants in the hyporheic zone: A review. *Science of the Total Environment*, 373(2-3), 435–446. doi:10.1016/j.scitotenv.2006.11.004
6. Hinkle, S. R., Bencala, K. E., Wentz, D. A., & Krabbenhoft, D. P. (2014). Mercury and methylmercury dynamics in the hyporheic zone of an Oregon stream. *Water, Air, and Soil Pollution*, 225(1). doi:10.1007/s11270-013-1694-y
7. Gandy, C. J., Smith, J. W. N., & Jarvis, A. P. (2007). Attenuation of mining-derived pollutants in the hyporheic zone: A review. *Science of the Total Environment*, 373(2-3), 435–446. doi:10.1016/j.scitotenv.2006.11.004
8. Haggerty, R., Argerich, A., & Mart??, E. (2010). Development of a “smart” tracer for the assessment of microbiological activity and sediment-water interaction in natural waters: The resazurin-resorufin system. *Water Resources Research*, 46(4), 1–10. doi:10.1029/2007WR006670
9. Haggerty, R., Argerich, A., & Marti, E. (2010). Development of a “smart” tracer for the assessment of microbiological activity and sediment-water interaction in natural waters: The resazurin-resorufin system. *Water Resources Research*, 46(4), 1–10. doi:10.1029/2007WR006670
10. Ghaly, A. E., & Kok, R. (1988). The effect of sodium sulfite and cobalt chloride on the oxygen transfer coefficient. *Applied Biochemistry and Biotechnology*, 19(3), 259–270. doi:10.1007/BF02921498
11. Iarc, O. (2010). Table 9 Carcinogens Table : OSHA , IARC , NTP , ACGIH (March 2010) Chemical. *Safety And Health*, (March), 1–16.
12. Larsen, M., Borisov, S. M., Grunwald, B., Klimant, I., & Glud, R. N. (2011). A simple and inexpensive high resolution color ratiometric planar optode imaging approach: application to oxygen and pH sensing. *Limnology and Oceanography: Methods*, 9, 348–360. doi:10.4319/lom.2011.9.348

Supporting Data for Student Report

The following results are from experiments conducted from June 2016-July 2016. The experiments were conducted in a 150 ml beaker with a stir plate at a setting of 2. DO measurements were taken with the YSI Pro Plus DO probe. Resazurin kinetic values were analyzed using HORIBA FluoroMax 4.

From the measurements it was determined removing the cobalt chloride catalyst added to aid the deoxygenation rate did not slow the reaction between the dissolved oxygen and sodium sulfite. It did, however, reduce the rate at which sodium sulfite transforms resazurin to resorufin. The reaction order for the resazurin was determined to be first-order.

Table 1. Summary of DO kinetic results using 0.1 M Sodium Sulfite (Na_2SO_3) and 0.001 M Cobalt Chloride (CoCl_2). The reaction best fit resulted to be a first-order reaction.

Water Type	Raz Concentration [mg/L]	0.1 M Sodium Sulfite and 0.001 M Cobalt Chloride added [mL]	Rate Coefficient [1/sec]	R ²
DI	5	20	0.273	0.977
Tap	5	20	0.260	0.947
DI	5	20	0.223	0.970
Tap	5	20	0.316	0.993
DI	0	20	0.360	0.984

The following figures display the results illustrated in Table 1.

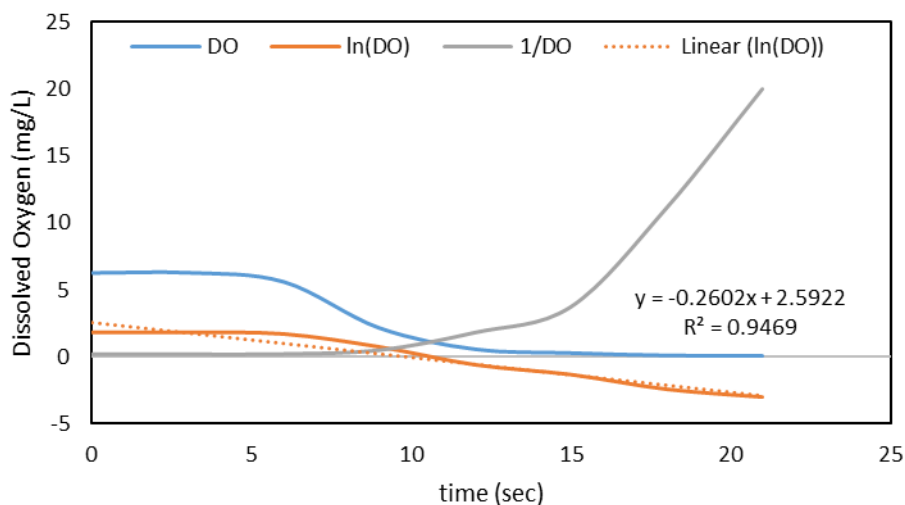


Figure 1. 5 mg/L Raz tap water solution with 20 ml of 0.1 M sodium sulfite and 20 ml of 0.001 M cobalt chloride added to solution. Dissolved Oxygen (DO) was recorded every 3 seconds. Only trendline and r-squared for first order kinetics shown.

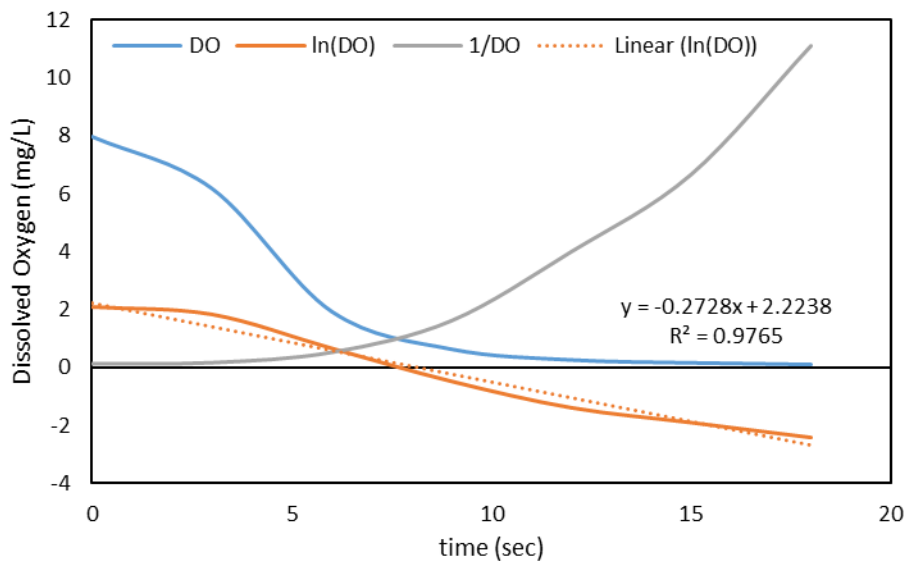


Figure 2. 5 mg/L Raz distilled water solution with 20 ml of 0.1 M sodium sulfite and 20 ml of 0.001 M cobalt chloride added to solution. Dissolved Oxygen (DO) was recorded every 3 seconds. Only trendline and r-squared for first order kinetics shown.

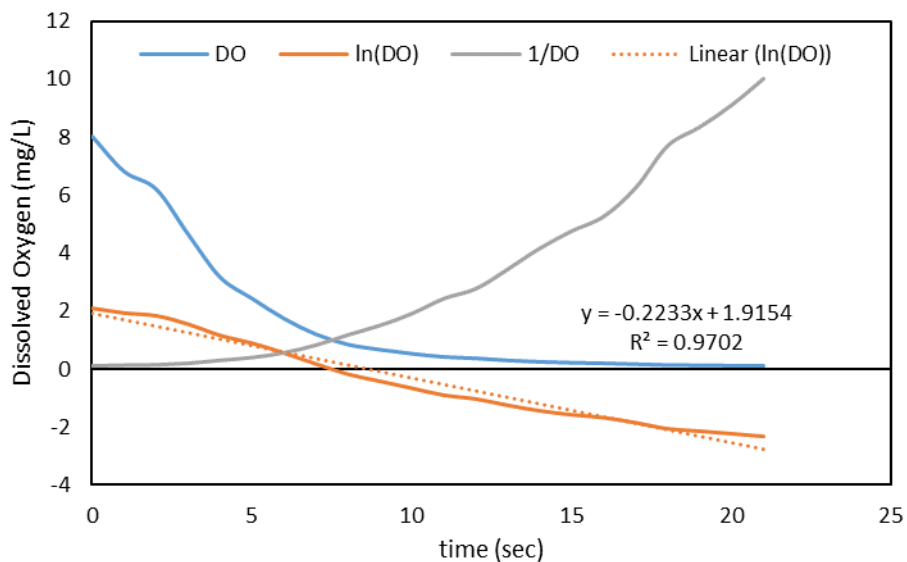


Figure 3. 5 mg/L Raz distilled water solution with 20 ml of 0.1 M sodium sulfite and 20 ml of 0.001 M cobalt chloride added to solution. Dissolved Oxygen (DO) was recorded every second. Only trendline and r-squared for first order kinetics shown.

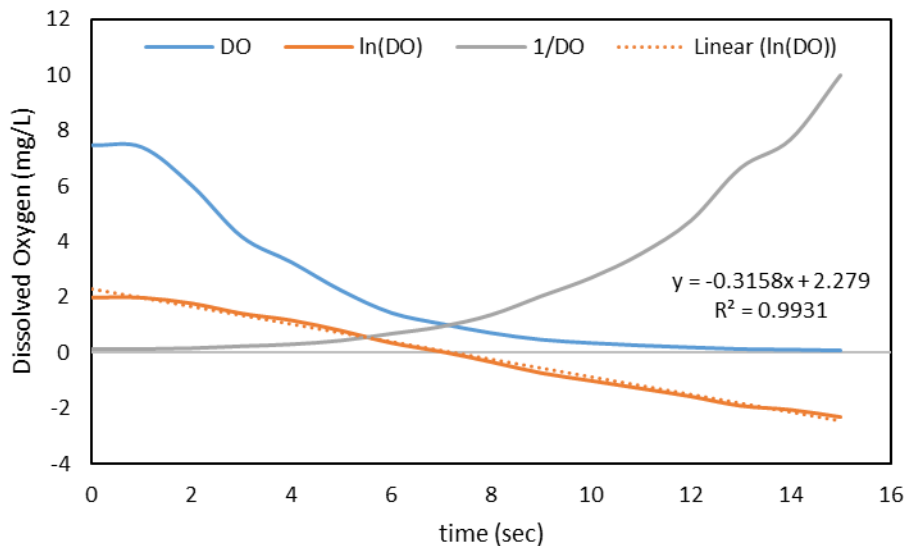


Figure 4. 5 mg/L Raz tap water solution with 20 ml of 0.1 M sodium sulfite and 20 ml of 0.001 M cobalt chloride added to solution. Dissolved Oxygen (DO) was recorded every second. Only trendline and r-squared for first order kinetics shown.

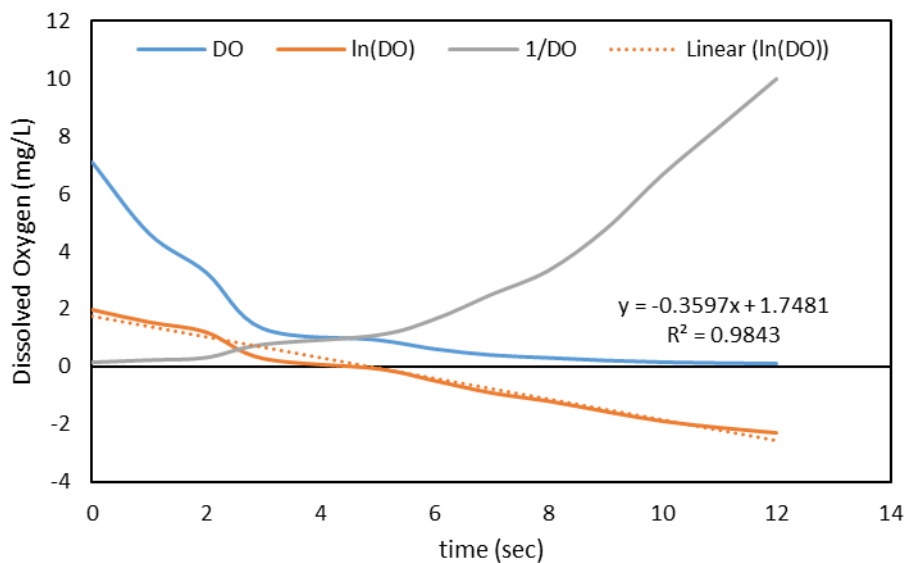


Figure 5. 0 mg/L Raz distilled water solution with 20 ml of 0.1 M sodium sulfite and 20 ml of 0.001 M cobalt chloride added to solution. Dissolved Oxygen (DO) was recorded every second. Only trendline and r-squared for first order kinetics shown.

Table 2. Summary of DO kinetic results using 0.1 M Sodium Sulfite (Na_2SO_3). The reaction resulted to be a first-order reaction.

Water Type	Raz Concentration [mg/L]	0.1 M Sodium Sulfite added [mL]	DO Rate Coef. [1/sec]	DO R^2
DI	5	20	0.340	0.989
DI	0	10	0.313	0.976
DI	5	10	0.340	0.990
DI	5	50	0.257	0.971
Tap	5	30	0.300	0.985
DI	5	50	0.204	0.969
Tap	5	30	0.222	0.970
Tap	5	20	0.297	0.985
DI	5	20	0.223	0.953
DI	0	20	0.334	0.989

The following figures display the results illustrated in Table 2.

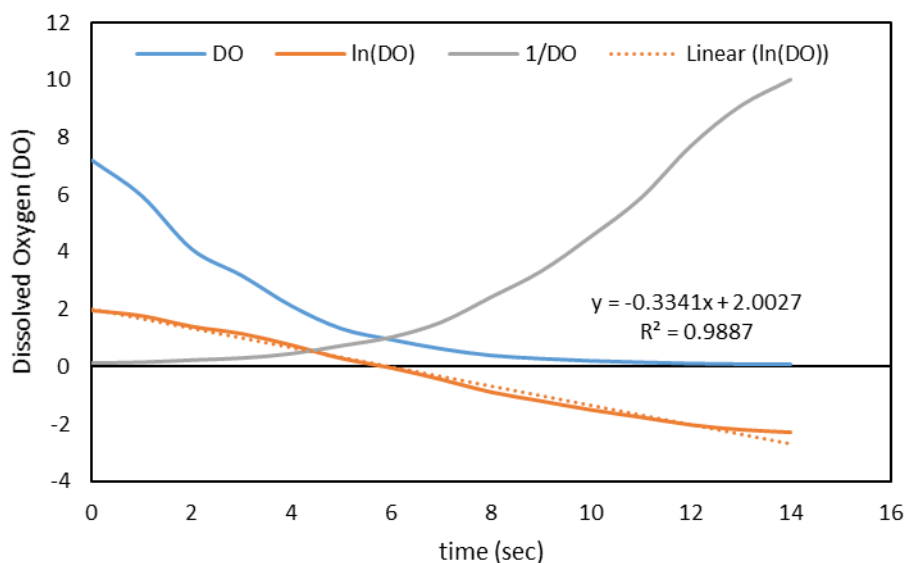


Figure 6. 0 mg/L Raz distilled water solution with 20 ml of 0.1 M sodium sulfite added to solution. Dissolved Oxygen (DO) was recorded every second. Only trendline and r-squared for first order kinetics shown.

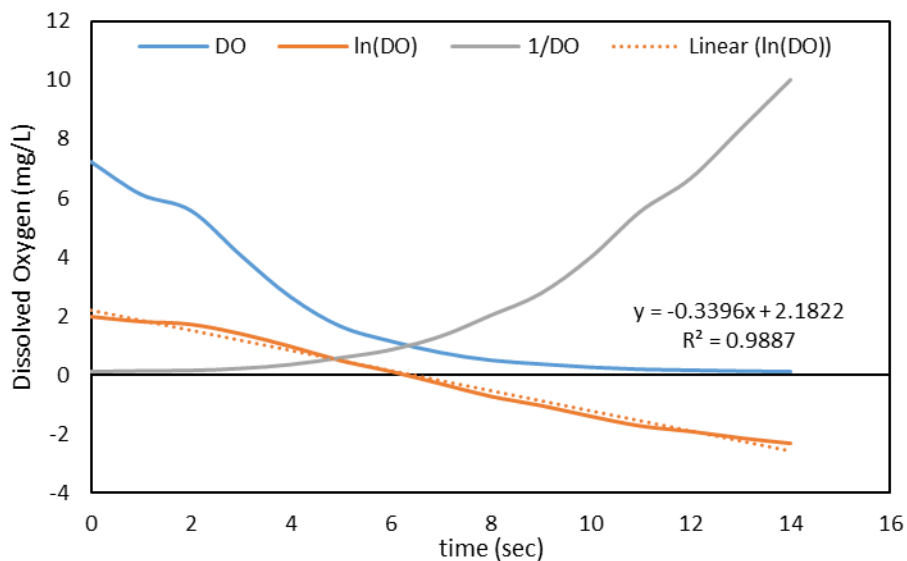


Figure 7. 5 mg/L Raz distilled water solution with 20 ml of 0.1 M sodium sulfite added to solution. Dissolved Oxygen (DO) was recorded every second. Only trendline and r-squared for first order kinetics shown.

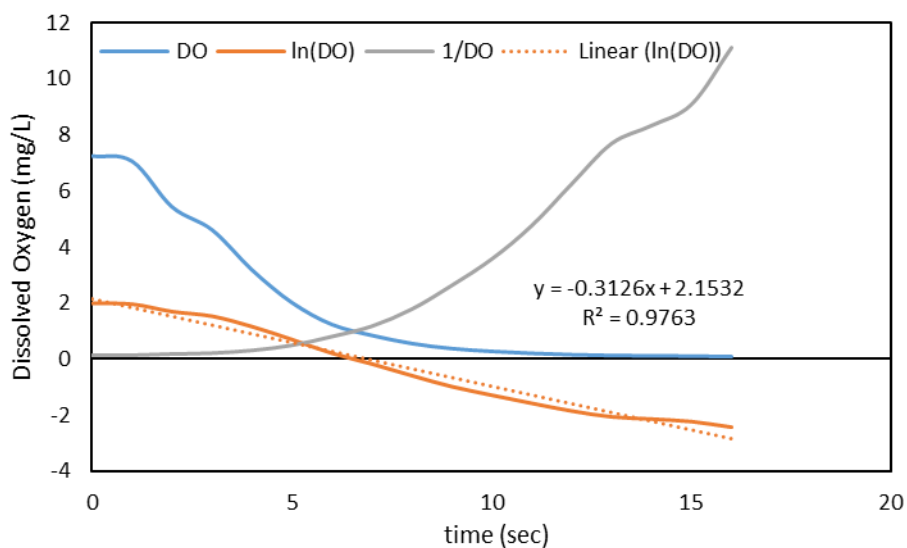


Figure 8. 0 mg/L Raz distilled water solution with 10 ml of 0.1 M sodium sulfite added to solution. Dissolved Oxygen (DO) was recorded every second. Only trendline and r-squared for first order kinetics shown.

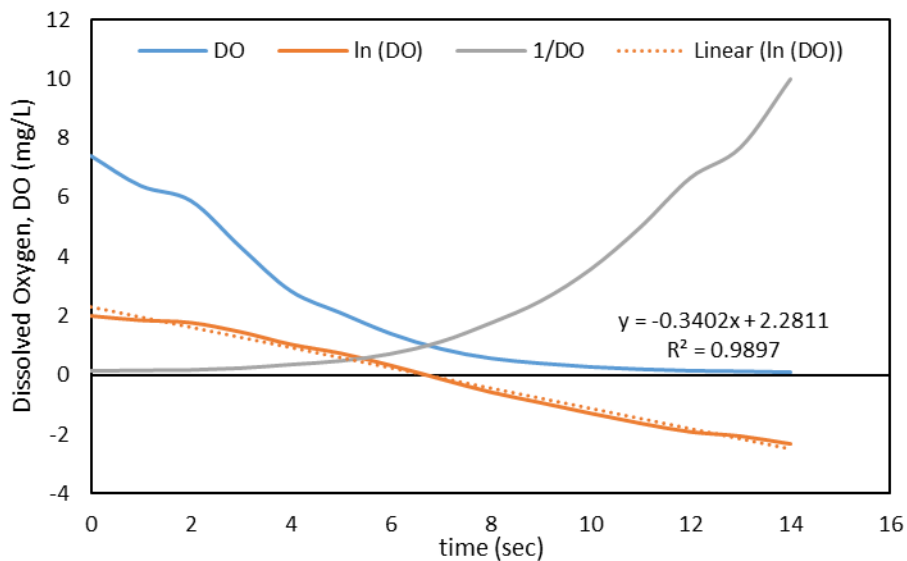


Figure 9. 5 mg/L Raz distilled water solution with 10 ml of 0.1 M sodium sulfite added to solution. Dissolved Oxygen (DO) was recorded every second. Only trendline and r-squared for first order kinetics shown.

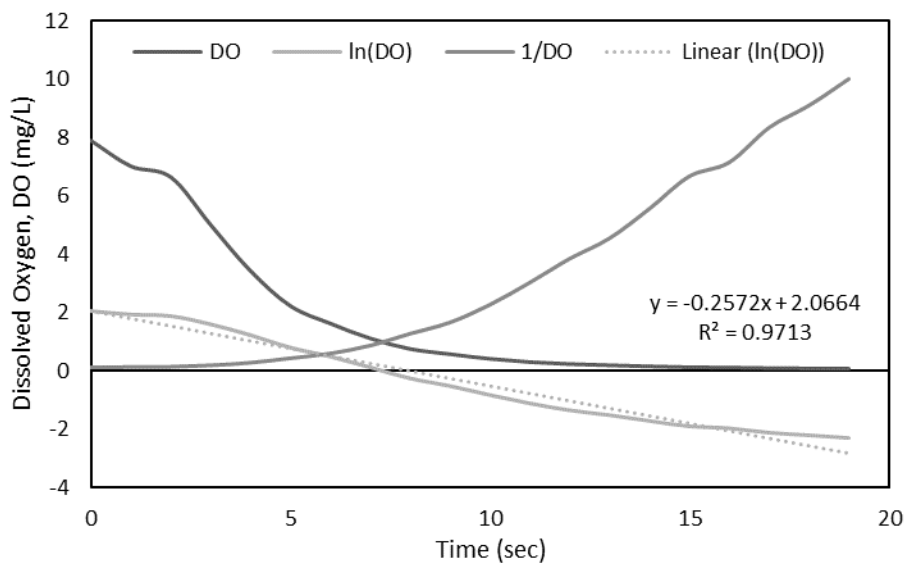


Figure 10. 5 mg/L Raz distilled water solution with 50 ml of 0.1 M sodium sulfite added to solution. Dissolved Oxygen (DO) was recorded every second. Only trendline and r-squared for first order kinetics shown.

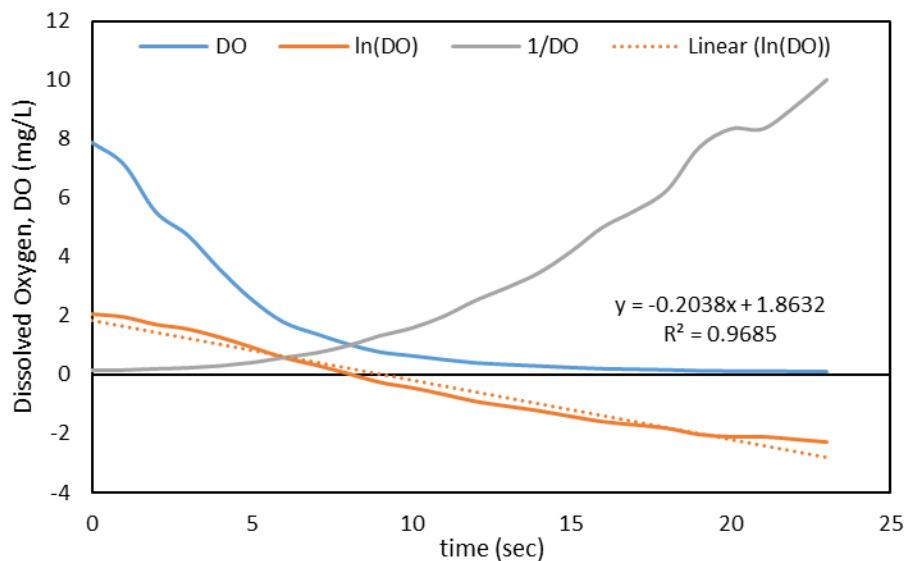


Figure 11. 5 mg/L Raz distilled water solution with 50 ml of 0.1 M sodium sulfite added to solution. Dissolved Oxygen (DO) was recorded every second. Only trendline and r-squared for first order kinetics shown.

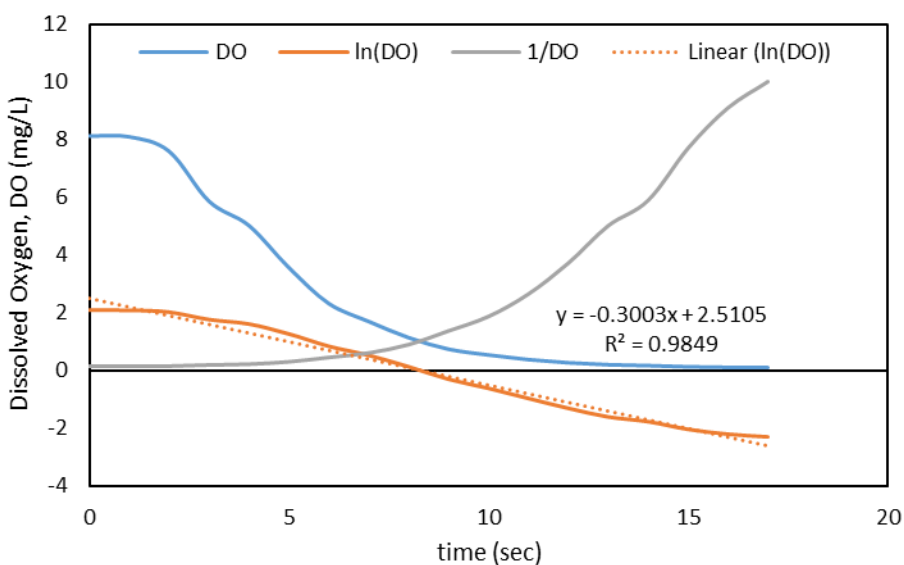


Figure 12. 5 mg/L Raz tap water solution with 30 ml of 0.1 M sodium sulfite added to solution. Dissolved Oxygen (DO) was recorded every second. Only trendline and r-squared for first order kinetics shown.

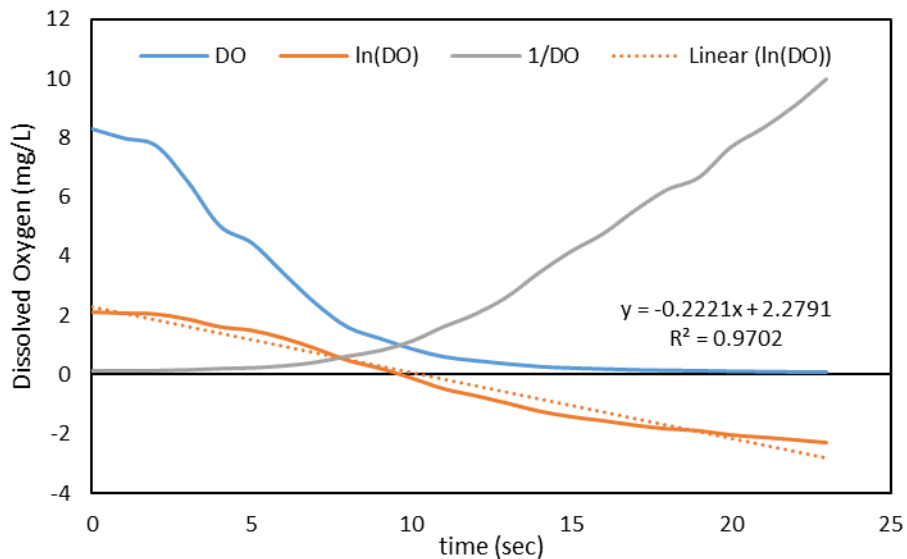


Figure 13. 5 mg/L Raz tap water solution with 30 ml of 0.1 M sodium sulfite added to solution. Dissolved Oxygen (DO) was recorded every second. Only trendline and r-squared for first order kinetics shown.

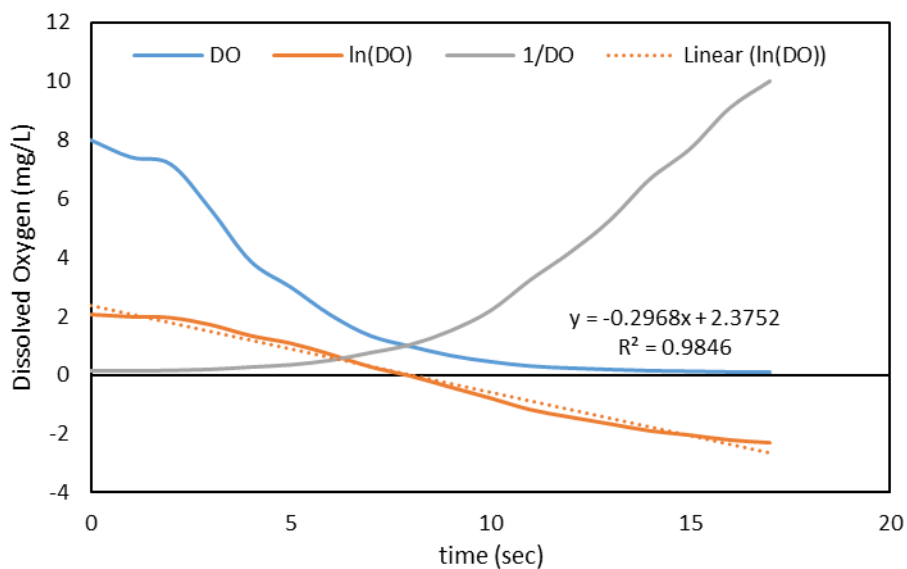


Figure 14. 5 mg/L Raz tap water solution with 20 ml of 0.1 M sodium sulfite added to solution. Dissolved Oxygen (DO) was recorded every second. Only trendline and r-squared for first order kinetics shown.

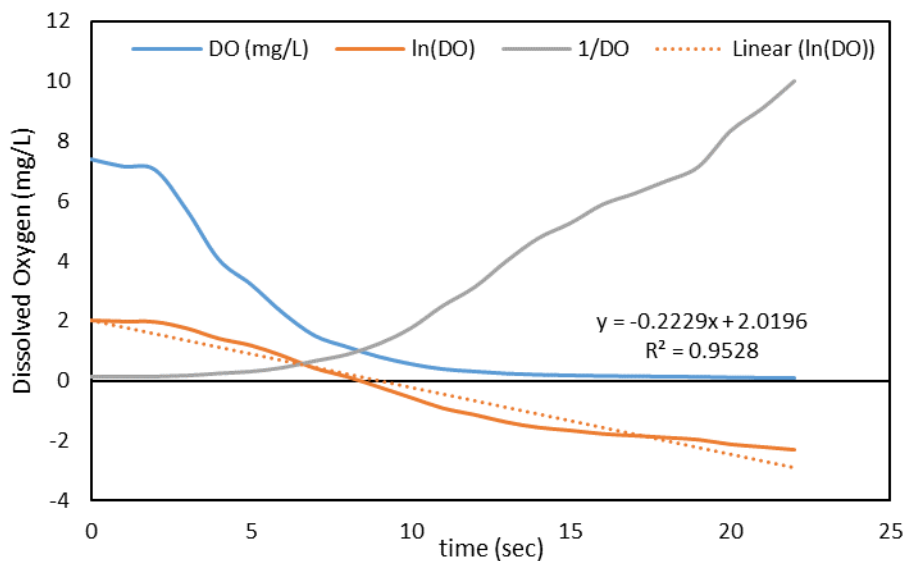


Figure 15. 5 mg/L Raz distilled water solution with 20 ml of 0.1 M sodium sulfite added to solution. Dissolved Oxygen (DO) was recorded every second. Only trendline and r-squared for first order kinetics shown.

Table 3. Summary of Raz kinetic results using 0.1 M Sodium Sulfite (Na_2SO_3). The rates coefficient seen are for the zero-order reaction.

Water Type	Raz Concentration [mg/L]	0.1 M Sodium Sulfite and 0.001 M Cobalt Chloride added [mL]	Rate Coefficient	R^2
DI	5	20	0.0523	0.977
DI	5	20	0.0194	0.993